Igneous layering in the syenites of Nunarssuit and West Kûngnât, South Greenland

Mark Edward Hodson

Thesis submitted for the degree of
Doctor of Philosophy
University of Edinburgh
1994

Declaration

I certify that the work presented in this thesis is my own, except where otherwise stated, and has not been previously submitted as a degree at this or any other university.

Mark Edward Hodson

Abstract

The genesis of the rhythmically layered syenites of Nunarssuit and West Kûngnât is considered, together with the post-crystallisation modification that the layers have undergone.

Field work was carried out to observe the layering phenomena exhibited by the two syenitic bodies. In both cases the layering developed close to the edge of the intrusion. The rhythmic layers are c.20cm thick and have a thin, c.3cm, melanocratic base. Over a short distance this grades into leucocratic syenite which has the same modal composition as homogeneous syenite above and below the layered series. Cumulus phases are pyroxene, olivine, feldspar, apatite and opaque oxides and sulphides. The occurrence of the Nunarssuit layered syenite is cyclic. In each cycle the bases of layers become more melanocratic up section. Each cycle is capped by a thick melanocratic layer. Two fully developed cycles are present. A third cycle starts to develop but then layering fades and the syenite becomes essentially homogeneous. Troughs, rich in mafic phases, and unconformities between layers are present in both layered series. Slumps and slump breccias are present in Nunarssuit.

Samples from across individual layers, groups of adjacent layers, distantly spaced layers, slump structures and breccias were collected. Electron probe, synchrotron XRF-microprobe and XRF whole-rock analysis were used to determine mineral and rock chemistry. $\delta^{18}O$ values were determined for feldspars from Nunarssuit samples. Grain size analysis, cathodoluminescence studies, and SEM and electron probe BSE image analysis were used for textural analysis. The composition of the magma from which the syenites crystallised was estimated and its physical and chemical properties determined.

The samples from the Nunarssuit layered syenite become more magnesian up section. In West Kûngnât the samples become more ferroan up section. In both intrusions samples from troughs are more magnesian than samples from adjacent syenite. Fluid dynamic calculations indicate that the crystallising magma convected turbulently. Crystals would have been kept in suspension in the body of the magma but may have settled in stagnant boundary layers along the bottom and sides of the chamber. Non-linear analysis indicates that the layer producing mechanism was chaotic. Textures and mineral chemistry were modified after crystallisation due to interaction with fluids. At high temperatures, below the solidus, small grains of

olivine and pyroxene were absorbed by larger grains of the same mineral species. At temperatures as low as c.450°C fluids reacted with the syenites and: 1) pyroxenes were partially altered to amphiboles and pyroxene rims were enriched in the acmite component, 2) olivines were altered to biotites, 3) feldspars exsolved and, 4) apatites and zircons lost some, or all, of their original zoning.

The layering could not have been generated by either crystal settling or *in situ* processes alone. The grains at the bases of layers are not hydraulically equivalent. This, together with the fact that the layers have sharp bases and grade rapidly into more leucocratic syenite, has been taken as evidence that the layers were generated by the periodic inhibition of feldspar nucleation. This may have happened either *in situ* or in the boundary layers. Several possible mechanisms can explain the inhibition of feldspar nucleation and it has not proved possible to choose between them. Convection currents scouring the crystal pile and earth movements disturbing the chamber floor generated the unconformities seen. Troughs were generated by crystal-melt slurries originating through the collapse of side-wall cumulates or the collapse of piles of crystals which accumulated up-slope under side-wall boundary layers. Side-wall collapse generated the breccias and slumps. It is not known why the modal contrast involved in the layers in Nunarssuit became greater up-section. The cyclicity of the layering in Nunarssuit was generated by magma chamber replenishment, possibly linked to volcanic eruption.

Acknowledgements

I would like to thank my supervisors, Ian Parsons and Brian Upton, for proposing this project, for showing me around Nunarssuit and Kûngnât and for putting up with me for three years. They have both been remarkably tolerant of my foibles and have done sterling service in teaching me how to be a scientist and write almost proper English. Adrian Finch deserves much credit for talking to me when I was an undergraduate and suggesting that I apply for this project rather than Godfrey's (sorry Godfrey). His help in the field was much appreciated as was his encouragement afterwards.

Peter Hill and Stuart Kearns, of the electron microprobe unit, have been responsible for helping with the production of most of the mineral data in this thesis. As a result of their proddings, cajolings and sarcasm I analysed a lot of (too many?) minerals for a lot of elements. Dodie James and Godfrey Fitton fulfilled a similar role in the case of XRF, they showed much patience with my uncanny XRF abilities. Dodie is particularly thanked for taking pity on me and fusing some discs after my third successive failure to get decent totals! The mystery of the cloudy discs remains but thankfully I have not got to do any more. Joe Smith helped arrange my trip to use the synchrotron XRF-microprobe at Brookhaven. Whilst I was there Mark Rivers ensured that I had sufficient beamtime and had good books to read in between times. Barry Dawson helped to prepare me mentally for the Brookhaven experience but the reality was even worse, particularly the snow storms. Mike Hall and Jane Foster supplied me with more thin sections than I've had hot dinners. Yvonne Cooper and Diane Batty taught me how to print and develop photos, Yvonne even taught me more sophisticated techniques such as "burning". Shane Voss and Ian Chisholm were witty and helped with computing difficulties. Tony Fallick at SURRC volunteered to do my oxygen isotope analyses and John Findlay helped with the SEM.

Ian and Brian did the bulk of the proof reading but the back up team of Ian Snape, Pauline Thompson and Barbara Page also shared the load. Thanks go particularly to Barbara who did the boring chapters (which ones are those?) and told me how to use semi-colons.

Money was mainly supplied by NERC, they coffed up for various conferences and the unexpected trip to the States. Financial thanks are also owed to Queens' College, Oxford who paid for me to go to Ardnamurchan where I saw my first "live" igneous

layer and The Mineralogical Society of Britain for a bursary which allowed me to go to Rum. One day I'll go back in the sunshine!

On my travels I've discussed igneous layering with many a wise old bird: Ian Parsons, Brian Upton, Bob Hunter, Claude Jaupart, Steve Sparks, Alex McBirney, Dick Naslund, Grant Cawthorn and Bill Brown. At Edinburgh Roy Gill and Nick Odling were always keen to know what I was up to.

Finally I'd like to thank my office mates for their companionship: Chris Salt for being a kindred spirit, Babs Page for finding us amusing and Jon Wilson for being too perplexed to protest (most of the time). Peripheral to us were Harriet Randle who, after two years, emerged (burst?) from the XP labs, Pauline Thompson who wandered around with not many clothes on throughout the winter months and Sally Brown who seems to have been in Greece longer than she's been in the office.

Contents.

Descriptive work

Interpretive work

Hypotheses

Appendices

Foldout of Figs. 2.2 and 2.5 inside back cover

Chapter 1: Introduction

1.1: Igneous layering

Igneous layering is a relatively common phenomenon in large basic intrusions whilst it occurs more rarely in syenitic and granitic intrusions. The layering may be defined by any one, or a combination of the following: modal variation of phases, variation in grain size, variation in mineral chemistry or by textural changes within an igneous rock. The study of igneous layering helps to promote the understanding of processes which occur as magma chambers crystallise.

Much of the early work on igneous layering was carried out by Wager and his co-workers (notably Deer and Brown) on the Tertiary layered intrusion of Skaergård[1] on the East Greenland coast. Wager and his colleagues (Wager and Brown, 1968) came to the conclusion that the majority of rhythmic igneous layering was generated by crystal laden plumes which descended down through the magma chamber from the roof zone and spread out on the chamber floor. "Normal" rock between the rhythms was generated by crystals settling from the main body of the magma. It was acknowledged that certain layering phenomena such as vertical layering must have formed by another mechanism. In the 1970s the common wisdom that rhythmic layering formed by crystal settling was called into question. Notable papers published at this time advocating a chemically controlled *in situ* mechanism for the generation of igneous layering were those by Campbell (1978) and McBirney and Noyes (1979). Some workers remained convinced that crystal settling occurred (e.g. Cox and Mitchell, 1988, Martin and Nokes, 1989). Theories for the subsolidus generation or modification of igneous layering have been developed (Hunter, 1987, McBirney, 1987, Petersen, 1987, Bédard *et al.*, 1988,). The majority of these models have been developed to explain, or tested on, basic intrusions.

1.2: Regional geology

1.2.1: Introduction

The Gardar province contains a collection of alkaline intrusions of Proterozoic age in the south of Greenland (Fig. 1.1). Early work was carried out by a number of workers (e.g. Giesecke, 1910, Steenstrup, 1881, Flink, 1898 and Ussing, 1912) but Wegmann

[1]In 1974 the Danish Geodetic Institute changed the official spelling of Skaergaard to Skaergård

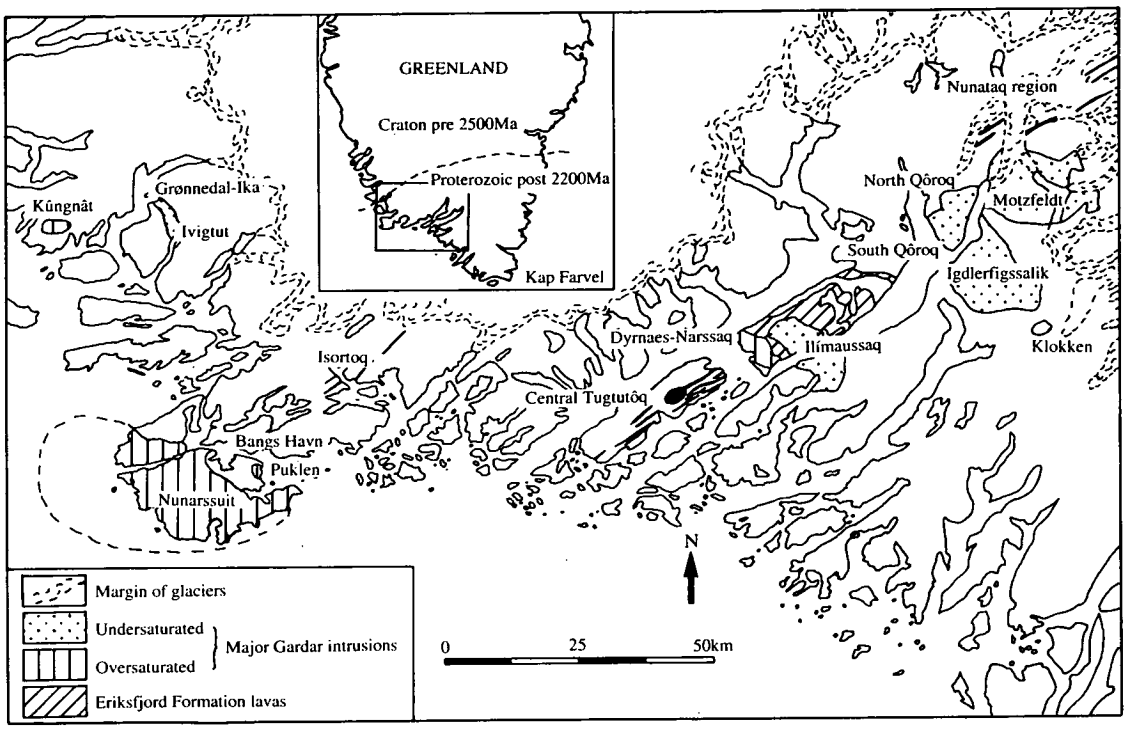

Fig. 1.1: Simplified geological map of south Greenland showing Gardar intrusions (from Emeleus and Upton, 1976).

(1938) carried out the first comprehensive study of the area and coined the term "Gardar Province". The area has been extensively mapped by the Geological Survey of Greenland (GGU), starting in the 1950s. It was at this time that the first work on Nunarssuit (Harry and Pulvertaft, 1963) and Kûngnât (Upton, 1960) was carried out. Reviews of the regional geology have been published by Upton, (1974), Emeleus and Upton, (1976) and Upton and Emeleus, (1987). Ferguson and Pulvertaft (1963), and more recently Upton, Parsons, Emeleus and Hodson (in prep.), reviewed the variety of layering phenomena observed in the province. Since 1963 the Nunarssuit intrusion has been studied by Anderson (1974), Butterfield (1980) and Parsons and Butterfield (1981), and the Kûngnât intrusion by McDowell and Wyllie (1971), Upton, Thomas and Macdonald (1972), Stephenson and Upton (1982). The nature of the subsolidus fluids associated with the Gardar intrusions were studied by Finch (1990).

The principle magmatic activity in the Gardar province is believed to have occurred in three phases at around 1300Ma, 1250 Ma and 1160 Ma respectively. (Blaxland *et al.*, 1978). The Kûngnât pluton was intruded 1245 +/- 17Ma (Emeleus and Upton, 1976) and the Nunarssuit syenite was intruded 1154 +/- 14Ma (Blaxland *et al.*, 1978).

1.2.2: Nunarssuit

The Nunarssuit complex is partially covered by the Davis Strait (Fig. 1.2) and measures at least 45km by 25km.

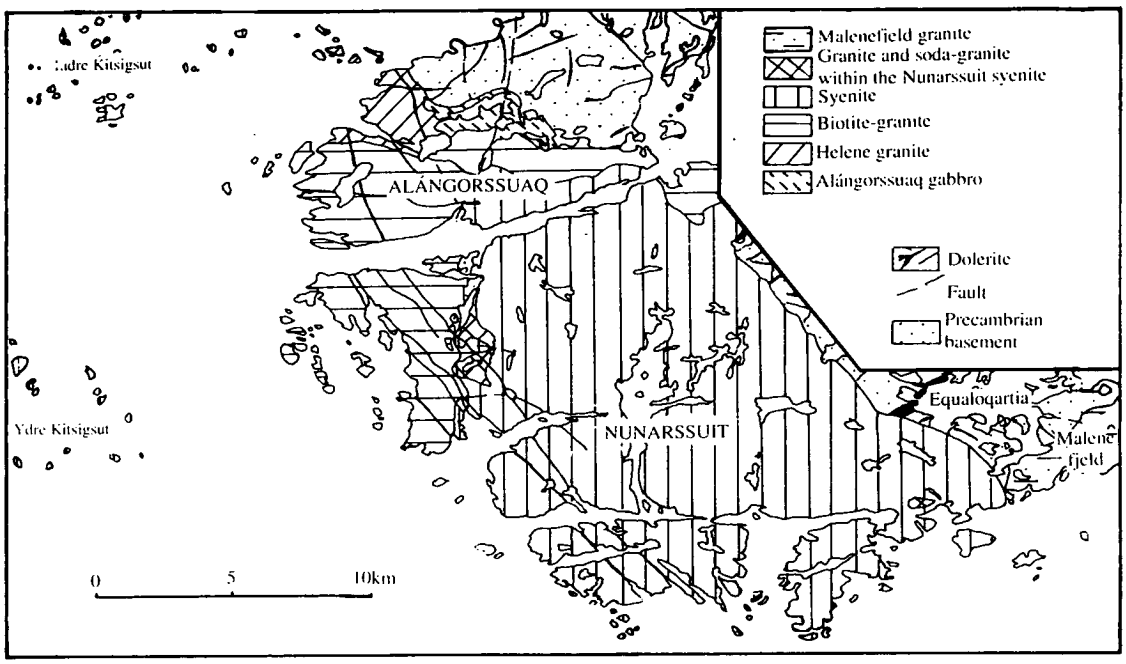

Fig. 1.2: Geological map of the Nunarssuit complex (from Emeleus and Upton, 1976).

It consists of the Alángorssuaq gabbro, Kitsigut syenite, main granites, Nunarssuit syenites and late granites (Harry and Pulvertaft 1963). Greenwood (Fig. 1.3, pers comm.) demonstrated that the 24km by 13km body of the Nunarssuit syenite consists of five arcuate bodies of syenite. Of these it is only the outermost mainland body that exhibits any notable layering. Individual layers typically consist of a sharply defined, melanocratic base rich in pyroxene, olivine and opaque oxides and sulphides which grades, over a few centimetres, into a more feldspathic layer. The thickness of individual layers varies but is typically in the order of a few tens of centimetres.

1.2.3: Kûngnât

The Kûngnât pluton (Fig. 1.4) measures about 5km by 2.5km. It consists of a marginal syenite unit, 2 intersecting syenite stocks and a narrow, nearly complete, ring dyke of troctolite and syenogabbro. The western stock comprises the Western Syenite Lower Layered Series (WLLS) and the Western Syenite Upper Layered Series (WULS). Together, these two series consist of up to 1800m of layered syenite which dips in from the intrusion margin towards a focus occupied by the eastern syenite intrusion.

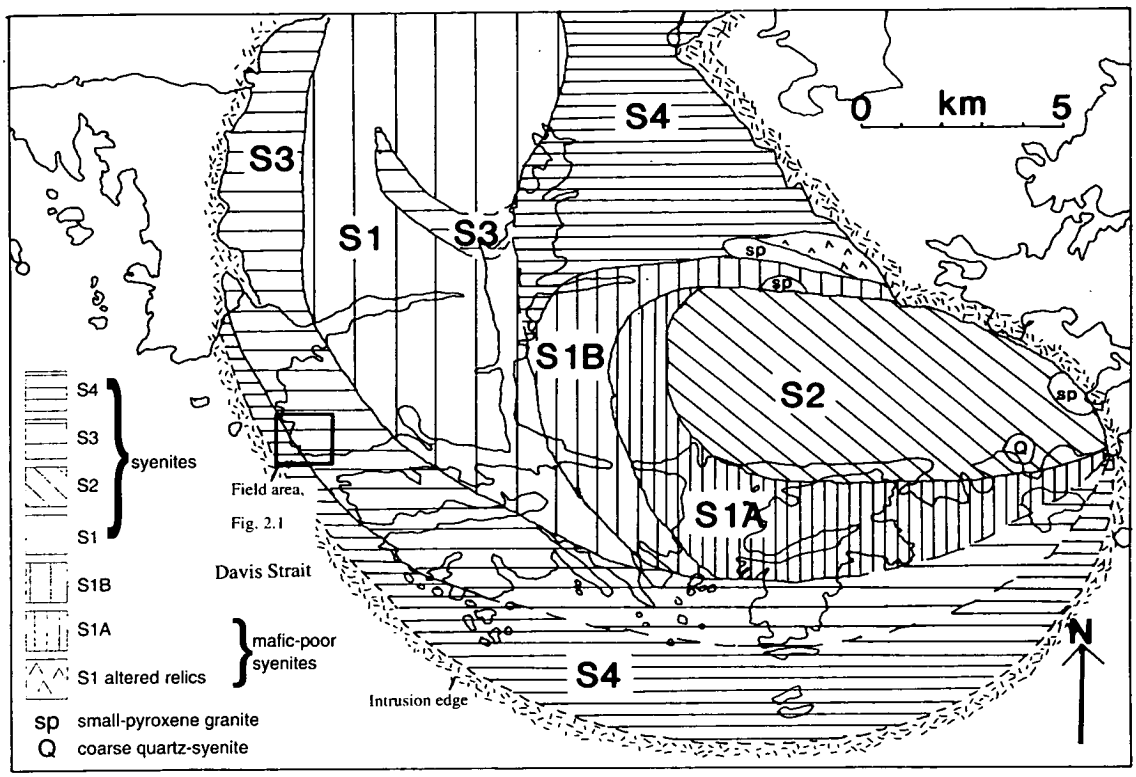

Fig. 1.3: Map of the Nunarssuit syenite showing the five zones defined by pyroxene chemistry. Field area marked by square (map supplied by P Greenwood).

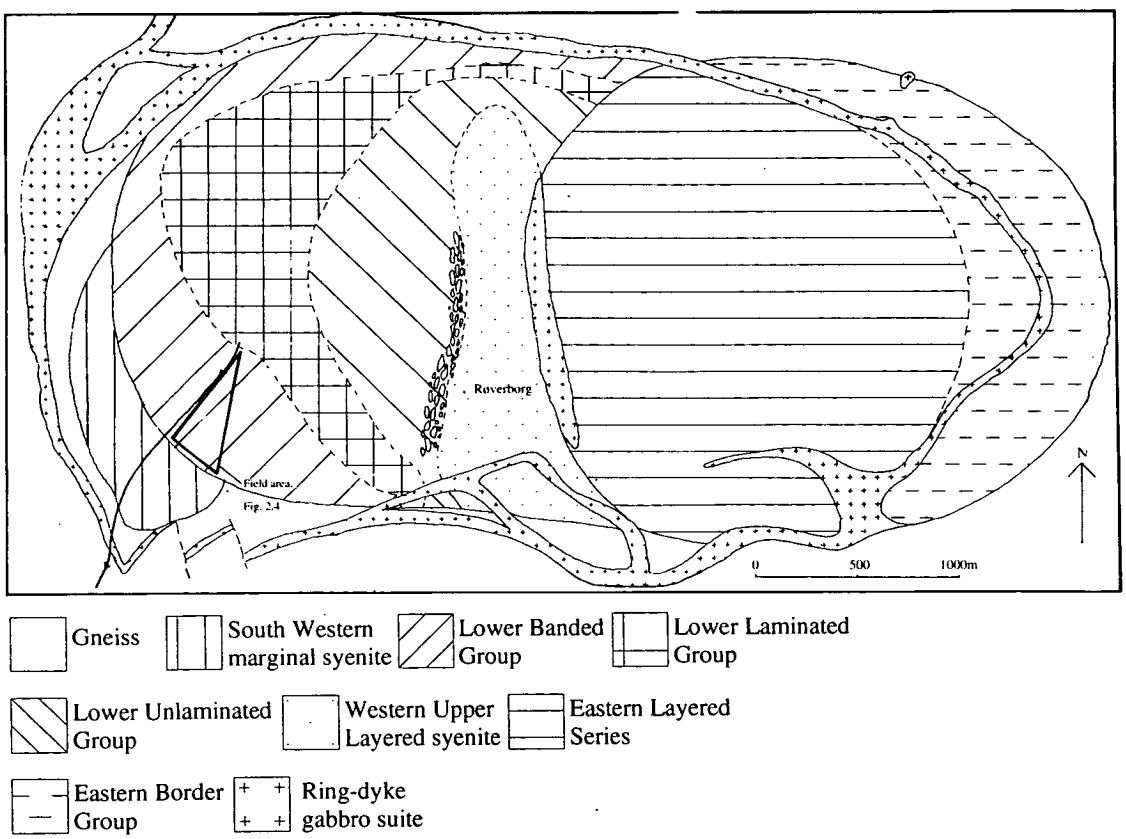

Fig. 1.4: Geological map of the Kûngnât pluton (from Upton, 1960).

The WLLS is separated into three sub-units: the lower banded group; the lower laminated group and the unlaminated group. The lower banded group is between 300 and 400m thick. Individual layers typically consist of a sharply defined base rich in olivine, pyroxene and opaque oxides which grades, over a few centimetres, into a more feldspathic layer. The thickness of individual layers varies but is typically in the order of a few tens of centimetres. The lamination of the lower laminated group is due to alignment of tabular feldspar crystals. The degree of lamination decreases up section. The syenites of the lower unlaminated group are homogeneous. The Upper Layered Syenite Series (WULS) overlies the WLLS unlaminated group. The base of the WULS is layered and is well exposed on the inaccessible south face of the Røverberg. Layering in this unit fades upwards until the highest syenites exposed on the Røverberg face are almost homogeneous.

1.3: Aims of the project

The aim of the project was, primarily, to examine the layering of the Nunarssuit and West Kûngnât syenites in the light of recent developments in theories to explain igneous layering. It was felt that a good test of recent hypotheses would be to apply them to evolved rocks and to see if they were still feasible. These two intrusions were chosen because of their good exposure and ready access. The layering of the intrusions had not been specifically investigated. Also since the leucocratic layers of the two intrusions were known to be more altered than the melanocratic layers, an explanation of this observation was sought. Recently attention has been focused on the subsolidus changes that can affect igneous rocks (Hunter, 1987; Finch, 1990) and the layered syenites were examined with a view to identifying what subsolidus modification could be detected.

1.4: Outline of thesis

The first section is descriptive. Field work was carried out in both Nunarssuit and West Kûngnât and the results are detailed in Chapter 2. The petrography of the syenites is described in Chapter 3. The major element chemistry of the minerals present in the two plutons is described in Chapter 4 and the chemistry of leucocratic and melanocratic samples is compared. In Chapter 5 trace element data for individual phases and whole-rock chemical data are presented. The next section contains interpretive work. In Chapter 6 the degree of subsolidus modification which the syenites from the two plutons have undergone is assessed. Chapter 7 deals with the

physical conditions in the magma chambers as the syenites crystallised. In Chapter 8 non-linear statistical methods are used to analyse the spacing of rhythmic layers from both plutons. The final section of the thesis deals with hypotheses of igneous layering. In Chapter 9 previous hypotheses for the generation of igneous layering are reviewed whilst in Chapter 10 hypotheses to explain the origin of the layering seen in the Nunarssuit and West Kûngnât syenites are presented.

Part 1

Descriptive work

Chapter 2 : Fieldwork

2.1: Nunarssuit

2.1.1: Introduction

Field work was carried out in an approximately $2km^2$ area north of the fjord Tasiussaq (Fig. 1.3 and Fig. 2.1). To the south and west the area is bounded by the sea. To the north there is a river valley with high, south-facing, crags to the north of it; layering can be seen in these cliffs. Traversing to the east the layering is less and less well defined. A west-east traverse was carried out working up through the entire modally layered succession. Detailed sampling was carried out along this traverse, with minor sampling being carried out to either side (Fig. 2.1 and 2.2. N.B. Fig. 2.2 is reproduced as a fold out at back of thesis). Appendix A lists sample numbers.

The petrography of the syenites is detailed in Chapter 3. Alkali feldspar is the dominant species. At the base of individual graded layers pyroxene is more abundant than the feldspar. In the thick melanocratic units (Units 5 and 8 in Figs. 2.1 and 2.2) pyroxene is the dominant phase with feldspar being present in lower concentrations than in the normal syenites. Olivine is more frequently seen than in the normal syenite. Often the feldspar is present as oikocrysts around smaller pyroxene crystals. Autoliths present in, and spatially close to, these melanocratic layers are also pyroxene- and olivine-rich.

The stratigraphic sequence has been separated into ten units shown diagramatically in Fig. 2.2, and summarised below. Each unit consists of a set of layers with a distinct character:

Unit 10: Upper layered syenite (layers faintly visible and irregularly spaced)
Unit 9: Upper layered syenite (layers faintly visible and fairly regularly spaced)
Unit 8: Middle melanocratic unit
Unit 7: Middle layered syenite (layers clearly visible and fairly regularly spaced)
Unit 6: Middle layered syenite (layers faintly visible and fairly regularly spaced)
Unit 5: Lower melanocratic unit
Unit 4: Transition unit
Unit 3: Lower layered syenite (layers clearly visible and fairly regularly spaced)
Unit 2: Lower layered syenite (layers faintly visible and irregularly spaced)
Unit 1: Homogeneous syenite

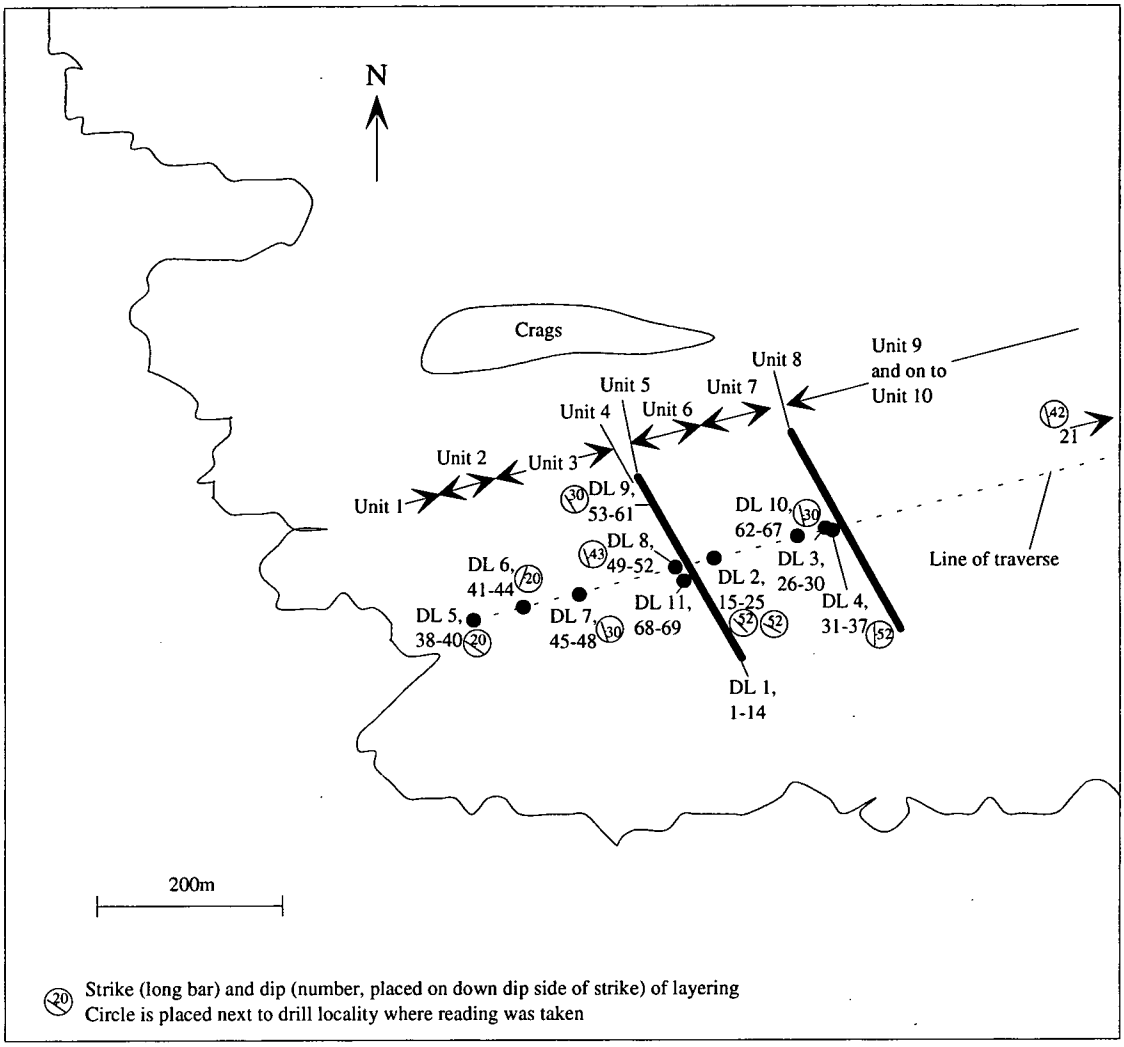

Fig. 2.1: Sketch map of field area showing drill localities (DL)

Overleaf and as a foldout at back of thesis

Fig. 2.2: Diagrammatic sketch section through the layered sequence of Nunarssuit. Shading represents increase in colour index of the bases of individual rhythms up section. DL indicates a drill locality. N.B. drawing is not to scale. Unit 1 = homogeneous syenite, Unit 2 = lower layered syenite (layers faintly visible and irregularly spaced), Unit 3 = lower layered syenite (layers clearly visible and fairly regularly spaced); Unit 4 = transition unit; Unit 5 = lower melanocratic unit; Unit 6 = middle layered syenite (layers faintly visible and fairly regularly spaced); Unit 7 = middle layered syenite (layers clearly visible and fairly regularly spaced); Unit 8 = middle melanocratic unit; Unit 9 = upper layered syenite (layers faintly visible and fairly regularly spaced); Unit 10 = Upper layered syenite (layers faintly visible and irregularly spaced).

Fig. 2.5: Diagrammatic sketch section through the lower layered series of West Kûngnât. DL indicates drill locality. Question mark above DL 12 indicates lack of certainty over stratigraphic relations between trough stacks and the rest of the stratigraphy. N.B. drawing is not to scale. Unit 1 = unlayered xenolith-rich syenite; Unit 2 = two series of trough stacks; Unit 3 = poorly layered syenite; Unit 4 = normally graded rhythmically layered syenite; Unit 5 = laminated syenite.

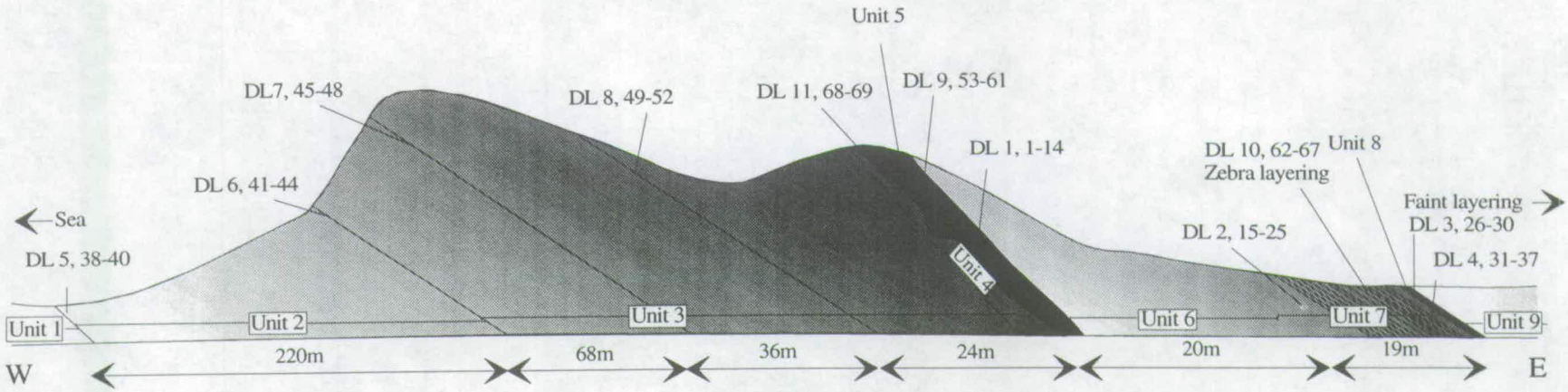

Figure 2.2

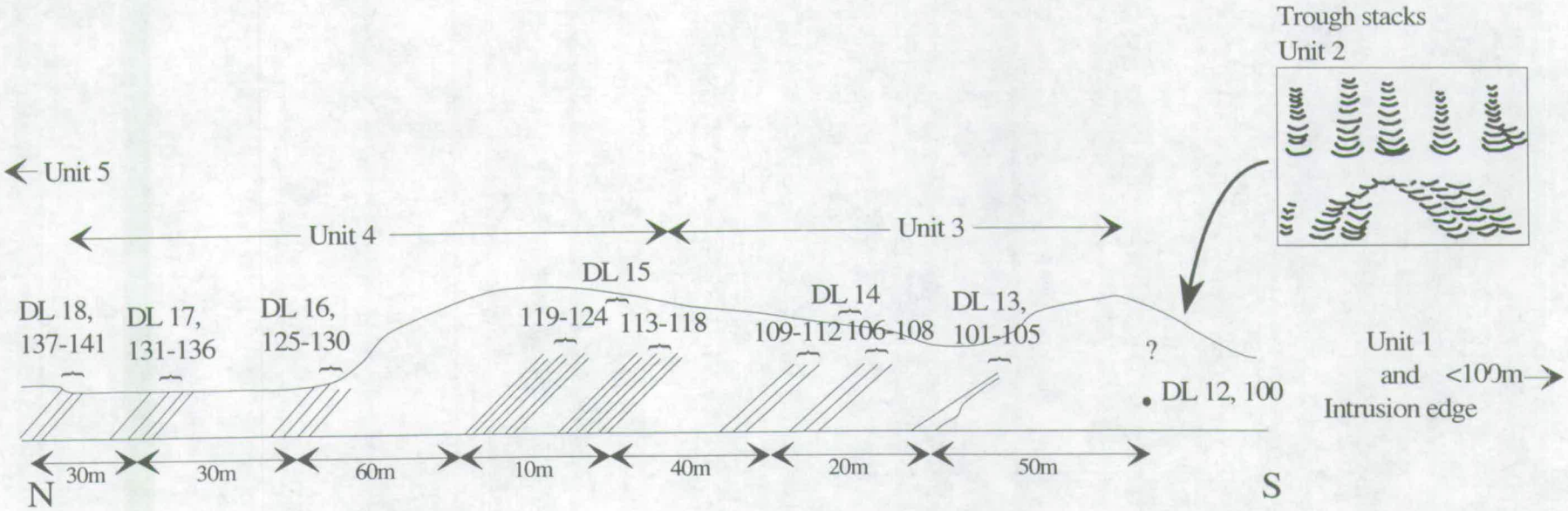

Figure 2.5

Units 9 and 10 (Figs. 2.1 and 2.2) probably include Harry and Pulvertaft's (1963) middle and upper layered zones. Certainly from their fig. 28 (present Fig. 2.3) this would seem to be the case, particularly since a xenolith horizon was found in Unit 10.

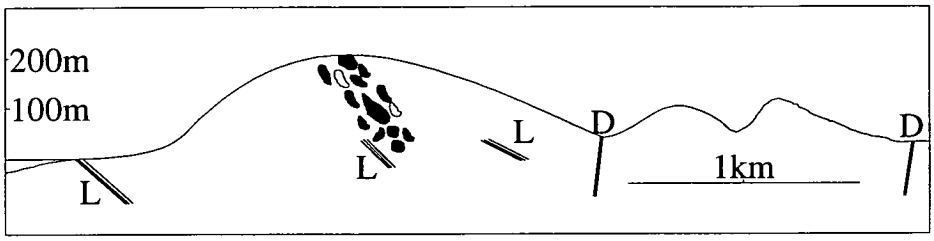

Fig. 2.3: Sketch cross section through the Nunarssuit syenite showing three layering horizons (L) two major dykes (D) and a xenolith horizon (from Harry and Pulvertaft 1963).

2.1.2: General observations

Rhythmic layering is present from the south coast to the south-facing crags labelled in Fig. 2.1. It was also observed on the coastal exposures seen during the boat trip to the field area approaching from the north. This makes the lateral extent of the layered series at least 15km from the south to the north. All the layers measured in the layered zone of SW Nunarssuit dip at about 30° to the east with a strike of between 340° and 360°. Harry and Pulvertaft (1963) carried out more extensive dip measurements over the whole of the Nunarssuit syenite and showed that the strike of the layering swings round to define an arc about a point in central Nunarssuit. This, together with the similarity of the layering to that seen in the West Kûngnât syenite, led Parsons and Butterfield (1981) to suggest that the dip of the layering was primary. The thickness of the individual layers varies between 5 and 80cm. On average the thickness of individual layers is about 20cm although this varies along strike. The normally-graded layers have a well-defined melanocratic base and grade up into normal syenite over a distance of a couple of centimetres. The stratigraphic thickness of the obviously layered zone, from the onset of regular rhythmic layering to the top of the second thick melanocratic unit (Unit 8 in Fig. 2.1), is approximately 86m. Below this there is a thickness of about 110m exhibiting faintly visible, irregularly spaced layering. Faintly visible, fairly regularly spaced, modal layering is also present above Unit 8. Gradually this faintly visible modal layering becomes irregularly spaced. The faintly visible layering above Unit 8 may be equivalent to the middle and upper layered zones as described by Harry and Pulvertaft (1963).

Various structures comparable to those in sedimentary rocks were observed; truncations (Plate 2.1a) of layers, or sets of layers, by the lowest member of the over-

lying series of layers generating low-angle cross bedding as is seen in fluvial deposits (Tucker, 1981); and trough structures are present. Near to the trough structures lenticular concentrations of mafic minerals can often be observed; it is thought that these are poorly preserved or poorly formed troughs. Slump structures (Plate 2.3a and b) and breccias (Plate 2.1c and d) are common near to the channels and troughs. These are best seen in and around the two thick melanocratic units. The breccias usually contain black, ultramafic clasts. It is thought that these clasts are fragments of disrupted melanocratic layers and they will be referred to as autoliths. No size sorting of mineral grains is seen. Grains are of a uniform size in the layered series although the autoliths are often finer grained than the surrounding syenite.

No mineral alignment or lamination was seen in the layered zone except in the two exceptionally thick melanocratic units. This planar fabric is usually poorly developed but, around autoliths and slumps, it is more pronounced. For example Plate 2.2a and c show what was referred to as a "comet structure" in the field. This consisted of a circular slumped region of more melanocratic material with a "tail" of syenite containing aligned feldspar and pyroxene behind it. The autoliths contain aligned pyroxene grains. This alignment is not concordant with the general layering. Layering always becomes more pronounced as the two melanocratic units are approached from below. Directly above these units the intensity of the layering drops to a minimum.

2.1.3: The detailed stratigraphy of the layered zone of SW Nunarssuit

The detailed stratigraphy of the layered zone of SW Nunarssuit is now described, starting from below, working upwards. All thicknesses are stratigraphic thickness unless otherwise stated. Drill locality positions are shown in Fig. 2.1.

Unit 1 - Homogeneous syenite

Homogeneous syenite is present from the west coast to drill locality 5 where the first layer was observed. Extrapolating from the map of Greenwood (Fig. 1.3) the thickness of the unit is c.500m.

Unit 2 - Lower layered syenite (layers faintly visible and irregularly spaced)

This unit is about 110m thick and starts where the first layer was observed. This first layer is planar, normally-graded showing grading over about 8cm from a relatively melanocratic base (with a colour index of c.25%) to syenite with the same colour

index as the unlayered syenite below (a colour index of c. 15%). The syenite directly above this layer appears to be homogeneous. About 30m further up the section a layered autolith was observed (Plate 2.1b). The autolith occurs in a patch of otherwise homogeneous syenite. It is about 1m wide and 2m long at outcrop. 2cm thick, randomly spaced, melanocratic layers, separated by normal syenite, run perpendicular to the strike of the layering seen elsewhere. The east edge of the autolith is obscured by gravel. The west and south edges are rimmed by a 0.5cm band of melanocratic material and a 20cm thick pegmatitic band outside the melanocratic rim. This autolith is inferred to have been derived from either the roof or the wall of the chamber.

Up section, faint layers, much the same as the first, occur at irregular intervals. The periodicity of layers becomes more regular up section. The colour index of the bases of rhythmic layers becomes higher up section, i.e. bases become more mafic and thus more visible. Several irregular, non-planar, melanocratic syenite layers are also present. These contain feldspars which are oikocrystic around pyroxenes. The end of the faintly layered syenite unit and the start of the more intensely layered syenite unit is placed arbitrarily at the location of drill locality 6. This is approximately 110m stratigraphically above drill locality 5. By this stage in the succession the layers occur at fairly regularly spaced intervals, 20cm on average.

Unit 3 - Lower layered syenite (layers clearly visible and fairly regularly spaced)

This unit is about 60m thick and consists of a series of graded layers (Plate 2.2b) which are between 5cm and 80cm thick. The average spacing of layers is about 20cm. Individual layers consist of a melanocratic band with a sharp base which grades upwards into normal syenite over 5cm at the most. Within this unit large-scale troughs occur which are thought to be genetically related to the over-lying lower melanocratic unit. The troughs contain melanocratic syenite that shows normal grading, are up to several metres wide and 70cm deep, and occur in approximately aligned vertical stacks which are continuous for stratigraphic distances greater than 30m. The tops of the stacks merge into the lower melanocratic unit. Small-scale unconformities between layers are seen. Often individual layers die out over a distance of 100m along strike but their place is taken up after a short break by another layer at a similar stratigraphic level. In places the replacing layer overlaps with the layer that dies out (Plate 2.2d). The top of Unit 3 is marked abruptly by a

slumped melanocratic layer, which is about 40cm thick and which defines the start of the transition unit between the clearly layered syenite and the first melanocratic unit.

Unit 4 - Transition unit

Within this unit various structures are seen. Patchy development of "inch-scale" or micro-rhythmic layering (Plate 2.4a) is seen developed on the SW face of a small crag about 20m north west of drill locality 11; this layering can be traced laterally for no more than 2m. Individual layers consist of a thin melanocratic base, about 1cm thick, which grades up into normal syenite within another centimetre; layers are approximately 3cm apart. Layering on nearby rock faces is of the type seen in the lower clearly layered unit.

Cross-cutting layers are seen at the top of Unit 4 (Plate 2.4b and c). A 4cm thick curved layer, that grades inwards with normal syenite present inside the arc, was observed; next to this curved layer are four relatively straight, 5cm thick, normally graded layers. The curved layer appears to cut across these straight layers without disrupting them.

Slumped and folded melanocratic layers, some of which are connected to the over-lying melanocratic layer are also present. An example of slumping is shown in Plate 2.3. Both troughs A and B have irregular erosive bases; rhythmic layering is seen stratigraphically below and above the troughs. It is thought that rhythmic layering was being produced when wall collapse occurred at the periphery of the magma chamber. Such collapses generated crystal-melt slurries which flowed into the centre of the magma chamber as slump and debris flows analogous to those which generate deep clastic sea deposits (Stow, 1986). A slurry-like stream formed trough B, then a second stream formed trough A, partially eroding the first trough. Melanocratic autoliths occur in the base of trough B

Within this unit autoliths on the scale of tens of centimetres are seen. These autoliths tend to be as melanocratic as the most melanocratic parts of the over-lying thick melanocratic unit but have a slightly finer grain size.

Unit 5 - Lower melanocratic unit

Due to outcrop geometry it is often hard to differentiate Units 4 and 5. They are probably genetically related. Many of the layers present in Unit 5 are markedly more melanocratic than the bases of the normally graded layers described previously. The

layers are of irregular thickness and spacing; most of the layers show normal grading. Feldspars sometimes occur as oikocrysts about pyroxene in the very melanocratic parts of the layers. The base of this unit is very irregular with folding and slumping along it (Plate 2.5a) and consequently the thickness of the unit varies between about 1m and 5m. Stacks of melanocratic troughs are developed both above and below the unit (Plate 2.5b and c), the bases or tops of which merge into the melanocratic unit. These stacks often penetrate down into the well-layered material to a height or depth of 30m although they appear not to disturb the layering. Unit 5 has a definite and sudden top where it is succeeded by another unit of faint layering.

Unit 6 - Middle layered syenite (layers faintly visible and fairly regularly spaced)

Unit 6 is about 10m thick and resembles Unit 2. Unit 6 is succeeded by a unit with more intense layering; the boundary between the two is rather arbitrary.

Unit 7 - Middle layered syenite (layers clearly visible and fairly regularly spaced)

This second unit of clearly layered syenite is about 10m thick. In places the normally graded layers consist of three separate sub-layers (Plate 2.6a): a melanocratic base that grades rapidly, over a thickness of about 1cm, into; normal syenite; and whiter syenite that contains feldspars that are whiter than those in the normal syenite. The whiter layer has positive relief. The spacing of the graded layers is up to about 20cm; the melanocratic base and leucocratic top are about 3cm thick with the normal syenite being about 9cm thick. In the field this layering was referred to as "zebra-layering" due to the marked colour contrasts between the melanocratic and leucocratic portions of individual layers. Over a stratigraphic height of 8m, approximately 15m below the top of Unit 7, the exact position of the base of each normally graded layer was recorded (Plate 2.6b). These data were used for non-linear dynamic analysis in Chapter 8. This unit has a definite top. The over-lying unit is another very melanocratic unit. Troughs of melanocratic syenite stacked on top of each other occur in Unit 7 without deforming the layers in any way. The tops of the trough stacks are obscured by Unit 8.

Unit 8 - Middle melanocratic unit

This unit is about 1m thick; like Unit 5 it contains many autoliths and slump structures. Again some feldspars are present as oikocrysts.

Unit 9 - Upper layered syenite (layers faintly visible and fairly regularly spaced)

Initially this faint layering is laterally and vertically continuous (Plate 2.6c). The layering gradually becomes less clearly visible over a thickness of several hundred metres until eventually the rocks appear wholly unlayered.

Unit 10 - Upper layered syenite (layers faintly visible and irregularly spaced)

Above the faintly layered unit the rock is largely homogeneous; layering occurs at irregular intervals in the stratigraphy. About 10m up into the homogeneous syenite there is a deformed melanocratic layer, about 15cm thick. Melanocratic autoliths and xenoliths of metabasite occur about 10cm below this. Both the melanocratic layer and the autoliths are fine grained with respect to the surrounding syenite. This xenolith layer is probably the southern continuation of the Mercurius Havn - Kap Desolation zone reported by Harry and Pulvertaft (1963). If this is the case then the underlying syenite described previously is probably equivalent to the middle layered zone of Harry and Pulvertaft (1963) and one of the irregular occurrences of layering is probably equivalent to their upper layered zone.

2.1.4: Interpretation of field observations

2.1.4.1: Sedimentary-style features

1) The **grading of the layers**, with dense minerals concentrated at the base of the layer, is consistent with them being derived by a gravity sorting process. This could either have been a sedimentation process affecting the whole magma chamber (Sparks *et al.*, 1993) or a more local process due to the action of currents on an unconsolidated crystal pile (Conrad and Naslund, 1989).

2) The **unconformities** seen (Plate 2.1a) could have been produced by erosion of the crystal pile by a convection current or a crystal-melt slurry and the deposition of another layer on the new floor.

3) **Troughs** could have been produced by erosion and deposition from a crystal-melt slurry.

4) Lateral **fading out of layers** would occur if the layers were produced by crystal-laden currents flowing along the magma chamber floor. Eventually these currents would die out, having deposited their load and the layer generated by the current would also die out.

5) **Slumps** (Plate 2.5a) may have been produced by the collapse of either side-walls or loosely consolidated piles of crystals, which accumulated up slope below boundary layers, resulting in crystal slurry mass flows.
6) **Slump breccias** (Plate 2.1c) may have been produced by side-wall collapse. Disruption of previously solid material is necessary to explain the brecciated material.
7) The **melanocratic units** could have been produced by wall collapse resulting in crystal slurry mass flows.

2.1.4.2: Non-sedimentary-style features

1) The **onset** and **sporadic occurrence up section of layering** indicates that some critical limit must be reached before layering can be produced. This critical limit is most likely to be of a physiocochemical nature.
2) The **grading of the layers** could be related to either inhibition of nucleation (Parsons and Becker, 1987) or relative ease of nucleation (Wager, 1959); phases with the simplest structure (olivine and pyroxene) are supplemented by a phase with a more complicated structure (feldspar) up through each layer.
3) The **inch-scale layering** (Plate 2.4a) is unlikely to have formed by a sedimentary-style process when it is "surrounded", both laterally and vertically by larger scale layering; a chemical origin seems more likely. There is a general consensus in the literature that inch-scale layering is generated by an *in situ* process (Irvine, 1987a).
4) The **crossed layers** (Plate 2.4b and c) could not be generated by deposition; at least one of the layers must have been produced after the crystal pile had been deposited.
5) The **cyclic increase in visibility of layering** up section is probably related to the supply of crystals with more mafic phases being available for the bases of individual rhythms up section. Some sort of control involving nucleation rates, diffusion rates, under-cooling and crystal growth rates seems likely.

Plate 2.1

(a) Normally-graded layers from Unit 3, Nunarssuit exposed on coast. Arrow indicates a set of layers truncated by an over-lying layer. This is thought to be related to erosion and layer formation.

(b) Layered syenite autolith in Unit 2. Notebook is 20cm long.

(c) Slump breccia in Unit 4. Dark blobs are mafic to ultramafic cumulates thought to have been transported from the wall of the chamber after wall collapse by a crystal slurry. Hammer handle is 30cm long.

(d) Sketch of (c), black shading represents mafic cumulate autoliths, stipple represents melanocratic syenite.


a)

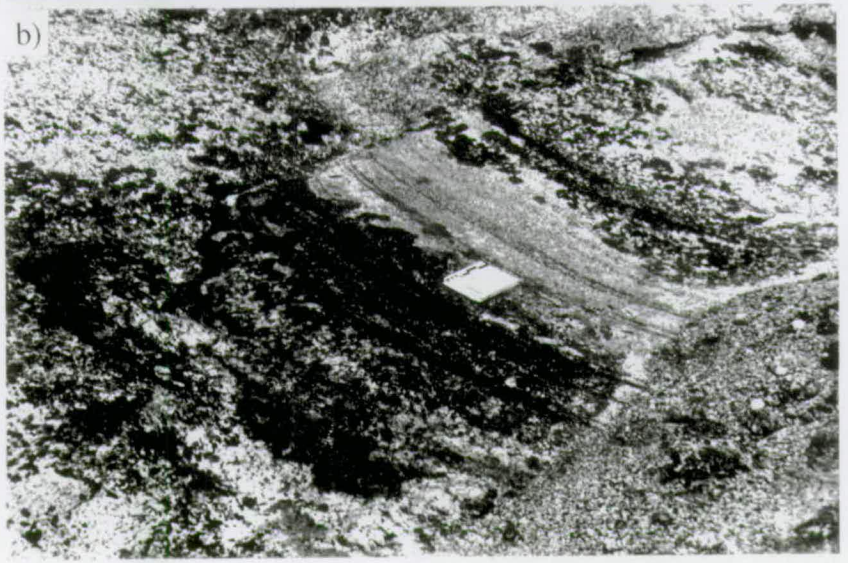
b)


c)


d)

Plate 2.2

(a) Comet structure from Unit 4. The roughly circular head of the comet is composed of mafic (to ultramafic?) cumulate. Tail contains aligned pyroxenes and feldspars, pyroxene content gradually reducing away form head to that of the surrounding syenite. Hammer handle is 30cm long.

(b) Rhythmic layering in Unit 3.

(c) Sketch of (a)

(d) Rhythmic layering in Unit 3, some layers fade along strike.

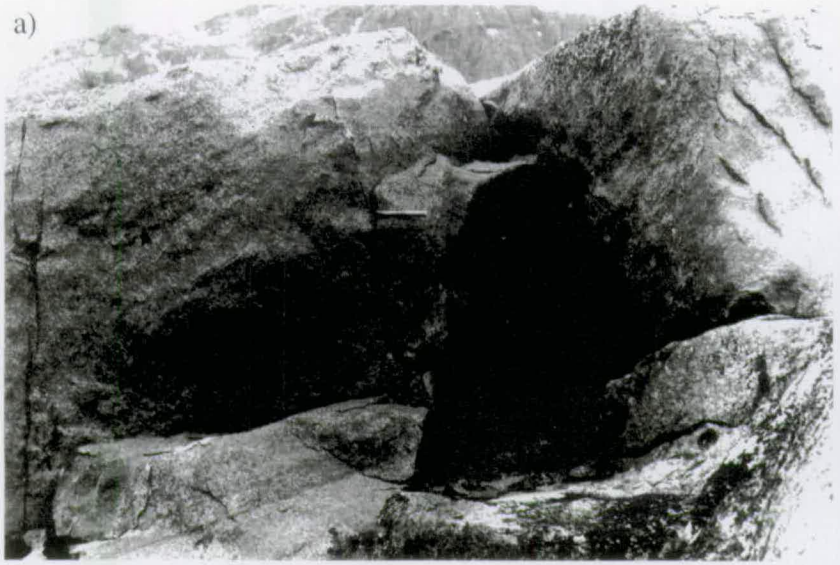
a)


b)

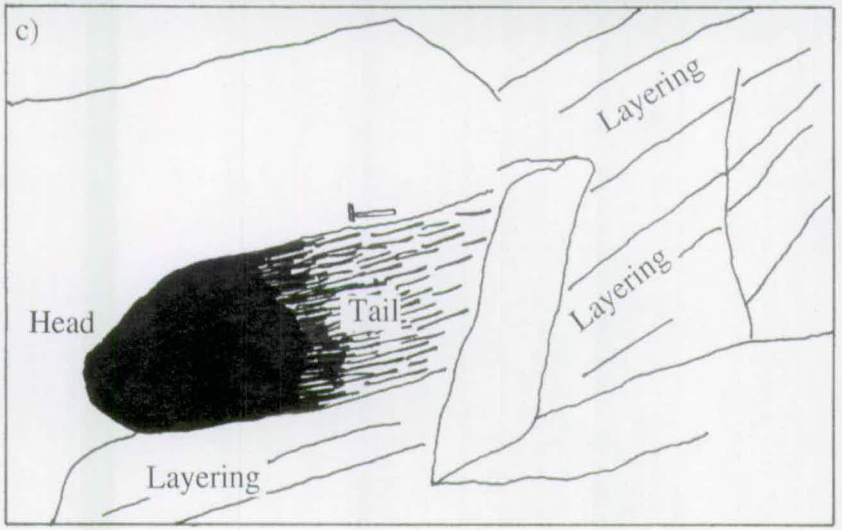
c)
Layering
Layering
Head
Tail
Layering

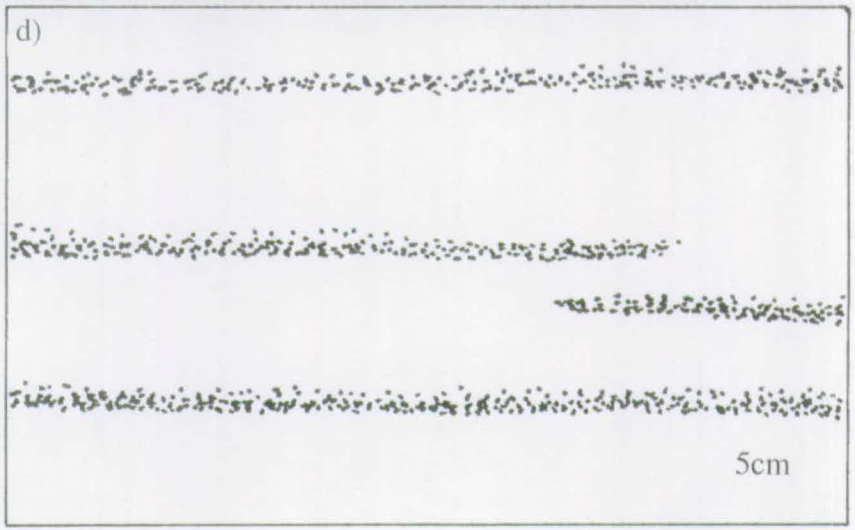
d)
5cm

Plate 2.3

(a) Two overlapping troughs in Unit 4. Layer formation was interrupted by the deposition of large trough structures, probably from a crystal-melt slurry generated by wall collapse. Both troughs have an erosive base; trough B formed first and then trough A. Rhythmic layering is present above the troughs.

(b) Sketch of (a), stipple marks base of troughs

a)

b)

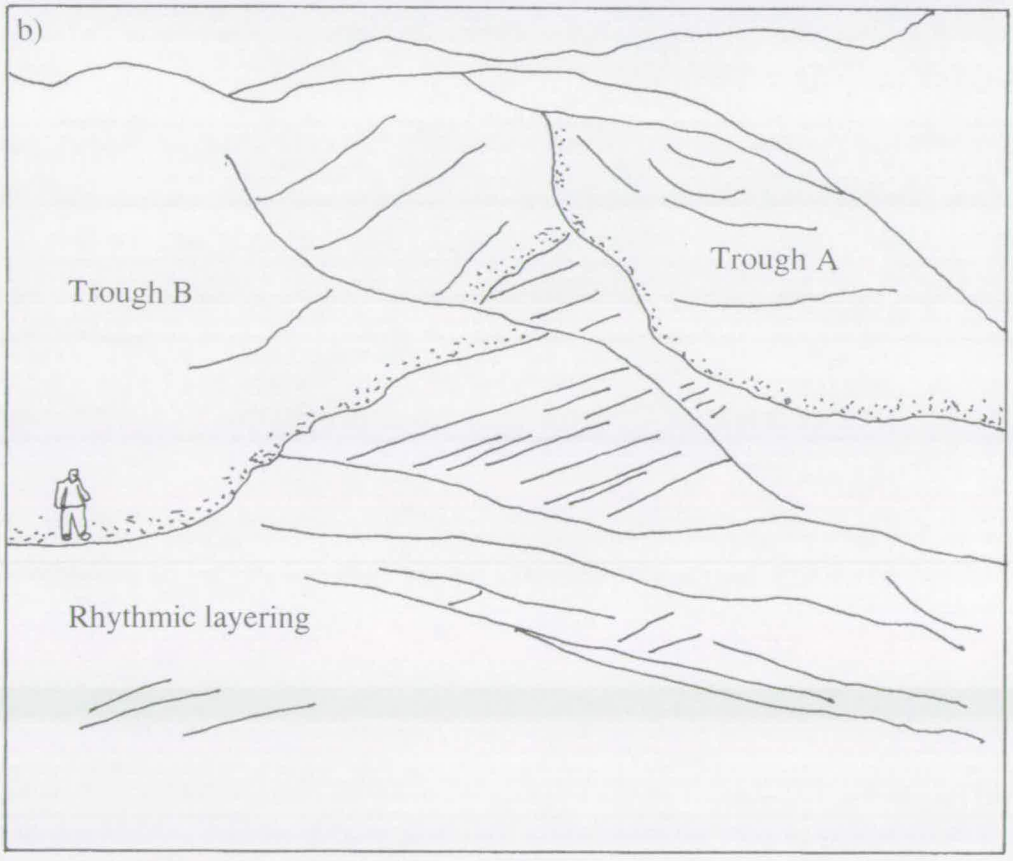

Plate 2.4

(a) Isolated outcrop of microrhythmic layering. Layering on nearby rock faces is on a scale of tens of centimetres. Hammer handle is 30cm long.

(b) Crossed layers in Unit 4. One set of rhythmic layers runs from the top right to the bottom left of picture. The other set of layers curves in from the top left towards the centre of the picture. Notebook is 20cm long.

(c) Sketch of (b), note layer truncation to the left of the notebook and the fading of layers to the right of the notebook.

a)

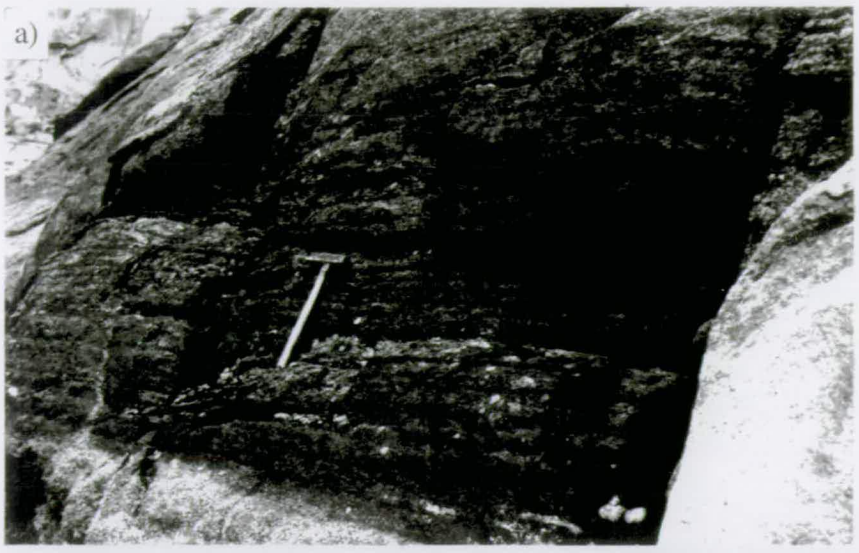

b)

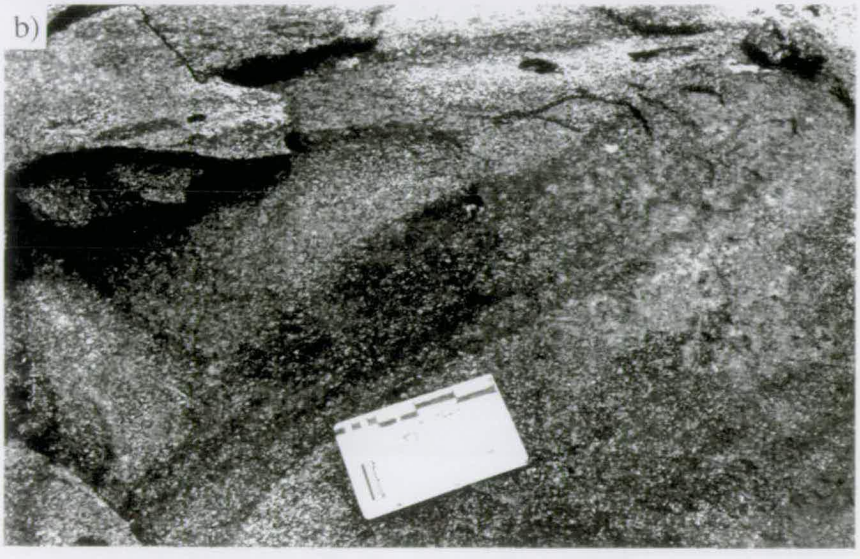

c)

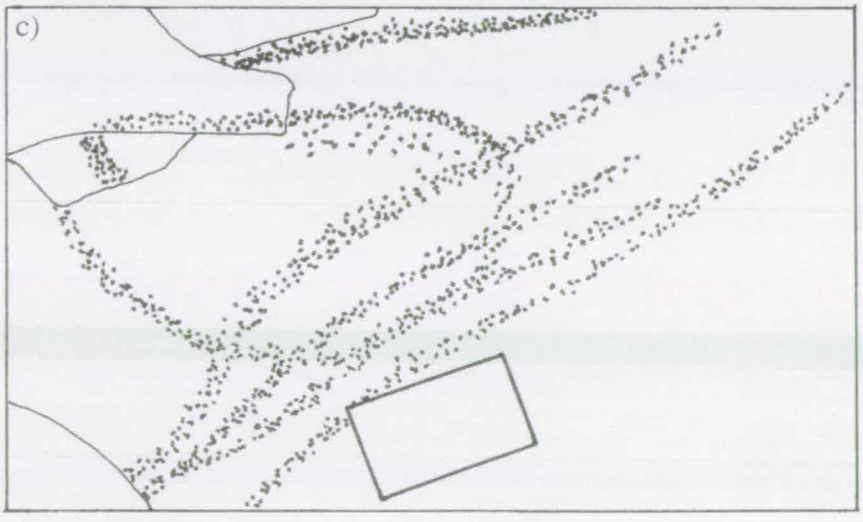

Plate 2.5

(a) Slumped base of Unit 5. Syenite within the slump is layered. The shorter of the two hammer handles is 30cm long.

(b) Stacked series of troughs contained melanocratic syenite. Troughs merge with top of Unit 5 and extend up-section into Unit 6. The axial planes of the troughs appear to be vertical. Dark, near vertical streaks in background are surface outcrop stains.

(c) Sketch of (b)

a)

b)

c)

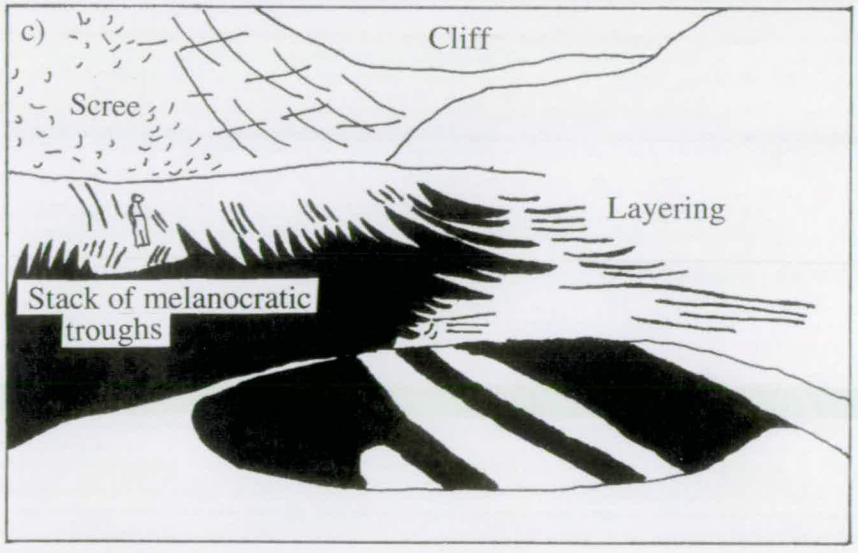

Plate 2.6

(a) Zebra layering in Unit 7, three distinct sub layers are visible; a melanocratic base; a "normal" middle; and a leucocratic top. Notebook (ringed) is 20cm long, glove is about 20cm long

(b) Rhythmic layering in Unit 7. The spacing of layers was measured for non-linear dynamic analysis. Notebook (ringed) is 20cm long.

(c) Faint layering in cliffs, Unit 9. The layering (just visible) runs parallel to the strike of the rock slope. Dark near vertical streaks are stains on rock, not igneous layering.

a)

b)

c)

2.2 West Kûngnât

2.2.1 Introduction

Field work was carried out around the main glacial valley of West Kûngnât. The area was bounded to the east by the crags of the Røverborg, to the south by gneiss, to the west by 920m Ridge and to the north the layering faded out upwards into unlayered syenite (Fig. 2.4).

Syenite near the contact of the intrusion was examined on the rock faces exposed through the snow to the south of the main valley. Layering stratigraphically above this was examined in the main river valley. A south-north traverse along the main glacial valley, sampling the layered succession, was carried out (Fig. 2.5, N.B. Fig. 2.5 is reproduced as a foldout at back of thesis). Appendix A lists sample numbers.

The petrography of the syenites is detailed in Chapter 3; dominant phases are feldspars and pyroxenes; smaller quantities of olivine and opaque oxides are also present. Oikocrysts of amphibole and biotite occur in melanocratic troughs, seen in a rock face above the glacial river valley; oikocrysts are not seen elsewhere in the layered succession. For the purposes of description the lower layered group has been separated into five units. Each unit consists of a set of layers or layering phenomena with a distinct character. The stratigraphy is shown diagramatically in Figs. 2.4 and 2.5 and is summarised below:

Unit 5: Laminated syenite
Unit 4: Normally graded rhythmically layered syenite
Unit 3: Poorly layered syenite
Unit 2: Two series of trough stacks
Unit 1: Unlayered, xenolith-rich syenite
Unit 1 is in contact with the intrusion wall.

2.2.2 General observations

The layered succession is well exposed in the main West Kûngnât river valley that runs perpendicular to the strike of the layering. The layered syenite exposed at the south end of the valley is only about 100m away from the southern contact of the intrusion. The layers at the south end of the valley dip at 30° to the north, striking

---

Figure 2.4 (overleaf): Sketch section of valley where fieldwork was carried out (DL - drill locality).

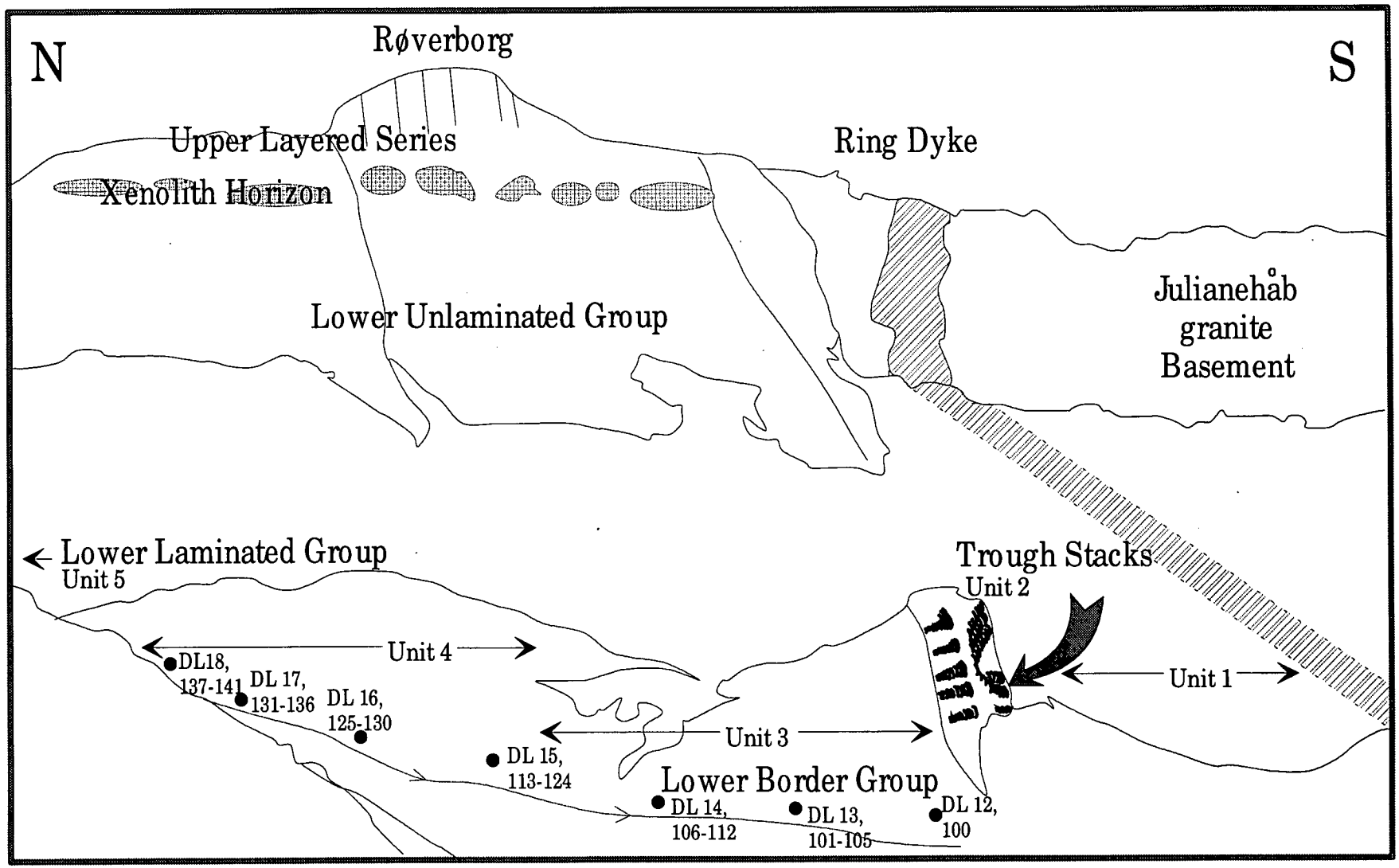
N
Røverborg
S
Upper Layered Series
Xenolith Horizon
Ring Dyke
Julianehåb
granite
Basement
Lower Unlaminated Group
Lower Laminated Group
Unit 5
Trough Stacks
Unit 2
Unit 4
Unit 1
Unit 3
DL18,
137-141
DL 17,
131-136
DL 16,
125-130
DL 15,
113-124
Lower Border Group
DL 14,
106-112
DL 13,
101-105
DL 12,
100

roughly EW. This dip steadily increases along the valley until it reaches 40° at the stratigraphically highest locality that was drilled. Upton (1960) showed that the strike of the layering swings round so that the layers always dip towards a focus which lies to the east of the Røverberg in the younger eastern syenite stock. For this reason it is thought that the original dip of the layers is preserved. Above the highest drill locality rhythmic layering fades away and the rock develops a feldspar lamination. North of the river valley syenite terraces are present up to the top of 920m Ridge. These terraces are formed from leucocratic rock layers underlain by more easily weathered, melanocratic layers about 1m thick. Layer thickness varies from a few centimetres to tens of centimetres. In parts of the sequence the layers are very regular and are laterally continuous on the outcrop scale. Within individual layers, sharp melanocratic bases rich in olivine, pyroxene and opaque oxides grade up into a feldspathic layers in less than half the thickness of the layer. No size sorting of mineral grains is seen. No grain alignment is seen in the rhythmically layered syenite. Some discordances and trough structures occur. Rhythmic layering is seen within the troughs. Sets of troughs occur around the lower parts of the NW and N slopes of 920m Ridge and the western face of Nisseborg as well as at the southern contact of the intrusion. The axial planes of these troughs usually appear to be vertical.

2.2.3 The detailed stratigraphy of the West Kûngnât layered sequence

Unit 1 - Unlayered, xenolith-rich syenite

This unit was exposed through snow above the main glacial valley less than 20m away from the inferred southern contact of the intrusion. The stratigraphic thickness of this unit is unknown since its base is not exposed. There is less than 50m stratigraphic thickness between these outcrops and Unit 2. The syenite is largely homogeneous but contains a large number of xenoliths on the tens of centimetres scale. The majority of these are gneiss but at least one is aplitic syenite. Below this xenolith, which is rimmed by pegmatite, are some narrow melanocratic layers (Plate 2.7a), about 3cm thick and separated from each other by c.30cm. The layering is curved, following the shape of the aplite xenolith, and fades away from the xenolith over a distance of about 30cm.

Unit 2 - Two series of trough stacks

This unit is about 50m thick. Two series of regularly spaced, horizontally aligned, stacks of troughs (Plate 2.7b and c) were observed about 50m east of the outcrop of Unit 1. Both dip north towards the centre of the intrusion with dips apparently

conformable to those of the parallel modal layering in the Unit 3 above. These trough stacks have many features in common with those in the UZa trough zone of the Skaergård intrusion. The two series occur one above the other separated by a stratigraphic thickness of c.10m of syenite that sometimes shows faint, normally-graded rhythmic layering. In the lower series consists six trough stacks are visible. The widths of the bases of the trough stacks vary between 5m and 13m; the centres of troughs at the base of adjacent stacks are separated laterally by c.26m. In the upper series seven trough stacks are exposed. The bases of these trough stacks are all c.8m wide; the centres of troughs at the base of adjacent stacks are separated laterally by c.13m. The trough stacks extend through a stratigraphic sequence of between 5 and 20m. The individual troughs that compose the stacks show normal density-grading and are up to 80cm deep. Syenite with faintly visible normally graded rhythmic layering occurs laterally between stacks. Layers are, on average, about 20cm thick, grading from a more melanocratic base up into normal syenite over a distance of about 5cm. The layers appear to merge into the individual trough wing tips.

The number of troughs within each stack is usually >10 but <40. The syenite within the troughs is more melanocratic than that seen at the base of nearby graded layers and contains c.1cm amphibole and biotite oikocrysts not seen in the surrounding syenite. Whereas troughs in the upper series are stacked directly on top of each other, those in the lower series are laterally displaced so that the trough stacks appear to be draped over an antiformal structure. This latter is possibly a ridge on the magma chamber floor, that is picked out by curved, normally-graded layers between the trough stacks.

The lower trough stack series

The six trough stacks in the lower series will be referred to as T1:0 through T1:5 numbering working from west to east. These troughs are poorly developed relative to the upper trough stack series. The spacing of the troughs is remarkably regular:

T1:0 - 26m - T1:1 - 26m - T1:2 - 29m - T1:3 adjacent to T1:4 - snow - T1:5

Distances are between the centres of the lowest observable troughs in each stack.

Trough stack T1:0 (Plate 2.8a and b) consists of a series of trough structures loosely associated together although not stacked on top of each other, over a lateral distance of about 3.5m and a vertical distance of 5m. Underlying this collection of troughs are normally graded syenite layers with a little cross-bedding.

Trough stacks T1:1 and T1:2 (Plate 2.8 c and d) are more regular and the individual troughs are stacked precisely on top of one another, each trough cutting into the under-lying one. The base of T1:1 was obscured by snow. The trough at the snow line is 13m wide. The stack is about 10m high. Stack T1:2 is similar except that its base was visible. 5m up from the lowest exposure of T1:1 a thin, tapered, slightly curved sliver of leucocratic material is seen within a trough (Plate 2.9a), it is about 50cm long and up to 5cm wide. This leucocratic material strongly resembles the syenite surrounding the trough stacks both in its shape and mineralogy. As shown in Plate 2.9a the normal syenite just above the trough where the sliver is seen has a groove in it that is the same shape as the sliver. The sliver of syenite resembles a detached autolith, the relevance of which is discussed in section 2.2.4. A rectangular block of normal syenite was seen at the top of one of the troughs in T1:2 (Plate 2.9b) but there was no place visible in the surrounding syenite which this block could have been detached.

The trough axes of T1:3, T1:4 and T1:5 (details in Figs. 2.4 and 2.5) are systematically offset to the west in an upward sequence and T1:1 and T1:2 are linked by a broad triangular zone, both stacks being slightly displaced to the east. T1:2 and T1:3 are separated by an antiform (Plate 2.9c and d). This antiform is picked out by faint normally graded rhythmic layers which are on average about 20cm thick and trace out the outline of the antiform. The trough stacks are displaced so as to be roughly parallel to the adjacent limb of this antiform.

Between the lower and upper trough stack series there is about 10m of syenite that, in places, exhibits rhythmic layering.

The upper trough stack series

The upper trough stack series consists of seven trough stacks, T2:1 to T2:7, numbering working from east to west. T2:1 is directly above T1:5. The individual troughs are better developed than those seen in the lower trough series, (T2:2 is shown in Plate 2.10a). As is seen in Figs. 2.4, 2.5 and Plate 2.7b the bases of the trough stacks in the upper series all occur at the same stratigraphic level. This was confirmed by building cairns at the base of each stack and sighting along them. The spacing of the stacks is not as regular as the lower series:

2:6 - 10m - T2:5 - 16m - T2:4 - 8m - T2:3 - 15m - T2:2 adjacent to T2:1

Distances are between the centres of the lowest observable troughs in the stack.

The troughs are all about 8m wide at the base of an individual trough stack but get narrower up the sequence. Although the trough stacks start at the same stratigraphic level they fade out irregularly up section. The tips of the lower troughs of T2:1 and T2:2 interdigitate (Plate 2.10b) and show no signs of deformation. The degree of interdigitation between T2:1 and T2:2 increases until about three metres up from the base of the trough stacks they merge.

2m stratigraphically above the upper trough stack series are much smaller channel structures (Plate 2.10c), about a metre wide and up to 20cm deep. These have an apparently random distribution. Also at this stratigraphic level are some normally graded rhythmic layers (Plate 2.10d), about 20cm thick, with unconformities visible between them.

Unit 3 - Poorly layered syenite

From the start of the outcrop at the south of the main glacial river valley up to drill locality 15 (Fig. 2.4, 2.5) layering occurs in an irregular manner over a stratigraphic thickness of about 45m. Normally graded layers vary in thickness from 10cm to about 50cm. The average spacing is about 20cm. The layers have well-defined melanocratic bases which grade over one or two centimetres into normal syenite. It is thought that palaeo-magma chamber floor topography is seen in this section (Plate 2.11a and b). The syenite to the left of the fault plane down-faulted with either subsequent layers on the left banking up against the fault scarp or pre-existing layers being deflected upwards by the faulting.

Unit 4 - Normally-graded, rhythmically layered syenite

Over a stratigraphic thickness of about 60m, from drill locality 15 to drill locality 18, regular normally-graded rhythms are seen. Individual rhythms are on average 20cm thick. At drill locality 15 (Plate 2.11c), over a stratigraphical thickness of 7m, the spacing of the layers was measured. These data are used for non-linear dynamic analysis in Chapter 8. After drill locality 18 the layering becomes more irregular and is last seen about 50m below the summit of 920m Ridge.

Unit 5 - Laminated syenite

Stratigraphically above drill locality 18 the syenite begins to develop a lamination due to parallelism of feldspars. By the time the summit of 920m Ridge is reached the lamination is pronounced and the syenite is jointed along the lamination planes. The rocks lying stratigraphically above this height were not accessible and therefore not

studied. The west face of Røverborg clearly shows that there is a region of unlayered syenite that is then succeeded by a xenolith-rich zone and the upper layered series, (Upton, 1960)

2.2.4 Interpretation of field observations

2.2.4.1 Sedimentary style features

1) The **grading of the layers**, with dense minerals concentrated at the base of the layer, is consistent with them being derived by a gravity sorting process. This could either be a sedimentation process affecting the whole magma chamber (Sparks *et al.*, 1993) or the action of currents on an unconsolidated crystal pile (Conrad and Naslund, 1989).

2) **Troughs** could have been produced by erosion and deposition from crystal-melt slurries.

3) The **stacking of the troughs** could have been a function of rapid accumulation of the crystal pile at the floor of the magma chamber. Stacks of sandstone troughs are relatively common in the North Sea and are associated with rapid subsidence (Einsele, 1992).

4) The thin sliver of leucocratic syenite in trough T1:1 and the block of leucocratic syenite in T1:2 may be **autoliths**. These could have been plucked off the wall or floor of the chamber by the streams responsible for the formation of the troughs.

5) The **interdigitation** of troughs in stacks T2:1 and T2:2 (Plate 2.10b) could have been produced by a single stream of crystal-melt slurry switching between two positions. In sedimentary geology interdigitating troughs generated by the process of streams switching course (known as avulsion) is relatively common in fluvial environments (Einsele, 1992).

2.2.4.2: Non-sedimentary-style features

1) The **onset** and **sporadic occurrence up section of layering** indicates that some critical limit must be reached before layering can be produced. This critical limit is most likely to be of a physicochemical nature.

2) The **grading of the layers** could be related to either inhibition of nucleation (Parsons and Becker, 1987) or relative ease of nucleation (Wager, 1959); phases with the simplest structure (olivine and pyroxene) are supplemented by a phase with a more complicated structure (feldspar) up through each layer.

3) The **spacing of the trough stacks** may be a function of convection, the spacing of the troughs being equal to the width of two roller convection cells (Irvine, 1987a and

Chapter 9.8). Alternatively it could be a function of the way that fluid flows down slope (Chapter 10.9).

Plate 2.7

(a) The rounded pale patch in the centre of the picture is an aplitic syenite xenolith. The xenolith is rimmed by pegmatite; underneath this are some narrow melanocratic layers. Notebook is 20cm long.

(b) The trough stack locality. The Lower trough stack series is unclear; the bases of the upper trough stacks are seen as a dark band running from left to right about one third of the way up the picture. The outcrop is shown diagramatically in Figs. 2.4 and 2.5 and Plate 2.7c.

(c) Sketch of (b) with trough stacks visible in (b) labelled

a)

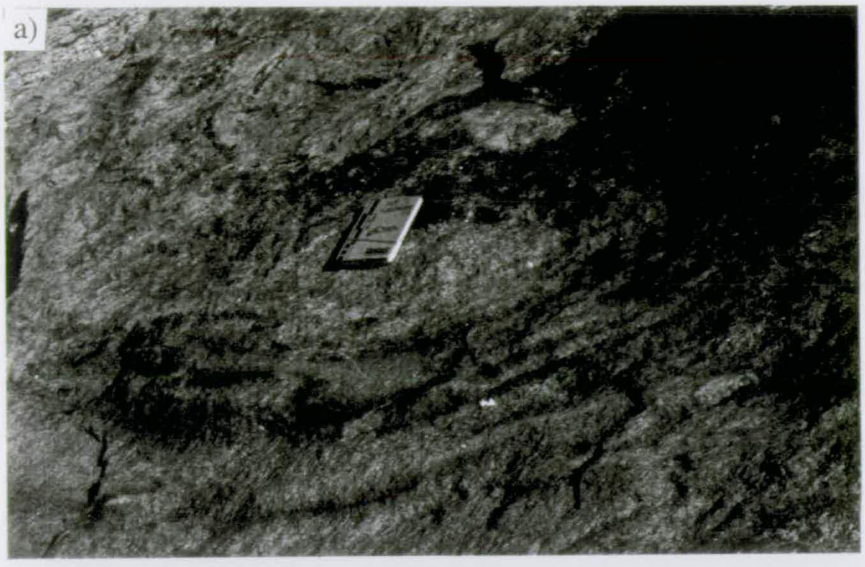

b)

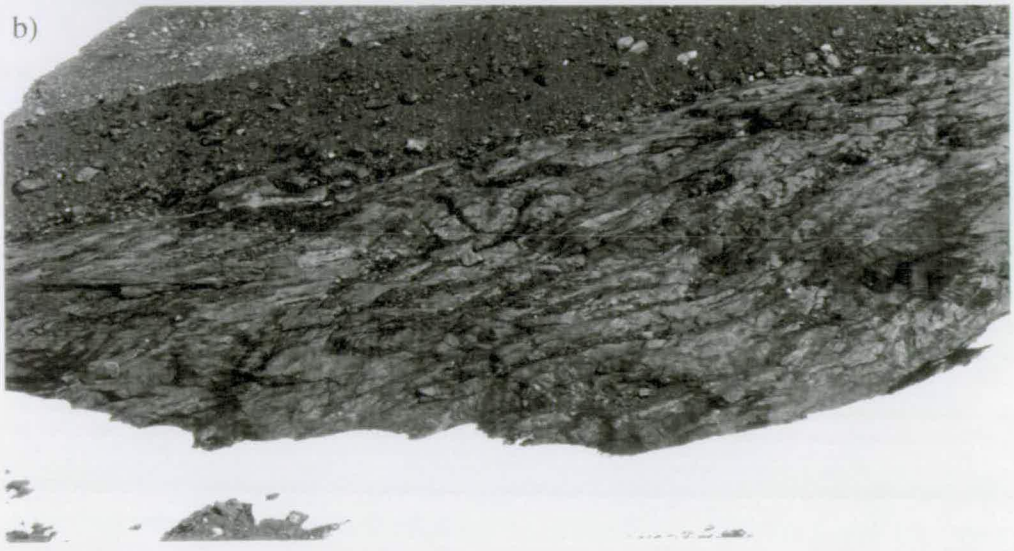

c)

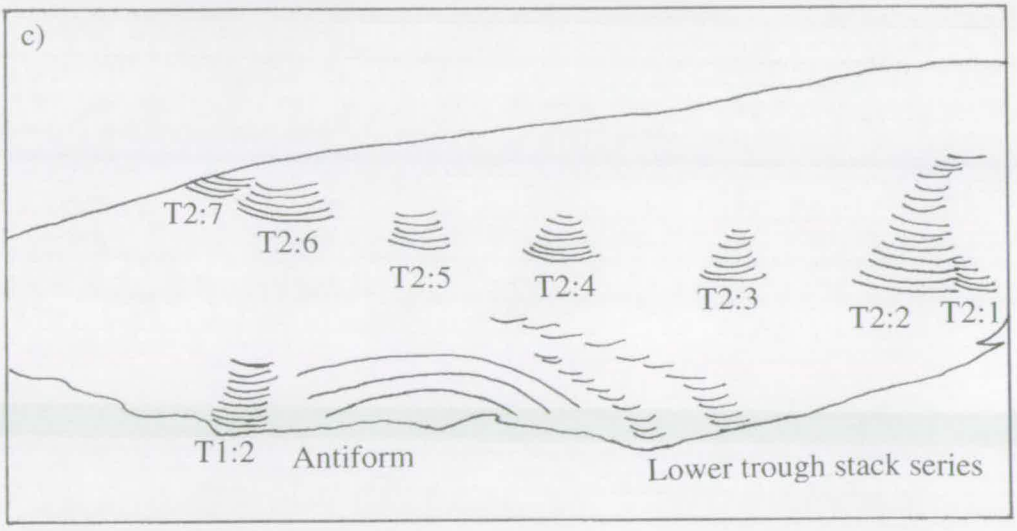
T2:7
T2:6
T2:5
T2:4
T2:3
T2:2
T2:1
T1:2
Antiform
Lower trough stack series

Plate 2.8

(a) T1:0, a series of channels loosely associated together, the dark material is melanocratic syenite within the troughs.

(b) Sketch of (a).

(c) T1:2, the dark material is melanocratic syenite within the troughs. Notebook is 20cm long.

(d) Sketch of (c).


a)


c)

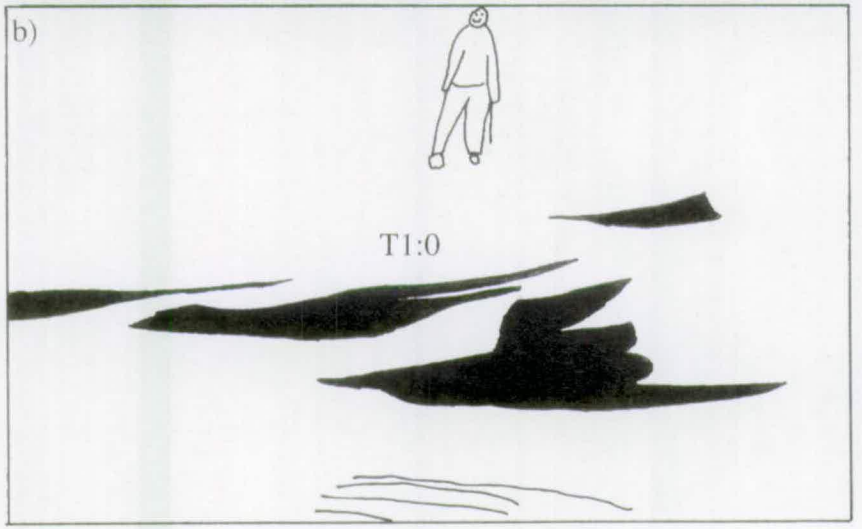
b)
T1:0

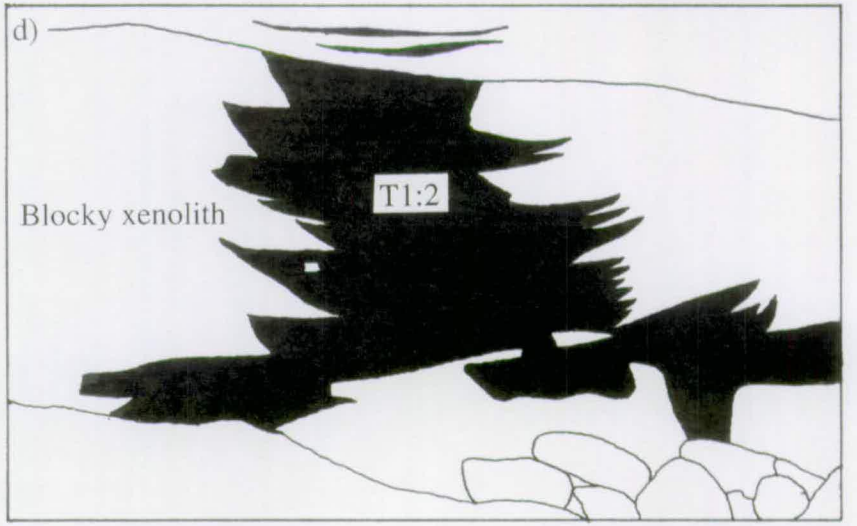
d)
Blocky xenolith
T1:2

Plate 2.9

(a) A sliver of leucocratic syenite in a trough from T1:1. The three dimensional shape of the sliver may be tabular or rod-like. Its upper surface has the same shape as the lower surface of the over-lying host syenite. The sliver may be an autolith or it could be host syenite trapped between two irregularly shaped troughs. Lens cap is c.5cm in diameter.

(b) Sketch of blocky xenolith of host syenite within a trough from T1:2. Position of trough in relation to T1:2 is shown in a sketch in the top right hand corner.

(c) Field photograph of the antiform separating T1:2 and T1:3; antiform picked out by rhythmic layers.

(d) Sketch of (c).


a)

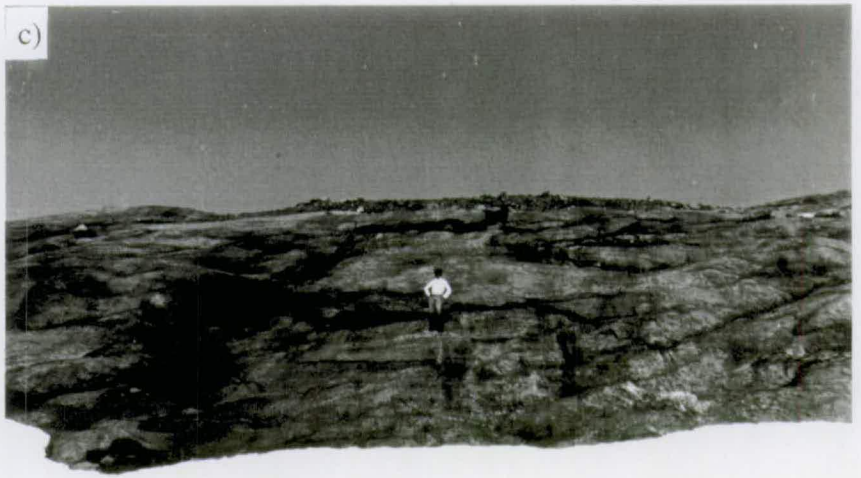
c)

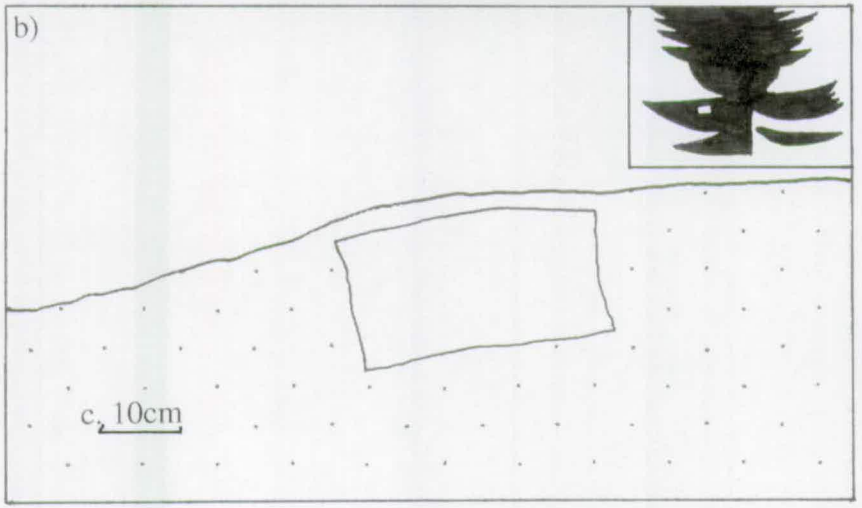
b)
c. 10cm

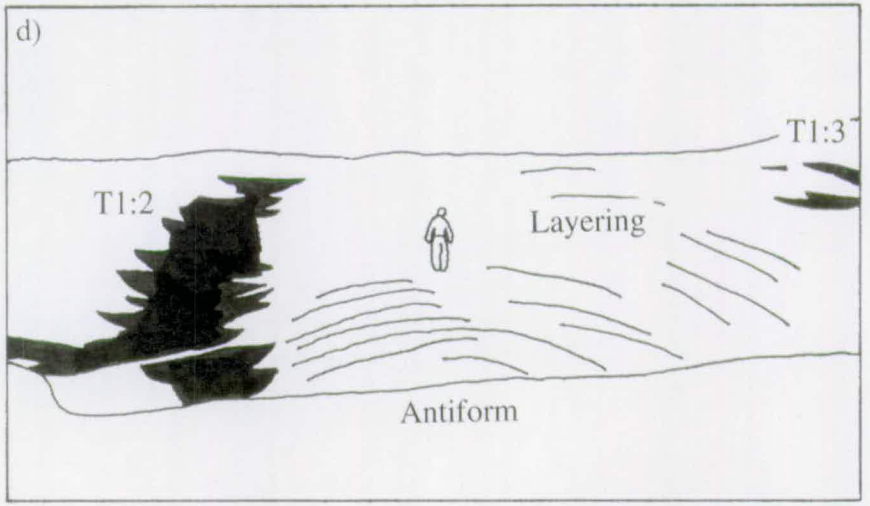
d)
T1:3
T1:2
Layering
Antiform

Plate 2.10

(a) T2:2, note grading of individual troughs. Hammer handle is 60cm long.

(b) Interdigitating trough tips of trough stacks T2:1 and T2:2. Notebook is 20cm long.

(c) Smaller scale trough structures and unconformities above Upper trough stack series.

(d) Rhythmic layering above Upper trough stack series. Notebook is 20cm long.


a)


b)


c)


d)

Plate 2.11

(a) Possible magma chamber floor faulting. Rhythmic layers are seen at left hand side of picture and centre of picture. Layers at bottom middle of picture can be traced upwards to the top right; these layers are concave up as if they have been deflected and stop halfway up the picture. It is suggested that they are truncated by a fault plane and that the faulting caused the upwards deflection of the layers.

(b) Sketch of (a)

(c) Rhythmic layering at locality DL 15 where spacing of layers was measured for non-linear dynamic analysis.

a)

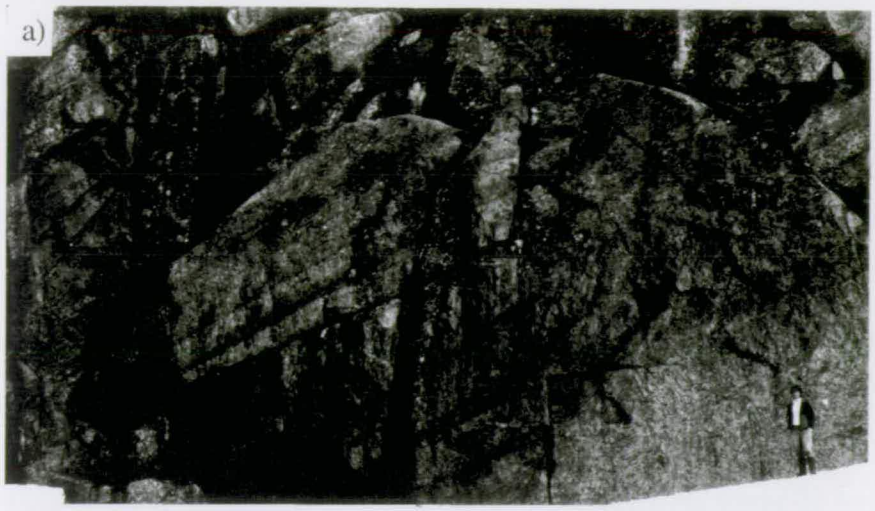

b)

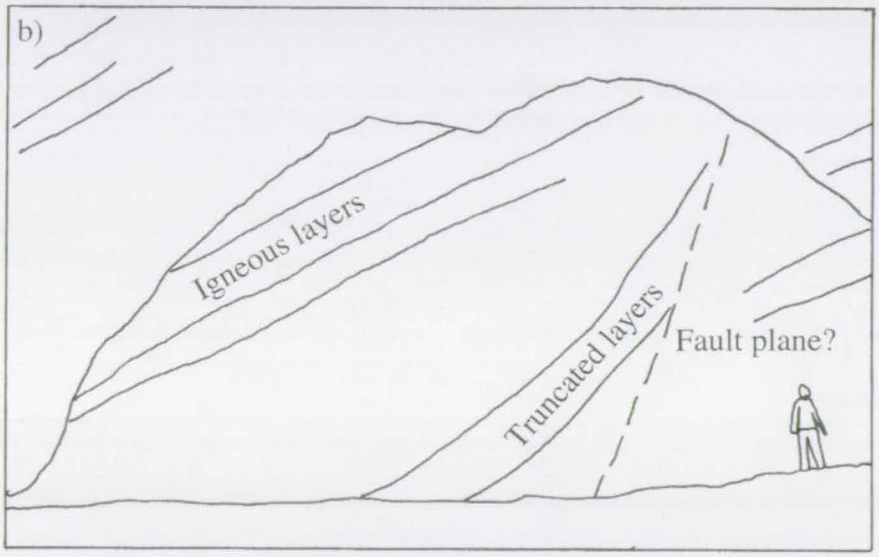

c)

Chapter 3 - Petrography

3.1: Introduction

In this chapter the petrography of the layered syenites from Nunarssuit and West Kûngnât is described. Where used, cumulate terminology follows the guide lines set down by Irvine (1982). The use of this terminology is kept to a minimum due to the different uses of the word cumulate in the literature. A cumulate is defined as "An igneous rock characterised by a cumulus framework of touching mineral crystals or grains that were evidently formed and concentrated primarily through fractional crystallisation, ... either by crystals separating from the liquid (crystal settling), liquid separating from the crystals (convecting away) or by some other mechanism" Irvine (1982). In the case of Nunarssuit and West Kûngnât the melanocratic facies described are obviously cumulates, the bulk compositions do not represent liquid compositions and there is evidence that current action led to the concentration of the mafic grains (Chapters 2 and 10). The obvious cumulus phases are pyroxene, olivine (when present) and apatite. Opaque oxides and sulphides have a somewhat ambiguous mode of occurrence, often occurring as irregular rounded blobs mantling olivines and pyroxenes but also occurring as isolated crystals mantled with biotite within feldspar. According to the above definition the leucocratic facies would also be termed cumulates even if they just represent the normal crystallisation product of a syenitic magma, providing that some residual magma separated from the crystals. Again pyroxene, olivine and apatite are cumulus phases. The mode of occurrence of the opaque oxides and sulphides is ambiguous.

The classification of the feldspar grains is less obvious, particularly since the shape of the crystals has been modified by sub-solidus processes. In the case of the melanocratic facies the feldspars often have very irregular shapes and mantle other grains. Occasionally an inclusion free crystal is seen. It appears that the feldspars continued to crystallise after the mafic phases and apatite, whether this occurred during the formation of a touching crystal framework (cumulus crystallisation phase) or afterwards, during the solidification of the intercumulus liquid, is not clear. In the case of the leucocratic facies feldspar must have been a cumulus phase. The loss of original grain shape and any original zoning makes it impossible to determine how much postcumulus growth these feldspars have experienced.

The problems of identifying postcumulus feldspar growth makes the classification of these rocks as ortho- (25-50 vol% postcumulus material) meso- (7-25 vol% postcumulus material) or adcumulates (0-7 vol% postcumulus material) far from certain but they are most likely to be mesocumulates.

In this chapter the petrography of the Nunarssuit and West Kûngnât layered syenites is discussed. After this the grain size of pyroxenes and olivines in the two intrusions is determined. The petrography of the two layered series is then compared.

3.2 Nunarssuit

The petrography of the melanocratic bases of the layers (Plate 3.1a) is described and compared with that of, (i) the leucocratic material from the remainder of the layers (Plate 3.1b), (ii) the thick melanocratic units and the autoliths found within them (Plate 3.1c) and, (iii) the melanocratic troughs (Plate 3.1d).
In general there is an inverse correlation between the colour index of a sample and its degree of sub-solidus modification. Thus the melanocratic base of a layer is less altered than the overlying leucocratic part; the melanocratic bases of layers from the markedly layered syenite units are less altered than the melanocratic bases of layers from the faintly layered syenite units. Table 3.1 shows the modes of various facies from the layered sequence.

3.2.1 Feldspar

3.2.1.1 Petrography

Feldspars at the base of layers are sub- to euhedral and up to 8mm by 3mm in section; it is not clear whether they are partly cumulus or wholly intercumulus. They usually mantle or enclose the other minerals present in the sample. This is not necessarily a primary texture as the original shape of the feldspar crystals has almost certainly been lost (see Chapter 6.2). Partial sericitisation of the feldspars has caused optical turbidity (Plate 3.2a). Feldspars are predominantly film perthites, although patch (Plate 3.2b) and braid (Plate 3.2b) perthites are also present. Film and braid perthite crystals have swapped rims (complex irregular interpenetrating boundaries between two crystals as illustrated in Plate 3.2c, see also Smith and Brown, 1988 pp 603-604) and pleated rims (braid perthite coarsens at the rims of crystals producing a texture which looks like pleats in cloth as illustrated in Plate 3.2b).

Facies / Phase	Melanocratic base of layer at base of faintly layered syenite (6-41, Unit 2)	Melanocratic base of layer at top of clearly layered syenite (8-51, Unit 3)	Lower thick melanocratic unit (9-56, Unit 5)	Mafic cumulate autolith (11-69, Unit 4)	Homogeneous unlayered syenite (MH-NUN-92 9, Unit 1)	Leucocratic portion of layer at base of faintly layered syenite (6-42,Unit 2)	Leucocratic portion of layer at top of clearly layered syenite (8-52, Unit 3)
Non-turbid feldspar	4	30	23	31	17	18	16
Turbid feldspar	70	7	14	25	63	67	71
Total feldspar	74	37	37	56	80	85	87
Pyroxene	6	25	25	20	8	10	6
Olivine	<1	29	29	18	4	<1	<1
Amphibole	11	1	2	2	5	5	4
Biotite	3	<1	<1	0	<1	<1	<1
Opaque oxides and sulphides	2	5	7	4	1	<1	<1
Apatite	1	1	1	<1	<1	<1	<1

Table 3.1: Modal content of different facies from the Nunarssuit layered syenite expressed as percentages. Over 2000 points were counted for each sample. Due to the coarse grain size accuracy is probably no greater than 5%.

Feldspars are less anhedral within the leucocratic portions of the rhythmic layers than in the melanocratic bases. Feldspars from the leucocratic portions contain a higher proportion of patch and film perthite. Almost all grains have complex swapped rims and pleated rims. Little braid perthite is present. Feldspars in the thick melanocratic units and in the mafic autoliths are anhedral and appear to have grown between pyroxene and olivine grains as an intercumulus phase. They are less turbid and contain a smaller proportion of patch and film perthite and more braid perthite. The more mafic a sample (higher colour index) the less turbid feldspar it contains (Fig. 3.1)

3.2.1.2 Cathodoluminescence petrography

Rae and Chambers (1988) showed that changes in alkali feldspar CL are associated with textural changes in feldspars (turbidity and coarsening of perthite) which are generally accepted to result from fluid-feldspar interaction (Worden *et al.*, 1990).

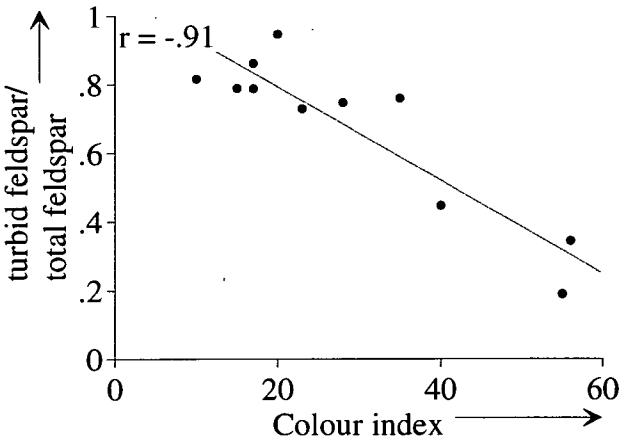

Fig. 3.1: Plot showing inverse correlation between colour index (= %vol mafic minerals in sample) and the proportion of feldspar in the sample which is turbid.

Pristine feldspars luminesce bright blue whereas optically turbid feldspars luminesce red or dull blue. Finch and Walker (1991) defined a feldspar luminescence index (f.l.i.) of a sample as the ratio of red luminescing feldspar to total feldspar; the f.l.i. is here defined as the ratio of non-sky blue luminescing feldspar to total feldspar. Table 3.2 compares the average f.l.i. of various facies from the Nunarssuit layered sequence. The data suggest that the more leucocratic samples have undergone more interaction with fluid than the melanocratic samples.

Facies	Average feldspar luminescence index	Relative alteration
Melanocratic base of layer at base of faintly layered syenite (Unit 2)	85	High
Melanocratic base of layer at top of clearly layered syenite (Unit 3)	60	Moderate
Lower thick melanocratic unit (Unit 5)	20	Low
Mafic syenite xenolith (from Unit 4)	20	Low
Homogeneous unlayered syenite (Unit 1)	92	High
Leucocratic portion of layer at base of faintly layered syenite (Unit 2)	93	High
Leucocratic portion of layer at top of clearly layered syenite (Unit 3)	94	High

Table 3.2 Average feldspar luminescence indices (feldspar luminescence index is defined here as the ratio of non-sky blue luminescing feldspar to total feldspar) for different facies from the Nunarssuit layered syenite.

3.2.1.3 Scanning electron microscopy

Brown and Parsons (1994) suggested that feldspars develop micropores as a consequence of the release of elastic strain energy when the feldspar is altered by interaction with a fluid. These holes are associated with optical turbidity of feldspars and are visible in SEM. A detailed discussion of feldspar micropores is provided by Walker (1991). A brief study of feldspars from the Nunarssuit layered series showed

that feldspars from the leucocratic facies contain a higher volume of micropores than those from the melanocratic facies.

3.2.2 Pyroxene

In all facies pyroxene occurs as a cumulus phase. The melanocratic bases of individual layers contain euhedral to subhedral pyroxenes up to 2mm by 1mm in section. The most common colour in thin section is pale brown, often grading to green at crystal edges and along cracks (Plate 3.2d, 3.3a). Exsolved, needle-like crystals (Plate 3.3b) of an Fe-Ti oxide are often present as inclusions around the centre of crystals. These crystals are too small to analyse using the electron probe but are probably titanomagnetites; inclusions of apatite and magnetite are also present. Alteration to a green/brown pleochroic amphibole has either given rise to irregular shaped blobs within the crystal (Plate 3.3b and c), (often surrounded by green pyroxene) or, less commonly, to almost total alteration of the pyroxenes (Plate 3.3d).

Pyroxenes from the leucocratic portions of the layers are more altered, commonly displaying wholesale alteration to amphibole. Pyroxenes from the thick melanocratic units and mafic cumulate autoliths are more idiomorphic and less altered. Mafic cumulate autoliths contain pyroxenes which are aligned in a preferred orientation (Plate 3.1c). Pyroxenes also show preferred orientation in the slumps associated with Units 5 and 8, the thick melanocratic units.

3.2.3 Olivine

In all facies olivine occurs as a cumulus phase. Olivines occur as rounded, straw coloured, elongate crystals up to 3mm by 2mm in section. They contain inclusions of apatite, and less commonly, of magnetite. Grains are often densely cracked; the cracks, along which grains alter to iddingsite and magnetite, have a preferred orientation (Plate 3.4a) thought to be related to compaction of the cumulate pile.

Within the leucocratic layers very little of the olivine is fresh. Magnetite and iddingsite are present as alteration products along cracks in the crystals and within the body of the crystals. Within the thick melanocratic units and mafic cumulate autoliths, olivine is largely unaltered; some magnetite is present along cracks.

3.2.4 Amphibole

In melanocratic bases of the layers amphiboles occur as anhedral alteration products of pyroxenes (see section 3.2.2. Plates 3.3b, c and d) and, in extreme cases, less than

10% of the original pyroxene remains. All the amphiboles are pleochroic green, green/brown, brown. Inclusions of apatite and magnetite are common.

A greater proportion of the pyroxene is altered to amphibole in the leucocratic portions of layers. As well as being present in recognisably altered pyroxene grains, amphiboles, up to 3mm in length in any orientation, which contain no pyroxene occur. These are often angular in shape and appear to have formed interstitially to feldspar grains. These amphiboles would appear to be postcumulus. Within the thick melanocratic units and mafic cumulate autoliths, amphibole is rare and is present only as irregular patches within pyroxene grains.

3.2.5 Biotite

Small crystals of biotite are present, largely grouped together to form fringes on magnetite and ilmenite grains (Plate 3.4b), but also as discrete, angular, anhedral, sub-millimetre crystals. Biotite appears to be either postcumulus or the product of sub-solidus reactions.

There is no difference in the mode of occurrence of biotite within the different facies in the layered sequence.

3.2.6 Minor phases

Apatite

Apatite is present in all facies of the layered sequence as small well-formed crystals up to 1mm in length. It occurs within feldspar, olivine, pyroxene, amphibole, and ilmenite but is predominantly present in the later four phases and is thus concentrated in the bases of layers. Apatite is a cumulus phase. Finch (1990) defined a number of zoning styles (Fig. 3.2) which are observed in apatites from the Late Igdlerfigssalik centre (a nepheline syenitic centre in the Gardar province). Zoning in apatites was observed using back-scattered electron imaging on the Cameca electron-probe (Plate 3.5a and b). Table 3.3 shows the relative proportions of different zoning styles, these results are discussed in Chapter 6.6. The apatites luminesce yellow.

Facies	Oscillatory (Fig. 3.2a)	Concentric (Fig. 3.2b)	Fracture (Fig. 3.2c)	No zoning
Melanocratic base of layer (Unit 3)	14	18	2	66
Leucocratic portion of layer (Unit 3)	5	25	1	69
Thick melanocratic unit (Unit 5)	18	18	3	61

Table 3.3: Average % of zoning styles in apatites from different facies of the Nunarssuit layered syenite.

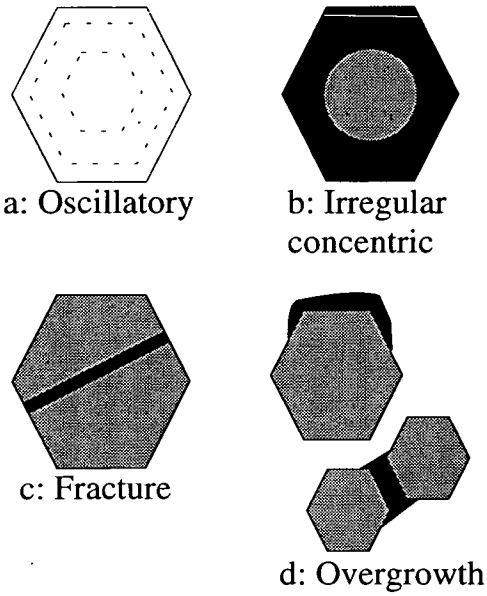

Fig. 3.2: Apatite zoning classification scheme. A: Oscillatory, primary magmatic zoning; B: Irregular concentric zoning, may be a primary magmatic feature or produced by post-crystallisation modification by fluids; C: Fracture zoning produced by percolation of fluids along cracks; D: Overgrowth produced by precipitation of apatite after crystallisation of primary grains, may occur in magma or subsequent to solidification. E: Chaotic (not figured) either a complex superposition of many types of zoning pattern or irregular dissolution and reprecipitation. After Finch (1990)

Opaque oxides and sulphides:

Ilmenite occurs in all facies of the Nunarssuit layered sequence as rounded blobs less than 1mm in diameter. It occurs as discrete grains mantling other mafic phases and as inclusions in pyroxenes and amphiboles. Ilmenite appears to be both a cumulus phase (inclusions in mafic phases) and a postcumulus phase (mantling olivine and pyroxene). Ilmenites show multiple twinning but not exsolution textures.

Magnetite occurs in all facies as a cumulus phase but in very low concentrations. It is slightly more common in the more melanocratic facies than in the leucocratic facies. It also occurs as an alteration product of olivine. When it is present as a primary phase magnetite shows exsolution and oxidation to ilmenite. There is no difference between facies in the style of oxidation and exsolution in magnetite grains.

Iron and copper sulphides occur in all facies as irregular blobs and appear to be a product of a sulphide cumulus melt phase. No chemical analyses were carried out on the sulphides.

Other phases:

In all the facies sphene, zircon, quartz and carbonate are present. Sphene, zircon and quartz are readily identified under the microscope. The carbonate is most readily detected by its orange cathodoluminescence and is most likely to be calcite (Miller, 1988). Zircons can be shown to be zoned using back-scattered electron-imaging (Plate 3.5c to f). This zoning shows both primary and sub-solidus features and is discussed in Chapter 6.8.

3.2.7 Low temperature alteration products

Intergrowths of chlorite, amphibole and clay minerals are present in some samples (Plate 3.4c). The intergrowths are irregular in shape and several millimetres across. The intergrowths penetrate along the pleats at the rims of feldspars indicating that they grew after the feldspars became pleated. This occurs at temperatures below 450°C (Brown and Parsons, 1994). The intergrowths can not be replacing the feldspar isochemically. Either the bulk chemistry of the rock is being altered or the growth of the intergrowths is linked to the break-down of other phases elsewhere in the rock. Due to the relative freshness of most grains it is assumed that this stage of alteration has had little effect on the final mineralogy of the syenites.

Plate 3.1[1]

(a) Melanocratic sample from the base of a layer in Unit 7, Nunarssuit. White grains are feldspar, high relief light grey grains are olivines, dark grey grains are pyroxenes, black grains are opaque oxides, amphibole and biotite. Sample 10-66, field of view 22mm x 14mm, ppl.

(b) Leucocratic material from mid-way up a layer in Unit 7, Nunarssuit. The majority of the field of view is feldspar; that in the upper part of the picture is less turbid than that in the lower part. Dark grey and black phases are altered pyroxene, amphibole and biotite. Sample 10-63, field of view 22mm x 14mm, ppl.

(c) Mafic cumulate autolith from Unit 5, Nunarssuit. White grains are feldspar, high relief light grey grains are olivines, dark grey grains are pyroxenes, black grains are opaque oxides, amphibole and biotite. Pyroxenes are orientated from top right to bottom left. Sample 9-57, field of view 22mm x 14mm, ppl

(d) Melanocratic material from a trough present in Unit 4, Nunarssuit. White grains are feldspar, high relief light grey grains are olivines, dark grey grains are pyroxenes, black grains are opaque oxides, amphibole and biotite. Sample 1-10, field of view 22mm x 14mm, ppl

[1]Plates 3.1a to d and Plates 3.6 a to d are all the same scale.

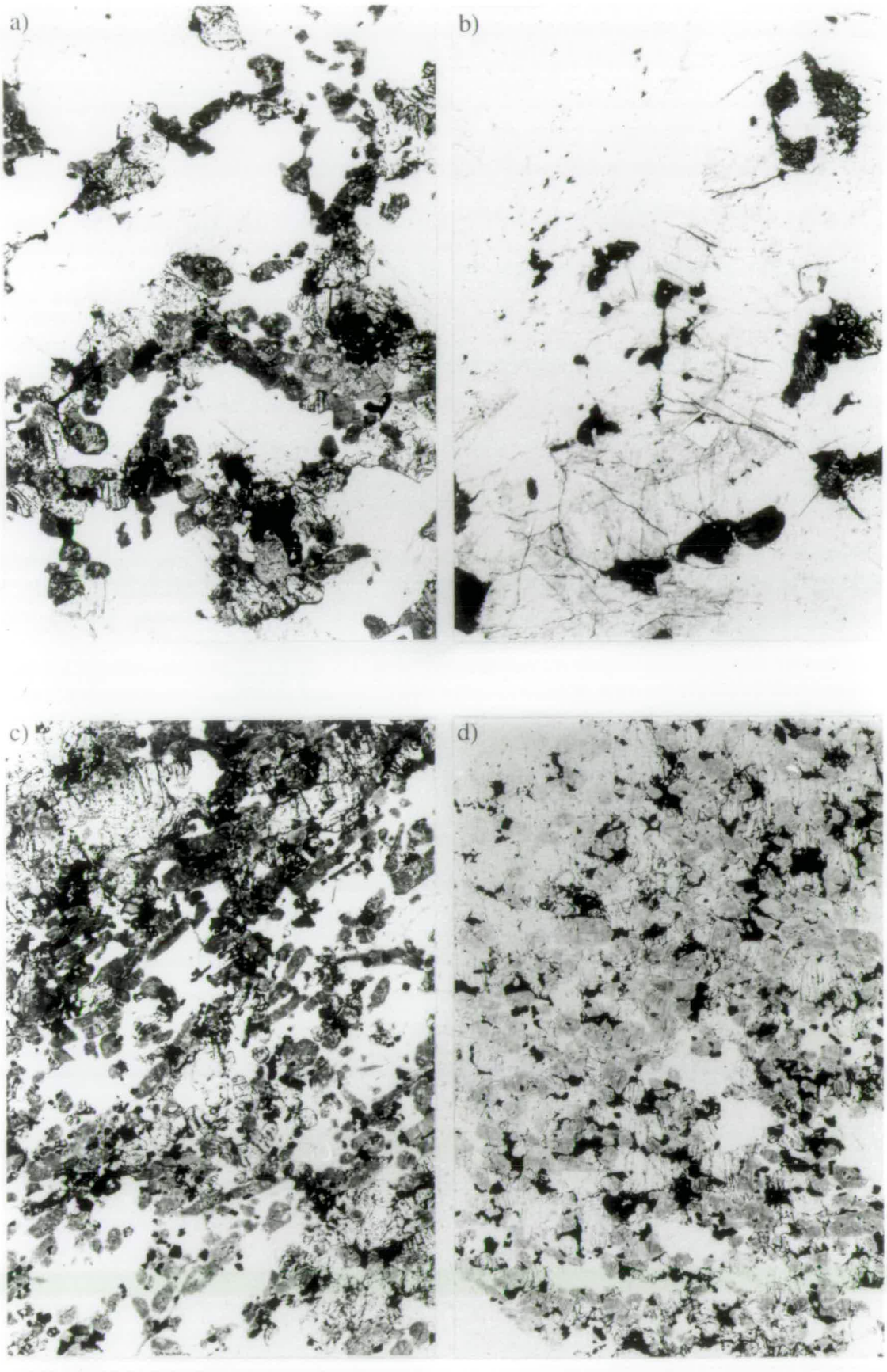
a)
b)
c)
d)

Plate 3.2

(a) Turbid feldspar in the host syenite between trough stacks, West Kûngnât. Sample 31, field of view 13mm x 21mm, ppl.

(b) Feldspar from Nunarssuit showing: i) a pleated rim along its lower left hand margin; ii) possible braid perthite in the lower left of the crystal and; iii) patch perthite midway up the right hand side of the crystal. Sample 4-34, field of view 3mm x 4mm, xpl.

(c) A swapped rim (running from top to bottom of photograph) between two feldspar grains from Nunarssuit. sample 4-34, field of view 0.75mm x 1mm, xpl.

(d) Irregularly zoned pyroxene grain from Nunarssuit, lighter shades of grey are enriched in the acmite component and depleted in the hedenbergite and diopside components. Sample 2-25, field of view 2mm x 3mm, ppl

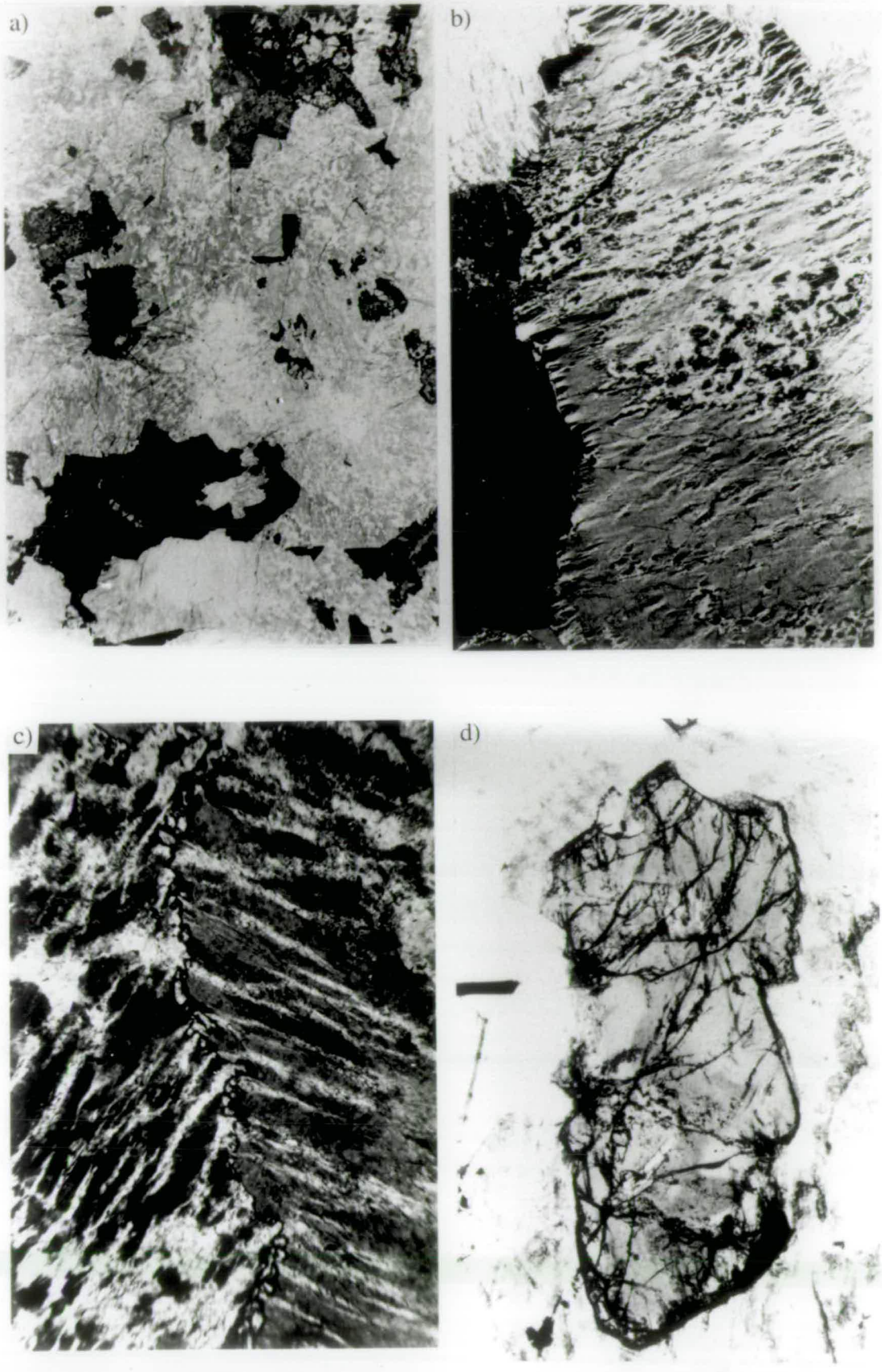
a)
b)
c)
d)

Plate 3.3

(a) Irregularly zoned pyroxene grain from Nunarssuit, lighter tones of grey are enriched in the acmite component and depleted in the hedenbergite and diopside components. Sample 2-21, field of view 15mm x 25mm, ppl.

(b) Pyroxene grain showing: i) exsolution of an Fe-Ti phase (straight black lines) and; ii) slight alteration to amphibole (irregularly shaped dark patches in body of crystal. Sample 4-34, Nunarssuit, field of view 15mm x 25mm, ppl.

(c) Most of the field of view is of a pyroxene being altered to amphibole (dark grey and black), the grain is still predominantly pyroxene. An altered olivine grain is present in the bottom right of the picture. Sample 2-25, Nunarssuit, field of view 15mm x 25mm, ppl.

(d) Central-left portion of picture is of a pyroxene being altered to amphibole, the grain is predominantly amphibole which shows well developed cleavage. Sample 10-66, Nunarssuit, field of view 35mm x 55mm, ppl

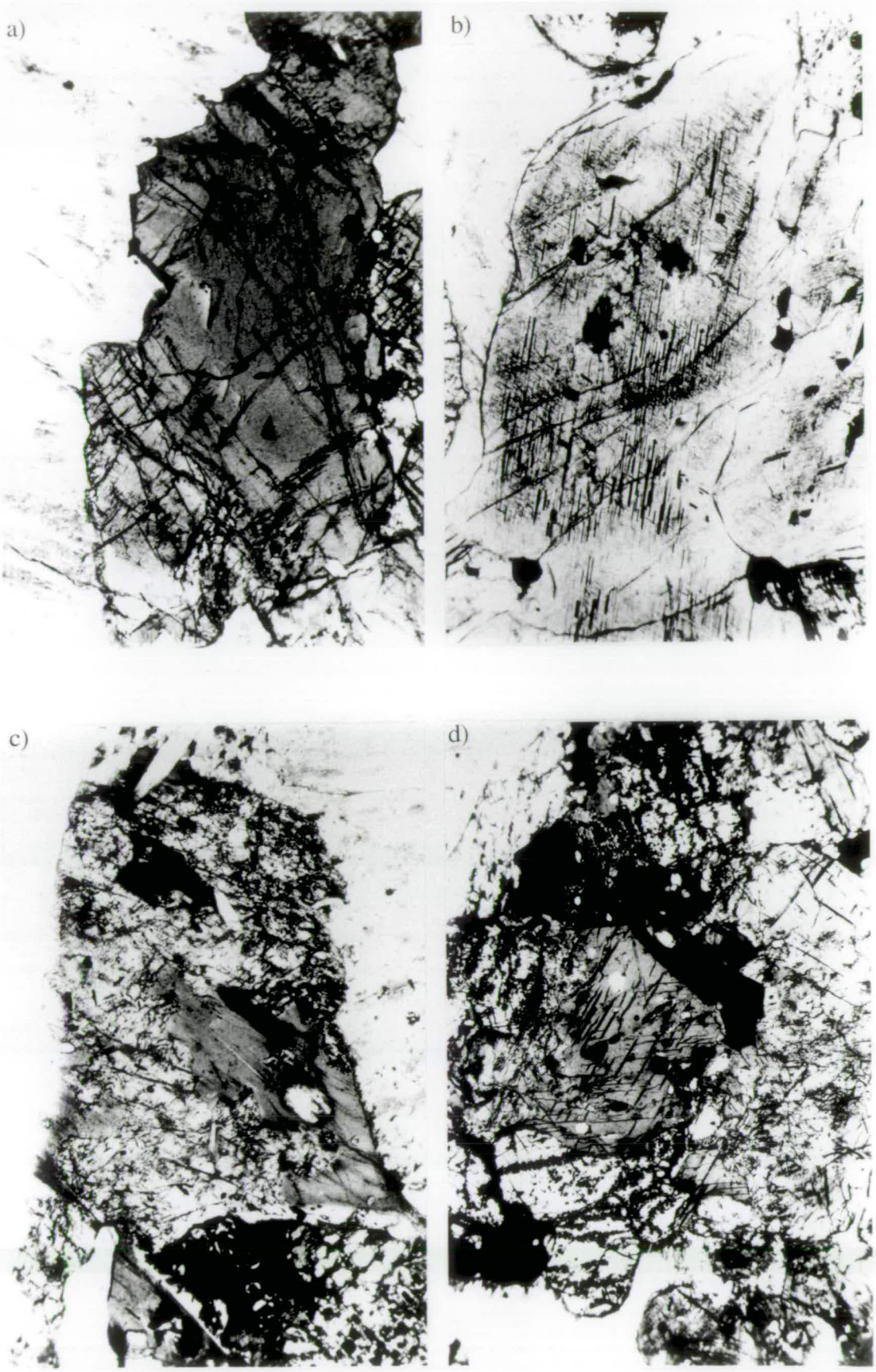
a)
b)
c)
d)

Plate 3.4

(a) Four olivine grains (centre of picture, light grey) with aligned cracks now occupied by magnetite. Also present are pyroxenes (darker grey) and an intercumulus opaque phase. Sample 1-10, Nunarssuit, field of view 25mm x 35mm, ppl.

(b) Biotite (dark grey) fringes around opaque phases. Sample 9-57, Nunarssuit, field of view 2mm x 25mm, ppl.

(c) Heavily altered pyroxene now largely replaced by opaque phases and sheet silicates. On the lower side of the altered grain the sheet silicate is seen penetrating along the pleats at the rim of a feldspar. Sample 2-21, Nunarssuit, field of view 4mm x 2.5mm, ppl.

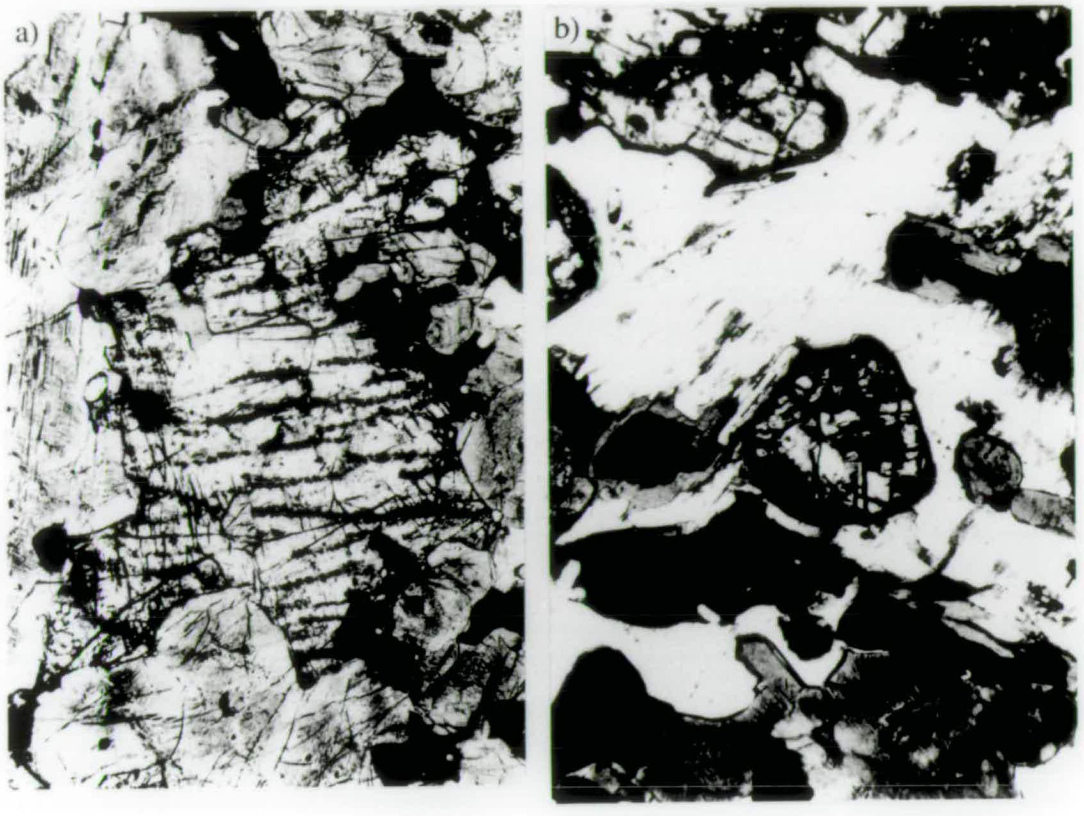
a)
b)

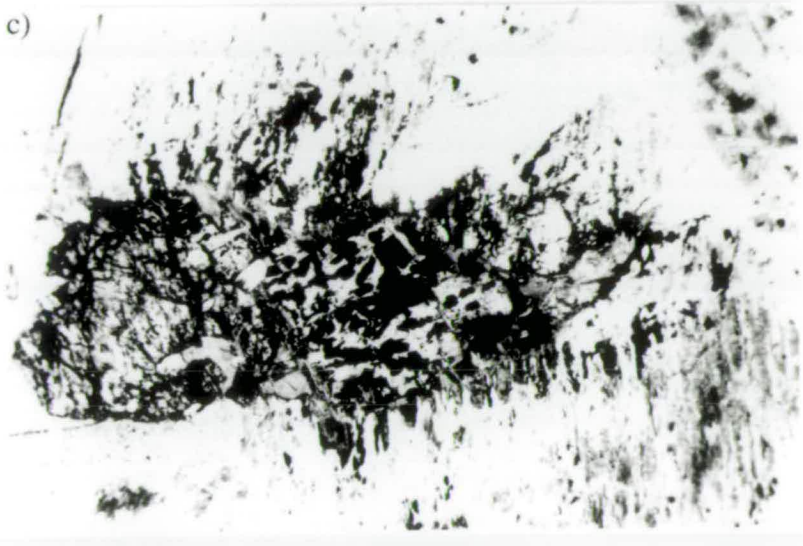
c)

Plate 3.5

(a) An apatite showing concentric magmatic zoning. Nunarssuit sample, field of view 0.1mm x 0.15mm, BSEI.

(b) The upper apatite shows at least a three phase growth history (growth of central magmatic zoned apatite, dissolution of right hand side of crystal, growth of outer crystal) and evidence for subsequent modification (curved zoning in top left of crystal). The lower grain shows a similar growth history. Nunarssuit sample, field of view 0.1mm x 0.15mm, BSEI.

(c) A zircon. The main zoning feature is post-crystallisation modification of the zoning resulting in the lighter grey irregular zones. Cracks both predate (are truncated by) and post date (cross) the irregular zoning. Sample 7-45, Nunarssuit, field of view 0.37mm x 0.34mm, BSEI.

(d) The zircon has an irregular core, is oscillatory zoned and is corroded along its upper right edge. The bevelled corners of an inner zone of the crystal indicate that the crystal was not growing continuously but underwent a period of erosion. Sample 4-34, Nunarssuit, field of view 0.15mm x 0.14mm, BSEI.

(e) The zircon shows evidence for several periods of growth, truncated zones are seen near the lower edge of the grain. Sample 14-108, West Kûngnât, field of view 0.7mm x 0.6mm, BSEI.

(f) The zircon shows magmatic oscillatory zoning near the centre of the grain and post-magmatic irregular zoning along the left edges of the grain. The irregular zoning is problematic; the dark zoning appears to be the latest (the edge of the dark zones are irregular and not parallel to the earlier formed oscillatory zoning) and yet cracks run through this and are truncated/cut by the lighter zones which seems to indicate that the lighter zoning is the latest. Sample 28M, West Kûngnât, field of view 0.4mm x 0.4mm, BSEI.

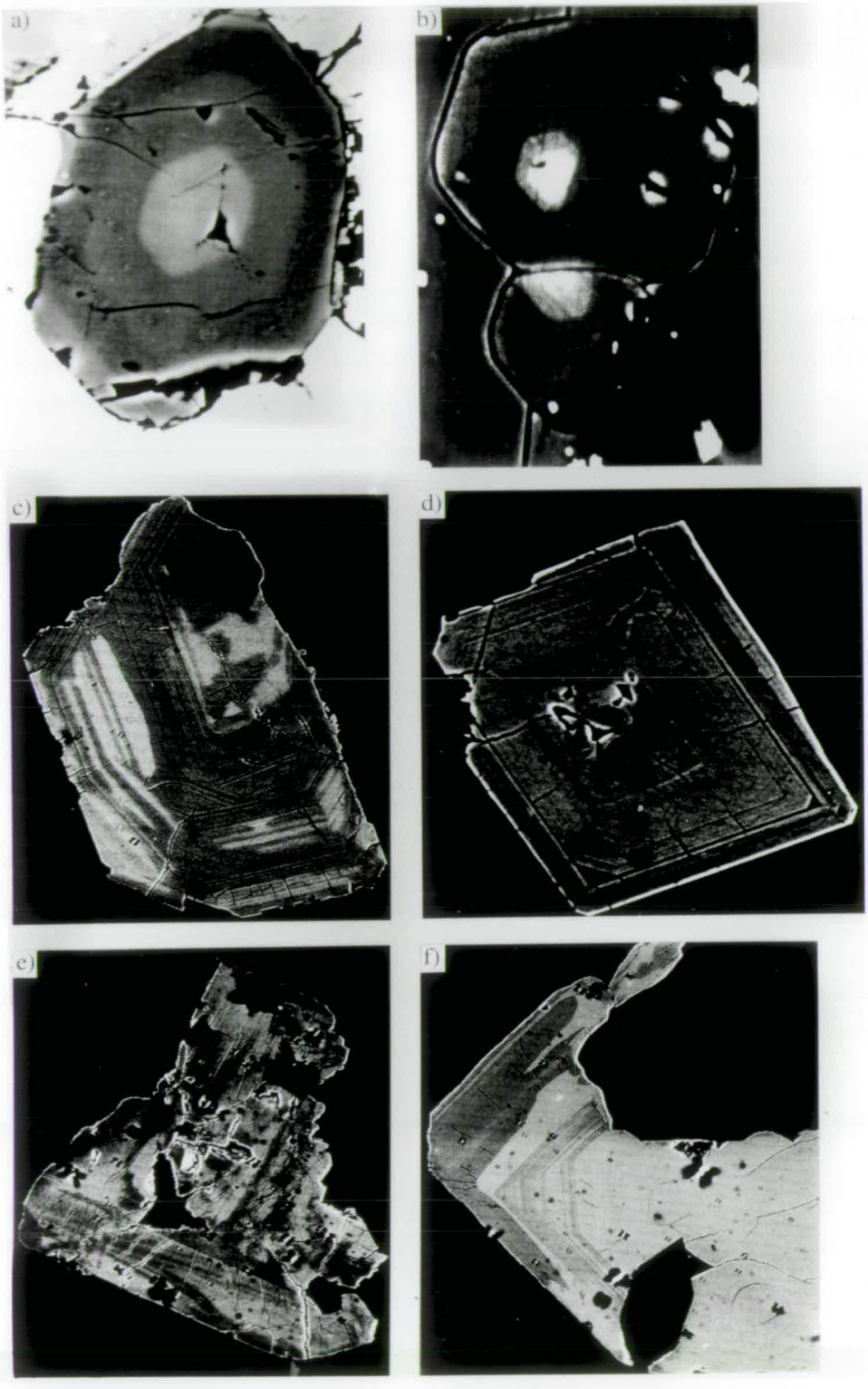
a)
b)
c)
d)
e)
f)

3.3 West Kûngnât

The reader is referred to Chapter 3.2 for a description of the melanocratic bases of layers from Nunarssuit; these are contrasted in the following sections with those from West Kûngnât. Following this, the melanocratic bases of the layers seen in West Kûngnât (Plate 3.6a) are compared with (i) the leucocratic material from the remainder of the layers (Plate 3.6b); (ii) the trough stack syenite (Plate 3.6c); and (iii) the host syenite that surrounds the trough stacks (Plate 3.6d). As in Nunarssuit, there is a general inverse correlation between the colour index of a rock and the degree of sub-solidus alteration it has undergone. The degree of alteration of the West Kûngnât rocks is greater than that in Nunarssuit. Table 3.4 shows the modes of various facies from the layered sequence.

Facies / Phase	Melanocratic portion of layer	Leucocratic portion of layer	Trough stack syenite	Syenite surrounding trough stack
Non-turbid feldspar	21	6	15	13
Turbid feldspar	30	84	30	67
Total feldspar	51	90	45	80
Pyroxene	20	6	17	4
Olivine	10	<1	8	3
Amphibole	13	3	22	8
Biotite	2	<1	5	<1
Opaque oxides and sulphides	3	<1	2	3
Apatite	<1	<1	1	1

Table 3.4: Modal content of the different facies from the West Kûngnât layered syenite expressed as percentages.

3.3.1 Feldspar

3.3.1.1 Petrography

Feldspars within the layers are like those in the Nunarssuit layers in terms of habit: those in melanocratic bases are anhedral; those in leucocratic layers are subhedral. It is not clear to what extent the feldspars are cumulus and to what extent they are post-cumulus. They are far more turbid than those in Nunarssuit; feldspars within the leucocratic portions of layers are more turbid than those in the melanocratic bases of layers. Feldspars are predominantly film and patch perthites (Plate 3.2b) with braid perthites being relatively rare compared to the Nunarssuit melanocratic layers. Feldspars in the host syenite around the trough stacks are the same in habit and degree of alteration as those in the leucocratic layers. Feldspars within the trough stacks themselves tend to be the same in habit but are more turbid than those in the melanocratic layers. Generally the more mafic a sample (higher colour index) the less turbid feldspar it contains (Fig. 3.3)

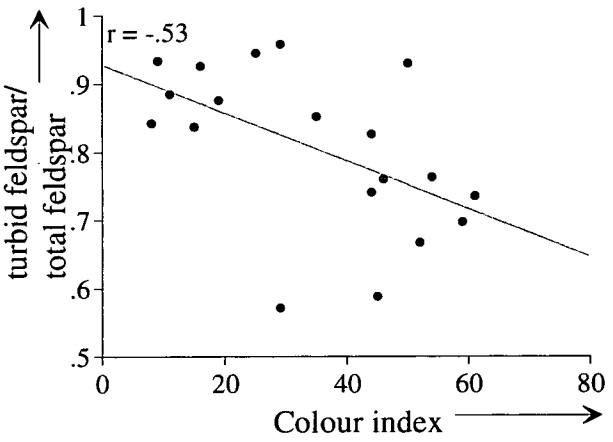

Fig. 3.3: Plot showing inverse correlation between colour index (= %vol mafic minerals in sample) and the proportion of feldspar in the sample which is turbid.

3.3.1.2 Cathodoluminescence petrography

Unlike in Nunarssuit, feldspars in all facies have high f.l.i.s (Table 3.5). This is in agreement with the findings of Finch (1990).

Facies	Average feldspar luminescence index	Relative alteration
Melanocratic base of layer	98	High
Leucocratic portion of layer	100	High
Trough stack syenite	83	High
Syenite surrounding trough stack	100	High

Table 3.5: Average feldspar luminescence indices for different West Kûngnât layered sequence facies.

3.3.1.3 Scanning electron microscopy

As in Nunarssuit, micro-pores are associated with optical turbidity of the feldspars.

3.3.2 Pyroxene

Pyroxene occurs as a cumulus phase. Pyroxenes in the melanocratic bases of layers and troughs tend to be the same in habit and degree of alteration as those in the melanocratic bases of the Nunarssuit layers. The pyroxenes in the leucocratic portions of the layers and in the host syenite tend to be more altered. As in Nunarssuit, the pyroxenes are variably altered to amphibole.

3.3.3 Olivine

Olivine occurs in lower concentrations in West Kûngnât than in Nunarssuit but is still a cumulus phase. Olivines in the melanocratic bases of layers and troughs tend to be the same in habit and degree of alteration as those in the melanocratic bases of layers of Nunarssuit. The olivines in the leucocratic portions of the layers and in the host syenite are more altered than those from the melanocratic facies; more magnetite and iddingsite are present. Often grains are completely psuedomorhped by magnetite and iddingsite.

3.3.4 Amphibole

Within the melanocratic bases of layers, the leucocratic bases of layers and the host syenite surrounding the trough stack amphiboles have the same habit as those seen in Nunarssuit. Amphibole is thought to be a post-cumulus phase or the product of subsolidus reactions. In the trough stacks large, centimetre-scale crystals of amphibole occur (Plate 3.5c). These are occasionally coarsely intergrown with biotite. The crystals contain irregularly shaped pyroxene, rounded olivines, opaque oxides and apatite crystals. The concentration of apatite within these amphiboles is far greater than the concentration of apatite within the rocks as a whole. These amphiboles are often irregularly zoned. The amphiboles appear to have originated by alteration of pyroxenes; their large size and the continued existence of pyroxene grains leads to the suggestion that once growth had been initiated these grains grew as a primary phase within a loosely consolidated crystal mush and not by alteration of pyroxene.

3.3.5 Biotite

Biotite is thought to be either a post-cumulus phase or the product of subsolidus reactions. Within all the facies biotite occurs as aggregates of small crystals in fringes on opaque oxides like the biotites in Nunarssuit and as discrete irregularly shaped grains up to 0.5mm in length. Within the trough stacks, biotite also occurs as large, centimetre-scale crystals. The large biotites are sometimes intergrown with amphibole. Like the large amphibole crystals in the trough stacks, the biotites contain irregularly shaped pyroxenes, rounded olivines, opaque oxides and apatites. The concentration of apatites in the biotite crystals is greater than is seen in the rock as a whole.

3.3.6 Minor phases

Apatite

As in Nunarssuit, apatite is a cumulus phase and occurs predominantly within the mafic phases. In the trough stacks, apatite is present to an exceptionally high level in the large crystals of biotite and amphibole. The relative proportions of the various types of apatite zoning are shown in Table 3.6, the significance of these results is discussed in Chapter 6.6. Upton (1960) reported that the proportion of apatite present in the syenites decreases up section; this trend was not observed in the present study. It could be the case that the sampled section was to small to observe the decrease in apatite up section.

Facies	Oscillatory (Fig. 3.2a)	Concentric (Fig. 3.2b)	Fracture (Fig. 3.2c)	No zoning
Trough stack	7	3	1	87
Large amphiboles and biotites within trough stacks	7	25	0	68
Syenite surrounding trough stacks	4	7	0	89
Melanocratic base of layer	4	12	3	81
Leucocratic portion of layer	7	12	3	78

Table 3.6: Average percentage of different zoning schemes in apatites from the West Kûngnât layered series.

Opaque oxides and sulphides:

The occurrence of these ilmenites, magnetites and Fe and Cu sulphides is the same as in Nunarssuit. Grains occur as discrete grains mantling other phases (post-cumulus) and as inclusions in olivines and pyroxenes (cumulus). Upton (1960) observed a decrease in opaque oxide concentration up section. As with apatites this trend was not detected in the present study, but this may be due to the smaller section sampled. Upton (1960) reported the occurrence of chalcopyrite, pyrrhotite and pentlandite in the Western Lower Layered Series, no chemical analyses were carried out on the sulphides in this study.

Other phases:

Sphene, zircon and carbonate are present in all facies. As in Nunarssuit the carbonate luminesces orange and is most likely to be calcite (Miller, 1988). Unlike Nunarssuit quartz is not present. Zircon zoning is discussed in Chapter 5.5.

3.3.7 Low temperature alteration products

Intergrowths of chlorite, amphibole and clay minerals occur as in Nunarssuit

Plate 3.6[2]

(a) Melanocratic base to a layer from West Kûngnât. White and very light grey grains are feldspar, higher relief and slightly darker grey grains are olivines, darker grains are pyroxene, very dark grey grains are biotite and amphibole and black grains are opaque oxides. The irregular grey shape near the middle of the picture is a hole in the slide. Sample 15-113, field of view 14mm x 22mm, ppl.

(b) Leucocratic material form mid-way up a layer in West Kûngnât. White and very light grey grains are feldspar, higher relief and slightly darker grey grains are olivines, darker grains are pyroxene, black grains are amphibole, biotite and opaque oxides. Sample 15-116, field of view 14mm x 22mm, ppl.

(c) Melanocratic sample from within a trough from the trough stack locality of West Kûngnât. The large black irregular shapes are each aggregates of two or three biotite and/or amphibole crystals; the small white grains within the amphiboles and biotites are apatites, other grains within the amphiboles and biotites are olivines and pyroxenes. Sample 30, field of view 14mm x 22mm, ppl.

(d) Leucocratic syenite from between the troughs at the trough stack locality, West Kûngnât. Sample 29, field of view 14mm x 22mm, ppl.

[2]Plates 3.1a to d and Plates 3.6 a to d are all the same scale.

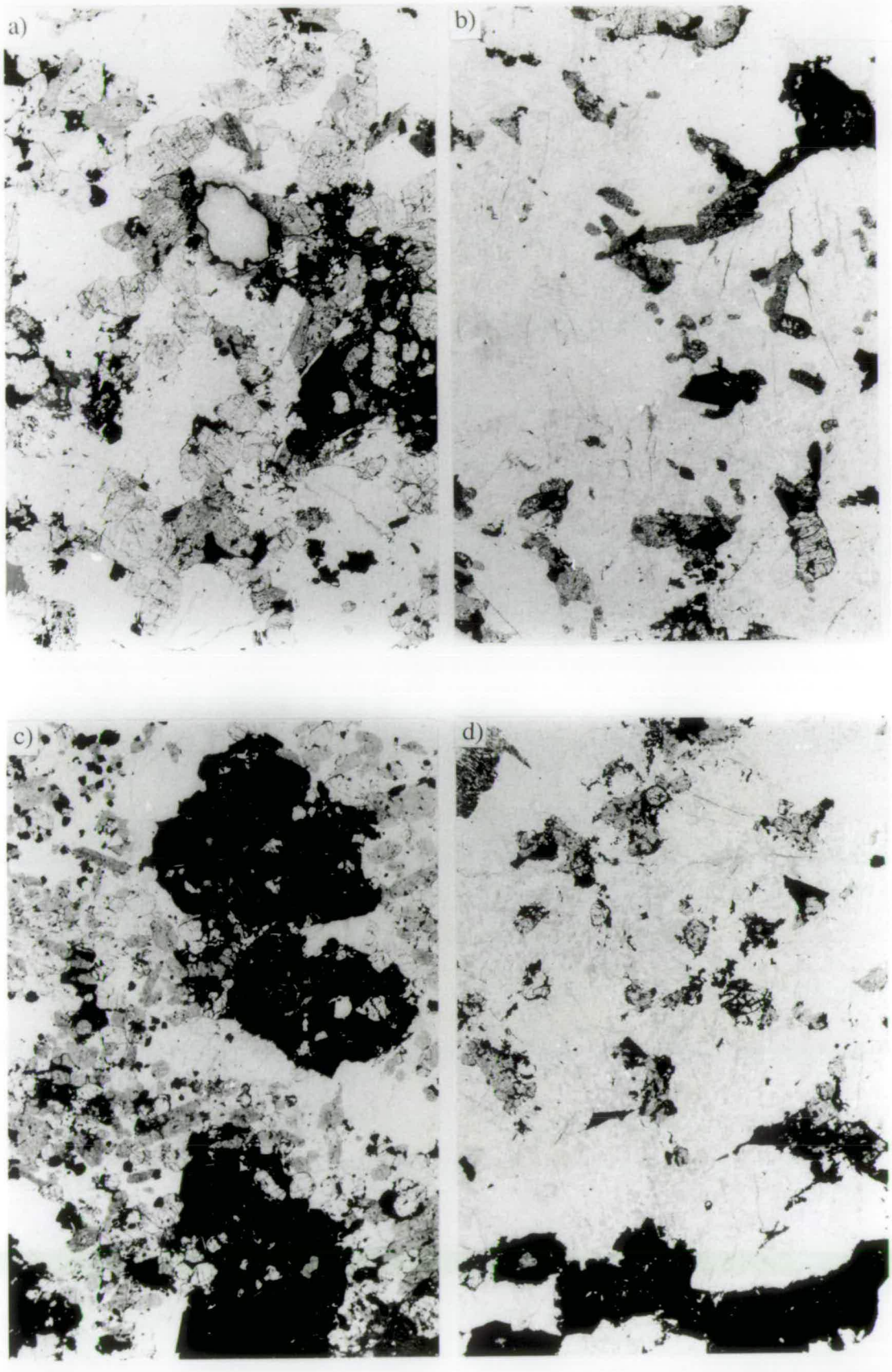
a)
b)
c)
d)

3.4 Grain size analysis of Nunarssuit and West Kûngnât

Grain size analysis is important for many reasons. It is necessary to know grain dimensions to calculate accurate settling rates and critical viscosities and to see if grains in the same horizon are hydraulically equivalent (see Chapter 7.7). Graded layers may be size graded with a decrease (normal grading) or increase (reverse grading) in grain size up section. From purely qualitative observations no grain size variation for pyroxene and olivine appears to be present between the melanocratic facies in either Nunarssuit or West Kûngnât. This was confirmed quantitatively. Qualitative observations indicate that the rhythmic layers of Nunarssuit and West Kûngnât are not size graded. Unfortunately insufficient grains occur in the leucocratic facies to carry out this analysis. On the grounds that the study confirmed qualitative observations on grain size variations between the different melanocratic facies it is thought that there is no size grading in the layers of either Nunarssuit or West Kûngnât.

In recent years much progress has been made in determining actual grain dimensions from two dimensional thin sections (Naslund *et al.*, 1986; Marsh, 1988; Cashman and Marsh, 1988; Renner, 1989). An accepted measurement of grain size is to measure the long and short apparent axes (Fig. 3.4)

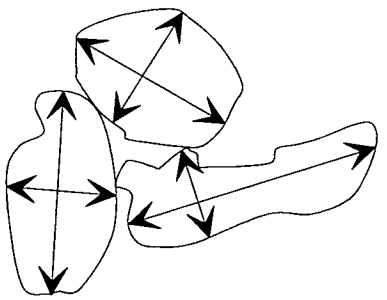

Fig. 3.4: Long and short apparent axes for three randomly shaped grains. The long axis is the length of the grain measured parallel to the direction of maximum elongation of the grain, the short axis is the maximum distance across the grain measured perpendicular to the direction of maximum elongation.

Frequency distribution plots of both the long and short apparent axes produce plots with an uneven bimodal distribution. The peaks on these graphs correspond to real axial lengths (Fig. 3.5).

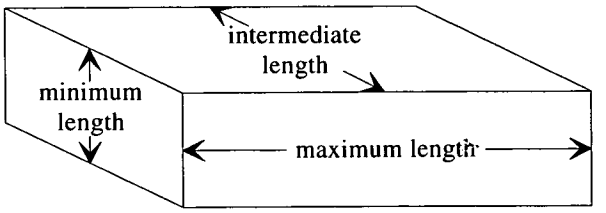

Fig. 3.5: Diagram showing both the maximum, intermediate and minimum lengths of an ideal cuboidal crystal.

A plot of the apparent long axis gives the long and intermediate axes whilst a plot of the apparent short axis gives the intermediate and short axes (Mingard, 1990).

Renner (1989) measured the dimensions of olivine crystals in a komatiite, the reported error of these measurements was 2% of the mean length of the crystals. Measurements were made using a video camera and digitiser tablet. The video camera pictures of thin sections were transferred to a computer where lengths were measured using digitising software. Using the same system Mingard (1990) estimated that errors were of the order of 5% of the measured length. This system was not available for use so the analysis was performed manually. Photographs of thin sections were taken, 6 A4 photographs covering one 3cm by 2cm thin section. Measurements were taken directly from the photographs using a ruler. A photograph of a grid of 1mm squares was taken to check for distortion at the edges of the photographs; no distortion was present. This manual system avoids the problems of resolution limit and grain misidentification possible with an automated system. The problem of large grains being more frequently intersected by the plane of the section with respect to small grains still remains; this can lead to a biasing of the measurements in favour of large grains.

The majority of pyroxene and olivine grains are sub to euhedral and it was assumed that little or no adcumulus growth had occurred on these grains. No attempt was made to analyse feldspars. Whilst feldspar was obviously a cumulus phase the irregular grain shapes now present indicate that substantial postcumulus growth has occurred. No regular zoning is preserved so it is impossible to tell what the original shape of the feldspar grains was. The results of the present study are summarised below in Table 3.7.

Table 3.7 Summary of results of grain size analysis. Dimensions in mm, a, b and c represent the short, intermediate and long axes respectively.

Intrusion	Sample	Olivine			Pyroxene		
		a	b	c	a	b	c
West Kûngnât	18-141 (Unit 4)	0.65	0.65	1.25	0.5	0.8	1.5
	15-113,115 (Unit 4)	0.65	1.18	1.25	0.45	1.15	1.48
	13-103 (Unit 3)	0.5	0.9	1.6	0.55	0.8	1.4
	29 (Host, Unit 2)	0.5	0.7	1.2	0.5	1	1.5
	30 (Trough, Unit 2)	0.5	0.55	0.8	0.55	1.05	1.5
Nunarssuit	10-66 (Unit 7)	0.65	0.65	1.23	0.6	0.6	1.0
	9-60 (Unit 5)	0.45	0.6	1.4	0.45	0.6	1.15
	9-56 (Unit 5)	0.6	0.65	1.45	0.45	0.7	1.05
	8-51 (Unit 3)	0.6	0.6	1.3	0.65	0.65	1.1
	9 (Unit 1)	0.5	0.6	1.37	0.5	0.7	0.9

Pyroxenes from West Kûngnât are slightly larger than those from Nunarssuit. Olivines within the melanocratic troughs in West Kûngnât are slightly smaller than those in the other West Kûngnât facies. However grain sizes, shapes and configurations tend to change as rocks cool, in order to obtain a lower surface energy (Hunter, 1987). In slowly-cooled plutonic rocks this may lead to very different textures from those produced when the crystals first come into contact. This is discussed in Chapter 6.9.

3.5 A comparison of the petrography of the layered successions of Nunarssuit and West Kûngnât.

In both Nunarssuit and West Kûngnât feldspars are predominantly perthitic, turbid, have pleated and swapped rims and are irregular in shape. In Nunarssuit there is a marked inverse correlation between the colour index of a rock and the proportion of feldspar that is turbid in that sample (Fig. 3.1). This correlation is also seen in West Kûngnât (Fig. 3.3) but it is less obvious. The f.l.i. is high in all West Kûngnât facies (Table 3.5) whilst in Nunarssuit it is lower in the melanocratic facies than in the leucocratic facies (Table 3.4).

The pyroxenes in West Kûngnât show better developed irregular zoning along their rims and cracks to a pale green colour than those from Nunarssuit. Pyroxenes in melanocratic xenoliths from Nunarssuit and those in slump structures in Nunarssuit have a preferred orientation. Olivines are modally more abundant in the melanocratic facies of Nunarssuit than in West Kûngnât (Tables 3.1 and 3.4). They appear to be slightly more altered in West Kûngnât than in Nunarssuit. In West Kûngnât amphiboles and biotites occur as oikocrysts in the trough stacks.

In the trough stacks of West Kûngnât apatites are concentrated in the oikocrysts of amphibole and biotite. In West Kûngnât a higher proportion of apatites show no zoning than in Nunarssuit (see Chapter 6.6). In both intrusions ilmenite is the most abundant opaque oxide phase. Magnetite (exsolved and oxidised) and Fe-Cu sulphides are also present. Both intrusions contain zircon, sphene and calcite. Quartz is present in Nunarssuit. Allanite is a very scarce component in the West Kûngnât layered sequence.

Average grain dimensions are shown in Table 3.7. Pyroxenes and olivines have roughly the same dimensions in both intrusions.

Chapter 4: Major element mineral chemistry

4.1: Introduction

Electron probe analysis was carried out on the rims and cores of pyroxenes and olivines and on biotites, amphiboles, feldspars, ilmeno-magnetites, apatites and zircons. For olivines and pyroxenes, only core compositions are plotted, there was no consistent variation between rims and cores. Operating conditions and detection limits are detailed in Appendix B.2. Typical analyses are presented in Appendix C. Results are presented for the layered syenites of Nunarssuit and West Kûngnât. The mineral chemistry of the two layered series is then briefly contrasted.

4.2: Nunarssuit.

Samples are grouped according to locality; leucocratic and melanocratic samples are therefore grouped together. No compositional variation in the minerals from adjacent leucocratic and melanocratic layers has been detected.

The samples are arranged in stratigraphic order; sample number 9 is the lowest and sample number 21 is the highest (see Fig. 2.1 for stratigraphic column). Samples 6 and 7 represent melanocratic syenite within the troughs.

4.2.1: Feldspar

Most feldspars in Nunarssuit are coarse perthites. To obtain an analysis that represents the bulk chemistry of the hyper-solvus feldspar which first crystallised it is necessary either to analyse braid perthite or to analyse large areas of patch perthite and then average the analyses (Brown *et al.*, 1983). Feldspar bulk compositions fall across the anorthoclase-sanidine boundary (Fig. 4.1). It appears that whereas feldspars from the rhythmically layered facies can not be differentiated by chemical means, those from the lower melanocratic unit (DL 9, Unit 5) are slightly more anorthite-rich, $An_{1.5\text{-}2.5}$ as opposed to $An_{<1.5}$. According to Nekvasil (1992) this implies a higher minimum crystallisation temperature. The feldspars which were analysed from DL 9 are texturally identical to those in melanocratic samples from other drill localities. It appears that the higher An content in DL 9 cannot be explained by differences in texture but must relate to the conditions of formation of the thick melanocratic layer (Unit 5).

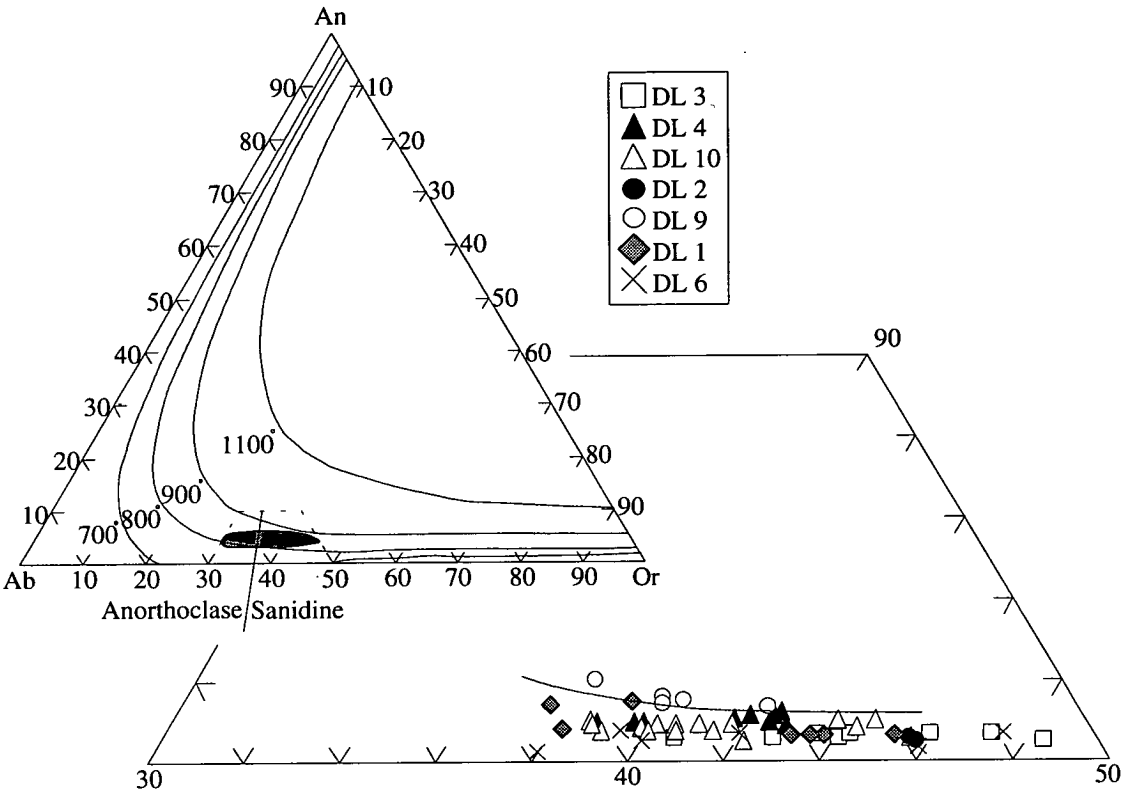

Fig. 4.1: Plot showing the composition of feldspars from the Nunarssuit layered syenite in terms of the albite, orthoclase and anorthite components. Superimposed on this are thermal contours for anhydrous conditions at 1kb (Nekvasil, 1992). These contours show minimum crystallisation temperatures.

Plots of Fe^{2+} (Fig. 4.2a) and Ba (Fig. 4.2b) against the fractionation index K-Ca show no trend, unlike the YGDC (Mingard (1990) where there is a positive correlation.

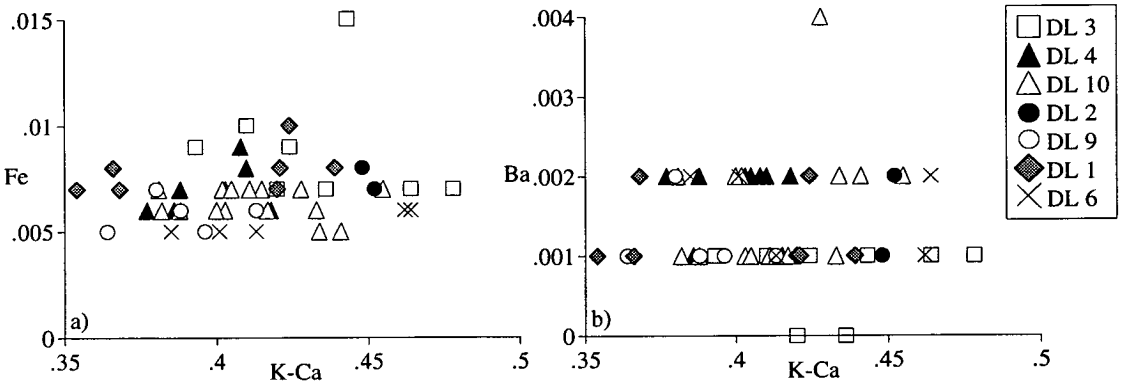

Fig. 4.2: a) total Fe as Fe^{2+} and b) Ba in feldspars from the layered syenite of Nunarssuit plotted against a feldspar fractionation index K-Ca.

4.2.2: Pyroxene

There is a general decrease in iron content of pyroxenes up section (Fig. 4.3).

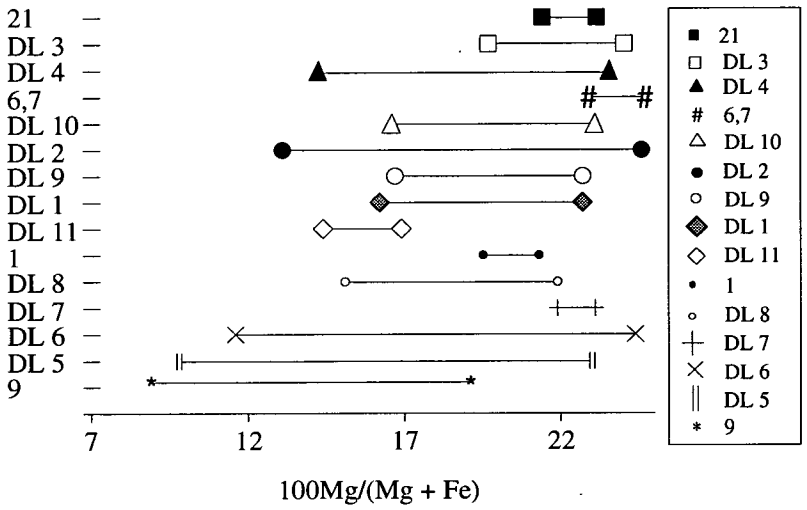

Fig. 4.3: Variation in Mg number up section in pyroxenes from the Nunarssuit layered syenites. Points show the maximum and minimum Mg number. Sample 9 is from below and sample 21 from above the layered zone. (See Appendix A for specimen localities)

All pyroxenes belong to a single high-Ca series and have <1 wt.% Na_2O. Analyses have been recast for Fe^{2+} and Fe^{3+}assuming that Fe^{3+} is equal to the sum of Na^+ and K^+ and that all remaining iron is Fe^{2+}. From Fig. 4.4 it can be seen that all compositions lie in the ferrosalite or hedenbergite fields of Deer *et al.* (1966). The pyroxenes define a field which plots on fractionation trends defined by pyroxenes from other over- and under-saturated complexes (Fig. 4.5); no fractionation trend is seen in terms of Di-Hd-Ac. Pyroxenes from 9, DL 5 and DL 6 are relatively enriched in acmite as is sample 2-27 from DL 2. An irregular variation in colour is seen in some pyroxenes. The change in body colour from brown to green correlates with enrichment in the acmite component with accompanying depletion in the diopside and hedenbergite components along crystal edges and cracks. Due to the irregular nature of this zoning it is ascribed to subsolidus processes (Chapter 6.3).

Aluminium (Fig. 4.6a) shows a strong negative correlation with Mg/(Mg+Fe) whilst only a slight negative correlation is apparent between Ti (Fig. 4.6b) and Mg/(Mg+Fe). This behaviour is similar to that observed in pyroxenes from Klokken (Parsons, 1979), Tugtutôq Central Complex (Upton *et al.*, 1990), and the YGDC (Mingard, 1990). All the samples have sufficiently low Al(vi) to fall within the field of igneous rocks of Aoki and Kushiro (1968).

When Al(iv) is plotted against Ti the majority of compositions lie below the line Al(iv)=2Ti (Fig. 4.7). This indicates that unlike the YGDC pyroxenes (Mingard, 1990) the pyroxenes are free of Ca-Ti and Ca- Tschermak's' molecule ($CaTiAl_2SiO_6$

and $CaAl_2SiO_6$ respectively). However, most of the aluminium in the pyroxenes is Al(iv). Both Ti and Al correlate negatively with Si but positively with calcium. The substitution $M^{2+} + 2Si^{4+} \rightarrow Ti^{4+} + 2Al^{3+}$ is therefore probably present, but in insufficient quantity to produce Ca-Ti-Tschermak's molecule.

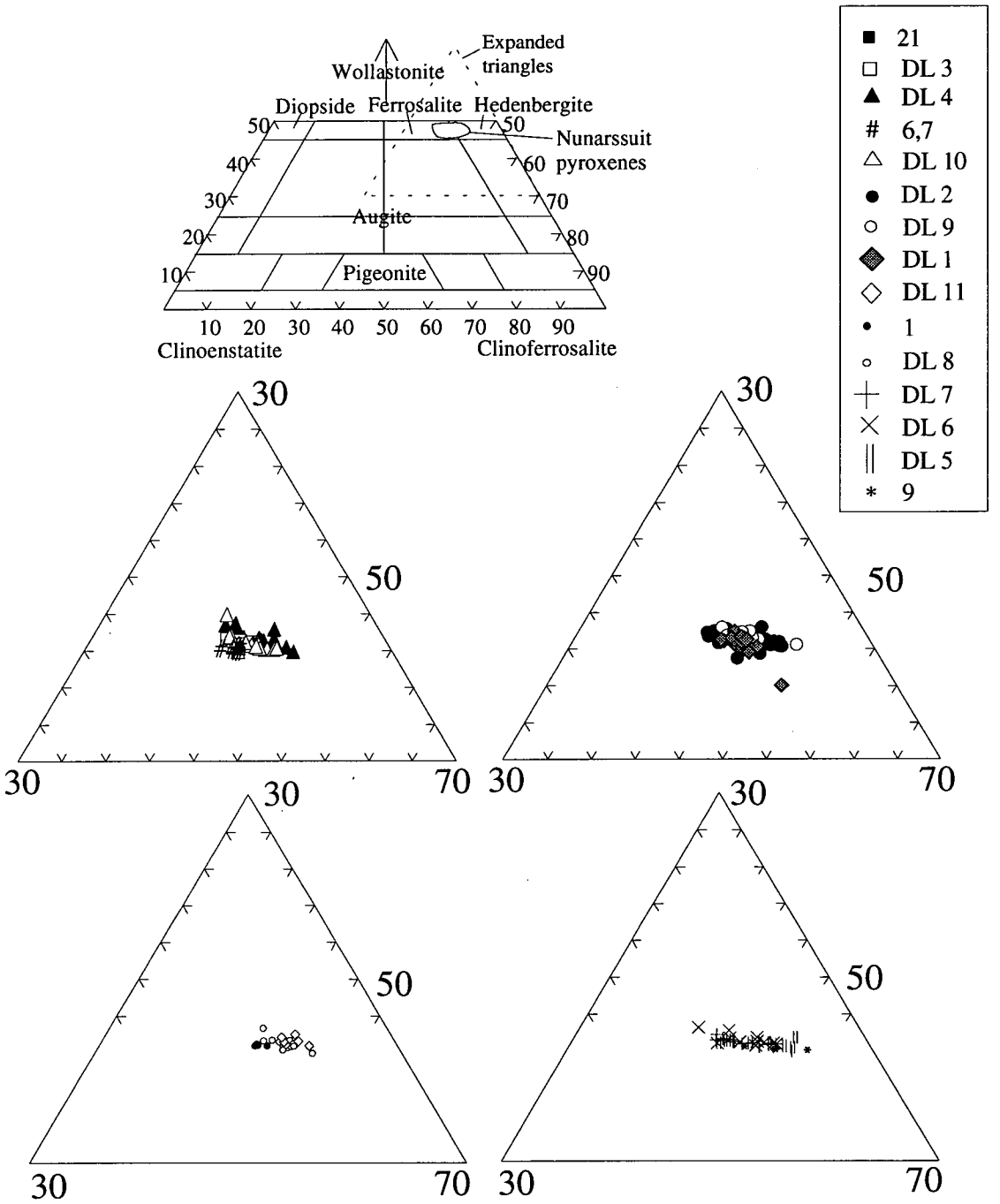

Fig. 4.4: Composition of the Nunarssuit layered syenite pyroxenes. Chemical field boundaries from Deer *et al.* (1966). Clinoenstatite = Mg, clinoferrosalite = Fe^{2+}+Mn, wollastonite = Ca (atoms per 4 oxygens)

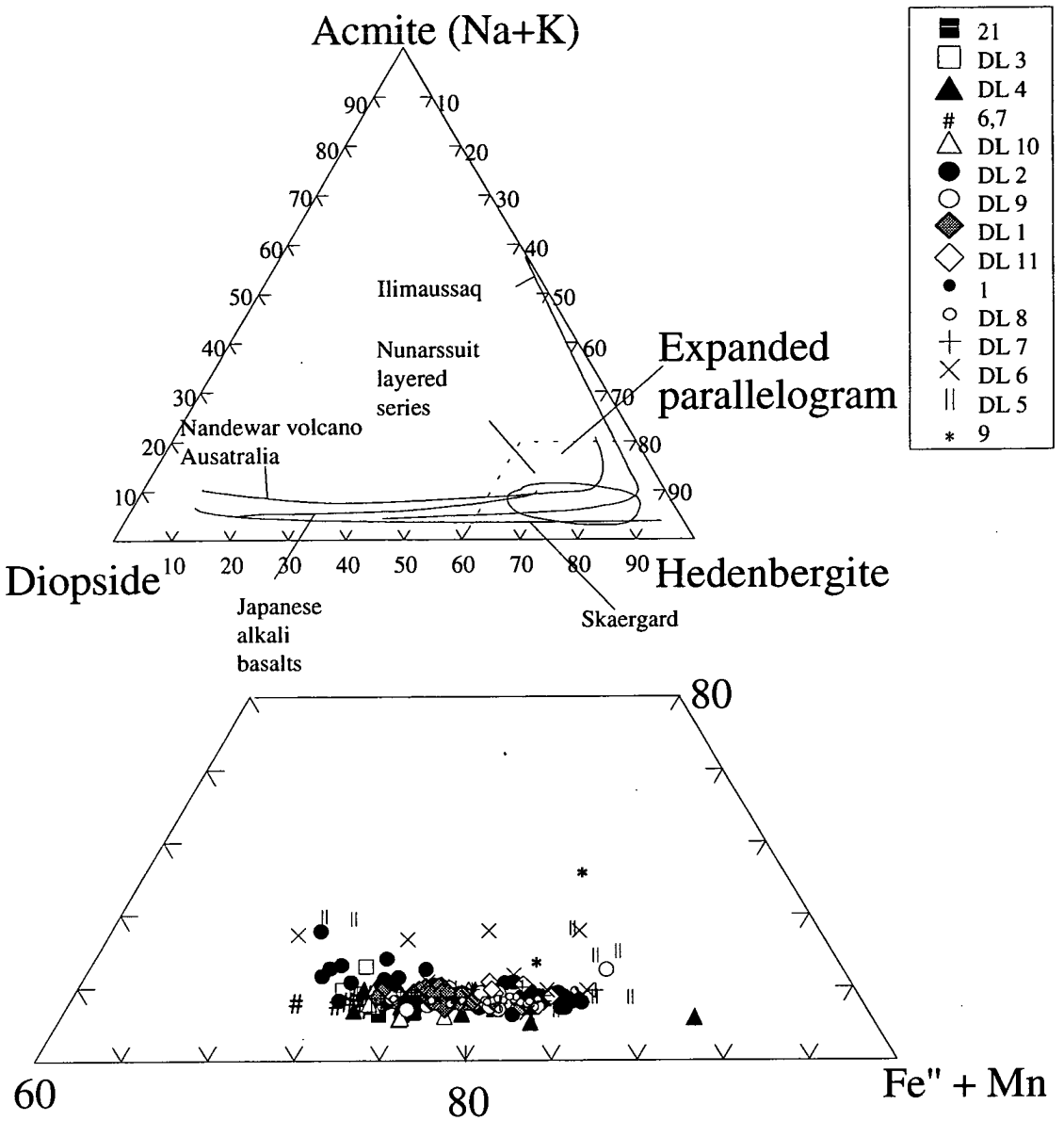

Fig. 4.5: Plot of Acmite (Na+K), Diopside (Mg) and Hedenbergite (Fe^{2+}+Mg) for pyroxenes (atoms per 4 oxygens) from Nunarssuit layered syenite. Trends from over-saturated (Skaergård, Japanese alkali basalts and Nandewar volcano) and under-saturated (Ilímaussaq) complexes are superimposed on the plot for comparison.

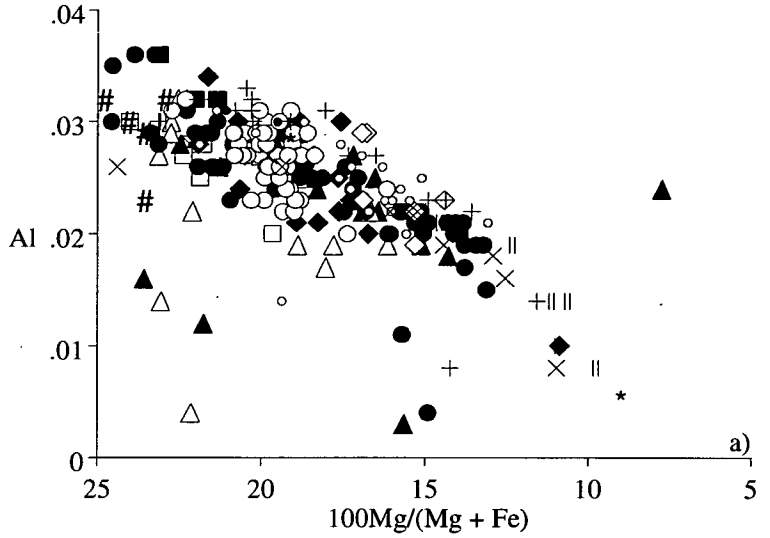

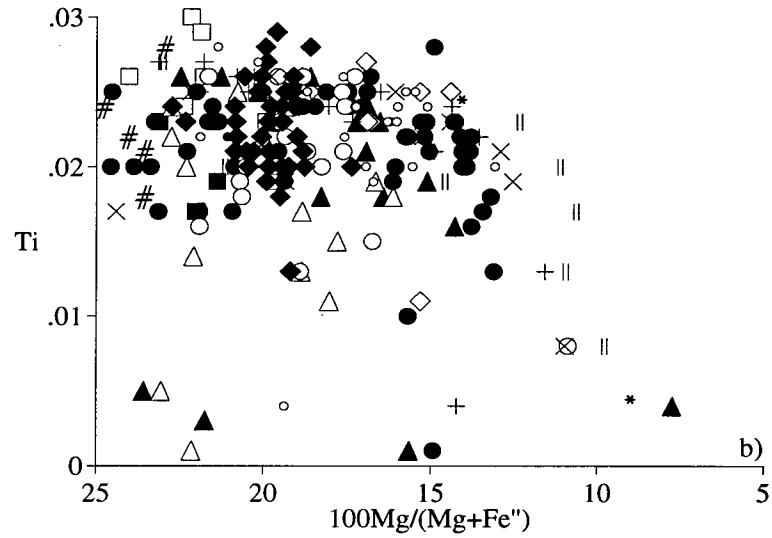

Fig. 4.6: a) Al and b) Ti plotted against 100*Mg no. for pyroxenes from the Nunarssuit layered syenite.

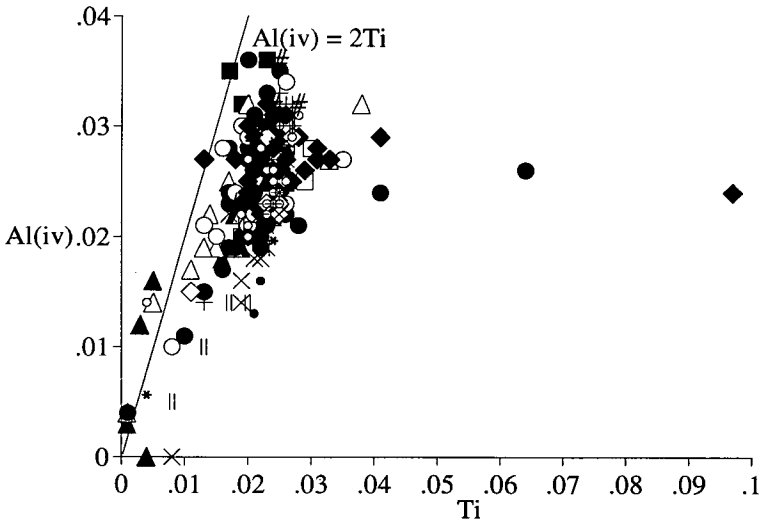

Fig. 4.7: Al (iv) (=2-Si) against Ti for pyroxenes from the Nunarssuit layered syenite.

4.2.3: Olivine

Olivines lie in the range Fo_{10}-Fo_3 (Fig. 4.8, 4.9). Variation within samples covers this range of compositions. There is a decrease in the iron content of olivines up section, particularly if DL 11 and 1 (autoliths), DL 9 and DL2 (thick melanocratic units and troughs) are ignored.

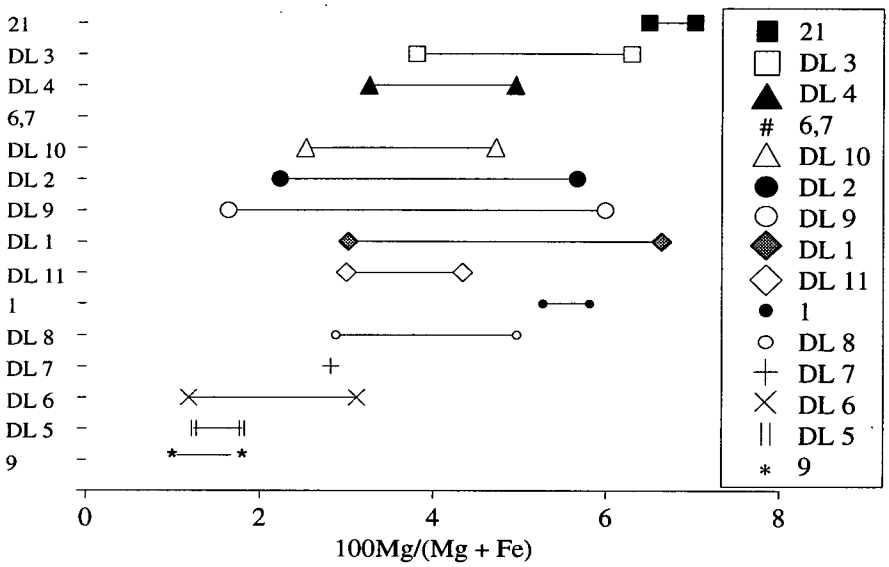

Fig. 4.8: Variation in Mg number up section in olivines from the Nunarssuit layered syenites. Points show the maximum and minimum Mg number. Sample 9 is from below and sample 21 from above the layered zone. (See Appendix A for specimen localities)

The maximum Ca content of the olivines is 0.18 wt.% (Fig. 4.10); most of the samples fall within the plutonic field of Simkin and Smith (1970), the others fall in the hypabyssal field. The olivines are less Ca-rich than those of the YGDC (Mingard, 1990) but are similar to those of the laminated and granular syenites of Klokken (Parsons, 1979). In the case of the layered syenites of Nunarssuit, Ca variation in olivines can not be due to differences in the height of the olivines in the intrusion itself since there is no consistent variation in Ca content of the olivines with stratigraphic height. Jurewicz and Watson (1988) suggested that a number of factors such as silica activity and melt composition could control the Ca content of olivines. Olivines from melanocratic and leucocratic layers have the same Ca content; Ca partitioning in olivines is therefore not directly related to the layering process.

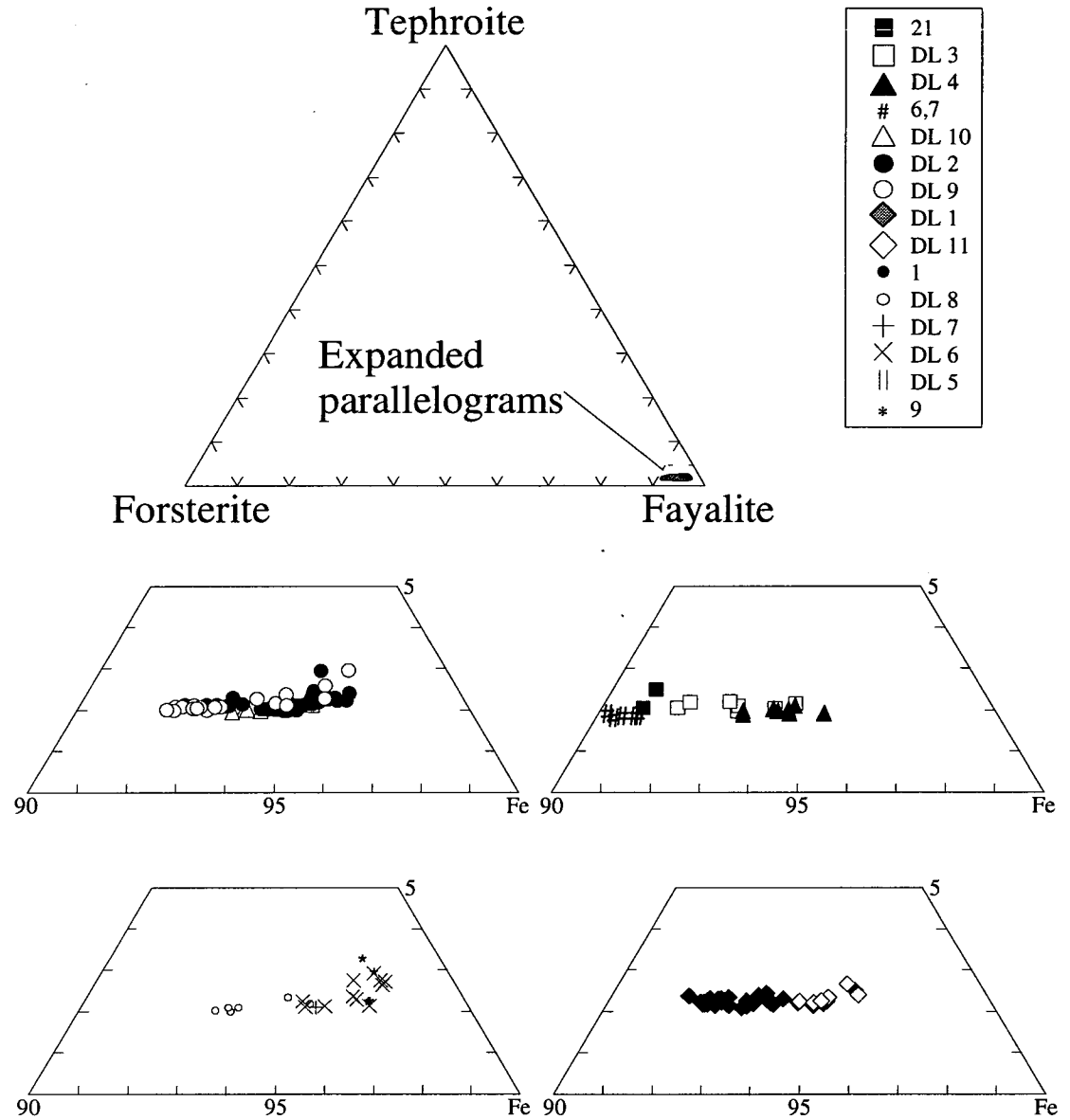

Fig. 4.9: Plot showing composition of olivines from Nunarssuit layered series in terms of Fe (fayalite), Mg (forsterite) and Mn (tephroite) end members.

Manganese increases regularly with Fe^{2+} from 1.6 wt.% to 2.6 wt.%. This range is similar to those reported by Simkin and Smith (1970) and for other Gardar intrusions such as Klokken (Parsons, 1979), Kûngnât (Chapter 4.2.3), the YGDC (Mingard, 1990) and the giant dykes of Isotoq (Becker, 1984). Chromium (maximum 0.03 wt.%), titanium (maximum 0.04 wt.%), aluminium (maximum 0.02 wt.%) and nickel (below detection limits) were present only in trace amounts. No regular zoning was detected in the olivines.

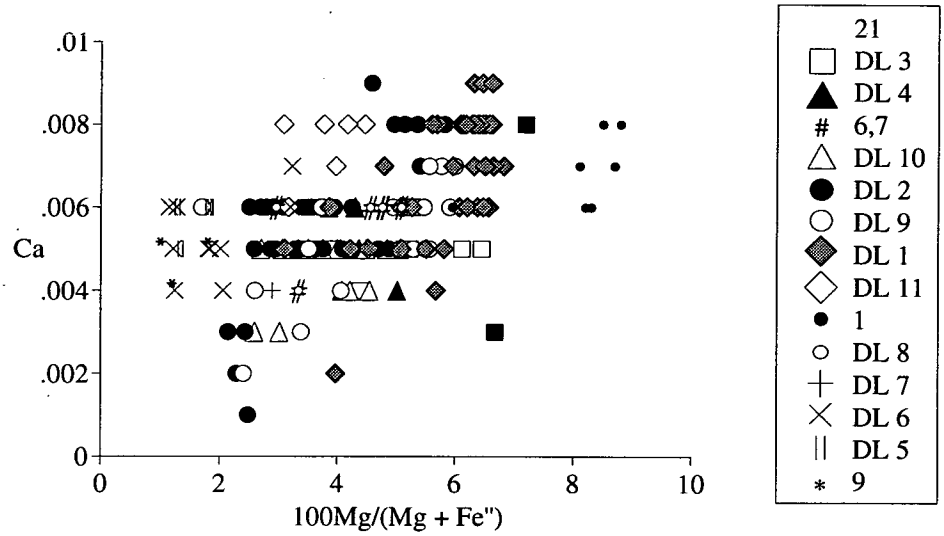

Fig. 4.10: Calcium content of Nunarssuit syenite olivines.

4.2.4: Amphibole

Amphiboles are considered to be secondary, formed by the alteration of pyroxenes (see Chapter 6.4). All iron is treated as Fe^{2+} since the complexity of the amphiboles prevent Fe^{3+} being calculated (Droop, 1987). Amphiboles get slightly more Mg rich up through the stratigraphy (Fig. 4.11a). The relatively Mg rich points from DL 2 are for sample 2-28.

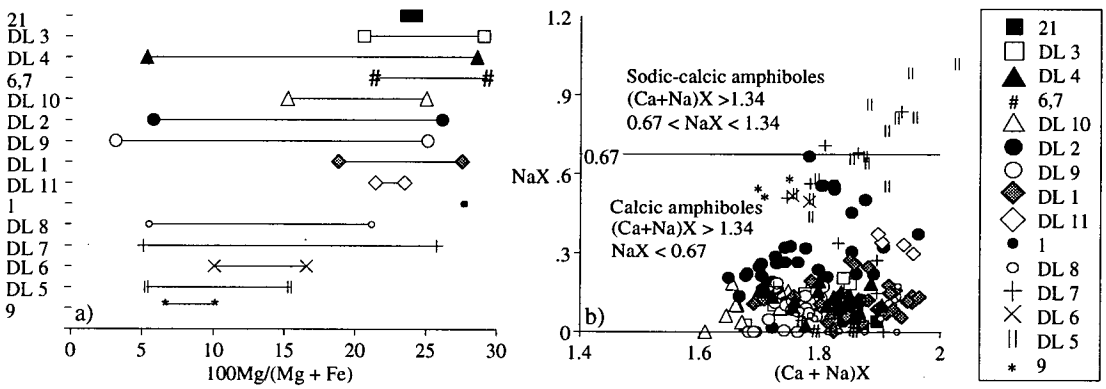

Fig. 4.11: a) variation in Mg number up section in amphiboles from the Nunarssuit layered syenites. Points show the maximum and minimum Mg number. Sample 9 is from below and sample 21 from above the layered zone. (See Appendix A for specimen localities), b) plot of Na in the X site against Ca+Na in the X site (atoms per 23 oxygens) for amphiboles form the Nunarssuit layered syenite shows that most of the amphiboles are classified as calcic amphiboles under the scheme of Leake (1978).

Nunarssuit syenite amphiboles are largely classed as calcic though some are sodic-calcic in the system of Leake (1978), Fig. 4.11b. The calcic-amphiboles are sodium-

rich, particularly DL 6 and sample 9. The sodic-calcic amphiboles are from localities DL 5 and 7. These samples contain quartz, possibly as a late-stage phase derived from magmatic or hydrothermal fluid.

The sodic-calcic amphiboles are katophorites, the calcic-amphiboles range from silicic ferro-edenites to ferro-pargasites; ferro-edenite is the most common composition (Fig. 4.12).

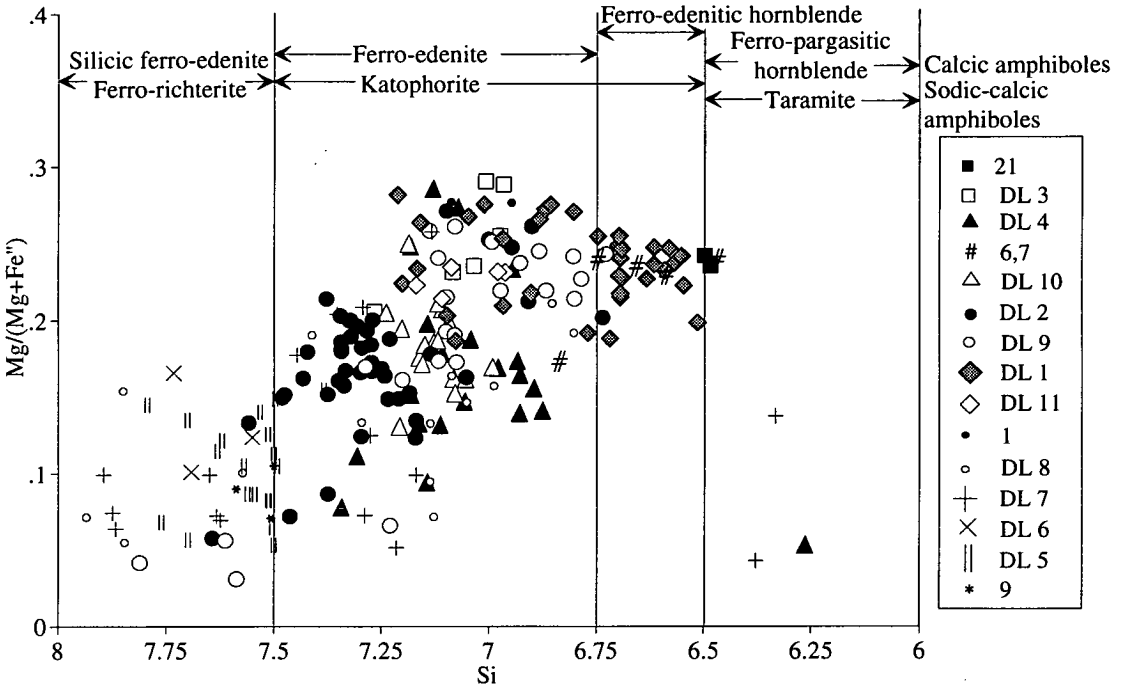

Fig. 4.12: Mg/(Mg+Fe) against Si (atoms per 23 oxygens)for amphiboles. Field boundaries from Leake (1978).

Fig. 4.13a shows compositions plotted on a diagram of Al(iv) + Ca against Si + Na + K after Becker (1984). Both the trend from calcic to sodic-calcic amphiboles (down the Al(iv) + Ca axis) and the trend from Fe to Mg rich amphiboles (towards lower values of Si + Na + K) are seen. The hydroxyl group is partially replaced by fluorine (<1 wt%) and chlorine (<0.5 wt%). Mitchell (1990) suggested that all amphibole compositions should be plotted in a prism with axes for silicon content, magnesium number and calcium in the amphibole X site (see Leake, 1978 for amphibole site occupancies); for ferroan amphiboles this plot could be projected onto the silicon-calcium face of the prism. Most amphiboles from the Nunarssuit layered sequence plot close to the primary magmatic trend exhibited by amphiboles from over-saturated syenites (Fig. 4.13b).

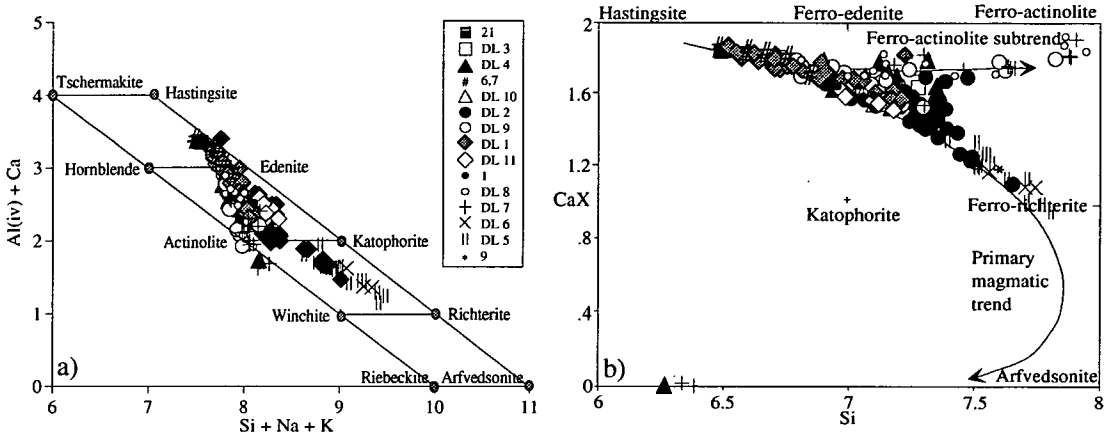

Fig. 4.13: a) Plot of Al (iv) + Ca vs Si+Na+K (atoms per 23 oxygens) for Nunarssuit syenite amphiboles, after Giret *et al.* (1980), modified by Becker (1980), b) plot of Ca on the X site vs Si (atoms per 23 oxygens) for Nunarssuit syenite amphiboles (after Mitchell 1990).

Amphiboles from DL 7 and some from DL 9 and 8 plot closer to the ferro-actinolite subtrend; Mitchell interpreted this trend as indicating growth of the amphiboles at lower temperatures than those which lie on the primary magmatic trend. The DL 7 points (7-45) are from the analysis of a fibrous amphibole associated with chlorite, the DL 8 points (8-50, 8-52) are from leucocratic portions of layers, the DL 9 points (9-61) are from a sample close to the top of the first thick melanocratic layer adjacent to leucocratic syenite. Compositions are plotted in terms of $Mg:Fe^{2+}+Mn:Na+K$ on Fig. 4.14. most of the Nunarssuit syenite amphiboles follow the Helene granite trend most closely. Sample 9, DL 5 and DL 6 follow the Kûngnât trend more closely than the Helene granite trend. Fig. 4.15 shows that Na is substituting for Ca.

Fig. 4.16 shows two clear trends. For amphiboles with less than 0.85 Na per unit formula the exchanges

$$XFe^{3+} \rightarrow YNa^{+}(1)$$

and

$$XSi^{4+} \rightarrow YNa^{+} (2)$$

(where X and Y are different species)

seem to have occurred. These exchanges are seen in some DL 9 points (9-61), DL 7, DL 8 and some DL 2 points (2-19,24,25). In amphiboles with more than c.1.0 Na per formula unit the exchanges

$$NaSi \rightarrow XY \quad (3)$$

and

$$NaFe^{3+} \rightarrow XY \quad (4)$$

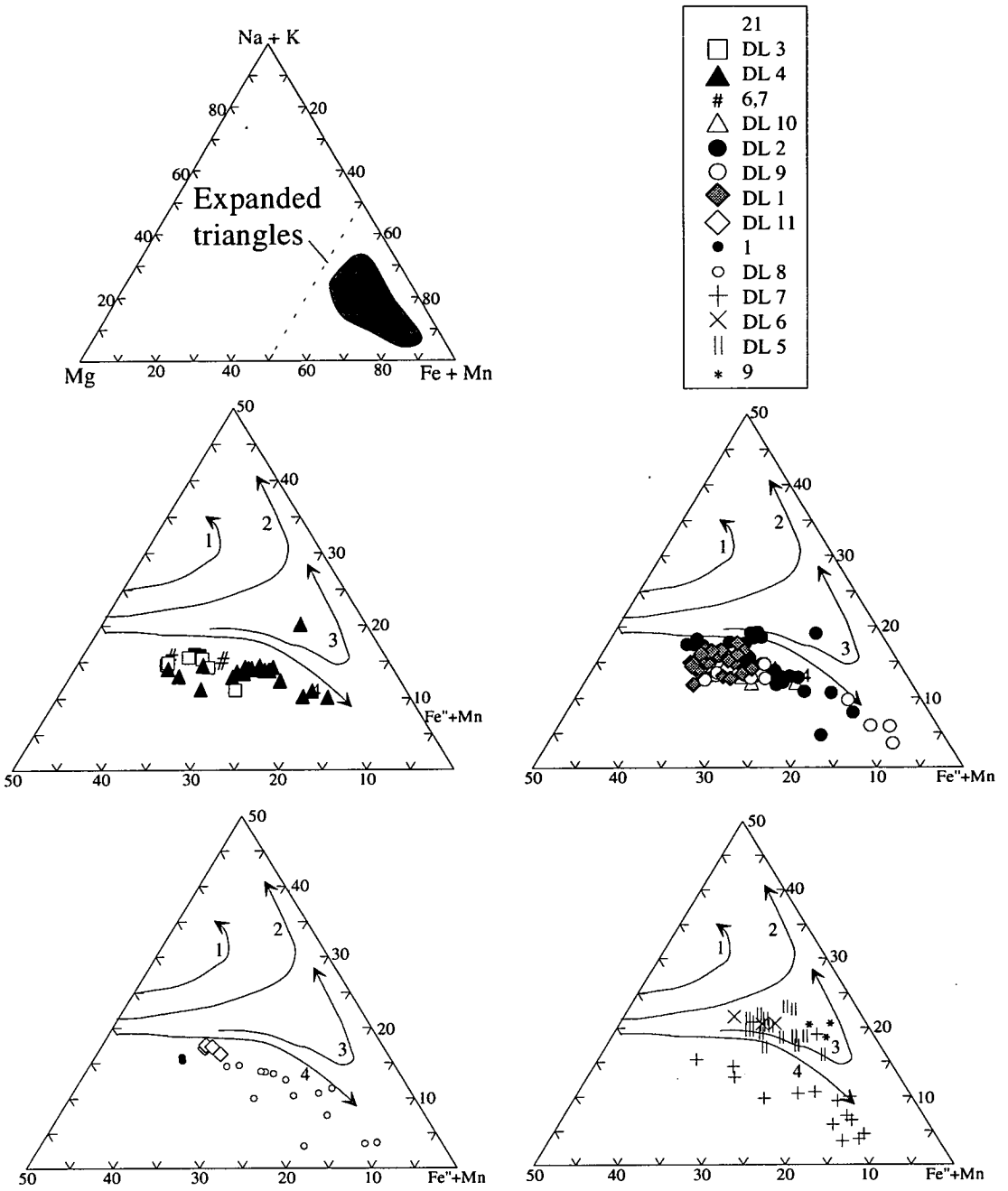

Fig. 4.14. Amphiboles plotted in terms of Mg:Na+K:Fe+Mn (atoms per 23 oxygens). Trends for the under-saturated complexes of South Qôroq (1) (Stephenson and Upton, 1982) and Ilímaussaq (2) (Larsen, 1976), and the over-saturated complexes of Kûngnât (3) (Stephenson and Upton, 1982) and the Helene Granite, Nunarssuit (4) (Butterfield, 1980) are shown for comparison.

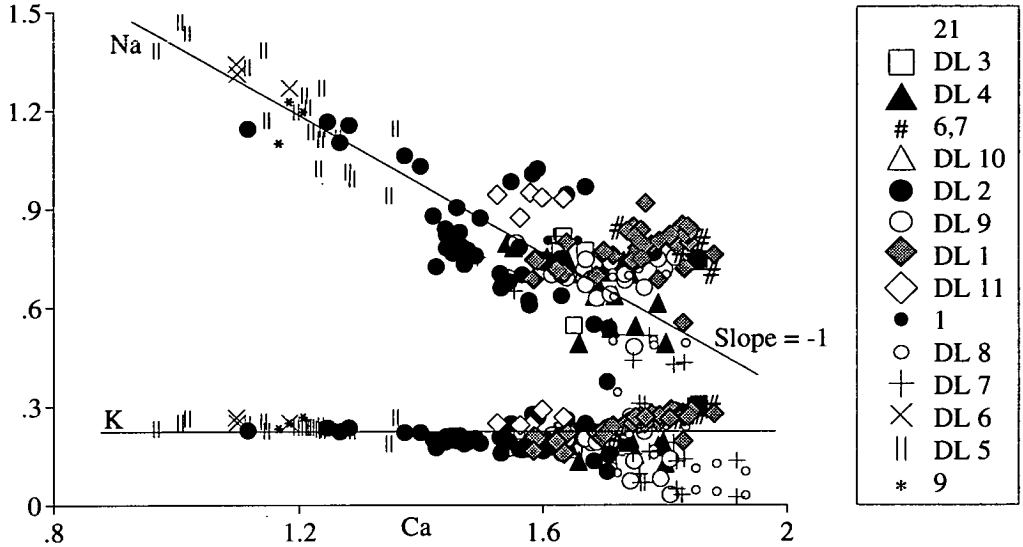

Fig. 4.15: Na and K plotted against Ca for Nunarssuit amphiboles. The antipathetic correlation of Na and Ca indicates that the two elements are involved in an exchange reaction.

seem to have occurred. These exchanges are less well defined than (1) and (2), they are most marked in sample 9, DL 5 and DL 6.

Fig. 4.17a shows two trends. The dominant trend suggests that Ca and Al(iv) are coupled whilst the second trend indicates little correlation between Ca and Al(iv). This second trend is shown by the same amphiboles which showed the Ferro-actinolite subtrend in Fig. 4.13b. It is thought that all these trends are due to alteration of the amphiboles after they formed from the pyroxenes. Fig. 4.17b shows that Al is largely tetrahedrally co-ordinated as in the pyroxenes.

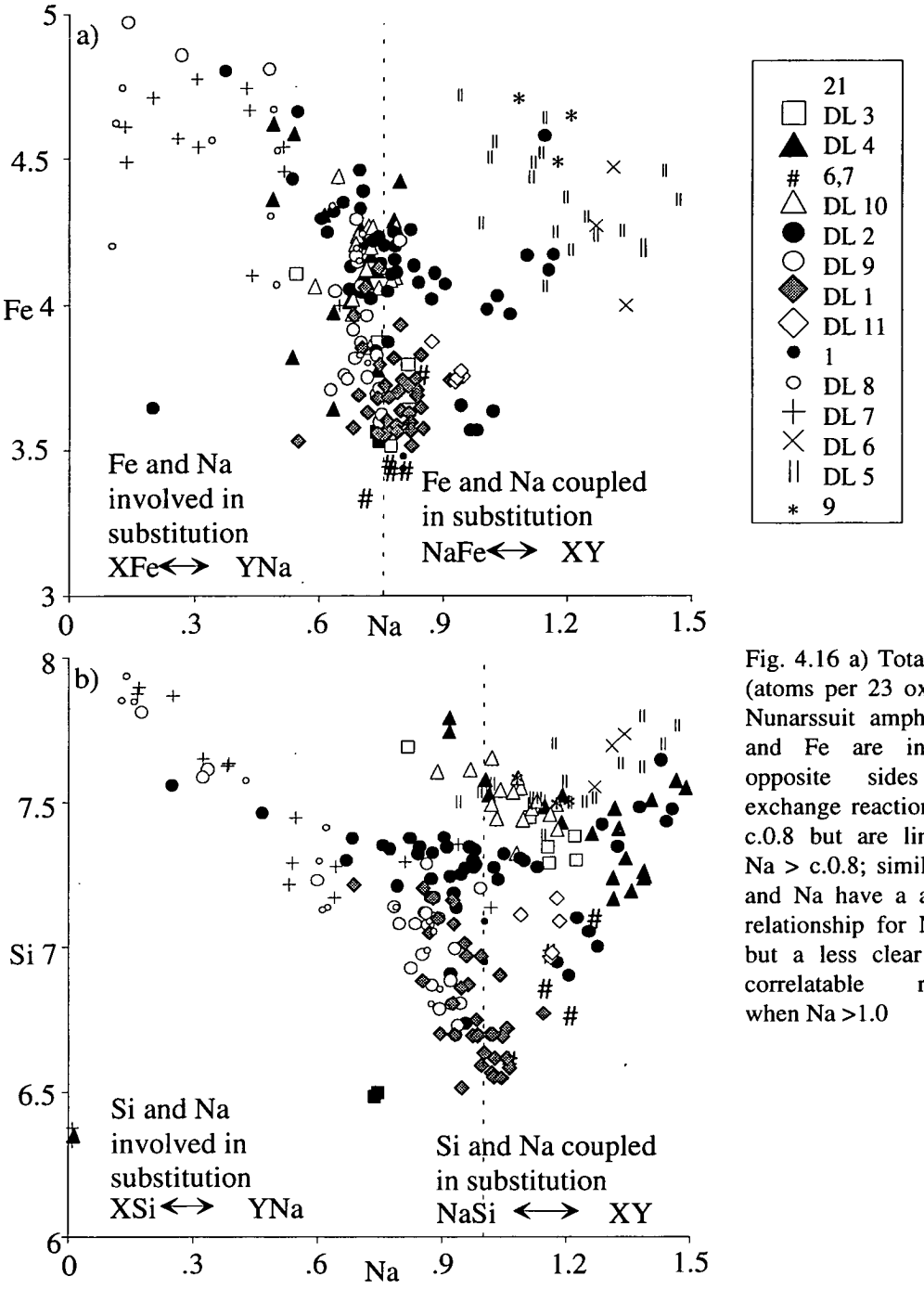

Fig. 4.16 a) Total Fe vs Na (atoms per 23 oxygens) for Nunarssuit amphiboles. Na and Fe are involved in opposite sides of an exchange reaction for Na < c.0.8 but are linked when Na > c.0.8; similarly, b) Si and Na have a antipathetic relationship for Na < c.1.0 but a less clear positively correlatable relationship when Na >1.0

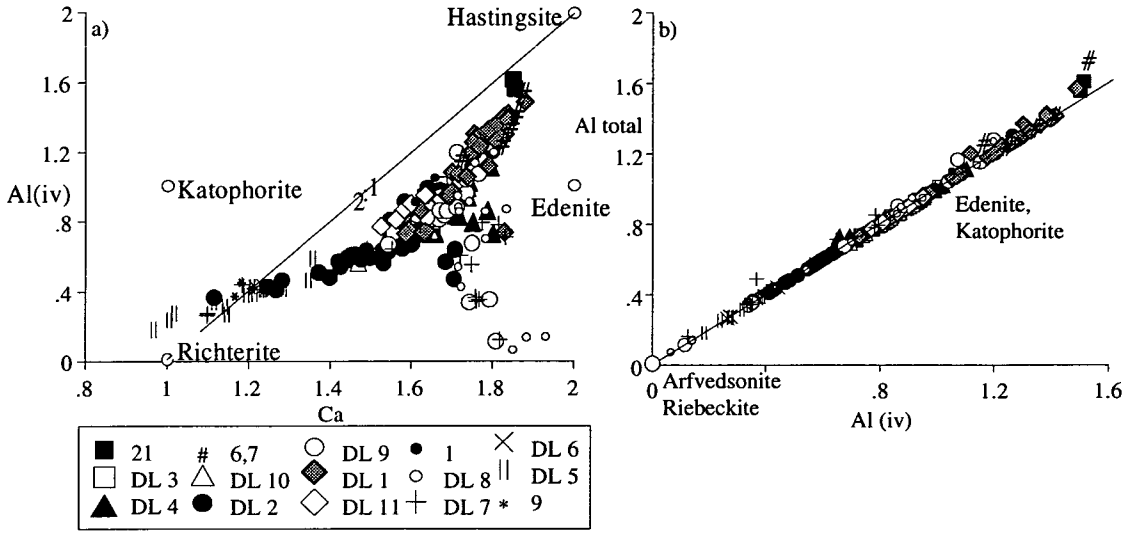

Fig. 4.17: a) Plot of tetrahedrally co-ordinated Al against Ca for Nunarssuit amphiboles indicating that the substitution deduced from Fig. 4.19 could be CaAl(iv) ⇔ NaSi, b) plot of total Al against tetrahedrally co-ordinated Al shows that most Al is tetrahedrally co-ordinated as is seen in the pyroxenes.

4.2.5: Biotite

All iron was taken as Fe^{2+} and cation proportions calculated on the basis of 22 oxygens. All the biotites are annites, $Ann_{70\text{-}100}$ (Fig. 4.18a) according to the classification of Deer *et al.* (1966). The siderophyllite content is zero as in biotites from many other Gardar syenites (Parsons *et al.*, 1991). There appears to be a slight increase in the maximum Mg content of biotites up section (Fig. 4.18b).

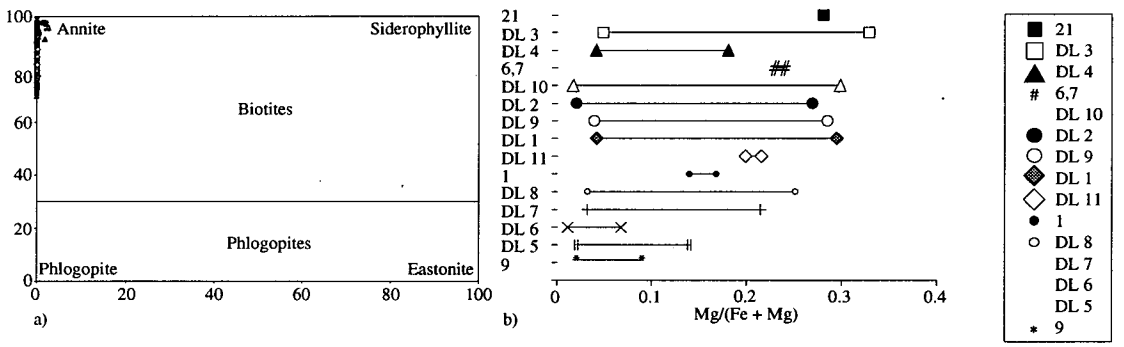

Fig. 4.18: a) biotite composition in terms of the end members phlogopite, annite, siderophyllite and eastonite. Fields from Deer *et al.* (1966), b) variation in Mg number up section in biotites from the Nunarssuit layered syenites. Points show the maximum and minimum Mg number. Sample 9 is from below and sample 21 from above the layered zone. (See Appendix A for specimen localities) variation in Mg number up section in the Nunarssuit layered syenites. Points show the maximum and minimum Mg number. Sample 9 is from below and sample 21 from above the layered zone.

Mn increases slightly with Fe^{2+} (Fig. 4.19) up to Fe/(Mg+Fe) = 0.95 where there is a sharp inflexion point and biotite becomes more strongly Mn enriched. This pattern is unlike that of the YGDC biotites (Mingard, 1990) where there is a gradual increase in Mn with Fe/(Mg+Fe). Stratigraphically distant rhythmically-layered localities (DL 2 and DL 8 and to a lesser extent DL 6,7 and 4) all show this sudden increase in Mn so it appears not to reflect a sudden change in magma-chamber chemistry.

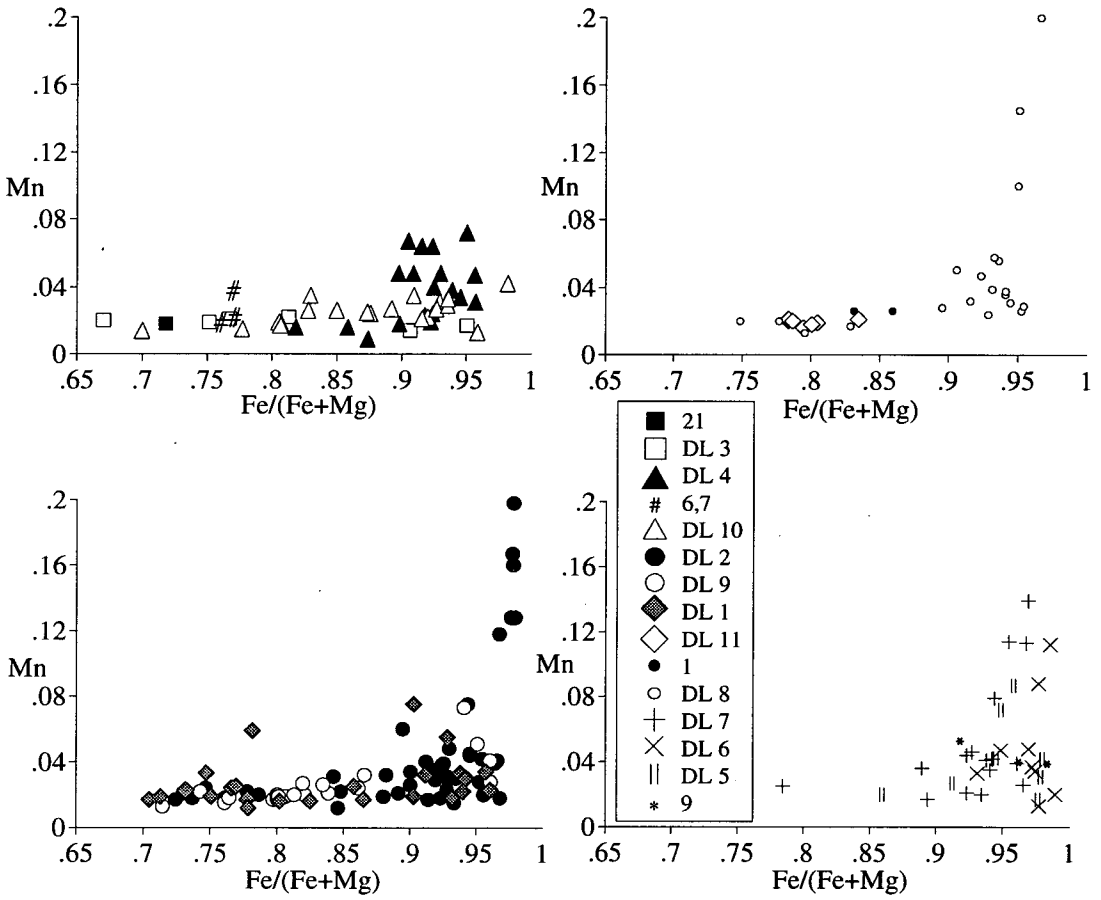

Fig. 4.19: Variation of Mn in biotites (atoms per 22 oxygens) plotted against Fe/(Fe+Mg) for biotites from the Nunarssuit layered syenite.

Biotites show a slight decrease in Ti with increasing Fe (Fig. 4.20), TiO_2 contents ranging from 0 wt.% to 5 wt.%.

Gardar biotites tend to be rich in fluorine but poor in chlorine (Parsons *et al.*, 1991). Fluorine content is controlled by both the fluorine content of late-stage metasomatic fluids and the iron content of the biotite. Wt.% F is plotted against Fe/(Fe+Mg) in Fig. 4.21 and shows a "iron-fluorine avoidance trend". "Iron-fluorine avoidance trend" is a term coined by Mason (1992) and refers to the commonly observed

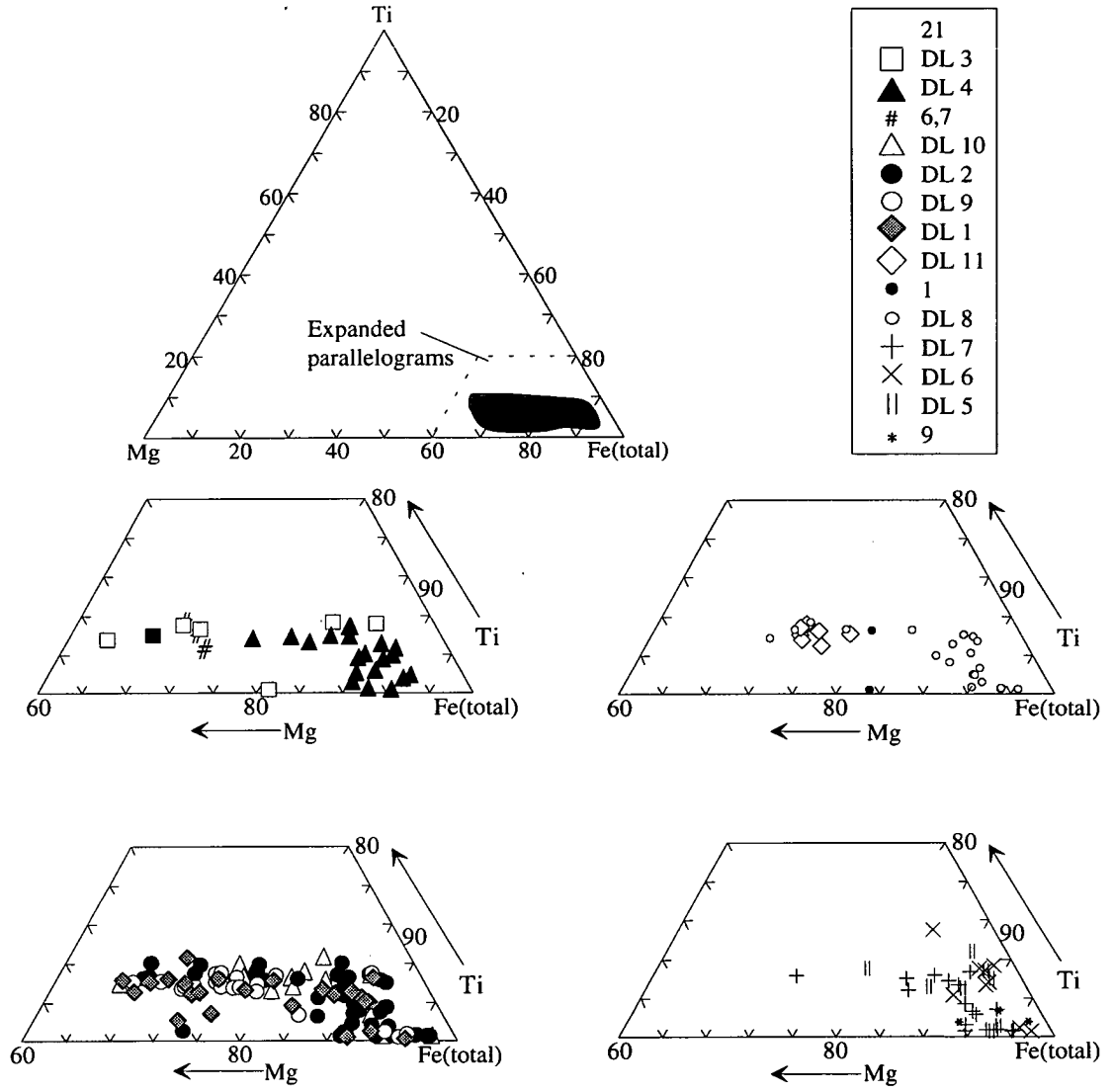

Fig. 4.20: Biotite from the Nunarssuit layered syenite plotted in terms of Mg:Ti:Fe(total).

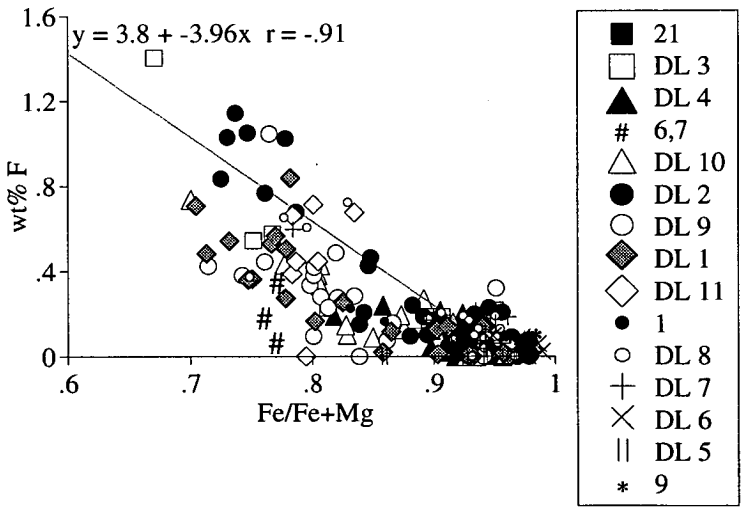

Fig. 4.21: Wt%F against Fe/Fe+Mg for biotites from the Nunarssuit layered syenite. The biotites define a triangular field with Fe correlated inversely with F content.

antipathetic relationship between concentrations of Fe and F in many ferromagnesian minerals. The trend is slightly steeper than the one reported by Finch (1990) for Nunarssuit syenites but the regression line plots closer to Fe/(Fe+Mg) = 1 at 0 wt.%F (ideal annite composition). The four data points for DL 2 which show the greatest F content are for sample 2-28, a melanocratic trough.

Biotite formation and growth may have taken place from the inter-cumulus fluid or in the subsolidus and is discussed in Chapter 6.5.

4.2.6: Minor Phases

Apatite

Apatites were analysed for the major elements Ca and P; the REE elements Ce, Pr, Nd, La; and the trace elements F, Na, Si, Fe and Mn. There is no significant variation between apatites from the different facies or different stratigraphic levels of the layered succession. The major elements Ca and P show little variation. Na_2O varies from 0.1 to 0.5 wt %, SiO_2 varies from 0.35 to 2.5 wt.%. Both elements show considerable within sample variation. Ce_2O_3, the most abundant REE, reaches values of 2.7 wt.%. The other REE decrease in abundance in the order Nd_2O_3, La_2O_3 and Pr_2O_3. Mn may substitute for Ca in apatites but was below detection limits in the Nunarssuit apatites. This finding agrees with that of Becker (1984) for the Giant Dykes of Isortoq.

The yellow cathodoluminescence of the apatites (Chapter 3.2.6) may be due to Mn or REE; without a spectroscope attached to the luminescence equipment it is impossible to differentiate between these different activators. Blue luminescing apatites from North Qôroq have been described by Rae (1988); the blue luminescence is thought to be due to Eu^{2+}. Finch (1990) reported red luminescing apatites from Igdlerfigssalik.

Apatite is part of a solid solution series with vitusite (5) and britholite (6). The Nunarssuit apatites are all nearly pure end member apatites.

$$Ca^{2+} + Ca^{2+} \rightarrow Na^{+} + RE^{3+} \qquad (5)$$

apatite vitusite

$$Ca^{2+} + P^{5+} \rightarrow RE^{3+} + Si^{4+} \qquad (6)$$

apatite britholite

Where seen most zoning is interpreted as modified magmatic zoning or secondary zoning. Some primary magmatic zoning is observed. In all cases the cores of the

apatites are probably the closest to the original composition of the apatite with an increase in RE, Si and Na outwards towards the rim. Fluorine contents range from 2.5 to 4.3 wt.%, within sample variation is 1-1.3 wt.%. Chlorine concentrations are, less than 0.1 wt.%.

The Nunarssuit apatites are not noticeably different from other Gardar syenite apatites, (Becker, 1984; Mingard, 1990).

Opaque oxides

Few magnetites were detected in the samples; most of those were exsolved and oxidised to ilmenite/magnetite intergrowths. Geothermometry using co-existing ilmenites and reconstructions of the original composition of the magnetite yielded low subsolidus temperatures which corresponded to the oxidation temperature of the magnetite (see Chapter 7.4). For this reason the primary composition of the magnetites could not be satisfactorily deduced. No hematite exsolution lamellae are visible in the ilmenites. Compositions are plotted on Fig. 4.22a and b. Ilmenites are almost pure $FeTiO_3$ but plot above the ilmenite-hematite solid solution line. This is thought to be due to the presence of MnO which is not included in the plot. Minor elements are plotted in Fig. 4.22c and d. The dominant minor element is Mn. Al, Mg, Cr and V are present in very low concentrations only.

Zircon

Zircon crystals occur occasionally at all stratigraphic levels in the Nunarssuit layered succession and in all facies. It is not possible to differentiate between crystals from different facies or stratigraphic heights in terms of their chemistry. Most of the zircon crystals show well developed oscillatory zoning; chemically this shows up in variation in zirconium and hafnium content. In back-scattered electron images dark areas are relatively zirconium-rich; lighter areas are relatively hafnium-rich. Irregular zoning is sometimes superimposed on this oscillatory zoning. It is thought that this represents subsolidus alteration. Hafnium content varies from 0.9 to 2.4 wt.%; within sample variation is 0.9 wt.%. Speer (1982) reported the exchange reaction

$$REE^{3+} + P^{5+} \rightarrow Zr^{4+} + Si^{4+} \qquad (7)$$

which represents a solid solution of zircon with its isostructural analogue, xenotime ($YSiO_4$). Most crystals contain <0.5 wt.% Y_2O_3 and are almost pure end-member zircons.

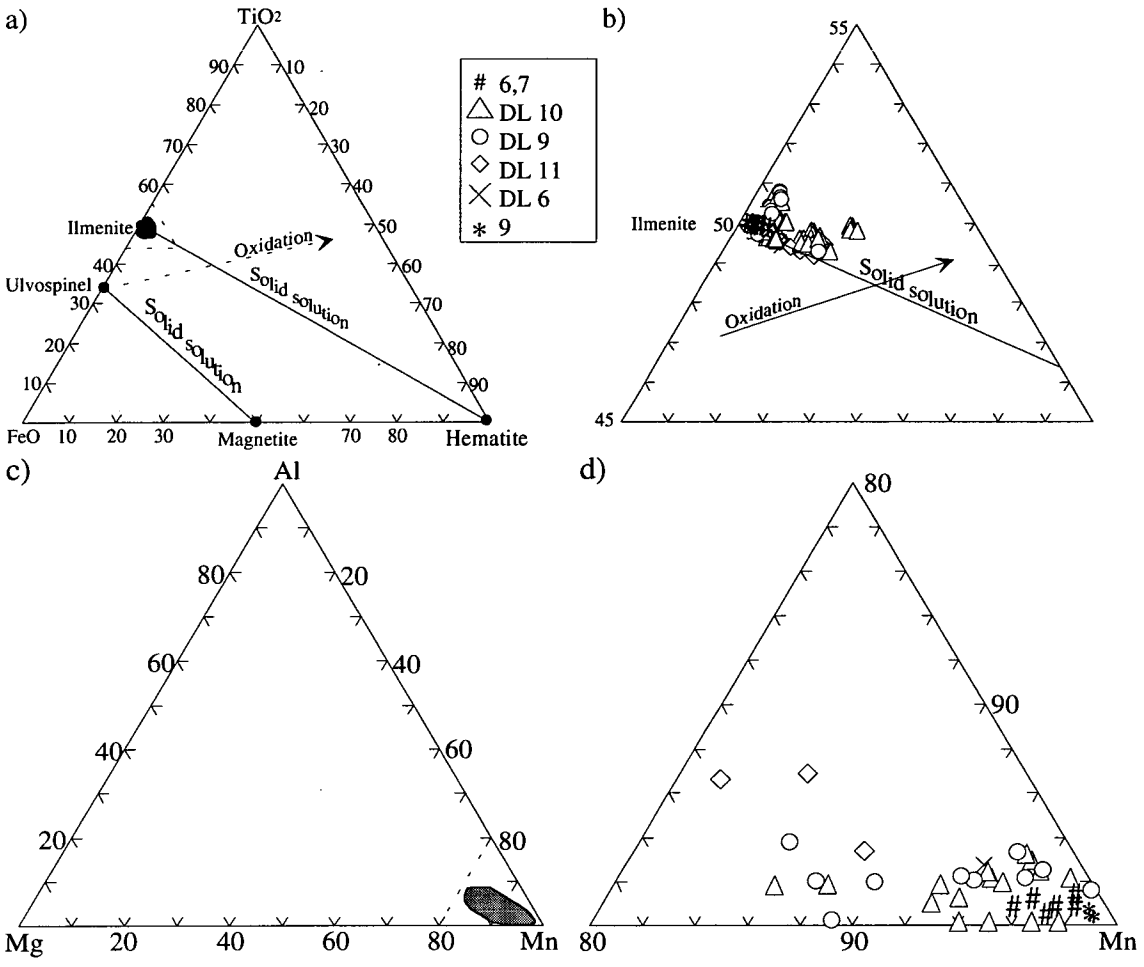

Fig. 4.22: a) and b) ilmenomagnetites plotted as $FeO:TiO_2:Fe_2O_3$ showing solid solution between ilmenite and hematite. c) and d) ilmenomagnetites plotted in terms of the minor elements MgO, MnO and Al_2O_3.

4.2.7: Summary

Olivines and pyroxenes become more magnesian up section. Biotites and amphiboles also show this trend but it is less marked. An explanation of this reverse cryptic zoning, based on the relative inclinations of the intrusion edge and the layering is presented in Chapter 10.8. These trends show a disturbance around the lower melanocratic unit (Unit 5), this disturbance is seen more clearly in the trace element composition of different phases (Chapter 5). Phases from sample 9 (lowest level) tend to be the most ferroan whilst phases from samples 6 and 7 (melanocratic troughs) tend to be the most magnesian. Pyroxenes from the lower levels (sample 9, DL 5 and DL 6) are richer in the acmite component than the other pyroxenes. Similar behaviour is also seen in the sodium content of the amphiboles. These samples contain quartz as a late-stage (possibly hydrothermal) phase. Phases in sample 2-28

(a melanocratic trough) are more magnesian than the surrounding syenite (DL 2). Pyroxenes show sub-solidus zoning both optically and chemically.

Feldspars in the layered succession of Nunarssuit show a slight compositional difference between the thick melanocratic layer facies and the rhythmic layers. The feldspar compositions in the lower thick melanocratic unit (Unit 5) indicate a higher minimum temperature of crystallisation than feldspar compositions in the rhythmically layered facies. Biotites show F-Fe avoidance. Amphiboles are largely calcic; others are calcic-sodic. The variation is inferred to reflect their subsolidus history. Some apatites preserve magmatic zoning, with Ca and P decreasing towards their rims. Primary and modified zoning in zircons is visible using cathodoluminescence and back-scattered electron imaging; zoning is usually due to varying hafnium and zirconium contents.

4.3: Kûngnât.

Samples are grouped according to locality. Leucocratic and melanocratic samples from DL localities are therefore grouped together. No chemical variation has been detected between adjacent leucocratic and melanocratic layers and the diagrams would be over-crowded and illegible if the samples were spilt into smaller groups.

The samples are arranged in stratigraphic order; DL 12 is the lowest; DL18 is the highest (see Fig. 2.4 for stratigraphic column). Samples from the trough stacks and the syenite which surrounds the troughs (host syenite) are plotted separately in many diagrams because the stratigraphic height of this locality with respect to the other localities is not clear.

4.3.1: Feldspar

Most feldspars in West Kûngnât are coarse perthites. Feldspar bulk compositions are shown on Fig. 4.23 and fall in the sanidine field; no consistent trends are present.

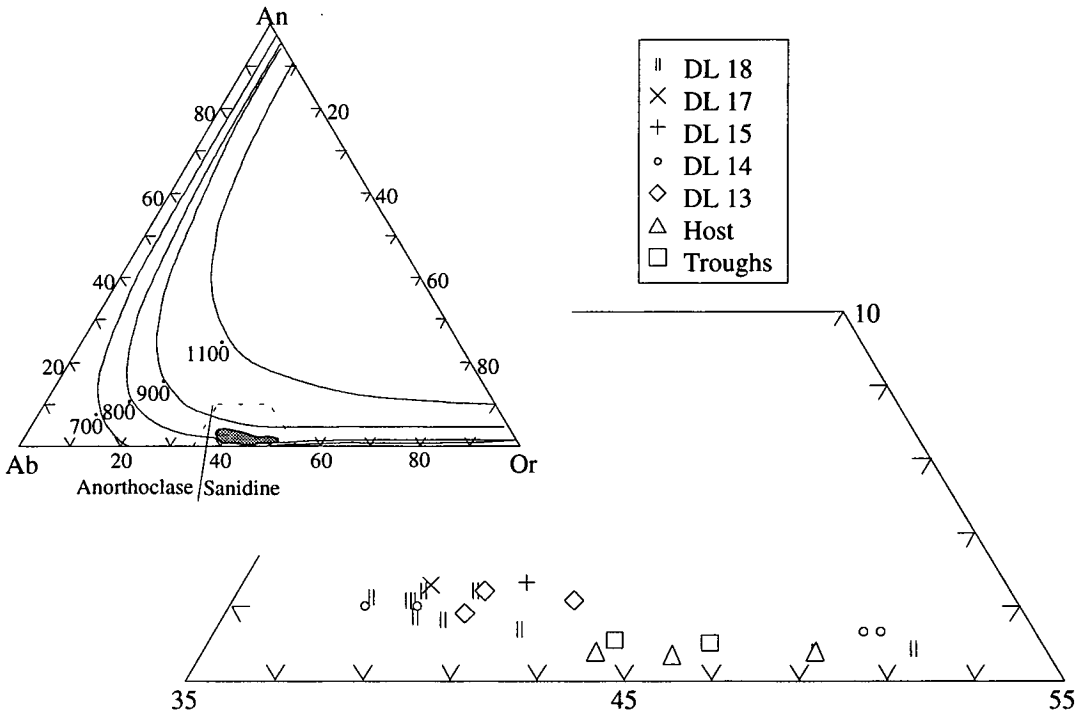

Fig. 4.23: Composition of feldspars from the layered syenites of West Kûngnât in terms of the albite, anorthite and orthoclase components.

Plots of Fe^{2+} (Fig. 4.24a) and Ba (Fig. 4.24b) against the fractionation index K-Ca do not reveal any trends.

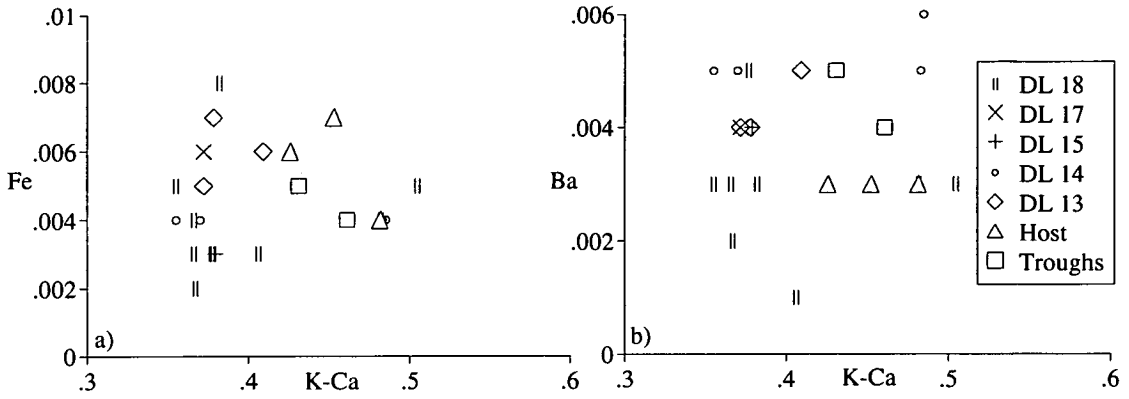

Fig. 4.24: a) total Fe as Fe^{2+} and b) Ba in feldspars from the layered syenite of West Kûngnât plotted against a feldspar fractionation index K-Ca.

4.3.2: Pyroxene

Pyroxene from the trough stacks is slightly more magnesian than that from the surrounding syenite (Fig. 4.25). Pyroxenes from DL 12 appear to be noticeably more magnesian than other pyroxenes in the succession. This may be due to the highly altered nature of samples from DL 12.

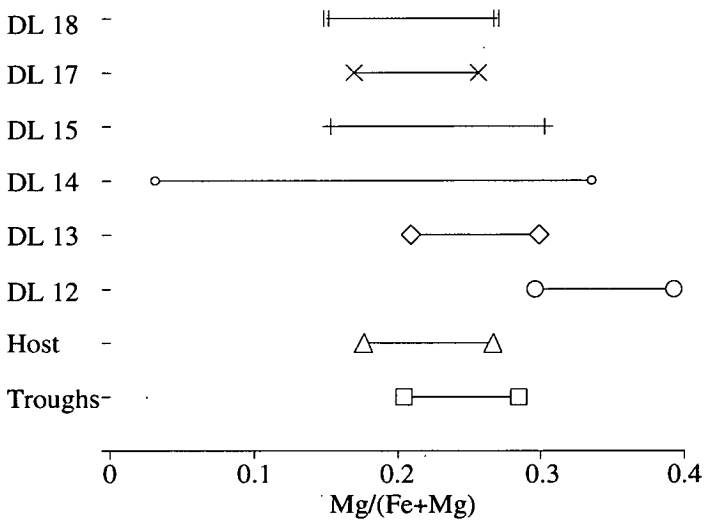

Fig. 4.25: Variation of Mg number, up section in, pyroxenes from the layered syenite of West Kûngnât. Points show the maximum and minimum Mg number.

All the pyroxenes belong to a single high-Ca series (Fig. 4.26) and have < 1 wt% Na_2O. Electron microprobe analyses have been recast for Fe^{2+} and Fe^{3+} assuming that Fe^{3+} is equal to Na^+ and K^+ and that the remaining Fe is Fe^{2+}. Compositions lie over the junction between the ferrosalite, hedenbergite, ferroaugite and ferrohedenbergite fields of Deer *et al.* (1966). The trough stack pyroxenes define a field which is less ferroan than the field defined by the host syenite pyroxene. There is a slight tendency for the fields defined by the localities to become more hedenbergitic up through the stratigraphic succession (Fig. 4.26 and 4.27). The pyroxenes define a field which

overlaps a fractionation trends defined by pyroxenes from other complexes (Fig. 4.27).

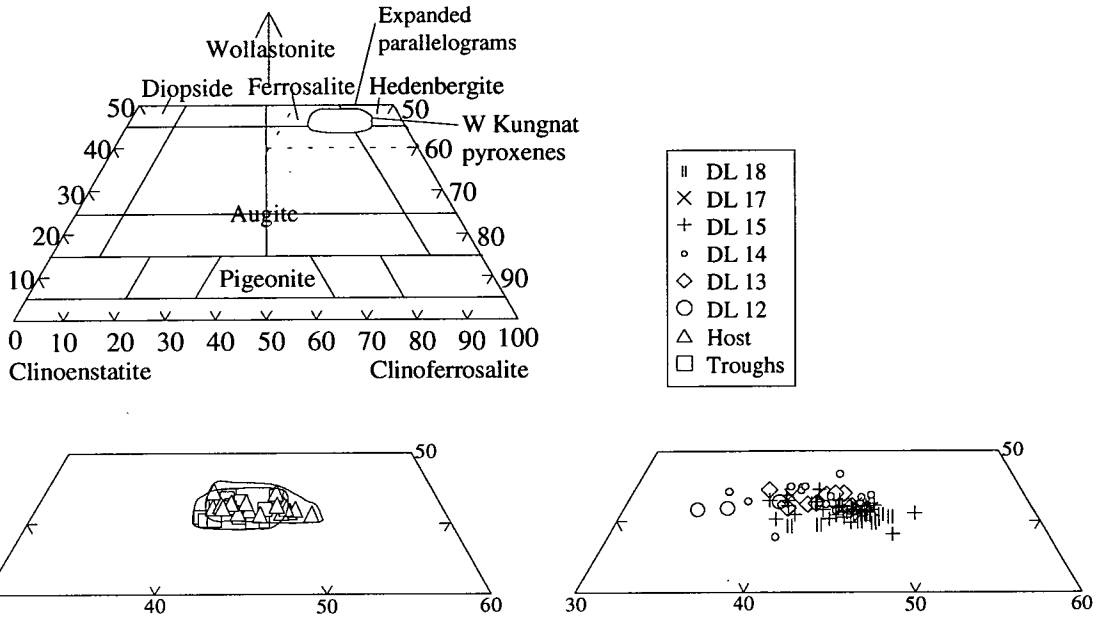

Fig. 4.26: Composition of the West Kûngnât layered syenite pyroxenes (atoms per 6 oxygens) Compositional fields form Deer *et al.* (1966). Clinoenstatite = Mg, clinoferrosalite = Fe^{2+}Mn, wollastonite = Cal.

Irregular zoning is seen in some pyroxenes. The nature of this zoning is described in section 4.2.2.

Aluminium (Fig. 4.28a) and titanium (Fig. 4.28b) show a slight negative correlation with Mg/(Mg+Fe). The ranges of aluminium and titanium for the given values of Mg/(Mg + Fe) are similar to those seen for low Mg/(Mg+Fe) pyroxenes from Klokken (Parsons, 1979), Tugtutôq Central Complex (Upton *et al.*, 1990), and the YGDC (Mingard, 1990). All the samples have sufficiently low Al(vi) to fall within the field of igneous rocks of Aoki and Kushiro (1968). When Al(iv) is plotted against Ti the majority of compositions lie on the line Al(iv)=2Ti (Fig. 4.28c). This indicates that the pyroxenes have a Ca-Ti Tschermak's molecule component ($CaTiAl_2SiO_6$, Larsen, 1976) which is produced by the reaction $M^{2+} + 2Si^{4+} \rightarrow Ti^{4+} + 2Al^{3+}$. Points above the line may also contain Ca-Tschermaks molecule $CaAl_2SiO_6$.

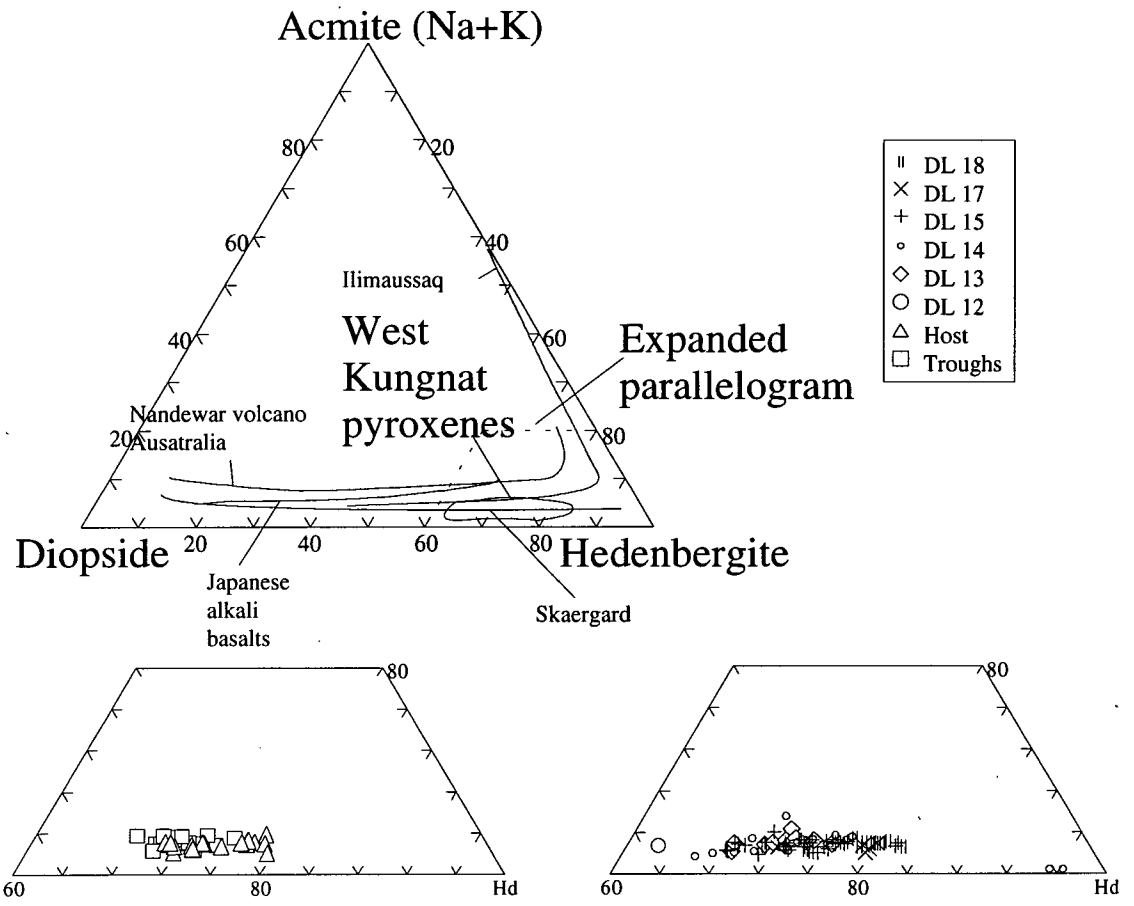

Fig. 4.27 Plot of acmite (Na+K), diopside (Mg) and ferrohedenbergite (Fe^{2+}+Mn) for pyroxenes from the West Kûngnât layered syenite. Trends from over-saturated (Skaergård, Japanese alkali basalts and Nandewar volcano) and under-saturated (Ilímaussaq) complexes are superimposed for comparison.

4.3.3: Olivine

Olivines lie in the range Fo_9-Fo_5 (Fig. 4.29 and 4.30). Variation within samples covers this range of compositions. The trough stack olivines are noticeably more magnesian than those from the surrounding syenite. There is a slight trend of increased tephroite and fayalite components in the olivines up through the succession. The maximum Ca content of the olivines is 0.1 wt.% (Fig. 4.31); the samples fall within the plutonic field of Simkin and Smith (1970). The olivines are less Ca-rich than those of the YGDC (Mingard, 1990) but similar to those of the laminated and granular syenites of Klokken (Parsons, 1979). In the case of the layered syenites of West Kûngnât, Ca variation in olivines can not be due to differences in the level of the intrusion since there is no consistent variation in Ca content of the olivines with stratigraphic height. Olivines from the trough stacks and surrounding syenite are also indistinguishable on the basis of their calcium contents although they have a wider range of Ca content than other localities.

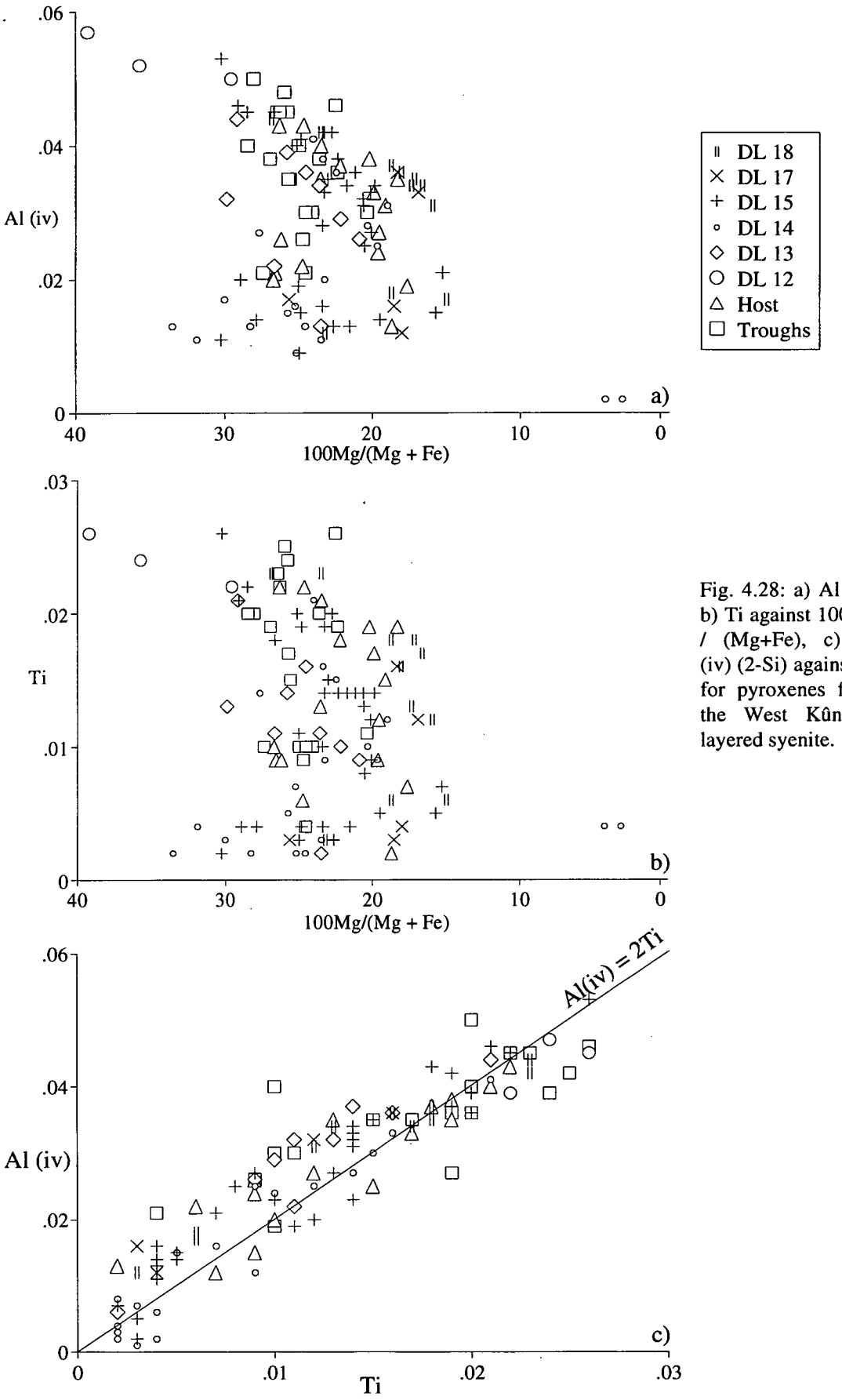

Fig. 4.28: a) Al and b) Ti against 100Mg / (Mg+Fe), c) Al (iv) (2-Si) against Ti for pyroxenes from the West Kûngnât layered syenite.

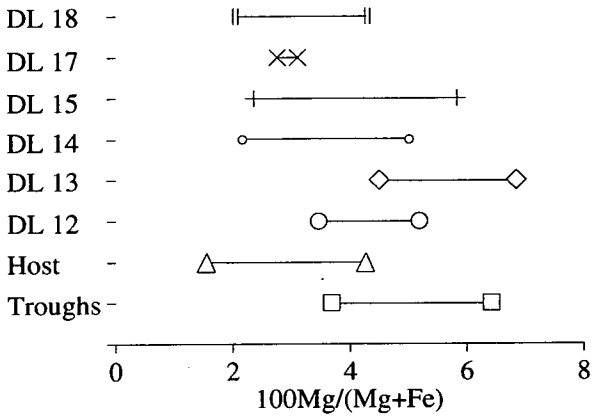

Fig. 4.29: variation of Mg number, up section, in olivines from the layered syenite of West Kûngnât. Points show the maximum and minimum Mg number. Variation of Mg number with stratigraphic height for pyroxenes from the layered syenite of West Kûngnât.

Jurewicz and Watson (1988) suggested that a number of factors, such as silica activity and melt composition, could control the Ca content of olivines. Olivines from melanocratic and leucocratic layers have the same Ca content; Ca partitioning in olivines is therefore not directly related to the layering process.

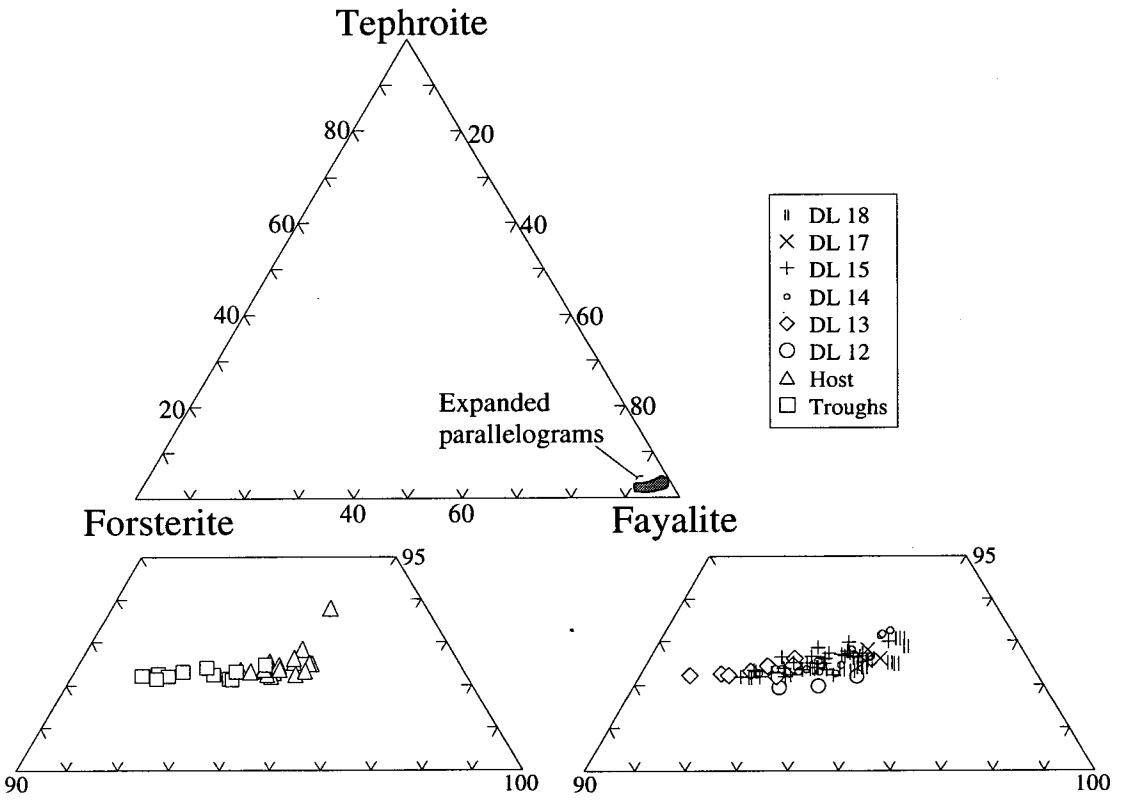

Fig. 4.30: Plot showing composition of olivines from the layered syenites of West Kûngnât in terms of Fe (fayalite), Mg (forsterite) and Ti (tephroite) end-members.

Manganese increases regularly with Fe^{2+} from 1.6 wt.% to 2.6 wt.%. This range is similar to those reported by Simkin and Smith (1970) and of other Gardar intrusions

such as Klokken (Parsons, 1979), Nunarssuit (this study), the YGDC (Mingard, 1990) and the giant dykes of Isotoq (Becker, 1984)

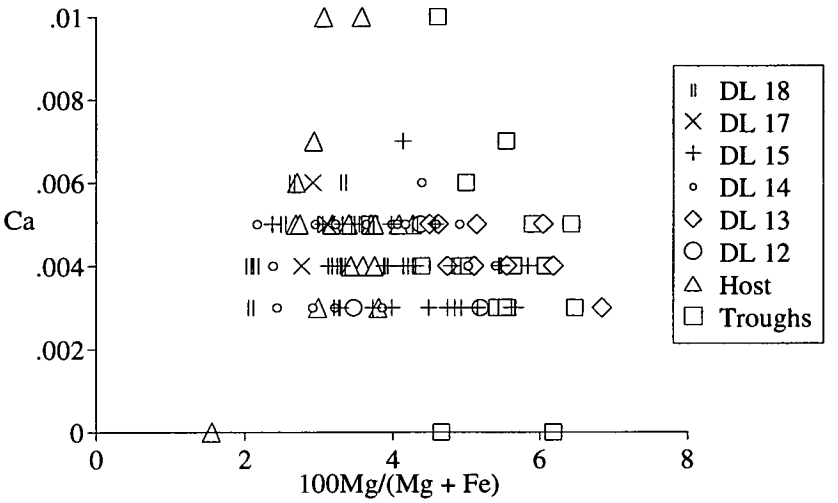

Fig. 4.31 Calcium (atoms per 4 oxygens) in the West Kûngnât layered syenite olivines.

Chromium (maximum 0.03 wt.%), titanium (maximum 0.05 wt.%), aluminium (maximum 0.02 wt.%) and nickel (below detection limits) are present only in trace amounts. No regular zoning was detected in the olivines.

4.3.4: Amphibole

Most of the amphiboles are considered to be secondary, formed by the alteration of pyroxenes (Chapter 3.2.2 and 6.4). It is not clear whether the large amphibole oikocrysts seen in the trough stacks are primary or the product of alteration. It is possible that the initial amphibole was the product of alteration of a pyroxene. The large oikocrystic amphibole could then have grown on the pre-existing amphibole. It is not possible to differentiate chemically between the large oikocrystic amphiboles and those which are the obvious product of alteration of pyroxenes. All iron was treated as Fe^{2+} since the complexity of the amphiboles prevent Fe^{3+} being calculated (Droop, 1987). Amphiboles from the trough stacks are more magnesian than those in the surrounding syenite (Fig. 4.32a).

West Kûngnât syenite amphiboles are calcic according to the system of Leake (1978), Fig. 4.32b. The calcic-amphiboles range from silicic ferro-edenites to ferro-pargasitic hornblendes (Fig. 4.33). The hydroxyl group is partially replaced by fluorine (<1 wt%) and chlorine (<0.5 wt%). Figure 4.34a shows compositions plotted on a diagram of Al(iv)+Ca against Si+Na+K after Becker (1984). Most amphiboles from the West Kûngnât layered sequence plot close to the ferro-actinolite sub-trend

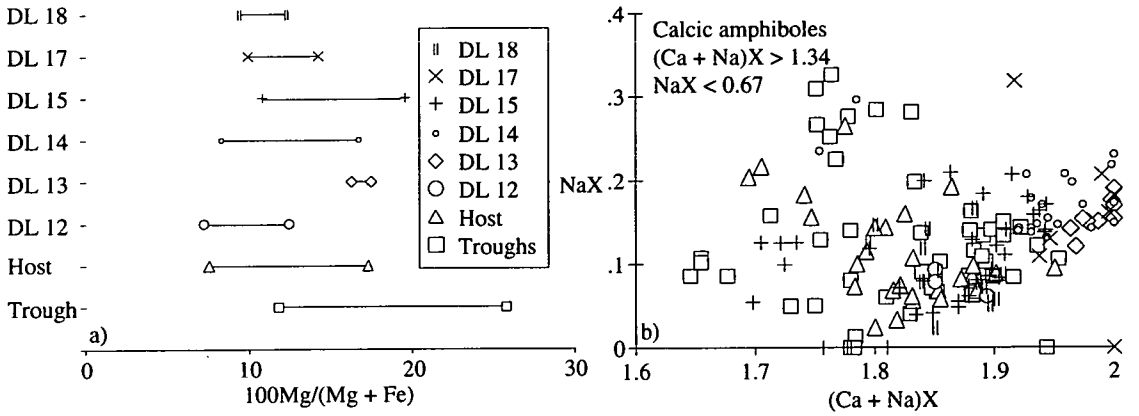

Fig. 4.32:a) variation of Mg number, up section, in amphiboles from the layered syenite of West Kûngnât. Points show the maximum and minimum Mg number, b) plot of Na in the X site against Ca+Na in the X site (atoms per 23 oxygens) for amphiboles from the layered syenites of West Kûngnât showing that amphiboles are classified as calcic amphiboles under the scheme of Leake (1978).

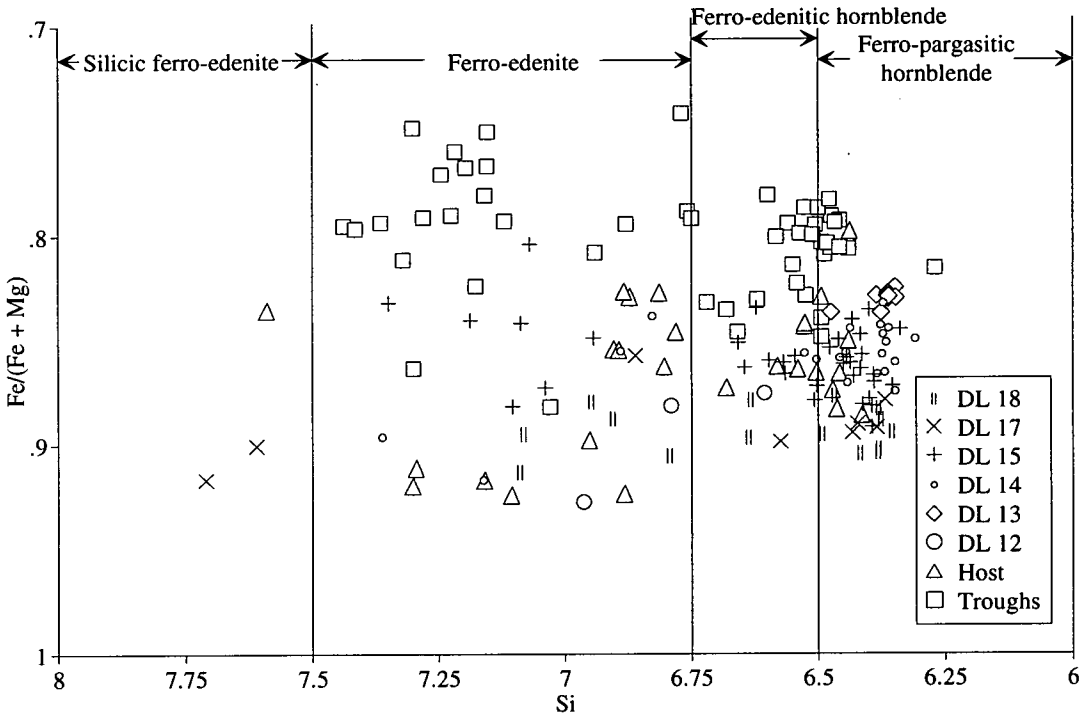

Fig. 4.33: Fe/(Fe+Mg) against Si (atoms per 23 oxygens) for amphiboles, fields from Leake (1978)

of Mitchell (1990) (Fig. 4.34b). Mitchell interpreted this trend as indicating growth of the amphiboles at lower temperatures than those which lie on the primary magmatic trend. Compositions are plottted in terms of $Mg:Fe^{2+}+Mn:Na+K$ on Fig. 4.35.

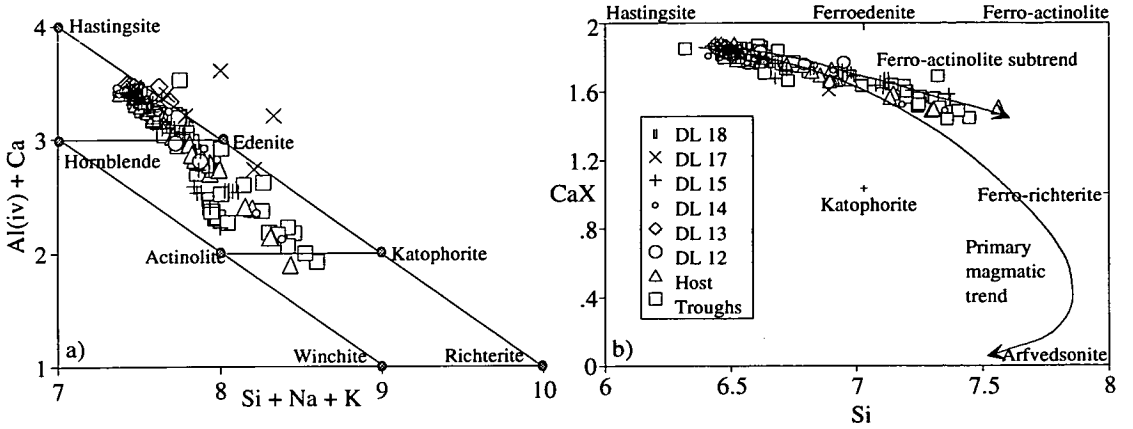

Fig. 4.34: a) plot of Al (iv)+ Ca against Si+Na+K (atoms per 23 oxygens) for amphiboles from the layered syenite of West Kûngnât, after Giret *et al.* (1980), modified by Becker (1980), b) plot of X site Ca against Si (atoms per 23 oxygens) for amphiboles from the layered syenite of West Kûngnât.

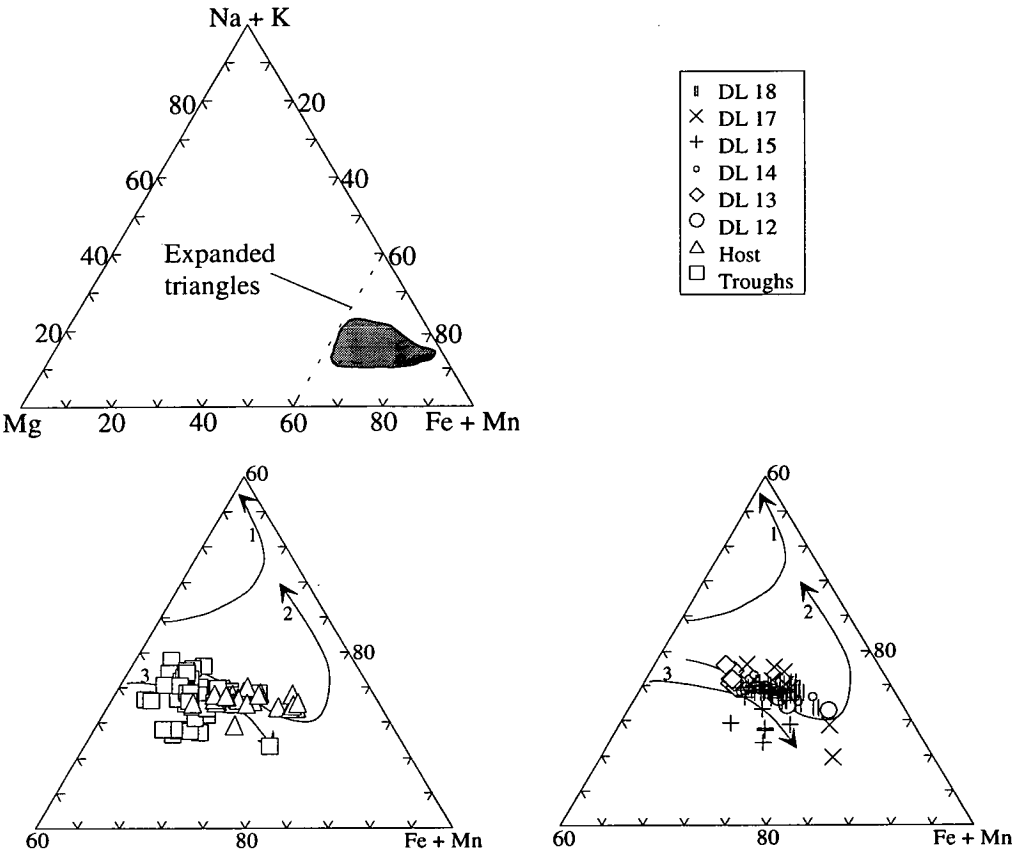

Fig. 4.35: Amphiboles in terms of Mg:Na+K:Fe+Mn. Trends for the under-saturated complexes of South Qôroq (1), (Stephenson and Upton, 1982) and Ilímaussaq (2), (Larsen, 1976) and the over-saturated complexes of Kûngnât (3), (Stephenson and Upton, 1982) and the Helene Granite, Nunarssuit (4), (Butterfield, 1980) are shown for comparison.

Unlike other Gardar intrusions (YGDC; Mingard, 1990; Giant dykes of Isortoq Becker, 1984) sodium does not appear to be substituting for calcium and potassium

seems to be correlated with calcium (Fig. 4.36). There is no clear relationship between silica and sodium (Fig. 4.37a) or iron and sodium (Fig. 4.37b).

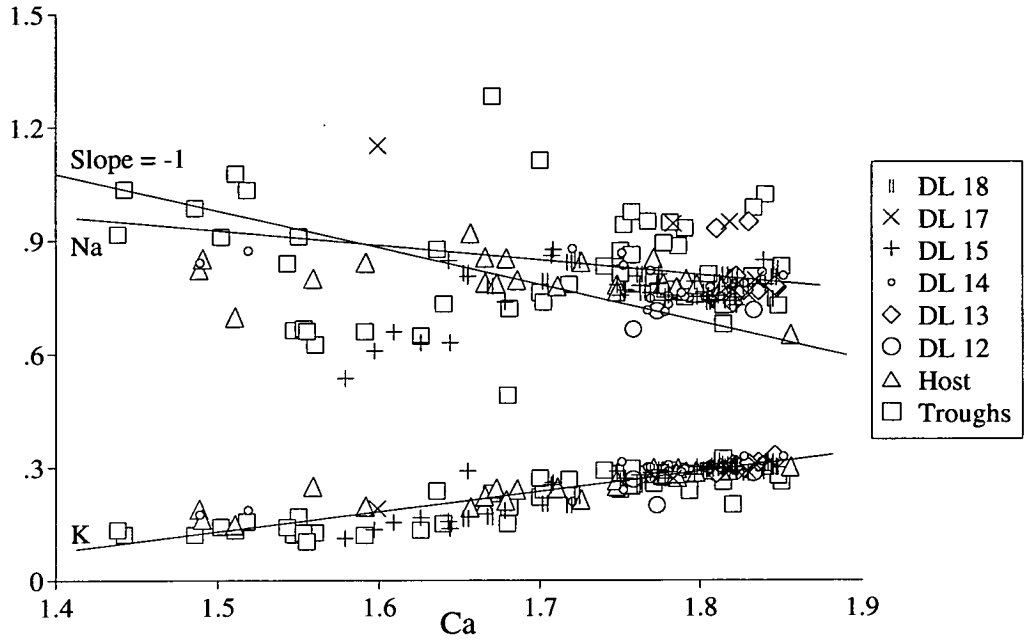

Fig. 4.36: Na and K plotted against Ca for amphiboles from the layered syenite of West Kûngnât.

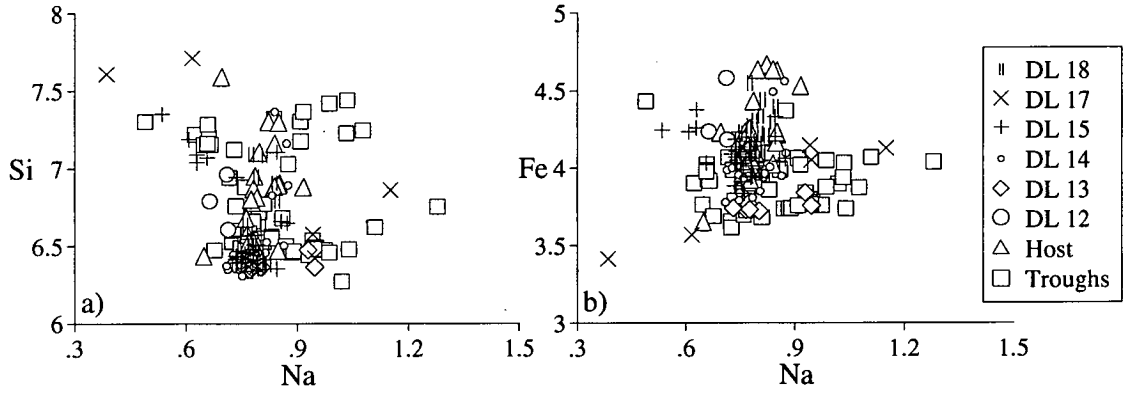

Fig. 4.37: a) total Fe against Na (atoms per 23 oxygens) for amphiboles from the layered syenite of West Kûngnât, b) Si against Na (atoms per 23 oxygens) plot for the amphiboles from the layered syenite of West Kûngnât. No clear trends are seen.

Figure 4.38a shows that Ca and Al(iv) are coupled. Figure 4.38b shows that Al is largely tetrahedrally co-ordinated as in the pyroxenes.

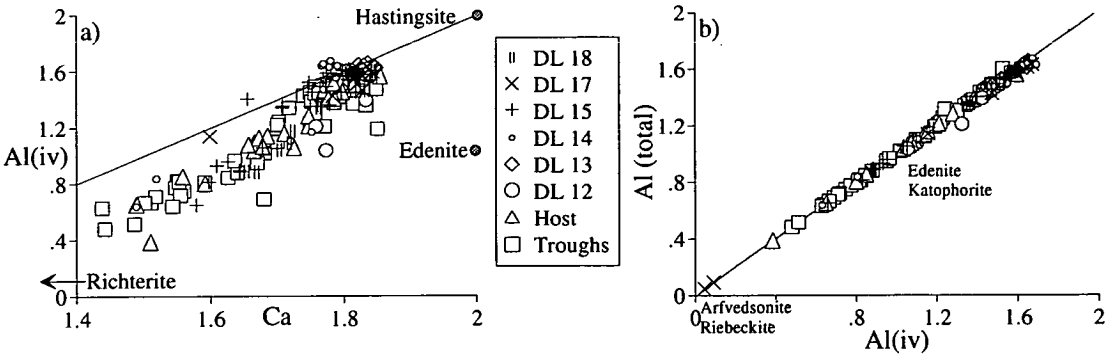

Fig. 4.38: a) plot of tetrahedrally co-ordinated Al against Ca for amphiboles from the layered syenite of West Kûngnât, indicates that Al(iv) and Ca are linked in an exchange reaction, b) plot of total Al against tetrahedrally co-ordinated Al shows that most Al is tetrahedrally co-ordinated.

4.3.5: Biotite

All iron was taken as Fe^{2+} and cation proportions calculated on the basis of 22 oxygens. All the biotites are annites, $Ann_{70\text{-}100}$ (Fig. 4.39a), according to the classification of Deer *et al.* (1966). The siderophyllite content in the biotites is zero as in many other Gardar syenites (Parsons *et al.*, 1991). There is no consistent chemical trend in biotite Fe content (Fig. 4.39b) but biotites from the trough stack appear to be more magnesian than those in the rest of the succession.

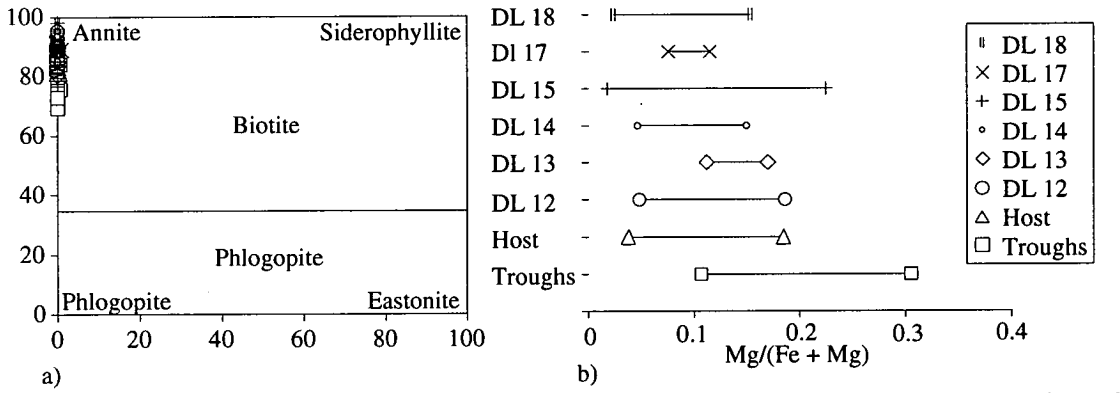

Fig. 4.39: a) biotite compositions in terms of the phlogopite, annite, siderophyllite and eastonite end members. Compositional fields from Deer *et al.* (1966), b) variation of Mg number, up section, in biotites from the layered syenite of West Kûngnât. Points show the maximum and minimum Mg number. Variation of Mg number with stratigraphic height for pyroxenes from the layered syenite of West Kûngnât.

The Mn content shows a slight correlation with Fe/(Fe + Mg) (Fig. 4.40) unlike biotite from the YGDC (Mingard, 1990) where there is a gradual increase in Mn with Fe/(Mg+Fe). The trough stack biotites tend to contain less manganese than those in the surrounding syenite. The variation in Mg:Ti:Fe is plotted in Fig. 4.41. TiO_2 contents range from 2 wt.% to 5 wt.%.

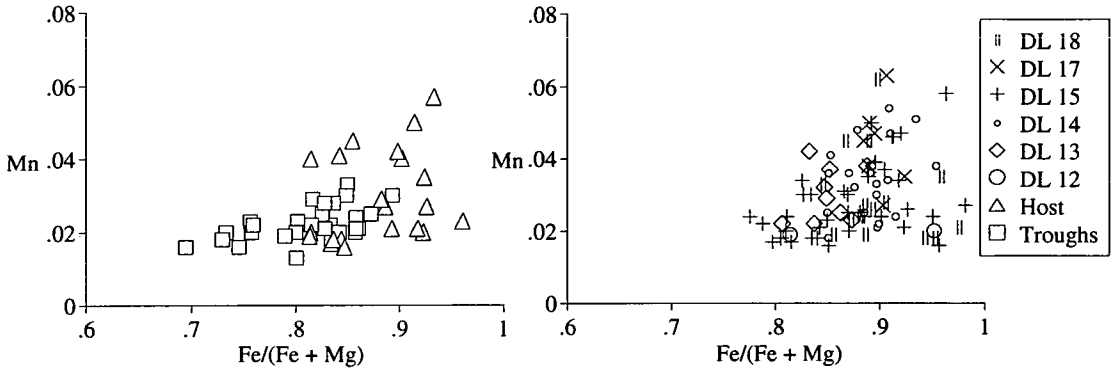

Fig. 4.40: Mn (atoms per 22 oxygens) plotted against Fe/Fe+Mg for biotites from the layered syenite of West Kûngnât.

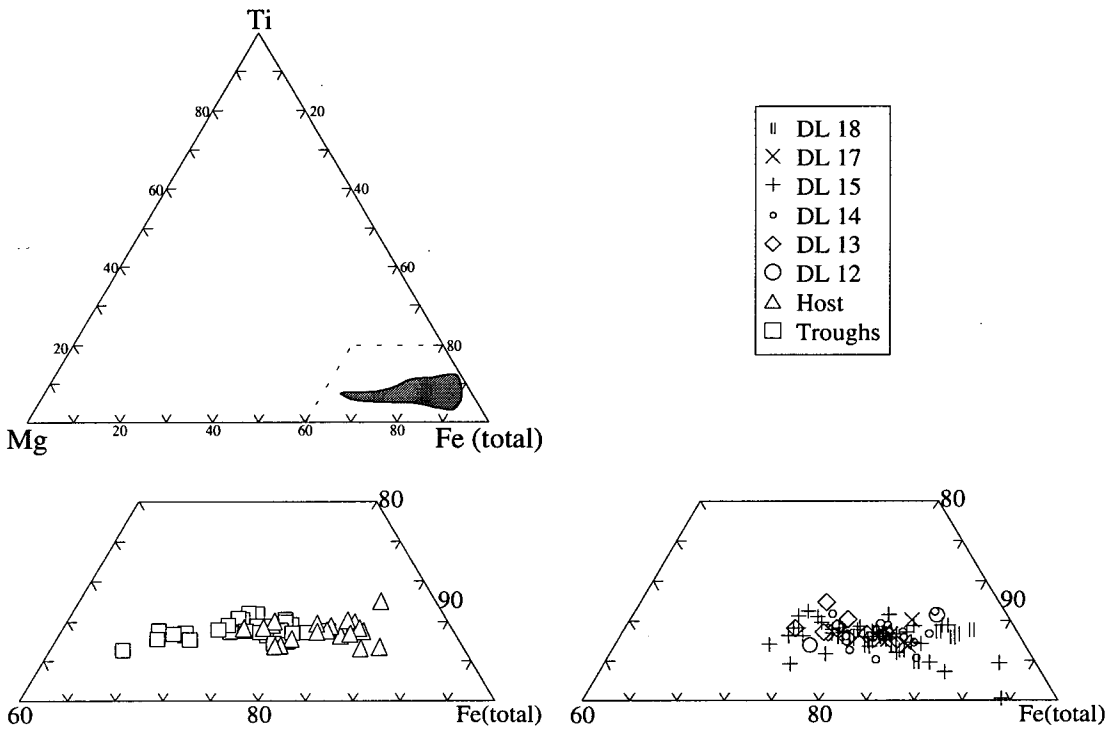

Fig. 4.41: Biotites from the layered syenite of West Kûngnât plotted in terms of Mg:Ti:Fe(total)

Gardar biotites tend to be rich in fluorine but poor in chlorine (Parsons *et al.*, 1991). Fluorine content is controlled by both the fluorine content of late-stage metasomatic fluids and the iron content of the biotite. Wt.% F is plotted against Fe/(Fe+Mg) in Fig. 4.42; the data define a roughly triangular field. This is due to F-Fe avoidance (Finch, 1990).

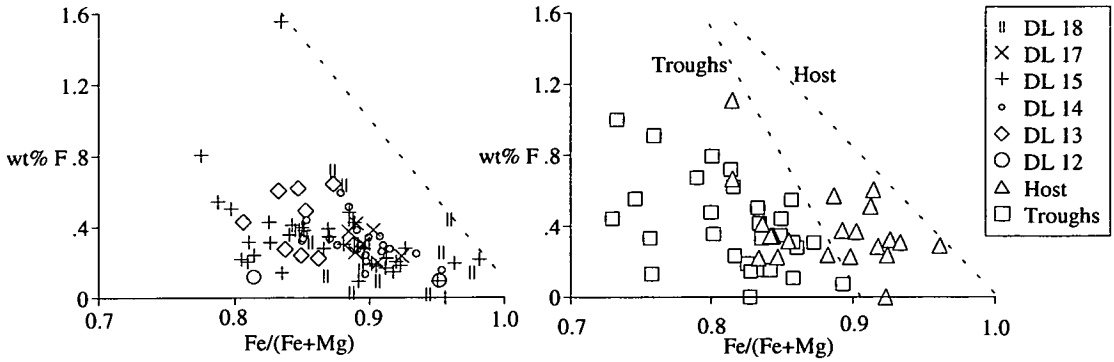

Fig. 4.42: Wt%F vs. Fe/Fe+Mg for biotites from the layered syenite of West Kûngnât. The biotites define triangular fields with Fe correlated antipathetically with F content.

4.3.6: Minor Phases

Apatite

Apatites were analysed for Ca, P, Ce, Pr, Nd, La, F, Na, Si, Fe and Mn. There is no significant variation between apatites from the different facies or different stratigraphic levels of the layered succession. Ca and P show little variation. Na_2O varies from 0.1 to 0.7 wt % and SiO_2 varies from 0.3 to 2.2 wt.%. Both components show considerable within-sample variation. Ce is the most abundant REE and Ce_2O_3, reaches values of 1.0 wt.%. The other REE decrease in abundance in the order Nd_2O_3, La_2O_3 and Pr_2O_3. Mn substitutes for Ca in apatites but was below detection limits in the Nunarssuit apatites; this finding agrees with that of Becker (1984) for the Giant Dykes of Isortoq. Fluorine contents range from 2.8 to 5.2 wt.%; within-sample variation is 1-1.3 wt.%. Chlorine concentrations are less than 0.1 wt.%.

The West Kûngnât apatites are not noticeably different from other Gardar syenite apatites, (Becker, 1984, Mingard, 1990). Aspects of apatite chemistry and zoning discussed in section 4.2.6 are equally valid for the West Kûngnât apatites.

Opaque oxides

Few magnetites were detected in the samples; most of those were exsolved and oxidised to ilmenite/magnetite intergrowths. Geothermometry using co-existing ilmenites and reconstructions of the original composition of the magnetite yielded low subsolidus temperatures which corresponds to the oxidation temperature of the magnetite (see Chapter 7.4). The initial composition of the magnetites can not, therefore, be satisfactorily deduced. No hematite lamellae are visible in the ilmenites. Ilmenite compositions are plotted on Fig. 4.43a and b. Ilmenites are almost pure but plot above the ilmenite-hematite solid solution line. This is thought to be due to the

presence of MnO. Minor elements are plotted in Fig. 4.43c and d. The dominant minor element is Mn. Al, Mg, Cr and V are present in very low concentrations only.

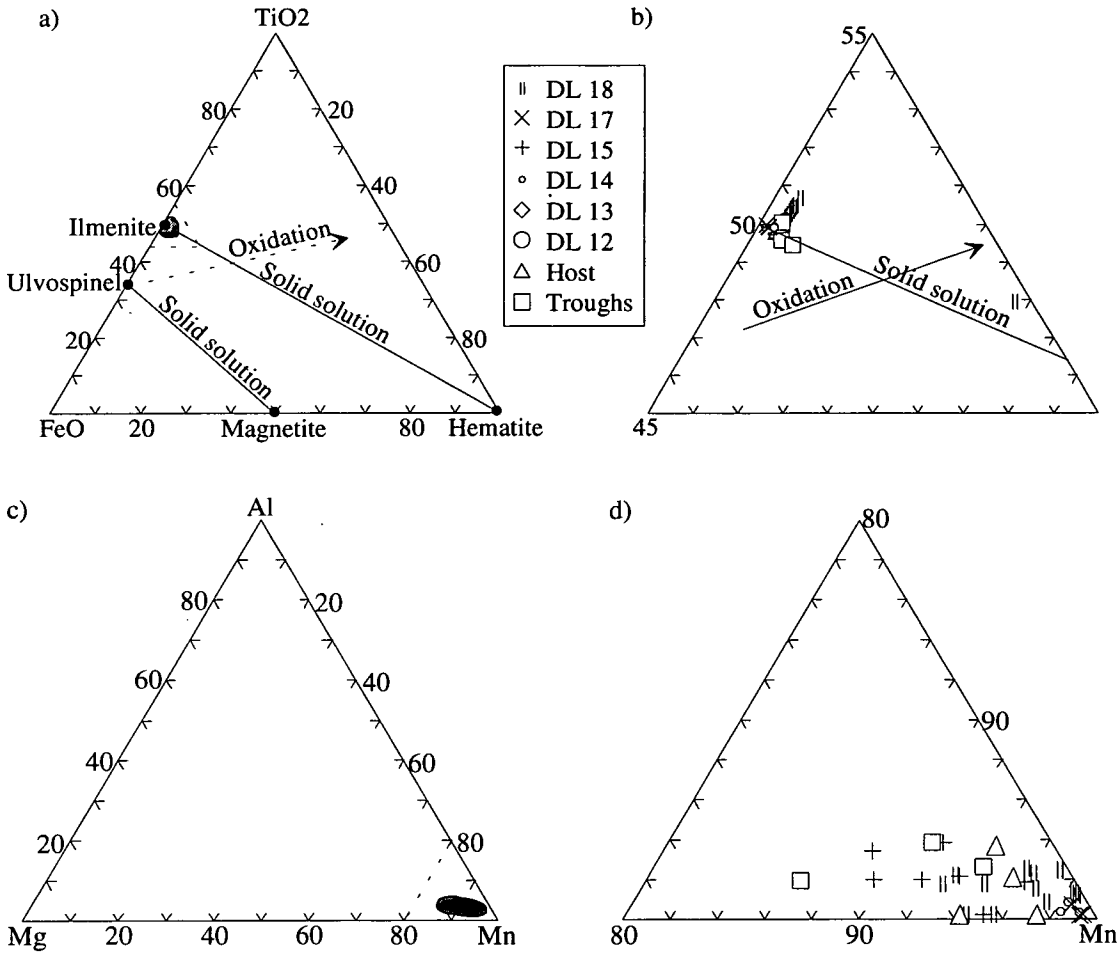

Fig. 4.43 a) and b) ilmenomagnetites plotted as $FeO:TiO_2:Fe_2O_3$, c) and d) ilmeno-magnetites plotted in terms of the minor elements Al, Mg and Mn.

Zircon

Zircon crystals occur occasionally at all stratigraphic levels in the West Kûngnât layered succession and in all facies. Hafnium content varies from 0.6 to 2.0 wt.%, within sample variation is 1.0 wt.%. Most crystals contain <0.5 wt.% Y_2O_3 and are almost pure end-member $ZrSiO_4$. The discussion of zircon chemistry and zoning in section 4.2.6 is equally valid for the West Kûngnât zircons.

4.3.7: Summary

Phases from the trough stacks are more primitive than equivalent phases within the surrounding leucocratic syenite. It is not possible to differentiate, by chemical means, the large biotite and amphibole oikocrysts from smaller biotites and amphiboles within the troughs. Little primary zoning remains. Pyroxenes show subsolidus zoning both optically and chemically. Biotites show F-Fe avoidance. Amphiboles are calcic. Some apatites preserve magmatic zoning, Ca and P concentrations decreasing towards the rim. Zircons show both primary magmatic and sub-solidus zoning.

4.4: A comparison of the major element mineral chemistry of the layered successions of Nunarssuit and West Kûngnât.

4.4.1: General comments

The major element mineral chemistry of the two intrusions is broadly similar. This is not surprising since syenites are the crystallisation products of such evolved magmas and most solid solution series have reached nearly ideal pure end-member compositions. One quite major difference in the major element mineral chemistry exists; the minerals of Nunarssuit show reverse cryptic layering (become more magnesian up section), whilst those of West Kûngnât do not show a definite trend. In both intrusions minerals from troughs are more magnesian than those in the surrounding syenite (sample 2-28 and the rest of DL 2 in Nunarssuit and the trough stack locality in West Kûngnât).

4.4.2: Feldspar

Feldspars from West Kûngnât and Nunarssuit are invariably perthitic. Feldspars from Nunarssuit contain slightly less An and Or but more Ab than those from West Kûngnât. This is unsurprising after a consideration of the feldspar phase diagram. By the time a magma is crystallising syenites the melt from which the feldspars precipitate has reached the bottom of a thermal "valley" in the feldspar phase diagram around these compositions; this effectively fixes the compositions of the feldspars until the solvus is crossed. The Nunarssuit feldspars are slightly more ferroan but less Ba-rich than the West Kûngnât feldspars.

4.4.3: Pyroxene

West Kûngnât pyroxenes are slightly more magnesian than those from Nunarssuit, and contain less wollastonite and acmite components. West Kûngnât pyroxenes contain some Ca-Ti Tschermak's component whereas those from Nunarssuit do not. Pyroxenes from both intrusions have undergone subsolidus alteration resulting in enrichment of the acmite component along rims and cracks.

4.4.4: Olivine

Olivines from West Kûngnât and Nunarssuit have compositions in the range $Fo_{1\text{-}9}$ with less than 5% tephroite component. The olivines have a range of Ca contents largely plotting in the plutonic fields of Simkin and Smith (1970), though some olivines from Nunarssuit plot in the lower portion of the hypabyssal field.

4.4.5: Amphibole

Amphiboles from Nunarssuit have higher Mg/(Mg+Fe) values than those from West Kûngnât. Nunarssuit amphiboles are either calcic or sodic-calcic according to Leake's (1978) classification whereas West Kûngnât amphiboles contain less sodium and are all calcic. Nunarssuit amphiboles plot on the primary magmatic trend defined by Mitchell (1990). Those from West Kûngnât plot on the ferro-actinolite sub-trend, inferred by Mitchell to represent formation of amphiboles at lower temperatures than the magmatic trend, and are therefore inferred either to have undergone subsolidus modification or to be formed in the sub-solidus.

4.4.6: Biotite

Biotites from West Kûngnât and Nunarssuit are annites with practically no siderophyllite component; they have the same range of Mg/(Fe+Mg), 0 to 0.3, the Nunarssuit biotites are slightly more magnesian than those form West Kûngnât. On average biotites from both intrusions contain the same concentration of manganese but those from Nunarssuit have a greater spread of values. All biotites show Fe-F avoidance trends.

4.4.7: Minor phases

Ilmenospinel

Both West Kûngnât and Nunarssuit contain low concentrations of exsolved magnetites. The dominant opaque oxide is ilmenite. The ilmenite is almost pure $FeTiO_3$ in which the only significant substitution is by manganese.

Apatite and zircon

The apatites from Nunarssuit contain substantially more REE than those from West Kûngnât. There are no significant compositional differences between the zircons in West Kûngnât and Nunarssuit. Both the apatites and zircons have essentially ideal end-member compositions with substitutions of REEs.

Chapter 5. Trace element mineral chemistry and whole-rock chemistry.

5.1: Introduction

Trace element analysis of feldspar, pyroxene, olivine, amphibole and biotite was carried out at Brookhaven National Laboratory, Upton, USA using the synchrotron XRF-microprobe. Appendix B.2 gives details of the analytical technique, its drawbacks, detection limits for the various elements analysed in each phase, partition coefficients for mineral/melt partitioning and typical analyses and the range of values obtained. In this chapter trace element data will be presented in turn for each phase analysed. Since less data are available than for major elements, both Nunarssuit and West Kûngnât are dealt with together. Figs. 5.2 and 5.3 show trends in the trace element content of various phases from Nunarssuit and West Kûngnât respectively. Samples are arranged in stratigraphic order from the bottom to the top of the layered zone. Each point on the graphs represents a single analysis and the different analyses of a given phase from the same sample are linked by horizontal lines. Following this, whole-rock XRF data are presented. The use of XRF whole-rock data in the study of layered intrusions is rife with problems. Parsons, (1979) noted that the regular cryptic variation seen in the Klokken syenites from individual mineral analyses does not show up in whole-rock analyses. The Klokken rocks consist of up to 80% feldspar of constant composition. Cryptic variation in the mafic phases is largely obscured by variations in the proportions of different mafic minerals and the feldspar/mafic mineral ratio. Compaction of the cumulate pile and the circulation of post-cumulus fluid can strongly affect the trace element composition of the final solidified rock. An additional problem with syenites is that many elements which are incompatible in basic rocks partition into the solid phase in syenite magmas (Table 5.1, Table 5.2 for trace element partition coefficients).

K, Rb, Ba (LIL)	Fsp
Zr	Zircon, sphene, pyroxene
Nb (HFS)	Sphene, alteration products
Ti	Pyroxenes, sphene, Ti-Fe oxides
Ce, La, Nd (LREE)	Zircon, apatite
Th, U (HREE)	Apatite

Table 5.1: Trace elements and the phases which they partition into compatibly relative to trachytic melt.

Partition coefficient data for syenites or trachytes are sparse due to the experimental problems of modelling Fe-rich systems. Table 5.2 lists the most suitable partition coefficients available for various trace-elements. Where no partition coefficients

were available for trachytes or syenites values quoted are either for andesites or rhyolites. It is felt that the andesite values are more realistic since the degree of polymerisation of syenites is similar to that of andesites (Chapter 7.5.1) and Mysen and Virgo (1980) argue that the structure of the melt is a more important control on partitioning than the precise composition of the melt.

Table 5.2. Partition coefficients for trace elements analysed using the XRF-microprobe at Brookhaven. (W) = Wörner *et al.* (1983), values for phonolites; (H) = Henderson (1982) values for andesite except for Sr (rhyolite) and biotite (rhyolite); (L) - Lemarchand *et al.* (1987), values for trachyte; (F) = Frey *et al.* (1978), values for basalts; (P) = Pearce and Norry (1979), values for "acid" magmas (Pearce and Norry determined these coefficients using a compilation of previously published data for magmas with greater than 60% SiO_2); (M) = Mahood and Stimac (1990), values for trachytes. Amphibole figures are for hornblende.

Element	Phase				
	Feldspar	Pyroxene	Olivine	Amphibole	Biotite
Zn	0.05 (W)	0.4 (H)	0.7 (H)	0.69 (H), 3.3 (W)	20 (H)
Ge	-	-	-	-	-
Rb	0.16 (L)	0.04 (L)	0.08 (L)	0.14 (L)	3.3 (H)
Sr	9.4 (H)	0.1 (H)	0.01 (F)	3.1 (W)	0.12 (H)
Y	-	4 (P)	0.01 (P)	6 (P)	-
Nb	-	0.8 (P)	0.01 (P)	4 (P)	-
Mo	-	-	-	-	-
Ta	0.05 (L)	0.47 (L)	0.14 (L)	1.02 (L)	-
Ni	-	2-4 (F)	3.8-35 (F))	-	-
Cu	-	-	-	-	-
Ga	-	0.3-0.8 (H)	0.04 (H)	-	-
Zr	0.17 (L)	1.02 (L)	0.07 (L)	0.5 (W), 4 (P)	-
Hf	0.08 (L)	0.95 (L)	0.09 (L)	0.84 (L)	2.1 (H)
Ba	5.4 (M)	-	-	-	-

Most of the whole-rock data are from Nunarssuit. On the basis of the reverse cryptic variation seen in the major element trends of the minerals from the Nunarssuit layered succession it was felt that the Nunarssuit whole-rock data would be more interesting than that of West Kûngnât. Some whole-rock XRF data for the trough stacks and surrounding syenites in West Kûngnât is also discussed. Representative XRF analyses are presented in Appendix E.

Samples numbers are listed in Appendix A.

5.2: Feldspar

The analysed elements which are above detection limits are Zn, Rb, Sr, Y, Mo, Ni, Cu, Ga, Zr and Ba. Ti and Nb were below detection limits (see Appendix B.2). Fewer feldspars than other phases were analysed using the XRF-microprobe. Most of the points analysed luminesced red when analysed using cathodoluminescence apparatus and thus analyses may not represent primary compositions (Chapter 3.2.1, and Finch (1990)). In the Nunarssuit feldspars Ni content decreases up section (Fig. 5.2a) and Ba content increases up section (Fig. 5.2b). In West Kûngnât no stratigraphic trends were seen but the trough stack feldspars contain less Zn and Ga than the surrounding syenite (Figs. 5.3a and 5.3b). Perhaps a more interesting result lies in the comparison of the trace element compositions of blue and red luminescing feldspars from the same sample (Fig. 5.1).

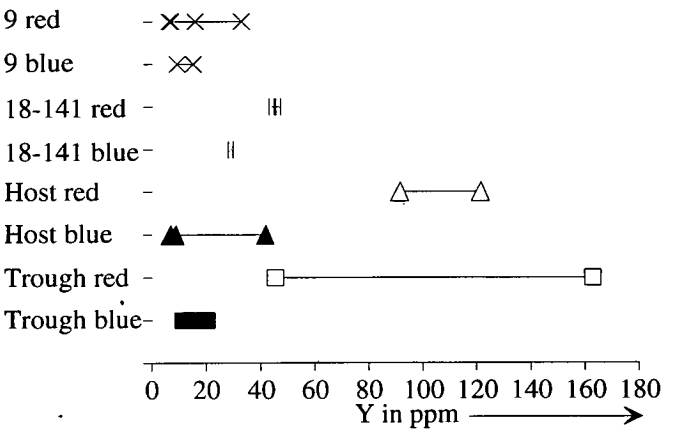

Fig. 5.1: Y content of red and blue luminescing feldspars. Sample 9 is from normal syenite from below the zone of layering (Unit 1),Nunarssuit. The other samples are from West Kûngnât. Trough samples are 26 and 30, host samples are 31 and 36, 18-141 is from the melanocratic base of a rhythm in Unit 4. N.B. samples are not arranged in stratigraphic order

Analyses of blue and red luminescing feldspars were carried out on sample 9 from Nunarssuit and samples 18-141, 31 (host syenite next to the trough stacks) and 26 and 30 (syenite from the trough stacks) from West Kûngnât. For all these samples the red luminescing feldspar contained more Sr, Y, Mo, Cu and Ga than the blue luminescing feldspar.

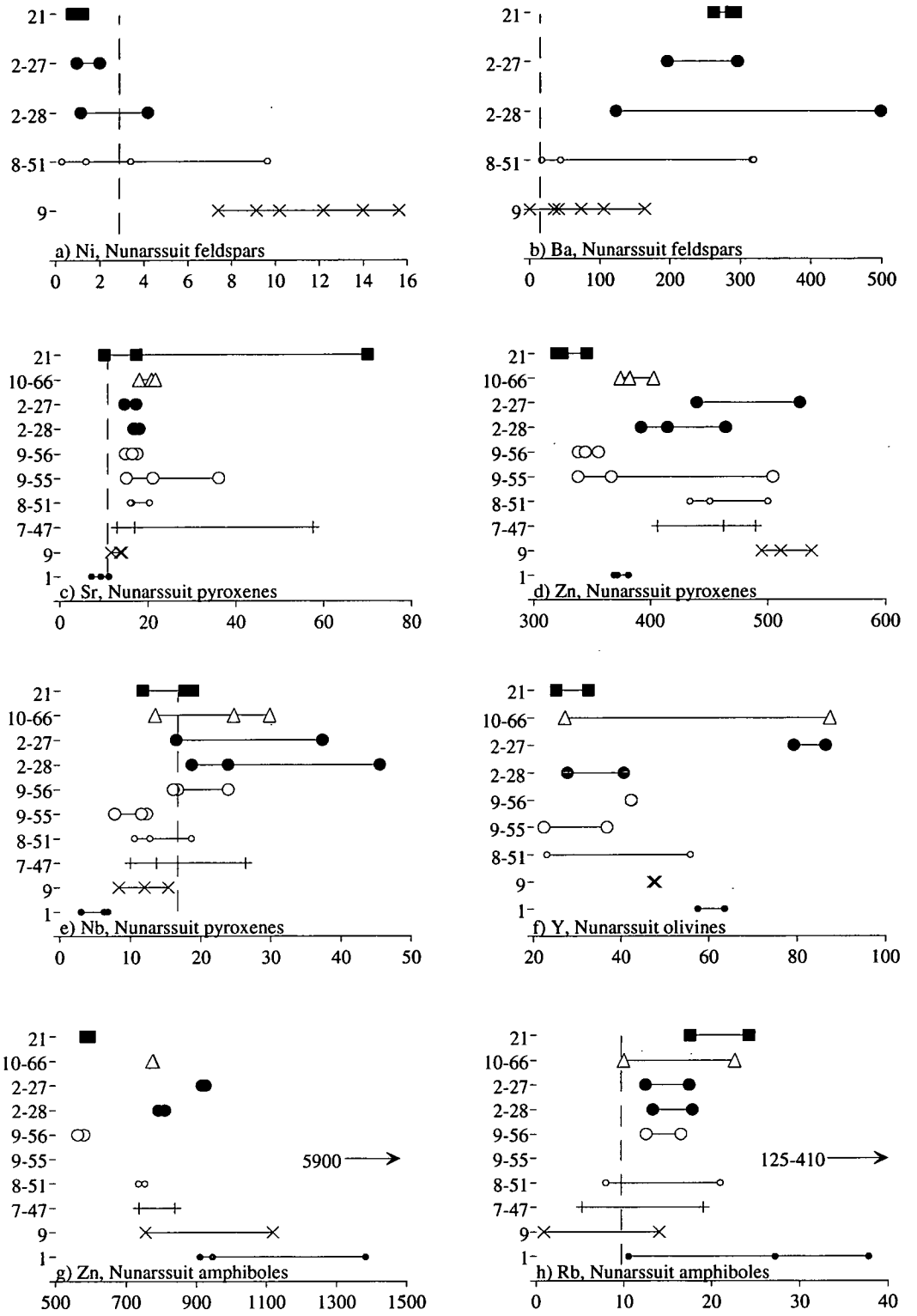

Fig. 5.2a-h: Samples are arranged in stratigraphic order, dashed lines show detection limits, (see over).

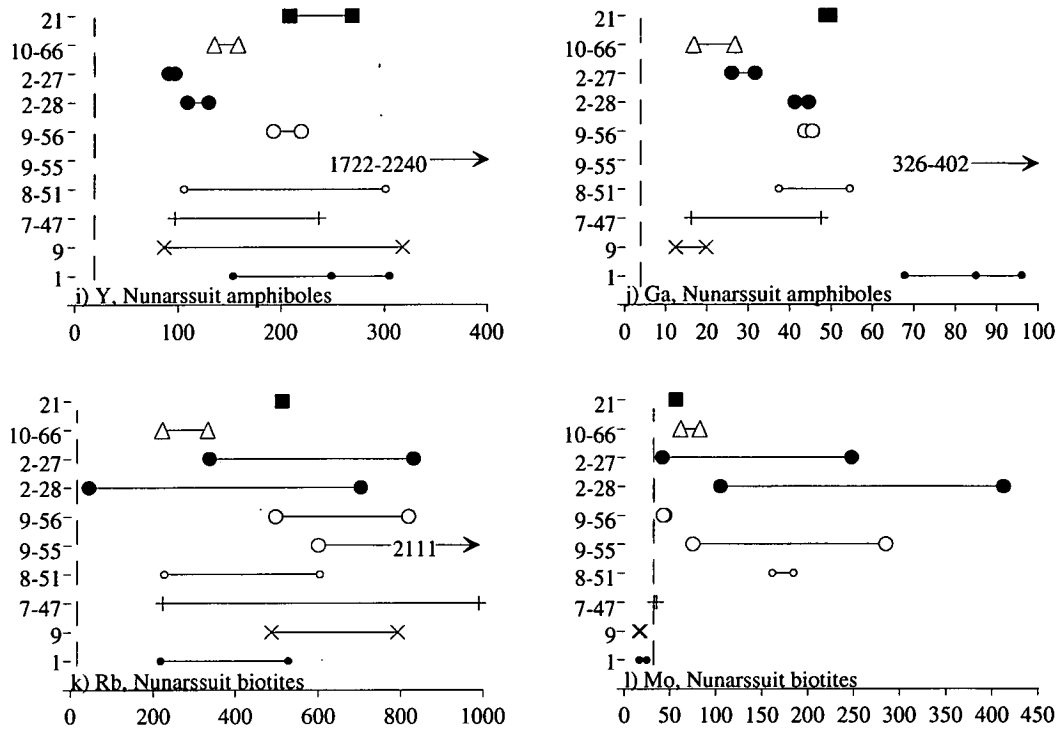

Fig. 5.2i-l: Trace element trends in various phases from Nunarssuit. Samples are arranged in stratigraphic order (see Figs. 2.1 and 2.1 for section). Dashed lines show detection limits, on graphs d), f) and g) detection limit plots to left of the data. Sample 1 is a melanocratic autolith from Unit 10, sample 9 is normal syenite from below the zone of layering (Unit 1), 7-47 is from the melanocratic base of a rhythm in Unit 3, 8-51 is from the melanocratic base of a rhythm in Unit 3, 9-55 and 9-56 are melanocratic and more leucocratic samples from the lower melanocratic unit, Unit 5, 2-28 is a sample from a melanocratic trough in Unit 7, 2-27 is a sample of leucocratic syenite close to the trough, 10-66 is from the melanocratic base of a rhythm in Unit 7 and 21 is from the melanocratic base of a faint rhythm in Unit 10.

5.3: Pyroxene

The analysed elements which are above detection limits are Zn, Ge, Sr, Y, Nb, Mo, Ga and Zr. Rb, Ta, Ni and Cu are below detection limits (see Appendix B.2). In Nunarssuit, pyroxene Sr contents show a general increase up section (Fig. 5.2c). There is a decrease up to Unit 5 (DL 9, the Lower Melanocratic Unit), then an increase at Unit 5 and a further decrease in the concentration Zn (Fig. 5.2d) and Ge whilst Nb (Fig. 5.2e) increases up to Unit 5 and then decreases. There is no consistent stratigraphic trend in Y, Mo, Ga and Zr contents. In West Kûngnât the pyroxene from host syenite around the trough stacks is richer in Zn than in the trough stacks themselves (Fig. 5.3c) and Sr levels show a decrease from DL 13 to DL 18 (Fig. 5.3d). There are no trends in Ge, Y, Nb, Mo, Ga and Zr contents.

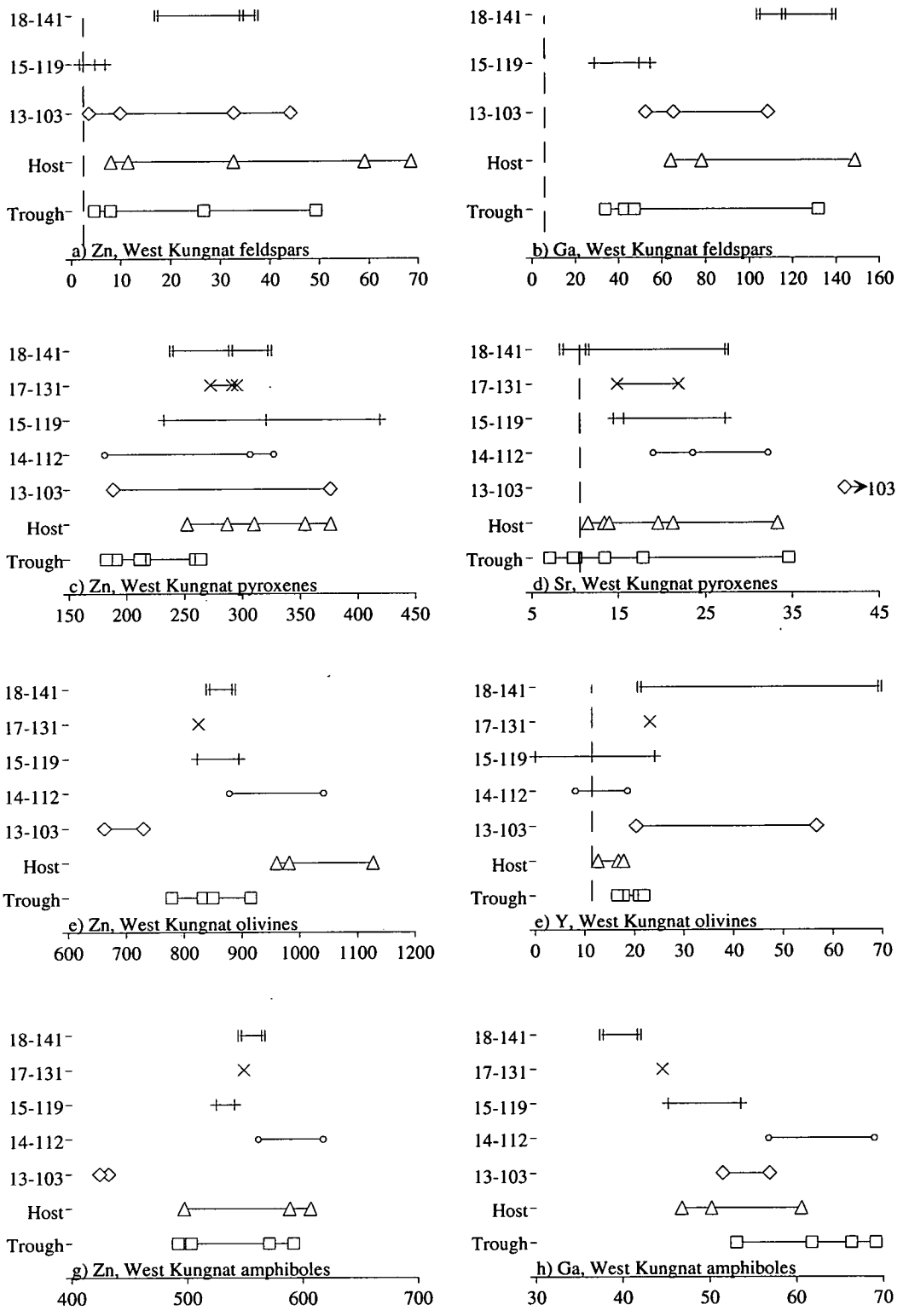

Fig. 5.3a-h: Samples are arranged in stratigraphic order, dashed lines show detection limits (see over).

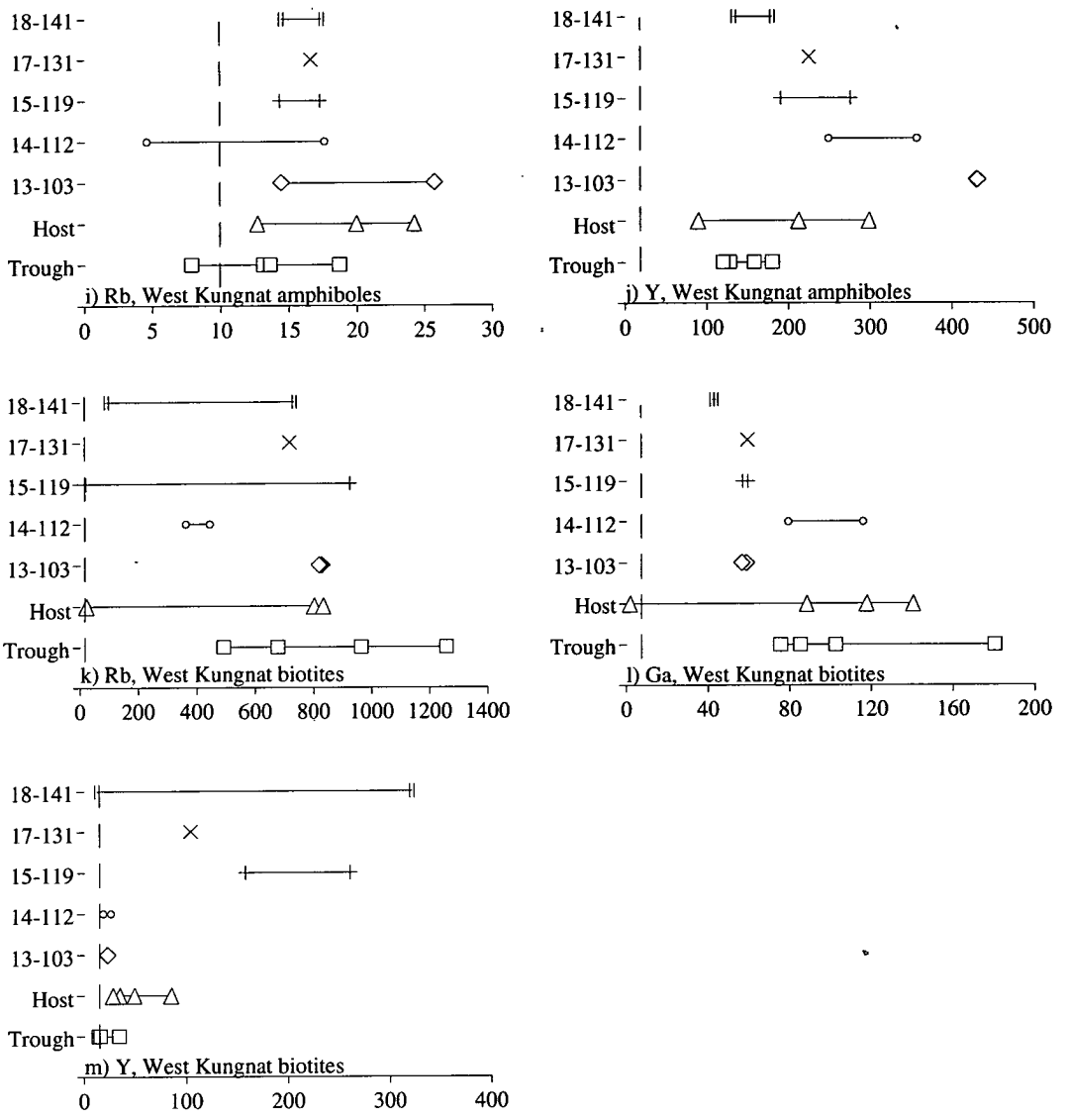

Fig. 5.3: Trace element trends in various phases from West Kûngnât. Samples are arranged in stratigraphic order (see Figs. 2.4 and 2.5 for section). Detection limits are shown by dashed lines as in Fig. 5.2. Trough samples are samples 26 and 30, host samples are samples 31 and 36, 13-103 is from the leucocratic portion of a rhythm in Unit 3, 14-112 is from the leucocratic base of a rhythm in Unit 3, 15-119 is a sample from the melanocratic base of a rhythm in Unit 4, 17-131 is from the melanocratic base of a rhythm in Unit 4 and 18-141 is from the melanocratic base of a rhythm in Unit 4.

5.4 Olivine

The analysed elements which are above detection limits are Zn, Sr, Y and Mo. Ge, Rb, Ta, Ni, Cu, Ga, Zr and Hf are below detection limits (see Appendix B.2). In Nunarssuit there is a rough decrease in Y content up section (Fig. 5.2f), with a jump in the trend at Unit 5. Zn, Sr and Mo show no trend. In West Kûngnât none of the above elements show a consistent stratigraphic trend although Zn contents are lower

(Fig. 5.3e) and Y contents are higher (Fig. 5.3f) in the trough stack olivines than in those of the surrounding syenite.

5.5: Amphibole

The analysed elements which are above detection limits are Zn, Rb, Sr, Y, Nb, Ga, Zr and Hf. Ge, Mo, Ta, Ni and Cu are below detection limits (see Appendix B.2). In Nunarssuit the amphibole Zn (Fig. 5.2g) levels decrease up section with a jump at Unit 5 whilst Rb increases up section (Fig. 5.2h). Y (Fig. 5.2i) shows no trend up to Unit 5 and then decreases. Ga, Hf and Zr all increase up to Unit 5 and then show a minimum at sample 10-66 (Fig. 5.2j). Sr shows no trend. In West Kûngnât the trough stack amphiboles are richer Ga (Fig. 5.3l) but poorer in Rb (Fig. 5.3h), Sr and Hf than the surrounding syenite. From DL 13 to 18 there is a general increase in Zn (Fig. 5.3g) and Sr and a decrease in Y (Fig. 5.3j), Nb, Ga, Zr and Hf.

5.6: Biotite

The analysed elements which are above detection limits are Zn, Rb, Sr, Y, Nb, Mo and Ga. Ge, Ta, Ni, Cu and Hf are below detection limits (see Appendix B.2). In Nunarssuit there is a decrease in Rb content up section to Unit 5 and then a curved trend with a maximum at 10-66 (Fig. 5.2k), Mo contents increase up section to Unit 5 and then decrease (Fig. 5.2l). Zn, Sr, Y, Nb and Ga show no trend. In West Kûngnât the trough stack biotites are richer in Rb (Fig. 5.3k) and Ga and poorer in Y (Fig. 5.3m) than those in the surrounding syenite. There is a general decrease in Ga (Fig. 5.3l) from DL 13 to DL 18. Zn, Sr, Y, Nb and Mo show no trend.

5.7: Nunarssuit whole-rock chemistry

5.7.1 Introduction

Cryptic variation in the Nunarssuit pluton is detectable in the whole-rock analyses. Elements analysed for were Si, Al, Fe, Mg, Ca, Na, K, Ti, Mn, P, Nb, Zr, Y, Sr, Rb, Th, Pb, Zn, Cu, Ni, Cr, Ce, Nd, La ,V, Ba and Sc. Ni, Cr and V were below detection limits. Typical XRF whole-rock data is presented in Appendix E.

5.7.2: CIPW Norms

CIPW norms were calculated for a range of samples at various heights in the stratigraphy and from various facies. Typical norms are presented in Appendix E. Samples from the base of the layered succession (MH-NUN-92 9 and 14, DL 6 and DL 7) were quartz-normative. Samples 10-53 and 10-66 (from the leucocratic portions of rhythms) were also quartz-normative. The other samples (MH-NUN-92 1, 4, 5, 6, 15, 16, DL 10 and 9-57) were all olivine-hypersthene-normative except MH-NUN-92 3 (meta-basite xenolith) which was nepheline-normative. This sample contains far more anorthite in its norm than the other samples. Other normative minerals were orthoclase, albite, anorthite, diopside, magnetite, ilmenite and apatite. A few samples (6-41, 6-44 and MH-NUN-92 14) contain acmite. This is thought to reflect an increased Na content in these samples due to subsolidus alteration (see Chapter 6)

5.7.3: Element variation with stratigraphic height

Syenite autoliths (MH-NUN-92 4 and 1), xenoliths (MH-NUN-92 3) and troughs (troughs from DL 3 and 4) contain higher concentrations of the major elements which enter the mafic minerals and lower concentrations of the major elements which enter the felsic minerals (e.g. Na_2O, Fig. 5.4a), this trend is also seen in the trace elements Rb, Pb, Zn, Cu, Ba (e.g. Rb, Fig. 5.4b). This trend is seen to a lesser extent in the samples from the melanocratic bases and leucocratic portions of layers from the same drill locality.

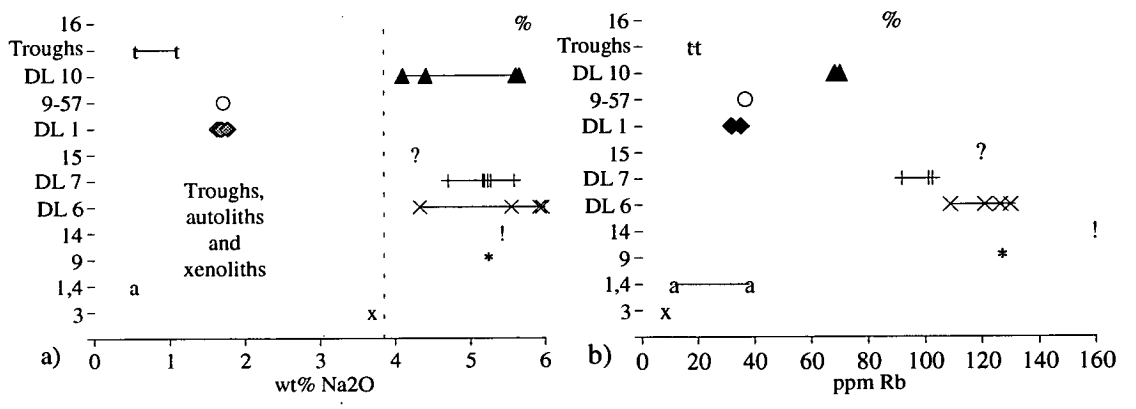

Fig. 5.4: a) variation of Na_2O with height. Samples which do not come from the repeated rhythms have a distinct chemistry. In this case the samples contain less Na_2O than the layers. b) ignoring the samples from troughs, autoliths and xenoliths Rb concentration decreases up section. Troughs, autoliths and xenoliths contain less Rb than the samples from the layers.

The only elements to show any consistent variation with stratigraphic height are Rb (a decrease in concentration up through the stratigraphy, Fig. 5.4b) and Ba (a slight

increase up through the stratigraphy, Fig. 5.5a). The range of the other elements is constant up section (e.g. La, Fig. 5.5b). Mg number calculated as Mg/(Mg + Fe^{2+}) increases up section to DL 10 and then decreases (Fig. 5.6).

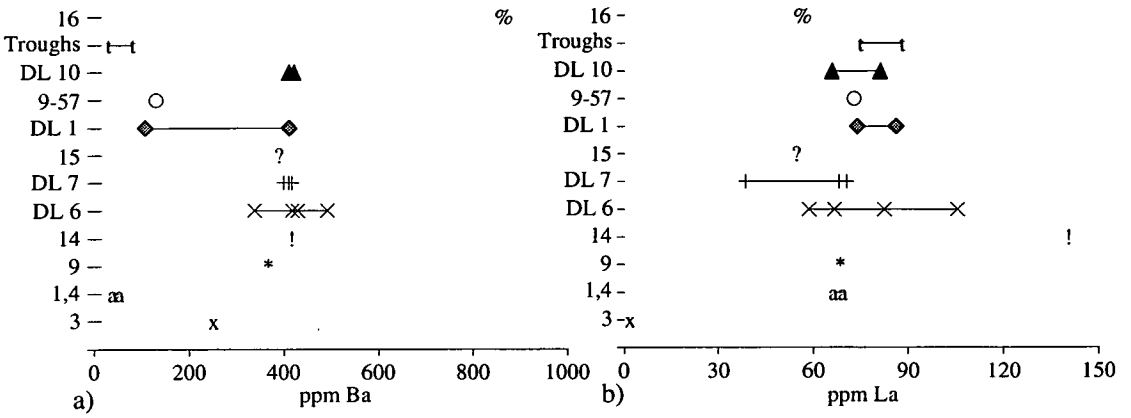

Fig. 5.5 a) Ba concentration increases up section (ignoring troughs, autoliths and xenoliths). b) La concentration shows no variation with stratigraphic position, troughs, autoliths and xenoliths have the same range of concentrations as the layers.

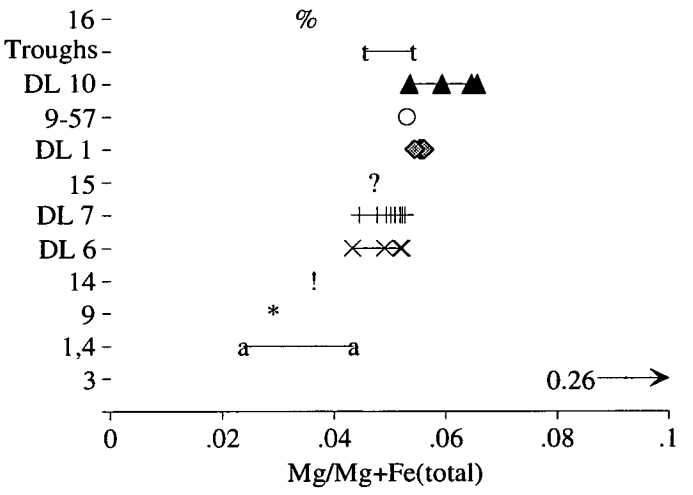

Fig. 5.6 Mg number calculated as Mg/(Mg + total Fe) increases up section to DL 10 and then decreases. Troughs and autoliths fit on this trend. The meta-basite xenolith MH-NUN-92 3 does not fit on this trend.

5.7.4: Element variation with mafic content

Elements which are partitioned compatibly into either mafic or felsic minerals will have a zig-zag concentration profile up through the stratigraphy as the melanocratic bases of layers alternate with more leucocratic rock. The total Fe and Mg content of the samples is taken as a measure of the concentration of mafic minerals. Plots of total Fe+Mg against different elements generally produce straight lines. Positive correlations are seen against Ca, Ti, Mn, P, Y, Zn, Cu, Ce, Nd, Sc, Y, Zn, Cu, Nd, Sc (Fig. 5.7a); negative correlations are seen against Al_2O_3, Na_2O, SiO_2, K_2O, Sr, Rb, Pb, Ba (Fig. 5.7b, c and d); no correlation is seen against Nb, Zr, La and Th (Fig. 5.7c

and d). Elements which show a positive correlation are those which enter mafic minerals whilst those which show a negative correlation are those which enter felsic minerals. Sample MH-NUN-92 3 plots off these trends; this sample is a meta-basite. Sample MH-NUN-92 6 plots above the trend for P_2O_5 on Fig. 5.7a. This is because this sample contains a large amount of cumulus apatite. Samples MH-NUN-92 1,4 and 5 plot below the observed trend. No thin sections are available for these samples but the lack of correlation is presumably due to these samples being apatite-poor relative to the concentration of other mafic minerals. These samples are also deficient in Ca relative to the correlation seen between Ca and Fe+Mg.

All the syenite samples fit on the observed whole-rock trends, apart from the plot of Fe+Mg against P_2O_5 (Fig. 5.7a), regardless of their colour index. It is felt that this is a good indication that the syenite autoliths seen are indeed co-magmatic with the layered syenites. Sample MH-NUN-92 3, the meta-basite, plots off many of the observed trends because the meta-basite is a xenolith.

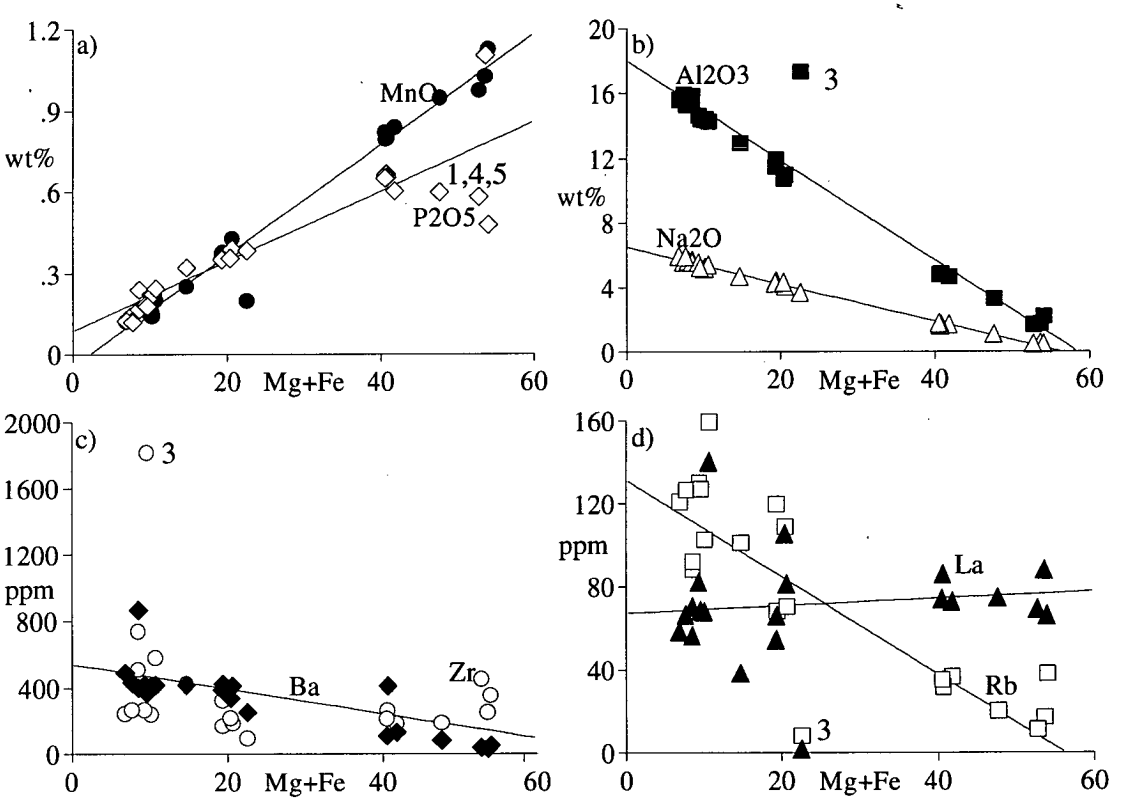

Fig. 5.7: a) positive correlation of MnO and P_2O_5 with Fe+Mg. The point which lies off the Mn trend is sample MH-NUN-92 3. The high Fe+Mg points lying off the P_2O_5 trend are discussed in the text. b) negative correlation of AL_2O_3 and Na_2O with Fe+Mg. The point which lies off the Al_2O_3 trend is sample MH-NUN-92 3. c) negative correlation of Ba with Fe+Mg, Zr shows no trend with Fe+Mg. d) negative correlation of Rb with Fe+Mg, La shows no trend with Fe+Mg. The point which lies off the Rb trend and has less La than the other samples is sample MH-NUN-92 3.

The main control on the concentration of Ba and Rb in the syenites is the concentration of feldspar. However Ba content increases up section (Fig. 5.5a) and Rb decreases up section (Fig. 5.3b, ignoring samples from troughs, autoliths and xenoliths) independently of feldspar concentration. Ba is compatible in alkali feldspar whilst Rb is incompatible (see Table 5.2 for partition coefficients). The REE are incompatible, it is surprising that whilst La shows no correlation with Mg+Fe, Nd and Ce are positively correlated with Mg+Fe. This implies that there is a mafic phase which fractionates the REE. La, Nb and Th show no trend with either Mg+Fe or stratigraphy. The increase in Mg number and Ba concentration up section together with the decrease in Rb up section indicate that the Nunarssuit layered syenite is inversely cryptically zoned.

5.7.5: Comparison with the Klokken layered syenites

Parsons (1979, fig. 7) presents plots of whole-rock data from the Klokken intrusion of South Greenland. Similar plots for the Nunarssuit syenite are presented below. Nunarssuit layered syenites plot in the same field as the Klokken layered syenites on plots of FeO:MgO:Na_2O+K_2O and K_2O:CaO:Na_2O (Fig. 5.8) The meta-basite xenolith, MH-NUN-92 3, plots off these trends.

In a Ca:Fe:Mg diagram the two intrusions plot differently. Parsons (1981, fig. 4) plotted the compositions of samples which were likely to represent liquid compositions (the dark grey fields and the heavy dotted line in Fig. 5.9), together with pyroxene and olivine compositions on a Ca:Fe:Mg plot and noted the similarity between the trend shown by the possible liquids and the $CaSiO_3$-$FeSiO_3$ phase boundary which was deduced experimentally by various workers (e.g. Yoder, Tilley and Schairer, 1963 and Lindsley and Munoz, 1969). Cumulate rock was not plotted but plotted on either side of the line depending on whether pyroxene or olivine was the cumulus phase.

Only the meta-basite (MH-NUN-92 3) plotted near this trend. The autoliths MH-NUN-92 1 and 4 and material from melanocratic troughs (MH-NUN-92 5 and 6, 9-57 and DL 1) are the most ferroan compositions, containing a high proportion of olivine. The leucocratic samples MH-NUN-92 15,14 and 16 have a decreasing Fe content and an increasing Ca content. This trend is clear from the colour-index of the samples, MH-NUN-92 15 being the most melanocratic. The melanocratic samples from DL 6, 7 and 10 are more ferroan than the leucocratic samples as a consequence of the higher concentration of olivine in these samples. Samples from DL 10 are more

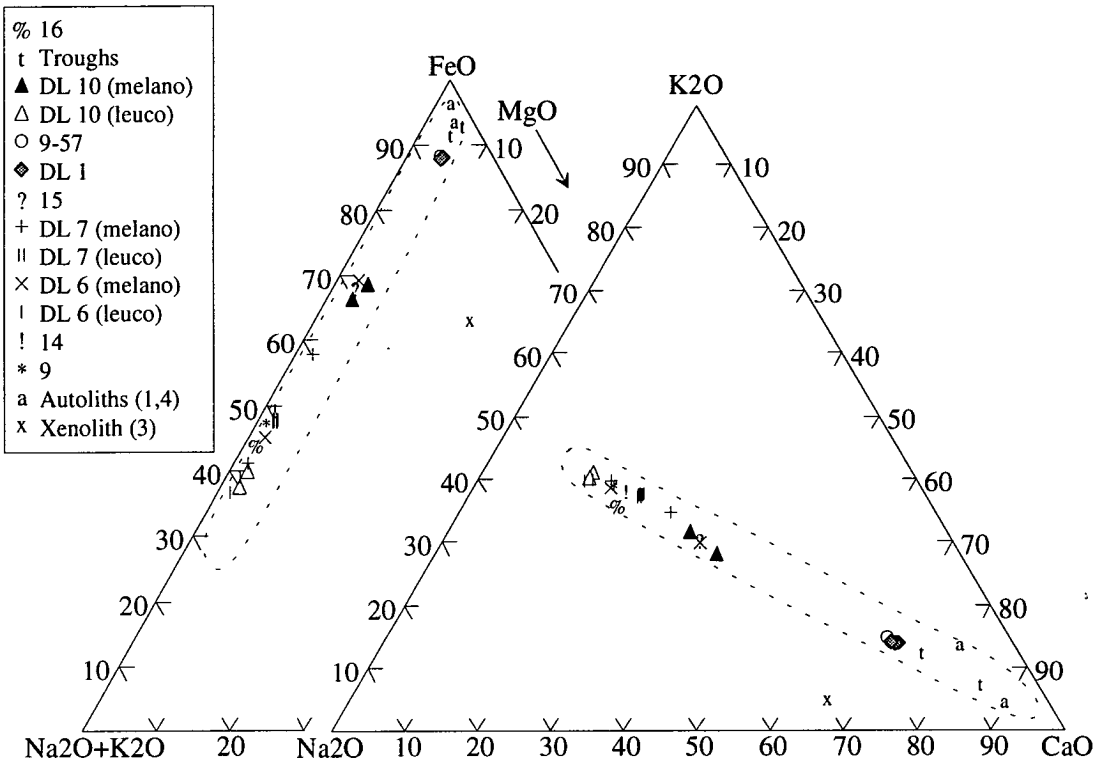

Fig. 5.8 Plots of Na2O+K2O:FeO:MgO and Na2O:K2O:CaO for whole rock analyses from the Nunarssuit layered syenite. Samples plot in the same fields as the Klokken syenites (shown by dashed lines, Parsons, 1979) Sample outside the field is MH-NUN-92 3.

magnesian than those from DL 6 or 7, reflecting the apparent inverse cryptic zoning of the layered series already mentioned in section 5.7.4. Point P is where the composition P1 (which is taken as the liquid composition from which the syenite crystallised, see Chapter 7.3) plots.

The liquid from which the Nunarssuit syenites crystallised may have been more ferroan than that which crystallised the Klokken syenites, so the fact that composition P does not plot close to the liquid line of Klokken, as defined by Parsons (1981), is not necessarily significant. However it is surprising that the syenites of Klokken and Nunarssuit appear to have similar compositions on the basis of Fig. 5.8 but that leucocratic Nunarssuit syenite, which must have a composition fairly similar to the crystallising liquid, does not plot close to the likely liquid compositions identified by Parsons (1981). Samples MH-NUN-92 1, 4, 5, 6, 9-57 and DL 1 are obviously enriched in iron relative to a coexisting melt due to the concentration of olivine. The melanocratic portions of DL 6, 7 and 10 are more iron-rich than the leucocratic samples from the same localities due to the higher concentration of mafic phases.

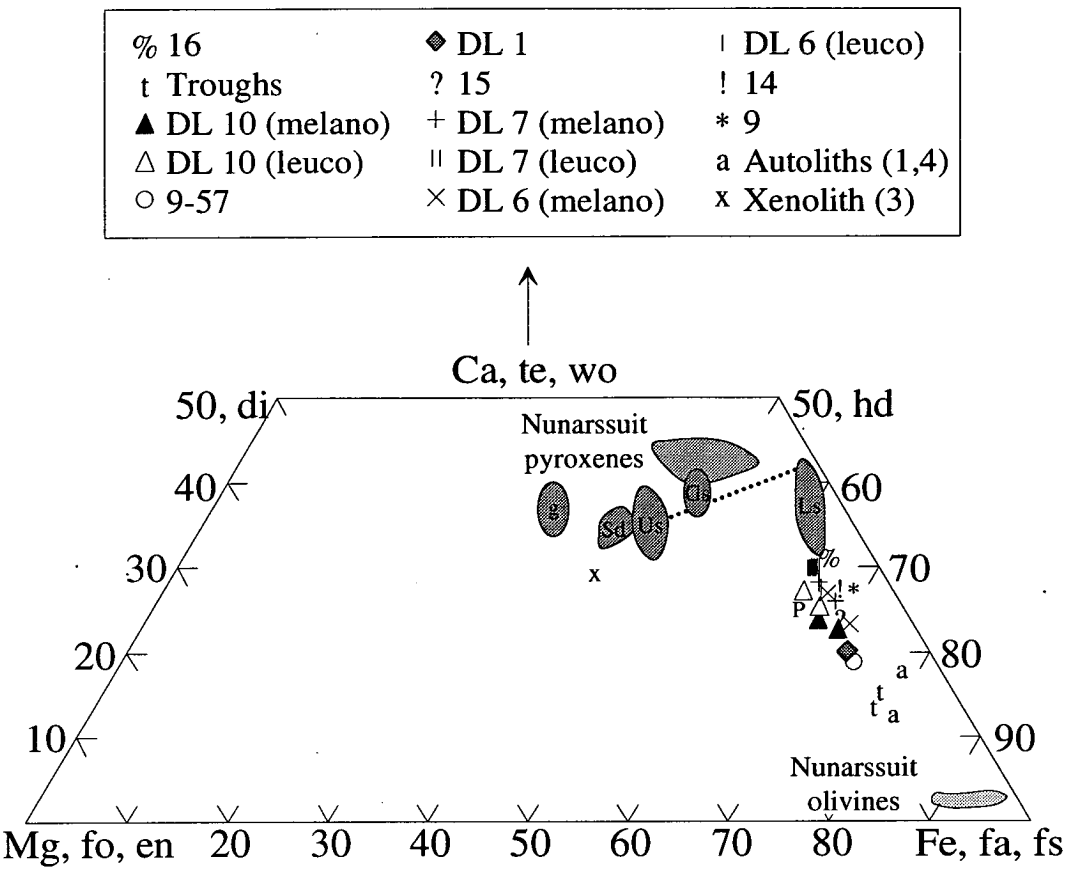

Fig. 5.9: Plot of Nunarssuit whole-rock samples in terms of atomic % (Mg:Ca:Fe). Superimposed on this are: the field for Nunarssuit olivines (in terms of forsterite (fo), tephroite (te) and fayalite (fa), the light grey field), the field for Nunarssuit pyroxenes (in terms of enstatite (en), diopside (di), hedenbergite (hd) and ferrosalite (fs), the mid-grey field), the postulated liquid line for Klokken (the dark dotted line, from Parsons, 1981,) and the samples thought to approximate to liquid compositions in Klokken, (the dark grey fields, g = gabbro, Sd = syenodiorite, Us = unlaminated syenite, Gs = granular syenite, Ls = laminated syenite, from Parsons, 1981).

It is not obvious where the crystallising liquid for the Nunarssuit syenite should plot. If P is a suitable composition to crystallise the Nunarssuit syenites then, following Parsons (1981) Fig. 5.9 implies that the leucocratic syenite sample MH-NUN-92 16 is a pyroxene-rich cumulate, whilst MH-NUN-92 14 and 15 are olivine-rich cumulates. On the basis of field observations this is not a reasonable conclusion since samples 16, 14 and 15 closely resemble MH-NUN-92 9 and the rest of the unlayered syenite. Whilst all the syenites are probably cumulates the leucocratic unlayered syenites appear to have accumulated the same minerals. An alternate explanation is that the Parsons analysis is not relevant due to the complicating factors of subsolidus biotite and amphibole growth (both of which have high Fe to Ca contents) and substitution of Na for Ca in the pyroxenes, which drives compositions away from the Ca corner of the plot, towards the Fe corner. A simpler explanation is that the composition P is not a suitable for the magma which crystallised to produce the

syenites. According to this argument a more suitable composition would have been more calcic and less magnesian and ferroan.

The conclusions derived from Fig. 5.9 are that: 1) MH-NUN-92 3 is not comagmatic with the Nunarssuit syenites, 2) the autoliths and troughs of Nunarssuit are enriched in olivine relative to the surrounding syenite and 3) the melanocratic portions of layers are more Fe-rich than the adjacent leucocratic portions of layers.

5.8 West Kûngnât whole-rock chemistry

Samples from the troughs stacks and the surrounding syenite were analysed. Typical norms are presented in Appendix E. Samples from the troughs and surrounding syenite were olivine-normative. Other normative minerals were hypersthene, orthoclase, albite, anorthite, diopside, magnetite, ilmenite and apatite. Upton *et al.* (1971, table 1) analysed various rocks from West Kûngnât and calculated norms. Three samples (26004,26005 and 26470) came from the layered succession, and were collected from roughly the same locality. 26004 was nepheline-normative (1.8% nepheline), 26005 was olivine normative and 26470 was quartz normative (0.2% quartz). The overlying syenites are all quartz normative. Variation between the whole-rock chemistry of the troughs and surrounding syenite is masked due to the high concentration of feldspars of constant composition, Parsons (1979) reported a similar problem for the Klokken syenites. For example the range of Mg number for whole-rock analyses of the troughs is the same as that for the surrounding syenite. This is surprising since the mafic minerals in the troughs tend to be more primitive than those in the surrounding syenite (Chapter 4.3).

5.9: Summary and conclusions

The reader is referred to Appendix B.2 for the various problems associated with XRF-microprobing and the interpretation of the results obtained. In the following section it is assumed that the analyses obtained represent the composition of the phase which I meant to analyse. It has been assumed that the phases crystallised in equilibrium with the melt surrounding them and that the concentration of elements with a negative partition coefficient between a particular phase and melt should increase up section and that the concentration of elements with a positive partition coefficient between a particular phase and melt should decrease up section. Table 5.2 lists partition coefficients.

5.9.1: Nunarssuit

The Sr content of pyroxenes and the Rb content of amphiboles increases up section. This is normal cryptic layering. The Ba content of feldspars and the Y content of amphibole increases up section whilst the Zn and Ge content of pyroxenes and the Y content of olivines decreases up section. This is reverse cryptic zoning. The Zn content of amphiboles decreases up section, there is dispute in the literature as to whether Zn is partitioned preferentially into amphibole or silicic melt (Henderson 1982, Wörner *et al* 1983). The Nb (partition coefficient less than 1) content of pyroxenes and the Mo (no suitable published partition coefficients) content of biotites increase up to Unit 5 and then decrease. The Ga (no suitable published partition coefficients), Hf (partition coefficient less than 1) and Zr (published partition coefficients are both greater than 1 (Pearce and Norry 1979) and less than 1 (Wörner *et al.* 1983)) contents of amphiboles increase up to unit 5 and then show a curved trend with a minimum at 10-66, the Rb (partition coefficient greater than 1) content of biotite shows the opposite trend, decreasing up to Unit 5 and then curving with a minimum at 10-66.

Sample MH-NUN-92 1, a melanocratic autolith from Unit 10, sits at the bottom of the normal cryptic zoning trend in Sr for pyroxene and at the bottom of the Y trends for olivine (reverse cryptic zoning) and amphibole. Sample MH-NUN-92 1 sits at the high end of the trends for Rb in amphibole and Zn in pyroxene. Samples 9-55, 9-56 and 2-28 always sit at inflection points or reversals on all the trends.

In Nunarssuit any trace element which shows a trend of either increasing or decreasing concentration up section in a particular phase has that trend interrupted at Unit 5, the lower melanocratic unit. This is taken as evidence that the formation of Unit 5 involved a major disruption of normal crystallisation conditions in Unit 5. It is not obvious from this trace element data at what level the syenite represented by sample 1 crystallised. The evidence for reverse and normal cryptic layering is contradictory. Appendix B.2 details possible reasons for problems in interpreting the data.

The whole-rock data for Nunarssuit indicates that the layered series is cryptically zoned in a reverse sense, that is the concentration of elements with partition coefficients greater than 1 increases up section (Ba), whilst the concentration of elements with partition coefficients less than 1 decreases up section (Rb). The autoliths and troughs have a higher concentration of mafic elements as is expected

from their mineralogy. They fit on the trend produced by a plot of Mg/Mg+Fe against height in the intrusion. In DL 2 (Chapter 4) phases in the troughs tend to be more magnesian than the surrounding syenite and it was expected that the troughs and autoliths would have a higher Mg/Mg+Fe ratio than the layered syenite. Models which explain the apparent reverse cryptic zoning seen in the whole-rock analyses are discussed in Chapter 10.8

5.9.2: West Kûngnât

The Zn (partition coefficient less than 1) and Ga (no suitable published partition coefficients) content of feldspars, the Zn (partition coefficient less than 1) contents of pyroxenes and olivines, the Rb (partition coefficient less than 1) and Hf (partition coefficient less than 1) contents of amphiboles and the Y (no suitable published partition coefficients) content of biotites is greater in the syenite surrounding the trough stacks than in the trough stacks themselves. The Rb (partition coefficient greater than 1) content of biotites is greater in the trough stacks than in the syenite surrounding them. These results imply that the phases in the trough stacks crystallised from a less evolved melt than the syenite surrounding the trough stacks. The Y (partition coefficient less than 1) content of olivines is greater in the troughs than in the syenite surrounding the trough stacks whilst the Sr (partition coefficient greater than 1) content of amphiboles is greater in the surrounding syenite than in the trough stacks. These results imply that the phases in the trough stacks crystallised from a more evolved melt than the syenite surrounding the trough stacks.

The Y content of amphiboles decreases up section from 13-103 to 18-141, this is normal cryptic layering. The Sr content of pyroxenes decreases up section from 13-103 to 18-141 and the Sr content of amphiboles increases up section from 13-103 to 18-141. This is reverse cryptic layering. The Zn (partition coefficient greater than 1 according to Wörner *et al.*, 1983, less than 1 according to Henderson 1982) content of amphiboles increases up section from 13-103 to 18-141 and the Ga (no suitable published partitioning coefficients) content of biotites decreases down section from 18-141 to 13-103. In both the Zn amphibole trend and Ga biotite trend sample 14-112 is enriched relative to the trend.

In no cases do either the trough stacks or the syenite surrounding the trough stacks fit on the trends reported for drill localities 13 to 18. Whole-rock analyses indicate that the troughs and surrounding syenites have much the same Mg/Mg+Fe ratio, any

variation could be masked by the presence of a high concentration of feldspars of constant composition (Parsons, 1979).

The evidence for reverse and normal cryptic layering between 13-103 and 18-141 is contradictory. The majority of the trace element data suggests that the phases present in the trough stacks crystallised from a less evolved melt than the surrounding syenite. It is confusing that phases from the trough stacks or the syenite surrounding them do not fit on the trends between 13-103 and 18-141 since samples 13-103 to 18-141 occur stratigraphically higher than the trough stack locality. Appendix B.2 details possible reasons for problems in interpreting the data.

5.9.3: Trace element contents of feldspars

The reason for the blue and red luminescence of feldspars is a matter of some debate. De St. Jorne and Smith (1988) argued that the blue luminescence was due to high Ga contents however Finch (1990) found that Ga contents were higher in red luminescing feldspars from the Blå Måne Sø intrusion than in blue luminescing feldspars from the same intrusion. The XRF-microprobe data presented here also shows this trend. Geake *et al.* (1977) suggested that the blue luminescence of feldspars was due to point defects within the crystal structure, Rae and Chambers (1988) supported this theory and also showed that although the red luminescence peak is present in blue luminescing feldspars, the blue peak dominates so that the red peak is not seen optically. Rae and Chambers (1988) also showed that the iron content of the feldspars is proportional to the intensity of the red luminescent peak. Finch (1990) presented textural evidence that supported the hypothesis that metasomatised feldspars luminesce red.

The widely held view on the reason for red luminescence of feldspars is that the blue luminescence of fresh feldspars is inhibited, possibly by the eradication of defects within the crystal structure, whilst the red luminescent peak increases in intensity due to increasing iron contents in the feldspar, these changes being bought about by feldspar-fluid interaction. Whilst the author has no reason to disagree with the above theories the results from the XRF-microprobe (Fig. 5.1) indicate that other elements (in this case Sr, Y, Mo, Cu and Ga) may have a role to play in feldspar luminescence. The exact role played by iron in enhancing the red luminescence peak is not known and it could be that a variety of elements can fulfil this role.

Part 2

Interpretive work

Chapter 6: Subsolidus modification of the igneous layering in the Nunarssuit and West Kûngnât syenites.

6.1: Introduction

The four preceding chapters described observations in the layered rocks of Nunarssuit and West Kûngnât. Chapters seven to ten will address the question of what occurs in magma chambers as they solidify and how igneous layering may form. The purpose of this chapter is to assess the extent to which the layered rocks of Nunarssuit and West Kûngnât have been modified since crystallisation. The extent to which the chemistry of feldspars, pyroxenes, apatites, zircons and titanomagnetites and the grain size of pyroxenes and olivines has been modified subsequent to crystallisation is assessed. The question of whether the biotite and amphibole in the layered syenites is a post-cumulus or sub-solidus phase is addressed. The degree of compaction of the crystal mush is assessed and then models are presented to explain the differences in subsolidus modification of the leucocratic and melanocratic layers.

Diagenesis has been acknowledged as a major process effecting the textures and composition of sedimentary rocks for many years. Diagenetic processes are defined as "the sum total of processes that bring about changes in a sediment or sedimentary rock subsequent to deposition" (Berner, 1980); diagenetic processes include compaction, recrystallisation, dissolution, replacement, authigenesis (development in place during or after deposition) and cementation. Diagenesis occurs at low temperatures but there is a continuum between diagenetic and metamorphic processes. In recent years many authors (Parsons and Brown, 1984; Hunter, 1987; Boudreau, 1987) have drawn attention to the processes that affect minerals and rocks after they have crystallised. Parsons and Brown (1984) recognised three stages in the history of igneous rocks: 1) magmatic growth - nucleation and growth; 2) subsolidus transformation - phase transformation and exsolution; 3) deuteric alteration - visible modification of microtextures, often involving a fluid. The deuteric stage is restricted to alteration that does not involve large amounts of water introduced from outside (i.e. hydrothermal alteration). The subsolidus and deuteric stages are analogous to diagenesis in sedimentary rocks and it is the subsolidus and deuteric modification of the layered rocks of the Nunarssuit and West Kûngnât syenites with which this chapter is concerned.

6.2: Feldspar

Hypersolvus feldspars are perhaps the mineral species that best illustrate subsolidus and deuteric alteration processes. Above the solvus a single homogeneous feldspar crystallises (a to b in Fig. 6.1). As the temperature falls the solvus is crossed (b in Fig. 6.1) and the feldspar exsolves coherently producing sanidine- and albite-rich lamellae. By processes of coarsening (and simultaneous Si and Al ordering) a braid perthite is eventually produced (Plate 3.2b). This can occur down to temperatures as low as 450°C (Brown and Parsons, 1994) in the stability field of low microcline. Below this temperature only deuteric processes affect the feldspar. There is evidence for higher temperature deuteric processes but when the braid perthite stage is reached no further coherent exsolution occurs.

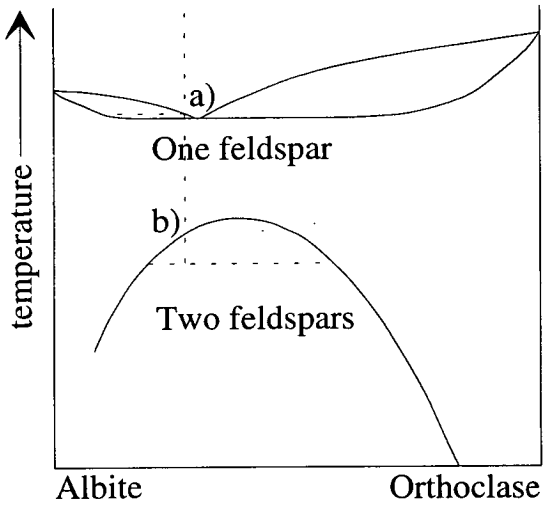

Fig. 6.1: Feldspar phase diagram. a) as the liquid cools it precipitates a single feldspar, b) when the solvus is crossed the single feldspar exsolves forming two feldspars.

Perthite coarsens to produce incoherent or semi-coherent patch perthite (Plate 3.2b); associated with this is the generation of micropores which give the feldspar a turbid appearance (Plate 3.2a). Braid perthite sometimes coarsens at the edge of crystals to give "pleated" rims (Plate 3.2b); feldspar-feldspar grain boundaries develop "swapped" rims (Plate 3.2c and Smith and Brown, 1988 pp 603-604); these processes are thought to relate to fluid being present along feldspar rims. The formation of swapped rims, together with post-cumulus growth has resulted in the loss of the original feldspar morphology. Formation of patch perthite involves dissolution and reprecipitation (Brown and Parsons, 1994) and oxygen isotopic exchange is likely to occur with the deuteric fluid so that the feldspars inherit the δO^{18} signature of the deuteric fluid.

In both Nunarssuit and West Kûngnât feldspars have undergone more deuteric alteration in the leucocratic facies than in the melanocratic facies. This is seen by the relative proportion of turbid to non-turbid feldspar; the f.l.i. of the feldspars (sections 3.2.1 and 3.3.1) and the more complex grain boundaries of feldspars in the leucocratic facies. Oxygen isotope work carried out by previous workers (Finch and Walker, 1991; Mingard, 1990) and Fallick for the present study (Table 6.1) gives the same magmatic values of δO^{18} for feldspars from leucocratic and melanocratic facies. No attempt was made to separate cloudy and clear feldspars as previous workers (Walker, 1991) have found that both types of feldspar were isotopically identical. Results are shown in Table 6.1. All the samples apart from MH-NUN-92 15, 68 and 69 fall in the magmatic field; MH-NUN-92 15, 68 and 69 are all from the same locality and appear to have interacted with meteoric water. These feldspars are identical to those from the other samples when viewed using optical microscopy. Since all three samples give consistent meteoric values this is taken as being not due to analytical error or sample contamination. The fluid that altered the feldspars, apart from those from MH-NUN-92 15, 68 and 69, is interpreted as having been the hydrous-rich residual fluid left after the syenites had crystallised. It is not known why samples MH-NUN-92, 68 and 69 then took on a meteoric signature whilst the other samples did not.

Sample	$\delta^{18}/_{00}$SMOW
MH-NUN-92 4	8.2
MH-NUN-92 10	6.1
MH-NUN-92 14	6.5
MH-NUN-92 15	4.3
MH-NUN-92 16	6.4
20 (DL 2)	6.3
32 (DL 4)	7.4
33 (DL 4)	8.6
35 (DL 4)	7.0
36 (DL 4)	7.0
46 (DL 7)	8.0
48 (DL 7)	6.7
49 (DL 8)	6.4
50 (DL 8)	6.6
51 (DL 8)	5.9
52 (DL 8)	5.9
54 (DL 9)	7.1
59 (DL 9)	7.3
68 (DL 11)	4.4
69 (DL 11)	4.5

Table 6.1: Oxygen isotope results for Nunarssuit samples. Oxygen isotope determinations were carried out at SURRC, East Kilbride, by Tony Fallick on feldspar separates from Nunarssuit; the feldspars were separated in Edinburgh. Samples were crushed using a jaw crusher and Tema; sieves of 180 μm and 210μm were then used to separate material of the right size for oxygen isotope work. Feldspars were separated from other grains by floating them in tetrabromoethane. Further purification of the feldspar separate was achieved using a Franz electromagnetic separator.

6.3: Pyroxene

Pyroxenes in the layered syenites frequently have irregular zoning involving enrichment in the acmite component, with accompanying depletion in the diopside and hedenbergite components, along crystal edges and cracks (Plate 3.2d, 3.3a). Similar zoning was reported by Parsons and Brown (1988) in pyroxenes from the Klokken intrusion where it was suggested that it was due to reactions like the one shown below involving peralkaline deuteric fluids; this zoning is seen most intensely in the leucocratic facies.

$$Fe_2Si_2O_6 + Na^{+}_{(aq)} \Leftrightarrow NaFeSi_2O_6 + Fe^{2+}_{(aq)} + e^{-}_{(aq)} \qquad (1)$$

Ferrosalite + sodium from the fluid ➛ acmite + iron in the fluid

6.4: Amphibole

The majority of the amphiboles in Nunarssuit and West Kûngnât are the product of alteration of pyroxenes (Chapter 3.2.2 and 3.3.2), a few amphiboles appear to be intercumulus phases (Chapter 3.2.4 and 3.3.4) whilst many appear to be subsolidus in origin (Figs. 4.13b and 4.34b). Crystallisation of the syenites probably occurred between 950-750°C (Chapter 7.4.1). The amphiboles present in the syenites would only have formed at the lower end of this temperature range (Gilbert *et al.*, 1982) by which stage the syenites must have been almost entirely solid. If the amphiboles are derived by a reaction involving pyroxenes and the mixing of Fe and Mg is ideal in pyroxenes and amphiboles then plots of the ratio Fe/Fe+Mg in amphiboles against Fe/Fe+Mg in pyroxenes should plot on lines of constant Kd ($Kd = \left[\left(X^{Px}_{Fe}.X^{Amph}_{Mg}\right)/\left(X^{Px}_{Mg}.X^{Amph}_{Fe}\right)\right]$, where $X^{Px}_{Fe} = [Fe/(Fe+Mg)]^{pyroxene}$) in the same way as they do for biotites and olivines (Chapter 6.5 and Parsons *et al.*, 1991). Plots for the amphiboles and pyroxenes of Nunarssuit (Fig. 6.2) do not plot on lines of constant Kd.

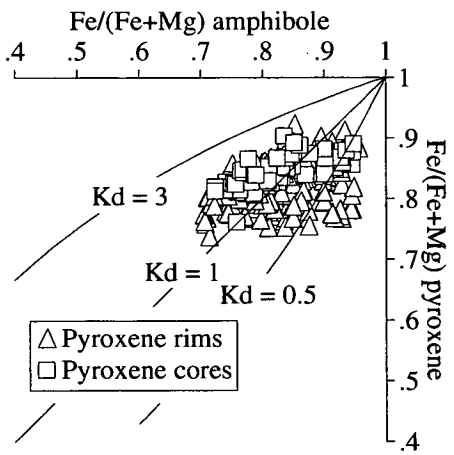

Fig. 6.5: Plots of Fe/(Fe+Mg) of amphibole against Fe/(Fe+Mg) pyroxene for the layered syenite of Nunarssuit.

However plots for amphiboles and pyroxenes from West Kûngnât (Fig. 6.3a and b) define a trend which lies between the lines Kd = 1 and Kd = 0.5, for the layered series the correlation is seen best when amphiboles are plotted against pyroxene rims.

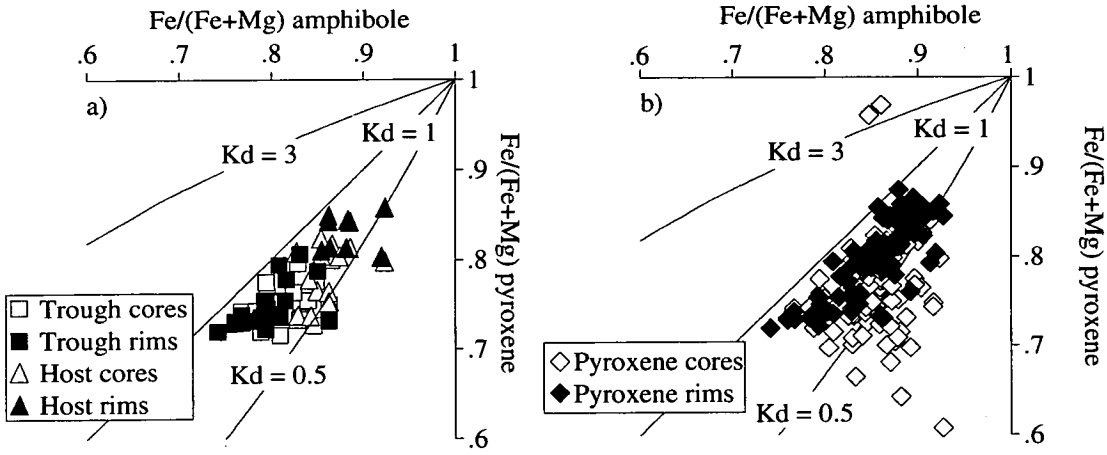

Fig. 6.3: a) trough stack localities, West Kûngnât and b) the layered syenite of West Kûngnât.

The Nunarssuit plot indicates that either the mixing of Fe and Mg in the pyroxenes and amphiboles is non-ideal or that the reaction which generated amphiboles in Nunarssuit involved other Fe and Mg bearing phases as well as pyroxene. Chemical variation in the pyroxenes from Nunarssuit is reflected in the chemical variation of the amphiboles. Pyroxenes and amphiboles from the lower part of the succession, (sample 9, DL 5 and DL 6), are the most sodic and sample 2-28 contains the most magnesian pyroxenes and amphiboles from DL 2. Since the amphiboles inherited the chemical signature of the pyroxenes it seems likely that pyroxene was the dominant phase in the amphibole producing reaction.

The plots for West Kûngnât indicate that pyroxene was involved in a reaction which generated amphibole, and that Fe and Mg mixed ideally in the two phases. The fact that the plots lie more parallel to lines of constant Kd when rim compositions of pyroxenes are used rather than cores implies that the rims of pyroxenes reacted to produce the amphiboles and that the cores of pyroxenes were less involved in the reaction.

It would seem logical that, given the similarities in composition and conditions of formation, amphiboles in Nunarssuit and West Kûngnât were produced by the same reaction. If this was the case it is not obvious why the mixing of Fe and Mg should

have been non-ideal in Nunarssuit and ideal in West Kûngnât. It is possible that the difference in the plots is due to the temperature interval that the amphiboles grew over being different in Nunarssuit and West Kûngnât

6.5: Biotite

In most studies of the Nunarssuit and West Kûngnât syenites (Upton, 1960; Butterfield, 1980) biotites have been treated as a post-cumulus phase which grew out of the inter-cumulus fluid. Powell (1978) suggested, on textural grounds, that biotite was probably a subsolidus phase in the Igdlerfigssalik syenites. Hewitt and Wones (1984) showed that iron-rich biotites are only stable below 800°C at the QFM oxygen fugacity buffer and c.2kb. Dachs (1994) futher constrained the stability of Fe-rich biotites to temperatures below c.550°C at the QFM buffer. Parsons *et al.*, (1991), calculated temperatures of formation for biotites from the Klokken intrusion and concluded that biotites in this intrusion formed at c.600°C, about 300°C subsolidus. It is therefore possible that biotites in the intrusions of Nunarssuit and West Kûngnât are a subsolidus phase, forming after the syenite solidified. Parsons *et al.*, (1991), suggested two reactions that could be responsible for the production of biotite in the Klokken syenites:

$$KAlSi_3O_8 + Fe_3O_4 + H_2O \rightarrow KFe_3AlSi_3O_{10}(OH)_2 + 1/2O_2 \qquad (2)$$

sanidine + magnetite + water → annite + oxygen

and

$$KAlSi_3O_8 + 3/2Fe_2SiO_4 + H_2O \rightarrow KFe_3AlSi_3O_{10}(OH)_2 + 3/2SiO_2. \qquad (3)$$

sanidine + fayalite + water → annite + silica

For reaction (2) to be applicable to Mg-bearing biotites, other phases such as pyroxene would be required to participate in the reaction to provide magnesium.

Figs. 6.4, 6.5 and 6.6 are plots of Fe/(Fe+Mg) of biotite against Fe/(Fe+Mg) of coexisting pyroxene rims and cores and olivine rims and cores from the intrusions of Nunarssuit and West Kûngnât. Superimposed on this graph are Kd isopleths for the Fe-Mg partitioning between biotite and either olivine or pyroxene, $(Kd = \left[\left(X^{Ol}_{Fe}.X^{Biot}_{Mg}\right)/\left(X^{Ol}_{Mg}.X^{Biot}_{Fe}\right)\right]$, where $X^{Ol}_{Fe} = \left[Fe/(Fe+Mg)\right]^{olivine}$ etc.). For syenite samples from Klokken (Parsons *et al.*, 1991) plots of Fe/(Fe+Mg) of biotite against

Fe/(Fe+Mg) of olivine fit a curve consistent with a constant Kd approximately equal to 3.02. Parsons *et al.* (1991) argued that this is good evidence for reaction (3) being

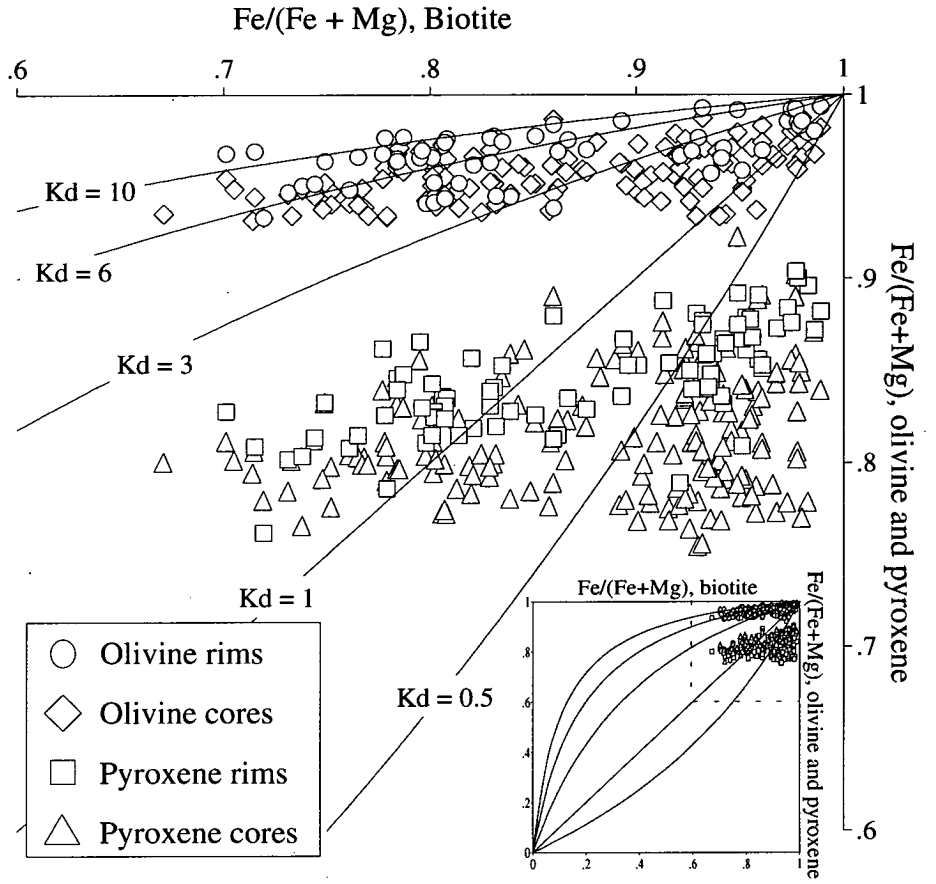

Fig. 6.4. Distribution of iron and magnesium between coexisting biotite and olivine or pyroxene for rocks from the Nunarssuit layered syenite. See text for definition of Kd.

the dominant biotite producing reaction in the Klokken syenites. The biotites and coexisting olivines and pyroxenes from the Nunarssuit and West Kûngnât syenite show a less exact relationship; the biotite-olivine data plot more closely along the isopleths than the biotite-pyroxene data. The reason for the less exact relationship for Nunarssuit and West Kûngnât compared to Klokken may be due to the fact that data on biotites in gabbros are also plotted for Klokken which constrains the magnesian part of the curve. Also the biotites would have grown over a range of temperatures which would affect the position of the data points. It seems likely that a reaction involving olivine as a major reagent was responsible for the formation of biotite in Nunarssuit and West Kûngnât. Parson *et al.* (1991) calculated the temperature of formation of biotite from the reaction represented by equation (3) using equation (4) given below. The assumptions necessary to apply this equation are discussed in

Parsons *et al.* (1991). No attempt has been made in this present study to apply the equation directly to the Nunarssuit and West Kûngnât rocks. However, a comparison of the assumptions made by Parsons *et al.* (1991) and their relevance to the present study has been carried out and indicates that equation (4) (and also a similar equation which is applicable to reaction (2)) would yield lower temperatures of formation of the biotites than the c.600°C obtained for the Klokken biotites.

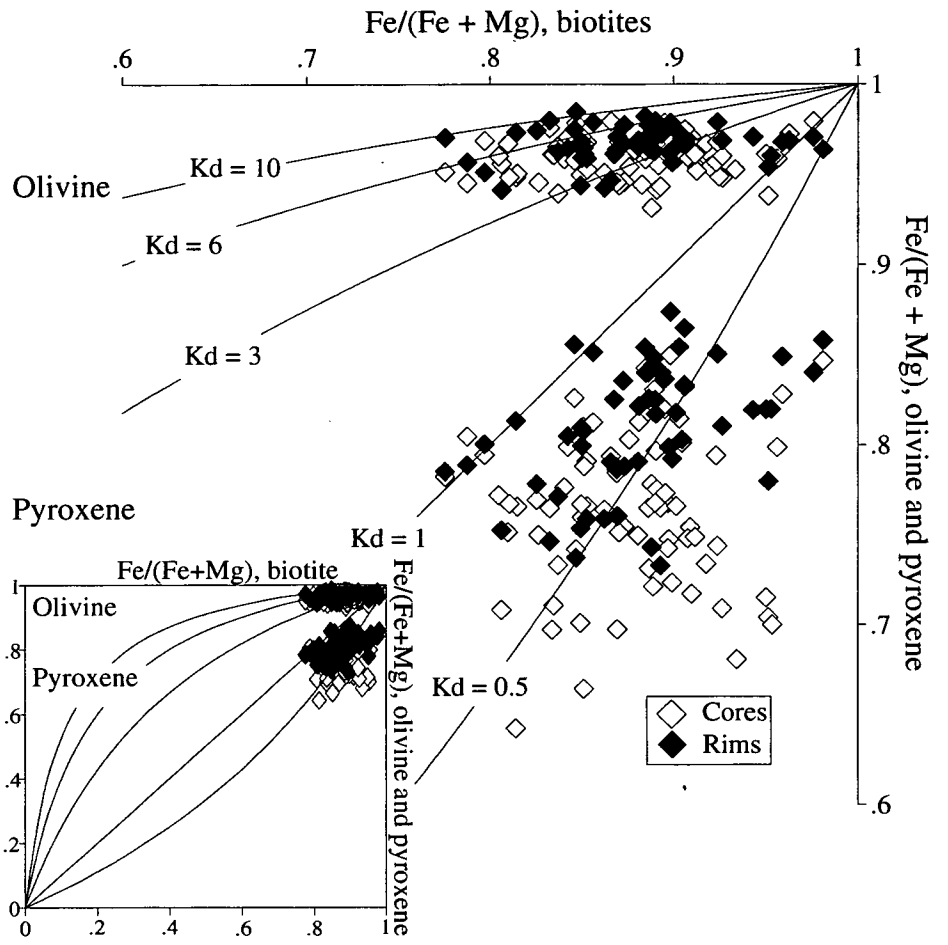

Fig. 6.5. Distribution of iron and magnesium between coexisting biotite and olivine or pyroxene for rocks from the West Kûngnât layered syenite. See text for definition of Kd.

Parsons *et al.* (1991) assume that the oxygen fugacity was controlled by the QFM buffer, this controls values of silica activity. The assumption is probably not so valid for Nunarssuit and West Kûngnât but remains a good estimate. Quartz is only occasionally seen as an accessory phase in Nunarssuit and more rarely still in the layered syenite of West Kûngnât. Quartz is present further up section in West Kûngnât. Feldspar, olivine and biotite compositions in the three intrusions are very similar so that to a first approximation assumptions about sanidine and fayalite

activities are applicable to Nunarssuit and West Kûngnât. Biotites are very iron rich, contain largely OH rather than F and almost no Cl in all three intrusions. The major difference between the three intrusions is the water content of the crystallising magma. The Klokken magma was probably water saturated by the time that syenites were crystallising (Parsons, 1979) where as the magmas of Nunarssuit and West Kûngnât appear to have been relatively anhydrous. This means that the water fugacity value used in equation (4) by Parsons *et al.* (1991) is too high for the Nunarssuit and West Kûngnât magmas. Reducing the value of this term results in reducing the value obtained for the temperature of formation of biotite. Thus it seems likely that the biotites of the Nunarssuit and West Kûngnât syenites are subsolidus in origin and that they are produced by a reaction involving olivine.

$$\log f_{H2O} = \frac{-4996}{T} + 8.47 + 3\log X_{Fe}^{Biot} + \frac{3}{2}\log a_{SiO2} - \log a_{san}^{AF} - \frac{3}{2}\log a_{fa}^{Oliv} + 2\log X_{OH}^{Biot} \qquad (4)$$

where: f_{H2O} = fugacity of water

T = temperature of biotite growth

X = mole fraction

a = activity

Biot = biotite

Fe = formula iron content

OH = formula hydroxyl content

SiO_2 = silica

AF = alkali feldspar

san = sanidine component of alkali feldspar

Oliv = olivine

fa = fayalite component of olivine

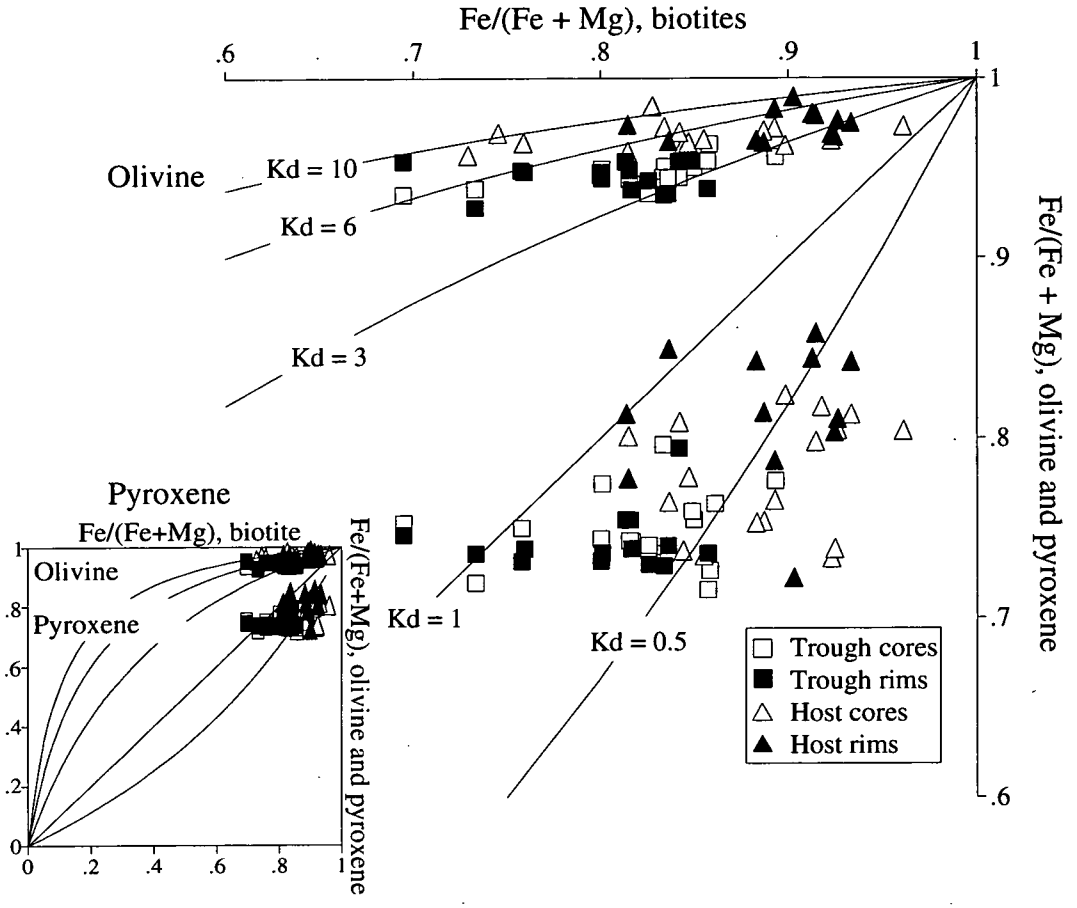

Fig. 6.6. Distribution of iron and magnesium between coexisting biotite and olivine or pyroxene for rocks from the trough stacks at the base of the West Kûngnât layered syenite. See text for definition of Kd.

6.6: Apatite

Finch (1990) defined a number of zoning styles exhibited by apatites (Fig. 3.2). Finch (pers comm.) states that concentric and fracture zoning are produced by the action of late-stage fluids on the apatite and that apatites which show no zoning have not been affected by late-stage fluids. Finch considered that apatites were second only to feldspar microtextures in sensitivity to late-stage fluids. In Nunarssuit (Table 3.3), essentially the same proportion of apatites from all facies are unzoned indicating that they have all experienced the same amount of late-stage fluid interaction. In West Kûngnât (Table 3.6) apatites in all facies have the same proportion of unzoned apatites. This proportion is greater than in Nunarssuit, indicating that the Nunarssuit syenites have seen more late-stage fluid than the West Kûngnât syenites. This conclusion, however, contradicts conclusions drawn on the basis of the degree of alteration of feldspars, pyroxenes and olivines. The apatites

within the large biotites and amphiboles in the trough stacks of West Kûngnât are more often zoned than those not so enclosed. However why the large amphiboles and biotites appear to have experienced more fluid than the surrounding rock is not so readily explicable.

6.7: Ilmenospinel

As for the feldspars, there is a solvus which governs the solid solution of magnetite-ulvöspinel. At magmatic temperatures a single phase crystallises, but, as the solvus is crossed, ulvöspinel exsolves from the magnetite. The ulvöspinel may subsequently be oxidised to ilmenite. Various geometries of exsolution exist; trellis and sandwich intergrowths (Fig. 6.7a and b respectively) and granular exsolution (Fig. 6.7b). Buddington and Lindsley (1964) demonstrated that granular exsolution occurs in titanomagnetites which have been more extensively deuterically altered than those which exhibit trellis and sandwich intergrowths.

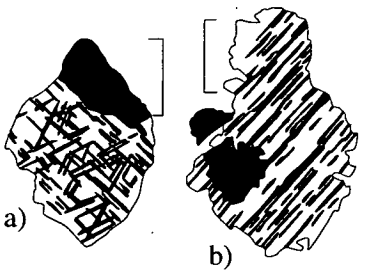

Fig. 6.7: Ilmenospinel exsolution textures, ilmenite black, scale bars 0.5mm. a) rather regularly shaped ilmenite at margins of ilmenomagnetite showing trellis intergrowths, b) rounded granule of ilmenite with irregular boundary enclosed in ilmenomagnetite showing sandwich intergrowth (from Parsons, 1980, fig. 8).

Magnetite occurs rarely in the syenites of Nunarssuit and West Kûngnât. Whenever it is present it shows either trellis or sandwich intergrowths. No granular exsolution has been observed in magnetites from the layered series of the two intrusions.

6.8: Zircon

Zircons show: a) regular oscillatory zoning (e.g. the middle portion of the grain in Plate 3.5f), interpreted as primary magmatic zoning; b) transgressive oscillatory zoning (e.g. portions of the grain in Plate 3.5c where one planar zone is truncated by another), interpreted as growth, cessation of growth and then growth again within the magma chamber and; c) transgressive unzoned regions (e.g. the lighter portions in the centre and around the edge of the grain in Plate 3.5c), interpreted as being due to deuteric alteration of the zircon. Annealed cracks are associated with the transgressive unzoned regions. Cracks within the body of the grain are truncated by

the transgressive unzoned regions of the crystals and these are thought to have been annealed during the alteration of the zircon (Harley pers comm., e.g. cracks in the grain of Plate 3.5f). Deuteric alteration results in an increase of the hafnium content of the zircons. Thus zircons give evidence for several stages of growth in the magma chamber and also for subsequent sub-solidus modification. Examples of the above types of zoning can be found in zircons from all facies in the Nunarssuit and West Kûngnât layered syenite.

6.9: Crystal size distribution

Crystal size distribution theory was developed by Marsh, Cashman and Ferry (Marsh, 1988; Cashman and Marsh, 1988; Cashman and Ferry, 1988). The parameter crystal population density (=n) is defined as the gradient of the curve on a cumulative frequency graph of the number (N) of crystals of a length less than a stated length (L, Fig. 6.8); length is defined as maximum length parallel to direction of elongation of a grain in thin section (Fig. 6.9).

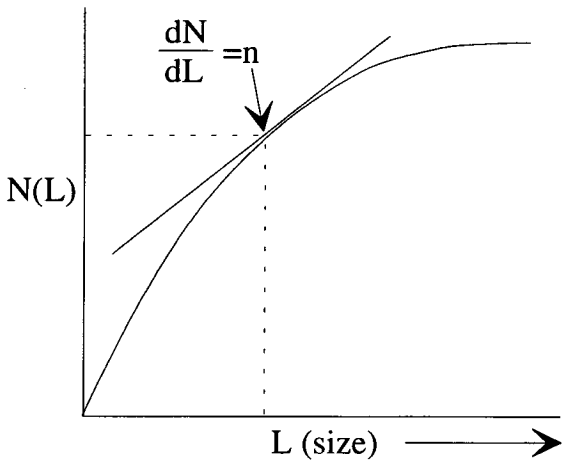

Fig. 6.8: Population density (n) = gradient of size cumulative frequency graph

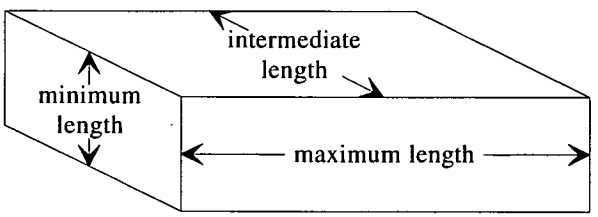

Fig. 6.9: Diagram showing the maximum, intermediate and minimum lengths of an ideal cuboidal crystal.

Such curves were plotted for olivines and pyroxenes from the layered series of Nunarssuit and West Kûngnât. The equations which define the curves were obtained mathematically (using the Computer Associate program CA-Cricket Graph v1.3) to

an order of 2 decimal places and up to cubic L terms. Curves fit the equations to a precision of r^2=0.99. The equations were differentiated to obtain the gradient of the curves. Plots of ln (n) against L were produced.

According to Cashman and Marsh (1988) the shape of such plots is affected by a variety of processes (Fig. 6.10). If the crystals grew and the rock solidified with no modification the plots should be straight lines. Crystal settling should produce plots with a reduction in gradient at coarse grain sizes for samples composed of settled grains, i.e. a cumulate pile at the bottom of a magma chamber (relative enrichment in coarse grain sizes). Subsolidus grain annealing due to such processes as Oswald ripening should produce bell-shaped curves, the negative gradient of the plot at fine grain sizes indicates negative growth, i.e. resorption.

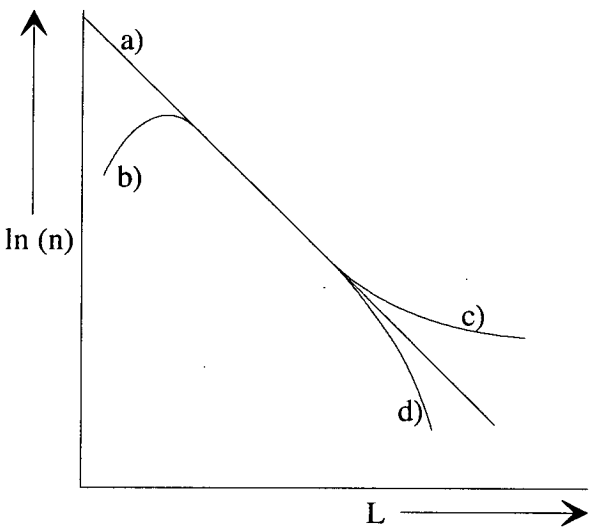

Fig. 6.10: a) theoretical CSD modified by; b) annealing of small crystals; c) accumulation of large crystals by settling; d) loss of large crystals by settling.

Olivines: samples from DL 10 in Nunarssuit, and DL 13, trough stacks and host syenite from West Kûngnât gave bell-shaped curves (Fig. 6.11c) indicative of annealing; samples from DL 8 and 9 from Nunarssuit and 15 from West Kûngnât produced curves (Fig. 6.11b) which could be interpreted either as indicating a reduction in the numbers of smaller grains or a reduction in the number of larger grains. These problematic curves have similar gradients at the high L end to those of the more readily explained bell shaped curves of the other olivines. For this reason they are interpreted as showing the beginnings of annealing and the loss of some small grains although the process has not gone as far as in the samples which gave bell-shaped curves.

Pyroxenes: A sample from DL 18, West Kûngnât, produced a curve indicative of accumulation of larger grains by crystal settling (Fig. 6.11e). Pyroxenes from other samples from Nunarssuit and West Kûngnât produced problematic curves like those of the olivines (Fig. 6.11d). Again these are interpreted as indicating the onset of annealing.

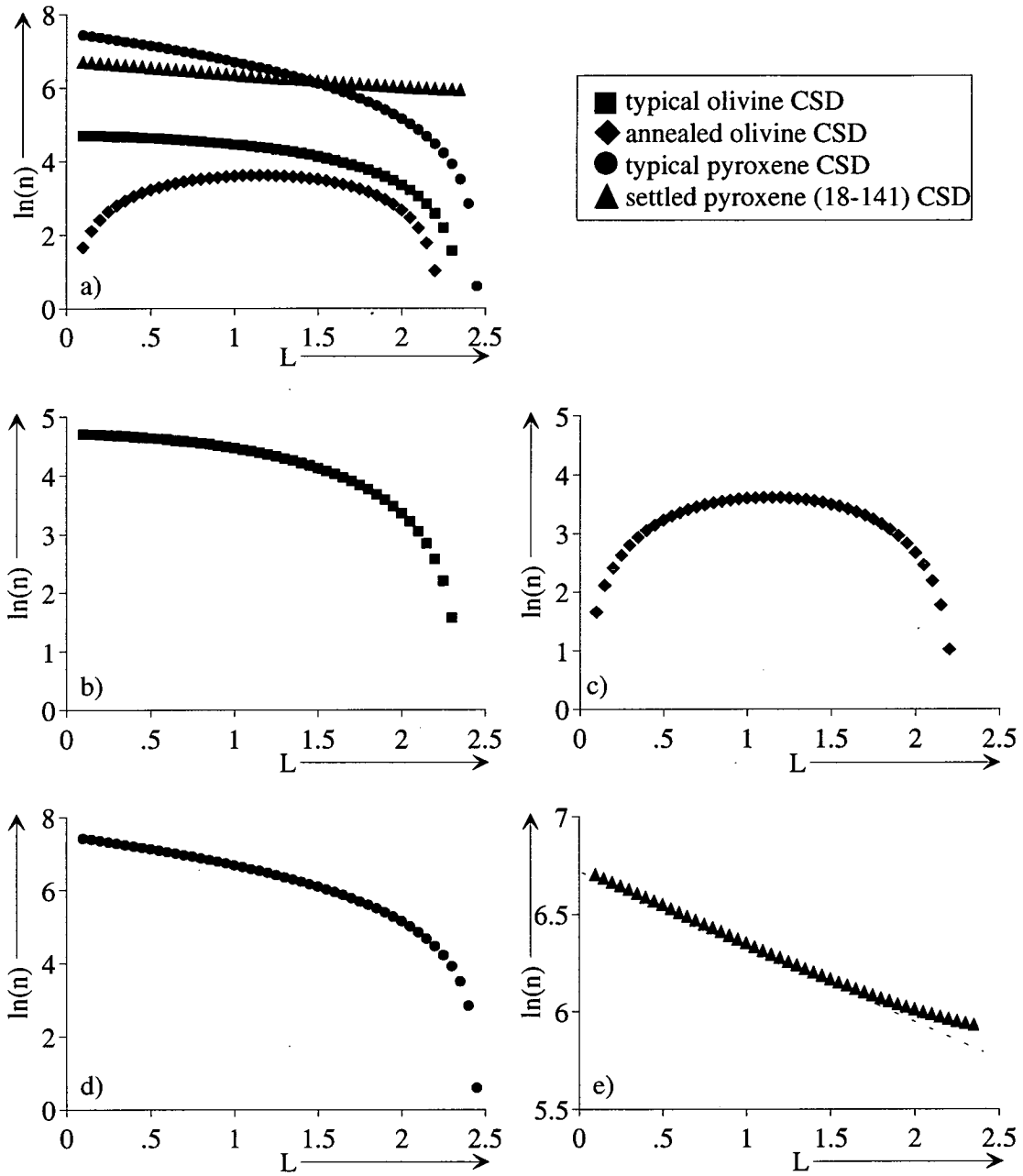

Fig. 6.11: a) typical CSDs from this study; b) typical CSD given by olivines from DL 8, and 9 from Nunarssuit and DL 15 from West Kûngnât; c) typical CSD given by olivines from both Nunarssuit and West Kûngnât indicating annealing; d) typical CSD given by pyroxenes from Nunarssuit and West Kûngnât; e) CSD given by pyroxenes from 18-141.

Crystal size distribution theory yields problematic curves for most samples from Nunarssuit and West Kûngnât. They are, however, interpreted as indicating some degree of annealing. Some olivine populations give "text-book" curves which indicate annealing and one pyroxene curve indicates crystal settling. Regardless of the interpretation, the grain size populations are not those expected from simple nucleation and growth.

6.10: Compaction

Sparks *et al.*, (1985) calculated that compaction of a cumulate pile can reduce porosities to less than 1% and, if only one cumulus mineral is involved, generate essentially monomineralic rocks. Compaction can alter texture and, indirectly, mineral composition (by dissolution-reprecipitation mechanisms). Higgins (1991) suggested that compaction can generate lamination in igneous rocks. Hunter (1993) concluded that rocks do not reach full textural equilibrium with angles of 120° between adjacent grain boundaries at the triple junction of three grains unless they have been compacted and that compaction is a potential mechanism for the formation of adcùmulate textures. A preliminary survey of the angles at grain triple junctions, on both the Nunarssuit and West Kûngnât syenites, indicated that the majority of grains were not in textural equilibrium. Most of the layered syenites of Nunarssuit and West Kûngnât possess no igneous lamination, have non-equilibrium angles between adjacent grain boundaries at grain triple junctions and possess orthocumulate textures. This suggests that little compaction has occurred. Most rocks which show mineral lamination are associated with slumps indicating that flow of a crystal mush affected the degree of lamination of mineral grains, probably by producing a shear stress in excess of any stress due to convection currents. Other mineral lamination occurs in and around melanocratic autoliths. These were probably denser than the surrounding magma and the crystal pile on which they must have come to rest; the mineral lamination could have been produced by a local increase in the degree of compaction.

6.11: The subsolidus modification of the syenites

Pyroxenes in the leucocratic facies of Nunarssuit and West Kûngnât appear to have undergone more subsolidus modification than those in the melanocratic facies (acmite-enriched grain rims are more common and the ratio of pyroxene to amphibole is smaller in the leucocratic facies relative to the melanocratic facies). Other phases appear to have undergone the same degree of subsolidus alteration in both leucocratic and melanocratic facies. Feldspars in leucocratic facies are more altered than those in melanocratic facies but this is thought to be brought about by lower temperature processes than the other subsolidus modifications. The fluid responsible for the subsolidus alteration of the various phases must have been more concentrated in the leucocratic facies to explain the higher degree of subsolidus modification of the pyroxenes in these facies. The fluid responsible for the growth of intercumulus amphiboles (Chapter 3.2.4 and 3.3.4) must have been a late stage residual melt left after the majority of the syenite had crystallised. The fluid responsible for the enrichment in acmite at the rims of pyroxenes, the growth of biotite and the alteration of olivine may have been either a late stage hydrous melt or a hydrothermal fluid. The fluid which altered the feldspars must have been deuteric. Two alternate hypotheses are presented which explain how late stage residual melt was present in the solidifying pile of crystals.

The first relates to dihedral angles. The dihedral angle is defined as the angle between two adjacent grain boundaries and a fluid phase (Hunter, 1987; Harte *et al.*, 1993 and references therein). If the dihedral angle is less than 60° the fluid can form an interconnected network (Fig. 6.12a). If the dihedral angle is greater than 60°, the fluid is trapped in isolated pockets (Fig. 6.12b).

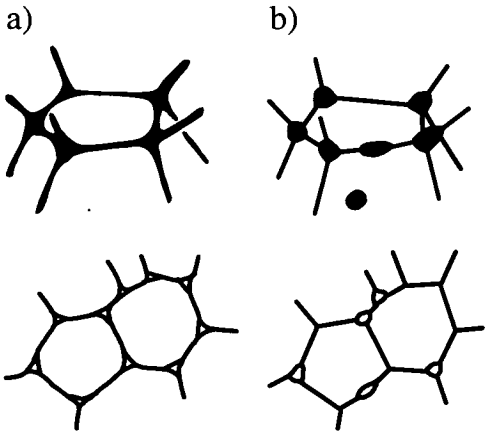

Fig. 6.12: The three dimensional geometry of fluid-filled pores (or any second phase) along the edges of cumulus grains (a) and at the corners or trapped in local energy minima along the edges and faces of cumulus grains (b) for dihedral angles of less than or greater than sixty degrees, respectively. The lower diagrams show the corresponding appearance of the pores in a two-dimensional section. Note that for $\theta < 60^{o}$, the second phase is present at all the cumulus grain triple junctions but that for $\theta > 60^{o}$ a random section may not intersect all the pores or second-phase grains; many of the triple junctions will appear "dry" (from Hunter, 1987).

If the phases in the leucocratic layers typically had dihedral angles less than 60° whereas the melanocratic layers typically had dihedral angles greater than 60°, then late stage fluid could have flowed through the leucocratic layers altering the minerals whereas in the melanocratic layers the fluid would have had a restricted amount of contact with the minerals in the layers. Alkali feldspar-alkali feldspar dihedral angles in melts of felsic composition (Harte *et al.*, 1993 Table 1) are less than 60°. No data is available for other phases in felsic melts. Insufficient data is available to assess this hypothesis.

The second explanation relates to packing. Differences in packing were first suggested by Upton (1961) to explain differences in alteration in the syenites in the north-west of the Grønnedal-Íka complex which is another syenitic intrusion of the Gardar province. Since the melanocratic layers contain more pyroxene and olivine than the leucocratic layers, and these minerals typically form crystals smaller than the feldspars, the porosity of the leucocratic layers would be greater than the porosity of the melanocratic layers (Fig. 6.13). This would have caused late-stage magmatic fluid to concentrate in the leucocratic layers which would accordingly show more subsolidus modification than the less porous melanocratic layers.

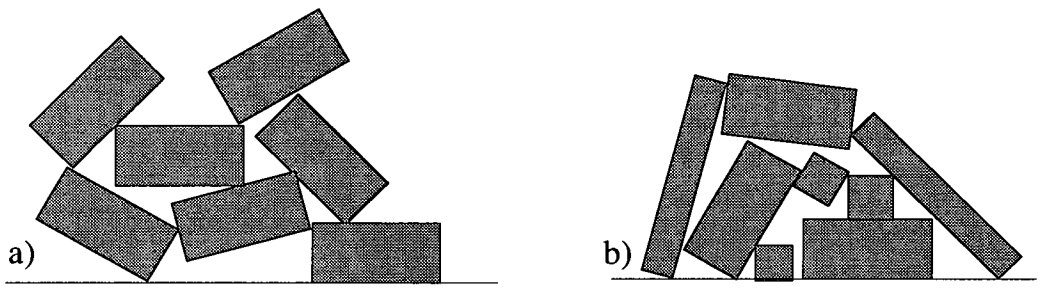

Fig. 6.13: a) Loosely packed large crystals. relatively high porosity; b) more compactly packed range of crystal sizes, lower porosity

The above hypotheses relate to fairly high subsolidus temperatures and can explain the source of the melt responsible for the changes in chemical zonation of pyroxenes, apatites and zircons. However, the deuteric exsolution textures in feldspars form at temperatures below 450°C (Brown and Parsons, 1994) and another mechanism is required to explain why the feldspars in the leucocratic layers show more deuteric alteration than those in the melanocratic layers. Clay minerals sometimes grow along and between the pleated edges of feldspars (Plate 3.4c) and in the Klokken syenites biotites have been seen with this relationship to feldspar (Parsons *et al.*, 1991). Subsolidus biotite and amphibole growth may have occurred during feldspar alteration although these hydrous phases probably began to grow at higher

temperatures. It is also possible that the acmite enrichment seen in pyroxene rims may have occurred at these low temperatures (Finch, 1990). The oxygen isotope signature of the feldspars in Nunarssuit and West Kûngnât (section 6.2) indicate that the deuteric fluid involved in the alteration of the feldspars was magmatic in origin. At this time it is not possible to say why the feldspars in the leucocratic layers are more deuterically altered than those in the melanocratic facies but for some reason the leucocratic facies must contain more deuteric fluid than the melanocratic facies at temperatures below 450°C. Perhaps the feldspars in the leucocratic layers were more reactive. If the feldspars in the leucocratic layers initially had more water dissolved in them, which later exsolved (Worden *et al.*, 1990), the feldspar in the leucocratic layers might be more porous and thus be more altered by water at lower temperatures.

6.12: Summary

Both leucocratic and melanocratic facies have undergone some degree of subsolidus alteration. It would appear that whereas feldspars and pyroxenes from leucocratic facies are more altered than those in melanocratic facies, apatites, ilmenospinels and zircons are altered to a similar degree regardless of the colour index of the host rock. Feldspars have lost their original shapes, a variety of minerals no longer preserve their original chemistry along the grain rims. Pyroxenes reacted to produce amphibole and olivines produced biotite, both these reactions probably occurred in the sub-solidus. Crystal size distributions indicate that the original grain size distribution of olivines and pyroxenes after crystallisation has been lost due to annealing. The non-equilibrium dihedral angles between grains and the orthocumulate textures indicate that little compaction occurred. Mineral lamination is most marked around slump structures (indicating that the lamination is due to flow of the crystal mush) and dense melanocratic autoliths (indicating that the lamination is due to compaction).

The reason that pyroxenes in the leucocratic facies underwent more sub-solidus modification than those in the melanocratic facies is probably that the cumulus minerals in the leucocratic facies were less well packed so that more intercumulus liquid was present. This liquid fractionated, leaving a water-rich residue which reacted with the surrounding syenite. At lower temperatures feldspars were altered by a deuteric fluid which had a magmatic origin. It is not known why the feldspars in leucocratic layers underwent more alteration than those in melanocratic facies.

Chapter 7: Physical conditions within magma chambers and their affect on crystal settling, with particular reference to the magma chambers of Nunarssuit and West Kûngnât.

7.1: Introduction

Understanding the processes that occur during the solidification of a magma chamber requires the knowledge of a number of variables, most importantly the temperature, pressure, viscosity, density and chemical composition of the magma. Useful geothermometers and geobarometers, that use the chemical compositions of co-existing phases, are not available since syenites do not contain many minerals that are suitable for these purposes. Viscosity and density are controlled by both the chemical composition and the crystal content of the magma. Viscosity and density calculations derived on a theoretical and experimental basis have existed for many years (e.g. Shaw, 1972); variables in these calculations, such as crystal and volatile content, are themselves poorly constrained. Calculations for parameters such as fluid dynamic constants need values of density, viscosity, pressure and temperature differences driving convection. The choice of values for independent variables can introduce over four orders of magnitude uncertainty into calculations! With this caveat in mind this chapter discusses the likely physical conditions within the magma chambers of Nunarssuit and West Kûngnât and how these conditions affect convection and crystal settling. To fulfil this aim a number of questions are addressed:

1) what was the likely rheology of the magmas?
2) what are the most likely compositions of the magmas that crystallised to produce the syenites of Nunarssuit and West Kûngnât?
3) what were the crystallisation temperatures and pressures of these magmas?
4) what were the viscosities and densities of these magmas and how were they affected by varying temperature and crystal content?
5) did convection occur in these magma chambers, and if it did what form did this convection take and how was it affected by changes in temperature and temperature gradient driving convection?
6) could crystal settling occur in these magma chambers and if it did how would it be affected by changes in temperature, viscosity, temperature gradient driving convection and crystal content?

In all of the calculations acceleration due to gravity is taken as 980 cms^{-2} and values for coefficients of thermal expansion and thermal diffusivity are taken from Bagdassarov and Fradhov (1993), which deals specifically with convection in evolved magma chambers

7.2: Is "magma" a Newtonian fluid?

Newtonian fluids are those in which viscosity is constant at constant temperature and pressure, i.e. strain increases linearly with shear stress (e.g. water, Fig. 7.1a). Non-Newtonian fluids are those in which shear stress is not linearly proportional to strain; (e.g. tomato ketchup, a pseudoplastic fluid, Fig. 7.1b, treacle, possibly a Bingham plastic, Fig. 7.1c and sugar solution, a dilatant Fig. 7.1d)).

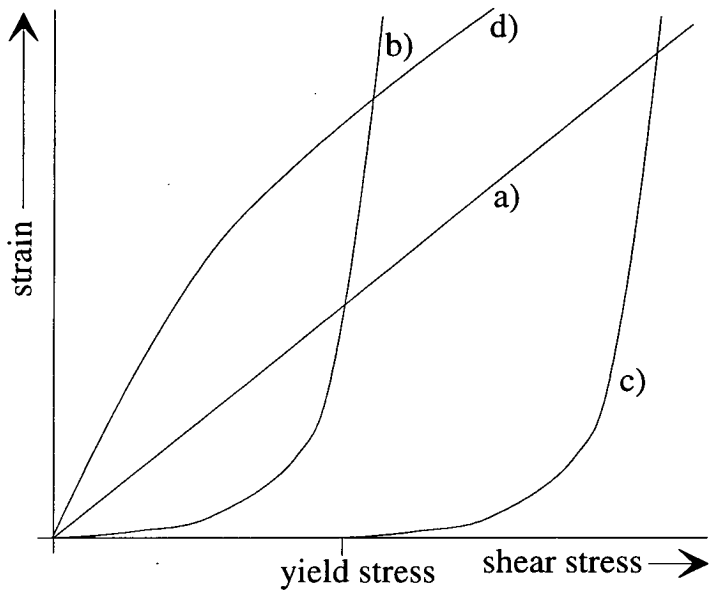

Fig. 7.1: Stress/strain relations in fluids of different rheologies; a) Newtonian, where stress is proportional to strain; b) pseudoplastic, where strain is initially low for the applied stress but then increases rapidly; c) Bingham plastic, where strain occurs after a critical yield stress is exceeded; d) dilatant, where the strain is initially high for the applied stress but then decreases.

Pseudoplastic fluids initially show a low strain with applied stress. When a critical limit is reached the strain increases rapidly. Bingham plastics show no strain until a critical stress (the yield stress) is reached; strain then increases rapidly. Barnes and Walters (1985) claimed that yield stresses did not exist and that strain at low stresses is just difficult to measure. In a series of experiments using precise flow meters they claimed to detect flow at very low stresses in previously reported Bingham plastics. The response of the fluid to stress was divided into three sections (Fig. 7.2). At first (I) the fluid behaved as a Newtonian fluid. When stress reached a critical level, the strain rose rapidly giving a power law relationship with stress (II). Finally a "Newtonian plateau" (III) was reached where strain increased linearly with stress.

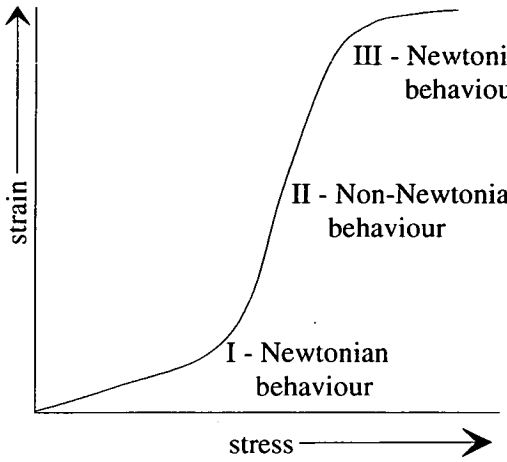

Fig. 7.2: Stress/strain behaviour of a "Bingham plastic" (after Barnes and Walters, 1985).

Dilatants initially show a high strain for an applied stress. As the applied stress increases, the strain increases less rapidly. In experiments to determine the effect of particle shape on crystal settling rate (Chapter 7.7.3) a variety of fluids has been used e.g. oils (McNown and Malaika, 1950) and glycerine (Komar and Reimers, 1978). Such fluids have been chosen for their ready availability and high viscosity, which causes particles to settle slowly and thus aids observation. The rheology of these fluids is never stated but is obviously important. For example as a crystal settling in a dilatant begins to rotate the stress exerted on the fluid will increase, the strain will not increase proportionally and the crystal could conceivably be stabilised.

Since basaltic lavas appear to be Bingham fluids, it is often assumed that all magmas are Bingham fluids as well (e.g. Rice, 1993). It has been argued by McBirney and Noyes (1979) that yield stress could prevent crystals from sinking in a fluid which is only slightly less dense than the crystals, or alternatively, that yield stress could prevent crystals from rising in a fluid after buoyant crystals have been carried to the bottom of the magma by a current. If yield stress does not exist such arguments are irrelevant.

Parsons and Butterfield (1981), by dividing the mass of individual grains by the cross section that they presented as they settled downwards in the magma, calculated that the cumulus phases (fayalite, hedenbergite and feldspar) in the Klokken laminated syenite would all have exerted approximately the same downward force whilst settling through the magma. They argued that crystals settled when they reached a size sufficient to overcome the yield stress of the magma. Certainly from Parsons and Butterfield's evidence the Klokken laminated syenite magma would appear to have behaved as a Bingham plastic.

It is generally accepted that bubble- and crystal-free magma is Newtonian (Mazurin, 1986). However, most magmas are unlikely to be bubble- and crystal-free. In a recent review, Bottinga (1994) presented evidence that magmas are non-Newtonian at high stresses, but concluded that it was unclear whether magmas were Newtonian at low stresses. There is a tendency in the literature to assume that crystallising magmas are Newtonian (RSJ Sparks and C Jaupart, pers comms.). The assumption of a Newtonian rheology is probably reasonable for the basic melts from which most of the layered cumulates described in the literature formed. However, for more evolved melts the assumption is far less valid. Basic melts are composed largely of small silicon-oxygen tetrahedra whereas volatile-free felsic melts contain large silicon and oxygen polymers which are responsible for the higher viscosities of these evolved melts; relatively strong forces exist between the polymers and these forces would contribute towards a yield stress. Syenitic magmas are likely to depart from the Newtonian ideal and possess a yield stress. In the rest of this and subsequent chapters however, they will be treated as Newtonian because: 1) suitable equations for non-Newtonian behaviour of fluids appear to be unavailable, and 2) this will allow comparison with work done on basic and ultrabasic intrusions.

7.3: Parental magma composition

Normally, parental magma compositions are determined by sampling the chilled margin of an intrusion. In neither Nunarssuit nor West Kûngnât is a chilled margin available. Another method is to analyse the matrix of a co-genetic dyke that contains a phenocryst assemblage that is the same as that of the cumulus phases present in the cumulate. There are no such dykes in Nunarssuit or West Kûngnât. However, Martin (1985) lists the phenocryst assemblage of a variety of compositionally-grouped dyke types from the Tugtutôq-Ilímaussaq dyke swarm. Trachyte dykes from this dyke swarm have a phenocryst assemblage (ferroaugitic pyroxene, perthite, apatite, opaque oxides and olivine) that is very similar to the cumulus assemblage present in the syenites of Nunarssuit and West Kûngnât except that the olivine is more magnesian. According to Martin's calculations quartz was on the verge of becoming a crystallising phase. Due to the similarities between the phenocryst assemblage in the trachyte dykes and the cumulus assemblages present in Nunarssuit and West Kûngnât it was decided to use a trachyte chill from the Tugtutôq-Ilímaussaq dyke swarm as an approximation for the magma composition which crystallised syenites. The dyke sample used is one of the Main Series dykes in the Nunataq region and is taken from Upton and Fitton (1985, no.5 in Table 1); it will be referred to from now on as P1.

This composition is very similar to the most primitive Klokken syenites (140183), the marginal augite syenite of the Ilímaussaq intrusion (40528), the West Kûngnât lower layered syenite (26470) and the unlayered Nunarssuit syenite (9). These compositions are reproduced in Table 7.1 below.

Table 7.1: Composition of: P1, trachyte chill taken as parental magma composition for Nunarssuit and West Kûngnât. Fe_2O_3 recalculated to FeO and Fe_2O_3 assuming a Fe_2O_3/FeO ratio of 0.15 (as suggested by Brooks, 1976); 140183, fine-grained granular syenite from the top of the Klokken layered series (analysis also contains 0.39 H_2O and 0.09 CO_2, Parsons (1979); 40528 (GGU sample), Ilímaussaq augite syenite marginal zone, total Fe recalculated to FeO and Fe_2O_3 after Brooks (1976), Upton and Emeleus 1987; 26470 (GGU sample), syenite from the lower banded group, West Kûngnât (Upton 1960); 9 (sample from this study), unlayered syenite at the base of the layered series of Nunarssuit, total Fe recalculated to FeO and Fe_2O_3 after Brooks (1976).

Sample	SiO_2	Al_2O_3	FeO	Fe_2O_3	MgO	CaO	Na_2O	K_2O	TiO_2	MnO	P_2O_5	Total
P1	59.64	15.14	7.74	1.16	0.72	2.42	5.26	5.73	1.13	0.20	0.30	99.43
140183	60.40	15.30	5.01	2.44	0.70	3.40	4.22	5.48	1.26	0.21	0.40	98.82
40528	54.99	15.48	10.02	1.50	1.60	4.39	4.79	4.64	1.95	0.22	0.76	100.35
26470	59.9	15.1	7.8	2.5	0.6	3.9	5.2	5.2	1.1	0.19	n.d.	101.49
9	61.87	14.43	8.13	1.22	0.28	2.55	5.24	5.012	0.767	0.181	0.178	99.81

CIPW norms are shown in Table 7.2, more norms are presented in Appendix E. P1 is more potassic but less calcic than samples 9 (Nunarssuit) and 26470 (West Kûngnât) so its norm contains more orthoclase and less anorthite. Sample 9 is more silicic than P1 and the norm contains free silica, a relatively high proportion of hypersthene and no olivine. Sample 26470 contains less Na^+ relative to Fe^{3+} than P1 and so contains more magnetite and consequently less hypersthene and olivine.

Table 7.2: CIPW norms of P1, 140183, 40528, 26470 and 9. Qtz - quartz, Ortho = orthoclase, Alb = albite, Anorth = anorthite, Neph = nepheline, Diop = diopside, Hyp = hypersthene, Ol = olivine, Mt = magnetite, Il = ilmenite, Ap = apatite.

Sample	Qtz	Ortho	Alb	Anorth	Neph	Diop	Hyp	Ol	Mt	Il	Ap
P1	0	34.05	44.76	0.78	0	8.14	2.38	5.34	1.69	2.16	0.7
140183	6.91	32.77	36.13	6.7	0	6.63	3.92	0	3.58	2.42	0.94
40528	0	22.4	14.36	5.75	10.16	7.05	0	34.05	1.78	3.03	1.44
26470	0	30.28	43.35	2.46	0	14.51	1.29	2.47	3.57	2.06	n.d.
9	3.17	29.66	44.4	1.05	0	9.24	8.83	0	1.77	1.46	0.41

The volatile content of the magma also has to be estimated since volatiles are lost from the magma during cooling. I have considered fluorine, chlorine and water as these are the three most common volatiles which affect the viscosity of magmas. The Gardar plutons were emplaced during a continental rifting event (see Chapter 1). The Kenyan rift system may be taken as a modern analogue to the Proterozoic Gardar rift system. Bailey and MacDonald (1987) report a strong positive correlation between Zr, Y, F and Cl for recent trachytic glasses from the Kenyan rift system. Assuming a

similar relationship for the Nunarssuit and West Kûngnât magmas and using Zr contents of 350ppm and Y contents of 40ppm (trace element analysis of P1) gives fluorine contents of 1000-2000ppm and chlorine contents of up to 1000ppm. These figures are rough estimates, there is no reason why all rifts should show the same, if any, correlation between trace elements such as Zr and Y and Cl and F. However, it seems reasonable to assume that these numbers are at least the right order of magnitude. Syenites are saturated when they contain 5% H_2O at 1000°C and 1 kb (Parsons and Butterfield, 1981). There is no evidence in the Nunarssuit and lower West Kûngnât rocks that they were vapour-saturated and so, as a first approximation, the magma from which they crystallised from may be considered as essentially anhydrous. Calculations are presented using viscosities and densities for both anhydrous melts and those containing 1wt% H_2O. Since the magmas were essentially anhydrous the true water content probably lies between these two[1]. Fluorine may be treated as water in viscosity calculations (Dingwell *et al.*, 1985) and is thus included in the estimate of 1wt% H_2O by default. The effect of chlorine and any other volatiles was ignored.

7.4: Conditions of temperature and pressure at the onset of crystallisation of the Nunarssuit and West Kûngnât syenite

7.4.1: Temperature

Various studies on syenites have determined temperatures at the onset of crystallisation; Table 7.3 lists these temperatures and the methods used to determine them.

Table 7.3: Published temperatures for the onset of syenite crystallisation.

Intrusion	Temperature	Method used	Reference
Nunarssuit	>830°C	Feldspar thermometry	Butterfield (1980)
Nunarssuit	840-980°C	Magnetite-ilmenite thermometry	Buddington and Lindsley (1964)
Ilímaussaq	900°C	Mineral stability	Larsen (1976)
Ilímaussaq	830°C	Nepheline thermometry	Larsen (1976)
Klokken	840°C	Magnetite-ilmenite thermometry	Parsons (1981)
Klokken	900-920°C	Mineral stability	Parsons (1981)

[1]The upper figure was chosen purely for illustrative reasons and could lie anywhere between 0 and the saturation level.

In the course of the present study a variety of geothermometers has been used to try to determine temperatures at the onset of crystallisation of the Nunarssuit and West Kûngnât syenites, temperatures obtained are presented below.

Feldspars: Nekvasil's 1992 geothermometer for ternary feldspars uses the distribution of all three feldspar components between the two feldspar phases so that the chemical potential is the same in both phases. In the present study the thermometer is applied to just one feldspar and so rather than a specific temperature being determined a minimum temperature of crystallisation is obtained instead. This thermometer gives minimum crystallisation temperatures of 750-850°C (at pressures of 1 to 3 kb) for the Nunarssuit and West Kûngnât braid perthites.

Pyroxenes: Ferrohedenbergite is stable below 965°C (Deer *et al.*, 1966); above this temperature it inverts to a pyroxenoid which belongs to an iron-rich β-wollastonite solid solution. The pyroxene in Nunarssuit and West Kûngnât is hedenbergite and not the product of inversion of another phase. This gives a maximum temperature for the crystallisation of the pyroxene.

Pyroxene and olivine: The thermometer of Kawasaki and Ito (1993) uses the partitioning of Fe and Mg between olivines and pyroxenes to determine the temperature of crystallisation of co-existing olivines and pyroxenes which are in equilibrium with each other. Unlike the thermometer of Powell and Powell (1978) this thermometer is based upon actual experimental data. This thermometer gives temperatures of 650-900°C for Nunarssuit and 650-850°C for West Kûngnât. Calculations carried out on all facies give this range of temperatures.

Biotites: Annites are stable below about 550°C at pressures of c.2kb when oxygen fugacity is buffered by the QFM buffer (Dachs, 1994). It is thought that biotite is not a primary cumulus phase but represents either an inter-cumulus phase or alteration product.

Amphiboles: Edenite is not stable above 825°C at 1kb; ferro-richterite is stable below 700°C at the QFM buffer; hastingsite and pargasite are stable at 600°C at P_{fluid}=1000kb at the QFM buffer (Gilbert *et al.*, 1982). It is thought that amphibole is not a primary cumulus phase but represents either an inter-cumulus phase or alteration product.

Opaque oxides: The thermometer of Anderson and Lindsley (1988) uses the partitioning of Fe, Mg, Mn, Al Ti and V between co-existing ilmenites and magnetites to determine temperatures of crystallisation. This thermometer gives temperatures of 600-750°C and log oxygen fugacities of -26 to -19 when applied to bulk compositions of ilmenites and exsolved magnetites. All the magnetites used

were exsolved and oxidised. Magnetite exsolves at about 600°C. The calculated temperatures are likely to represent oxidation temperatures.

The maximum temperature at the onset of crystallisation is constrained by the stability of ferrohedenbergite to 965°C. Feldspars constrain the minimum temperature of crystallisation to 750°C. Upton (1960) concluded that the temperature of the West Kûngnât syenite magmas, on intrusion, were unlikely to have exceed 900°C, whilst in an experimental study McDowell and Wyllie (1971) concluded that the West Kûngnât feldspars crystallised above 800°C. On the basis of the above an initial crystallisation temperature of 850°C has been assumed for calculations concerned with the behaviour of the magma. In comparison, magmas of basaltic composition usually begin to crystallise at about 1300°C.

7.4.2: Pressure

Pressure is more poorly constrained than temperature. as there are no suitable geobarometer assemblages in the Nunarssuit and West Kûngnât syenites. The Nunarssuit and West Kûngnât syenites contain xenoliths of supracrustal rock. The maximum uneroded thickness of supracrustal rocks preserved in the Gardar is 3km (Parsons, 1981). The magmas must have been in contact with these supra-crustal rocks in order to contain xenoliths of them and must therefore have been emplaced at a minimum depth of 3km. A pressure of 1kb is used in calculations on magma behaviour on the basis of 1kb = 3km depth.

7.5: Viscosity and density - assumptions, controls and calculations

7.5.1: Viscosity

Viscosity of magma affects a variety of processes including settling rates, convection and hence cooling rates. Viscosity is controlled by the degree of polymerisation of the melt. A pure silica melt may be imagined as a net-work of silica tetrahedra linked by bonds between the oxygens at the corners of the tetrahedra (Fig. 7.3a). Al_2O_3, TiO_2 and P_2O_5 melts also behave like this; these oxides are known as network formers. The oxygens involved in bonding the tetrahedra together are known as bridging oxygens. Oxides such as Na_2O, K_2O, CaO, Fe_2O_3, FeO, MgO, MnO, H_2O and the elements F and Cl break the oxygen to oxygen bonds and are known as network modifiers (Figs. 7.3b, 7.4 and 7.5).

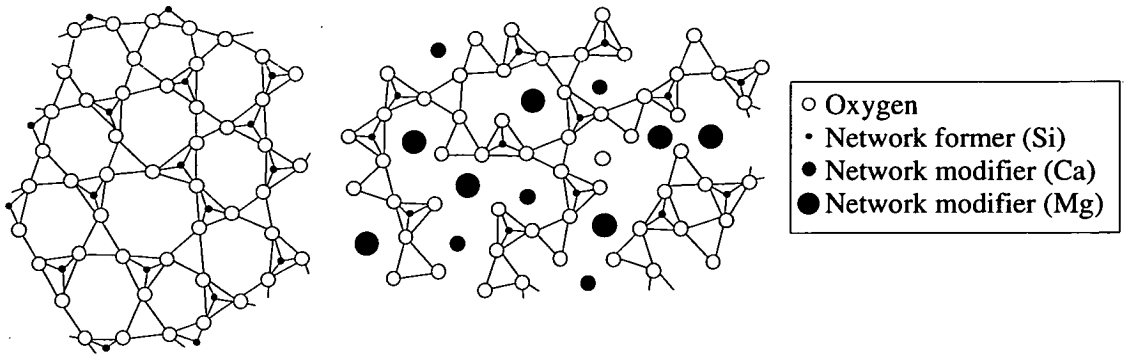

Fig. 7.3: a) pure silica melt network; b) modified silicate melt structure. After Best (1982).

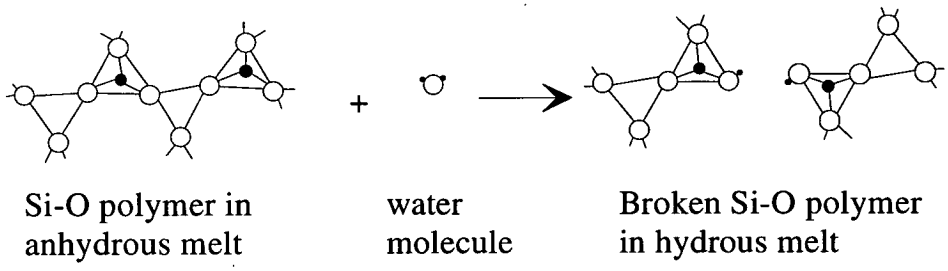

Fig. 7.4: Mechanism for reaction of network modifiers with silica network. Network modifier could be any oxide. After Best (1982).

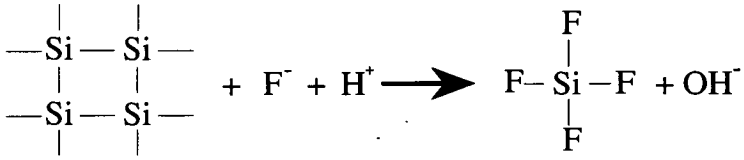

Fig. 7.5: Mechanism for reaction of fluorine with silica network. After Norton (1992).

Oxygens that are not involved in bonding the tetrahedra together are known as non-bridging oxygens (NBO). Details of this model are given by Hess (1980). A semi-quantitative measure of viscosity is the NBO/T ratio (Henderson *et al.*, 1985) where T is the number of network forming oxide tetrahedra. Appendix F gives details of how to calculate NBO/T ratios; typical values are given in Table 7.4. A more quantitative viscosity calculation was presented by Shaw (1972) and it is this calculation that is in current use in today's literature. However, there are a number of problems with this model that will be outlined before determining the viscosity of P1.

Table 7.4: Typical values of NBO/T from Norton, 1992; Mysen, 1987 and Henderson *et al.*, 1985.

Magma type	Basalt	Rhyolite	Andesite	P1
NBO/T	0.76	0.10	0.27	0.25

Shaw's model takes into account the presence of water but not halogens or other "volatile or minor constituents"; it takes no account of crystal content or bubbles. Values of viscosity calculated in Shaw's paper vary by less than 2 log units from viscosities measured in the laboratory for anhydrous melts. When compared to measurements of the viscosity of hydrous melts, the calculation results were found to be within known probabilities of experimental error except at high pressures and high water contents. Accuracy decreases above viscosities of 10^8 poise. The results of using Shaw's calculation on P1 are plotted in Fig. 7.6a and given in Table 7.5.

Fluorine has been treated as if it were water (cf. Dingwell *et al.*, 1985) and other volatiles have been ignored. The calculation is explained in Appendix F. Norton (1992) reviewed various models for calculating the viscosity of melts. For crystal contents of less than 60% of the total volume of the magma she found that the Einstein-Roscoe equation (1) gave the best fit to experimental data:

$$\eta = \eta_{melt} (1-1.35\phi)^{-2.5} \quad ...(1)$$

where: η_{melt} = viscosity calculated after Shaw (1972)

ϕ = the volume fraction of solids i.e. fraction of total volume of magma occupied by crystals

Table 7.5: Viscosities and densities of P1 and P1+1%H2O at various temperatures, pressure = 1kb. Viscosities were calculated by the method of Shaw (1972) and densities by the method of Bottinga *et al.* (1982). Viscosities and densities of other compositions were calculated for comparison. Compositions were taken from Middlemost (1985) and are all averages based on at least 200 analyses. The basalt analysis is number 4 in table 5.1.1, the rhyolite analysis is number 5 in table 8.3.2, the andesite analysis is number 2 in table 7.1.1 and the granite analysis is number 3 in table 9.3.

Sample	Temperature in °C	viscosity in poise	density in gcm^{-3}
Dry P1	950	7.08×10^5	2.54
	900	2.00×10^6	2.54
	850	6.20×10^6	2.55
	800	2.12×10^7	2.56
	750	8.26×10^7	2.57
	700	3.67×10^8	2.58
P1 + 1%H_2O	950	1.49×10^5	2.51
	900	3.85×10^5	2.52
	850	1.09×10^6	2.53
	800	3.40×10^6	2.54
	750	1.19×10^7	2.55
	700	4.72×10^7	2.56
Basalt	1300°C	8.4×10^1	2.67
Rhyolite	850°C	5.4×10^9	2.35
Andesite	1000°C	3.5×10^4	2.56
Granite (1% H_2O)	850°C	2.4×10^7	2.37

Fig. 7.6b shows the effect of increasing crystal content on P1 viscosity at 850°C. Above $\phi = 0.6$ the equation ceases to be realistic and Norton recommends the use of the equations developed by Gay *et al.* (1969). This equation was developed to model the flow of industrial slurries through pipes. Both these calculations contain crystal content terms, which are not known for magma chambers. The equation derived by Gay *et al.* contains a shear rate term. Shear rate is poorly constrained in magmas but Spera *et al.* (1988) claimed that it lies between 3 x 10^{-8} and 10^{-7} s^{-1} for silicic magmas. Numerical modelling (not presented here) of the equation presented by Gay *et al.* indicates that variations of one degree of magnitude in the shear rate affect the resultant viscosity by about a factor of 2. Variations in the crystal content of the magma and the maximum possible crystal content of the magma have a much greater effect on the results of the equation.

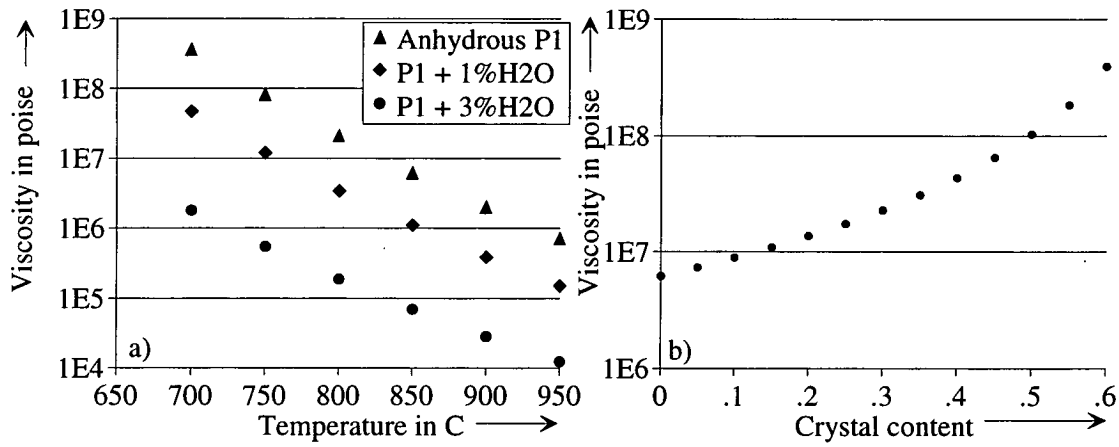

Fig. 7.6:a) Effect of decreasing temperature on viscosity of P1; b) effect of increasing crystal content (expressed in terms of fraction of total volume of magma occupied by crystals) on viscosity of anhydrous P1 at 850°C using the Einstein-Roscoe equation (1).

Shaw's equations were used to calculate viscosity without then using the Einstein-Roscoe equation or the equations developed by Gay *et al.* (1969) for the following reasons:

1) since the crystal content is poorly constrained any crystal content value would be little more than a guess.

2) for crystal contents up to 25 vol% the viscosity of a magma is affected by less than an order of magnitude.

3) in the engineering literature it has been shown that for a crystal content of less than 25 vol%, a suspension is relatively free-moving. Between 25 and 50 vol.% crystal content, solid-solid interactions have a greater impact on viscosity and the suspension behaves as a viscous mush. Above 50 vol% crystal content the system

behaves as a solid. Thus, the method of Gay *et al.* would be of use for calculating the behaviour of a crystal mush flowing down the side-wall of a magma chamber but appears to be unsuitable for calculating the behaviour of crystallising, convecting magma.

4) use of Shaw's equations allows comparison with previous work.

Compared to the uncertainty in some of the other parameters points 1) and 2) produce only minor errors. Some workers (e.g. Sparks *et al.*, 1993) have concluded that the crystal content, excluding cumulate layers, is always less than 1 vol% of the magma chamber.

7.5.2: Density

Density affects convection, cooling and settling or flotation. Any crystal more dense than the fluid that surrounds it, can potentially settle through that fluid (see section 7.7 for a discussion of this). Densities have been calculated for P1 and P1 + 1%H_2O at various temperatures using the method and data of Bottinga *et al.*, (1982, see Appendix F for details). Results are summarised in Table 7.5. Table 7.6 shows densities of phases present in the Nunarssuit and West Kûngnât syenites.

Phase	Density in gcm^{-3}
P1	2.54 - 2.58
P1 + 1%H20	2.51 - 2.56
pyroxene	3.5
olivine	4.35
feldspar	2.59
biotite	3.3
amphibole	3.4
apatite	3.2
ilmenite	4.7
magnetite	5.2
zircon	4.6
quartz	2.7

Table 7.6: Densities of P1 and P1 + 1%H_2O at 1kb pressure and 950-750°C and phases present in the Nunarssuit and West Kûngnât syenites (mineral densities from Deer *et al.*, 1966)

7.6: Convection

If a temperature difference exists between two points in a fluid then that fluid will convect. There are two main dimensionless numbers that are used to describe the convective state of magma chambers: the Rayleigh number, (Ra, section 7.6.2) and the Prandtl number, (Pr, section 7.6.3). The significance of the Prandtl number is a matter of some debate. If a crystallising magma convects then the moving fluid will

affect the spatial distribution of the crystals. It has been suggested by some workers (e.g. Sparks *et al.*, 1984) that the upward vertical convective velocity of magma may be sufficient to prevent crystals from settling. However, Marsh and Maxey (1985) state that convective velocity decreases to zero within boundary layers at the edge of magma chambers, and that crystal settling would not be hindered by the up flow of magma within such layers.

7.6.1: The temperature gradient driving thermal convection

The temperature within the body of a magma chamber may be relatively well constrained by geothermometers and experiments but the temperature at the edge of a magma chamber is not and could theoretically vary between the initial wall-rock temperature and the liquidus of the magma. Carrigan (1988) suggested that the initial wall-rock temperature should be used as the temperature at the edge of the magma because this linked "the thermal regime of the magma to that of the host". For Nunarssuit and West Kûngnât the initial wall-rock temperature is estimated at 300°C based on the average continental geotherm and the fact that the temperature would have been raised slightly above this because of rifting. This gives an initial value of Δ T of 550°C. Worster *et al.*, (1990) envisaged a magma chamber in which a solid crust of crystals formed at the roof of the chamber (Worster *et al.*, fig.1, present Fig. 7.7).

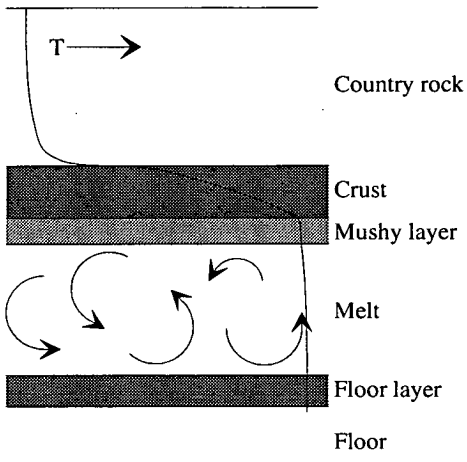

Fig. 7.7: From Worster *et al.*, (1990) showing temperature gradient in crystallising magma.

Below this is a "mushy" layer consisting of crystals bound together in a framework with buoyant residual magma between the crystals. This mushy layer does not take part in convection either because the framework is rigid or because there is a high viscosity contrast between the mushy layer and the melt. The temperature difference driving convection is that between the main body of magma and the base of the mushy zone. The temperature at the base of the mushy zone may be close to that of

the main body of the magma and so the temperature difference driving convection may be as little as 0.1°C. Thus the temperature difference driving convection used in equations may vary between 550°C and 0.1°C

7.6.2: Rayleigh number (Ra)

The Rayleigh number indicates the likelihood and nature of the thermal convection of a magma. Magmas convect if Ra > 1700. Between Ra = 1700 and Ra = 10^4 convection is ordered and steady and typically, rounded convection cells form (Fig. 7.8a). For Ra>10^4, convection is turbulent and tie-dependent (Fig. 7.8b).

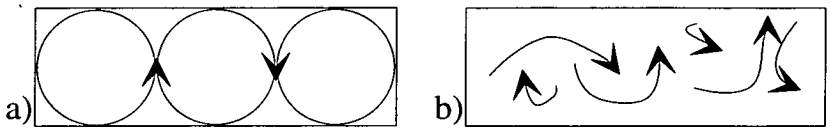

Fig. 7.8: a) regular, ordered, steady convection; b) turbulent, time dependent convection.

The Rayleigh number is given by:

$$Ra = (g\alpha\Delta T\rho L^3)/(\eta\kappa) \quad ...(2)$$

where: g = gravitational acceleration = 980 cms^{-2}

α = coefficient of thermal expansion = 5 x 10^{-3} K^{-1}

ΔT = temperature contrast driving convection in °C

ρ = density in gcm^{-3}

L = thickness of convecting layer in cm

η = viscosity in poise

κ = thermal diffusivity = 5 x 10^{-3} cm^2s^{-1}

L, the thickness of the convecting layer is poorly constrained for Nunarssuit and West Kûngnât. The thickness of the convecting layer is not known and it is not obvious that the entire chamber acted as a single convecting layer. Furthermore, in a layered magma chamber undergoing multi-diffusive convection (section 7.6.6) it is not possible to calculate the thickness of individual convecting layers (A Rice pers comm.). Thus any value given as L will be largely a guess although it is unlikely to have been greater than the maximum thickness of the intrusion under consideration; the value chosen is 1 x 10^5cm (1km). ΔT, the temperature difference driving convection is unknown (section 7.6.1) and may lie between 0.1°C and 550°C. Viscosity varies from 1.49 x 10^5 (wet, 950°C) and 3.67 x 10^8 (dry, 700°C) poise, density varies from 2.58 (dry, 950°C) to 2.51 (wet, 700°C) gcm^{-3}. Using the above values, the Nunarssuit and West Kûngnât magmas would have had a Rayleigh

number of between 6.84 x 10^8 (dry, ΔT = 0.1°C) and 1.07 x 10^{16} (wet, ΔT = 650°C). The range is illustrated in Fig. 7.9. Basaltic magma chambers typically have Ra = 10^{12} to 10^{16} (McBirney, 1984; Martin and Nokes, 1989).

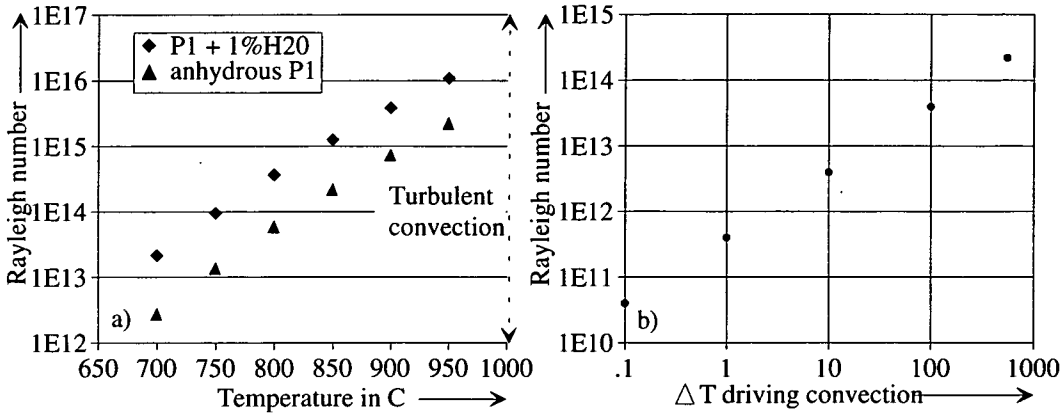

Fig. 7.9: a) variation of Rayleigh number with temperature (and viscosity) for anhydrous P1 and P1 + 1%H_2O, ΔT = 10°C, L = 10^5cm; b) variation of Rayleigh number with temperature driving convection for P1 at 850°C, viscosity = 6.20 x 10^6poise, density = 2.55gcm^{-3}.

7.6.3: Prandtl number (Pr)

The Prandtl number gives the rate at which temperature contrast is reduced by heat diffusion to the surrounding rocks. Some workers (e.g. Marsh and Maxey, 1985) suggest that flow is laminar when Pr > 10^5, whereas others believe that convection depends only weakly on the Prandtl number at high Prandtl numbers (e.g. Krishnamurthi, 1970). Many authors believe that all magma chambers undergo turbulent convection. The Prandtl number is given by:

$$Pr = \eta/(\rho\kappa) \quad ...(3)$$

where: ρ = density in gcm^{-3}

η = viscosity in poise

κ = thermal diffusivity = 5 x 10^{-3} cm^{2}s^{-1}

For values of viscosity and density of 1.49 x 10^5 poise and 2.51 gcm^{-3} (wet, 950°C) to 3.67 x 10^8 poise and 2.58 gcm^{-3} (dry, 700°C) the Prandtl number ranges from 2.84 x 10^7 to 1.19 x 10^8 which may be compared with typical values of 10^4 to 10^7 for basaltic magmas (Mingard, 1992).

7.6.4: Boundary layers

As magma crystallises, a zone of decoupling develops between the well-mixed convecting interior of the chamber and the margins of the chamber where

crystallisation occurs. This zone is known as a boundary layer (McBirney and Noyes, 1979). Gradients of heat, composition and momentum define thermal, compositional and mechanical boundary layers respectively. Momentum is transferred more rapidly than heat and elements so the mechanical boundary layer is generally thicker than the others (McBirney, 1984). Boundary layers will be referred to in section 7.6.5, 7.7 and in Chapters 9 and 10.

7.6.5: Convective velocity

Marsh and Maxey (1985) provide calculations for peak (i.e. maximum) convective velocity in the body of the magma chamber:

$$U_0 = (0.258\kappa Ra^{1/2})/L \quad ...(4)$$

where: U_0 = typical velocity found within the chamber

κ = thermal diffusivity = 5×10^{-3} cm^2s^{-1}

Ra = Rayleigh number

L = thickness of convecting layer in cm

Marsh and Maxey state that the constant 0.258 may lie in the range 0.2-0.3. Compared to other potential errors this is negligible. The results obtained using values of L of $1 \times 10^5 cms^{-1}$ and Ra between 6.84×10^8 and 1.09×10^{16} vary between 3.37×10^{-4} and 1.35 cms^{-1} which is considerably lower than values for more basic magmas which are typically within the range 0.0258 to 2.58 cms^{-1} for a convecting layer of a similar size. Within the mechanical boundary layer the velocity will decrease to zero.

7.6.6: Compositional convection

Compositional convection may result from density differences between residual fluid in a boundary layer and the main body of magma. If the residual liquid is less dense than the main magma then it will rise through the main magma. If the boundary layer is horizontal it reaches a critical thickness before the fluid rises through the chamber. Sparks and Huppert, (1984) introduced the term "fractionation density". This is defined as "the ratio of the gram formula weight to molar volume of the chemical components in the liquid phase that are being removed by fractional crystallisation". Fractionation densities of the cumulus phases of Nunarssuit and West Kûngnât were calculated (Table 7.7); all except feldspar are greater than the densities of P1 and P1 + 1%H_2O at the same temperature.

Phase	Fractionation density
Pyroxene	3.13
Olivine	6.13
Feldspar	2.33
Apatite	6.53
Ilmenite	5.06
Magnetite	4.80
P1	2.53
P1 + 1%H_2O	2.55

Table 7.7: Fractionation densities of average cumulus phases from Nunarssuit and West Kûngnât at 850°C and densities of P1 and P1 + 1%H_2O at 850°C. Fractionation densities calculated after Sparks and Huppert, (1984), magma densities calculated after Bottinga *et al.*, (1982).

The fractionation density of the crystallising assemblage is equal to the weighted sum of the individual fractionation densities of the phases which are crystallising. The fractionation densities of the Nunarssuit and West Kûngnât cumulus assemblages are greater than those of the magmas so the residual liquid would be less dense; compositional convection could have occurred during the evolution of the Nunarssuit and West Kûngnât magma chambers. This could have led to liquid stratification and double diffusive convection (Turner and Campbell, 1986).

7.7: Crystal settling

Darwin (1844) observed lavas on the Galapagos Islands which were rich in feldspar phenocrysts and suggested that this might have come about through crystal settling. In 1915 Bowen reported diopside and forsterite crystals sinking in a diopside-forsterite-silica melt although later he stated that "there is a common impression that I am a proponent of crystal settling...the impression has never had any justification" (1956). Since the 1970s the reality of crystal settling has been the matter of intense debate.

7.7.1: Arguments and evidence for and against crystal settling

Density contrasts: The simplest argument in favour of crystal settling is that particles should sink in a fluid if the particles are more dense than the fluid. Plagioclase is often less dense than basaltic magma and this has led to many workers dismissing crystal settling as a mechanism for the formation of igneous layering (McBirney and Noyes, 1979). Whilst it is true that plagioclase is less dense than basaltic magma this does not mean that crystal settling does not occur. Some layered intrusions do not contain plagioclase (e.g. Nunarssuit and West Kûngnât) and it may be possible for plagioclase to settle if grains are aggregated to other, more dense particles. Wager and Brown (1968) and Irvine (1978, 1980) suggested that

plagioclase could be carried down to the bottom of a magma chamber in density currents.

Yield stress: The yield stress of magma has also been the subject of much debate (see section 7.2). Rice (1993) argued that "measured yield strengths for magmas forbid crystal settling" whilst Parsons and Butterfield (1981) showed that the cumulus phases of the Klokken laminated syenite would all have exerted the same downward force when suspended in the magma and could thus have settled having overcome the magma yield strength. The Klokken syenite is similar to that of Nunarssuit and West Kûngnât; the main difference is that in its final stages the Klokken magma contained more water (evidence for the presence of a free vapour phase comes from the presence of druses in the layered syenites). To further complicate matters Barnes and Walters (1985) argued that yield strengths do not exist. If they are correct then arguments that yield strengths can prevent crystal settling are irrelevant; if magmas do possess yield strengths then the work of Parsons and Butterfield (1981) shows that they can be overcome. Considering the above it seems unlikely that "yield stresses for magmas forbid crystal settling" although in individual cases it may prevent settling.

Velocities: It has been argued by some workers (e.g. Sparks *et al.*, 1984) that if the convective velocity of the magma is greater than the settling velocity of the particles then the particles will remain in suspension and will not settle. Marsh and Maxey (1985) point out that convective velocity decreases to zero in the mechanical boundary layer and so once particles are carried into the boundary layer by a convective current they will be able to settle.

Hydraulic equivalence: If crystals settle out of a magma and accumulate on the magma chamber floor, it would be reasonable to expect that all the grains at a given horizon are hydraulically equivalent, that is, if the grains were dropped from the same height above the floor of the magma chamber they would arrive at the floor of the magma chamber together. The major cumulus grains in the layers of Nunarssuit and West Kûngnât are not hydraulically equivalent e.g. the settling rate of the olivine present in these layers is approximately twice that of the pyroxene (section 7.7.3), although apatite, ilmenite and magnetite are hydraulically equivalent. A layering scheme predicted on this basis would be something along the lines of an olivine-rich layer, followed by a feldspar- and pyroxene-rich layer, followed by an apatite-, ilmenite- and magnetite-rich layer. Some workers (e.g. Jackson, 1961) take the lack

of hydraulic equivalence as evidence against crystal settling but this ignores such effects as current reworking and settling from different heights in the magma chamber.

Critical viscosities: Sparks *et al.*, (1993) carried out a series of experiments on silicon carbide grit in a tank of water that was initially convecting. They observed that when the grit reached a critical concentration, convection was damped and the grit sank. They calculated that this could only happen because the viscosity of the water was below a critical value; above this value particles could not settle. The critical viscosity was defined as a function of both the fluid properties and the particle properties and so the critical viscosity for a given fluid is phase dependent. Critical viscosities are calculated for the various cumulus phases from Nunarssuit and West Kûngnât in section 7.7.2

Grain size distributions: Conrad and Naslund (1989) argued that, if crystals have accumulated by crystal settling, size grading should be seen with the largest crystals of the densest phases being concentrated at the base of layers. The grain size of these phases should decrease upward through the layer as is seen in some layers from the Skaergård Upper Zone A. Conversely if crystals nucleate and grow *in situ* there should be an inverse correlation between mode of a given phase and its grain size since individual nuclei will compete for the necessary components to grow. Examples of both types of grain distribution are seen in the rock record. What the above analysis ignores is the effect of a constant supply of growing crystals and subsolidus re-equilibration (Boudreau, 1987; Hunter, 1987; Chapter 6.9). There is no grain size variation within the rhythmic layers of Nunarssuit and West Kûngnât but this may be due to resorption of smaller grains and growth of larger grains by ripening.

Chemical variation within layers: Conrad and Naslund (1989) suggested that minerals in layers formed by density or convection currents re-depositing and sorting grains present at the bottom of the magma chamber would not show any systematic chemical variation. Minerals in layers formed by rhythmic nucleation or *in situ* crystallisation should show chemical variation because they are generated by chemical gradients or changes in magma chemistry. Again this argument ignores the effects of sub-solidus re-equilibration. No consistent variation in mineral composition has been detected within layers.

Experimental evidence: Wolf and Wyllie (1986) reported the ease with which feldspar crystals settled in melted West Kûngnât syenite (sample 26005 from Upton *et al.*, 1971) at temperatures above 850°C. Unfortunately this evidence for crystal settling is not very convincing. The melt used was artificially hydrated, sometimes by up to 5% and it is not reported at which water contents settling occurred. The pressure at which the experiments were conducted is not realistic and may have had an effect on convection. The shape and dimensions of the experimental capsule relative to the feldspar crystals is not stated and may be unrealistic. Finally the melt in the capsule may not have been convecting, it is not stated whether a temperature gradient existed in the capsule.

Evidence from lavas: Circumstantial evidence for crystal settling was described by Cox and Mitchell (1988). They reported two lavas from Deccan traps which were thought to be cogenetic; an aphyric lava and a slightly more evolved plagioclase-phyric lava. Calculations showed that, to relate the aphyric lava to the parental magma a combination of clinopyroxene, olivine and plagioclase crystals had to be removed. The matrix of the porphyritic lava could be related to the parental magma in a similar fashion but contained an excess of plagioclase phenocrysts. Cox and Mitchell suggested that because, compared to the aphyric lava, the phyric lava was slightly more evolved, slightly more Fe-rich and thus slightly more dense, plagioclase could not sink whereas clinopyroxene and olivine could. They also suggested that phenocrysts of clinopyroxene, olivine and plagioclase had sunk in the magma chamber from which the aphyric lava was derived. Evidence against crystal settling comes from the Hawaiian lava lakes. Large olivine phenocrysts and aggregations of phenocrysts have not sunk in the less dense lava (Helz, 1993). Olivine settling is thought to be prevented by turbulent convection, rising vesicles and melt and particle-particle interaction. However, there are reports of pillow lavas from Iceland, Réunion and Cyprus having concentrations of olivine phenocrysts at their bases. Since modern day pillow lavas are homogeneous when extruded it is difficult to propose a hypothesis other than crystal settling to explain these olivine concentrations.

7.7.2: Critical viscosities

Sparks *et al.*, (1993) define a critical viscosity whereby crystals may settle through the magma chamber if the actual viscosity of the magma is less than the critical viscosity.

Critical viscosity is defined as:

$$\eta_{crit} = [(\rho_{particle}-\rho_{fluid})gd^2/18]^{3/2} \times [(Ra_{Crit}\eta\kappa)/(\alpha\Delta T g\rho_{fluid})^{1/2} \times \kappa^{-1} \quad ...(5)$$

where: η_{crit} = critical viscosity above which a phase can not sink in poise

$\rho_{particle}$ = particle density in gcm^{-3}

ρ_{fluid} = fluid density in gcm^{-3}

g = gravitational acceleration = 980 cms^{-2}

d = particle diameter in cm

Ra_{Crit} = Rayleigh number at which fluid starts to convect = 10^3

α = coefficient of thermal expansion = 5×10^{-3} K^{-1}

ΔT = temperature difference driving convection

κ = thermal diffusivity = 5×10^{-3} cm^2s^{-1}

η = viscosity of the fluid in poise

In the following discussion it should be remembered that the equations presented by Sparks *et al.* were developed from a consideration of the settling behaviour of a single phase and do not attempt to consider the affect that several phases of differing densities would have on the critical viscosity. Figs. 7.10 and 7.11 show a series of graphs of critical viscosities of the cumulus phases of Nunarssuit and West Kûngnât plotted against temperature difference driving convection (section 7.6.1). Graphs are plotted for both P1 and P1 + 1%H2O, the sloping solid lines show the critical viscosity for different phases whilst the dashed horizontal line in each graph shows the actual viscosity of the syenitic magma at the temperature and water content under consideration. Actual viscosities and critical viscosities are lower for P1 + 1%H_2O than for the anhydrous P1. In all cases the viscosities of P1 and P1 + 1%H_2O are greater than the critical viscosities of apatite, magnetite and ilmenite which will therefore not sink. At high temperatures and for low temperature differences driving convection the critical viscosities of olivine, pyroxene and feldspar are greater than the actual viscosities of the magma so that according to Sparks *et al.*, (1993) these phases could sink. As temperature falls and the temperature difference driving convection rises the viscosity of the magmas increases more rapidly than the critical viscosities so that, at temperatures of 750°C for anhydrous P1 and 700°C for P1 + 1%H_2O, the critical viscosities of all the cumulus phases in the syenites of Nunarssuit and West Kûngnât are less than the actual magma viscosities and, according to Sparks *et al.*, (1993), none of the phases can sink.

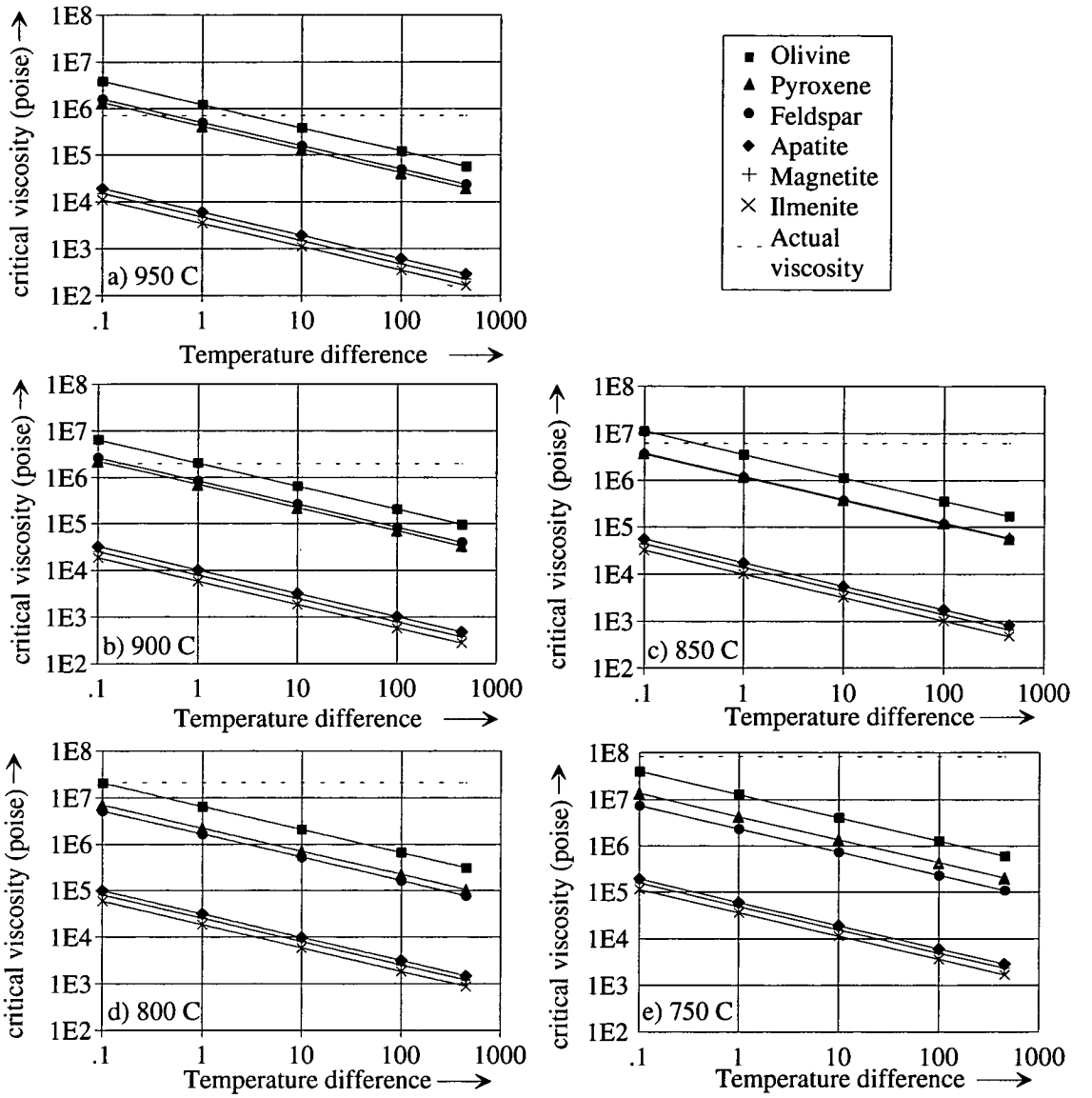

Fig. 7.10: Graphs of critical viscosities against temperature difference driving convection for anhydrous P1 magma assuming a critical Rayleigh number of 10^3, densities as given in Tables 7.5 and 7.6. Critical viscosities for olivine (0.5x0.7x1.3mm), pyroxene (0.5x0.8x1.0mm), feldspar (1.0x5.0x5.0mm), apatite (0.1x0.1x1.0mm), magnetite (0.1x0.1x0.1mm) and ilmenite (0.1x0.1x0.1mm) are shown by the sloping solid lines. The horizontal dashed line shows the actual viscosity of magma at stated temperature. If the critical viscosity is less than the actual viscosity settling can not occur.

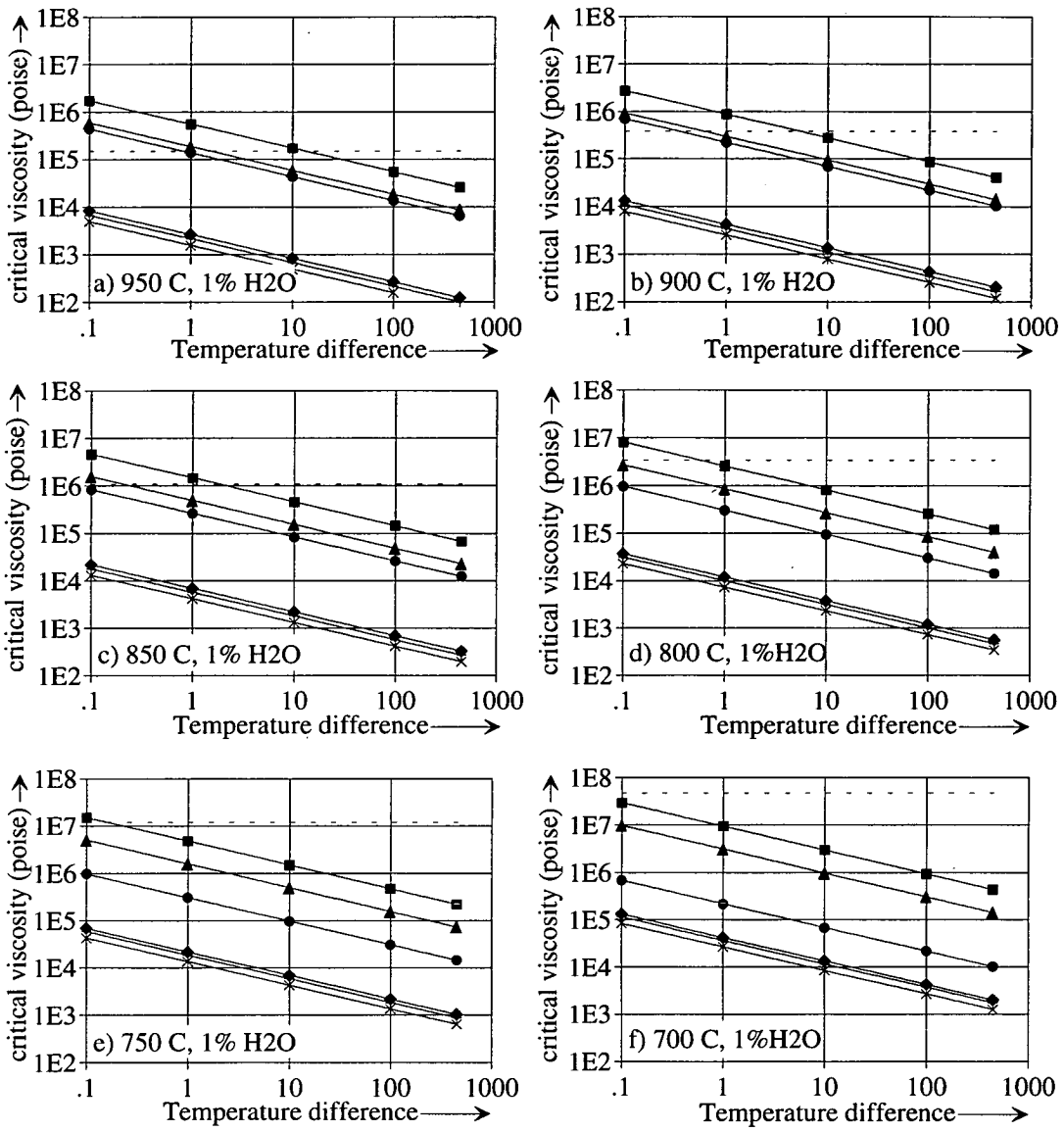

Fig. 7.11: Graphs of critical viscosities against temperature difference driving convection for hydrous P1 + 1% H_2O magma assuming a critical Rayleigh number of 10^3, densities as given in Tables 7.5 and 7.6. Critical viscosities for olivine (0.5x0.7x1.3mm), pyroxene (0.5x0.8x1.0mm), feldspar (1.0x5.0x5.0mm), apatite (0.1x0.1x1.0mm), magnetite (0.1x0.1x0.1mm) and ilmenite (0.1x0.1x0.1mm) are shown by the sloping solid lines. The horizontal dashed line shows the actual viscosity of magma at stated temperature. If the critical viscosity is less than the actual viscosity settling can not occur. Key as for Fig. 7.10.

7.7.3: Settling velocity calculations

The equation normally used to calculate the settling velocity of crystals in a magma was developed by Stokes for the settling of an individual spherical particle in a Newtonian fluid that has a diameter much greater than that of the particle under consideration. Terminal settling velocity V is given by:

$$V = [gd^2(\rho_{particle}-\rho_{fluid})]/(18\eta) \quad ...(6)$$

where: V = terminal settling velocity (cms^{-1})

g = gravitational acceleration = 980 cms^{-1}

$\rho_{particle}$ = density of settling particle (gcm^{-3})

ρ_{fluid} = density of fluid

η = viscosity (poise)

d = particle diameter (cm)

The above equation has been modified by various authors to take into account the non-spherical shape of settling particles and particle-particle interaction.

McNown and Malaika (1950) carried out experiments on small metal ellipsoids and various other shapes settling in oil and interpreted the relationship:

true velocity = Stokes velocity/constant (K) ...(7)

The diameter term in Stokes equation is replaced by a term = $2(abc)^{1/3}$ where a, b and c are the semi-axes of an ellipse: a is the semi-axis parallel to the direction of movement, b and c are interchangeable. They produced a theoretical graph (Fig. 7.12, their fig. 1) for ellipsoids. The constant K is read off the y axis for various values of a,b and c and for a constantly rotating particle (McNown and Malaika observed that all particles rotated for [2]Re<1) all possible combinations of a,b and c are used to find an average value. Experimentation showed that this method gave realistic velocities not only for ellipsoids but also for other shapes; McNown and Malaika concluded that the dimensions, not the shape of the particle, were the dominant control on settling velocity.

Komar and Reimers (1978) carried out experiments on pebbles settling in glycerine; they determined a more complicated relationship than that of McNown and Malaika. They used the Corey Shape Factor (CSF = $a/(b-c)^{1/2}$), and an average

---

[2]Re = Reynolds number and is defined as (Peak convective velocity in boundary layer x thickness of boundary layer)/kinematic viscosity, obviously for the high viscosities and low convective velocities calculated Re will be much less than 1. The Reynolds number gives an indication of how a magma flows along a cylindrical conduit, for Re>500 the flow is turbulent for Re<500 the flow is laminar.

diameter (D_i = (a.b.c)$^{1/3}$, where c, b and a are the major, intermediate and minor ellipse diameters) to calculate the settling velocity as $V = [(\rho_{particle}-\rho_{fluid})gD_i^2]/[18\eta f(csf)]$ where $f(csf) = 0.946(CSF)^{-0.378}$ for $0.4 < CSF < 0.8$ and $f(csf) = 2.18 - 2.09CSF$ for $CSF < 0.4$. Their work did not deal with non-ellipsoids but it is implied that the equation would hold for prisms.

Kerr and Lister (1991) carried out a theoretical analysis of the settling of ellipsoidal particles; they then extended this work concluding that the settling velocity of non-ellipsoidal particles is well approximated by ellipsoidal particles of equivalent volume and aspect ratios.

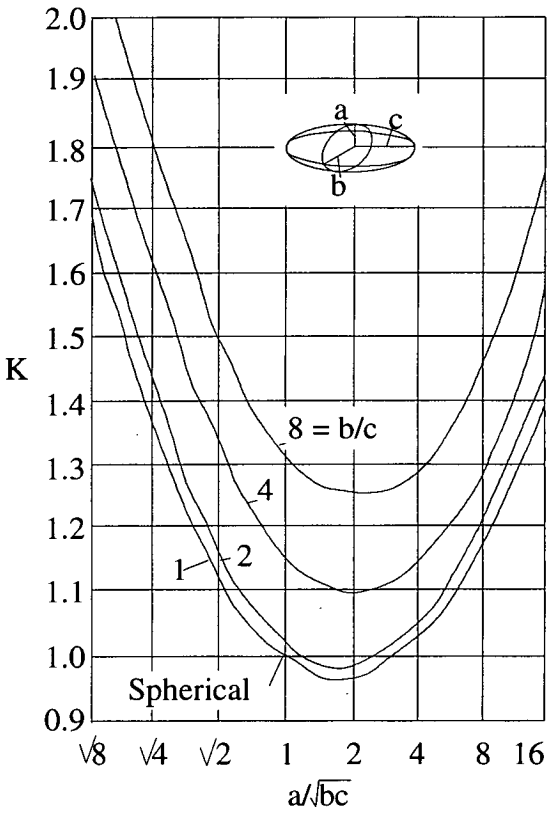

Fig. 7.12: Graph of a/√bc against K (from McNown and Malaika, 1950).

They calculated the settling velocity as true velocity = Stokes velocity x constant (S). S is read off the graph (Fig. 7.13, their fig. 1). The value of the particle radius used in calculating the Stokes settling velocity is given by d = (a.b.c)$^{1/3}$ where a,b and c are principal diameters, such that c>b>a.

The methods of Komar and Reimers (1978) and of Kerr and Lister (1991) are very similar and numerical modelling carried out in the course of this study shows that they produce nearly identical results. The calculations of McNown and Malaika produce velocities which are less than 5% greater than these.

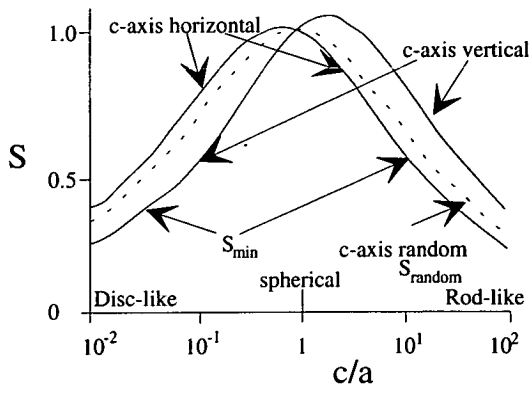

Fig. 7.13: Graph of S against c/a (from Kerr and Lister, 1991).

This difference is so small that the method of McNown and Malaika has been adopted for the calculations in this study purely for the reason that this method predates the others. None of the above formulae take into account the effect that the presence of other particles has on a settling particle. This leads to a reduction in the settling velocity of the particle and is known as the Bagnold effect (Wadsworth, 1973). This is quantified by:

$$\text{True velocity} = V_0(1 - \phi)^n \qquad ...(8)$$

where: V_0 = free fall velocity

ϕ = volume fraction of solids

n = poorly constrained constant somewhere between 2 and 4

Table 7.8 gives values of settling velocities for the cumulus phases in Nunarssuit and West Kûngnât using equations (6), (7) and (8). Figure 7.14a shows how the velocity

Table 7.8: Settling velocities, and critical viscosities (after Sparks *et al.*, 1992), using a viscosity of 6.20×10^6 poise, magma density of 2.53, mineral densities as in Table 7.6, $\Delta T = 10^0C$; ϕ = volume fraction of solids. Convective velocity = 3.37×10^{-4} to 1.35 cms^{-1}.

Phase	Settling velocity in cms^{-1} ($\phi = 0$)	Settling velocity in cms^{-1} ($\phi = 0.3$)	Settling velocity in cms^{-1} ($\phi = 0.5$)	Critical viscosity
Pyroxene	4.45×10^{-8}	1.53×10^{-8}	5.56×10^{-9}	3.84×10^5
Olivine	8.92×10^{-8}	3.06×10^{-8}	1.11×10^{-8}	1.12×10^6
Feldspar	3.70×10^{-8}	1.27×10^{-8}	4.63×10^{-9}	3.69×10^5
Apatite	1.88×10^{-9}	6.46×10^{-10}	2.35×10^{-10}	5.51×10^3
Ilmenite	2.34×10^{-9}	8.04×10^{-10}	2.93×10^{-10}	4.38×10^3
Magnetite	1.91×10^{-9}	6.54×10^{-11}	2.38×10^{-10}	3.21×10^3

is affected by the concentration of particles and Fig. 7.14b shows how the settling velocity varies with temperature (and viscosity). It can be seen that the velocities are at least five orders of magnitude less than the calculated peak convective velocity (3.37×10^{-4} to $1.35 cms^{-1}$). Even taking into account the poor constraints on all these velocities, particles should remain suspended in the body of the magma chamber.

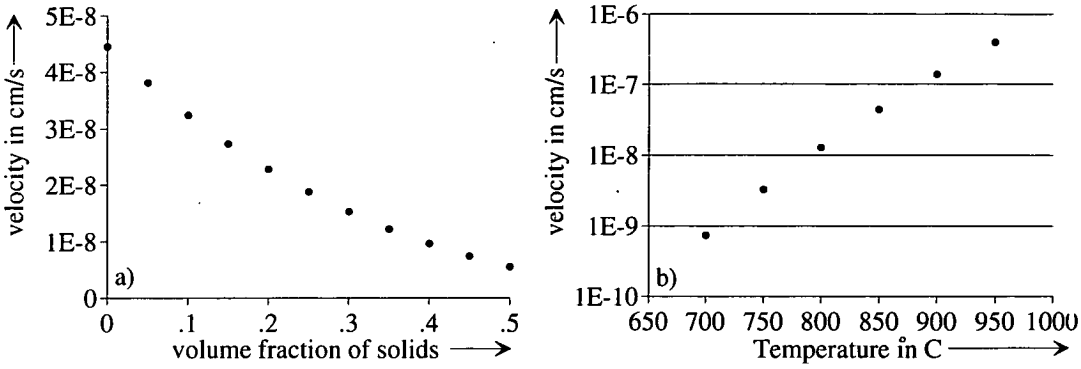

Fig. 7.14: a) Effect of suspended solids on terminal velocity of a pyroxene falling through P1, viscosity = 6.2 x 10^6poise and density 2.55gcm^{-3}; b) effect of decreasing temperature (and increasing viscosity) on terminal velocity of an individual pyroxene crystal (density 3.5 gcm^{-3}) falling through a fluid of composition P1.

As convective velocity decreases towards zero through the mechanical boundary layer, a level will be reached where the terminal velocity of the particles is greater than the convective velocity. Any particles which are in this zone will be able to settle. Typical settling velocities in basaltic magma are generally four or five orders of magnitude greater than those shown and tend to be three or four orders of magnitude less than typical basaltic convective velocities.

7.8: Summary

The rheology of magma is still far from certain. Experimental evidence (Barnes and Walters, 1985) suggests that Bingham plastics do not exist. However field evidence suggests that magmas do possess a yield stress (Parsons and Butterfield, 1981) and that crystals can settle once they exert a downwards force greater than this yield stress. Some workers, however, do not accept this (e.g. Rice, 1993). The composition of the magma which crystallised to give the Nunarssuit and West Kûngnât syenites is not known. These intrusions do not possess chilled margins and estimates of the magma composition have been made on the basis of the composition of Main Series trachytic dykes from the Nunataq region of the Gardar, these dykes have a phenocryst assemblage similar to that of the cumulus phases in the syenites. The magma composition chosen is similar to that of primitive syenite compositions from the layered syenites of Klokken and Ilímaussaq. The temperature and pressure of crystallisation of the syenites are poorly constrained due to a lack of suitable geothermometers and geobarometers; these are, however, estimated at 850°C and 1kb respectively. The assumed magma compositions, temperatures and pressures were used to calculate the viscosities and densities of the magmas using the methods of

Shaw (1972) and Bottinga *et al.*, (1982). Magma viscosities and densities were calculated for anhydrous magma and magma containing 1% water. In all cases the density of the magma was less than that of the cumulus phases. If the magma was stagnant this means that the cumulus phases would have sunk through the magma. Fluid dynamic constants such as the Rayleigh number were calculated and these indicate that the magmas of Nunarssuit and West Kûngnât would have convected turbulently. Calculated settling velocities using Stokes law and the modifications of McNown and Malaika (1950) are several orders of magnitude less than convective velocities calculated using the equation of Marsh and Maxey (1985). If these calculations are realistic then convection would have prevented particles from settling through the main body of magma. However, at the edge of magma chambers boundary layers are inferred to develop where velocity decreases to zero; any crystals within these layers would be able to settle and any crystals carried along by convection currents with no vertical component of motion would begin to settle downwards. Calculations using the equations of Sparks *et al.*, (1993) indicate that olivine, pyroxene and feldspar could have settled through the magma chambers of Nunarssuit or West Kûngnât but that apatite, magnetite and ilmenite could not. Similar calculations carried out on typical basaltic magmas indicate that olivine and pyroxene crystals would probably be able to settle though feldspar crystals would normally not be dense enough and would float.

On the basis of the calculations carried out in this chapter it is not possible to dismiss crystal settling. Certainly the calculations imply that it is unlikely that any of the cumulus phases could settle through the body of convecting magma. However, settling could occur through boundary layers where convective velocity decreases to zero. It should also be borne in mind that the equations used, and the variables inputted into them, are far from certainties.

Chapter 8: Non-linear dynamic analysis of the spacing of rhythmic layers in Nunarssuit and West Kûngnât.

8.1: Introduction

The spacing of rhythmic layers often appears to be approximately regular over a scale of a few metres of stratigraphic sequence. Frequency plots, developed for the study of non-linear dynamics, can be used to assess whether or not the layer-producing mechanism was periodic, chaotic (i.e. follows definite rules but is unpredictable) or random. In an ideal situation the number of variables, (referred to as the embedding dimension in the non-linear dynamic literature), required to describe the underlying dynamics can be determined. This would permit realistic limits to be placed on the degree of complexity required to explain the system. Such a procedure could, in principle, be used to distinguish between the mechanisms for layering suggested in the literature.

8.2: Frequency distribution plots

A frequency distribution with a marked mode (Fig. 8.1a) is indicative of a completely regular, predictable mechanism. An example of such a mechanism would be the time taken for successive oscillations by a frictionless pendulum. Conversely a plot such as Fig. 8.1b indicates an unpredictable mechanism, that is one which is controlled by many variables and has reached criticality[1]. An example of such a mechanism would be one which produces earthquakes. An intermediate non-Gaussian distribution (Fig 8.1c) indicates a chaotic mechanism, that is a mechanism described by non-linear equations. An example of such a mechanism would be that involved in the Belousov-Zhabotinskii reaction in which a solution oscillates between being blue and being red in colour (Scott, 1992). A frequency plot of time spent being blue would resemble Fig. 8.1c.

[1] A system may be considered to have reached criticality when it can switch, at random, between two contrasting phase-states, e.g. the growth of a pile of sand being deposited as a series of grains are dropped from above. The slope of the pile will reach a stable angle ϕ. Once this angle is reached the system may be said to have reached criticality. The additional of a single grain of sand may cause no change to the slope or it may raise the angle of the slope slightly above ϕ and cause an avalanche.

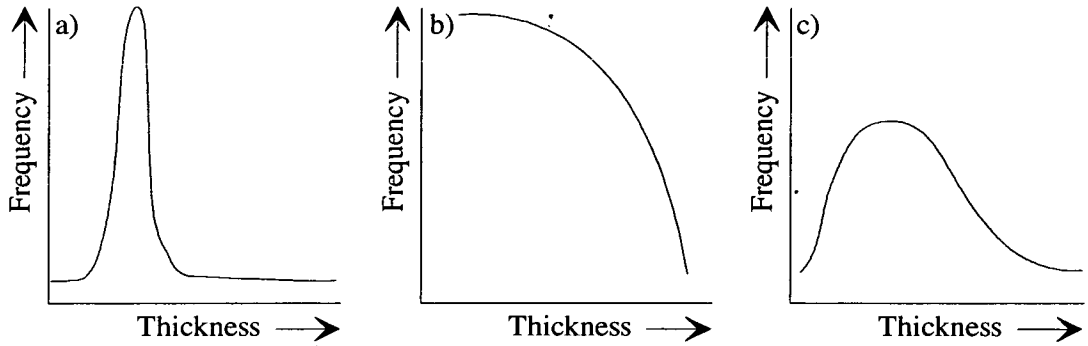

Fig. 8.1: Theoretical frequency distribution charts for the thickness of layers where the layering mechanism is: a) regular and predictable, b) unpredictable and c) chaotic (distribution is non-Gaussian).

8.3: Return maps and strange attractors

An attractor is defined as a set of points in phase space[2] to which the representative point of a dissipative system tends as the system evolves in time; attractors represent, in phase space, the stable condition that processes return to after they undergo a period of apparently random behaviour. The form of the attractor is governed by a number of factors, not least the number of variables in the equations which produce the series that the attractor describes. A point attractor is produced by a completely regular, predictable mechanism. A strange attractor is the name given to a fractal distribution, rather than a single point attractor and it is characteristic of chaotic processes.

A return map is simply an xy scatter plot ($x=x_n$, $y=x_{n+1}$) of a number of intra-related data series which have time as one variable. Only one data series is required. Subsequent series are generated artificially from the first giving coordinates of the form (n, n+1). For example Fig. 8.2, a two dimensional return map of the series 1,5,2,4,6 uses 5,2,4,6 as its second series. The first data point would have (1,5) as its co-ordinate, the second (5,2) etc. For a simple dynamical process with one variable, a two dimensional attractor would be sufficient to represent the system, but attractors may be n-dimensional where n is an integer and n-1 is the number of degrees of freedom (i.e. number of dynamical variables) in the system. A plot on an xy (n, n+1) graph gives a two dimensional slice through an attractor, a plot on a xyz

[2]"Phase space is a co-ordinate system whose co-ordinates are all the variables that enter the mathematical formulation of the system (i.e., the variables necessary to completely describe the state of the system at any moment)" (Tsonis, 1992)

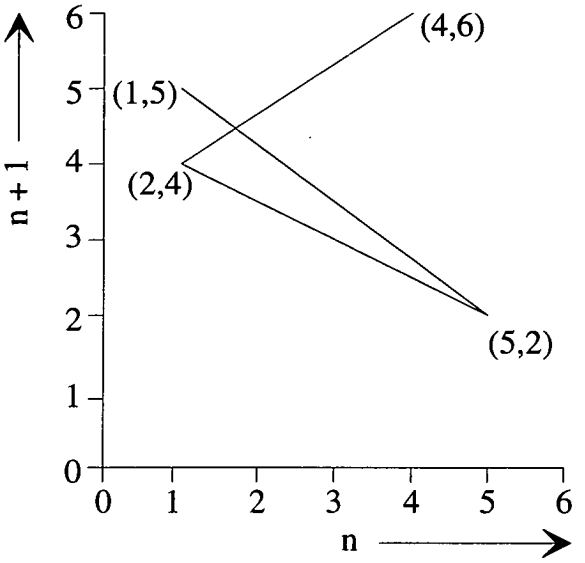

Fig. 8.2: A return map for the series 1,5,2,4,6. Co-ordinates are (1,5), (5,2), (2,4), (4,6).

(n, n+1, n+2) graph gives a three-dimensional section through an attractor. For systems with more than three co-ordinates it becomes very difficult to use graphical return maps to model attractors. The way that higher dimensions are dealt with will be covered in the next section. Processes which can be described by a set of non-linear equations, i.e. chaotic processes, will map out strange attractors when plotted on a return map (Fig. 8.3a). Random processes produce "tangled ball of string" plots on return maps with little structure (Fig. 8.3b),whereas linear periodic processes may produce linear plots (Fig. 8.3c) or point attractors (not figured, these plot as a single point on a return map).

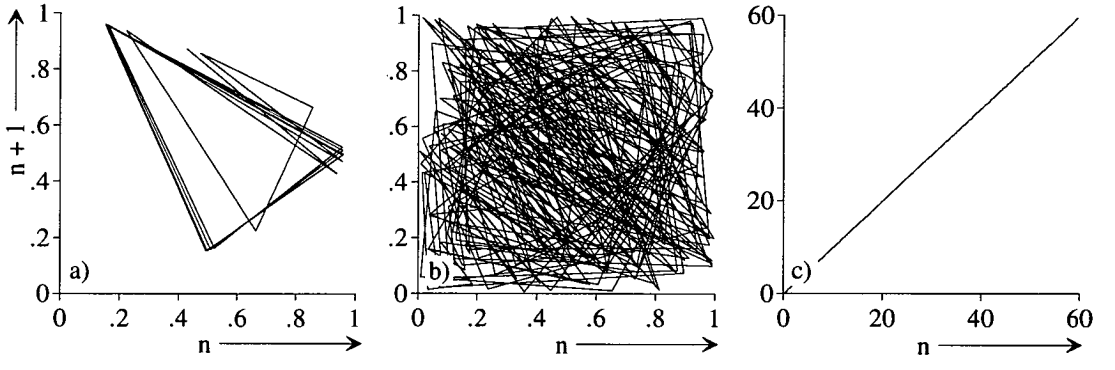

Fig. 8.3: Return maps generated by: a) non-linear equation, b) random data series and c) linear equation; each of the return maps is plotted for 300 data points. a) The equation used is x = (3.836x)*(1-x), the initial value of x is 0.65. After only a few iterations the system repeatedly traces out a triangular pattern, in detail the trace never repeats itself. b) The random data series was generated using the random number command on Excel 4, 5 figure random numbers are generated which are greater than 0 and less than 1. c) The equation used is y = 2x, for x = 0.1, 0.2, 0.3...30.0. The values of y were used to generate the return map.

8.4: Correlation mapping

As stated above, return maps for more than three dimensions are very difficult to plot. Correlation plotting overcomes this problem. Correlation plots are produced as follows:

1) Calculate the distance between all points on the return map generated by the data under consideration. This can be done using simple Pythagorean geometry i.e. if Rij is the distance between two points which have co-ordinates (Xi, Yi) and (Xj, Yj) (Fig. 8.4) then:

$$Rij = [(Xj-Xi)^2 + (Yj-Yi)^2]^{1/2}$$

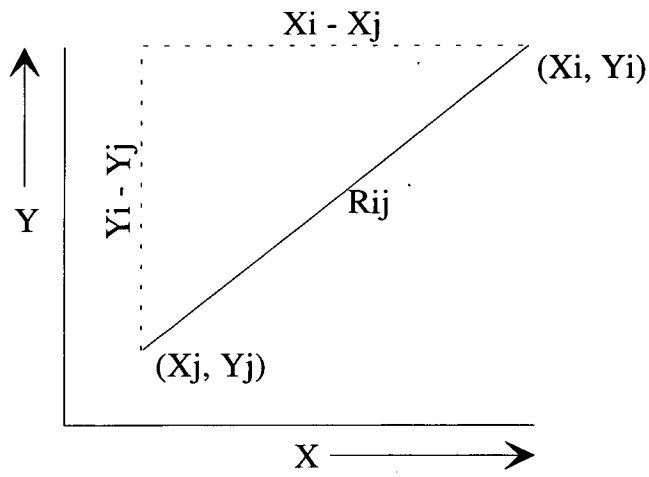

Fig. 8.4: The distance Rij between the points (Xj, Yj) and (Xi, Yi) = $[(Xj - Xi)^2 + (Yj - Yi)^2]^{1/2}$

Pythagorean geometry still applies regardless of the number of dimensions used and can easily be extended to an arbitrary number of dimensions by adding extra co-ordinates to the right-hand-side of the equation (e.g. = $[...+((Zj-Zi)^2]^{1/2}$). All repeat distances are discarded i.e. if the distance from point A to point B is calculated then the distance from point B to point A is not used in the analysis since Rij = Rji . No values of Rij = 0 are used so the total number of points in a two dimensional map is $N_{map} = N(N-1)/2$, N = number if data points.

2) Plot a cumulative frequency graph. First take the log of the values of Rij and sort them into ascending order and then calculate the correlation factor C. C is the number N of values of Rij below a stated value of Rij termed R. This value is then normalised by dividing by [N(N-1)/2]. Log C is then plotted against log R (Grassberger and Procaccia, 1983). This plot should generate a straight line though there may be a flattening out at both the top and bottom of the line due to sampling effects (Fig. 8.5a).

3) The discrete histogram is generated by plotting the log of the normalised difference between successive values of C in the series against values of log R. If a process is truly chaotic and governed by one attractor the topography of the histogram will mimic the topography of the cumulative frequency curve (Fig. 8.5b). If an attractor and a repeller are involved in the process the histogram will be bi-modal.

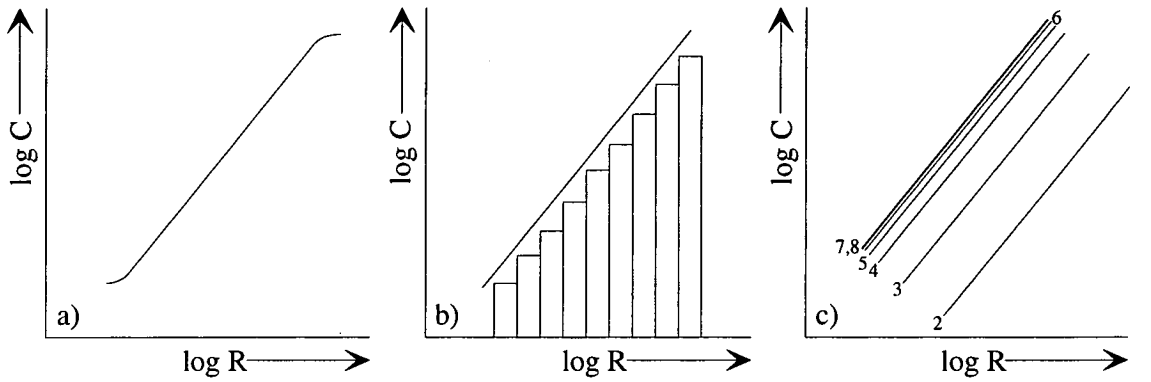

Fig. 8.5: Correlation maps. a) Example of a log-log cumulative frequency plot (see text for details), b) Combined cumulative frequency and discrete histogram plot (see text for details), c) cumulative frequency plot for successive dimensions, curves start to overlap when dimensionality = 7 (see text for details).

Successive dimensional plots i.e. (n, n+1), (n, n+1, n+2), (n, n+1, n+2, ...n+(d-2)) where d = dimensionality of the plot, will, for chaotic mechanisms, generate cumulative frequency plots where the lines slowly move closer together (Fig. 8.5c). When the curves start to overlap, the dimension of the superimposed curve is the embedding dimension of the process which gives a good indication of the number of dynamical variables involved in the process. Random processes never reach a point where successive dimensional lines superimpose themselves and linear processes quickly reach a limit.

Cumulative plots may be compared for different data sets with equal numbers of data points in them. In Fig. 8.6, line two is said to be more clustered than line one in both cases since there are more small values of R. Better clustered data sets have stronger attractors and the mechanisms which generate the data are more predictable provided that they are not lying in the random to unclustered region of phase space. It should be obvious from two-dimensional return maps whether the data lie in the clustered-random or random-unclustered region of phase space. Figure 8.7 illustrates the

geometrical picture of the predictability of regular (predictable) or clustered (reasonably predictable) layering compared with a random process.

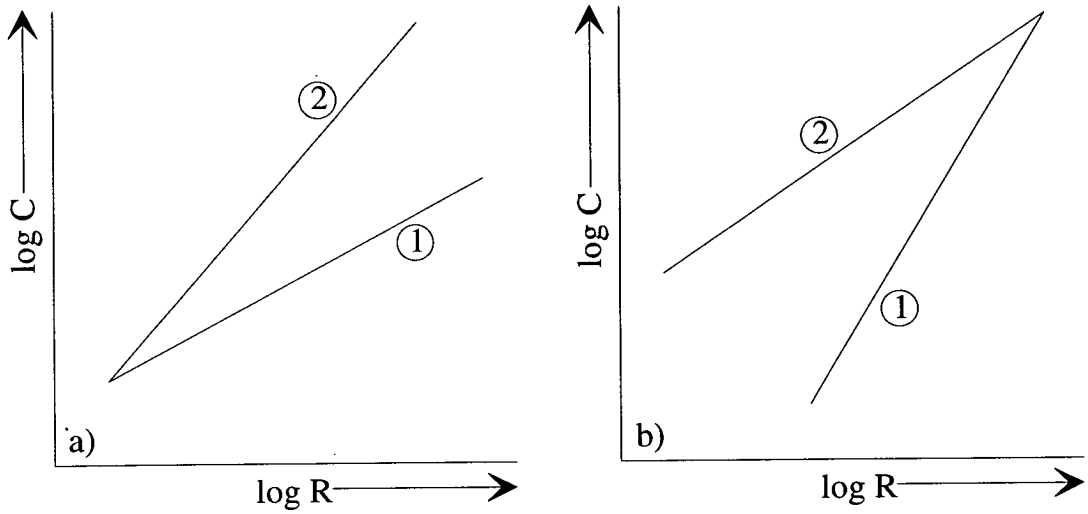

Fig. 8.6: Cumulative frequency plots. In both cases the data series generating line 2 is said to be more clustered since there are a greater number of small values of R in the series.

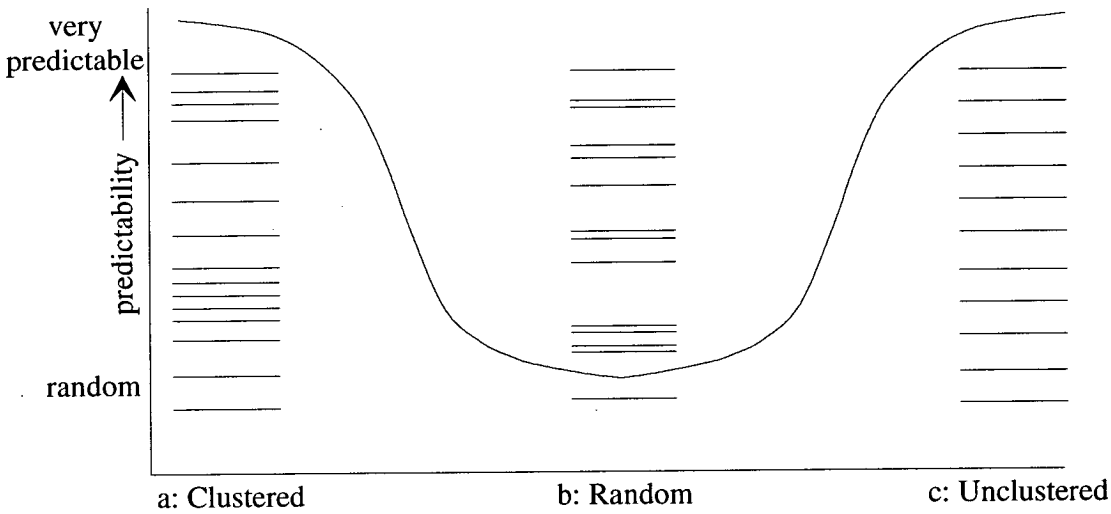

Fig. 8.7: Geometrical picture of the predictability of: a) a clustered, reasonably predictable series (chaotic), b) a random, unpredictable series and c) an unclustered predictable series (periodic).

8.5: Application to the layered series of Nunarssuit and West Kûngnât

The thickness of layers within a 10m stratigraphic sequence in Nunarssuit and 7.6m sequence in West Kûngnât were measured in order to test whether these data could be used to determine the regularity or non-regularity of the layering. The non-linear dynamic techniques described above have been applied to both data sets. Results and interpretations will be presented followed by problems with these techniques.

8.5.1: Frequency distribution plots.

Both the data set from Nunarssuit (Fig. 8.8a) and that from West Kûngnât (Fig. 8.9a) have frequency distributions indicative of mechanisms which are neither regular (equal spacing of layers), or critical point phenomena (fractal spacing of layers), but which denote some intermediate (chaotic) state.

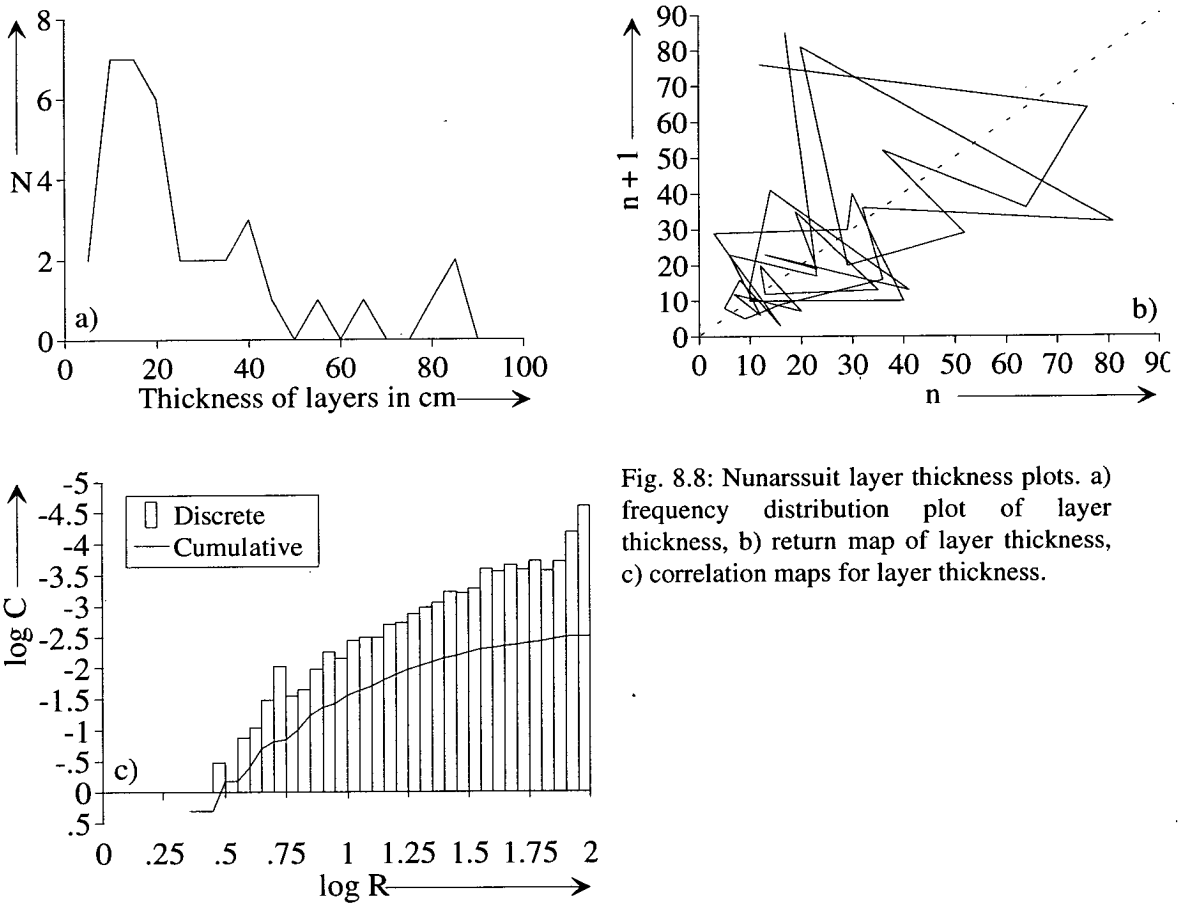

Fig. 8.8: Nunarssuit layer thickness plots. a) frequency distribution plot of layer thickness, b) return map of layer thickness, c) correlation maps for layer thickness.

8.5.2: Return maps and strange attractors.

The return map for the West Kûngnât (Fig. 8.9b) data shows a definite attractor. For example, when the layering is displaced from the cluster of points around (10,10), it rapidly returns. The Nunarssuit data (Fig. 8.8b) are harder to interpret. The data show some indication of a strange attractor in that there is a bunching of points around (15,15) but no geometrical shape is defined. To complicate matters the points lie very roughly along a 45° line which is an indicator that the mechanism which produces the layering is partially described by linear equations. Unfortunately there are not enough data to generate meaningful three dimensional return maps so a fuller representation of the attractors can not be plotted.

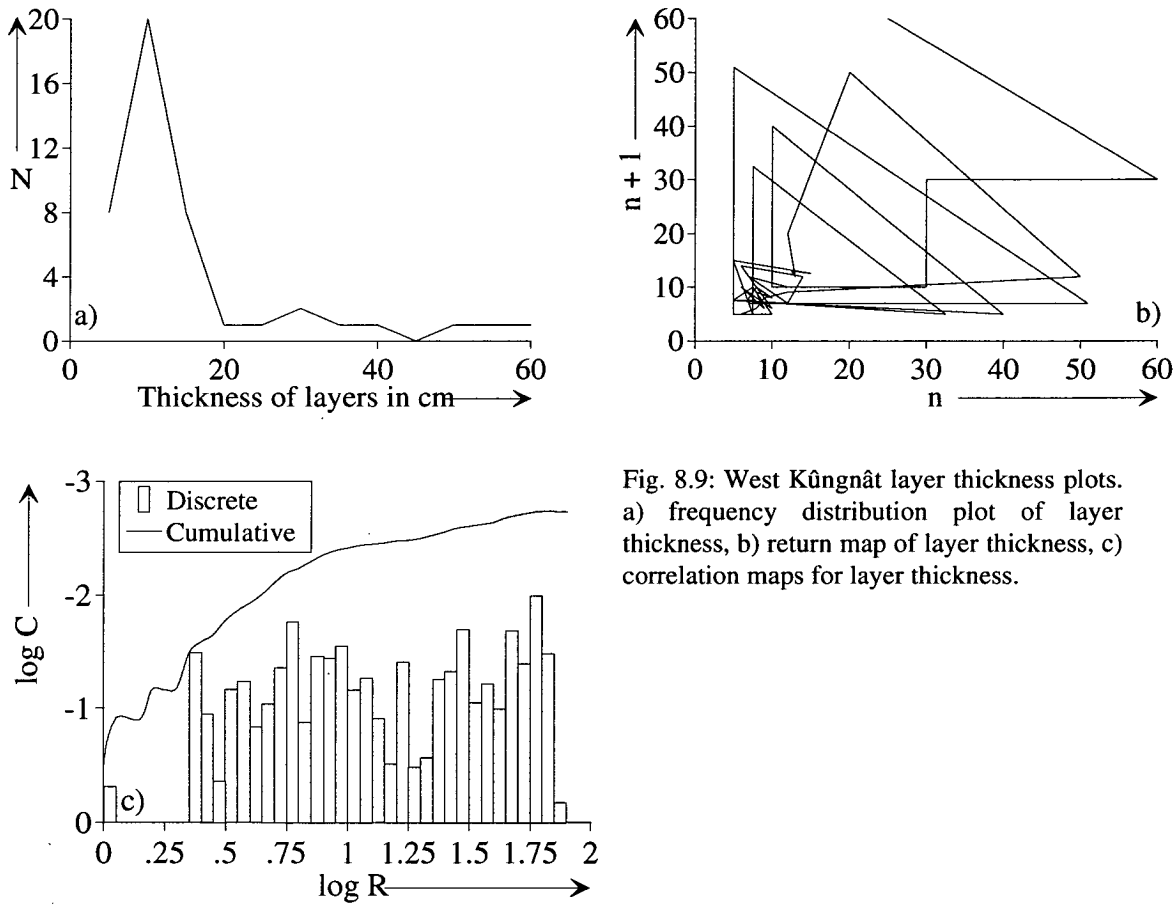

Fig. 8.9: West Kûngnât layer thickness plots. a) frequency distribution plot of layer thickness, b) return map of layer thickness, c) correlation maps for layer thickness.

8.5.3: Correlation mapping.

The Nunarssuit data (Fig. 8.8c) produce a cumulative curve which has a small straight segment. The discrete histogram roughly mimics the topography of the cumulative curve indicating that the mechanism responsible for the layering at Nunarssuit was chaotic. The West Kûngnât data (Fig. 8.9c) produce a cumulative curve which has a longer straight segment than the Nunarssuit curve but the discrete histogram has a bimodal distribution which may indicate that both an attractor and repeller may be involved in the layer-producing mechanism. The fact that the histogram does not mimic the topography of the cumulative curve indicates that the system may not be entirely chaotic. There are insufficient data to determine the embedding dimensions of the two data series

Comparing the cumulative curves of both Nunarssuit and West Kûngnât (Fig. 8.10) it is seen that the West Kûngnât layers are more clustered than those at Nunarssuit.

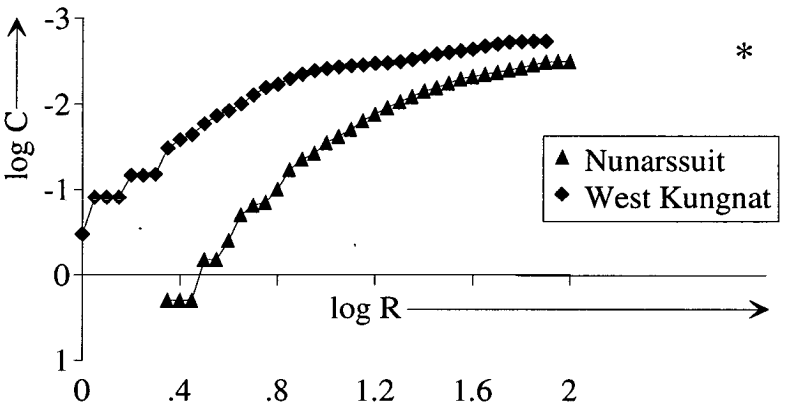

Fig. 8.10: Combined correlation plot for Nunarssuit and West Kûngnât. The two series converge towards *

8.6: Statistical significance

The number of data points used in the above plots was 36 for Nunarssuit and 50 for West Kûngnât. Given the small number of data points it is possible that the above plots are not statistically significant. It is not known to the author whether the frequency distribution plots are statistically significant or not, however these plots definitely show that the spacing of the layers is neither absolutely regular or totally random but lies somewhere between the two. This observation makes qualitative sense.

Pearce (1994) has used the thickness of successive zones of oscillatory zoned plagioclase to produce return maps. He states that "60 measurable zones is a large

number for a zoned crystal". Despite this small number of data points he has obtained meaningful results which suggests that the return maps for the Nunarssuit and West Kûngnât data series may also be meaningful. The conclusions drawn form the return maps (that the mechanism responsible for the layering is at least partially non-linear) confirm qualitative observations. It is not possible to predict the thickness of successive layers but it is usually possible to correctly predict what order of magnitude the thickness will lie in. Also it seems reasonable that layer production is partially controlled by crystal nucleation and growth rates which are non-linear.

Tsonis (1992) states that the minimum number of data points necessary to determine embedding dimensions depends on the value of the embedding dimension. For an embedding dimension of 4 he suggests that a raw data set of 5000 points may be sufficient to perform accurate analysis. The mechanisms responsible for producing layering probably have embedding dimensions of three or four but the possibility of measuring 5000 plus stratigraphically successive layers seems highly unlikely, certainly it is not possible in any of the Gardar layered intrusions. Therefore the correlation maps are probably not statistically significant. However the observation that the layer thickness of West Kûngnât is more predictable than Nunarssuit makes qualitative sense in that the Nunarssuit layers have obviously been disturbed by more currents than the ones at West Kûngnât.

8.7: Conclusions

The above plots seem to indicate that chaotic processes are responsible for the layering at both West Kûngnât and Nunarssuit. No information on the actual mechanisms is provided but the appearance of an attractor in the two-dimensional return map for West Kûngnât indicates that the mechanism may be dependent on only a few dynamical variables. Recent models such as that of Sparks *et al.*, (1993) fulfil this criterion. The layering of West Kûngnât is more clustered, and thus more predictable, than that of Nunarssuit (Fig. 8.10). This is perhaps not surprising since there is much evidence for current action in Nunarssuit in terms of small unconformities and breccias whilst the West Kûngnât magma chamber appears to have been less turbulent. These currents may have modified original layer thickness.

Part 3

Hypotheses

Chapter 9: A review of hypotheses for the genesis of igneous layering.

9.1: Introduction

In this chapter a number of models for the generation if igneous layering phenomena are reviewed. These models were predominantly produced in the years since the Nato ASI meeting on igneous layering held in the Gardar province of Greenland in 1986 (Parsons, 1987). In view of their importance, two older models, those of (i) Wager and his co-workers and (ii) McBirney and Noyes (1979) are also included. The theoretical models of Hort *et al.*, (1993), Sparks *et al.*, (1993), Boudreau (1987) and Wang and Merino (1993) are reviewed first. Equations presented by Hort *et al.*, (1993) and Sparks *et al.*, (1993) are applied to the Nunarssuit and West Kûngnât syenites. Intrusion-specific models are then reviewed. Firstly models developed for the Skaergård intrusion of east Greenland are reviewed (Wager and Brown, 1968, McBirney and Noyes, 1979, Irvine, 1987a and Conrad and Naslund, 1989), then those specific to intrusions in the Gardar province of Greenland (Parsons and Becker, 1987 (Klokken), Larsen and Sørensen, 1987 (Ilímaussaq) and Mingard, 1990 (Younger Giant Dyke Complex) and, finally, a recent model for the formation of layering on the Scottish island of Rum is reviewed (Bédard *et al.*, 1988).

9.2: Hort, Marsh and Spohn, 1993

Hort *et al.* (1993) produced a theoretical model that generated igneous layering between two phases, A and B, through oscillatory nucleation and crystal settling. The model is governed by two dimensionless numbers, the Avrami number (Av) and the settling number (Se). A qualitative description of the model is given below. The phase diagram for A and B is a simple binary; the model is summarised in Fig. 9.1. Initial undercooling (Fig. 9.1a) results in the nucleation and growth of phase A, leading to two effects: 1) the liquid composition is driven towards the liquidus of A (i.e. becomes less A-rich); and 2) the heat of crystallisation buffers the temperature and therefore the degree of undercooling decreases. The decrease in undercooling causes a cessation in nucleation and crystals already present coarsen and settle generating a layer of A crystals at the base of the magma chamber. This reduces the number of crystals extracting component A from the liquid. The temperature is now not buffered and undercooling begins again.

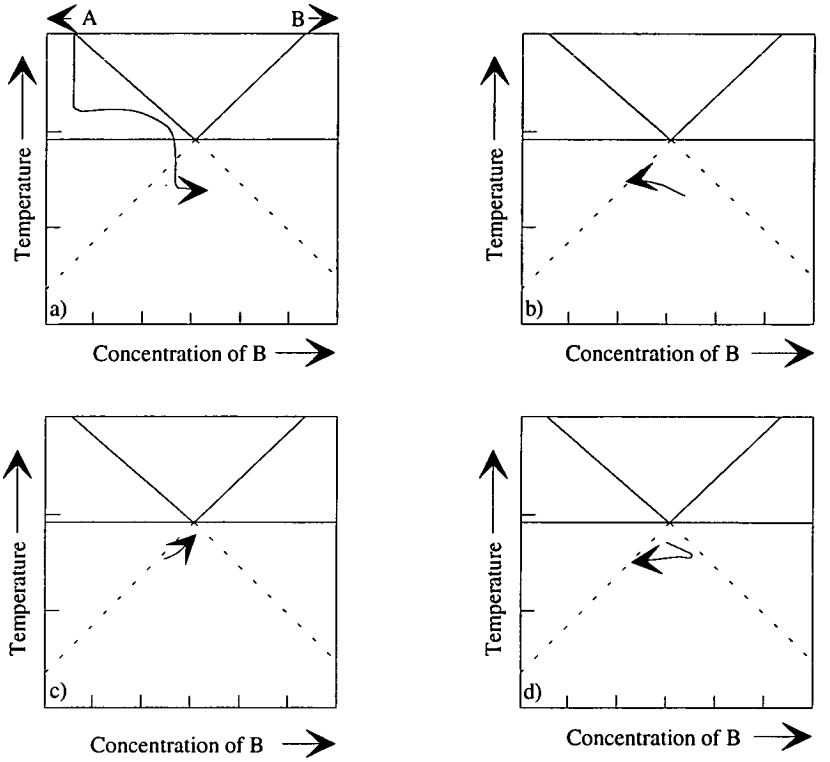

Fig. 9.1: a) the liquid is supercooled and A crystallises and the liquid is driven towards its eutectic. Heat of crystallisation buffers the temperature and the degree of undercooling decreases. Nucleation is inhibited and crystals grow and settle. Undercooling occurs again, A crystallises again and the liquid composition is driven over the metastable extension of the B liquidus; b) the liquid is now more undercooled with respect to B than A. A-rich crystals have settled so that they no longer remove A from the liquid, B crystallises and drives the liquid composition back over the metastable extension of the B liquidus; c) the liquid is now more undercooled with respect to A than B. B crystals have settled so that they no longer remove B from the liquid. A crystallises and drives the liquid composition back towards the metastable extension of the A liquidus; d) the cycle continues (after Hort *et al.*, 1993).

Any crystals which are already present grow rapidly, driving liquid compositions towards the metastable extension of the liquidus of A. A second nucleation event may occur. The liquid composition crosses the metastable extension of the liquidus of B. The degree of undercooling below the A liquidus decreases whilst the degree of undercooling below the B liquidus increases.

Two processes now operate (Fig. 9.1b): 1) large crystals of A grow and settle, thereby reducing the number of crystals extracting component A from the liquid and; 2) crystals of B nucleate and grow. These processes drive the liquid composition back towards the metastable extension of the B liquidus. The system then oscillates (Figs. 9.1c and d) until there is no residual melt left in the system. The model uses an unrealistic binary system and relies on undercooling to start crystallisation. Hort *et al.*, calculated that a "layering window" exists. Within this window, which is defined

by viscosity, nucleation and growth rates and intrusion size, layering can form. Below the window particles remain in suspension, whereas above the window, particles nucleate and settle so rapidly that the intrusion solidifies very rapidly as a homogeneous body (in extreme cases as a glass).

The three key equations presented by Hort *et al.*, (1993) are complex dimensionless equations which were solved with a finite difference technique. Solutions to the full set of equations allow the prediction of the thickness of alternating A-rich and B-rich layers. No attempt has been made in the present study to solve these equations for the Nunarssuit and West Kûngnât syenite. Hort *et al.*, (1993) present four simplified equations which predict whether or not crystal settling can occur. These equations, together with typical input values for syenitic magmas are shown below. Values of crystal nucleation and growth rate are taken from Hort and Spohn (1991), values of other variables are those which were used or calculated in Chapter 7. The Avrami number (Av) measures the importance of heat transfer relative to the kinetics of crystallisation; as Av increases, cooling becomes slower relative to the time taken for crystallisation and growth. The settling number (Se) is the ratio between the thermal and settling time scales; as Se increases, cooling becomes slower relative to the rate of crystal settling. For small values of Se the magma cools too rapidly for crystals to settle. For values of Se below the critical settling number (Se_{crit}) less than 5% of the crystals settle during the crystallisation process. The critical settling number defines the lower boundary of the "layering window". Hort *et al.*, (1993) demonstrate that most points which fall above the "layering window" are geologically unreasonable. A line defined by $t_{Se}=t_{kin}$ (crystal settling time scale = kinematic time scale) plots below the upper limit of the layering window (Fig. 9.2).

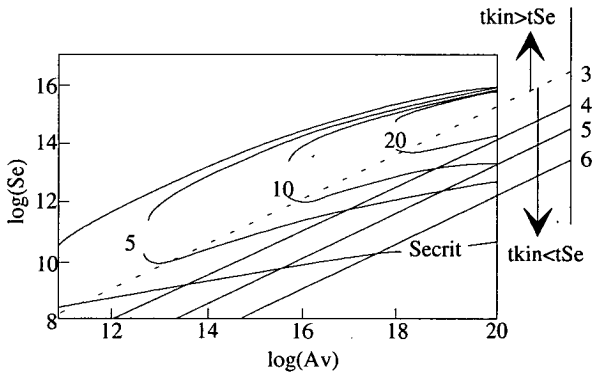

Fig. 9.2: Lower solid line shows the critical settling number. Above the dashed line $t_{kin}>t_{Se}$. Contours show number of layers for a given set of conditions (after Hort *et al.*, 1994, their figure 8)

By using equation (2) and fixing all variables but H and μ_o, Hort *et al.*, (1993) show that intrusions are likely to plot below the line $t_{Se}=t_{kin}$. Using the figures given below and fixing $t_{Se}=t_{kin}$ results in $H\mu_o = 0.29$ which is clearly unrealistic. Reasonable values

of H and μ_o define points which plot below the $t_{Se}=t_{kin}$ line, i.e. $t_{Se}>t_{kin}$. The calculations give results which imply that igneous layering can form in the Nunarssuit and West Kûngnât intrusions ($Se>Se_{crit}$). Some of the variables (growth rate, crystallisation rate, viscosity of melt, density difference between the melt and the crystals) are very poorly constrained and the shape factors f and σ are not defined.

The main problems with this model are that it considers an unrealistic binary system and requires a degree of initial undercooling. However it provides a useful qualitative framework for the discussion of the formation of igneous layering.

$$Av \equiv \sigma I_m U_m^3 \left(\frac{H^2}{\kappa}\right)^4 \qquad ...(1)$$

$$\frac{t_{Se}}{t_{kin}} = \left(\frac{H\mu_o}{fU_m^2 \Delta\rho g}\right)^{1/3} x\left(\sigma I_m U_m^3\right)^{1/4} \qquad ...(2)$$

$$\log(Se) = \frac{3}{4}\log(Av) = 3\log\left(\frac{t_{Se}}{t_{kin}}\right) \qquad ...(3)$$

$$\log(Se_c) \approx -11.49 - 5.34x(\log(Av))^{1/2} + 16.90x(\log(Av))^{1/3} \qquad ...(4)$$

where: Av = Avrami number = 8×10^{29} (calculated value)

Se = settling number = 1.26×10^{16} (calculated value)

Se_{crit} = critical settling number = 5.75×10^{11} (calculated value)

$$\frac{t_{Se}}{t_{kin}} = \frac{\text{settling time scale}}{\text{kinematic time scale}} = 128.4 \text{ (calculated value)}$$

σ = shape factor of crystals (undefined) = 1

I_m = maximum nucleation rate in $m^{-3}s^{-1} = 5 \times 10^4 m^{-3}s^{-1}$

U_m = maximum growth rate in $ms^{-1} = 10^{-8} ms^{-1}$

H = thickness of the intrusion in $m = 10^3 m$

κ = thermal diffusivity in $m^2s^{-1} = 5 \times 10^{-7} m^2s^{-1}$

μ_o = viscosity of magma in $Pas^{-1} = 6.2 \times 10^5 Pas^{-1}$

f = shape factor in Stoke's law (undefined) = 1

$\Delta\rho$ = density difference crystal/melt in $kgm^{-3} = 0.03 - 2.70 \times 10^3 kgm^{-3}$

g = acceleration due to gravity in $ms^{-2} = 9.8 ms^{-2}$

9.3: Sparks, Huppert, Koyaguchi and Hallworth, 1993

Sparks *et al.*, (1993) carried out experiments on silicon carbide particles suspended in turbulently convecting water. At very dilute concentrations, convection kept most of the particles in suspension although some settling occurred from the boundary layer at the base of the tank. Above a critical concentration convection was damped and the particles settled according to Stoke's Law. A sharp interface descended through the chamber, separating convecting, particle-free fluid above and non-convecting, sedimenting fluid below. Sparks *et al.*, extrapolated these results to magma chambers (their fig. 1, present Fig. 9.3). They envisaged a convecting magma chamber cooling from above. Crystals nucleate and grow within the body of the chamber; they are kept in suspension by convection though some settling occurs within the boundary layer at the base of the chamber (Fig. 9.3a). The concentration of crystals reaches the critical concentration, convection is damped and sedimentation occurs (Fig. 9.3b). As the lower layer sediments, the upper layer continues to cool; crystallisation continues and convection starts again (Fig. 9.3c). A graded bed is formed by the sedimenting event (Fig. 9.3d); some of the lower density crystals may be swept up into the new convecting layer.

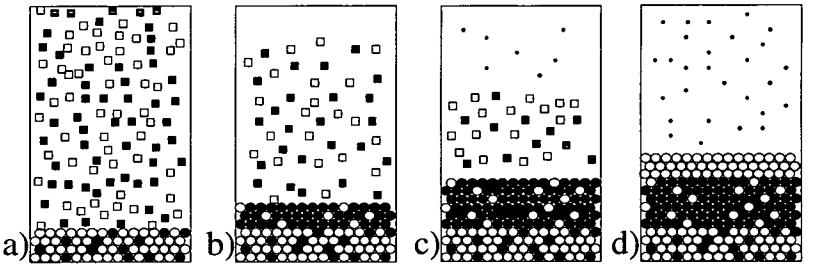

Fig. 9.3: Sequence of events in a magma chamber precipitating two phases of different size and density (from Sparks *et al.*, 1993).

Sparks *et al.*, (1993) produced equations which: 1) predict the critical concentration of individual phases above which sedimentation occurs and; 2) predict the critical viscosity above which crystals can not settle and the model is not valid. Application of the equation which calculates critical viscosity to the magmas of Nunarssuit and West Kûngnât (Chapter 7.7) indicates that olivine, pyroxene and feldspar may settle provided that the magma is hot enough and a low temperature difference drives convection; the other cumulus phases, apatite, ilmenite and magnetite could not settle. Sparks *et al.*, (1993) also present an equation (equation (5) below) to calculate the critical concentration of a phase which damps convection. Once the critical concentration is known the thickness of the layer (h) generated by the settling crystals can be calculated using equation (6) below.

Using the values for coefficient of thermal expansion, densities and temperature driving convection for which magma viscosity is less than the critical viscosity given in Chapter 7.7.2 generation of monomineralic layers several cm thick is predicted. For example at 850°C, the critical viscosity for pyroxene is greater than that of the magma P1+1%H_2O at temperature differences driving convection of 0.1°C. Under these conditions, equations (5) and (6) predict a pyroxene layer that is 3.7cm thick (for an arbitrary porosity of 0.5). This is in the same range as the thicknesses of the melanocratic bases of the rhythmic layers of Nunarssuit and West Kûngnât.
The critical concentration is given as:

$$C^* = \frac{\rho_P}{\rho_P - \rho_O}\alpha(T_O - T_U) \qquad ...(5)$$

where: C^* = critical concentration in wt% of a phase which damps convection

ρ_P = particle density in $kgm^{-3} = 3.5 \times 10^3\ kgm^{-3}$

ρ_O = density of the fluid in kgm^{-3} at $T=T_O = 2.53 \times 10^3 kgm^{-3}$

α = coefficient of thermal expansion of the fluid in $K^{-1} = 5 \times 10^{-3}$

$T_O - T_U$ = temperature difference driving convection in K = 0.1K

T_O = temperature in the lower layer where crystals are settling in K

T_U = temperature in the upper convecting layer in K

The thickness of the layer generated is then calculated as follows:

$$h = \left(\frac{C^*}{100}\right)\left(\frac{H}{\phi}\right) \qquad ...(6)$$

where: h = thickness of layer in $m = 3.7 \times 10^{-2}m = 3.7cm$ (calculated value)

C^* = critical concentration in wt% of particles which damps convection

$= 1.8 \times 10^{-3}$ wt% (calculated value)

H = chamber thickness in $m = 1 \times 10^3 m$

ϕ = porosity of the layer as fraction of inter cumulus = 0.5

The main problem with the model of Sparks *et al.*, is that eventually feldspar would reach its critical concentration and settle thereby generating a feldspar rich layer, such a layer is not observed in Nunarssuit or West Kûngnât. Sparks *et al.*, (1993) do not state how the presence of a variety of different phases affect critical concentrations. Also the large number of assumptions necessary to apply these equations (see Chapter 7) means that the results may vary by several orders of magnitude. However, on the basis of the results of calculations, using equation (5) in

Chapter 7 and equations (5) and (6) in the present chapter, this model appears to be reasonable and whilst it can not be used to mathematically model igneous layering it is a useful qualitative model.

9.4: Boudreau, 1987

Boudreau (1987) put forward a model for the generation of "inch-scale layering" in the Stillwater Complex that included "crystal ageing". The layering consists of alternations of orthopyroxenite and anorthosite layers on a scale of a few tens of millimetres. Surface energy makes a large contribution to the total free energy of crystals so larger crystals have a lower free energy than small crystals because of the higher surface to volume ratio of the latter. This results in the larger crystals being less soluble than the smaller crystals. Boudreau assumed an initially unlayered distribution of crystallites of different phases (Fig. 9.4a).

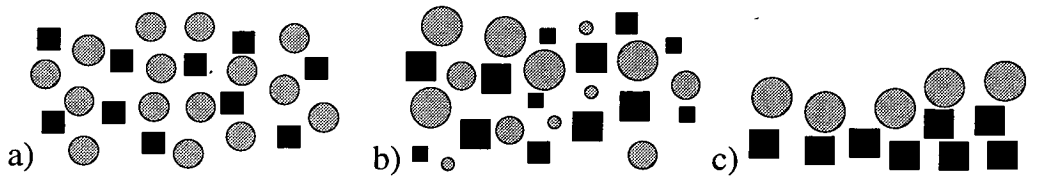

Fig. 9.4: a) initially an uniform distribution of crystallites exists near the floor of the magma chamber; b) small crystals dissolve and large crystals grow thereby reducing porosity; c) monomineralic grain contacts are more stable (lower surface energy) than bimineralic grain contacts so that grains in contact with grains of another phase dissolve. This generates a near monomineralic layer which has low porosity. Crystallites form above the layers and the process then repeats (after Boudreau, 1987).

Any grains which are marginally larger than those of the same phase in the surrounding area will be energetically favoured and grow at the expense of the smaller grains (Fig. 9.4b). As grains grow they will start to touch each other. The surface energy of contacts between grains of the same phase is lower than that of contacts between grains of different phases. This favours mineral segregation and fine-grained monomineralic layers develop (Fig. 9.4c). The influence of the large crystals decreases exponentially away from them so that new nuclei can grow to form crystallites above the original layer. Boudreau also suggested that macro-rhythmic layering may be "sharpened up" by crystal ageing, causing initial variations to be intensified.

9.5: Wang and Merino, 1993

Wang and Merino (1993) presented a mathematical treatment of oscillatory crystallisation controlled by feedback between concentrations of reactant species and mineral growth rates. They (their fig. 2, present Fig. 9.5) first considered growth of an idealised plagioclase (An_{33}, $Na_{2/3}Ca_{1/3}Al_{4/3}Si_{8/3}O_8$) at a reaction front in a silicate fluid containing an excess of calcium and a deficiency of aluminium relative to the concentrations in plagioclase. They assumed that the growth rate of plagioclase is proportional to the concentration of calcium and aluminium. Sodium was ignored because it diffuses rapidly and silicon was ignored because its concentration is assumed to be constant.

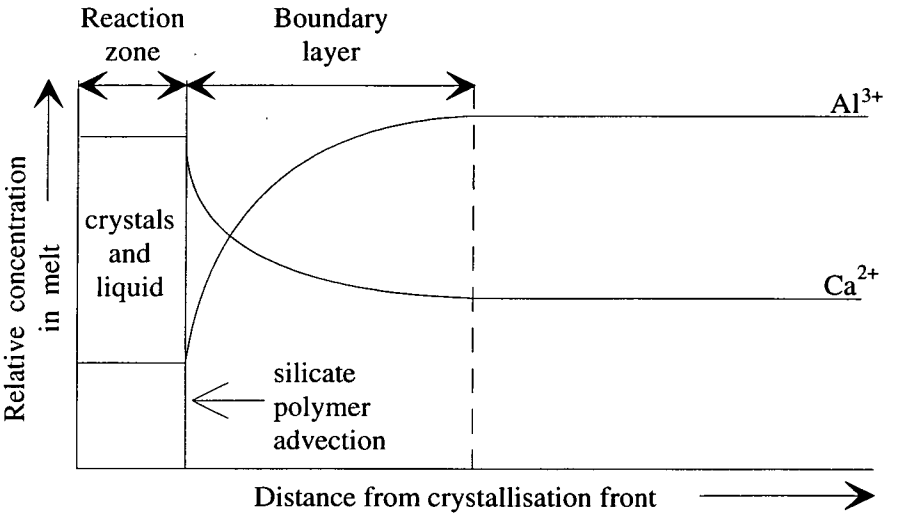

Fig. 9.5: Model system for the crystallisation of minerals from a liquid. The origin is placed at the left side of the reaction zone, within which crystals coexist with liquid. Outside of the reaction zone there is only melt on the right and only crystals on the left. Nucleation and crystal growth take place only within the reaction zone, and concentration profiles of chemical species remain roughly flat across it. Silicate polymers advect toward the reaction zone, carrying other ions. The boundary layer is defined by the distance at which species concentrations first become approximately constant. Shown are typical profiles of Ca^{2+} and Al^{3+} concentrations (relative to that of Si^{4+}) in the liquid during crystallisation of An_{33} plagioclase. For crystallisation of plagioclase An_{33} the concentrations of Ca^{2+} and Al^{3+}, relative to Si^{4+}, beyond the boundary layer are assumed to be > 1/8 and < 1/2 respectively therefore Ca^{2+} starts to accumulate in the reaction zone and Al^{3+} starts to become depleted. Feedback is then triggered which produces concentration and mode oscillations (from Wang and Merino, 1993).

According to this hypothesis plagioclase crystallises and grows in a reaction zone. Because the calcium content of the liquid is greater than that of the plagioclase, calcium becomes concentrated in the liquid in the reaction zone. The rise in calcium concentration causes the plagioclase to grow more and more rapidly once growth has started. Plagioclase growth causes a depletion in aluminium in the surrounding fluid.

Eventually the concentration of aluminium becomes so low that the growth rate of plagioclase decreases and calcium diffuses away out of the reaction zone slowing growth further. Aluminium concentration begins to recover and growth of plagioclase begins again. Wang and Merino developed equations for their model and then applied them to the growth of biotite and plagioclase thereby showing that this can generate repetitive "inch-scale layering".

Wang and Merino considered that the feedback was more likely to occur if two or more mineral species were crystallising because several species may accumulate in the reaction zone and catalyse or inhibit nucleation and growth. They stated that "The model requires that the diffusivities of the accumulated species (Ca^{2+} in the example given) are greater than the diffusivities of the depleted species (Al^{3+} in the example given). Species with low charge-to-size ratios are therefore more likely to accumulate in the liquid because they have higher diffusivities. Thus the occurrence of inch-scale igneous layering by this mechanism is most likely to occur in magmas rich in ions with low charge-to-size ratios such as Na^{+}, K^{+} and Ca^{2+}. This prediction coincides with the relatively common occurrence of rhythmic layers in alkaline rocks." It should be pointed out that whilst rhythmic layering is relatively common in alkaline rocks, the "inch-scale" igneous layering which this model predicts is not.

9.6: Wager and Brown, 1968 (Skaergård)

Wager and his co-workers (notably Deer and Brown) carried out the early work on the layered intrusion of Skaergård. Along with H.H. Hess and E.D. Jackson (1961) who worked on the Stillwater intrusion Wager pioneered the study of igneous layering in the 1940s to 1960s. The book published by Wager and Brown (1968) contains much valuable data on layered intrusions from around the world.

The Skaergård intrusion was intruded in the Tertiary during the rifting of the NE Atlantic and is located on the East coast of Greenland. The intrusion is split into a marginal border series, an upper border series and a layered series. These series all show differentiation trends from troctolite and olivine gabbro to olivine ferrodiorite. Rhythmic layering is extensively developed in the layered series; trough structures, "inch-scale" layering and cross-bedding are also present.

Wager *et al.*, thought that all the cumulus phases seen in Skaergård (plagioclase, olivine, pyroxene, magnetite and apatite) could have settled through the magmas

although turbulence in the magma was capable of keeping abundant plagioclase, (and sometimes other minerals), in suspension. They believed that the interaction of two types of convection current were responsible for the development of rhythmic layering seen in the Skaergård intrusion. The rhythmic layering commonly consists of an alternation of layers of uniform, "average rock" and thin, apparently gravity-stratified layers. Wager proposed that the uniform average rock accumulated by crystals settling through the magma chamber which was convecting in a slow, steady laminar fashion. Magma below the roof of the intrusion cooled and crystallised until it was denser than the underlying magma. Eventually this layer became unstable and sank, as a single descending column of dense liquid, through the magma chamber. These downward plunging convection currents, containing a mix of liquid and crystals, spread out along the floor of the magma chamber and came to rest, depositing their crystal load as a gravity-stratified layer. These rapid dense currents occurred intermittently through out the evolution of the magma chamber. Wager *et al.* took the presence of low density xenoliths in the rhythmic layering as evidence for the rapidly descending crystal-laden currents arguing that the xenoliths were dragged down against their tendency to float. As evidence for the steady convection currents they took the accumulation of large plagioclase crystals in the upper border group (at the top of the layered series). They argued that plagioclase would have sunk if the magma had been stagnant. If the magma had been convecting gently then the ascending convection cells could have carried up plagioclase which was only slightly denser than the magma but not the denser pyroxene and olivine grains.

Wager and Brown (1968) also put forward a hypothesis for the formation of the trough layering (a series of stacked troughs) seen in the Upper Zone (UZa) of Skaergård. The troughs are usually about 20m wide but vary between widths of 10 to 50m. Mapping shows that the troughs form a fan which converges to the east. The Skaergård trough stacks are separated by uniform rock, uniform rock also occasionally occurs between troughs in a single stack. The axial planes of the troughs shift laterally northwards with height in the trough stacks. The troughs are less regularly spaced than those of the West Kûngnât trough stack series. The mineralogy of the troughs involves more magnesian olivines and pyroxenes and more calcic feldspars than those of West Kûngnât although like the West Kûngnât rocks the troughs crystallised from an evolved magma (in this case a ferrodioritic magma). Individual troughs show gravity stratification. Wager *et al.* interpreted the individual troughs to be the product of deposition from the rapid, dense currents described above. The stacks of troughs were interpreted as being the product of deposition from

a succession of currents although no reason was suggested for the persistence of the dense currents in the same position. The uniform rock found between troughs was interpreted as being deposited from the steady convection currents although it is also suggested that the uniform rock may partially have formed as levees alongside the irregular currents which produced the troughs. Sometimes two adjacent troughs give place upwards to one which; this was interpreted as being due to a broadening of the current producing one of the troughs, presumably at the expense of the other. Later detailed mapping of these troughs by Irvine led to a different hypothesis being put forward (Irvine, 1987a).

9.7: McBirney and Noyes, 1979 Skaergård

McBirney and Noyes (1979) proposed two models for an *in situ* rhythmic crystallisation origin for the igneous layering of the Skaergård intrusion, East Greenland. They dismissed an origin involving a "rain" of settling crystals because: 1) they thought that plagioclase was too light to sink in the Skaergård magmas; 2) modal variation is not correlatable with size so that minerals at the bases of layers are not hydraulically equivalent; 3) convection would have been sufficiently vigorous to keep grains in suspension; and 4) some layers are vertical.

They dismissed the idea that layers could be deposited by density currents because: 1) layers start very close to the margins of the intrusion; 2) the layers have a large lateral extent; 3) crystals within layers do not bank up against xenoliths (although this is presented as a field observation by McBirney and Noyes (1979), and other workers e.g. I Parsons pers. comm.) have observed layers which are banked up against the xenoliths); and 4) some layers are vertical. They favour an *in situ* origin because; 1) they believe igneous layering to be produced by a mechanism that is an inherent feature of slow magmatic crystallisation; and 2) the trace element contents of oxide minerals and pyroxenes from a set of layers in the Upper Zone A show systematic differences from one level to the next.

In their first model, temperature increases inwards from the edge of the magma chamber towards the centre and, at any given point, temperature slowly decreases with time. When the temperature reaches a certain value, and provided that the relevant components have a high enough concentration, a phase A nucleates and grows at the crystallisation front (Fig. 9.6a); this generates a zone of fluid at the crystallisation front that is depleted in component A and crystallisation ceases. The

zone widens as component A diffuses in to the crystallisation front from the body of the magma. At a given time after the first nucleation event and at a given distance from the original crystallisation front, the concentration of components is sufficiently high and temperature is sufficiently low for nucleation to occur again (Fig. 9.6b). Thermal diffusion is more rapid than chemical diffusion so temperature will always reach the degree of undercooling necessary for nucleation at a certain point before the magma at that point becomes too depleted in A for nucleation to occur.

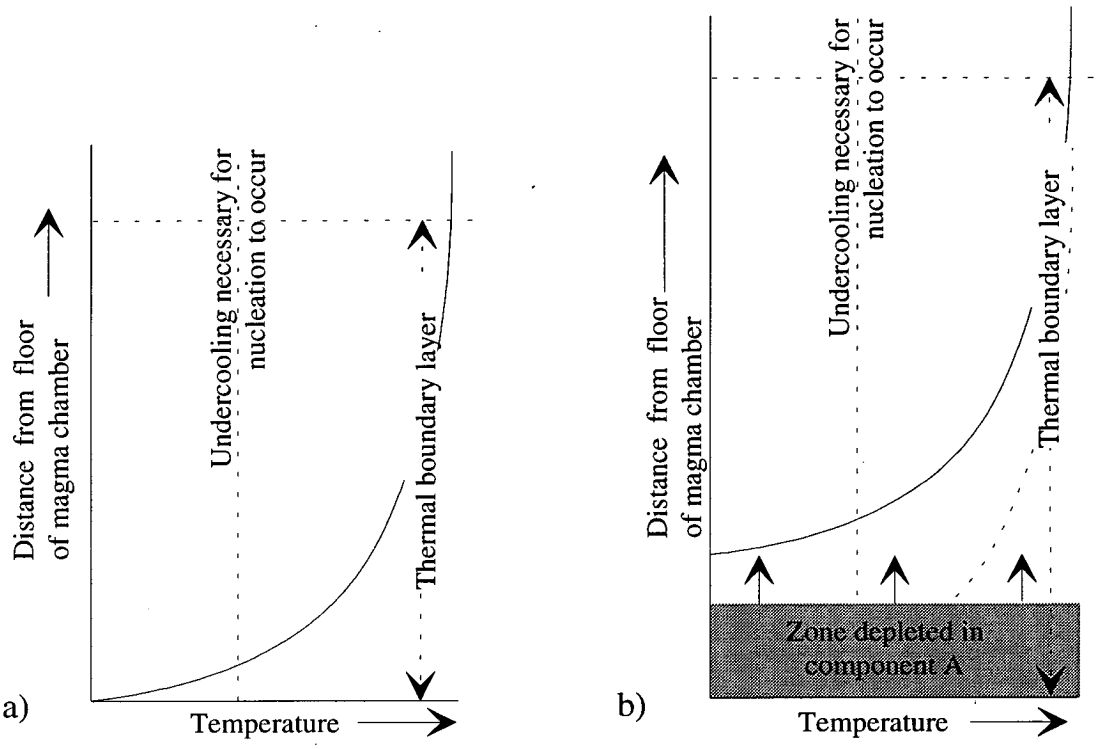

Fig. 9.6: a) magma at base of boundary layer is sufficiently undercooled for nucleation of A to occur; time passes, nutrients diffuse towards crystallites and crystals grow; zone depleted in nutrients advances into boundary layer; temperature falls; b) outside of zone depleted in nutrients temperature is low enough for nucleation to occur again.

The second model which is proposed in the paper deals with double diffusive convection and was thought to apply only to the boundary layer at the base of the magma chamber. For a fluid to become stratified there must be vertical differences in the concentrations of two components which have different diffusivities and opposing effects on the density of the fluid, in a magma the requisite components are heat and composition. McBirney and Noyes envisaged crystallisation at the floor of the magma chamber removing dense elements and creating both compositional and density gradients which decreased upwards and were gravitationally stable. Such a situation would have applied to the Nunarssuit and West Kûngnât magmas during the

crystallisation of the syenites (Chapter 7.6.6). They suggested that the magma cooled from the top of the chamber so that cooler denser magma overlay warmer less dense magma, obviously such an arrangement was gravitationally unstable. The envisaged conditions are shown in Fig. 9.7.

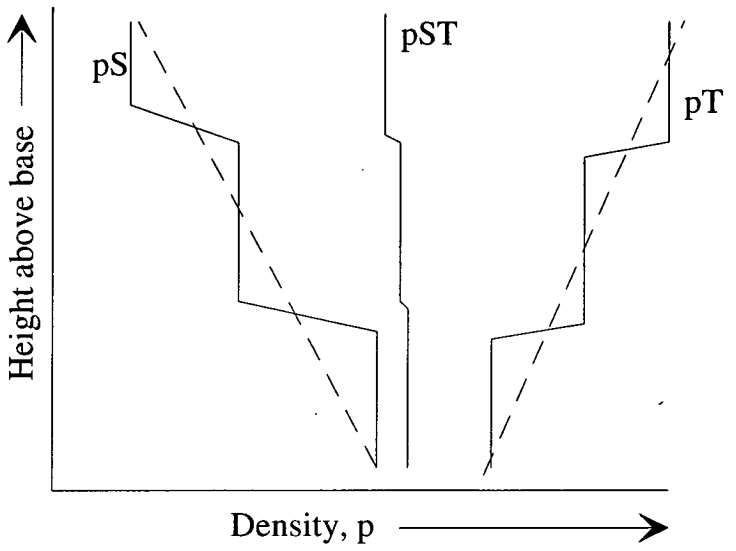

Fig. 9.7: Schematic diagram illustrating the initial distribution of density (broken lines) resulting from gradients of composition (pS) and temperature (pT) in a tholeiitic magma that is losing heat through its roof and crystallising in the bottom. After the smooth gradients breakdown into convecting layers they are divided by step-like interfaces (solid lines) and the resulting density distribution due to the combined effects of both factors has a form like that of pST (after McBirney and Noyes, 1979).

If the rate of heat diffusion and its effect on density exceeded that of the composition of the liquid then the effect of upward heat loss would not have been offset by chemical diffusion. In order to reach a gravitationally stable condition the fluid would have broken up into a series of convecting layers which were separated by sharp interfaces where a stable step in density and temperature was maintained by the relative concentrations and rates of diffusion of heat and chemical components. It is not wholly obvious how McBirney and Noyes expected a rhythmically stratified boundary layer to generate rhythmic layering but it appears that they envisaged each magma layer crystallising to produce a rhythmic layer. As crystallisation proceeded the magma layer adjacent to the chamber floor would have become less and less stable until it mixed with the overlying layer which proceeded to crystallise and produce another rhythmic layer.

Although the Nunarssuit and West Kûngnât syenitic magmas may have become stratified (Chapter 7.6.6) it is not possible to say whether they did or did not. It is possible to produce a model to explain the layering without appealing to a stratified magma chamber. It seems likely that the constant current activity, for which there is strong evidence for, in the Nunarssuit syenite would have constantly disrupted a

stratified boundary layer and prevented its development. This model fails to explain the onset and cessation of rhythmic layer production.

9.8: Irvine, 1987a (Skaergård)

Irvine (1987a) put forward a model to explain a series of trough stacks in the upper zone (UZa) of Skaergård. It appears to be the only recent model which attempts to describe how a series of trough stacks formed. The model is summarised in Fig. 9.8 (Fig. 9.8 is a small portion of fig. 41 in Irvine 1987a). Irvine envisaged the Skaergård magma chamber as having been divided into a number of independently convecting layers. In this model the layer at the base of the chamber is relatively thin and was responsible for the generation of a ridged topography on the chamber floor. Temperature decreased upwards through this layer. This lower layer convected in a laminar fashion and split into a series of roller convection cells. The descending limbs of the roller convection cells moved away from the body of the magma chamber, cooled and became supersaturated with the cotectic assemblage of cumulus minerals. The crystals nucleated, grew and precipitated below the descending limbs of the convection cells.

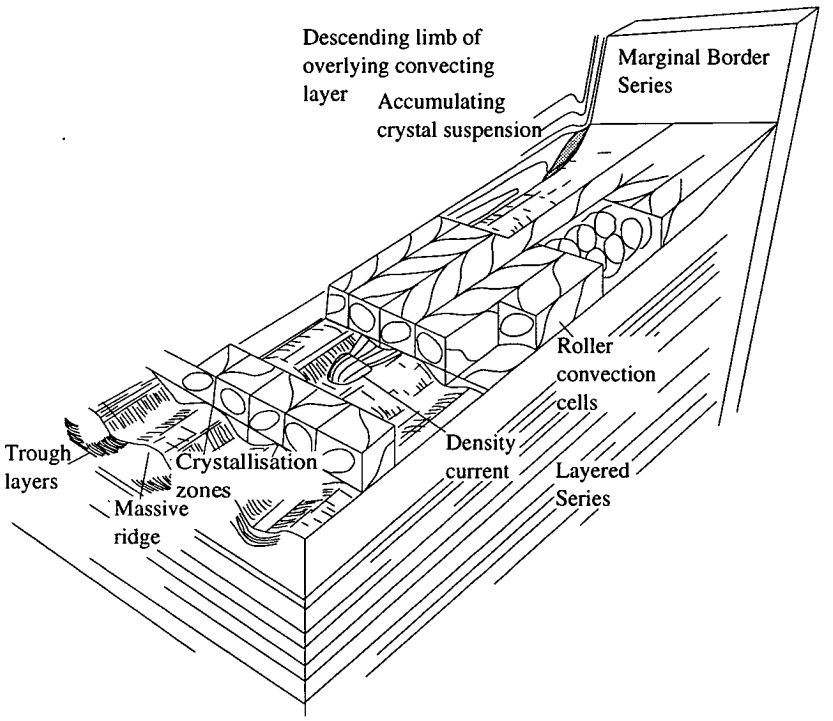

Fig. 9.8: Roller convection cells in a lower layer of the Skaergård magma giving rise to troughs and ridges, see text for details (from Irvine 1987a).

The ascending limbs of the roller convection cells move towards the body of the magma, heat up and become under-saturated; no mineral precipitation occurs. This generates a ridged topography on the magma chamber floor. At the same time, mineral grains are accumulating as an unstable crystal mush at the edge of the intrusion; these grains are precipitated from the descending limb of a large convection cell in the overlying convecting layer. This accumulation of crystals undergoes periodic slumping; crystal slurries flow down the troughs in the magma chamber floor, lose energy and are deposited as graded deposits. The convecting layer that contains the roller convection cells thins towards the edge of the intrusion. As it thins the roller convection cells migrate towards the centre of the intrusion where the liquid is thicker; this accounts for the northward shift of the troughs.

Irvine (1987a) also outlined a model, based on tank experiments, that can generate modally graded layers. As a density current flows across a surface it leaves a tail. Material at the head of the current is carried past the nose of the current and down onto the floor (see Fig. 9.9a) to form the bottom of the tail left by the density current; material at the back of the density current is stripped away to form the top of the tail. If the density current is made up of a crystal slurry then the tail will form a density-graded deposit.

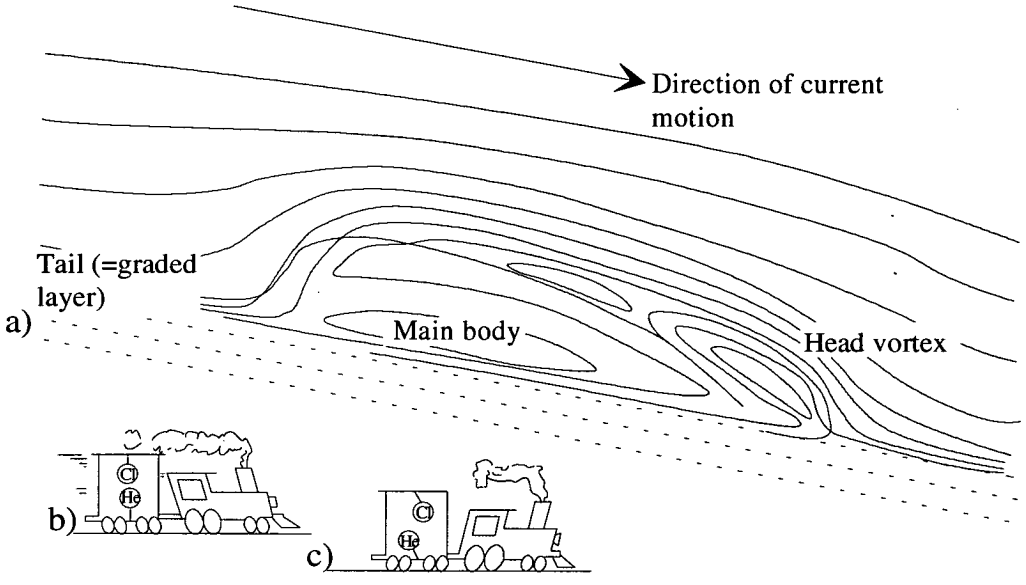

Fig. 9.9: a) in a density current flowing down a slope the densest particles are carried to front of the current and are incorporated into the base of tail. The least dense particles move to the back of current and are incorporated into the top of the tail; b) and c) illustrate the development of inertial sorting velocities (from Irvine 1987a).

The densest particles will have the greatest momentum and, as the density current is slowed by the drag effects of the cumulate floor and the overlying liquid, these particles will shift forward to the front of the density current (like the Cl-filled balloon in Fig. 9.9b). In moving forward, the densest particles will be preferentially caught up in the slurry that is carried to the bottom of the density current and deposited as the bottom of the tail to the current. The less dense particles will have lagged behind these dense particles (like the He-filled balloons in Fig. 9.9c) and will be caught up by the drag on the upper surface of the density current and move to form the top of the tail to the current. Thus the tail produces a density-graded deposit generated by the density current. Irvine points out that size-graded beds can not be generated if the settling minerals have a limited size range (as in Klokken) or if the settling minerals have a density very similar to the liquid that they are settling through.

9.9: Conrad and Naslund, 1989 (Skaergård)

Conrad and Naslund (1989) carried out a detailed study of modally-graded rhythmic layers in the Layered Series of Skaergård. They favoured a model in which crystallisation occurred "essentially *in situ* on the floor of the magma chamber". In this model the pile of crystals generated was redistributed by density and convection currents to generate the layers. This model was favoured because: 1) layers are density stratified with the densest grains at the base, as predicted by a gravitational sorting mechanism. By contrast *in situ* models predict an inverse correlation between grain size and modal proportions, which is not seen; 2) there was no primary chemical variation within layers; *in situ* models generate layering by changes in magma chemistry or by crystallisation along chemical diffusion gradients which would produce systematic variation in the major element chemistry of the phases in the layers; 3) layers are observed to fade along strike in a fashion reminiscent of graded beds in stream channels. Cross-bedding and troughs are also seen which are readily explained by current activity.

9.10: Parsons and Becker, 1987 (Klokken)

Klokken is an oversaturated intrusion in the Gardar province of South Greenland which consists of a gabbroic sheath and syenites. Parsons and Becker (1987 and references therein) produced a model that involved both crystal settling and oscillatory nucleation to explain the inversely graded macro-rhythmic layering which

is seen in the laminated syenites of the intrusion. Within individual layers the concentration of Fe-rich clinopyroxene increases upwards relative to the concentration alkali feldspar; crystal sizes are such that the feldspar, olivine and pyroxene grains present in the layers would all have exerted the same downwards force in the magma; this led Parsons and Butterfield (1980) to suggest that growth to a critical size was an essential factor in crystal sorting. The hydraulic equivalence of the cumulus phases at the base and at the top of individual layers led Parsons to suggest a chemical model for the origin of the inverse-grading.

Parsons and Becker envisaged a trachytic magma close to, or at, water saturation crystallising both feldspar and clinopyroxene in eutectic proportions (feldspar is the dominant phase). Parsons and Becker point out that this is an unusual situation for the Gardar syenites, evidence that $P_{H2O} \approx P_{Total}$ comes in the form of drusy cavities which are found in the layered syenites. Crystallisation of the feldspar causes an increase in P_{H2O} that depresses the melting curves of the trachytic magma and thus reduces the amount of undercooling (Fig. 9.10). This in turn, inhibits feldspar nucleation and growth relative to that of pyroxene. Further undercooling inhibits pyroxene nucleation and olivine and magnetite become dominant.

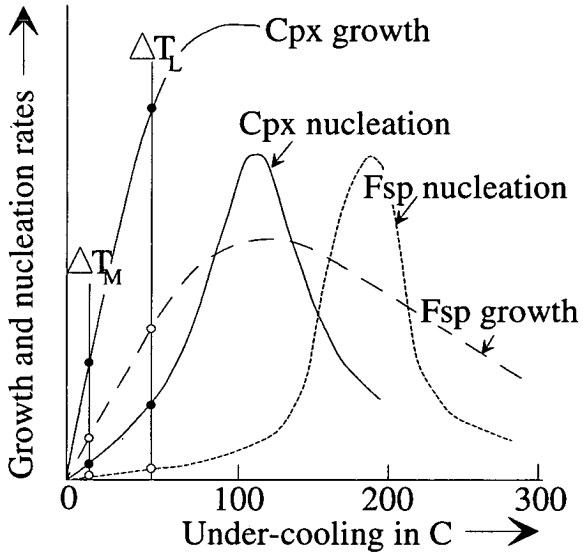

Fig. 9.10: Nucleation and growth rates of feldspar and clinopyroxene against degrees of undercooling. At undercoolings of ΔT_L feldspar is the dominant phase that crystallises and a leucocratic layer is generated. As feldspar crystallises P_{H2O} builds up and the melting curve of the magma is depressed, undercooling reduces to ΔT_M and pyroxene is now the dominant phase that crystallises and a melanocratic layer is generated. Pressure is released and the degree of undercooling returns to ΔT_L, (after Parsons and Becker, 1987).

The ease of crystallisation below the equilibrium crystallisation temperature is a function of the entropy of fusion of the solids. Pressure is then released and the system returns to crystallising feldspar as the dominant phase. Pressure release is achieved by ring-faulting; this apparently random event is favoured by the authors because the layers do not repeat in a regular fashion and are often truncated by layers of granular syenite which are thought to have detached from the roof of the chamber and sunk through the magma.

This model is not really relevant to the layering seen in Nunarssuit and West Kûngnât since the differences in nucleation and growth rate of the different phases only become marked when the magma is saturated or nearly saturated with water.

9.11: Larsen and Sørensen, 1987 (Ilímaussaq)

Ilímaussaq is an alkaline intrusion in the Gardar Province, thought to have formed through three main intrusive events. The first gave rise to the augite syenite which is present as an incomplete outer shell of the intrusion. The second phase consisted of alkali acid rocks and the third, agpaitic rocks. Included in the agpaitic rocks are the layered kakortokites. The main layered kakortokite sequence is c.200m thick and consists of 29 major rhythmic units. A fully developed unit consists of a lower black layer rich in arfvedsonite, a middle red layer rich in eudialyte and an upper white layer rich in alkali feldspar. Nepheline is present in all the layers. The lower contact of each unit is abrupt whilst within the unit there is a graded transition when passing between layers. Ussing (1912) proposed an origin by repeated variations in pressure controlling the crystallising assemblage. Rather than appeal to pressure, Larsen and Sørensen appeal to a layered magma chamber to explain the repetitive units and variations in the degree of undercooling brought about by gradual volatile loss and the relative rate of nucleation of the cumulus minerals arfvedsonite, eudialyte and feldspar to explain individual units.

Within the lowest layer of magma Larsen and Sørensen suggested that arfvedsonite, eudialyte, feldspar and nepheline were on the liquidus. Arfvedsonite and eudialyte nucleate at lower degrees of undercooling than feldspar and nepheline and could therefore grow and start settling before feldspar and nepheline as the layer of magma cooled. Volatiles were slowly lost from the layer of magma and so the liquidus rose and the degree of undercooling increased. Feldspar and nepheline were now the dominant phases which crystallised and settled. As the crystals settled to the floor of

the magma chamber, their density differences intensified the separation initially brought about by the differences in nucleation rates. Ultimately the magma layer became unstable and mixed with the overlying layer. The sharp base to the next layer was due to the sudden increase in the volatile concentration of the magma. The overlying layer would began to crystallise and another unit was generated. Alternately the next unit may have started to form within the original crystallising layer as the crystallisation of large amounts of volatile-free feldspar and nepheline caused an increase in the concentration of volatiles within the magma layer.

As with the model of Parsons (1979) this model is not really relevant to the layering seen in Nunarssuit and West Kûngnât since the differences in nucleation and growth rate of different phases only becomes marked when the magma is saturated or nearly saturated with water.

9.12: Mingard, 1990 (Younger Giant Dyke Complex)

The Younger Giant Dyke complex (YGDC) is a dyke swarm of Gardar age that was intruded during extensional continental magmatism. Dykes are up to 800m wide and the complex can be traced intermittently over 145km. Mingard (1990) suggested a model for the formation of layering in the YGDC that involved the settling of particles which crystallised in the thermal boundary layer at the margins of the intrusion. The magma chamber was undergoing turbulent convection and only at the chamber margins was undercooling sufficient for nucleation to occur. Crystals either settled through the boundary layers and accumulated at the floor of the chamber or were carried down to the floor by thermal convection currents. The majority of the layers are not graded but are olivine cumulates with a sharp base and top, over and underlain by a plagioclase and olivine cumulate. Mingard suggested that the lack of grading means that the olivine in the olivine cumulates was not separated from plagioclase under the influence of gravity as currents swept across the floor but that plagioclase nucleation was periodically suppressed. When plagioclase nucleation was suppressed olivine crystals were carried down to the bottom of the chamber by a density current. The olivine settled to form a layer of olivine cumulate; the remaining liquid then attained the cotectic and resumed olivine and plagioclase crystallisation. Provided that the olivine settled sufficiently rapidly there would be a sharp boundary between the olivine and olivine plus plagioclase cumulates. Mingard suggested a variety of reasons for the suppression of plagioclase nucleation: 1) raising the temperature of the magma; 2) raising the P_{H2O} of the magma; 3) introducing a more

olivine saturated magma into the chamber; but did not come up with an argument for favouring one reason over another.

9.13: Bédard, Sparks, Renner, Cheadle and Hallworth, 1988 (Rum)

Rum is a small island off the west coast of Scotland whose geology is dominated by a major igneous central complex of Palaeocene age. The layered complex of Rum consists of the Eastern Layered Series, the Western Layered Series and the Central Series. The layering seen in the Eastern Layered Series of Rum consists of 15 major peridotite-troctolite repetitions. This layering has been explained in terms of a replenishment model (Huppert and Sparks, 1980, and references therein). In their most basic form the replenishment models generate each peridotite-troctolite cycle by closed system fractionation of a mafic parental basalt. This basalt first crystallises olivines (peridotite), then olivine and feldspar (troctolite) and then olivine, feldspar and pyroxene (gabbro) as it evolves. The chamber is then replenished by another injection of mafic basalt and another cycle is generated. The model of Huppert and Sparks (1980) is illustrated in Fig. 9.11a. Harker (1908) proposed a sill-complex model for the formation of the layering but this fell out of favour when it was shown that the layers were cumulates and did not represent liquid compositions.

Bédard *et al.*, (1988) proposed an intrusive origin for some of the peridotite layers and a metasomatic origin for some of the gabbroic layers seen on Rum. Bédard *et al.* (1988) envisaged an initially layered troctolitic body into which picritic sills were injected. The picrite crystallised to produce peridotite cumulates. The residual basaltic liquid then metasomatised some of the troctolite to produce gabbro. This model is illustrated in Fig. 9.11b. Bédard *et al.* quote several pieces of evidence to support this model. Peridotite layers truncate both underlying and overlying allivalite layers. Replenishment models can account for the truncation of the underlying layers by ponding of the replenishing magma and thermal erosion of the underlying troctolite but it is harder to account for the truncation of the overlying layers. In contrast the model whereby the peridotite layers are intrusive sills can readily account for the truncation of both under- and overlying allivalite layers. The allivalite layers are laterally impersistent. This is hard to explain using the replenishment models, but again is readily explained by an intrusive model for the origin of the peridotite layers. The mineral chemistry of the layers can not be fully explained by fractionation and recent interpretations involve the percolation of an intercumulus

melt through the cumulus pile; the injection model can explain the mineral chemistry.

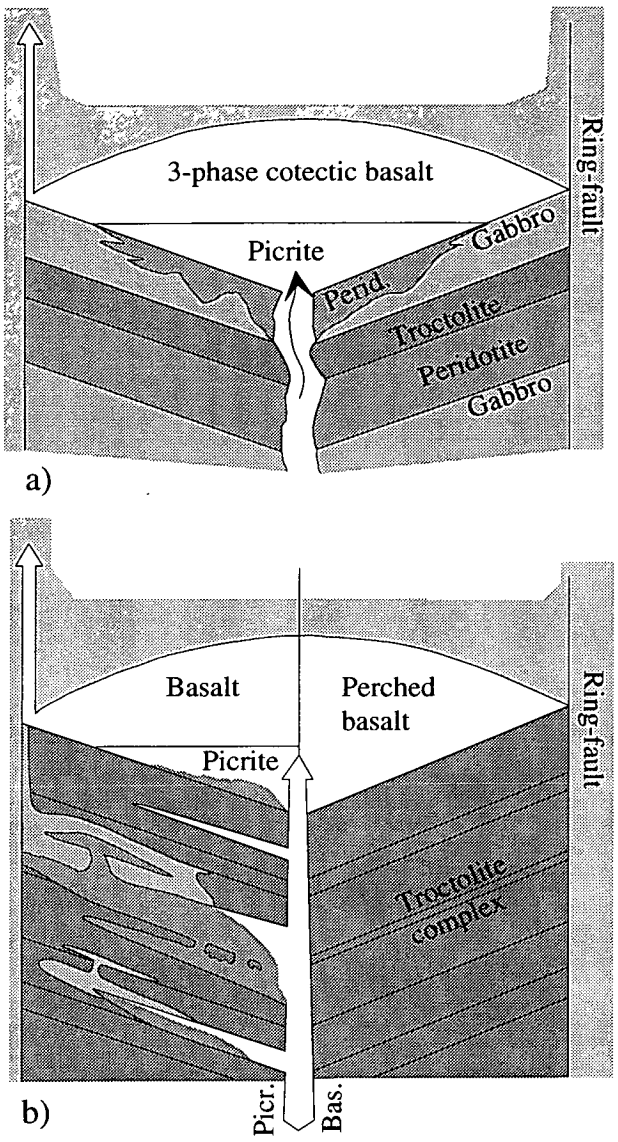

Fig. 9.11: a) Replenishment model of Huppert and Sparks (1980). The dense, replenishing picritic magma ponds under the basalt and interrupts the deposition of "basaltic" cumulates. After a period of peridotite deposition, the two layers mix and gabbroic or troctolitic cumulate are then deposited. If the picrite/basalt interface intersects the sloping cumulate floor, then time-correlative cumulates may display lateral facies changes. Because the replenishing picrite is hot and undersaturated in plagioclase and pyroxene, it could melt the basaltic cumulate floor and cause channelling.

b) Two stage intrusive model proposed in this (Bédard *et al.*'s) paper, same symbols as in Fig. 9.11a. On the right is a schematic representation of the cumulates derived from a magma chamber replenished by two phase basalts (ol + plag). This leads to the development of a troctolitic complex. Subsequently, picritic magma rises through the earlier troctolitic cumulates, forming sills on its way to the chamber/ cumulate interface. Assimilation of troctolite allows some of the picritic sills to coalesce. Residual three-phase (plag + cpx + ol) magma is eventually expelled from partially solidified picritic sills and reacts with the host troctolites to form metasomatic gabbros (from Bédard *et al.*, 1988).

Bédard *et al.* proposed that the parental liquid to the peridotite sills is a picritic basalt. They present data showing that 30% to 50% residual basalt must have remained after the peridotite had crystallised. Bédard *et al.* suggested that this residual melt could have metasomatised some of the allivalite layers to generate the layered gabbros seen in the layered succession. They considered that the layered gabbros are metasomatic in origin because: 1) they contain troctolite and anorthosite which is indistinguishable from the anorthosite and troctolite layers, 2) in some cases the layered troctolites extend into the gabbro, 3) gabbro-troctolite contacts are locally

discordant to plagioclase lamination seen in the troctolites and 4) the gabbros contain curved pyroxenite layers which could be interpreted as metasomatic fronts.

Whilst this model would not appear to be directly relevant to the layering features of Nunarssuit and West Kûngnât it is important because it shows: 1) that the often held belief that the stratigraphic succession of layers represents a time sequence with the oldest layers at the bottom of the stratigraphy and the youngest at the top may be incorrect and, 2) that metasomatism can be an important agent in the generation of igneous layering.

9.14: Summary

Models for the genesis of igneous layering can be split up into various groups (Irvine 1987b). Some are qualitative, others quantitative. Some invoke crystal settling whereas others suppose layers grew through *in situ* crystallisation. Some of the models are of general application whereas others are restricted to particular intrusions. It is generally the case that intrusion-specific models are qualitative (e.g. Conrad and Naslund, 1989) whilst general models are more quantitative (e.g. Sparks *et al.*, 1993). Settling and *in situ* models have been proposed that are both general (Sparks *et al.*, 1993, Wang and Merino, 1993) and intrusion specific (Parsons and Becker, 1987). It is hard to argue against intrusion-specific qualitative models since these are designed to fit the observations made in their particular intrusion. It is the quantitative general models which are more open to criticism. These often consider simplified, unrealistic systems (e.g. the simple binary AB system of Hort *et al.*, 1993) and the equations contain terms such as viscosity, density, coefficients of thermal diffusivity and conductivity and crystal nucleation and growth rates which are poorly constrained for trachytic magmas. Some of the variables in the equations, such as nucleation and growth rate, are so poorly constrained as to make the results to the equations meaningless. A major problem is that the theoretical magmas considered are invariably basic melts which have better constrained variables, (from experimental evidence), than evolved melts. Problems with the true rheology of the magma and the grain sizes and shapes also serve to reduce the accuracy of the equations. The theoretical model of Sparks *et al.*, (1993) would appear to be very useful. As a qualitative model it is easy to understand and simple equations are presented which are easy to apply and give reasonable results. The model has two main drawbacks: 1) it implies that feldspar-rich layers should be generated when feldspar reaches its critical concentration, and 2) it does not deal quantitatively with

magmas containing a mix of different mineral species. The double-diffusive convection model of McBirney and Noyes (1979) is, at first sight, appealing, but it does not explain the onset and cessation of rhythmic layering. Also the postulated stratified boundary layer would have been constantly disrupted by current activity in Nunarssuit. It is not obvious how the layers of magma would evolve during crystallisation.

There is a consensus within the literature that micro-rhythmic layering is the product of an *in situ* process related to diffusion and/or nucleation. The origin of macro-rhythmic layers is far more controversial in origin. Origins suggested within the literature include variations in crystal supply related to nucleation and growth (Parsons and Becker, 1987), *in situ* crystallisation with diffusion-nucleation effects (McBirney and Noyes, 1979), deposition from magmatic density currents (Irvine, 1987b) and intrusion as separate sheets (Bédard *et al.*, 1988). It seems likely that there is no one correct solution but that macro-rhythmic layering is the product of a variety of processes operating together. The dominant process may vary from intrusion to intrusion and possibly even within intrusions.

The genesis of various sedimentary-style structures seen within layered complexes is less contentious. Local unconformities are inferred to have been formed by current erosion and a layer formation mechanism, whereas convoluted layering is regarded as having been produced by slumping of the cumulate pile or drag from density currents. Autoliths are usually derived from wall or roof zones; trough layering is generated by deposition of crystals from slurry-like streams (see Chapter 10.9 for an alternative model to that of Irvine, 1987a); wall-rock collapse can generate slumping, slump-breccias and slurry-like streams resulting in troughs.

Chapter 10: Models for the genesis of layering and sedimentary structures in Nunarssuit and West Kûngnât

10.1: Introduction

In this chapter a number of factors, relevant to models for the genesis of rhythmic layering in the Nunarssuit and West Kûngnât syenites, are reviewed. Following this, models for the formation of the rhythmic layering in the two intrusions are presented. Questions considered in developing the models are:

1) what initiates and terminates rhythmic layer formation?
2) can we dismiss an origin for igneous layering by crystal settling or *in situ* processes?
3) could crystal settling and/or *in situ* processes produce the modal variations seen?
4) what mechanisms could inhibit feldspar nucleation and growth?
6) what could cause the increase in the visibility and the cyclicity of the rhythmic layering in Nunarssuit?
7) is the Nunarssuit syenite inversely cryptically layered, and if so what could bring this about?
8) how do troughs form?
9) how does micro-rhythmic layering form?
10) are there any features which sedimentary processes can not explain?

10.2: What initiates and terminates rhythmic layer formation?

In the Nunarssuit layered syenites layering starts gradually and having reached a peak in intensity ultimately fades up section (Harry and Pulvertaft, 1963 and Chapter 2.1). In West Kûngnât the rhythmic layering is initially irregularly spaced, the layering becomes more regularly spaced before it ultimately passes up into laminated syenite (Upton, 1960 and Chapter 2.2). Some critical variable must control the onset and termination of rhythmic layer production.

In the model of Parsons and Becker (1987) rhythmic layering is only produced when the Klokken magma approaches water saturation. In Ilímaussaq the lowest exposed kakortokites are layered, layering ceases up section after 29 major rhythmic units. Larsen and Sørensen (1987) attributed the termination of the rhythmic layering to an increase in cooling rate so that magma layers crystallised before the crystals of the

different mineral species had time to separate from each other. Wager and Brown (1968) suggested that rhythmic layering was produced by density currents generated by the sinking of crystal laden magma from the top of the chamber. This occurred randomly so that the start and finish of rhythmic layering production could not be predicted.

Hort *et al.*, (1993) and Sparks *et al.*, (1993) provide equations which define "layering windows" on the basis of the physical properties of the crystallising magma. Magmas would only produce rhythmic layering when they entered the "layering window". In the model of Hort *et al.*, (Chapter 9.2) the major controls on the position of magma chamber conditions relative to the "layering window" which could change during magma chamber evolution are the vertical thickness of the intrusion and viscosity. In the model of Sparks *et al.*, (Chapter 7.7.2 and 9.3) the variables which could change as the magma evolved are the temperature difference driving convection and the viscosity of the magma. It is not possible to chart accurately the change in any of these variables in the Nunarssuit and West Kûngnât magma chambers.

The development of rhythmic layering may be influenced by proximity to the intrusion wall. The rhythmic layering of West Kûngnât is developed close to the intrusion wall and that of Nunarssuit is inferred to be although the edge of the intrusion is under water. Proximity to the chamber wall could be an important factor if rhythmic layers are generated in part by density currents flowing down the walls of magma chambers and across the floor of the chamber. Irvine (1987a) envisaged currents sweeping down the walls and along the floor of the Duke Island and Skaergård magma chambers to generate rhythmic layering. Mingard (1990) attributed the olivine-rich rhythmic layering of the YGDC to the descent of olivine-rich crystal-melt plumes down the side-walls of the chamber. Proximity to the chamber wall does not however explain the initiation and cessation of rhythmic layering.

In Nunarssuit a xenolith horizon is present in Unit 10, the unit where layers are faintly visible and irregularly spaced, above the main layered series. In West Kûngnât it is highly likely that a xenolith horizon exists below the layered series adjacent to the intrusion edge. As evidence for this, Unit 1, adjacent to the intrusion edge, is xenolith-rich. A xenolith horizon is also seen in the cliffs of the Røverberg in West Kûngnât just below the Upper Layered Series (Chapter 2.2 and Upton, 1960). Generation of such horizons may involve a change in the vertical thickness of the intrusion, which is a variable in the mathematical model of Hort *et al.*, (1993). The

motion of the xenoliths falling through the chamber may disrupt the convective pattern or the layering of the magma.

Another point to bear in mind is the nature of non-linear systems. In Chapter 8 I showed that the mechanism responsible for igneous layering production may be non-linear. In chemistry the phenomenon of a system having two stable states between which it oscillates is known as bistability (Atkins, 1986) and results from a series of non-linear reactions controlling the production of a final compound. Magma chambers may have two stable states, layer producing and homogeneous rock producing, between which they can alternate in a fashion similar to chemical reactions and oscillating chaotic systems. If this is the case it may be impossible to determine accurately what causes the switch other than saying vaguely that a slight change in pressure, composition, crystal shape, rate of crystal rotation or some other variable could be sufficient.

It seems likely that some change in the physical properties of the magmas of Nunarssuit and West Kûngnât caused the initiation and cessation of rhythmic layering. Likely key factors are the viscosity of the magma, the degree of undercooling of the magma, the temperature difference driving convection, the rate of cooling of the magma and magma chamber height. Other factors such as the concentration of particular elements may also be important. It is not possible to say which variable changes or how it might change to terminate the production of the rhythmic layering.

10.3: Igneous layering: generation by crystal settling or *in situ* processes?

The cumulus phases present in the Nunarssuit and West Kûngnât layered syenites are all denser than the magma from which they crystallised (Table 7.5). However the settling velocity of the phases is much less than the convective velocity of the magma (Chapter 7.6.5 and 7.7.3). It seems likely that the turbulent convection of the magma would have kept the crystallising minerals in suspension within the main body of the magma chamber. Within the boundary layers at the edge of the magma chamber (Chapter 7.6.4) convective velocity decreases to zero, and crystals could settle. Thus crystals would accumulate at the foot of boundary layers adjacent to the magma chamber wall, and along the floor of the magma chamber. Crystals in the upper boundary layer may have sunk into the main body of the magma. Alternatively the

crystals could have remained in suspension in the upper boundary layer. The crystals in the boundary layer would have concentrated until the boundary layer became unstable and sank as a crystal-rich plume, to the bottom of the chamber. A new boundary layer would then have developed. Crystal settling could occur and, if the modal proportions of crystals which settled varied temporally, could produce igneous layering. Subsequent current modification of the accumulated crystals would account for the unconformities seen (Chapters 2.1.4 and 2.2.4 and e.g. Plate 2.1a).

A degree of under-cooling is usually required before crystals nucleate and grow. The release of latent heat of crystallisation at the solidification front at the base of the magma would reduce the degree of under-cooling, potentially inhibiting crystallisation. However, if it is assumed that crystallisation was not totally inhibited at the solidification front the layering could have been produced in place if rates of nucleation and crystal growth of different phases varied temporally.

10.4: Would crystal settling and/or *in situ* processes give rise to the modal variations seen?

The unlayered syenite above and below the Nunarssuit layered succession appears to be modally equivalent to the syenite in the leucocratic portions of the rhythmic layers. The unlayered syenite is assumed to be the eutectic crystallisation product of a trachytic liquid. If so, crystal settling would not produce the layering seen. If the melanocratic bases of the layers were the product of separation of pyroxenes and olivines from feldspars in the crystallising eutectic liquid it would be expected that the layers had an upper portion that was depleted in pyroxene relative to the unlayered syenite. This is not the case. This argument also applies to the layered syenite of West Kûngnât where the leucocratic syenite above the melanocratic bases of layers and surrounding the trough stacks is thought to represent the eutectic crystallisation product of a trachytic liquid. As has been mentioned in Chapter 7.7.1 the grains at the base of the layers are not hydraulically equivalent. If the layers were formed by settling from a suspension of crystals which consisted of the cumulus phases seen in the melanocratic bases of layers, a layering scheme of basal olivine cumulate, grading into a feldspar- and pyroxene-rich layer, grading into an apatite, ilmenite and magnetite layer would be expected. The above two arguments indicate that if the layers accumulated by crystal settling, nucleation and growth of feldspar must have been inhibited relative to the mafic phases. Current modification, and

possibly subsolidus processes, would then have removed any degree of hydraulic equivalence.

An *in situ* mechanism for the generation of igneous layering would also have to involve a phase inhibiting factor. This could either be a direct chemical control such as the depletion of components required by a crystallising phase or some kinetically related inhibitor such as the degree of under cooling affecting nucleation rates. Any chemical depletion mechanism must affect the whole magma chamber rather than act locally. Typical diffusion rates for ionic species in magmas are in the order of $1x10^{-3}$ to $1x10^{-1}$ cms^{-1} (calculated using values of D_0 for pantellerites and pitchstone from Henderson *et al.*, 1985) whilst typical nucleation and growth rates are 3 to 7 orders of magnitude smaller than this (Cashman, 1990; Kirkpatrick, 1981 and Hort and Spohn, 1991). Thus any chemical depletion would be removed by diffusion more rapidly than growing crystals could be affected by the depletion. If the magma was layered the double-diffusive interfaces between layers might inhibit diffusion so that depletion could affect a single layer rather than the whole chamber.

10.5: Mechanisms for inhibiting feldspar nucleation and growth

A number of mechanisms for the inhibition of feldspar relative to other phases are present in the literature. Parsons (1979) suggested that the degree of under-cooling of the magma could generate the layering scheme seen in Klokken since pyroxenes nucleate more rapidly at lower degrees of undercooling than feldspars. Larsen and Sørensen used a similar model to account for the rhythmic layering of the Ilímaussaq kakortokites. These models only apply to magmas which are saturated or nearly saturated with water and as such appear not to be applicable to the Nunarssuit and West Kûngnât magmas. Mingard (1990) suggested that the bases of individual layers seen in the YGDC could have been generated by the influx of new magma which was saturated in olivine and pyroxene but not feldspar. It is not possible to discount this model, though it seems unlikely that there would be so many reinjection episodes following one after another. Although this model offers an explanation as to why layering starts and stops the question is transferred to what triggers the start of magma injection and what causes it to stop. Mingard (1990) also suggested that raising the temperature of the magma could drive the magma composition temporarily off the eutectic to a point where feldspar nucleation and growth were inhibited. The rise in temperature could be brought about by the influx of new magma or periodic nucleation and release of latent heat. Brandeis *et al.*, (1984)

showed that nucleation at the base of magma chambers could occur in a series of sharp pulses followed by longer periods of crystal growth. In their modelling the nucleation pulses gave rise to thermal oscillations which could be sustained if the interior of the magma chamber was above the liquidus temperature. The thermal oscillations affected magma within a few cm of the crystallisation front and could thus generate the melanocratic bases of the rhythmic layers seen in Nunarssuit and West Kûngnât.

Naney and Swanson (1980) showed that increases in the concentrations of Fe and Mg could inhibit feldspar nucleation and growth in granitic melts. They postulated that this could be due to depolymerisation of the melt bought about by the network-modifying nature of FeO and MgO (Chapter 7.5.1). Crystallisation of the leucocratic syenite in Nunarssuit and West Kûngnât from composition P1 would have resulted in enrichment of the total Fe and Mg content of the residual liquid[1]. Fe and Mg contents might have built up in the magma until a critical concentration was reached and feldspar nucleation was inhibited. The melanocratic facies of both layered sequences contain a lot more apatite than the leucocratic facies. F contents would have increased whilst the leucocratic facies crystallised. F is a net-work modifier and so as F content built up the melt would have become less and less polymerised. This might have made it easier for pyroxenes and olivines to nucleate since they contain shorter silicate units than feldspar which is a framework silicate.

It would appear that feldspar nucleation and growth was inhibited during the formation of the melanocratic rhythms but it is not obvious what the inhibiting mechanism was. A variety of viable mechanisms exist and, as has been found previously (Mingard, 1990) it is impossible to choose between them.

[1]this result was obtained using modal proportions of phases as given in Tables 3.1 and 3.4 and assuming that: all the amphibole represents altered pyroxene, all the biotite was derived from olivine and that 20% of feldspar growth was post-cumulus.

10.6: Possible causes for the increase in visibility of the Nunarssuit layering

In the layered series of West Kûngnât the modal contrast involved in the layering remains the same throughout the layered succession. In Nunarssuit two fully developed and one partially developed cycle of the modal contrast between the base and overlying leucocratic syenite of individual layers increasing up section are seen. If the same layer producing mechanism was at work in Nunarssuit and West Kûngnât then either an additional factor had to be at work in Nunarssuit or the mechanism at West Kûngnât was damped. Upton (1960) suggested that the West Kûngnât magma chamber was a closed system. P Greenwood (Fig. 1.3) showed that the Nunarssuit syenite consists of a series of subunits defined in terms of pyroxene chemistry. These subunits presumably represent fresh impulses of magma. On a large scale the Nunarssuit syenite was not a closed system and the magmas producing the individual subunits may also have behaved as open systems. This may be an important factor in explaining why the layering styles of Nunarssuit and West Kûngnât are different although it is not possible at the present time to suggest how this may be brought about.

For the bases of layers to have become more olivine and pyroxene-rich feldspar nucleation must have been inhibited to a progressively greater extent. This could have been achieved if the degree of under-cooling of the magma slowly decreased. However this would also be reflected in a change of the modal content of the leucocratic portions of the layers. What is required is a mechanism which causes an increase in the amplitude of oscillations between the conditions producing leucocratic syenite and those producing the melanocratic bases of the layers. A mechanism analogous to chemical reactions driven by a linked catalyst and activator is presented below.

The activator would be an element which was partitioned into mafic phases relative to felsic phases so that its concentration increased during the crystallisation of leucocratic syenite (the dot-dashed line in Fig. 10.1) whilst the catalyst would be an element which was preferentially partitioned into the melt relative to the cumulus phases, i.e. the catalyst is incompatible, so that its concentration increased during crystallisation (the dashed line in Fig. 10.1). When the activator reached a critical level feldspar nucleation and growth would be inhibited thereby generating the mafic layers (the dotted line in Fig. 10.1), this situation applies to the layers at West

Kûngnât. At Nunarssuit the action of the catalyst would be superimposed on this. As the concentration of the catalyst built up feldspar nucleation and growth would be increasingly inhibited relative to the other cumulus phases when the activator reached its critical concentration. This would result in a higher concentration of mafic phases in the bases of the rhythms (the solid line in Fig. 10.1).

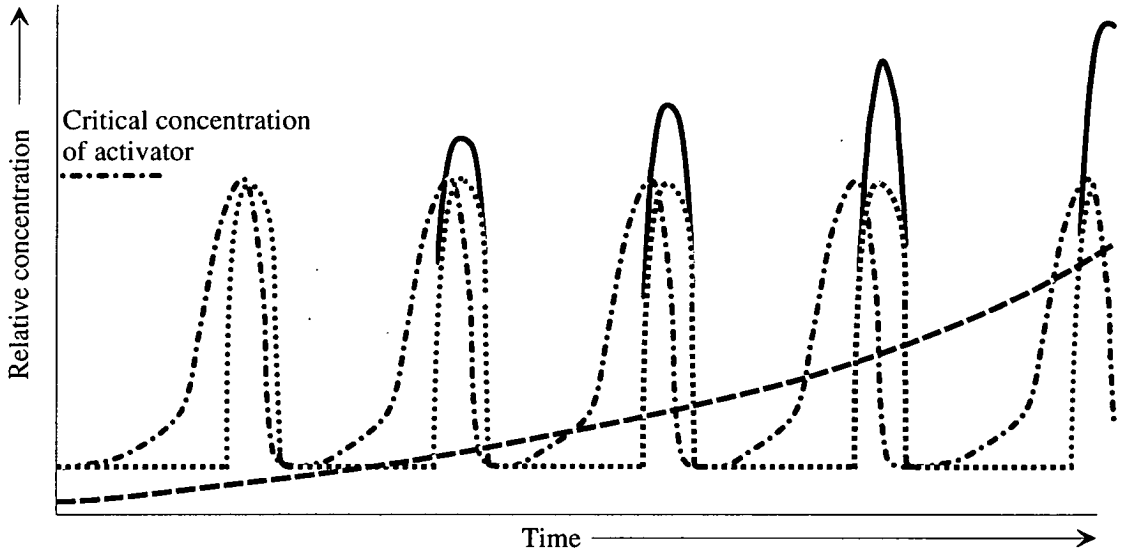

Fig. 10.1 The dotted line represents the variation in the concentration of mafic phases crystallising with time in the absence of the catalyst (dashed line), the oscillations generate igneous layering resembling that seen in West Kûngnât. The dashed line represents a catalyst for mafic phase nucleation and growth which only works when the activator reaches a critical concentration. The dot-dashed line represents the concentration of the activator, an element which is partitioned compatibly into mafic phases, but not leucocratic phases, relative to the melt. The activator increases in concentration as leucocratic syenite crystallises in the Nunarssuit magma chamber. The critical concentration of the activator is reached and the nucleation and growth of feldspar is inhibited. The combined effects of the increasing concentration of the catalyst and the oscillating concentration of the activator is to cause an increase in the concentration of the mafic phases crystallising to give the bases of the layers of Nunarssuit with time (solid line).

Possible activators are F, Fe and Mg which would have built up in the residual fluid as leucocratic syenite crystallised. These elements would depolymerise the melt and inhibit feldspar nucleation. Alternatively Na and K could have acted as catalyst poisoners so that the catalyst only worked after the relative concentrations of Na and K had decreased due to feldspar crystallisation.

Identifying a catalyst is harder as most elements are compatible in either mafic of felsic phases (Table 5.1). Volatile species such as Cl or CO_2 are incompatible but depolymerise melts and would thus inhibit feldspar nucleation and growth. Perhaps the effect of a volatile phase by itself is insufficient to produce the layering scheme

seen but the combined effect of a depolymerising volatile and fluctuating Fe and Mg concentration is sufficient.

A problem with this model is that as more mafic phases crystallised the magma might become more silicic. This would depend on the relative concentration of silica in the cumulus assemblages. If the crystallising magma did become more silicic compositional convection might occur and the silicic magma would accumulate at the roof of the intrusion.

An alternative to this chemically driven model is one in which the chemical inhibition of feldspar nucleation and growth is coupled to a physical winnowing of the melanocratic layers. In this model melanocratic layers would be produced by the inhibition of feldspar nucleation and growth, this could be due to high levels of Fe and Mg in the melt. Convection currents winnowed the melanocratic layers entraining feldspar into suspension whilst the denser mafic phases remain at rest on the floor of the magma chamber. As crystallisation progressed the strength of the winnowing currents increased and greater quantities of feldspar were entrained into suspension resulting in an increase in the mafic content of the melanocratic layers.

Current strength would have increased in the magma if there was an increase in the value of the Rayleigh number. The variables most likely to change, which affect the Rayleigh number (Chapter 7.6.2, equation 2) are the temperature difference driving convection, the density of the magma, the thickness of the convecting layer and the viscosity of the magma. As the magma crystallises the temperature difference driving convection is likely to decrease as the magma cools, this would lower the Rayleigh number. In Chapter 7.6.6 it was shown that the fractionation density of the crystallising assemblages of Nunarssuit and West Kûngnât was greater than that of the magma so the density of the magma would have decreased as crystallisation progressed, this would lower the value of the Rayleigh number. If the magma chamber convected as a single layer the thickness of the convecting layer would decrease as crystallisation proceeded, reducing the value of the Rayleigh number. However, it seems likely that the magma chamber would have been compositionally layered (Chapter 7.6.6) and it is not possible to determine the thickness of individual layers or chart their evolution with time. The viscosity of the magma may have increased or decreased during crystallisation, this would depend on melt composition, crystal content and temperature. An increase in viscosity would reduce the value of the Rayleigh number. The majority of variables which control the

Rayleigh number would have changed to reduce the Rayleigh number during crystallisation, this would have resulted in a reduction in the strength of potential winnowing currents.

Another problem with this hypothesis is that the concentration of feldspar would gradually increase either in the body of the chamber, if it remained in suspension, or in the leucocratic layers where the feldspar settled after it was winnowed out of the underlying melanocratic layer. This is not observed. Finally an increase in the removal of feldspar from the melanocratic layers would result in a reduction in the number of crystals making up the melanocratic layers which would thus be expected to decrease in thickness as they became more mafic, again this is not observed.

It would appear that the increase in modal contrast between melanocratic bases and adjacent leucocratic syenite is due to chemical affects rather than increased degrees of winnowing of cumulus feldspar. It should be stressed however that this conclusion is based on a qualitative assessment of the available data and can not be proved at the present time.

10.7: Mechanism which could cause the cyclicity in the layering patterns of Nunarssuit

The cyclicity of the rhythmic layering in Nunarssuit is described in Chapter 2.1. Two fully developed cycles are seen. Each cycle is capped by a thick layer which is very melanocratic. This layer has an irregular base which is thought to indicate an origin by slumping, and a fairly regular top above which another cycle begins. A third cycle is only partly developed, after an initial increase in visibility the bases of the rhythms become progressively less visible until the syenite is once again homogeneous. The thick melanocratic layers mark an event which interrupts the evolution of the magma and resets it to the conditions just before rhythmic layering production was initiated.

It is suggested that syenites may have a mafic sheath like some granites (Naney and Swanson, 1980) which would be redistributed over the magma chamber floor in the event of side-wall collapse. As crystallisation proceeded volatile concentrations would have built up. This could trigger an eruption which resulted in side-wall collapse generating the thick melanocratic layer at the top of the cycle and rehomogenising the magma so that homogeneous syenite crystallised until layer producing conditions were reattained. After the second eruption a permanent fissure

could have been established which prevented volatile concentration from building up to critical levels.

Alternatively a large influx of syenitic magma could enter the chamber and disturb the ambient conditions so that it was not possible to produce rhythmic layering. After a short period of mixing rhythmic layer producing conditions could be re-established. Either the new magma could be laden with olivine and pyroxene crystals which formed the thick melanocratic layer or the replenishment of the chamber could cause side-wall collapse producing the thick melanocratic layers. After the second replenishment event conditions remained unsuitable for large scale production of rhythmic layering. The above two hypotheses are not mutually exclusive.

The Mg/Mg+Fe number of samples (DL 9, DL 1) from the first thick melanocratic layer fit in the observed trend of whole rock Mg number (Chapter 5.7.3). If the layered sequence is inversely cryptically layered this implies that the material in the thick melanocratic layers crystallised in sequence with the surrounding syenite. If the layered sequence is not inversely cryptically layered (section 10.8) then the material in the thick melanocratic layers crystallised before that of the surrounding syenite. The major and minor element trends of individual phases are interrupted at the first thick melanocratic layer (Chapters 4 and 5), samples from the thick melanocratic layer tend to have relatively high Mg number maxima and minima. The material in the thick melanocratic units probably originated as crystals which adhered to the side-walls of the magma chamber forming a mafic sheath to the chamber. When this sheath formed is more debatable and hinges on whether the Nunarssuit layered syenites are inversely cryptically layered or not.

10.8: Explanations for the Mg/Fe enrichment trend seen in the Nunarssuit layered syenite

Reverse cryptic layering has been reported to occur at the bases of a number of layered intrusions, (Muskox, Irvine and Smith, 1967; Great Dyke, Wilson, 1982; Stillwater, Raedeke and McCallum, 1984). Wilson and Larsen, (1985) reported reversals in the cryptic layering of the Hyllingen complex, Norway. Raedeke and McCallum suggested that the basal magnesium enrichment trend seen at Stillwater was due to equilibration between the cumulus phases and trapped intercumulus liquid. Initially the intercumulus liquid was of fairly constant composition and was more ferroan than the cumulus phases. Re-equilibration resulted in Fe enrichment of

the cumulus phases. Raedeke and McCallum postulated that initial porosity of the crystal pile decreased as crystallisation proceeded so that the volume of liquid available for post-cumulus reequilibration decreased. Thus cumulus phases became less ferroan up section due to the decrease in postcumulus reequilibration. Raedeke and McCallum also suggested that variation in the degree of assimilation of country rock and replenishment of the magma chamber with melt from successively more magnesian magmas could cause or enhance the reverse cryptic layering seen.

In the Hyllingen intrusion modal and cryptic layering are strongly discordant (Wilson and Larsen, 1982). At times the cryptic layering is of a reversed nature, compositions become more primitive up section. Wilson *et al.*, (1987) postulated crystallisation from a stratified magma against an inclined side-wall to explain these observations (Fig. 10.2).

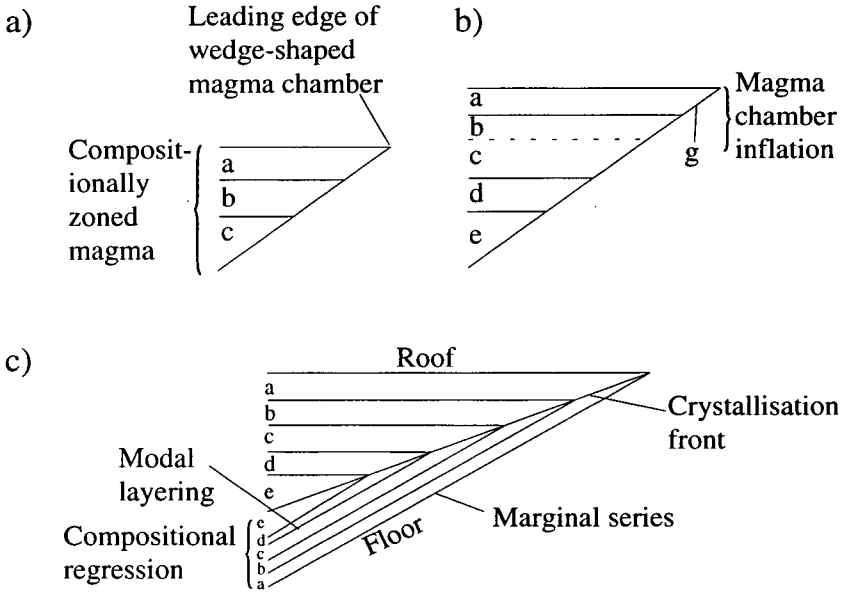

Fig. 10.2: Formation of a compositional reversal at the base of a layered intrusion by elevation of zoned magma along an inclined floor. a and b: Inflation of a wedge-shaped chamber due to elevation of zoned resident magma by a dense influx. The "new" floor at the leading edge of the wedge (at g) first comes into contact with the most buoyant, evolved magma layer (a), followed by successively denser, less evolved magma during continued inflation. c: Crystallisation during inflation produces a basal reversal (compositional regression a-e). Modal layering develops when the rate of cooling decreases sufficiently to allow oscillatory nucleation. It is parallel with the crystallisation front and consequently discordant to the magma stratification (from Wilson *et al.*, 1987).

In their model modal layering is produced by oscillatory nucleation against the side-wall of the chamber. The magma is stratified, becoming more evolved upwards. Mineral composition within the modal layers is governed by the layer of magma

which the crystals formed in. Primitive, dense magma is intruded into the bottom of the chamber and the magma layers are pushed upwards. In this way the modal layers come into contact with more primitive magma.

In Nunarssuit there is no evidence for differing degrees of assimilation of country rock; detailed isotopic work could confirm this. It is likely that the composition of the cumulus crystals was modified by the intercumulus liquid (Chapter 6) but there is no reason to suppose that the degree of modification decreased in a regular fashion up section. It is possible that the layering was produced by the repeated injection of small volumes of magma (section 10.5) and this magma may have become systematically more magnesian. It is not possible to prove or disprove this hypothesis. The model of Wilson *et al.* (1987) may be applicable to the Nunarssuit layered syenites however it seems unnecessarily complicated. An alternative is a model in which the syenite has normal cryptic layering which is discordant to the modal layers due to the inclination of the chamber floor (Fig. 10.3). Modal layers accumulate parallel to the chamber floor but the chemistry of the phases present in the layers is controlled by the stratified magma and so cryptic layers are discordant to the modal layers. The traverse of the layered syenites was carried out at an angle to the dip of the modal layers and so the stratigraphy may have been crossed obliquely, moving into more magnesian cryptic layers.

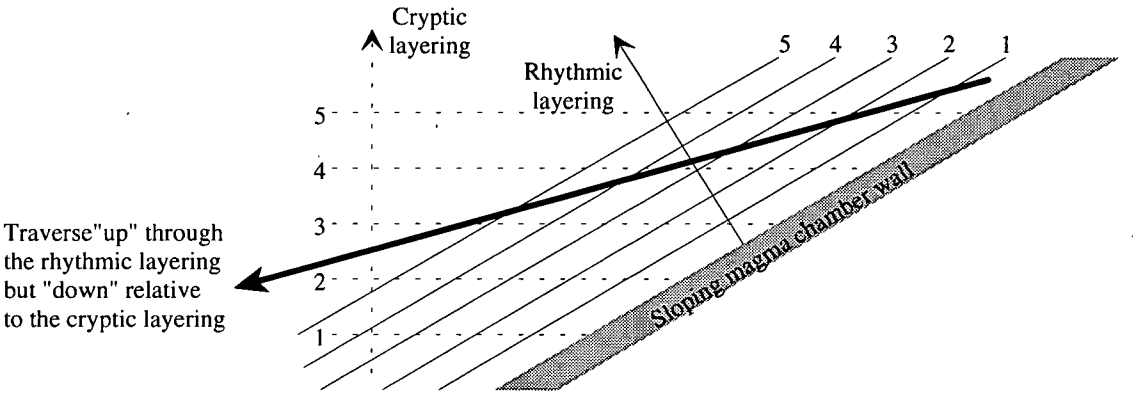

Fig. 10.3: Schematic layered magma chamber with an inclined floor. Rhythmic layers form in the sequence 1 to 5, cryptic layering parallel to the horizontal forms in the sequence 1 to 5, 5 being the most evolved. A traverse up through the rhythmically layered sequence could go down into successively more primitive cryptic layers.

To determine whether this scenario is applicable to the Nunarssuit layered series would require detailed mapping along individual layers to try and detect lateral chemical variation. It should be possible to sample along the strike of some layers for

several tens of metres. Due to the lack of vertical relief in the field area it would not be possible to sample chemical variation of the layers in the dip direction for more than a few metres. In other parts of Nunarssuit this sort of sampling may be possible. A major problem with this model is that the stratified magma would have been disrupted by the sedimentary like currents of crystal-melt slurry for which there is much field evidence in Nunarssuit.

It is felt that none of the above models is totally applicable to the Nunarssuit syenite. However it seems likely that the observed trends are due to a degree of subsolidus modification coupled with a degree of discordancy between modal and cryptic layering.

10.9: Mechanisms for the formation of troughs

Individual troughs are thought to have formed by the deposition of mafic phases from a stream of crystal-melt slurry. There are several potential sources for this slurry. Side-wall collapse would generate streams of crystal-melt slurry which might have been mafic-rich. Alternatively crystals could accumulate at the edge of the intrusion, causing a loosely consolidated pile of crystals to develop, when the slope of this pile reached a critical angle it would collapse and crystal-melt slurry would flow across the chamber floor. The presence of the slump structures and breccias in Nunarssuit (Chapter 2.1.2 and 2.1.3, Plate 2.1c and d, Plate 2.2a and b, Plate 2.3, Plate 2.5a) provide circumstantial evidence that large scale side-wall or crystal pile collapse occurred. The mafic phases in the troughs tend to be more magnesian than those in the surrounding syenite (Chapter 4.2, 2-28 relative to the other samples from DL2 and Chapter 4.3, the mafic phases in the trough stacks relative to those in the surrounding syenite). This suggests that the troughs contain earlier formed mafic phases than the surrounding syenite and leads me to favour early side-wall cumulates rich in mafic phases as a source of the slurries. The slurry could be channelised by chamber wall topography (Fig. 10.4) floor topography (Fig. 10.5 and Irvine, 1987a), or it could form a stream as it flowed down the wall after side-wall collapse.

Stacks of troughs (Plates 2.5b and c and Plates 2.7b, 2.8, 2.10a) are thought to have been produced by the intermittent flow of slurry along the same path. The stream of slurry may have been constrained to flow along the same path by:
1) scalloping of the chamber wall. Scalloping has been observed in experiments involving the cooling of NH_4Cl solution (Bédard *et al.*, 1992, present Fig 10.4).

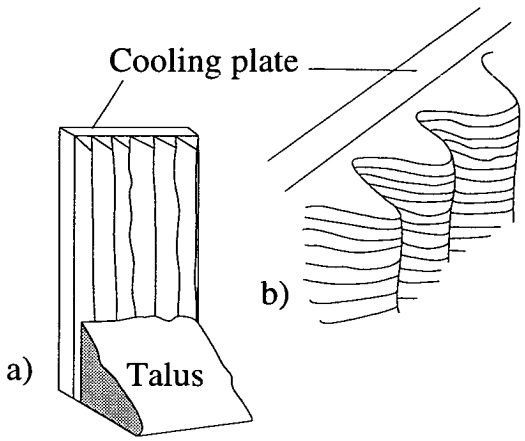

Fig. 10.4: a) a sketch illustrating the groove structures which developed in an experiment carried out by Bédard *et al.*, (1992) when NH_4Cl solution was cooled using a vertical plate, b) a close up of the groove structures (after Bédard *et al.*, 1992).

The banded division of the Marginal Border Group of the Skaergård intrusion contains "colloform" banding (Wager and Brown, 1968; Irvine 1987a and 1987b). This colloform layering is broadly parallel to the intrusion wall and would have given the wall a corrugated topography;

2) the topography of the magma chamber floor (Fig. 10.5). A model whereby the descending limbs of roller convection cells become supercooled and precipitate crystals and the ascending limbs warm up and do not precipitate crystals thereby generating a trough and ridge topography on the magma chamber floor has been suggested by Irvine (1987a, Chapter 9.8) to account for the trough stacks in the Skaergård intrusion, or;

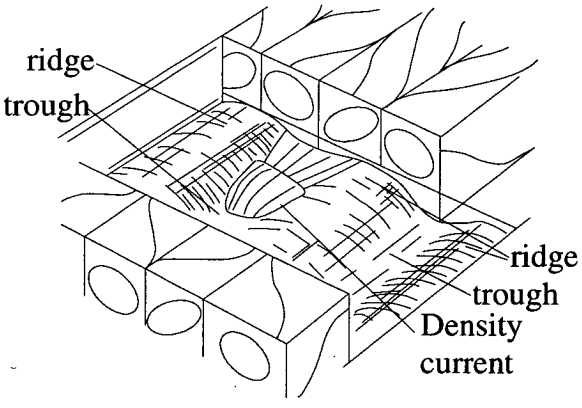

Fig. 10.5 The position of the density current is controlled by magma chamber floor topography (a detail from Irvine, 1987a fig. 41, see present Fig. 8.6 for a full extract of the diagram)

3) the first stream eroding a channel which subsequent streams occupied (Fig. 10.6)

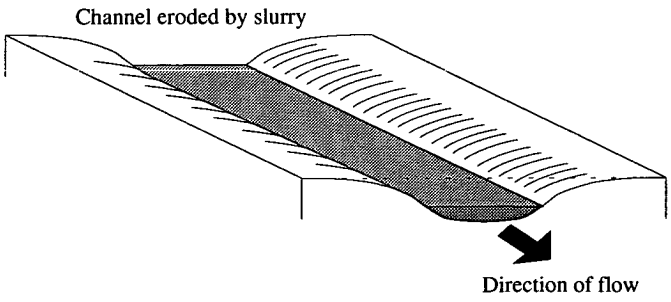

Fig. 10.6: The initial slurry stream erodes a channel which controls the position of subsequent streams.

In the case of the West Kûngnât trough stacks (Chapter 2.2.3) the regular position of the troughs may be a function of fluid flow down an incline, this is discussed below. The trough stacks could be formed in the same way that Irvine (1987a) suggests that the Skaergård trough stacks formed (Fig. 10.6 and Chapter 9.8). However, the mafic phases in the troughs are more magnesian than those in the surrounding syenite and are thought to represent an earlier phase of crystallisation. There is also no theoretical basis for the size of Irvine's roller convection cells which were drawn to the necessary size to fit the hypothesis. In West Kûngnât the diameter of these convection cells (half the width of a trough) would be around 2.5m to 8m; this would also have been the thickness of the layer containing the convection cells. Unfortunately it is not possible to calculate the thickness of this layer by independent means (A Rice, pers. comm.). An alternate model for the generation of the trough stacks seen in West Kûngnât has been developed.

When a broad band of viscous fluid is released so that it flows down a slope the leading edge of the fluid initially develops a sinusoidal pattern. Flow is fastest at the down slope cusps of the wave front and slowest at the up slope cusps so that gradually a series of regularly spaced streams of fluid develop (Huppert, 1982, present Fig. 10.7c). This effect can be seen using washing up liquid or oil and an inclined sheet of glass. It is suggested that a mafic side-wall cumulate could have formed as a sheath around the West Kûngnât magma chamber (Fig. 10.7a). As crystal growth proceeded this side-wall cumulate could have become gravitationally unstable (Fig. 10.7b). This could have been aided by the addition of fluid from a hydrothermal system or the presence of volatiles which had diffused up to the top of the magma chamber. The side-wall cumulate would eventually have detached from the side-wall and flowed down the side of the magma chamber as a crystal-melt slurry. Initially the flow would have developed a sinusoidal profile; this would have developed into a series of streams (Fig. 10.7c). At the bottom of the chamber the streams would have flowed across the chamber floor and deposited crystals from suspension (Fig. 10.7d). As the streams flowed over the floor they would have lost

momentum, both due to friction and cooling and it would have become harder and harder for the streams to propagate forwards. Ultimately the fast moving streams near the edge of the intrusion would have buckled and flowed over the older, now stationary streams (Fig. 10.7e and f).

This model explains why the mafic phases of the troughs are more magnesian than those in the surrounding syenite. It explains why trough stack formation stopped, the supply of slurry was exhausted. The lateral off-setting of the troughs could be due to banking up of the streams against a mound or ridge in the chamber floor. The generation of the two sets of trough stacks could be due to a cessation in slurry flow before another mass became unstable and broke away from the wall of the chamber. The model can also explain the high proportion of apatite crystals in the biotite and amphibole oikocrysts of the troughs. Volatiles would diffuse to the top of the chamber and, as their concentration built up small vapour bubbles would form. The presence of these could facilitate the growth of volatile bearing phases, i.e. amphibole, biotite and apatite. The model relies on the troughs being relatively close to the chamber margin.

Fig. 10.7 (over): a) in the initial stages of magma chamber evolution a mafic sheath forms around the West Kûngnât magma chamber, crystal settling may be occurring and a hydrothermal system may be set up. Volatiles slowly rise to the top of the magma chamber. The increase in concentration of volatiles stimulates growth of amphibole, biotite and apatite, b) as crystallisation proceeds the side-wall cumulate becomes gravitationally unstable and begins to sag, c) ultimately the side-wall cumulate becomes detached from the wall and flows down the chamber, initially as a relatively straight slurry front but gradually developing into, first a sinusoidal profile and then a series of regularly spaced streams, d) the slurry streams flow across the magma chamber floor depositing crystals from suspension. As the streams flow they cool and loose momentum, it becomes harder and harder for the streams descending the walls to propagate forwards, e and f) eventually the streams along the chamber floor are almost stationary, further up the walls the streams buckle and ride over the old stream generating a new series of troughs. Ultimately the supply of slurry is exhausted and no more troughs are generated.

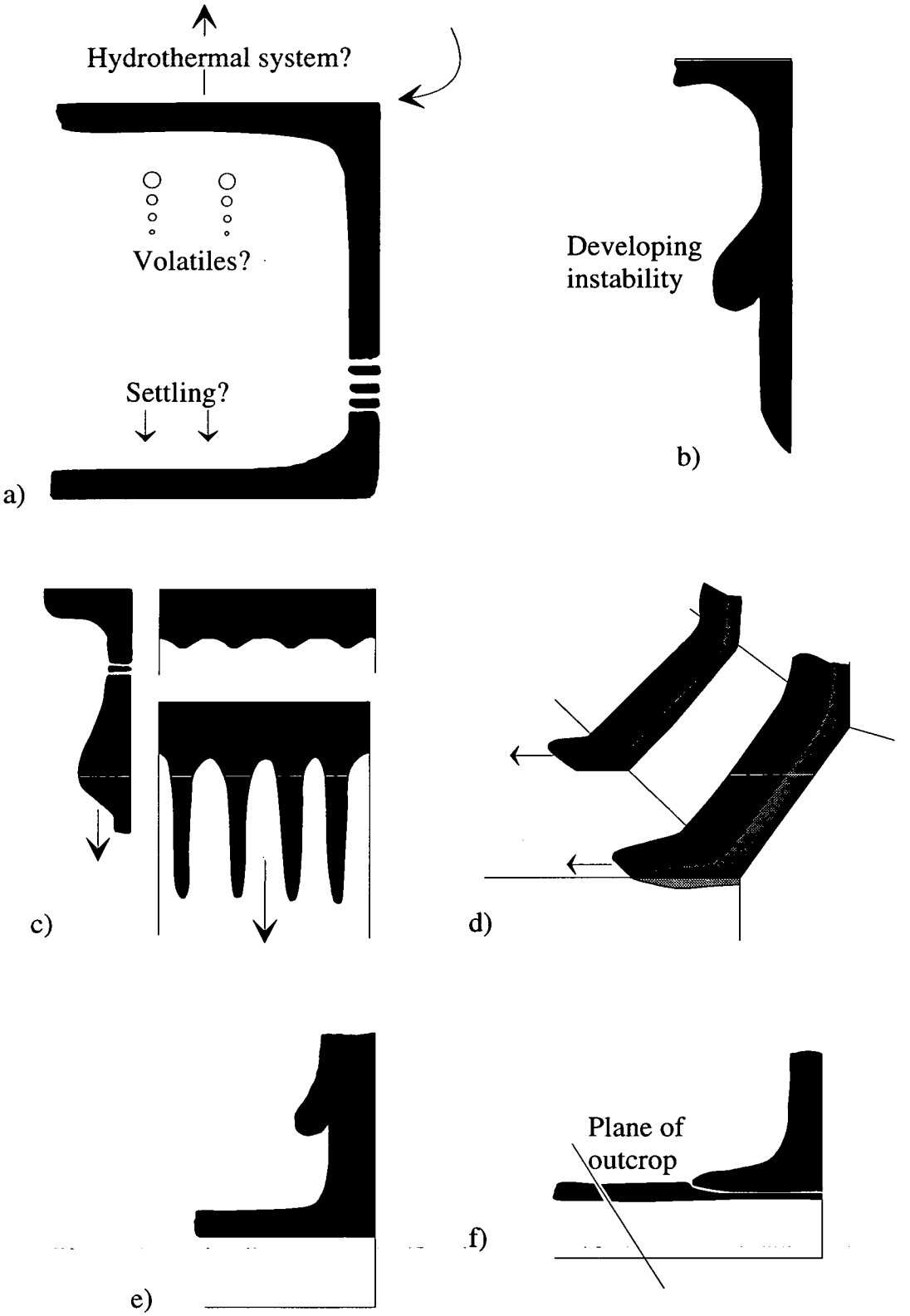
Hydrothermal system?
Volatiles?
Settling?
a)
Developing
instability
b)
c)
d)
e)
Plane of
outcrop
f)

10.10: Mechanisms for the formation of micro-rhythmic layering

Micro-rhythmic layering is seen in one isolated outcrop in Nunarssuit (Chapter 2.1.3 and Plate 2.4a). The micro-rhythmic layering occurs on an isolated rock face, nearby outcrops all show macro-rhythmic layering. It seems logical to suggest that this isolated occurrence of micro-rhythmic layering was produced by a localised fluctuation in the chemical or physical conditions of the magma. Within the literature it seems accepted that micro-rhythmic layering is produced by "micro-rhythmic differentiation by crystal nucleation, resorption and coarsening phenomena" (Irvine, 1987b).

10.11: Features in the Nunarssuit and West Kûngnât syenites which can not be explained by sedimentary style processes

The crossed layer observed in Nunarssuit (Chapter 2.1.3, Plate 2.4b and c) can not be explained in terms of sedimentary processes. At least one of these layers must have been produced by a process operating on the crystal pile. Some form of process involving subsolidus diffusion is suggested.

10.12: Synthesis

The magma chamber of Nunarssuit developed a mafic margin like those observed in some granites (Naney and Swanson, 1980) due to the relatively high Fe+Mg content of the magma. The magma was depleted in Fe and Mg by the crystallisation of the mafic phases at the edge of the intrusion. The phases seen in the leucocratic syenite began to crystallise in eutectic proportions. Compositional convection occurred during crystallisation giving rise to a stratified magma chamber. Crystallisation took place, predominantly, in the boundary layers where undercooling was greatest. Crystals which precipitated in the stagnant boundary layers settled to the floor of the magma chamber. Any crystals which formed in the body of the magma chamber were held in suspension by the convective motion of the magma.

As leucocratic syenite accumulated the Fe and Mg content of the magma slowly increased until it reached a critical level, feldspar nucleation and growth was inhibited relative to pyroxenes and olivines and a melanocratic layer accumulated on the chamber floor. The growth of the mafic phases depleted the magma in Fe and Mg and feldspar began to crystallise again. This cycle repeated, generating layers rich in

mafic minerals. Whilst this was occurring convection currents occasionally scoured the bottom of the magma chamber redistributing the layers and removing all traces of hydraulic equivalence. The redistribution of the crystal pile produced unconformities. The currents also produced layers which petered out along strike or down dip. Small-scale earth movements also altered the position of the horizontal and caused unconformities to be produced. Disruption of earlier formed layers and side-wall collapse generated slump breccias. Unstable piles of crystals built up at the edge of the chamber which occasionally collapsed and flowed across the chamber floor to produce troughs and slump structures.

As the cycle of melanocratic and leucocratic settling assemblages continued the concentration of an incompatible element built up. This promoted pyroxene and olivine nucleation when feldspar nucleation was inhibited so that melanocratic bases become more mafic up section. As this element became more concentrated, the magma chamber became increasingly unstable, until eruption occurred. This caused slumping of the side-walls which generated a thick melanocratic layer. The chamber was replenished with fresh magma which initially crystallised leucocratic syenite. A few streams of crystal-melt slurry persisted after the eruption and main episode of side-wall collapse and generated large scale troughs. The magma chamber gradually reverted to pre-eruption conditions and layering was once again produced. The cycle then repeated. After the second eruption a fissure was established leading to the external environment and conditions never developed to the extremes which they had reached before. Layering was sporadically produced but never to the previous extent. Roof collapse produced the xenolith horizon and altered the height of the chamber. The degree of under-cooling, the temperature driving convection or the viscosity of the magma may have changed so that conditions did not favour layering production.

In West Kûngnât the chamber was initially sheathed by a mafic layer. The trachytic magma began to crystallise leucocratic syenite. The side-wall cumulates became unstable and flowed down the chamber walls as a crystal-melt slurry generating a series of trough stacks. Concurrent with this a slight amount of rhythmic layering was produced by the depletion/enrichment of Fe and Mg and the inhibition of feldspar nucleation and growth. Layers initially draped over a mound or ridge on the chamber floor against which streams of the crystal-melt slurry banked up. Eventually the side-wall cumulate had wholly collapsed and trough stack production ceased. Rhythmic layering production continued for some time as the magma composition oscillated between being sufficiently Fe and Mg rich to inhibit feldspar nucleation

and growth and being sufficiently Fe and Mg poor for feldspar to nucleate and grow more rapidly than the other cumulate phases. Ultimately the magma ceased to be able to produce igneous layering as conditions changed and it was no longer in the layering window.

Subsequent to deposition the syenites of both Nunarssuit and West Kûngnât were subject to a variety of processes. Sub-solidus grain growth and absorption resulted in the loss of small pyroxene and olivine grains and the growth of feldspar grains so that porosity was reduced and the original shape of the feldspar crystals was lost. These sub-solidus processes, driven by diffusion gradients and kinetics produced small amounts of micro-rhythmic layering in Nunarssuit and also the strange structure which appears to be two layers crossing each other. Subsolidus modification to the original chemistry may have resulted in the reverse cryptic layering seen in Nunarssuit. Reduction of porosity by crystal growth was sufficiently rapid relative to the loading of the crystal pile by freshly deposited grains that little compaction occurred. Pyroxenes were altered to produce amphiboles, olivines were altered to produce biotites. These reactions occurred either at or below the solidus. The nature of the fluid is not known, it must either have been a late-stage hydrous melt or a hydrothermal fluid. Feldspars interacted with hydrous fluids (which had a magmatic origin) after the syenite had solidified and lost their original microstructures. The alteration of the olivines and pyroxenes probably occurred at a higher temperature than the alteration of the feldspar and involved a different fluid. However this is not certain, it could be that the fluids involved were genetically related.

Chapter 11: Summary

Nunarssuit and Kûngnât are relatively evolved, silica-saturated complexes in the alkaline Gardar Province of South Greenland and were intruded during Proterozoic continental rifting events. This activity lasted from c.1320 to 1120 Ma B.P. The Kûngnât pluton was intruded 1245 +/- 17Ma B.P. (Emeleus and Upton, 1976) and the Nunarssuit syenite was intruded 1154 +/- 14Ma B.P. (Blaxland *et al.*, 1978). The initial work on Kûngnât was carried out by Upton (1960) and the initial work on Nunarssuit by Harry and Pulvertaft (Harry and Pulvertaft, 1963).

The Nunarssuit syenite is part of a larger complex which consists of gabbros, syenites and granites. Greenwood, (pers comm.) showed that the syenite is composed of five compositionally distinct units. It is in the outer unit, close to the south western contact of the magma chamber, that rhythmic layering is developed. The Kûngnât complex consists of the Western and Eastern Kûngnât syenites, the marginal syenite and a syenogabbro-troctolite ring-dyke. The West Kûngnât syenitic stock is thought to have behaved essentially as a closed system. In the Western Syenite Lower Layered Series, rhythmic layering is seen near the base of the series, close to the wall. Up section the rhythmic layering fades and passes up into laminated syenite and then unlaminated syenite. Further up the succession, in the Western Syenite Upper Layered Series rhythmic layering is once again present.

The Nunarssuit and West Kûngnât Lower Layered Series syenites are probably mesocumulates though the problem of identifying postcumulus growth makes this far from certain. Cumulus phases are pyroxene, olivine, ilmenite, magnetite and Fe-Cu sulphides, apatite and feldspar. Feldspar is the dominant cumulus phase. Biotite and amphibole are the products of alteration of olivine and pyroxene respectively. Some of the feldspar is thought to be intercumulus in origin. The rhythmic layering is defined by variation in the modal content of feldspar. Individual layers are, on average, c.20cm thick with thin melanocratic bases (c.3cm) grading, within a few cm into leucocratic syenite which resembles the unlayered, homogeneous syenite seen in the intrusions. A variety of sedimentary-like structures (e.g. troughs, unconformities, slumps and slump breccias), are seen in the two intrusions. The feldspars are cloudier and the olivines and pyroxenes are more altered in the leucocratic syenites than in the melanocratic syenites. An extensive suite of samples was collected from both layered syenite successions.

Samples from adjacent melanocratic and leucocratic layers have the same mineral chemistry. Minerals from melanocratic trough layers are generally more magnesian than those from adjacent leucocratic syenite. The minerals in the Nunarssuit layered succession get more magnesian up section whilst those from West Kûngnât get slightly more ferroan up section. In both intrusions trace element compositions of individual minerals show conflicting trends, some elements decrease in concentration up section whilst others increase up section. These trends are seen in both compatible and incompatible elements.

Whole-rock analyses of the Nunarssuit layered syenite reflect the alternating concentrations of mafic and felsic layers. Most elements show a correlation with the total Fe and Mg content of the sample. However, Ba increases up section whilst Rb decreases up section. The ratio of Mg to Mg+Fe also decreases up section. It is possible that the Nunarssuit syenites are reversely cryptically zoned, however it could also be that the rhythmic layering and the cryptic layering are not parallel and that the sample traverse was carried out obliquely to both sets of layering which resulted in sampling being carried out up section relative to the modal layering but down section relative to the cryptic layering (see Fig. 10.3). No difference was apparent between the ratio of Fe to Mg in the whole-rock chemistry of the West Kûngnât trough stacks and adjacent leucocratic syenite.

Syenites from both layered successions have undergone subsolidus modification. Feldspars have lost their primary microstructures through interaction with low temperature (<450°C) hydrothermal fluids. Pyroxene rims have been modified through interaction with alkali-rich fluid. In the subsolidus, pyroxenes have been altered to amphiboles and olivines to biotites. Feldspars, pyroxenes and olivines are more altered in leucocratic facies than in melanocratic facies. The changes to pyroxenes and olivines may occur at low temperatures, possibly as low as 450°C or lower, it is not known whether the fluid was a late stage hydrous melt or a hydrothermal fluid. Some apatites and zircons have lost some or all of their primary zoning characteristics through subsolidus fluid interaction, again this fluid may have been a late stage hydrous melt or a hydrothermal fluid. The exsolution textures of ilmenospinels also indicate a limited amount of modification by fluids at low temperatures. Small grains of pyroxene and olivine have been absorbed by the larger grains. None of the syenites have undergone much compaction, probably as a result of low initial porosity and rapid intercumulus growth relative to the rate of crystal build up on the floor of the chamber. Possible explanations as to why leucocratic

facies are more altered than the melanocratic ones include, (i) feldspar being more equidimensional and larger than the other minerals so that leucocratic layers would have been more porous and thus would have contained more intercumulus fluid and (ii) feldspars in the leucocratic layers containing more dissolved water which later exsolved leaving the leucocratic layers permeable and more reactive

Chilled margins are absent from the Nunarssuit and West Kûngnât syenites so a best guess has to be made for the composition of the magma from which they began to crystallise. A chilled dyke margin from the Tugtutôq-Ilímaussaq dyke swarm was chosen since this dyke has a phenocryst assemblage very similar to that of the cumulus phases in the Nunarssuit and West Kûngnât syenites. Calculations show that, at likely liquidus temperatures, the magma was less dense that the cumulus phases so that crystal settling might have been able to occur. However the magma probably convected turbulently and since convective velocity would have been faster than settling velocity crystal settling could have occurred only in the boundary layers of the magma.

Non-linear dynamic analysis of the layer spacing in both intrusions indicates that the layer-producing mechanism was chaotic, i.e. it followed definite rules but was unpredictable. Only a few variables, (four or five at the very most), should be required to model the layer-producing mechanism. The layering at West Kûngnât is more predictable than that at Nunarssuit which contains more unconformities and shows more evidence for current activity.

Recent mathematical models predict that the trachytic magmas of Nunarssuit and West Kûngnât could have given rise to cumulate layering. Application of these models requires the use of poorly constrained variables and unrealistic one or two phase systems and is thus not wholly satisfactory. The more qualitative models proposed to explain the layering seen in other plutons are, to some extent applicable to Nunarssuit and West Kûngnât. In one sense, qualitative models are more satisfactory than the quantitative models as they can be tailored to individual intrusions and do not require exact knowledge of the physical properties of the magmas. However, it is hard to prove or disprove such models and they can not be used in a predictive sense.

It is concluded that the production of the rhythmic layering in Nunarssuit and West Kûngnât required the periodic inhibition of feldspar nucleation relative to the other

phases as has also been proposed for some of the layering in the YGDC, (Mingard, 1990). A variety of models for the suppression of feldspar nucleation exist, including (i) temperature rises due to magma replenishment, (ii) release of latent heat of crystallisation, (iii) depolymerisation of the magma or (iv) the influx of new magma for which feldspar was not on the cotectic. It is impossible to choose between the various models. Crystals are inferred to have accumulated by settling from the boundary layers and unstable piles of crystal may thus have developed underneath the side-wall boundary layers. Periodical collapse of these crystal accumulations may have given rise to density currents which flowed across the chamber floor causing erosional and subsequent depositional features (e.g. unconformities and troughs). A xenolith horizon is present above the main layered series of Nunarssuit. Xenoliths are likely to be present below the layered syenites of the Lower Layered Series, West Kûngnât. The xenoliths are thought to have exerted some control on the rhythm layering by either changing the effective vertical dimension of the chamber or disrupting the convective regime.

Troughs and trough stacks were produced by deposition of mafic phases from crystal-melt slurries derived mainly from side-wall collapse but also from the collapse of unstable crystal piles. The unstable side-wall cumulates were mafic early-crystallisation products analogous to the mafic rims which form around some granitic plutons, which explains why the trough phases are more magnesian than those in the surrounding syenite. Earth movements and convection currents scouring the bottom of the magma chamber would mix up the crystals removing any hydraulic equivalence and would generate the observed unconformities.

The layering at Nunarssuit is further complicated by the increase in modal contrast of the melanocratic bases up section whilst the leucocratic portions of the layers remain the same. Thus there was an "increase in the amplitude of the oscillation" between the conditions in which normal leucocratic syenite was produced and those in which feldspar nucleation was inhibited. It is suggested that some chemical factor promoted the nucleation of olivine and pyroxene, but only when feldspar was inhibited. Thus the feldspar inhibiting mechanism produced rhythmic layering as in West Kûngnât but superimposed on this was the effect of the promotion of pyroxene and olivine nucleation due to the presence of a chemical species which gradually increased in concentration but was only active when feldspar growth was inhibited. This situation is rather like that of a catalyst and activator where the catalyst can only act when the activator is present. The cyclicity of the Nunarssuit layering can be explained by

either, or both, magma chamber replenishment, and periodic eruption and resetting of magma chamber conditions preventing rhythmic layer production for a time. It is not known why the rhythmic layering ceased to form but this must have been influenced by changes in magma chamber geometry, magma chemistry, the degree of under-cooling or the temperature difference driving convection.

Future work on igneous layering in the field should concentrate on three dimensional sampling, the sample collections used in this study were largely two dimensional and it is impossible to get a full picture of the evolution of the magma chamber. Pb and Sr isotope studies would help to constrain processes occurring before, during and after crystallisation. In the laboratory any experiments dealing with crystal settling should be conducted with fluids whose rheology is fully understood. From the literature it is not clear whether the fluids which are being used, e.g. glycerol, are being chosen for any other reason than availability and ease of use. Experiments to determine parameters such as coefficient of thermal diffusivity need to be carried out on iron-rich silicic compositions so that theoretical models can be applied more accurately. Theoretical models need to be developed so that they can cope with a realistic mix of phases rather than just one or two.

This study has been of use in testing recent models for the genesis of igneous layering. Detailed chemical data, both major and minor have been obtained for both intrusions. It has been shown that the original chemistry and textures of the layered successions have been modified by subsolidus processes. Igneous layering could be produced by either crystal settling or *in situ* processes. In either case a mechanism is required to inhibit the nucleation of feldspar relative to the other cumulus phases. A start has been made in applying modern mathematical techniques to the analysis of layering. It is hoped that this study will further the understanding of the layered syenites of Nunarssuit and West Kûngnât and the genesis of igneous layering as a whole.

References

Abbey, S (1980) Studies on "standard samples" for use in the general analysis of silicate rocks and minerals. Part 6: 1979 edition of "usable" values. Geol. Surv. Canada. Paper **80** 1-14

Andersen, DJ and Lindsley, DH (1988) Internally consistent solution models for Fe-Mg-Mn-Ti oxides: Fe-Ti oxides. Am Miner **73** 714-726

Anderson, JG (1974) The geology of Alángorssuaq, Northern Nunarssuit complex, South Greenland. Unpubl. PhD thesis, University of Aberdeen

Aoki, K and Kushiro, I (1968) Some clinopyroxenes from ultramafic inclusions in Dreiser Weiher, Eiffel. Contr Miner Petrol **18** 326-337

Atkins, PW (1986) Physical chemistry (3rd edition). Oxford Univ Press 857pp

Bagdassarov, NS and Fradkov, AS (1993) Evolution of double diffusion convection in a felsic magma chamber. J Volc Geoth Res **54** 291-308

Bailey, DK and MacDonald, R (1987) Dry peralkaline felsic liquids and CO_2 flow through the Kenyan rift zone. In Mysen, BO (Ed) Magmatic processes: Physiochemical principles Geochem Soc. Spec. Pub. **1**, 91-105

Barnes, HA and Walters, K (1985) The yield strength myth? Rheol Acta **24** 323-326

Becker, SM (1984) Petrology of the giant dykes of Isortoq and feldspar variation in the Klokken Complex, South Greenland. Unpubl PhD thesis, University of Aberdeen

Bédard, JH, Kerr, RC and Hallworth, MA (1992) Porous sidewall and sloping floor crystallisation experiments using a porous mush: Implications for the self channelization of residual melts in cumulates. Earth Planet Sci Lett **111** 319-329

Bédard, JH, Sparks, RSJ, Renner, MJ, Cheadle, MJ and Hallworth, MA (1988) Peridotite sills and the metasomatic gabbros in the Eastern Layered Series of the Rhum complex. J Geol Soc Lond **145** 207-224

Berner, A (1980) Early diagenesis: A theoretical approach. Princeton Univ Press 241pp

Best, MG (1982) Igneous and metamorphic petrology. Oxford Freeman 630pp

Blaxland, AB, Breemen, O van, Emeleus, CH and Anderson, JG (1978) Age and origin of the major syenite centres of the Gardar: Rb-Sr studies. Geol Soc Am Bull **78** 231-244

Borthwick, J and Harmon, RS (1982) A note regarding ClF_3 as an alternative to BrF_5 for oxygen isotope analysis. Geochim Cosmochim Acta **46** 1665-1668

Bottinga, Y (1994) Non-Newtonian rheologies of homogeneous silicate melts. Phys Chem Min **20** 454-459

Bottinga, Y, Weill, DF, Richet, P (1982) Density calculations for silicate liquids 1. Revised method for aluminosilicate compositions. Geochim Cosmochim Acta **46** 909-919

Bowen, NL (1915) The crystallisation of haplobasaltic, haplodioritic and related magma. Am J Sci **40** 161-185

Boudreau, AE (1987) Pattern formation during crystallisation and the formation of fine-scale layering. In: Parsons, I (Ed) Origins of Igneous Layering. NATO ASI Series C196, D. Reidel Publishing Company, Dordrecht 453-471

Brandeis, G and Jaupart, C and Allègre, CJ (1984) Nucleation, crystal growth and the thermal regime of cooling magmas. J Geophys Res **89 (B12)** 10161-10177

Brooks, CK (1976) The Fe_2O_3/FeO ratio of basalt analyses: an appeal for a standard used procedure. Bull. Geol. Soc. Den. **25** 117-120

Brown, WL, Becker, SM and Parsons, I (1983) Cryptoperthites and cooling rate in a layered syenite pluton: A chemical and TEM study. Contr Miner Petrol **82** 13-25

Brown, WL and Parsons, I (1994) Feldspars in igneous rocks. In Parsons, I (Ed) Feldspars and their reaction. NATO ASI Series C421, D. Kulwer Academic publishers 449-499

Buddington, AF and Lindsley, DH (1964) Iron-titanium oxide minerals and synthetic equivalents. J Petrology **5** 310-357

Butterfield, AW (1980) Geology of the Western part of the Nunarssuit alkaline complex of south Greenland. Unpubl PhD thesis, University of Aberdeen.

Campbell, IH (1978) Some problems with the cumulus theory. Lithos **11** 311-323

Carrigan, CR (1988) Biot number and thermos bottle effect: Implications for magma-chamber convection. Geology **16** 771-774

Cashman, KV (1990) Textural constrains on the kinematics of crystallisation in igneous rocks. In: Nicholls, J and Russell, JK (Eds) Modern methods of igneous petrology: Understanding magmatic processes. Min Soc Am Reviews in Mineralogy **24** 259-313

Cashman, KV and Ferry, JM (1988) Crystal size distribution in rocks and the kinetics and dynamics of crystallisation III. Metamorphic crystallisation. Cont Min. Pet. **99** 401-415

Cashman, KV and Marsh, BD (1988) Crystal size distribution in rocks and the kinetics and dynamics of crystallisation II. Igneous crystallisation. Cont Min. Pet. **99** 292-305

Conrad, ME and Naslund, HR (1989) Modally-Graded Rhythmic Layering in the Skaergaard Intrusion. J Pet **30** 251-269

Cox, KG and Mitchell, C (1988) The importance of crystal settling in the differentiation of Deccan Trap basaltic magmas. Nature **333** 447-449

Dachs, E (1994). Annite stability revised. 1. Hydrogen-sensor data for the reaction annite = sanidine+magnetite+H_2. Cont Min Pet, **117**, 229-240.

Darwin, C (1844) Geological observations on the Volcanic islands, visited during the voyage of H.M.S. Beagle, together with some brief notices on the geology of Australia and the Cape of Good Hope. Being the second part of the geology of the Beagle, under the command of Capt. Fitzroy, R.N. during the years 1832 to 1836. Smith, Elder, London 175pp

De St. Jorre, L and Smith, DGW (1988) Cathodoluminescent gallium-enriched feldspars from the Thor Lake rare-metal deposit, Northwest Territories. Can. Mineral. **26**, 301-308

Deer, WA, Howie, RA and Zussman, J (1966) An introduction to the rock-forming minerals. Longman 528pp

Dingwell, DB , Scarfe, CM and Cronin DJ (1985) The effect of F on viscosities in the system Na_2O - Al_2O_3 - SiO_2. Am Miner **70** 80-87

Droop, GTR (1987) A general equation for estimating Fe^{3+} concentrations in ferromagnesian silicates and oxides from microprobe analyses, using stoichiometric criteria. Miner Mag **45** 201-9

Einsele G (1992) Sedimentary Basins. Springer Verlag 628pp

Emeleus, CH and Upton, BGJ (1976) The Gardar Period in southern Greenland. In: Escher and Watt (Eds) The Geology of Greenland. Gronl. Geol. Unders., Copenhagen 153-181

Evans, AM (1980) An introduction to ore geology (2nd edition). Blackwells Scientific Publications. 358pp

Ferguson, J and Pulvertaft, TCR (1963) Contrasted styles of igneous layering in the Gardar province of South Greenland. Min Soc Am Spec Pap **1** 10-21

Finch, AA (1990) The chemical and isotopic nature of fluids associated with alkaline magmatism, South Greenland. Unpubl PhD thesis, University of Edinburgh

Finch, AA and Walker, FDL (1991) Cathodoluminescence and microporosity in alkali feldspars from the Blue Moon Perthosite, S Greenland. Miner Mag **55** 585-589

Fitton, JG and Dunlop, HM (1985) The Cameroon line, W Africa, and its bearing on the origin of oceanic and continental alkali basalts. Earth Planet Sci Lett **72** 23-38

Fitton, JG, James, DE, and Thirlwall, MF (1984) A user's guide to the X-ray fluorescence analysis of rock samples. Unpubl. report, Univ of Edin (2nd Ed.)

Flink, G (1898) Berättelse om en mineralogiske Resa i Syd-Grønland 1897. Meddr om Grønland **14** 221-262

Frey, FA, Green, DH and Roy, SD (1978) Integrated models of basalt petrogenesis: a study of quartz tholeiites from south-east Australia utilising geochemical and experimental data. J Petrol. **19** 463-573

Gay, EC, Nelson, PA, Armstrong, WP (1969) Flow properties of suspensions with high solids concentrations. Am Inst Ch Eng J **15** 815-822

Geake, JE, Walker, G, Tefler, DJ and Mills, AA (1977) The cause and significance of luminescence in lunar plagioclase. Phil. Trans. Roy. Soc. Lond. **A285** 403-408

Giesecke, KL (1910) Karl Ludwig Gieseckes mineralogisches Rejsejournal über Grønland 1806-13 Meddr om Grønland **35** 532pp

Gilbert, MC, Heltz RT, Popp, RK and Spear, FS (1982) Experimental studies of amphibole stability. In: Veblen, DR and Ribbe, PH, (Eds) Amphiboles: Petrography and phase relationships, Am Min Soc Reviews in Mineralogy **9B** 229-346

Giret, A, Bonin, B and Leger, J-M (1980) Amphibole compositional trends in over-saturated and under-saturated alkaline plutonic ring complexes. Can Min. **18** 481-495

Grassberger, P and Procaccia, I (1983) Measuring the Strangeness of Strange Attractors. Phys. **D9**, 189-208

Harker, A (1908) The geology of the small isles of Inverness-shire (Sheet 60, Rhum, Canna, Eigg, Muck etc.). Memoir, Geological Survey of Scotland, Edinburgh, HMSO.

Harry, WT and Pulvertaft, TCR (1963) The Nunarssuit intrusive complex, S Greenland. Bull. Grønland geol. Unders. **36**

Harte, B, Hunter, RH and Kinney, PD (1993) Melt geometry, movement and crystallisation in relation to mantle dykes, veins and metasomatism. Phil Trans Roy Soc: Phys Sci Eng **342** 1-21

Helz RT (1993) Factors affecting the settling and aggregation of olivine in Kilauea Iki lava lake: Why is there no dunite layer? Conference abstract, Symposium on layering in igneous complexes, Johannesburg, South Africa

Henderson, P (1982) Inorganic geochemistry. Pergamon Press

Henderson, P, Nolan, J, Cunningham, GC and Lowry, RK (1985) Structural controls and mechanisms of diffusion in natural silicate melt. Contr Miner Petrol **89** 263-272

Hess, PC (1980) Polymerisation model for silicate melts. In: Hargraves, RB (Ed) Physics of magmatic processes. Princeton Univ Press 3-44

Hewitt, AD and Wones, DR (1984) Experimental relations in the micas. In: Bailey, SW (Ed) Micas, Am Min Soc Reviews in Mineralogy **13** 201-247

Higgins, MD (1991) The origin of laminated and massive anorthosites, Sept Iles layered intrusion, Quebec, Canada. Contr Miner Petrol **106** 340-354

Hort, M, Marsh, BD and Spohn, T (1993) An oscillatory nucleation model for igneous layering. Contr Miner Petrol **114** 425-440

Hort, M and Spohn, T (1991) Crystallisation calculations for a binary melt cooling at constant rats of heat removal: Implications for the crystallisation of magma bodies. Earth Planet Sci Lett **107** 463-474

Hunter, RH, (1987) Textural equilibrium in layered igneous rocks. In: Parsons, I (Ed) Origins of Igneous Layering. NATO ASI Series C196, D. Reidel Publishing Company, Dordrecht 453-471

Hunter, RH, (1993) Cumulate texture and physical process. Conference abstract, Symposium on layering in igneous complexes, Johannesburg, South Africa

Huppert, HE (1982) Flow and instability of a viscous current down a slope. Nature **300** 427-429

Huppert, HE and Sparks, RSJ (1980) The fluid dynamics of a magma chamber replenished by an influx of hot dense ultrabasic magma. Cont. Min. Pet. **75** 279-289

Irvine, TN (1978) Density current structure and magmatic sedimentation. Carnegie Institute of Washington Yearbook, **77** 717-725.

Irvine, TN (1980) Magmatic density currents and cumulus processes. Am J Sci, **280A** 1-58

Irvine, TN (1982) Terminology for layered intrusions. J Pet **23** 127-162

Irvine, TN (1987a) Layering and related structures in the Duke Island and Skaergaard intrusion: similarities, differences and origins. In: Parsons, I (Ed) Origins of Igneous Layering. NATO ASI Series C196, D. Reidel Publishing Company, Dordrecht 185-245

Irvine, TN (1987b) Processes involved in the formation and development of layered igneous rocks. Appendix II. In: Parsons, I (Ed) Origins of Igneous Layering. NATO ASI Series C196, D. Reidel Publishing Company, Dordrecht 649-656

Irvine, TN and Smith, CH (1967) The ultramafic rocks of the Muskox intrusion, Northwest Territories, Canada. In: Wyllie, PJ (Ed) Ultramafic and related rocks, New York, John Wylie and Sons 38-49

Irving, JA and Frey, FA (1984) Trace element abundance's in megacrysts and their host basalts: Constraints on partition coefficients and megacryst genesis. Geochim. Cosmochim. Acta **48** 1201-1221

Jackson ,ED (1961) Primary textures and Mineral associations in the ultramafic zone of the Stillwater Complex, Montana. U.S. Geol Surv Prof Paper **358** 106pp

Jurewicz, AJG and Watson, EB (1988) Cations in olivine. Part 1: Calcium partitioning between olivines and co-existing melts, with petrologic applications. Contr Miner Petrol **99** 176-185

Kawasaki, T and Ito, E (1993) Fe-Mg partitioning between olivine and Ca-rich clinopyroxene: Implications for Fe-Mg mixing properties of Ca-rich clinopyroxene. Technical report of ISEI SerA No **54** 50pp

Kerr, RC and Lister, JP (1991) The effects of shape on crystal settling and on the rheology of magmas J Geol **99** 457-467

Kirkpatrick, RJ (1981) Kinetics of crystallisation of igneous rocks. In: Lasaga, AC and Kirkpatrick, RJ (Eds) Kinetics of geochemical processes, Min. Soc. Am. Reviews in Mineralogy **8** 321-398

Komar, PD and Reimers, CE (1978) Grain shape effects on settling rates. J Geol **86** 193-209

Krishnamurthi, R (1970) On the transition to turbulent convection. Pt 2. The transition to time-dependent flow. J Fluid Mech **42** 309-320

Larsen, LM, (1976) Clinopyroxene and coexisting mafic minerals from Ilímaussaq intrusion, South Greenland. J Petrology **17** 258-290

Larsen, LM, and Sørensen, H (1987) The Ilímaussaq intrusion: Progressive crystallisation and formation of layering in agpaitic magma. In Fitton, JG and Upton, BGJ (Eds) The alkali rocks. Geol Soc Spec Publ **30** 473-488

Leake, BE (1978) Nomenclature of amphiboles. Can Min **16** 501-520

Lemarchand, F, Villemant, B and Calas, G (1987) Trace element distribution coefficients in alkaline series. Geochim. Cosmochim. Acta **51** 1071-1081

Lindsley, DH and Munoz, JL (1969) Subsolidus relations along the join hedenbergite-ferrosilite. Am J Sci **267-A (Schairer volume)** 295-324

Lu, F-Q Smith, JV, Sutton, SR, Rivers, ML and Davis, AM (1989) Synchrotron XRF analysis of rock forming minerals. Chem Geol **75** 123-143

Mahood, GA and Stimac, JA (1990) Trace element partitioning in pantellerites and trachytes. Geochim Cosmochim Acta **54** 2257-2276

Marsh, BD (1988) Crystal size distribution in rocks and the kinetics and dynamics of crystallisation I : Theory. Contr Miner Petrol **99** 277-291

Marsh, BD and Maxey (1985) On the distribution and separation of crystals in a convecting magma. J Volc Geoth Res **24** 94-150

Martin, AR (1985) The evolution of the Tugtutôq-Ilímaussaq dyke swarm, SW Greenland. Unpubl PhD thesis, University of Edinburgh

Martin, D and Nokes, R (1989) A fluid dynamical study of crystal settling in convecting magmas. J Petrology **30** 1-30

Mason, RA (1992) Models of order and Fe - F avoidance in biotite. Can Min **30** 343-354

Mazurin, OV (1986) Glass relaxation. J Non-cryst solids **87** 392-407

McBirney, AR (1984) Igneous petrology. OUP 504pp

McBirney, AR (1987) Constitutional Zone Refining of Layered Intrusions. In: Parsons, I (Ed) Origins of Igneous Layering. NATO ASI Series C196, D. Reidel Publishing Company, Dordrecht: 437-452

McBirney, AR and Noyes, RM (1979) Crystallisation and layering of the Skaergaard Intrusion. J. Pet **20** 487-554

McDowell, SD and Wyllie, PJ (1971) Experimental studies of igneous rock series: The Kûngnât syenite complex of Southwest Greenland. J Geol **79** 173-194

McNown, JS and Malaika, M (1950) Effects of particle size on settling velocities at low Reynolds numbers. Trans AGU **31** 74-82

Middlemost, EAK (1985) Magmas and magmatic rocks: An introduction to igneous petrology. London Longman 266pp

Miller, J (1988) Cathodoluminescence microscopy. In: Tucker, M (Ed) Techniques in sedimentology. Blackwells Scientific Publications 174-190

Mingard, S (1990) Crystallisation and Layering of the Younger Giant Dyke Complex, SW Greenland. Unpubl PhD thesis, University of Edinburgh

Mitchell, RH (1990) A review of the compositional variation of amphiboles in alkaline plutonic complexes. Lithos **26** 135-156

Mysen, BO (1987) Magmatic silicate melts: Relations between bulk composition, structure and properties. In: Mysen, BO (Ed) Magmatic processes: Physiochemical Principles. The Geochemical society Spec. Publ **1** 375-399

Mysen, BO and Virgo, D (1980) Trace element partitioning and melt structure: An experimental study at 1atm pressure. Geochim & Cosmochim Acta **44** 1917-1930

Naney, MT and Swanson, SE (1980) The effect of Fe and Mg on crystallisation in granite systems. Am Miner **65** 639-653

Naslund, HR, Conrad, ME, Urquhart and Turner, JS (1986) Computer simulations of apparent grain size in thin section, application to grain size variation in the Skaergaard Intrusion. (Abstract) EOS **67** 384

Nekvasil, H (1992) Ternary feldspar crystallisation in high temperature felsic magma. Am Miner **77** 592-604

Norton, G (1992) Silicate Rheology. Unpublished PhD thesis, University of Lancaster

Parsons, I (1979) The Klokken gabbro-syenite complex, S Greenland. Cryptic variation and origin of inversely graded layering. J Petrology **20** 653-694

Parsons, I (1980) Kspar and Fe-Ti oxide exsolution textures. Trans Royal Soc Edin: Earth Sci **71** 1-12

Parsons, I (1981) The Klokken gabbro-syenite complex, South Greenland: quantitative interpretation of mineral chemistry. J Pet **22** 233-260

Parsons, I (1987) Origins of igneous layering. NATO ASI series C **196**. D. Reidel Publishing Company, Dordrecht pp666

Parsons, I and Becker, SM (1987) Layering, compaction and post-magmatic processes in the Klokken Intrusion. In: Parsons, I (Ed) Origins of Igneous Layering. NATO ASI Series C196, D. Reidel Publishing Company, Dordrecht 29-92

Parsons, I and Brown, WL (1984) Feldspars and the thermal history of igneous rocks. In: Brown, WL (Ed) Feldspars and Feldspathoids. NATO ASI Series C137, D. Reidel Publishing Company, Dordrecht 317-371

Parsons, I and Brown, WL (1988) Sidewall crystallisation in the Klokken intrusion: zoned ternary feldspars and co-existing minerals. Contr Miner Petrol **98** 431-443

Parsons, I and Butterfield, AW (1981) Sedimentary features of Nunarssuit and Klokken syenites, S Greenland. J Geol Soc Lond **138** 289-306

Parsons, I, Mason, RA, Becker, SM and Finch, AA (1991) Biotite equilibria and fluid circulation in the Klokken stock, South Greenland. J Pet **32** 1299-1333

Pearce, JA and Norry, MJ (1979) Petrogenetic implications of Ti, Zr, Y and Nb variations in volcanic rocks. Contr Miner Petrol **69** 33-47

Pearce, TH (1994) Recent work on oscillatory zoning in plagioclase. In: Parsons, I (Ed) NATO ASI Series C421, D. Kulwer Academic publishers 313-349

Petersen, JS (1987) Solidification contraction: Another approach to cumulus processes and the origin of igneous layering. In: Parsons, I (Ed) Origins of Igneous Layering. NATO ASI Series C196, D. Reidel Publishing Company, Dordrecht 505-526

Powell, M (1978) The crystallisation history of the Igdlerfigssalik nepheline syenite intrusion, Greenland. Lithos **11** 99-120

Powell, R and Powell, M (1974) An olvine-pyroxene geothermometer. Contr Miner Petrol **48** 249-263

Rae, DA (1988) Metasomatism associated with the North Qôroq centre, Igaliko complex, South Greenland. Unpubl PhD thesis, University of Aston

Rae, DA and Chambers, AD (1988) Metasomatism in the North Qôroq centre, South Greenland: cathodoluminescence and mineral chemistry of alkali feldspars. Trans Roy. Soc. Edin.: Earth Sci. **79** 1-12

Raedeke, LD and McCallum, IS (1984) Investigations in the Stillwater Complex: Part II. Petrology and petrogenesis of the Ultramafic Series. J Pet **25** 395-420

Renner, R (1989) Cooling and crystallisation of komatiite flows from Zimbabwe. Unpubl PhD thesis, University of Cambridge

Rice, A (1993) Dynamics of magma chambers. In Flow and creep in the solar system: Observations, modelling and theory. In: Soone, D and Runcorn, SW (Eds) Flow and Creep in the Solar System: Observations, Modelling and Theory. NATO ASI Series C391 Kulwer Academic Publishers 289-306

Scott, S (1992) Clocks and chaos in chemistry. In The New Scientist guide to chaos, Hall, N (Ed). Penguin, 108-121

Shaw, HR (1972) Viscosities of magmatic silicate liquids: An empirical method of prediction. Am. J. Sci. **272** 870-893

Simkin, T and Smith, JV (1970) Minor element distribution in olivine. J Geol **78** 304-325

Smith, JV and Brown WL (1988) Feldspar minerals vol. 1. Springer-Berlin Heidelberg NY 828pp

Sørenson, H and Larsen, LM, (1987) Layering in the Ilímaussaq Intrusion, South Greenland. In: Parsons, I (Ed) Origins of Igneous Layering. NATO ASI Series C196, D. Reidel Publishing Company, Dordrecht 1-28

Sparks, RSJ and Huppert, HE (1984) Density changes during the fractional crystallisation of basaltic magmas: fluid dynamic implications. Contr Mineral Petrol **85** 300-304

Sparks, RSJ, Huppert, HE, Kerr, RC, McKenzie, DP and Tait, SR (1985) Postcumulus processes in layered intrusions. Geol. Mag. **122** 558-568

Sparks, RSJ, Huppert, HE, Koyaguchi, T and Hallworth, MA (1993) Origin of modal and rhythmic igneous layering by sedimentation in a convecting magma chamber. Nature **361** 246-249

Sparks, RSJ, Huppert, HE and Turner, JS (1984) The fluid dynamics of evolving magma chambers. Phil Trans R Soc Lond A **310** 511-34

Speer, JA (1982) Zircon. In: Ribbe, PH (Ed) Orthosilicates, Min Soc Am Reviews in Mineralogy **5** 67-112

Spera, FJ, Borgia, A, Strimple, J and Feigenson, M (1988) Rheology of melts and magmatic suspensions 1. Design and calibration of a concentric cylinder viscometer with application to rhyolitic magma. J Geophys Res **93** 10273-10294

Steenstrup, KJV (1881) Bemärkninger til et geognostisk Oversigtskaart over en Del af Julianeshaabs Disrtikt i 1876. Meddr om Grønland **2** 27-41

Stephenson, D and Upton, BGJ (1982) Ferromagnesian silicates in a differentiated alkaline complex: Kungnat Fjeld, South Greenland. Min. Mag. **46** 283-300

Stow, AD (1986) Deep clastic seas. In Reading, HG (Ed) Sedimentary Environments. and Facies Ed. Blackwells Scientific Publications 399-444

Tsonis, AA (1992) Chaos: From theory to application. Plenum Press 274pp

Tucker, ME (1981) Sedimentary petrology: An introduction. Blackwells scientific publications 252pp

Turner, JS and Campbell, IH (1986) Convection and mixing in magma chambers. Earth Science Reviews **23** 255-352

Upton, BGJ (1960) The alkaline igneous complex of Kûngnât Fjeld, South Greenland. Grøn. Geol. Und. Rap **123**

Upton, BGJ (1961) Textural features of some contrasted igneous cumulates from South Greenland. Grøn. Geol. Und. Rap **123**

Upton, BGJ (1974) The alkali province of SW Greenland. In: Sørensen, H (Ed) The Alkaline Rocks. Wiley, New York 221-238

Upton, BGJ and Emeleus, CH (1987) Mid-Proterozoic alkaline magmatism in S Greenland: The Gardar Province. In: Fitton, JG and Upton, BGJ (Eds) Alkaline igneous rocks. Geol Soc Spec Publ **30** 449-471

Upton, BGJ and Fitton, JG (1985) Gardar dykes north of the Igaliko syenite complex, S Greenland. Grøn. Geol. Und. Rap **127**

Upton, BGJ, Martin, AR and Stephenson, D (1990) Evolution of the Tugtutôq Central Complex, S Greenland: A high-level, rift axial, late-Gardar centre. J Volc Geoth Res **43** 195-214

Upton, BGJ, Thomas, JĖ and MacDonald, R (1971) Chemical variation within three alkaline complexes in S Greenland. Lithos **4** 163-164

Upton, BGJ, Emeleus, CH, Parsons, I and Hodson, ME (in preparation) Layering phenomena in alkaline igneous rocks of the Gardar province, South Greenland.

Ussing, NV (1912) Geology of the country around Julianehaab, Greenland. Meddr Grønland **38**

Wadsworth, WJ (1973) Magmatic Sediments. Minerals Sci. Eng. **5** 25-35

Wager, LR (1959) Differing powers of Crystal Nucleation as a Factor Producing Diversity in Layered Igneous Intrusions. Geol. Mag. **96** 75-80

Wager, LR and Brown, GM (1968) Layered Igneous Rocks. Oliver and Boyd, Edinburgh 588pp

Walker, FDL (1991) Micropores in alkali feldspars. Unpubl PhD thesis, University of Edinburgh

Wang, Y and Merino, E (1993) Magma Crystallisation by feedback between the concentrations of the reactant species and mineral growth rates. J Petrol **34** 369-382

Wegmann, CE (1938) Geological investigations in South Greenland. Part 1. On the structural divisions of South Greenland. Meddr om Grønland **113** (2) 149pp

Wilson, AH (1982) The geology of the Great Dyke, Zimbabwe: The ultramafic rocks. J Pet **23** 240-292

Wilson, JR and Larsen, SB (1982) Discordant layering relations in the Fongen-Hyllingen basic intrusion. Nature **299** 625-6

Wilson, JR and Larsen, SB (1985) Two dimensional study of a layered intrusion: the Hyllingen Series, Norway. Geol Mag **122** 97-124

Wilson, JR, Menuge, JF and Pedersen, S (1987) The southern part of the Fongen-Hyllingen layered mafic complex, Norway: Emplacement and crystallisation of compositionally stratified magma. In: Parsons, I (Ed) Origins of Igneous Layering. NATO ASI Series C196, D. Reidel Publishing Company, Dordrecht 145-184

Winick, H (1987) Synchrotron radiation. Sci Am **257** 72-81

Wolf, MB and Wyllie, PJ (1986) Crystal settling in hydrous syenite melt at 15kbar. Abstract for Geol Soc. Am. Cordilleran Section, 82nd annual meeting. Abstract with programs Geol. Soc. Am. **18**, pp200

Worden, RH, Walker, FDL, Parsons, I and Brown, WL (1990) Development of microporosity, diffusion channels and deuteric coarsening in perthitic alkali feldspar. Contr Miner Petrol **104** 507-515

Wörner, G, Beusen, J-M, Duchateau, N, Gijbels, R and Schmincke, H-U (1983) Trace element abundance's and mineral/melt distribution coefficients in phonolites from the Laacher See Volcano (Germany) Contr Miner Petrol **84** 152-173

Worster, MG, Huppert, HE and Sparks, RSJ (1990) Convection and crystallisation in magma cooled from above. Earth Planet Sci Lett **101** 78-89

Yoder, HS, Tilley, CE and Schairer, JF (1963) Pyroxenes and associated minerals in the crust and mantle. Carnegie Institute Yearbook **62**, 84-95

Appendices

Appendix A: Sample localities

Abbreviations:

t = examined in thin section, p = electron probed, c = point counted, s = grain size analysed, i = oxygen isotope analysis of feldspars, l = cathodoluminescence, x = XRF, X = synchrotron XRF microprobe

1:1 Nunarssuit

Sample	Locality	Unit	Description	
1	DL 1	4	Leucocratic syenite in layer below 2	p,t,
2-7			Alternate melanocratic bases of rhythms and over lying leucocratic tops of rhythms all below melanocratic trough	p,t
8-12			Melanocratic syenite in trough	p,t,x
13			Leucocratic syenite to side of trough	
14			Leucocratic syenite above trough	
15-28	DL2	7	Alternate melanocratic bases of rhythms and over lying leucocratic tops of rhythms. Sample 2-28 is of a melanocratic trough (first sample is from leucocratic top).	i,p,t,X
29	DL 3	8	Leucocratic syenite below trough	l,p,t
30			Melanocratic within trough	

31-36	DL 4	8	Alternate melanocratic bases, "normal" middles, and leucocratic tops of zebra layers.	i,l,p,t
38	DL 5	2	Leucocratic syenite below first layer	l,p,t,l
39			Melanocratic syenite at base of first layer	
40			Leucocratic syenite at top of first layer	
41-44	DL 6	2/3	Alternate melanocratic bases and over-lying leucocratic tops of rhythms	l,c,p,s,t,x
45-48	DL 7	3	Alternate melanocratic bases and over-lying leucocratic tops of rhythms	c,i,p,t,x,X
49-52	DL 8	3	Alternate melanocratic bases and over-lying leucocratic tops of rhythms	c,i,l,p,s,t,X
53	DL 9	5	Leucocratic syenite below thick melanocratic layer	c,i,l,p,s,t,x,X
54			Melanocratic syenite form thick layer	
55			Leucocratic syenite below thick melanocratic layer	
56			Melanocratic syenite from thick layer	
57			Melanocratic syenite autolith	

58-61			Melanocratic syenite form thick layer	
62-67	DL 10	7	Alternate melanocratic bases and over-lying leucocratic tops of rhythms	c,l,p,s,t,x,X
68-69	DL 11	4	Melanocratic syenite autoliths	c,i,l,p,t,x
MH-NUN-92 1		10	Melanocratic syenite autolith	p,t,x,X
MH-NUN-92 2		8	Melanocratic syenite	
MH-NUN-92 3		10	Metabasite xenolith	x
MH-NUN-92 4		10	Melanocratic syenite autolith	i,p,t,x
MH-NUN-92 5	DL 3	8	Melanocratic syenite in trough	x
MH-NUN-92 6	DL 4	8	Melanocratic syenite in trough	x
MH-NUN-92 7	DL 4	8	Melanocratic syenite in trough	
MH-NUN-92 8	DL 4	8	Leucocratic syenite just above trough	
MH-NUN-92 9		1	Leucocratic syenite	c,l,p,s,t,x,X
MH-NUN-92 10-13		2	Leucocratic syenite	i
MH-NUN-92 14	DL 6	2/3	Leucocratic syenite	i,x
MH-NUN-92 15	DL 11	4	Leucocratic syenite between autoliths	i,p
MH-NUN-92 16		9	Leucocratic syenite	i,x
MH-NUN-92 20		10	Slightly melanocratic base of rhythm	p
MH-NUN-92 21		10	Slightly melanocratic base of rhythm	p,X

1:2: West Kûngnât

Sample	Locality	Unit	Description	
100	12	3	Leucocratic unlayered syenite	
101-105	13	3	Alternate melanocratic bases and over-lying leucocratic tops of	c,l,p,s,t,x,X

			rhythms	
106	14	3	Leucocratic syenite below 107	c,l,p,s,t
107-112	14	3	Alternate melanocratic bases and over-lying leucocratic tops of rhythms	c,l,p,t,X
113-124	15	4	Alternate melanocratic bases and over-lying leucocratic tops of rhythms	c,l,p,s,t,X
125-130	16	4	Alternate melanocratic bases and over-lying leucocratic tops of rhythms	c,p,t
131-136	17	4	Alternate melanocratic bases and over-lying leucocratic tops of rhythms	c,l,p,t,X
137-141	18	4	Alternate melanocratic bases and over-lying leucocratic tops of rhythms	c,l,p,s,t,x,X
MH-KUN-92 22	15	4	Graded layer	
MH-KUN-92 23	Trough stacks	2	Melanocratic syenite in T1:1	c,p,t,x
MH-KUN-92 24	Trough stacks	2	Leucocratic host syenite next to T1:1	c,p,t,x
MH-KUN-92 25	Trough stacks	2	Melanocratic syenite in T1:1	c,p,t,x
MH-KUN-92 26	Trough stacks	2	Melanocratic syenite in T1:2	c,p,t,x,X
MH-KUN-92 27	Trough stacks	2	Leucocratic host syenite next to T1:2	p,t,x
MH-KUN-92 28	Trough stacks	2	Melanocratic syenite in T2:4	p,t,x
MH-KUN-92 29	Trough stacks	2	Leucocratic host syenite next to T2:5	p,st,,x
MH-KUN-92 30	Trough stacks	2	Melanocratic syenite in T2:5	c,p,s,t,x,X
MH-KUN-92 31	Trough stacks	2	Host syenite between T2:5 and T2:6	c,p,s,t,x,X

MH-KUN-92 32	Trough stacks	2	Melanocratic syenite in T2:4	p,t,x
MH-KUN-92 33	Trough stacks	2	Host syenite between T2:4 and T2:5	c,p,t,x
MH-KUN-92 34	Trough stacks	2	Leucocratic host syenite next to T2:3	p,t,x
MH-KUN-92 35	Trough stacks	2	Melanocratic syenite in T2:3	p,s,t,x
MH-KUN-92 36	Trough stacks	2	Leucocratic syenite above trough stacks	c,p,s,t,x,X
MH-KUN-92 37	920m ridge	5	Melanocratic base to rhythm	
MH-KUN-92 38		1	Homogeneous marginal syenite	p,t,x
MH-KUN-92 39		1	Homogeneous marginal syenite	p,t,x
MH-KUN-92 40		1	Trachyte back-veined by syenite (not *in situ*)	
MH-KUN-92 41		1	Homogeneous marginal syenite	

Appendix B: Analytical techniques

B.1: Electron microprobe

Mineral analyses were made on a Cameca Camebax Microbeam electron probe at the University of Edinburgh. WDS analyses used a spot beam (apart from feldspar analyses which were rastered over an area of $100\mu m^2$), an accelerating voltage of 20kV and a beam current of 20nA. Count times were 30 seconds on the peak and 10 seconds on the background. PAP corrections were applied according to the method of Pichou and Pichet (unpubl.). Standards and crystals used for analysis are given in Table B.1.

Table B.1: Standards used and crystals used to read elements. PET = penta eurythritol, LIF = Lithium fluoride, TAP = Thallium acid phthalate

Element	Standard	Crystal
F	Magnesium fluoride	TAP
Na	Jadeite	TAP
Mg	Periclase	TAP
Al	Corundum	TAP
Si	Wollastonite	TAP
Cl	Halite	PET
K	Orthoclase	PET
Ca	Wollastonite	PET
Ti	Rutile	PET
Cr	Metal	PET/LIF
Mn	Metal	LIF
Fe	Metal	LIF
Ba	Baryte	PET
V	Metal	LIF
P	Apatite	PET
Ce	Glass	LIF/PET
Pr	Glass	LIF
Nd	Glass	LIF
La	Glass	LIF/PET

Analytical precision and detection limits can be calculated from a single analysis using the equations:

$$2\sigma = \frac{2W}{\sqrt{T_p}(\sqrt{R_p} - \sqrt{R_b})} \quad \ldots.(1)$$

$$\text{det.lim.} = \frac{3W\sqrt{R_b}}{R_p\sqrt{T_b}} \quad \ldots (2)$$

Where: T_p = peak count time

T_b = background count time

R_p = peak count rate

R_b = background count rate

W = wt% element or oxide

These have been calculated for a representative analysis of each phase analysed, results are presented below.

	Olivine		
	Wt% Oxide	2σ	det. lim.
SiO_2	29.52	0.14	0.03
TiO_2	0.04	0.02	0.01
Al_2O_3	0.01	0.02	0.00
FeO	65.96	0.30	0.04
MnO	1.77	0.06	0.03
MgO	2.33	0.06	0.03
CaO	0.17	0.02	0.01
Total	99.76		

	Pyroxene		
	Wt% Oxide	2σ	det. lim.
SiO_2	48.37	0.17	0.03
TiO_2	0.74	0.03	0.02
Al_2O_3	0.60	0.03	0.02
FeO	25.13	0.20	0.04
MnO	0.68	0.05	0.03
MgO	3.43	0.06	0.02
CaO	20.42	0.11	0.02
Na_2O	0.53	0.04	0.03
Total	99.90		

	Biotite		
	Wt% Oxide	2σ	det. lim.
F	0.32	0.24	0.14
SiO_2	34.75	0.15	0.03
TiO_2	0.05	0.02	0.01
Al_2O_3	10.34	0.09	0.02
FeO	39.81	0.24	0.04
MnO	0.35	0.04	0.03
MgO	1.15	0.04	0.02
CaO	0.11	0.02	0.01
Na_2O	0.05	0.03	0.01
K_2O	8.60	0.08	0.02
Total	95.53		

	Amphibole		
	Wt% Oxide	2σ	det. lim.
F	0.17	0.37	0.08
SiO_2	43.06	0.16	0.03
TiO_2	1.33	0.02	0.01
Al_2O_3	6.15	0.07	0.02
FeO	27.93	0.79	0.45
MnO	0.40	0.04	0.03
MgO	4.88	0.04	0.01
CaO	10.24	0.08	0.02
Na_2O	2.11	0.07	0.03
K_2O	1.09	0.03	0.02
Total	97.36		

	Feldspar		
	Wt% Oxide	2σ	det. lim.
SiO_2	66.91	0.21	0.03
Al_2O_3	18.39	0.10	0.02
FeO	0.24	0.04	0.02
MgO	0.01	0.02	0.002
BaO	0.05	0.04	0.01
CaO	0.14	0.02	0.01
Na_2O	6.16	0.10	0.03
K_2O	7.51	0.08	0.02
Total	99.41		

	Magnetite		
	Wt% Oxide	2σ	det. lim.
SiO_2	0.07	0.03	0.01
TiO_2	7.23	0.20	0.07
Al_2O_3	0.53	0.04	0.02
FeO	85.50	0.37	0.05
MnO	0.26	0.04	0.03
MgO	0.02	0.03	0.004
Cr_2O_3	0.06	-0.17	0.02
V_2O_5	0.04	0.04	0.01
Total	93.71		

	Ilmenite		
	Wt% Oxide	2σ	det. lim.
SiO_2	0.02	0.02	0.03
TiO_2	0.10	0.02	0.01
Al_2O_3	44.49	0.28	0.05
FeO	0.01	0.03	0.05
MnO	52.93	0.51	0.08
MgO	1.49	0.07	0.04
Cr_2O_3	0.03	-0.09	0.08
V_2O_5	0.30	0.06	0.04
Total	99.37		

	Zircon		
	Wt% Oxide	2σ	det. lim.
SiO_2	33.00	0.15	0.04
Fe_2O_3	0.03	0.04	0.01
ZrO_2	65.32	1.00	0.25
HfO_2	0.93	0.15	0.08
P_2O_5	0.02	0.07	0.01
CaO	0.01	0.02	0.002
Al_2O_3	0.02	0.02	0.003
TiO_2	0.05	0.06	0.02
Ce_2O_3	0.02	0.06	0.002
La_2O_3	0.06	0.05	0.01
Nd_2O_3	0.001	0.08	0.0002
Y_2O_3	0.32	0.15	0.08
ThO_2	0.03	0.10	0.01
Total	99.81		

	Apatite		
	Wt% Oxide	2σ	det. lim.
SiO_2	0.45	0.03	0.02
FeO	0.16	0.04	0.02
Cl	0.01	0.03	0.002
F	3.16	0.65	0.39
P_2O_5	41.76	0.62	0.28
CaO	52.47	0.22	0.03
Na_2O	0.45	0.05	0.03
MnO	0.02	0.04	0.005
Ce_2O_3	1.41	0.18	0.11
La_2O_3	0.75	0.14	0.10
Nd_2O_3	0.72	0.13	0.08
Pr_2O_3	0.19	0.19	0.05
Total	103.53		

B.2: XRF microprobe

The XRF micro-probe was used in two modes, for trace element analysis and specifically for the quantitative analysis of rare earth elements. Most analyses were carried out using the former method since the latter had previously only been used to determine relative REE concentrations and was thus less certain to yield accurate and precise data. A brief study carried out on well characterised standards (Tables B.2 and B.3 below) shows that whilst the trace element data is probably accurate the XRF-microprobe is not sensitive enough to accurately analyse the low concentrations of REE present in the majority of phases. Full details of the operating conditions of the synchrotron XRF microprobe are not available, details may be obtained from either Lu *et al.* (1989) or Dr Mark Rivers, Beamline 26A, Brookhaven National Laboratory, Upton, New York, USA.

Analysis is as follows. A polished thin section of known thickness is prepared on a pure silica one inch round, a bonding agent such as araldite is used to stick the rock slice to the slide. The sample is placed in a lead lined room and is irradiated by a focused X-ray beam at room pressure. The X-ray source is a synchrotron which produces high quality X-rays. Details on the workings of synchrotrons may be found in Winick (1987). The sample is excited and emits X-rays. The X-rays given off by the sample are collected in a spectrometer, analysed by computer and displayed in the format of number of counts per second for wavelengths given off by different elements in the sample. Filters are placed between the sample and the spectrometer to absorb high intensity X-rays which would mask the other X-rays being emitted. A separate computer program is used to calculate the number of counts that a phase of a specified composition would yield under the same radiation and filtering conditions as the unknown phase, the thickness and density of the grain being analysed has to be taken into account as this influences the number of X-rays produced. The concentration of a given element is then calculated using the following formula:

$$ppmA = wt\%Fe.\frac{ctsA^{Actual}}{ctsFe^{Actual}}.\frac{ctsFe^{Predicted}}{ctsA^{Predicted}}.\frac{ppmA^{Predicted}}{ppmFe^{Predicted}}$$

where $ppmA$ = concentration of an element A

$ctsA^{Actual}$ = counts per second of a specific X-ray line given off by element A

$ctsFe^{Actual}$ = counts per second of a specific X-ray line given off by Fe

$ctsFe^{Predicted}$ = calculated number of counts per second of a specific X-ray given off by Fe in a phase which is the same as the one being analysed but is of stated composition, thickness and density

$ctsA^{Predicted}$ = calculated number of counts per second of a specific X-ray given off by A in a phase which is the same as the one being analysed but is of stated composition, thickness and density

$ppmA^{Predicted}$ = stated concentration of A in the theoretical phase used in calculations

$ppmFe^{Predicted}$ = stated concentration of Fe in the theoretical phase used in calculations

Precision has been quantitatively shown to be ±15% (M Rivers, pers comm.).

Comparison of XRF-microprobe analyses with ion-probe analyses of three standards (Table B.2) suggests that the analyses obtained were of a similar quality to ion-probe analyses.

Table B.2: Comparison of XRF-microprobe (XRFP) and ion-probe (IP) analyses (in ppm) of three well characterised standards. For all XRF analyses apart from Cr a 110 micron Al filter was placed between the sample and the detector to reduce the intensity of Fe Kα x-rays which tended to obscure the other high Z element x-rays. No analyses are presented for Ba or Sc. Sc x-rays have much the same wavelength as the Ca x-rays and are not resolvable. Similarly Ba x-rays are not resolvable from Ti x-rays. KH1 (pyroxene from Kilbourne Hole, Irving and Frey 1984), KH80A (amphibole from Kilbourne Hole, Irving and Frey 1984) and AZ192H (amphibole from Hoover Dam, no reference) ion-probe analyses are based on the average of at least 10 analyses.

		Zn	Ge	Rb	Sr	Y	Nb	Ta	Ni	Ga	Zr	Hf	Cr
KH1	XRFP	67	1	0	48	14	4	20	211	12	25	8	273
		70	3	2	41	13	4	15	220	13	23	5	270
	IP	-	-	e-8	45	12	0	-	-	-	27	1	295
KH80A	XRFP	49	-	14	625	24	26	8	151	26	99	4	38
		49	-	15	691	26	28	11	156	21	113	4	20
	IP	-		7	513	21	27	-	-	-	60	2	75
AZ192H	XRFP	49	-	10	589	20	24	10	133	16	89	4	20
		42	-	9	646	20	27	14	130	17	102	4	32
	IP	30	-	5	573	23	26	-	281	-	68	-	271

Quantitative analysis of REE had never been undertaken before. Two methods of analysis were carried out on the raw data of the number of counts per second of the X-rays emitted. The first method was as the above, the second used the ratio of (counts per second for the Lα X-ray/known concentration of REE) determined on a glass standard of known composition to calculate the concentration of a given element in a sample on the basis of the number of counts per second a specific X-ray line was yielding. The Lα line was used as this yielded results which were closest to those of the ion-probe. The results obtained using the second method are given in Table B.3

Table B.3: Comparison of REE analyses by XRF-microprobe (XRFP) and ion-probe (IP) for well characterised samples. KH1, KH80A, AZ195 as Table B.2 Durango-apatite (no reference).

		La	Ce	Nd	Pr	Sm	Eu	Gd
KH1	XRFP	28	40	42	52	-	-	-
	IP	2	6	7	1	3	1	3
KH80a	XRFP	-	-	29	0	34	0	0
	IP	6	18	18	3	5	2	6
AZ195	XRFP	-	42	21	39	22	-	-
	IP	9	27	21	-	-	-	-
Durango-apatite	XRFP	3000	4180	1500	484	509	-	590
	IP	4000	5000	1500	690	190	60	450

The analyses are closest for the apatite which has high concentrations of the REE. Perhaps the detection limits of the EDS xrf-probe were such that it was unable to perform accurate analyses for the pyroxene and amphiboles. Unfortunately due to time constraints on instrument use and the small size of apatite grains (for the most part smaller than the area of the beam) pyroxenes were concentrated on for REE analysis, the calculations which produced Table B.3 being carried out at a later time.

Detection limits.

Detection limits were calculated for the various elements analysed for in olivines, pyroxenes, feldspars, biotites and amphiboles. These are presented in Table B.4.
The detection limits of the probe are given by

Detection limit = actual concentration/(Area/MDL)

Area/MDL is a parameter that the probe produces for each X-ray line detected.

Detection limit in ppm	Phase				
	Feldspar	Pyroxene	Olivine	Amphibole	Biotite
Zn	3	5	6	6	7
Ge	5	3	4	5	5
Rb	20	7	10	10	14
Sr	30	10	10	10	14
Y	20	14	10	15	15
Nb	40	16	15	20	20
Mo	60	20	20	25	34
Ta	-	10	15	13	12
Ni	3	10	20	25	15
Cu	3	4	10	8	10
Ga	5	8	5	5	7
Zr	30	15	15	20	20
Hf	-	5	20	13	20
Ba	10	-	-	-	-

Table B.4. Average detection limits in ppm for elements analysed for on XRF-microprobe. Averages based on 15 analyses.

Problems interpreting the results obtained.

The main problem with the above results are the penetration of the X-ray beam into the sample. Unless the thickness of the grain being analysed is known it is not possible to say whether the beam has penetrated through the grain and into another one or not. Obviously this causes problems when interpreting data. In this study I felt that analyses of rims of grains were definitely unlikely to remain within a single grain whilst analyses towards the centre of grains were more likely to remain within a single grain.. Another problem is the novelty of some of the data, there are few published partition co-efficients available for the behaviour of the analysed elements in trachytic melts. The net result of the above problems is that whilst it is tempting to accept analyses for individual elements for a given phase which show a trend (e.g. decreasing Y levels in amphiboles up stratigraphy in West Kûngnât) it is not possible to categorically state that this is a primary magmatic trend in the phase of interest. If the analyses for one element are accepted as representing analyses of the grain of interest and not of a combination of the grain of interest and any grain(s) below it which may be penetrated by the beam then all elemental analyses for that grain must be accepted as being derived wholly from that grain. If all but one of the analysed elements show no trend one must resort to differences in compatability or mobility during weathering as an explaination. Since little relevant data is available for either of these two processes this is an unsatisfactory situation.

In the case of the trace element analyses Table B.2 shows that the XRF-microprobe is capable of producing analyses of a similar quality to the ion-probe. However the

standards analysed were mineral separates of known thickness and so the complicating factors of grain penetration and interference were avoided. In retrospect if the analyses were to be carried out again the author would first separate grains and make up mounts which were pure for a given phase.

The usefulness of the XRF-microprobe is limited by the problems of beam penetration. This problem is easily overcome by the preparation of mineral separates. Once this problem is overcome the XRF-microprobe appears to be able to produce analyses which are comparable to the ion-probe for a range of elements, particularly the transition metals which it is not possible to analyse using the ion-probe. Accurate REE analyses may also be produced provided that REE are present in levels higher than about 100ppm. Typical analyses are presented in Appendix C.

B.3: XRF whole-rock analysis

Whole-rock samples of fresh rock were crushed for XRF whole-rock analysis. Where possible 100g samples were crushed, because many samples were drill cores this was not always possible. Samples were always more than 50g in weight. Samples were crushed initially in a jaw crusher and then in a Tema tungsten carbide swing mill for one to three minutes to a grainsize of les than 200μm. Most samples were analysed for 10 major and 17 trace elements using a rhodium tube on a Philips PW1480 X-Ray fluorescence spectrometer. Some major element were determined with a chromium tube because the rhodium tube broke. Analysis of in house standards showed that this made no difference to accuracy or precision. Fused discs were prepared from samples to measure major elements, Johnson Matthey Spectroflux 105 was used to assist fusing. Pressed powder pellets were prepared for trace element analysis. Preparation procedures are described in Fitton *et al.* (1984) and Fitton and Dunlop (1985).

Matrix corrections for trace elements were made using mass absorption coeffiecinets based on the major element analyses. USGS and CRPG rock standards (Abbey, 1980) were used to calibrate each element. Six separate glass discs were made for sample 7-45 to measure within sample variation, a single glass disc of sample 1-8 was analysed 6 times to measure machine precision. Mean and standard deviation (2 σ) of the results are given below together with standard error ($2\sigma/\sqrt{n}$) as a measure of accuracy.

Sample 1-8	Mean (n=6)	Standard deviation	Standard error
SiO_2	41.36	0.027	0.011
Al_2O_3	4.81	0.019	0.008
Fe_2O_3	38.46	0.052	0.021
MgO	2.27	0.016	0.007
CaO	7.52	0.004	0.002
Na_2O	1.67	0.025	0.001
K_2O	1.481	0.003	0.001
TiO_2	3.383	0.005	0.002
MnO	0.803	0.007	0.003
P_2O_5	0.660	0.005	0.002

Sample 7-46	Mean (n=6)	Standard deviation	Standard error
SiO_2	60.11	0.227	0.092
Al_2O_3	14.383	0.031	0.013
Fe_2O_3	9.73	0.060	0.0246
MgO	0.52	0.021	0.009
CaO	3.19	0.014	0.006
Na_2O	5.2	0.042	0.017
K_2O	4.98	0.035	0.014
TiO_2	1.18	0.014	0.006
MnO	0.15	0.007	0.003
P_2O_5	0.22	0.003	0.001

B.4: Oxygen isotopes

50 to 100g samples of fresh rock were crushed using a jaw crusher and Tema tungsten carbide swing-mill down to a grain size of <200μm. Samples were seived and the 180μm to 212μm fraction used for separation. Feldspar was separated from he other minerals by flotation in tetrabromoethane. Futher separation was carried out using a Franz electromagnetic separator. Thin sections of samples of the feldspar separate were made. The image analysis software of the Cameca electron probe was used to confirm that the samples were over 99% pure feldspar. No attempt was made to separate cloudy and clear feldspar as a previous study by A.A. Finch and F.D.L. Walker had shown that cloudy and clear feldspars from the same rock had indistinguishable oxygen isotopes.

Oxygen was extracted from the feldspars following the method of Borthwick and Harmon (1982). Sample sizes were 10-15μm and reaction with ClF_3 was carried out at 670°C overnight. $\delta^{18}O$ data relative to SMOW were determined by gas source mass spectrometry on the CO_2 produced after oxygen extraction. The mass spectrometer was a VG SIRA10 with a reference gas calibrated against international carbonate and silicate standards (NBS 19 and NBS 28).

Appendix C: Representative electron probe analyses

Typical electron probe analyses for phases from Nunarssuit and West Kûngnât are presented below. The number of oxygen ions per formula is assumed to be:

Pyroxene	6
Olivine	4
Feldspar	32
Biotite	22
Amphibole	23
Apatite	26
Ilmenite	6
Magnetite	32
Zircon	16

Nunarssuit: Typical pyroxene analyses

	Unit 1			Unit 2/3						
	MH-NUN-92 9			41			42			43
	Px 1	Px 2	Px 3	Px 1	Px 2	Px 3	Px 1	Px 2	Px 3	Px 1
Na2O	0.504	1.604	0.842	0.530	0.524	0.720	0.465	0.572	0.567	0.647
MgO	3.431	1.569	2.490	2.277	3.252	2.723	3.971	2.204	2.547	3.451
AL2O3	0.576	0.104	0.404	0.374	0.501	0.459	0.586	0.336	0.404	0.559
SiO2	47.823	48.444	48.024	48.531	48.698	48.978	48.914	48.061	48.516	48.643
K2O	0.010	0.004	0.005	0.000	0.001	0.001	0.017	0.000	0.012	0.005
CaO	20.133	19.203	19.653	19.769	20.083	19.944	20.154	19.600	19.862	20.076
TiO2	0.786	0.120	0.767	0.669	0.836	0.717	0.814	0.609	0.756	0.857
Cr2O3	0.022	0.010	0.022	0.000	0.009	0.009	0.000	0.015	0.007	0.003
MnO	0.690	0.665	0.660	0.622	0.657	0.649	0.662	0.622	0.673	0.637
FeO	25.778	28.267	27.136	27.319	25.842	26.512	24.863	27.359	26.888	24.889
Total	99.752	99.989	100.005	100.091	100.402	100.713	100.446	99.377	100.232	99.765
Na	0.040	0.128	0.067	0.042	0.041	0.056	0.036	0.046	0.045	0.051
Mg	0.208	0.096	0.152	0.138	0.196	0.164	0.238	0.135	0.154	0.208
Al	0.028	0.005	0.019	0.018	0.024	0.022	0.028	0.016	0.019	0.027
Si	1.949	1.992	1.963	1.978	1.966	1.976	1.964	1.976	1.972	1.969
K	0.001	0.000	0.000	0.000	0.000	0.000	0.001	0.000	0.001	0.000
Ca	0.879	0.846	0.861	0.863	0.869	0.862	0.867	0.864	0.865	0.871
Ti	0.024	0.004	0.024	0.021	0.025	0.022	0.025	0.019	0.023	0.026
Cr	0.001	0.000	0.001	0.000	0.000	0.000	0.000	0.000	0.000	0.000
Mn	0.024	0.023	0.023	0.021	0.022	0.022	0.023	0.022	0.023	0.022
Fe	0.879	0.972	0.928	0.931	0.873	0.895	0.835	0.941	0.914	0.843
Total cats.	4.032	4.066	4.037	4.013	4.016	4.019	4.016	4.019	4.017	4.016

			Unit 5							
			55			56			57	
	Px 2	Px 3	Px 1	Px 2	Px 4	Px 1	Px 2	Px 3	Px 1	Px 2
Na2O	1.057	0.993	0.593	0.597	0.613	0.527	0.561	0.488	0.559	0.592
MgO	2.625	3.293	3.641	3.658	3.359	3.431	3.446	3.208	3.315	3.371
AL2O3	0.457	0.544	0.641	0.516	0.561	0.601	0.618	0.442	0.550	0.605
SiO2	48.951	49.368	48.722	48.743	47.718	48.369	48.382	48.390	48.431	48.326
K2O	0.017	0.000	0.002	0.006	0.006	0.002	0.008	0.012	0.001	0.006
CaO	19.835	20.298	20.533	20.565	19.877	20.430	20.309	20.122	20.343	20.466
TiO2	0.712	0.616	0.642	0.606	1.159	0.744	0.849	0.664	0.687	0.726
Cr2O3	0.019	0.000	0.012	0.004	0.034	0.013	0.003	0.018	0.015	0.015
MnO	0.621	0.616	0.607	0.659	0.661	0.678	0.668	0.649	0.682	0.629
FeO	25.923	24.365	24.850	25.096	26.524	25.133	25.236	25.613	25.668	25.039
Total	100.217	100.093	100.243	100.450	100.513	99.927	100.079	99.606	100.251	99.785
Na	0.083	0.077	0.046	0.047	0.048	0.041	0.044	0.039	0.044	0.047
Mg	0.158	0.197	0.219	0.220	0.203	0.207	0.208	0.195	0.200	0.204
Al	0.022	0.026	0.030	0.024	0.027	0.029	0.029	0.021	0.026	0.029
Si	1.982	1.986	1.964	1.964	1.936	1.960	1.958	1.970	1.961	1.961
K	0.001	0.000	0.000	0.000	0.000	0.000	0.000	0.001	0.000	0.000
Ca	0.860	0.875	0.887	0.888	0.864	0.887	0.881	0.878	0.882	0.890
Ti	0.022	0.019	0.019	0.018	0.035	0.023	0.026	0.020	0.021	0.022
Cr	0.001	0.000	0.000	0.000	0.001	0.000	0.000	0.001	0.000	0.000
Mn	0.021	0.021	0.021	0.022	0.023	0.023	0.023	0.022	0.023	0.022
Fe	0.878	0.820	0.838	0.845	0.900	0.852	0.854	0.872	0.869	0.850
Total cats.	4.027	4.021	4.024	4.029	4.038	4.023	4.023	4.018	4.027	4.026

		58			59			60		
	Px 3	Px 1	Px 2	Px 3	Px 1	Px 2	Px 3	Px 1	Px 2	Px 3
Na2O	0.572	0.462	0.526	0.601	0.487	0.493	0.553	0.515	0.518	0.593
MgO	3.475	3.069	3.121	2.971	3.112	3.673	3.827	3.313	3.515	3.036
AL2O3	0.605	0.487	0.516	0.418	0.463	0.559	0.582	0.635	0.567	0.635
SiO2	48.525	48.414	48.593	48.803	48.283	48.602	48.944	48.484	48.824	48.728
K2O	0.002	0.000	0.000	0.001	0.000	0.007	0.001	0.011	0.005	0.000
CaO	20.438	20.227	20.241	20.094	20.175	20.235	21.037	20.193	20.342	20.444
TiO2	0.667	0.839	0.819	0.507	0.682	0.664	0.537	0.864	0.831	0.779
Cr2O3	0.006	0.020	0.000	0.006	0.016	0.019	0.019	0.023	0.006	0.006
MnO	0.638	0.652	0.691	0.635	0.686	0.648	0.652	0.620	0.600	0.655
FeO	25.289	26.108	25.906	26.287	25.963	25.344	24.272	25.473	24.928	25.401
Total	100.446	100.279	100.412	100.324	99.867	100.245	100.425	100.131	100.136	100.276
Na	0.045	0.036	0.041	0.047	0.038	0.039	0.043	0.040	0.040	0.046
Mg	0.209	0.185	0.188	0.179	0.189	0.221	0.229	0.200	0.211	0.183
Al	0.029	0.023	0.025	0.020	0.022	0.027	0.028	0.030	0.027	0.030
Si	1.961	1.962	1.964	1.976	1.965	1.962	1.966	1.961	1.969	1.968
K	0.000	0.000	0.000	0.000	0.000	0.000	0.000	0.001	0.000	0.000
Ca	0.885	0.878	0.877	0.872	0.880	0.875	0.905	0.875	0.879	0.885
Ti	0.020	0.026	0.025	0.015	0.021	0.020	0.016	0.026	0.025	0.024
Cr	0.000	0.001	0.000	0.000	0.001	0.001	0.001	0.001	0.000	0.000
Mn	0.022	0.022	0.024	0.022	0.024	0.022	0.022	0.021	0.021	0.022
Fe	0.855	0.885	0.876	0.890	0.883	0.856	0.815	0.862	0.841	0.858
Total cats.	4.055	4.018	4.019	4.022	4.022	4.023	4.025	4.017	4.013	4.016

	62			63			64			65
	Px 1	Px 2	Px 3	Px 1	Px 2	Px 3	Px 1	Px 2	Px 3	Px 1
Na2O	0.600	0.634	0.520	0.541	0.663	0.411	0.580	0.621	0.578	0.368
MgO	3.310	3.232	4.054	3.916	3.965	3.565	3.654	3.328	3.184	3.761
AL2O3	0.567	0.363	0.622	0.465	0.667	0.569	0.597	0.512	0.391	0.085
SiO2	48.349	48.698	48.501	48.694	48.581	48.287	48.356	48.476	48.634	49.528
K2O	0.004	0.000	0.012	0.000	0.001	0.007	0.013	0.007	0.006	0.007
CaO	20.028	19.818	20.156	20.077	19.753	20.074	20.105	20.032	19.776	22.249
TiO2	0.804	0.369	0.781	0.449	0.666	0.706	0.814	0.549	0.499	0.038
Cr2O3	0.012	0.023	0.000	0.010	0.023	0.020	0.007	0.000	0.018	0.007
MnO	0.582	0.589	0.630	0.593	0.700	0.648	0.585	0.611	0.612	0.624
FeO	25.377	26.272	24.541	24.656	24.613	25.442	24.828	25.583	26.254	23.535
Total	99.633	99.997	99.817	99.400	99.631	99.730	99.540	99.719	99.951	100.202
Na	0.047	0.050	0.041	0.043	0.052	0.032	0.046	0.049	0.046	0.029
Mg	0.200	0.196	0.244	0.237	0.239	0.216	0.221	0.202	0.193	0.225
Al	0.027	0.017	0.030	0.022	0.032	0.027	0.029	0.025	0.019	0.004
Si	1.965	1.977	1.960	1.975	1.966	1.961	1.963	1.970	1.975	1.990
K	0.000	0.000	0.001	0.000	0.000	0.000	0.001	0.000	0.000	0.000
Ca	0.872	0.862	0.873	0.873	0.856	0.874	0.874	0.872	0.861	0.958
Ti	0.025	0.011	0.024	0.014	0.020	0.022	0.025	0.017	0.015	0.001
Cr	0.000	0.001	0.000	0.000	0.001	0.001	0.000	0.000	0.001	0.000
Mn	0.020	0.020	0.022	0.020	0.024	0.022	0.020	0.021	0.021	0.021
Fe	0.863	0.892	0.829	0.836	0.833	0.864	0.843	0.870	0.892	0.791
Total cats.	4.020	4.027	4.022	4.021	4.023	4.019	4.021	4.025	4.022	4.020

	Unit 8						Unit 10			
			29			30			MH-NUN-92 21	
	Px 2	Px 3	Px 1	Px 2	Px 3	Px 1	Px 2	Px 3	Px 1	Px 2
Na2O	0.650	0.625	0.554	0.754	0.570	0.627	0.573	0.554	0.402	0.417
MgO	3.374	2.978	3.873	3.951	3.885	4.236	3.510	3.968	3.872	3.817
AL2O3	0.404	0.448	0.593	0.593	0.531	0.627	0.425	0.569	0.684	0.661
SiO2	48.675	48.116	48.140	47.798	47.864	48.302	48.029	48.121	48.758	48.431
K2O	0.007	0.000	0.008	0.130	0.005	0.004	0.000	0.000	0.012	0.016
CaO	19.813	19.720	20.456	20.360	20.475	20.455	19.807	20.105	20.651	20.301
TiO2	0.420	0.616	0.861	0.981	0.947	0.847	0.604	0.796	0.557	0.616
Cr2O3	0.000	0.037	0.028	0.035	0.000	0.000	0.001	0.000	0.013	0.016
MnO	0.566	0.569	0.649	0.671	0.633	0.635	0.657	0.670	0.640	0.640
FeO	25.824	26.517	24.769	24.753	24.678	23.812	25.538	24.537	24.468	24.981
Total	99.733	99.627	99.932	100.026	99.587	99.546	99.145	99.319	100.057	99.896
Na	0.051	0.050	0.043	0.059	0.045	0.049	0.045	0.044	0.031	0.033
Mg	0.204	0.181	0.234	0.239	0.235	0.255	0.214	0.241	0.233	0.230
Al	0.019	0.022	0.028	0.028	0.025	0.030	0.020	0.027	0.032	0.032
Si	1.978	1.966	1.949	1.938	1.946	1.954	1.965	1.957	1.965	1.960
K	0.000	0.000	0.000	0.007	0.000	0.000	0.000	0.000	0.001	0.001
Ca	0.862	0.863	0.888	0.885	0.892	0.887	0.868	0.876	0.892	0.880
Ti	0.013	0.019	0.026	0.030	0.029	0.026	0.019	0.024	0.017	0.019
Cr	0.000	0.001	0.001	0.001	0.000	0.000	0.000	0.000	0.000	0.001
Mn	0.019	0.020	0.022	0.023	0.022	0.022	0.023	0.023	0.022	0.022
Fe	0.877	0.906	0.839	0.839	0.839	0.806	0.874	0.835	0.825	0.845
Total cats.	4.025	4.028	4.031	4.050	4.034	4.029	4.028	4.027	4.017	4.022

Typical olivine analyses

	Unit 1			Unit 2/3					Unit 5	
	MH-NUN-92 9			41		42			55	
	Ol 1	Ol 2	Ol 3	Ol 1	Ol 2	Ol 1	Ol 2	Ol 3	Ol 1	Ol 2
MgO	0.738	0.479	0.418	1.277	0.690	1.066	0.774	0.438	2.073	1.333
Al2O3	0.000	0.025	0.019	0.015	0.032	0.008	0.021	0.000	0.013	0.006
SiO2	28.879	28.873	28.883	29.778	29.429	29.542	29.666	29.442	29.489	29.600
CaO	0.126	0.122	0.148	0.208	0.144	0.332	0.139	0.169	0.134	0.095
TiO2	0.083	0.055	0.060	0.057	0.050	0.037	0.060	0.040	0.050	0.043
Cr2O3	0.018	0.003	0.016	0.010	0.000	0.020	0.026	0.001	0.000	0.006
MnO	1.803	1.999	2.151	1.735	2.224	1.711	1.874	2.193	1.704	1.996
Fe	68.235	68.759	68.656	67.813	66.774	66.397	67.362	66.777	66.433	67.530
Total	99.881	100.314	100.352	100.918	99.456	99.128	100.016	99.072	99.929	100.630
Mg	0.037	0.024	0.021	0.063	0.035	0.054	0.039	0.022	0.104	0.066
Al	0.000	0.001	0.001	0.001	0.001	0.000	0.001	0.000	0.001	0.000
Si	0.981	0.979	0.980	0.993	0.998	1.000	0.999	1.002	0.988	0.990
Ca	0.005	0.004	0.005	0.007	0.005	0.012	0.005	0.006	0.005	0.003
Ti	0.002	0.001	0.002	0.001	0.001	0.001	0.002	0.001	0.001	0.001
Cr	0.000	0.000	0.000	0.000	0.000	0.001	0.001	0.000	0.000	0.000
Mn	0.052	0.057	0.062	0.049	0.064	0.049	0.053	0.063	0.048	0.057
Fe	1.939	1.951	1.947	1.890	1.894	1.880	1.898	1.901	1.862	1.889
Total cats.	3.016	3.018	3.018	3.007	3.011	2.998	3.007	2.997	3.011	3.009

		56			57		58		59	
	Ol 3	Ol 1	Ol 2	Ol 3	Ol 1	Ol 2	Ol 1	Ol 2	Ol 1	Ol 2
MgO	2.157	2.333	2.248	1.947	2.164	2.177	1.459	1.373	2.011	1.595
Al2O3	0.011	0.009	0.019	0.021	0.025	0.021	0.004	0.009	0.015	0.008
SiO2	29.457	29.517	29.461	29.502	29.472	29.604	29.596	29.474	29.468	29.256
CaO	0.144	0.169	0.189	0.165	0.126	0.147	0.157	0.126	0.153	0.125
TiO2	0.050	0.040	0.038	0.047	0.032	0.043	0.030	0.057	0.037	0.037
Cr2O3	0.023	0.000	0.018	0.006	0.000	0.025	0.004	0.013	0.000	0.010
MnO	1.810	1.765	1.743	1.770	1.710	1.733	1.853	1.806	1.755	1.943
Fe	66.346	65.965	65.839	66.514	66.118	66.149	67.464	67.695	66.819	67.141
Total	100.047	99.804	99.672	100.160	99.658	99.979	100.572	100.752	100.277	100.272
Mg	0.108	0.116	0.113	0.097	0.108	0.109	0.073	0.069	0.100	0.080
Al	0.000	0.000	0.001	0.001	0.001	0.001	0.000	0.000	0.001	0.000
Si	0.986	0.988	0.989	0.989	0.989	0.990	0.990	0.987	0.986	0.984
Ca	0.005	0.006	0.007	0.006	0.005	0.005	0.006	0.005	0.005	0.004
Ti	0.001	0.001	0.001	0.001	0.001	0.001	0.001	0.001	0.001	0.001
Cr	0.001	0.000	0.000	0.000	0.000	0.001	0.000	0.000	0.000	0.000
Mn	0.051	0.050	0.050	0.050	0.049	0.049	0.052	0.051	0.050	0.055
Fe	1.858	1.847	1.848	1.865	1.856	1.850	1.887	1.896	1.869	1.889
Total cats.	3.015	3.010	3.020	3.029	3.010	3.013	3.009	3.030	3.013	3.031

			60			62		63		
	Ol 2	Ol 3	Ol 1	Ol 2	Ol 3	Ol 1	Ol 2	Ol 1	Ol 2	Ol 3
MgO	1.544	2.126	2.199	2.152	2.421	1.801	1.655	1.186	1.544	1.902
Al2O3	0.020	0.019	0.008	0.025	0.028	0.023	0.026	0.026	0.021	0.008
SiO2	29.396	29.442	29.649	29.756	29.784	29.271	29.266	29.643	29.397	29.414
CaO	0.135	0.160	0.186	0.182	0.211	0.122	0.118	0.071	0.134	0.144
TiO2	0.039	0.042	0.058	0.048	0.040	0.048	0.055	0.057	0.038	0.035
Cr2O3	0.015	0.009	0.000	0.009	0.023	0.000	0.000	0.007	0.015	0.028
MnO	1.708	1.763	1.737	1.724	1.692	1.708	1.697	1.792	1.707	1.659
Fe	66.126	66.451	66.460	66.311	65.785	67.393	66.909	67.487	66.126	66.284
Total	99.036	100.023	100.453	100.230	100.002	100.372	99.726	100.305	99.036	99.573
Mg	0.078	0.106	0.109	0.107	0.120	0.090	0.083	0.059	0.078	0.095
Al	0.001	0.001	0.000	0.001	0.001	0.001	0.001	0.001	0.001	0.000
Si	0.995	0.986	0.989	0.992	0.993	0.981	0.987	0.994	0.995	0.991
Ca	0.005	0.006	0.007	0.006	0.008	0.004	0.004	0.003	0.005	0.005
Ti	0.001	0.001	0.001	0.001	0.001	0.001	0.001	0.001	0.001	0.001
Cr	0.000	0.000	0.000	0.000	0.001	0.000	0.000	0.000	0.000	0.001
Mn	0.049	0.050	0.049	0.049	0.048	0.049	0.048	0.051	0.049	0.047
Fe	1.872	1.862	1.853	1.849	1.834	1.890	1.886	1.893	1.872	1.867
Total cats.	3.006	3.012	3.023	3.007	3.006	3.017	3.011	3.006	3.006	3.017

	Unit 8							Unit 10		
	64		65	29			30	MH-NUN-92 21		
	Ol 1	Ol 3	Ol 1	Ol 1	Ol 2	Ol 3	Ol 1	Ol 2	Ol 1	Ol 2
MgO	1.185	1.901	1.181	2.043	1.728	2.016	2.529	2.386	2.626	2.839
Al2O3	0.026	0.007	0.015	0.000	0.021	0.017	0.028	0.009	0.004	0.009
SiO2	29.642	29.412	29.219	29.204	28.958	29.234	29.316	29.365	29.831	29.583
CaO	0.071	0.145	0.150	0.141	0.105	0.147	0.126	0.130	0.071	0.232
TiO2	0.056	0.035	0.043	0.050	0.047	0.045	0.047	0.040	0.100	0.057
Cr2O3	0.008	0.028	0.003	0.000	0.018	0.000	0.010	0.000	0.004	0.015
MnO	1.792	1.660	1.880	1.658	1.706	1.733	1.703	1.806	2.061	1.680
Fe	67.486	66.283	66.709	66.008	66.715	66.100	65.484	65.363	65.254	65.196
Total	100.303	99.471	99.333	99.104	99.297	99.293	99.243	99.100	100.047	99.726
Mg	0.059	0.095	0.060	0.103	0.087	0.101	0.127	0.120	0.130	0.141
Al	0.001	0.000	0.001	0.000	0.001	0.001	0.001	0.000	0.000	0.000
Si	0.994	0.991	0.992	0.988	0.982	0.987	0.986	0.990	0.993	0.988
Ca	0.003	0.005	0.005	0.005	0.004	0.005	0.005	0.005	0.003	0.008
Ti	0.001	0.001	0.001	0.001	0.001	0.001	0.001	0.001	0.003	0.001
Cr	0.000	0.001	0.000	0.000	0.000	0.000	0.000	0.000	0.000	0.000
Mn	0.051	0.047	0.054	0.047	0.049	0.050	0.049	0.052	0.058	0.048
Fe	1.893	1.867	1.894	1.867	1.892	1.866	1.843	1.842	1.817	1.821
Total cats.	3.006	3.018	3.020	3.011	3.016	3.011	3.011	3.009	3.012	3.019

Typical braid perthite analyses

	Unit 2/3			Unit 5						
	42			43		54		56		
	Braid 1	Braid 2	Braid 3	Braid 1	Braid 2	Braid 1	Braid 2	Braid 1	Braid 2	Braid 3
NaO	5.837	6.786	6.532	6.175	6.916	6.726	6.798	6.934	6.531	6.807
MgO	0.013	0.002	0.010	0.017	0.013	0.020	0.025	0.012	0.017	0.000
Al2O3	18.766	18.755	18.732	18.536	18.866	18.921	18.891	19.031	18.870	19.033
SiO2	66.769	66.547	66.600	66.470	66.613	66.498	66.448	65.849	66.010	65.918
K2O	8.191	6.817	7.291	8.056	7.070	6.969	7.067	6.746	7.435	7.183
CaO	0.118	0.151	0.127	0.035	0.080	0.386	0.353	0.508	0.327	0.374
BaO	0.112	0.087	0.059	0.083	0.117	0.098	0.060	0.040	0.058	0.030
FeO	0.165	0.125	0.136	0.157	0.131	0.174	0.171	0.140	0.151	0.125
Total	99.971	99.269	99.489	99.528	99.807	99.792	99.814	99.260	99.398	99.469
Na	0.509	0.593	0.571	0.541	0.602	0.586	0.592	0.607	0.572	0.596
Mg	0.001	0.000	0.001	0.001	0.001	0.001	0.002	0.001	0.001	0.000
Al	0.994	0.996	0.994	0.987	0.999	1.002	1.001	1.013	1.005	1.013
Si	3.002	2.999	3.000	3.003	2.993	2.988	2.987	2.975	2.984	2.976
K	0.470	0.392	0.419	0.464	0.405	0.399	0.405	0.389	0.429	0.414
Ca	0.006	0.007	0.006	0.002	0.004	0.019	0.017	0.025	0.016	0.018
Ba	0.002	0.002	0.001	0.001	0.002	0.002	0.001	0.001	0.001	0.001
Fe	0.006	0.005	0.005	0.006	0.005	0.007	0.006	0.005	0.006	0.005
Total cats.	4.990	4.994	4.997	5.006	5.011	5.003	5.011	5.016	5.014	5.022

	Unit 7									
	64		65				66			
	Braid 1	Braid 2	Braid 1	Braid 2	Braid 3	Braid 4	Braid 1	Braid 2	Braid 3	Braid 4
NaO	6.885	6.342	6.241	7.031	6.741	6.991	6.814	6.989	6.269	6.712
MgO	0.025	0.027	0.018	0.015	0.012	0.020	0.000	0.010	0.015	0.003
Al2O3	18.969	18.808	18.798	18.814	18.840	18.730	18.791	18.815	18.821	18.919
SiO2	66.160	65.952	66.391	66.519	66.115	65.997	65.911	65.849	66.046	66.029
K2O	7.143	7.708	7.711	6.932	7.359	7.155	7.191	6.813	7.855	7.446
CaO	0.228	0.257	0.207	0.199	0.187	0.221	0.239	0.243	0.242	0.238
BaO	0.089	0.061	0.107	0.054	0.054	0.089	0.065	0.077	0.095	0.070
FeO	0.157	0.147	0.143	0.148	0.180	0.178	0.166	0.162	0.145	0.156
Total	99.656	99.302	99.616	99.711	99.488	99.381	99.178	98.960	99.489	99.573
Na	0.602	0.557	0.546	0.613	0.590	0.613	0.598	0.614	0.550	0.588
Mg	0.002	0.002	0.001	0.001	0.001	0.001	0.000	0.001	0.001	0.000
Al	1.007	1.004	0.999	0.997	1.003	0.998	1.003	1.005	1.003	1.007
Si	2.981	2.986	2.994	2.991	2.985	2.984	2.985	2.984	2.987	2.981
K	0.411	0.445	0.444	0.398	0.424	0.413	0.415	0.394	0.453	0.429
Ca	0.011	0.012	0.010	0.010	0.009	0.011	0.012	0.012	0.012	0.012
Ba	0.002	0.001	0.002	0.001	0.001	0.002	0.001	0.001	0.002	0.001
Fe	0.006	0.006	0.005	0.006	0.007	0.007	0.006	0.006	0.005	0.006
Total cats.	5.021	5.013	5.001	5.015	5.020	5.029	5.020	5.017	5.013	5.023

							Unit 8			
			67				29			30
	Braid 5	Braid 6	Braid 1	Braid 2	Braid 3	Braid 4	Braid 1	Braid 2	Braid 3	Braid 1
NaO	6.956	6.821	6.205	6.740	6.977	6.819	6.315	6.605	6.158	5.792
MgO	0.005	0.022	0.002	0.012	0.012	0.015	0.015	0.003	0.008	0.020
Al2O3	18.819	18.768	18.645	18.664	18.861	18.814	18.400	18.502	18.390	18.509
SiO2	66.667	66.414	66.583	66.481	66.292	66.179	66.863	66.846	66.915	66.643
K2O	7.152	7.206	8.033	7.561	6.818	7.329	7.258	6.957	7.505	8.398
CaO	0.194	0.194	0.137	0.122	0.236	0.236	0.143	0.140	0.139	0.113
BaO	0.100	0.070	0.100	0.213	0.103	0.050	0.046	0.066	0.051	0.055
FeO	0.147	0.192	0.198	0.178	0.196	0.193	0.259	0.251	0.244	0.189
Total	100.040	99.687	99.904	99.970	99.495	99.635	99.298	99.370	99.410	99.720
Na	0.605	0.596	0.542	0.588	0.610	0.596	0.552	0.577	0.538	0.507
Mg	0.000	0.001	0.000	0.001	0.001	0.001	0.001	0.000	0.001	0.001
Al	0.995	0.996	0.990	0.990	1.002	1.000	0.978	0.982	0.977	0.984
Si	2.991	2.991	2.999	2.993	2.987	2.985	3.015	3.010	3.016	3.007
K	0.409	0.414	0.462	0.434	0.392	0.422	0.417	0.400	0.431	0.483
Ca	0.009	0.009	0.007	0.006	0.011	0.011	0.007	0.007	0.007	0.005
Ba	0.002	0.001	0.002	0.004	0.002	0.001	0.001	0.001	0.001	0.001
Fe	0.006	0.007	0.007	0.007	0.007	0.007	0.010	0.009	0.009	0.007
Total cats.	5.018	5.016	5.008	5.023	5.012	5.024	4.981	4.986	4.980	4.996

Typical biotite analyses

	Braid 2	Braid 3	Braid 4	Braid 5
NaO	6.255	6.321	5.930	5.954
MgO	0.017	0.012	0.023	0.030
Al2O3	18.545	18.608	18.619	18.500
SiO2	67.050	67.099	66.898	66.744
K2O	7.476	7.764	8.233	7.846
CaO	0.167	0.157	0.160	0.158
BaO	0.000	0.012	0.030	0.031
FeO	0.187	0.189	0.174	0.399
Total	99.695	100.160	100.066	99.661
Na	0.545	0.549	0.516	0.520
Mg	0.001	0.001	0.002	0.002
Al	0.982	0.983	0.986	0.982
Si	3.012	3.007	3.005	3.007
K	0.428	0.444	0.472	0.451
Ca	0.008	0.008	0.008	0.008
Ba	0.000	0.000	0.001	0.001
Fe	0.007	0.007	0.007	0.015
Total cats.	4.983	4.998	4.996	4.986

	Unit 1			Unit 2/3
	MH-NUN-92 9			41
	Bt 1	Bt 2	Bt 3	Bt 1
F	0.036	0.061	0.077	0.060
Na2O	0.053	0.031	0.028	0.274
MgO	2.265	0.927	0.398	0.343
Al2O3	7.429	7.235	8.550	4.809
SiO2	30.644	36.418	35.302	42.130
K2O	2.938	7.852	8.274	4.983
CaO	0.326	0.000	0.000	0.011
TiO2	0.565	1.239	0.517	0.055
Cr2O3	0.000	0.018	0.000	0.018
MnO	0.314	0.247	0.240	0.795
FeO	45.493	42.171	42.535	42.223
Total	90.063	96.199	95.921	95.701
F	0.021	0.033	0.042	0.031
Na	0.019	0.010	0.009	0.088
Mg	0.623	0.235	0.102	0.085
Al	1.615	1.450	1.730	0.939
Si	5.654	6.191	6.059	6.978
K	0.691	1.703	1.812	1.053
Ca	0.064	0.000	0.000	0.002
Ti	0.078	0.158	0.067	0.007
Cr	0.000	0.002	0.000	0.002
Mn	0.049	0.036	0.035	0.112
Fe	7.019	5.995	6.106	5.849
Total cats.	15.833	15.813	15.962	15.146

	Unit 5									
	42			43	55		56		57	
	Bt 1	Bt 2	Bt 3	Bt 1	Bt 1	Bt 2	Bt 2	Bt 3	Bt 1	Bt 2
F	0.092	0.098	0.065	0.000	0.319	0.276	0.334	0.096	0.381	0.423
Na2O	0.085	0.051	0.163	0.023	0.053	0.101	0.050	0.028	0.054	0.086
MgO	0.637	1.046	0.594	0.492	1.151	4.051	4.575	4.508	5.997	6.692
Al2O3	7.620	11.191	9.514	9.553	10.341	10.757	11.358	10.967	10.369	10.381
SiO2	34.865	34.688	30.952	34.504	34.750	34.936	35.351	35.402	36.016	36.301
K2O	7.724	8.850	7.179	8.461	8.596	6.419	9.059	8.812	9.065	9.308
CaO	0.066	0.059	0.042	0.113	0.000	1.230	0.118	0.132	0.105	0.013
TiO2	3.813	5.763	3.018	3.530	0.048	3.545	3.278	3.783	3.396	3.378
Cr2O3	0.012	0.023	0.004	0.004	0.000	0.000	0.019	0.018	0.000	0.019
MnO	0.258	0.337	0.226	0.093	0.354	0.143	0.120	0.146	0.159	0.097
FeO	39.899	34.491	40.382	38.174	39.807	33.058	32.112	32.282	30.832	29.807
Total	95.071	96.597	92.139	94.947	95.419	94.516	96.374	96.174	96.374	96.505
F	0.050	0.051	0.037	0.000	0.172	0.144	0.172	0.049	0.195	0.215
Na	0.028	0.016	0.057	0.008	0.017	0.032	0.016	0.009	0.017	0.027
Mg	0.162	0.255	0.158	0.125	0.293	0.995	1.107	1.091	1.443	1.601
Al	1.537	2.160	2.007	1.913	2.083	2.089	2.174	2.098	1.973	1.963
Si	5.966	5.682	5.540	5.862	5.940	5.755	5.741	5.746	5.814	5.826
K	1.686	1.849	1.639	1.834	1.874	1.349	1.877	1.824	1.867	1.906
Ca	0.012	0.010	0.008	0.021	0.000	0.217	0.020	0.023	0.018	0.002
Ti	0.491	0.710	0.406	0.451	0.006	0.439	0.400	0.462	0.412	0.408
Cr	0.002	0.003	0.001	0.001	0.000	0.000	0.002	0.002	0.000	0.002
Mn	0.037	0.047	0.034	0.013	0.051	0.020	0.017	0.020	0.022	0.013
Fe	5.710	4.725	6.045	5.424	5.691	4.554	4.361	4.382	4.162	4.001
Total cats.	15.681	15.508	15.932	15.652	16.127	15.594	15.887	15.706	15.923	15.964

		58		59			60			62
	Bt 3	Bt 1	Bt 2	Bt 1	Bt 2	Bt 3	Bt 1	Bt 2	Bt 3	Bt 1
F	1.045	0.000	0.156	0.075	0.421	0.000	0.380	0.280	0.229	0.738
Na2O	0.032	0.030	0.020	0.065	0.057	0.027	0.054	0.053	0.009	0.065
MgO	5.445	1.429	3.225	3.127	4.555	3.713	4.548	4.278	4.263	6.962
Al2O3	10.502	7.295	9.729	9.997	10.468	10.165	11.074	11.497	10.999	10.812
SiO2	35.950	37.599	35.366	35.496	35.058	35.128	34.711	35.210	35.443	36.915
K2O	9.257	7.085	8.657	9.130	7.135	6.799	8.791	8.379	9.299	9.322
CaO	0.013	0.018	0.053	0.007	0.719	0.844	0.108	0.355	0.000	0.017
TiO2	3.071	0.347	1.386	3.648	3.496	3.181	3.001	3.750	2.931	3.166
Cr2O3	0.000	0.012	0.029	0.007	0.009	0.000	0.000	0.022	0.022	0.006
MnO	0.134	0.509	0.229	0.172	0.139	0.147	0.125	0.136	0.145	0.106
FeO	31.513	40.505	37.108	34.603	32.734	34.409	32.613	31.810	33.014	29.003
Total	96.962	94.829	95.958	96.327	94.791	94.413	95.405	95.770	96.354	97.112
F	0.536	0.000	0.082	0.039	0.219	0.000	0.198	0.144	0.118	0.371
Na	0.010	0.010	0.007	0.021	0.018	0.009	0.017	0.017	0.003	0.020
Mg	1.317	0.362	0.803	0.766	1.118	0.917	1.118	1.037	1.037	1.649
Al	2.008	1.459	1.916	1.937	2.032	1.986	2.152	2.204	2.116	2.024
Si	5.831	6.380	5.908	5.836	5.775	5.823	5.722	5.726	5.784	5.865
K	1.916	1.534	1.845	1.915	1.499	1.438	1.849	1.738	1.936	1.889
Ca	0.002	0.003	0.010	0.001	0.127	0.150	0.019	0.062	0.000	0.003
Ti	0.375	0.044	0.174	0.451	0.433	0.397	0.372	0.459	0.360	0.378
Cr	0.000	0.002	0.004	0.001	0.001	0.000	0.000	0.003	0.003	0.001
Mn	0.018	0.073	0.032	0.024	0.019	0.021	0.017	0.019	0.020	0.014
Fe	4.275	5.748	5.184	4.758	4.509	4.770	4.496	4.326	4.506	3.854
Total cats.	16.288	15.615	15.965	15.749	15.750	15.511	15.960	15.735	15.883	16.068

			63			64			65	
	Bt 2	Bt 3	Bt 1	Bt 2	Bt 3	Bt 1	Bt 2	Bt 3	Bt 1	Bt 2
F	0.129	0.383	0.154	0.092	0.102	0.148	0.434	0.089	0.068	0.000
Na2O	0.078	0.085	0.042	0.190	0.070	0.050	0.036	0.338	0.038	0.055
MgO	2.797	4.447	1.632	1.668	3.716	3.930	5.147	3.442	0.411	1.635
Al2O3	10.458	10.124	9.878	10.519	10.798	10.043	10.224	10.933	9.667	10.585
SiO2	35.034	35.077	34.767	34.901	35.109	35.851	35.794	34.895	34.651	34.206
K2O	8.050	8.384	8.606	8.189	9.024	9.042	9.137	6.496	8.373	8.613
CaO	0.341	0.248	0.028	0.053	0.048	0.000	0.011	0.600	0.000	0.021
TiO2	3.448	3.238	2.254	4.430	4.138	3.538	3.256	2.684	0.022	3.721
Cr2O3	0.010	0.006	0.023	0.020	0.000	0.000	0.012	0.007	0.015	0.026
MnO	0.169	0.133	0.214	0.158	0.252	0.187	0.108	0.183	0.284	0.190
FeO	35.175	32.772	38.248	34.337	32.205	33.684	31.986	34.759	41.345	36.839
Total	95.689	94.897	95.846	94.557	95.462	96.473	96.145	94.426	94.874	95.891
F	0.067	0.201	0.082	0.049	0.053	0.076	0.224	0.047	0.037	0.000
Na	0.025	0.027	0.014	0.061	0.022	0.016	0.012	0.109	0.013	0.018
Mg	0.689	1.098	0.410	0.415	0.909	0.956	1.250	0.851	0.106	0.407
Al	2.038	1.977	1.961	2.068	2.088	1.932	1.964	2.137	1.970	2.083
Si	5.792	5.812	5.857	5.822	5.760	5.852	5.834	5.788	5.990	5.712
K	1.698	1.772	1.850	1.742	1.888	1.883	1.900	1.375	1.847	1.835
Ca	0.060	0.044	0.005	0.010	0.008	0.000	0.002	0.107	0.000	0.004
Ti	0.429	0.403	0.286	0.556	0.511	0.434	0.399	0.335	0.003	0.467
Cr	0.001	0.001	0.003	0.003	0.000	0.000	0.002	0.001	0.002	0.003
Mn	0.024	0.019	0.031	0.022	0.035	0.026	0.015	0.026	0.042	0.027
Fe	4.863	4.541	5.389	4.790	4.419	4.598	4.360	4.821	5.978	5.145
Total cats.	15.686	15.895	15.888	15.538	15.693	15.773	15.962	15.597	15.988	15.701

	Unit 8							Unit 10
		29			30			MH-Nun-92 21
	Bt 3	Bt 1	Bt 2	Bt 3	Bt 1	Bt 2	Bt 3	Bt 1
F	0.102	0.227	0.186	0.216	1.404	0.577	0.546	0.406
Na2O	0.051	0.116	0.115	0.092	0.063	0.050	0.061	0.063
MgO	1.512	4.482	2.025	1.065	7.710	5.260	5.648	6.482
Al2O3	9.910	9.430	10.583	10.906	10.859	10.825	10.863	11.173
SiO2	33.774	35.625	35.717	34.489	36.497	35.289	35.451	34.136
K2O	8.514	7.057	7.841	8.066	8.459	8.482	8.112	5.829
CaO	0.031	0.143	0.071	0.031	0.015	0.007	0.045	0.284
TiO2	1.276	0.048	3.848	3.736	3.041	3.603	3.872	3.461
Cr2O3	0.000	0.006	0.025	0.023	0.034	0.013	0.013	0.000
MnO	0.200	0.155	0.098	0.119	0.148	0.148	0.139	0.127
FeO	39.426	34.558	34.927	36.353	27.922	30.872	30.413	29.436
Total	94.796	91.847	95.436	95.096	96.152	95.126	95.163	91.397
F	0.055	0.123	0.097	0.114	0.712	0.299	0.281	0.214
Na	0.017	0.038	0.037	0.030	0.020	0.016	0.019	0.021
Mg	0.388	1.144	0.497	0.266	1.842	1.283	1.370	1.614
Al	2.009	1.903	2.056	2.154	2.051	2.088	2.083	2.199
Si	5.809	6.100	5.887	5.780	5.850	5.776	5.769	5.702
K	1.868	1.541	1.649	1.724	1.730	1.771	1.684	1.242
Ca	0.006	0.026	0.013	0.006	0.003	0.001	0.008	0.051
Ti	0.165	0.006	0.477	0.471	0.367	0.444	0.474	0.435
Cr	0.000	0.001	0.003	0.003	0.004	0.002	0.002	0.000
Mn	0.029	0.022	0.014	0.017	0.020	0.021	0.019	0.018
Fe	5.671	4.949	4.815	5.095	3.743	4.226	4.139	4.112
Total cats.	16.017	15.853	15.545	15.660	16.342	15.927	15.848	15.608

Typical amphibole analyses

	Unit 1			Unit 2/3						
	MH-NUN-92 9			41		42		43		
	Am 1	Am 2	Am 3	Am 1	Am 2	Am 1	Am 2	Am 1	Am 2	Am 3
F	0.810	0.785	0.760	0.777	0.789	1.229	0.982	1.110	1.075	0.961
Na2O	3.720	3.795	3.431	3.706	4.572	4.539	4.322	4.465	4.695	4.079
MgO	2.073	1.355	1.827	3.117	1.108	3.033	2.320	2.429	1.323	2.547
Al2O3	1.976	2.129	1.740	3.142	1.451	0.994	1.820	1.680	1.321	2.201
SiO2	46.112	45.853	46.837	46.358	47.607	49.620	48.035	47.697	48.133	46.884
K2O	1.185	1.096	1.014	1.311	1.279	1.165	1.225	1.248	1.223	1.111
CaO	6.922	6.740	6.716	7.954	5.872	5.742	6.548	6.669	5.821	7.203
TiO2	1.817	1.505	0.544	1.917	2.606	0.626	1.673	1.766	1.708	1.740
Cr2O3	0.031	0.006	0.029	0.001	0.000	0.018	0.000	0.010	0.000	0.000
MnO	0.527	0.581	0.616	0.412	0.550	0.464	0.523	0.501	0.564	0.486
FeO	33.044	33.994	34.766	30.499	32.964	32.002	32.004	31.315	32.321	31.617
Total	98.217	97.839	98.280	99.194	98.798	99.432	99.452	98.890	98.184	98.829
F	0.417	0.406	0.389	0.391	0.404	0.611	0.493	0.561	0.548	0.487
Na	1.173	1.205	1.078	1.145	1.434	1.383	1.332	1.383	1.468	1.267
Mg	0.502	0.331	0.441	0.740	0.267	0.710	0.549	0.578	0.318	0.608
Al	0.379	0.411	0.332	0.590	0.277	0.184	0.341	0.316	0.251	0.416
Si	7.500	7.507	7.589	7.384	7.699	7.795	7.632	7.620	7.761	7.513
K	0.246	0.229	0.210	0.266	0.264	0.233	0.248	0.254	0.252	0.227
Ca	1.206	1.182	1.166	1.358	1.018	0.967	1.115	1.142	1.006	1.237
Ti	0.222	0.185	0.066	0.230	0.317	0.074	0.200	0.212	0.207	0.210
Cr	0.004	0.001	0.004	0.000	0.000	0.002	0.000	0.001	0.000	0.000
Mn	0.073	0.081	0.085	0.056	0.075	0.062	0.070	0.068	0.077	0.066
Fe	4.495	4.655	4.711	4.063	4.459	4.205	4.253	4.184	4.359	4.238
Total cats.	15.800	15.786	15.682	15.831	15.809	15.614	15.740	15.759	15.699	15.782

	Unit 5							Unit 5		
	55			57				58		60
	Am 1	Am 2	Am 3	Am 1	Am 2	Am 3		Am 1	Am 2	Am 1
F	0.636	0.672	0.705	1.012	0.547	0.170	F	0.780	0.689	1.436
Na2O	2.188	2.305	2.240	2.412	2.391	2.116	Na2O	2.252	2.213	2.417
MgO	4.595	4.560	5.137	5.245	4.387	4.881	MgO	4.067	3.595	4.958
Al2O3	5.075	4.325	4.495	5.000	6.819	6.145	Al2O3	4.442	4.627	6.645
SiO2	43.405	44.437	45.061	43.917	42.697	43.057	SiO2	44.362	43.859	42.051
K2O	1.089	0.981	0.941	1.074	1.172	1.090	K2O	1.035	1.044	1.340
CaO	10.081	9.744	9.925	9.792	10.025	10.245	CaO	9.414	9.496	10.486
TiO2	1.523	1.408	1.031	1.538	1.807	1.328	TiO2	1.468	1.491	2.067
Cr2O3	0.016	0.003	0.000	0.006	0.000	0.013	Cr2O3	0.000	0.000	0.023
MnO	0.449	0.498	0.476	0.425	0.386	0.396	MnO	0.462	0.466	0.394
FeO	29.129	29.654	28.892	27.876	28.717	27.932	FeO	30.368	30.736	27.020
Total	98.186	98.587	98.903	98.297	98.948	97.373	Total	98.650	98.216	98.837
F	0.323	0.340	0.352	0.510	0.276	0.087	F	0.395	0.352	0.723
Na	0.682	0.714	0.686	0.745	0.739	0.660	Na	0.699	0.692	0.746
Mg	1.100	1.086	1.209	1.245	1.042	1.170	Mg	0.970	0.864	1.176
Al	0.961	0.815	0.837	0.939	1.281	1.166	Al	0.838	0.880	1.247
Si	6.973	7.099	7.119	6.993	6.802	6.927	Si	7.101	7.076	6.695
K	0.223	0.200	0.190	0.218	0.238	0.224	K	0.211	0.215	0.272
Ca	1.735	1.668	1.680	1.671	1.711	1.766	Ca	1.615	1.642	1.789
Ti	0.184	0.169	0.122	0.184	0.217	0.161	Ti	0.177	0.181	0.248
Cr	0.002	0.000	0.000	0.001	0.000	0.002	Cr	0.000	0.000	0.003
Mn	0.061	0.067	0.064	0.057	0.052	0.054	Mn	0.063	0.064	0.053
Fe	3.914	3.962	3.817	3.712	3.826	3.758	Fe	4.065	4.147	3.598
Total cats.	15.836	15.781	15.725	15.764	15.908	15.888	Total cats	15.738	15.762	15.827

	Unit 7									
		62			63	64			65	
	Am 2	Am 1	Am 2	Am 3	Am 1	Am 1	Am 2	Am 3	Am 1	Am 2
F	0.931	0.459	0.626	0.691	0.702	0.576	0.648	0.351	0.484	0.482
Na2O	2.420	2.316	2.386	2.401	2.226	2.169	2.494	1.903	2.169	2.177
MgO	4.885	3.706	4.427	3.900	3.658	4.402	3.883	4.105	3.329	4.313
Al2O3	6.683	4.300	4.225	4.210	4.289	4.527	4.274	4.291	4.693	3.885
SiO2	42.070	44.261	44.139	44.028	44.522	44.002	43.793	44.871	43.254	44.847
K2O	1.402	0.938	1.052	1.042	0.966	0.956	1.034	0.936	1.034	0.866
CaO	10.603	9.156	9.176	9.033	9.259	9.344	9.107	9.603	9.334	9.233
TiO2	2.027	0.996	1.425	1.394	0.621	1.430	1.490	1.069	1.421	1.219
Cr2O3	0.016	0.016	0.018	0.025	0.007	0.009	0.019	0.028	0.023	0.010
MnO	0.383	0.475	0.445	0.479	0.469	0.431	0.453	0.462	0.439	0.413
FeO	27.079	31.019	30.139	30.504	31.520	29.331	30.113	30.269	30.738	29.781
	98.499	97.642	98.058	97.707	98.239	97.177	97.308	97.888	96.918	97.226
F	0.471	0.235	0.319	0.354	0.357	0.295	0.333	0.178	0.251	0.246
Na	0.750	0.727	0.745	0.754	0.694	0.680	0.786	0.592	0.689	0.681
Mg	1.164	0.894	1.062	0.941	0.876	1.061	0.941	0.982	0.812	1.037
Al	1.260	0.820	0.802	0.804	0.813	0.863	0.819	0.812	0.906	0.739
Si	6.728	7.162	7.108	7.128	7.155	7.118	7.118	7.203	7.082	7.239
K	0.286	0.194	0.216	0.215	0.198	0.197	0.214	0.192	0.216	0.178
Ca	1.817	1.587	1.583	1.567	1.594	1.620	1.586	1.652	1.638	1.597
Ti	0.244	0.121	0.173	0.170	0.075	0.174	0.182	0.129	0.175	0.148
Cr	0.002	0.002	0.002	0.003	0.001	0.001	0.002	0.004	0.003	0.001
Mn	0.052	0.065	0.061	0.066	0.064	0.059	0.062	0.063	0.061	0.056
Fe	3.622	4.198	4.059	4.130	4.236	3.968	4.093	4.064	4.209	4.020
Total cats.	15.924	15.770	15.811	15.777	15.706	15.742	15.805	15.692	15.790	15.698

	Unit 8						Unit 10		
		29			30			MH-NUN-92 21	
	Am 3	Am 1	Am 2	Am 3	Am 1	Am 2	Am 3	Am 1	Am 2
F	0.564	0.015	1.090	0.813	1.216	0.909	1.206	0.842	0.805
Na2O	2.054	1.746	2.615	2.376	2.505	2.509	2.634	2.323	2.374
MgO	2.752	4.435	4.891	4.872	6.142	6.019	5.235	4.583	4.601
Al2O3	3.926	3.889	4.452	4.280	4.771	5.394	4.971	8.006	8.544
SiO2	44.396	45.215	43.838	44.064	44.197	43.868	43.636	39.300	40.466
K2O	0.741	0.819	1.090	1.020	1.015	1.049	1.103	1.447	1.464
CaO	9.477	9.587	9.485	9.419	9.586	9.811	9.540	10.473	10.777
TiO2	0.647	0.726	1.571	1.465	1.436	1.306	1.808	2.722	2.629
Cr2O3	0.001	0.000	0.000	0.006	0.000	0.006	0.000	0.020	0.009
MnO	0.577	0.458	0.436	0.442	0.429	0.393	0.427	0.345	0.367
FeO	32.707	30.556	28.262	28.792	26.726	26.472	27.221	25.524	26.588
	97.842	97.446	97.730	97.549	98.023	97.736	97.781	95.585	98.624
F	0.290	0.008	0.553	0.413	0.610	0.457	0.610	0.440	0.408
Na	0.647	0.544	0.814	0.741	0.770	0.773	0.816	0.745	0.738
Mg	0.666	1.062	1.170	1.167	1.451	1.424	1.247	1.129	1.099
Al	0.751	0.737	0.842	0.811	0.892	1.010	0.937	1.561	1.614
Si	7.207	7.267	7.035	7.085	7.007	6.966	6.974	6.498	6.485
K	0.153	0.168	0.223	0.209	0.205	0.213	0.225	0.305	0.299
Ca	1.649	1.651	1.631	1.623	1.629	1.669	1.634	1.856	1.850
Ti	0.079	0.088	0.190	0.177	0.171	0.156	0.217	0.338	0.317
Cr	0.000	0.000	0.000	0.001	0.000	0.001	0.000	0.003	0.001
Mn	0.079	0.062	0.059	0.060	0.058	0.053	0.058	0.048	0.050
Fe	4.441	4.107	3.793	3.872	3.544	3.516	3.638	3.530	3.563
Total cats.	15.672	15.686	15.758	15.746	15.727	15.780	15.745	16.013	16.016

Typical apatite analyses

	Unit 2/3				Unit 5					
	43				54				56	
	Ap 1	Ap 2	Ap 3	Ap 4	Ap 1	Ap 2	Ap 3	Ap 4	Ap 1	Ap 2
F	3.160	2.578	3.871	3.322	3.760	4.191	4.099	4.306	4.577	3.729
Na2O	0.453	0.383	0.361	0.237	0.112	0.129	0.146	0.136	0.123	0.147
SiO2	0.454	1.431	0.394	0.629	0.858	0.353	0.569	0.620	0.486	0.916
P2O5	41.763	39.075	42.114	41.761	41.023	42.221	41.261	42.004	41.811	41.046
Cl	0.006	0.029	0.017	0.011	0.016	0.038	0.045	0.016	0.000	0.027
CaO	52.469	42.376	52.866	53.314	53.177	54.337	53.644	53.540	53.770	52.824
Ce2O3	1.408	2.672	1.130	1.169	1.165	0.637	0.751	0.991	0.695	1.154
Pr2O3	0.187	0.401	0.242	0.110	0.277	0.029	0.136	0.173	0.063	0.078
Nd2O3	0.722	0.934	0.659	0.523	0.622	0.339	0.514	0.524	0.337	0.659
La2O3	0.749	1.330	0.652	0.571	0.610	0.332	0.292	0.545	0.325	0.462
FeO	0.162	0.138	0.143	0.087	0.284	0.223	0.224	0.192	0.264	0.589
MnO	0.019	0.032	0.017	0.000	0.044	0.039	0.005	0.025	0.027	0.028
Total	101.552	91.379	102.466	101.734	101.948	102.868	101.686	103.072	102.478	101.659
F	1.691	1.517	2.061	1.770	2.017	2.219	2.202	2.284	2.442	2.002
Na	0.149	0.138	0.118	0.078	0.037	0.042	0.048	0.044	0.040	0.048
Si	0.077	0.266	0.066	0.106	0.146	0.059	0.097	0.104	0.082	0.155
P	5.981	6.153	6.001	5.957	5.892	5.983	5.932	5.964	5.970	5.899
Cl	0.002	0.009	0.005	0.003	0.005	0.011	0.013	0.005	0.000	0.008
Ca	9.509	8.445	9.534	9.625	9.665	9.744	9.761	9.622	9.717	9.609
Ce	0.087	0.182	0.070	0.072	0.072	0.039	0.047	0.061	0.043	0.072
Pr	0.012	0.027	0.015	0.007	0.017	0.002	0.008	0.011	0.004	0.005
Nd	0.044	0.062	0.040	0.031	0.038	0.020	0.031	0.031	0.020	0.040
La	0.047	0.091	0.040	0.035	0.038	0.020	0.018	0.034	0.020	0.029
Fe	0.023	0.021	0.020	0.012	0.040	0.031	0.032	0.027	0.037	0.084
Mn	0.003	0.005	0.002	0.000	0.006	0.005	0.001	0.003	0.004	0.004
Total cats.	17.625	16.916	17.972	17.696	17.973	18.175	18.190	18.190	18.379	17.955

	Unit 7									
		64			65				66	
	Ap 3	Ap 1	Ap 2	Ap 3	Ap 1	Ap 2	Ap 3a	Ap 3b	Ap 1	Ap 2
F	4.754	3.706	3.814	4.312	4.320	3.905	3.817	3.873	3.709	4.207
Na2O	0.102	0.201	0.213	0.183	0.204	0.228	0.217	0.224	0.190	0.160
SiO2	1.100	1.217	0.445	0.404	0.451	0.419	1.020	0.443	0.310	0.460
P2O5	40.349	40.239	41.809	41.880	42.102	41.319	40.212	41.252	42.714	41.445
Cl	0.023	0.000	0.016	0.012	0.011	0.037	0.008	0.010	0.010	0.021
CaO	52.459	52.179	53.228	53.679	53.643	53.251	52.229	53.769	53.959	53.830
Ce2O3	1.382	1.615	0.953	0.826	1.003	1.027	1.752	1.133	0.874	0.910
Pr2O3	0.008	0.286	0.032	0.220	0.153	0.087	0.201	0.136	0.281	0.073
Nd2O3	0.770	0.818	0.516	0.444	0.499	0.460	0.807	0.525	0.356	0.446
La2O3	0.561	0.812	0.498	0.398	0.501	0.613	0.781	0.482	0.386	0.344
FeO	0.389	0.418	0.134	0.269	0.183	0.199	0.278	0.239	0.268	0.157
MnO	0.039	0.013	0.000	0.050	0.028	0.009	0.061	0.019	0.061	0.052
Total	101.936	101.504	101.658	102.677	103.098	101.554	101.383	102.105	103.118	102.105
F	2.579	2.007	2.040	2.297	2.292	2.101	2.074	2.076	1.951	2.253
Na	0.034	0.067	0.070	0.060	0.066	0.075	0.072	0.074	0.061	0.053
Si	0.189	0.208	0.075	0.068	0.076	0.071	0.175	0.075	0.052	0.078
P	5.859	5.833	5.986	5.971	5.979	5.951	5.847	5.920	6.013	5.942
Cl	0.007	0.000	0.005	0.003	0.003	0.011	0.002	0.003	0.003	0.006
Ca	9.640	9.573	9.645	9.686	9.640	9.707	9.765	9.614	9.768	9.342
Ce	0.087	0.101	0.059	0.051	0.062	0.064	0.110	0.070	0.053	0.056
Pr	0.001	0.018	0.002	0.014	0.009	0.005	0.013	0.008	0.017	0.004
Nd	0.047	0.050	0.031	0.027	0.030	0.028	0.050	0.032	0.021	0.027
La	0.035	0.051	0.031	0.025	0.031	0.038	0.049	0.030	0.024	0.021
Fe	0.056	0.060	0.019	0.038	0.026	0.028	0.040	0.034	0.037	0.022
Mn	0.006	0.002	0.000	0.007	0.004	0.001	0.009	0.003	0.009	0.007
Total cats.	18.540	17.970	17.963	18.247	18.218	18.080	18.206	17.939	18.009	17.811

					67		
	Ap 3a	Ap 3b	Ap 3c	Ap 4	Ap 1	Ap 2	Ap 3
F	3.367	3.630	3.923	3.454	4.790	3.401	4.670
Na2O	0.189	0.218	0.194	0.189	0.200	0.191	0.226
SiO2	2.456	0.920	0.456	1.384	0.387	1.033	0.481
P2O5	37.898	40.856	41.935	39.178	41.465	41.859	41.781
Cl	0.013	0.002	0.017	0.017	0.024	0.007	0.027
CaO	49.547	52.613	53.584	52.011	53.477	52.719	53.037
Ce2O3	2.526	1.472	1.018	1.848	0.875	1.592	1.208
Pr2O3	0.249	0.000	0.211	0.217	0.037	0.110	0.110
Nd2O3	1.318	0.773	0.492	1.025	0.442	0.693	0.580
La2O3	1.146	0.673	0.509	0.993	0.444	0.806	0.575
FeO	0.955	0.233	0.233	0.323	0.341	0.557	0.158
MnO	0.001	0.035	0.040	0.004	0.040	0.012	0.019
Total	99.665	101.425	102.612	100.643	102.522	102.980	102.872
F	1.874	1.956	2.086	1.895	2.571	1.798	2.496
Na	0.064	0.072	0.063	0.063	0.066	0.062	0.074
Si	0.432	0.157	0.077	0.240	0.066	0.173	0.081
P	5.646	5.893	5.968	5.754	5.956	5.923	5.977
Cl	0.004	0.001	0.005	0.005	0.007	0.002	0.008
Ca	9.605	9.651	9.667	9.722	9.441	9.602	
Ce	0.163	0.092	0.063	0.117	0.054	0.097	0.075
Pr	0.016	0.000	0.013	0.014	0.002	0.007	0.007
Nd	0.083	0.047	0.030	0.064	0.027	0.041	0.035
La	0.074	0.042	0.032	0.064	0.028	0.050	0.036
Fe	0.140	0.033	0.033	0.047	0.048	0.078	0.022
Mn	0.000	0.005	0.006	0.001	0.006	0.002	0.003
Total cats.	18.101	17.949	18.043	17.986	18.272	17.835	8.814

Typical ilmenite analyses

	Unit 2/3	Unit 4	Unit 5							
	43	68			54					56
	Il 1	Il 1	Il 2	Il 3	Il 1	Il 2	Il 3	Il 4	Il 5	Il 1
MgO	0.030	0.035	0.000	0.000	0.013	0.013	0.033	0.025	0.071	0.065
Al2O3	0.032	0.053	0.042	0.042	0.009	0.093	0.017	0.023	0.028	0.019
SiO2	0.015	0.045	0.021	0.047	0.011	0.019	0.032	0.021	0.030	0.032
TiO2	53.706	52.107	51.706	51.214	53.261	52.932	53.545	54.022	52.904	53.334
V2O3	0.291	0.333	0.316	0.305	0.306	0.300	0.274	0.297	0.328	0.303
MnO	1.345	1.591	1.592	1.684	1.027	1.488	1.048	0.962	0.970	0.984
Cr2O3	0.000	0.018	0.037	0.020	0.136	0.000	0.000	0.000	0.009	0.000
FeO	46.162	45.227	44.929	44.386	46.557	44.488	46.861	46.587	46.487	46.464
Fe2O3	0.000	1.210	0.940	1.329	0.000	0.000	0.000	0.000	0.861	0.000
Total	101.582	100.618	99.583	99.027	101.320	99.334	101.810	101.936	101.689	101.202
Mg	0.002	0.003	0.000	0.000	0.001	0.001	0.002	0.002	0.005	0.005
Al	0.002	0.003	0.002	0.002	0.001	0.006	0.001	0.001	0.002	0.001
Si	0.001	0.002	0.001	0.002	0.001	0.001	0.002	0.001	0.001	0.002
Ti	2.003	1.966	1.972	1.964	1.994	2.013	1.995	2.006	1.975	1.998
V	0.012	0.013	0.013	0.012	0.012	0.012	0.011	0.012	0.013	0.012
Mn	0.057	0.068	0.068	0.073	0.043	0.064	0.044	0.040	0.041	0.042
Cr	0.000	0.001	0.001	0.001	0.005	0.000	0.000	0.000	0.000	0.000
Fe2	1.914	1.898	1.906	1.893	1.939	1.881	1.942	1.924	1.930	1.935
Fe3	0.000	0.046	0.036	0.051	0.000	0.000	0.000	0.000	0.032	0.000
Total cats.	3.990	4.000	4.000	4.000	3.996	3.977	3.997	3.986	4.000	3.994

	Unit 7									
						64				65
	Il 2	Il 3	Il 4	Il 5	Il 6	Il 1	Il 2	Il 3	Il 4	Il 1
MgO	0.070	0.060	0.018	0.015	0.000	0.041	0.080	0.068	0.017	0.027
Al2O3	0.004	0.023	0.030	0.038	0.023	0.013	0.013	0.032	0.023	0.034
SiO2	0.019	0.030	0.032	0.034	0.036	0.021	0.019	0.011	0.015	0.006
TiO2	53.506	53.431	53.418	53.863	53.538	52.749	53.164	53.518	52.867	53.198
V2O3	0.334	0.356	0.284	0.310	0.331	0.307	0.333	0.310	0.322	0.322
MnO	0.981	1.055	1.240	1.723	1.482	1.121	1.021	1.156	1.063	1.626
Cr2O3	0.000	0.073	0.000	0.022	0.000	0.000	0.000	0.000	0.056	0.000
FeO	46.796	46.535	46.767	46.017	46.238	46.233	46.639	46.839	46.475	46.019
Fe2O3	0.000	0.000	0.001	0.000	0.000	0.695	0.650	0.000	0.215	0.000
Total	101.711	101.563	101.790	102.022	101.648	101.181	101.919	101.934	101.053	101.232
Mg	0.005	0.004	0.001	0.001	0.000	0.003	0.006	0.005	0.001	0.002
Al	0.000	0.001	0.002	0.002	0.001	0.001	0.001	0.002	0.001	0.002
Si	0.001	0.001	0.002	0.002	0.002	0.001	0.001	0.001	0.001	0.000
Ti	1.995	1.994	1.992	2.000	1.997	1.979	1.980	1.992	1.987	1.994
V	0.013	0.014	0.011	0.012	0.013	0.012	0.013	0.012	0.013	0.013
Mn	0.041	0.044	0.052	0.072	0.062	0.047	0.043	0.048	0.045	0.069
Cr	0.000	0.003	0.000	0.001	0.000	0.000	0.000	0.000	0.002	0.000
Fe2	1.941	1.932	1.939	1.900	1.918	1.929	1.932	1.939	1.942	1.918
Fe3	0.000	0.000	0.000	0.000	0.000	0.026	0.024	0.000	0.008	0.000
Total cats.	3.997	3.995	4.000	3.990	3.994	4.000	4.000	4.000	4.000	3.998

					66				67	
	Il 2	Il 3	il 4	il 5	Il 1	Il 2	Il 3	Il 4	Il 1	Il 2
MgO	0.017	0.023	0.043	0.022	0.020	0.045	0.033	0.030	0.013	0.053
Al2O3	0.030	0.025	0.006	0.028	0.023	0.008	0.023	0.008	0.023	0.006
SiO2	0.006	0.000	0.019	0.004	0.011	0.000	0.015	0.019	0.009	0.011
TiO2	53.279	52.757	52.626	52.929	53.199	53.228	53.289	53.676	53.338	52.887
V2O3	0.322	0.312	0.285	0.333	0.319	0.318	0.306	0.293	0.284	0.316
MnO	1.711	1.930	1.440	2.288	1.147	1.027	0.967	1.005	1.784	1.553
Cr2O3	0.000	0.047	0.000	0.000	0.000	0.056	0.000	0.028	0.058	0.000
FeO	46.167	45.483	45.790	45.259	46.657	46.775	46.896	47.214	46.107	45.893
Fe2O3	0.000	0.221	0.710	1.154	0.774	0.684	0.977	0.199	0.000	0.719
Total	101.533	100.799	100.920	102.017	102.149	102.139	102.507	102.471	101.616	101.439
Mg	0.001	0.002	0.003	0.002	0.001	0.003	0.002	0.002	0.001	0.004
Al	0.002	0.001	0.000	0.002	0.001	0.000	0.001	0.000	0.001	0.000
Si	0.000	0.000	0.001	0.000	0.001	0.000	0.001	0.001	0.000	0.001
Ti	1.992	1.987	1.980	1.971	1.978	1.979	1.974	1.989	1.992	1.980
V	0.013	0.013	0.011	0.013	0.013	0.013	0.012	0.012	0.011	0.013
Mn	0.072	0.082	0.061	0.096	0.048	0.043	0.040	0.042	0.075	0.065
Cr	0.000	0.002	0.000	0.000	0.000	0.002	0.000	0.001	0.002	0.000
Fe2	1.920	1.905	1.916	1.874	1.929	1.934	1.932	1.945	1.915	1.910
Fe3	0.000	0.008	0.027	0.043	0.029	0.025	0.036	0.007	0.000	0.027
Total cats.	4.000	4.000	3.999	4.000	4.000	4.000	4.000	4.000	3.999	4.000

Typical magnetite analyses

	Unit 4		Unit 7	
	68		65	54
	Mt 1	Mt 3	Mt 1	Mt 1
MgO	0.005	0.000	0.012	0.020
Al2O3	0.138	0.350	0.138	0.525
SiO2	0.053	0.064	0.092	0.071
TiO2	3.925	2.522	5.016	7.231
V2O3	0.016	0.010	0.022	0.041
MnO	0.118	0.068	0.190	0.256
Cr2O3	0.035	0.022	0.000	0.000
FeO	34.370	33.209	34.743	37.219
Fe2O3	60.745	63.325	57.439	53.661
Total	99.405	99.571	97.651	99.024
Mg	0.002	0.000	0.005	0.009
Al	0.050	0.127	0.051	0.191
Si	0.016	0.020	0.029	0.022
Ti	0.910	0.584	1.183	1.674
V	0.004	0.003	0.006	0.010
Mn	0.031	0.018	0.050	0.067
Cr	0.009	0.005	0.000	0.000
Fe2	8.867	8.555	9.110	9.583
Fe3	14.100	14.677	13.550	12.431
Total cats.	23.990	23.989	23.984	23.987

Typical zircon analyses

	Unit 3			
	45			
	Zrn 1a	Zrn 1b	Zrn 1c	Zrn 1d
Al2O3	0.013	0.028	0.021	0.019
SiO2	31.145	32.486	31.761	32.542
ZrO2	61.810	64.112	63.163	63.543
P2O5	0.053	0.078	0.073	0.034
Y2O3	0.286	0.368	0.276	0.351
Ce2O3	0.002	0.011	0.023	0.019
La2O3	0.068	0.025	0.013	0.032
CaO	0.297	0.024	0.126	0.028
ThO2	0.026	0.059	0.061	0.083
HfO2	2.301	2.351	2.403	2.423
Fe2O3	0.559	0.064	0.473	0.157
Nd2O3	0.030	0.000	0.016	0.023
TiO2	0.067	0.045	0.040	0.050
Total	96.656	99.651	98.451	99.304
Al	0.002	0.004	0.003	0.003
Si	3.975	4.012	3.979	4.030
Zr	3.847	3.861	3.859	3.837
P	0.006	0.008	0.008	0.004
Y	0.019	0.024	0.018	0.023
Ce	0.000	0.000	0.001	0.001
La	0.003	0.001	0.001	0.001
Ca	0.041	0.003	0.017	0.004
Th	0.001	0.002	0.002	0.002
Hf	0.084	0.083	0.086	0.086
Fe	0.054	0.006	0.045	0.015
Nd	0.001	0.000	0.001	0.001
Ti	0.006	0.004	0.004	0.005
Total cats.	8.038	8.008	8.023	8.011

							Unit 3		Unit 7	
			48				50		67	
	Zrn 1e	Zrn 1f	Zrn 1a	Zrn 1b	Zrn 1c	Zrn 1d	Zrn 1a	Zrn 1b	Zrn 1a	Zrn 1b
Al2O3	0.028	0.021	0.023	0.023	0.021	0.026	0.017	0.013	0.013	0.006
SiO2	31.795	32.439	32.965	32.741	32.193	32.717	33.047	32.756	32.623	32.826
ZrO2	61.827	62.497	65.656	64.394	63.675	65.148	66.432	66.187	65.172	65.118
P2O5	0.087	0.087	0.089	0.112	0.117	0.096	0.069	0.126	0.055	0.073
Y2O3	0.372	0.462	0.047	0.428	0.720	0.478	0.132	0.321	0.914	0.320
Ce2O3	0.030	0.023	0.013	0.002	0.029	0.020	0.027	0.067	0.101	0.035
La2O3	0.046	0.021	0.020	0.023	0.000	0.016	0.023	0.000	0.052	0.075
CaO	0.158	0.020	0.017	0.006	0.088	0.011	0.024	0.015	0.050	0.017
ThO2	0.052	0.020	0.000	0.112	0.157	0.011	0.000	0.063	0.187	0.018
HfO2	2.355	2.329	1.877	1.939	1.718	2.030	1.215	1.064	1.440	1.583
Fe2O3	0.525	0.217	0.103	0.036	0.309	0.034	0.000	0.016	0.044	0.093
Nd2O3	0.020	0.001	0.034	0.055	0.080	0.045	0.009	0.000	0.026	0.000
TiO2	0.052	0.052	0.060	0.002	0.057	0.002	0.017	0.013	0.058	0.062
Total	97.348	98.191	100.904	99.872	99.165	100.635	101.012	100.640	100.735	100.226
Al	0.004	0.003	0.003	0.003	0.003	0.004	0.002	0.002	0.002	0.001
Si	4.016	4.051	4.009	4.025	3.993	4.000	4.007	3.990	3.988	4.016
Zr	3.808	3.805	3.893	3.860	3.851	3.884	3.928	3.932	3.885	3.885
P	0.009	0.009	0.009	0.012	0.012	0.010	0.007	0.013	0.006	0.008
Y	0.025	0.031	0.003	0.028	0.048	0.031	0.009	0.021	0.059	0.021
Ce	0.001	0.001	0.001	0.000	0.001	0.001	0.001	0.003	0.005	0.002
La	0.002	0.001	0.001	0.001	0.000	0.001	0.001	0.000	0.002	0.003
Ca	0.021	0.003	0.002	0.001	0.012	0.001	0.003	0.002	0.007	0.002
Th	0.002	0.001	0.000	0.003	0.004	0.000	0.000	0.002	0.005	0.001
Hf	0.085	0.083	0.065	0.068	0.061	0.071	0.042	0.037	0.050	0.055
Fe	0.050	0.020	0.009	0.003	0.029	0.003	0.000	0.001	0.004	0.009
Nd	0.001	0.000	0.001	0.002	0.004	0.002	0.000	0.000	0.001	0.000
Ti	0.005	0.005	0.005	0.000	0.005	0.000	0.002	0.001	0.005	0.006
Total cats.	8.029	8.013	8.003	8.006	8.023	8.008	8.003	8.004	8.020	8.007

		Unit 8								
		34								
	Zrn 1c	Zrn 1a	Zrn 1b	Zrn 2	Zrn 3a	Zrn 3b	Zrn 3c	Zrn 3d	Zrn 3e	Zrn 3f
Al2O3	0.021	0.032	0.028	0.015	0.017	0.030	0.023	0.009	0.009	0.025
SiO2	32.991	32.809	32.679	32.692	32.602	32.381	31.692	30.805	32.039	32.456
ZrO2	64.944	65.923	64.794	66.016	66.006	64.806	65.063	64.729	61.695	63.165
P2O5	0.076	0.000	0.099	0.142	0.108	0.119	0.144	0.128	0.096	0.103
Y2O3	0.306	0.093	0.847	0.029	0.593	0.766	0.604	0.720	0.728	1.702
Ce2O3	0.061	0.055	0.039	0.001	0.070	0.000	0.050	0.090	0.042	0.012
La2O3	0.043	0.049	0.057	0.002	0.022	0.057	0.046	0.000	0.000	0.004
CaO	0.017	0.036	0.006	0.014	0.003	0.029	0.011	0.015	0.043	0.021
ThO2	0.089	0.007	0.071	0.010	0.092	0.049	0.006	0.049	0.193	0.098
HfO2	1.353	1.877	1.550	1.864	0.987	1.166	1.307	1.244	1.323	1.120
Fe2O3	0.112	0.020	0.073	0.021	0.049	0.043	0.021	0.056	0.130	0.139
Nd2O3	0.000	0.115	0.013	0.000	0.020	0.068	0.051	0.022	0.022	0.084
TiO2	0.062	0.057	0.050	0.078	0.020	0.050	0.027	0.018	0.012	0.053
Total	100.073	101.074	100.304	100.886	100.588	99.565	99.046	97.886	96.334	98.981
Al	0.003	0.005	0.004	0.002	0.002	0.004	0.003	0.001	0.001	0.004
Si	4.033	3.995	4.003	3.982	3.980	3.991	3.944	3.896	4.064	4.021
Zr	3.872	3.915	3.870	3.921	3.929	3.895	3.948	3.992	3.816	3.816
P	0.008	0.000	0.010	0.015	0.011	0.012	0.015	0.014	0.010	0.011
Y	0.020	0.006	0.055	0.002	0.039	0.050	0.040	0.048	0.049	0.112
Ce	0.003	0.002	0.002	0.000	0.003	0.000	0.002	0.004	0.002	0.001
La	0.002	0.002	0.003	0.000	0.001	0.003	0.002	0.000	0.000	0.000
Ca	0.002	0.005	0.001	0.002	0.000	0.004	0.001	0.002	0.006	0.003
Th	0.002	0.000	0.002	0.000	0.003	0.001	0.000	0.001	0.006	0.003
Hf	0.047	0.065	0.054	0.065	0.034	0.041	0.046	0.045	0.048	0.040
Fe	0.010	0.002	0.007	0.002	0.004	0.004	0.002	0.005	0.012	0.013
Nd	0.000	0.005	0.001	0.000	0.001	0.003	0.002	0.001	0.001	0.004
Ti	0.006	0.005	0.005	0.007	0.002	0.005	0.002	0.002	0.001	0.005
Total cats.	8.008	8.007	8.015	7.998	8.010	8.014	8.009	8.012	8.016	8.031

	36 Zrn 1a	Zrn 1b	Zrn 1c	Zrn 1d	Zrn 2a	Zrn 2b
Al2O3	0.009	0.017	0.013	0.030	0.013	0.017
SiO2	32.816	32.846	32.734	32.869	31.936	32.490
ZrO2	65.558	65.525	64.614	64.406	63.740	64.497
P2O5	0.103	0.089	0.112	0.076	0.135	0.179
Y2O3	0.419	0.000	0.926	0.163	0.540	0.606
Ce2O3	0.059	0.054	0.015	0.050	0.000	0.034
La2O3	0.016	0.067	0.042	0.004	0.049	0.081
CaO	0.027	0.006	0.007	0.035	0.250	0.014
ThO2	0.138	0.126	0.100	0.023	0.158	0.114
HfO2	1.551	1.664	1.532	1.561	1.356	1.243
Fe2O3	0.030	0.031	0.021	0.053	0.203	0.020
Nd2O3	0.058	0.108	0.026	0.055	0.023	0.000
TiO2	0.000	0.047	0.048	0.093	0.128	0.043
Total	100.784	100.580	100.192	99.418	98.534	99.338
Al	0.001	0.002	0.002	0.004	0.002	0.002
Si	4.001	4.010	4.011	4.042	3.981	4.008
Zr	3.898	3.901	3.861	3.862	3.874	3.880
P	0.011	0.009	0.012	0.008	0.014	0.019
Y	0.027	0.000	0.060	0.011	0.036	0.040
Ce	0.003	0.002	0.001	0.002	0.000	0.002
La	0.001	0.003	0.002	0.000	0.002	0.004
Ca	0.003	0.001	0.001	0.005	0.033	0.002
Th	0.004	0.004	0.003	0.001	0.004	0.003
Hf	0.054	0.058	0.054	0.055	0.048	0.044
Fe	0.003	0.003	0.002	0.005	0.019	0.002
Nd	0.003	0.005	0.001	0.002	0.001	0.000
Ti	0.000	0.004	0.004	0.009	0.012	0.004
Total cats.	8.008	8.001	8.014	8.006	8.028	8.008

West Kungnat: Typical pyroxene analyses

Unit 2 (Troughs)

	MH-KUN-92 23			MH-KUN-92 25			MH-KUN-92 26		MH-KUN-92 28	
	Px 1	Px 2	Px 3	Px 1	Px 2	Px 3	Px 1	Px 2	Px 1	Px 2
NaO2	0.462	0.574	0.384	0.470	0.491	0.488	0.492	0.557	0.530	0.500
MgO	4.571	3.509	4.213	3.948	4.802	4.170	4.666	4.508	4.400	4.480
Al2O3	0.941	0.620	0.450	0.756	0.438	0.799	0.822	1.018	0.630	0.760
SiO2	48.371	48.444	48.916	48.501	49.601	48.707	49.644	49.216	48.310	48.750
K2O	0.006	0.006	0.000	0.001	0.001	0.000	0.006	0.000	no analyses made	
CaO	20.792	21.198	21.609	20.210	21.083	20.167	20.998	20.900	21.220	21.020
TiO2	0.764	0.347	0.138	0.636	0.339	0.674	0.631	0.846	0.280	0.470
Cr2O3	0.010	0.032	0.012	0.000	0.016	0.007	0.000	0.001	0.010	0.010
MnO	0.615	0.608	0.609	0.620	0.604	0.626	0.582	0.619	0.600	0.590
FeO	22.662	24.436	23.112	24.389	22.722	24.063	22.552	22.874	24.160	24.060
Total	99.194	99.773	99.444	99.532	100.097	99.701	100.393	100.539	100.140	100.640
Na	0.036	0.045	0.030	0.037	0.038	0.038	0.038	0.043	0.040	0.040
Mg	0.275	0.212	0.254	0.238	0.286	0.251	0.276	0.267	0.260	0.270
Al	0.045	0.030	0.021	0.036	0.021	0.038	0.038	0.048	0.030	0.040
Si	1.953	1.964	1.976	1.963	1.981	1.964	1.973	1.958	1.950	1.950
K	0.000	0.000	0.000	0.000	0.000	0.000	0.000	0.000	no analyses made	
Ca	0.900	0.921	0.935	0.877	0.902	0.871	0.894	0.891	0.920	0.900
Ti	0.023	0.011	0.004	0.019	0.010	0.020	0.019	0.025	0.010	0.010
Cr	0.000	0.001	0.000	0.000	0.001	0.000	0.000	0.000	0.000	0.000
Mn	0.021	0.021	0.021	0.021	0.020	0.021	0.020	0.021	0.020	0.020
Fe	0.765	0.828	0.781	0.826	0.759	0.811	0.749	0.761	0.820	0.810
Total cats.	4.019	4.033	4.023	4.017	4.017	4.015	4.008	4.014	4.050	4.040

Unit 2 (Host)

	MH-KUN-92 24			MH-KUN-	MH-KUN-92 31			MH-KUN-92 32		
	Px 1	Px 2	Px 3	Px 1	Px 1	Px 2	Px 3	Px 1	Px 2	Px 3
NaO2	0.627	0.360	0.495	0.560	0.489	0.474	0.518	0.476	0.468	0.514
MgO	3.087	4.621	3.316	4.730	4.147	4.419	4.147	3.182	3.475	3.409
Al2O3	0.408	0.450	0.642	0.420	0.839	0.907	0.741	0.720	0.699	0.495
SiO2	49.073	49.588	48.728	48.890	48.347	48.542	48.743	47.973	48.166	48.360
K2O	0.012	0.007	0.011	0.020	0.020	0.008	0.007	0.011	0.011	0.017
CaO	20.213	21.061	20.393	22.250	21.017	21.094	21.425	20.623	20.626	20.872
TiO2	0.244	0.292	0.502	0.180	0.684	0.724	0.435	0.626	0.560	0.294
Cr2O3	0.013	0.028	0.004	0.000	0.000	0.007	0.000	0.000	0.009	0.015
MnO	0.630	0.625	0.638	0.660	0.660	0.624	0.639	0.666	0.660	0.638
FeO	25.645	22.817	24.975	23.090	24.157	24.072	24.045	25.318	25.004	24.930
Total	99.952	99.849	99.705	100.780	100.361	100.872	100.699	99.594	99.678	99.542
Na	0.049	0.028	0.039	0.040	0.038	0.037	0.040	0.038	0.037	0.041
Mg	0.186	0.276	0.200	0.280	0.249	0.263	0.248	0.193	0.211	0.207
Al	0.019	0.021	0.031	0.020	0.040	0.043	0.035	0.035	0.033	0.024
Si	1.988	1.985	1.975	1.950	1.945	1.940	1.953	1.955	1.957	1.968
K	0.001	0.000	0.001	0.001	0.001	0.000	0.000	0.001	0.001	0.001
Ca	0.877	0.903	0.885	0.950	0.906	0.903	0.920	0.901	0.898	0.910
Ti	0.007	0.009	0.015	0.010	0.021	0.022	0.013	0.019	0.017	0.009
Cr	0.000	0.001	0.000	0.000	0.000	0.000	0.000	0.000	0.000	0.000
Mn	0.022	0.021	0.022	0.020	0.022	0.021	0.022	0.023	0.023	0.022
Fe	0.869	0.764	0.846	0.770	0.813	0.805	0.806	0.863	0.850	0.849
Total cats.	4.019	4.009	4.014	4.050	4.034	4.035	4.036	4.027	4.027	4.031

	Unit 3									
	MH-KUN-92 33		101			102			103	
	Px 1	Px 2	Px 1	Px 2	Px 3	Px 1	Px 2	Px 3	Px 1	Px 2
NaO2	0.547	0.408	0.543	0.468	0.473	0.481	0.687	0.522	0.348	0.553
MgO	3.439	4.401	3.907	4.702	3.656	4.480	4.041	4.225	5.107	4.042
Al2O3	0.571	0.476	0.620	0.465	0.537	0.822	0.268	0.748	0.675	0.707
SiO2	47.971	49.032	48.720	49.132	48.625	48.797	49.622	48.568	49.160	48.827
K2O	0.000	0.012	0.000	0.000	0.000	0.000	0.000	0.008	0.000	0.001
CaO	20.938	21.689	21.061	21.304	20.994	20.998	21.127	21.405	21.818	21.280
TiO2	0.407	0.215	0.335	0.349	0.312	0.457	0.080	0.522	0.419	0.352
Cr2O3	0.000	0.012	0.006	0.000	0.000	0.018	0.000	0.013	0.028	0.031
MnO	0.625	0.646	0.586	0.575	0.573	0.559	0.640	0.545	0.567	0.558
FeO	25.264	23.836	24.476	23.082	24.729	23.006	23.466	23.216	21.380	23.356
Total	99.761	100.727	100.253	100.077	99.899	99.618	99.932	99.772	99.501	99.707
Na	0.043	0.032	0.042	0.036	0.037	0.038	0.054	0.041	0.027	0.043
Mg	0.209	0.262	0.235	0.281	0.221	0.269	0.242	0.254	0.305	0.243
Al	0.027	0.022	0.029	0.022	0.026	0.039	0.013	0.036	0.032	0.034
Si	1.954	1.962	1.963	1.969	1.968	1.963	1.994	1.957	1.968	1.968
K	0.000	0.001	0.000	0.000	0.000	0.000	0.000	0.000	0.000	0.000
Ca	0.914	0.930	0.909	0.915	0.910	0.905	0.909	0.924	0.936	0.919
Ti	0.012	0.006	0.010	0.011	0.009	0.014	0.002	0.016	0.013	0.011
Cr	0.000	0.000	0.000	0.000	0.000	0.001	0.000	0.000	0.001	0.001
Mn	0.022	0.022	0.020	0.020	0.020	0.019	0.022	0.019	0.019	0.019
Fe	0.861	0.798	0.825	0.774	0.837	0.774	0.788	0.782	0.716	0.787
Total cats.	4.041	4.036	4.033	4.027	4.028	4.021	4.024	4.029	4.016	4.025

	Unit 3									
		115			116			117		
	Px 3	Px 1	Px 2	Px 3	Px 1	Px 2	Px 3	Px 1	Px 2	Px 3
NaO2	0.472	0.483	0.464	0.462	0.522	0.520	0.532	0.523	0.476	0.499
MgO	5.147	3.963	5.057	4.374	3.449	4.009	3.573	3.863	4.235	3.686
Al2O3	0.930	0.873	0.433	0.863	0.701	0.686	0.658	0.797	0.306	0.748
SiO2	48.908	48.510	49.830	48.732	48.963	48.944	48.814	48.677	49.471	48.604
K2O	0.013	0.005	0.011	0.001	0.002	0.016	0.000	0.018	0.008	0.014
CaO	20.953	20.409	21.299	20.273	20.621	20.554	20.659	20.609	21.562	20.445
TiO2	0.684	0.654	0.137	0.629	0.402	0.449	0.422	0.475	0.137	0.465
Cr2O3	0.000	0.010	0.004	0.015	0.007	0.000	0.004	0.042	0.032	0.022
MnO	0.595	0.612	0.640	0.607	0.557	0.633	0.573	0.589	0.630	0.558
FeO	22.265	23.991	22.144	23.623	24.404	23.531	24.527	23.975	22.833	24.492
Total	99.967	99.509	100.019	99.580	99.628	99.342	99.763	99.569	99.689	99.534
Na	0.037	0.038	0.036	0.036	0.041	0.041	0.042	0.041	0.037	0.039
Mg	0.306	0.239	0.300	0.263	0.208	0.241	0.215	0.233	0.254	0.223
Al	0.044	0.042	0.020	0.041	0.033	0.033	0.031	0.038	0.015	0.036
Si	1.954	1.961	1.986	1.963	1.980	1.977	1.973	1.967	1.989	1.969
K	0.001	0.000	0.001	0.000	0.000	0.001	0.000	0.001	0.000	0.001
Ca	0.897	0.884	0.910	0.875	0.893	0.890	0.895	0.892	0.929	0.887
Ti	0.021	0.020	0.004	0.019	0.012	0.014	0.013	0.014	0.004	0.014
Cr	0.000	0.000	0.000	0.000	0.000	0.000	0.000	0.001	0.001	0.001
Mn	0.020	0.021	0.022	0.021	0.019	0.022	0.020	0.020	0.021	0.019
Fe	0.744	0.811	0.738	0.796	0.825	0.795	0.829	0.810	0.768	0.830
Total cats.	4.022	4.016	4.017	4.015	4.012	4.013	4.019	4.019	4.018	4.018

Unit 4

	118			138			139		140	
	Px 1	Px 2	Px 3	Px 1	Px 2	Px 3	Px 1	Px 2	Px 1	Px 2
NaO2	0.481	0.330	0.665	0.473	0.396	0.470	0.497	0.496	0.348	0.421
MgO	4.649	3.951	4.439	2.893	4.144	3.008	3.121	2.756	4.001	2.607
Al2O3	0.935	0.272	0.843	0.697	0.873	0.701	0.743	0.639	0.259	0.351
SiO2	48.275	49.873	48.981	47.795	48.110	48.228	48.131	47.466	49.353	48.658
K2O	0.017	0.000	0.000	0.005	0.006	0.010	0.010	0.011	0.008	0.013
CaO	20.372	21.019	20.200	20.634	20.551	20.894	20.865	20.863	21.626	20.767
TiO2	0.595	0.092	0.679	0.560	0.751	0.417	0.539	0.377	0.097	0.204
Cr2O3	0.003	0.016	0.000	0.028	0.029	0.000	0.035	0.007	0.022	0.013
MnO	0.626	0.659	0.628	0.671	0.670	0.644	0.598	0.602	0.711	0.671
FeO	22.853	24.059	23.566	25.776	24.033	25.458	25.240	25.866	23.598	26.281
Total	98.808	100.270	99.999	99.534	99.563	99.831	99.778	99.221	100.023	99.985
Na	0.038	0.026	0.052	0.038	0.031	0.037	0.039	0.040	0.027	0.033
Mg	0.281	0.236	0.265	0.176	0.250	0.182	0.189	0.169	0.240	0.158
Al	0.045	0.013	0.040	0.034	0.042	0.034	0.036	0.031	0.012	0.017
Si	1.957	1.998	1.964	1.955	1.948	1.962	1.957	1.954	1.985	1.981
K	0.001	0.000	0.000	0.000	0.000	0.001	0.000	0.001	0.000	0.001
Ca	0.885	0.902	0.868	0.904	0.892	0.911	0.909	0.920	0.932	0.906
Ti	0.018	0.003	0.020	0.017	0.023	0.013	0.016	0.012	0.003	0.006
Cr	0.000	0.001	0.000	0.001	0.001	0.000	0.001	0.000	0.001	0.000
Mn	0.022	0.022	0.021	0.023	0.023	0.022	0.021	0.021	0.024	0.023
Fe	0.775	0.806	0.790	0.882	0.814	0.866	0.858	0.891	0.794	0.895
Total cats.	4.021	4.005	4.021	4.029	4.023	4.027	4.027	4.056	4.019	4.021

	141		
	Px 3	Px 1	Px 2
NaO2	0.487	0.448	0.531
MgO	3.008	4.729	3.200
Al2O3	0.735	0.930	0.382
SiO2	48.172	48.332	48.745
K2O	0.000	0.002	0.012
CaO	20.521	20.479	21.108
TiO2	0.574	0.742	0.185
Cr2O3	0.010	0.003	0.004
MnO	0.653	0.634	0.699
FeO	25.829	23.005	24.802
Total	100.149	99.304	99.669
Na	0.038	0.035	0.042
Mg	0.182	0.285	0.194
Al	0.035	0.044	0.018
Si	1.958	1.951	1.980
K	0.000	0.000	0.001
Ca	0.894	0.886	0.919
Ti	0.018	0.023	0.006
Cr	0.000	0.000	0.000
Mn	0.022	0.022	0.024
Fe	0.878	0.777	0.843
Total cats.	4.046	4.022	4.026

Typical olivine analyses

Unit 2 (Troughs)

	MH-KUN-92 23			MH-KUN-92 26	
	Ol 1	Ol 2	Ol 3	Ol 1	Ol 2
MgO	1.932	2.175	1.948	2.389	2.525
Al2O3	0.015	0.011	0.015	0.019	0.030
SiO2	29.320	29.247	29.230	30.034	30.067
CaO	0.118	0.187	0.174	0.120	0.137
TiO2	0.050	0.067	0.065	0.068	0.040
Cr2O3	0.026	0.025	0.023	0.009	0.013
MnO	1.872	1.923	1.985	1.866	1.845
FeO	66.225	66.072	66.147	65.508	65.614
Total	99.672	99.771	99.758	100.139	100.290
Mg	0.097	0.109	0.098	0.118	0.125
Al	0.001	0.000	0.001	0.001	0.001
Si	0.987	0.983	0.984	0.999	0.997
Ca	0.004	0.007	0.006	0.004	0.005
Ti	0.001	0.002	0.002	0.002	0.001
Cr	0.001	0.001	0.001	0.000	0.000
Mn	0.053	0.055	0.057	0.053	0.052
Fe	1.865	1.858	1.863	1.822	1.820
Total cats.	3.020	3.021	3.026	3.011	3.002

Unit 2 (Host)

	MH-KUN-92 28			MH-KUN-92 31			MH-KUN-92 32			
	Ol 3	Ol 1	Ol 2	Ol 3	Ol 1	Ol 2	Ol 3	Ol 1	Ol 2	Ol 3
MgO	2.310	1.850	0.000	1.790	1.066	1.501	1.424	1.249	1.451	1.474
Al2O3	0.030	0.020	65.670	0.020	0.011	0.026	0.026	0.015	0.017	0.021
SiO2	29.711	30.140	30.130	30.110	29.273	29.369	29.249	28.943	28.997	29.108
CaO	0.133	0.110	0.000	0.150	0.134	0.088	0.118	0.125	0.139	0.150
TiO2	0.080	0.000	0.030	0.000	0.062	0.078	0.095	0.037	0.053	0.062
Cr2O3	0.019	0.000	1.810	0.000	0.000	0.009	0.010	0.034	0.018	0.018
MnO	1.823	1.870	0.060	1.930	2.128	1.983	1.932	1.879	1.850	1.868
FeO	65.543	66.310	2.500	66.950	68.220	67.474	67.675	67.524	66.782	66.900
Total	99.713	100.300	100.200	100.950	100.931	100.529	100.621	99.805	99.307	99.601
Mg	0.115	0.090	0.120	0.090	0.053	0.075	0.071	0.063	0.073	0.074
Al	0.001	0.000	0.000	0.000	0.000	0.001	0.001	0.001	0.001	0.001
Si	0.994	1.000	1.000	1.000	0.982	0.984	0.982	0.981	0.984	0.985
Ca	0.005	0.000	0.000	0.010	0.005	0.003	0.004	0.005	0.005	0.005
Ti	0.002	0.000	0.000	0.000	0.002	0.002	0.002	0.001	0.001	0.002
Cr	0.001	0.000	0.000	0.000	0.000	0.000	0.000	0.001	0.000	0.000
Mn	0.052	0.050	0.050	0.050	0.060	0.056	0.055	0.054	0.053	0.054
Fe	1.834	1.840	1.820	1.860	1.913	1.891	1.899	1.913	1.895	1.892
Total cats.	3.009	3.000	3.000	3.000	3.018	3.013	3.025	3.018	3.014	3.013

Unit 3

	MH-KUN-92 33			101			102			103
	Ol 1	Ol 2	Ol 3	Ol 1	Ol 2	Ol 3	Ol 1	Ol 2	Ol 3	Ol 1
MgO	1.055	1.487	1.331	2.170	1.985	1.847	1.741	1.787	2.023	2.421
Al2O3	0.008	0.017	0.013	0.021	0.025	0.006	0.015	0.023	0.009	0.015
SiO2	29.070	29.309	29.365	29.365	29.339	29.202	29.192	29.356	29.354	29.157
CaO	0.157	0.112	0.144	0.122	0.119	0.112	0.127	0.148	0.133	0.104
TiO2	0.077	0.065	0.043	0.087	0.080	0.072	0.092	0.072	0.075	0.067
Cr2O3	0.025	0.006	0.012	0.004	0.000	0.006	0.001	0.019	0.000	0.025
MnO	2.378	2.009	2.088	1.890	1.788	1.937	2.120	1.995	2.010	1.857
FeO	67.414	67.599	67.638	66.002	65.824	66.055	65.951	65.707	66.440	65.606
Total	100.281	100.660	100.761	99.788	99.267	99.399	99.374	99.171	100.048	99.333
Mg	0.053	0.074	0.067	0.109	0.100	0.093	0.088	0.090	0.101	0.122
Al	0.000	0.001	0.001	0.001	0.001	0.000	0.001	0.001	0.000	0.001
Si	0.982	0.982	0.984	0.986	0.990	0.987	0.987	0.992	0.984	0.983
Ca	0.006	0.004	0.005	0.004	0.004	0.004	0.005	0.005	0.005	0.004
Ti	0.002	0.002	0.001	0.002	0.002	0.002	0.002	0.002	0.002	0.002
Cr	0.001	0.000	0.000	0.000	0.000	0.000	0.000	0.001	0.000	0.001
Mn	0.068	0.057	0.059	0.054	0.051	0.055	0.061	0.057	0.057	0.053
Fe	1.904	1.894	1.896	1.854	1.858	1.868	1.866	1.857	1.863	1.850
Total cats.	3.024	3.019	3.025	3.023	3.016	3.026	3.023	3.011	3.013	3.022

Unit 3

			114			115			116	
	Ol 2	Ol 3	Ol 1	Ol 2	Ol 3	Ol 1	Ol 2	Ol 3	Ol 1	Ol 2
MgO	2.675	2.358	1.849	1.350	0.910	2.248	2.126	1.928	1.502	1.777
Al2O3	0.008	0.011	0.015	0.015	0.019	0.008	0.002	0.008	0.563	0.000
SiO2	29.050	29.236	29.326	29.339	29.269	29.461	29.354	29.358	29.842	29.074
CaO	0.090	0.147	0.085	0.140	0.136	0.087	0.113	0.073	0.109	0.126
TiO2	0.075	0.082	0.038	0.022	0.055	0.057	0.080	0.067	0.087	0.085
Cr2O3	0.018	0.003	0.020	0.019	0.026	0.019	0.013	0.000	0.003	0.000
MnO	1.818	1.810	2.160	2.214	2.440	1.809	1.786	1.801	2.094	2.060
FeO	64.919	65.512	66.347	66.665	67.082	66.728	66.087	66.417	65.691	66.270
Total	99.036	99.160	99.862	99.880	100.005	100.423	99.603	99.668	100.421	99.392
Mg	0.135	0.119	0.093	0.068	0.046	0.112	0.107	0.097	0.074	0.090
Al	0.000	0.000	0.001	0.001	0.001	0.000	0.000	0.000	0.022	0.000
Si	0.983	0.986	0.986	0.989	0.989	0.983	0.987	0.988	0.991	0.984
Ca	0.003	0.005	0.003	0.005	0.005	0.003	0.004	0.003	0.004	0.005
Ti	0.002	0.002	0.001	0.001	0.001	0.001	0.002	0.002	0.002	0.002
Cr	0.000	0.000	0.001	0.001	0.001	0.001	0.000	0.000	0.000	0.000
Mn	0.052	0.052	0.062	0.063	0.070	0.051	0.051	0.051	0.059	0.059
Fe	1.837	1.848	1.866	1.880	1.896	1.863	1.858	1.869	1.825	1.875
Total cats.	3.053	3.012	3.013	3.018	3.015	3.015	3.012	3.011	3.012	3.014

Unit 4

		117		138		139	140		141	
	Ol 3	Ol 1	Ol 2	Ol 1	Ol 2	Ol 1	Ol 1	Ol 2	Ol 1	Ol 2
MgO	1.751	1.875	1.549	1.265	1.035	1.298	0.816	1.263	1.650	1.673
Al2O3	0.036	0.015	0.019	0.004	0.019	0.011	0.017	0.000	0.021	0.023
SiO2	29.384	29.382	29.403	28.796	28.946	28.539	28.986	29.050	29.286	29.296
CaO	0.085	0.111	0.092	0.111	0.164	0.106	0.094	0.070	0.123	0.141
TiO2	0.082	0.068	0.067	0.073	0.083	0.082	0.047	0.047	0.047	0.040
Cr2O3	0.006	0.009	0.000	0.006	0.015	0.000	0.001	0.004	0.039	0.009
MnO	1.937	1.834	1.917	1.972	2.061	1.955	2.364	2.085	1.964	1.929
FeO	66.581	66.080	66.539	67.847	67.720	67.054	67.741	67.614	66.431	65.916
Total	99.865	99.533	99.720	100.109	100.134	99.054	100.093	100.163	99.662	99.051
Mg	0.088	0.094	0.078	0.064	0.052	0.066	0.041	0.064	0.083	0.084
Al	0.001	0.001	0.001	0.000	0.001	0.000	0.001	0.000	0.001	0.001
Si	0.988	0.991	0.991	0.975	0.980	0.976	0.982	0.981	0.988	0.992
Ca	0.003	0.004	0.003	0.004	0.006	0.004	0.003	0.003	0.004	0.005
Ti	0.002	0.002	0.002	0.002	0.002	0.002	0.001	0.001	0.001	0.001
Cr	0.000	0.000	0.000	0.000	0.000	0.000	0.000	0.000	0.001	0.000
Mn	0.055	0.052	0.055	0.057	0.059	0.057	0.068	0.060	0.056	0.055
Fe	1.872	1.863	1.876	1.921	1.917	1.917	1.919	1.909	1.874	1.866
Total cats.	3.009	3.024	3.018	3.026	3.027	3.022	3.017	3.019	3.019	3.007

Typical braid perthite analyses

	Unit 2 (Troughs)		Unit 2 (Host)		Unit 3			Unit 3	
	MH-KUN-92 28		MH-KUN-92 35			102	105		107
	Braid 7	Braid 8	Braid 2	Braid 5	Braid 2	Bp2	Bp1	Bp4	Braid 1	Braid 2
Na2O	6.129	6.300	6.237	6.110	5.799	6.991	5.973	6.477	5.446	5.520
MgO	0.000	0.007	0.010	0.012	0.015	0.003	0.005	0.000	0.012	0.017
Al2O3	18.817	18.904	18.521	18.475	18.789	19.241	19.993	19.985	18.611	18.560
Si2O	66.260	66.320	65.873	65.383	66.408	64.718	66.063	65.565	65.340	65.317
K2O	8.213	7.746	7.506	7.912	8.584	7.442	7.054	7.002	8.595	8.551
CaO	0.255	0.281	0.197	0.176	0.220	0.476	0.515	0.602	0.334	0.323
BaO	0.092	0.064	0.172	0.145	0.169	0.125	0.095	0.094	0.307	0.305
FeO	0.100	0.133	0.167	0.179	0.111	0.309	0.391	0.289	0.102	0.098
Total	99.866	99.754	98.683	98.392	100.094	99.304	100.089	100.014	98.747	98.691
Na	0.536	0.550	0.550	0.542	0.507	0.617	0.519	0.564	0.483	0.490
Mg	0.000	0.000	0.001	0.001	0.001	0.000	0.000	0.000	0.001	0.001
Al	1.000	1.004	0.994	0.996	0.998	1.032	1.056	1.058	1.003	1.001
Si	2.989	2.988	2.998	2.992	2.992	2.946	2.960	2.946	2.988	2.989
K	0.473	0.445	0.436	0.462	0.493	0.432	0.403	0.401	0.501	0.499
Ca	0.012	0.014	0.010	0.009	0.011	0.023	0.025	0.029	0.016	0.016
Ba	0.002	0.001	0.003	0.003	0.003	0.005	0.004	0.004	0.006	0.005
Fe	0.004	0.005	0.006	0.007	0.004	0.006	0.007	0.005	0.004	0.004
Total cats.	5.015	5.007	4.998	5.011	5.009	5.062	4.973	5.007	5.002	5.005

	Unit 4		Unit 4						
		120	128	137					140
	Braid 8	BP2	Braid 1	Braid 2	Braid 3	Braid 4	Braid 5	Braid 6	Braid 2
Na2O	6.790	6.330	6.666	6.854	6.698	6.840	6.619	6.768	6.548
MgO	0.002	0.007	0.018	0.008	0.017	0.013	0.013	0.015	0.015
Al2O3	18.993	18.825	18.889	19.197	19.055	19.125	19.193	19.076	19.071
Si2O	65.736	65.732	63.881	65.837	65.867	65.988	65.864	65.933	65.845
K2O	6.559	7.111	6.842	6.928	6.971	6.848	7.070	6.864	7.335
CaO	0.493	0.665	0.642	0.445	0.420	0.550	0.604	0.603	0.358
BaO	0.262	0.100	0.247	0.294	0.143	0.117	0.204	0.161	0.079
FeO	0.102	0.184	0.147	0.093	0.207	0.064	0.087	0.078	0.085
Total	98.936	98.992	97.332	99.655	99.377	99.546	99.656	99.498	99.336
Na	0.597	0.557	0.598	0.599	0.587	0.598	0.579	0.592	0.574
Mg	0.000	0.000	0.001	0.001	0.001	0.001	0.001	0.001	0.001
Al	1.014	1.006	1.030	1.020	1.015	1.016	1.020	1.014	1.016
Si	2.979	2.982	2.955	2.970	2.976	2.974	2.970	2.974	2.977
K	0.379	0.411	0.404	0.399	0.402	0.394	0.407	0.395	0.423
Ca	0.024	0.032	0.032	0.022	0.020	0.027	0.029	0.029	0.017
Ba	0.005	0.004	0.004	0.005	0.003	0.002	0.004	0.003	0.001
Fe	0.004	0.003	0.006	0.003	0.008	0.002	0.003	0.003	0.003
Total cats.	5.001	4.997	5.030	5.019	5.011	5.013	5.012	5.012	5.013

Typical biotite analyses

Unit 1

	MH-KUN-92 23			MH-KUN-92 25			MH-KUN-92 26			
	Bt 1	Bt 2	Bt 3	Bt 1	Bt 2	Bt 3	Bt 1	Bt 2	Bt 3	Bt 4
F	0.418	0.505	0.442	0.072	0.106	0.280	0.154	0.189	0.232	0.357
NaO2	0.089	0.171	0.189	0.088	0.201	0.255	0.274	0.260	0.259	0.205
MgO	3.731	3.795	3.460	2.389	3.054	3.081	3.706	3.867	4.096	4.542
Al2O3	9.978	10.307	9.835	10.124	10.672	10.466	11.193	11.167	10.957	10.835
SiO2	34.262	34.326	34.198	34.035	34.750	35.113	34.872	34.200	34.371	34.852
K2O	8.485	8.678	7.153	8.527	7.406	7.864	8.607	8.261	8.377	7.775
CaO	0.153	0.034	0.474	0.021	0.210	0.217	0.021	0.130	0.180	0.303
TiO2	4.060	3.805	3.488	4.067	4.579	4.385	5.118	5.119	4.766	4.454
Cr2O3	0.019	0.009	0.000	0.018	0.023	0.007	0.000	0.015	0.003	0.000
MnO	0.127	0.156	0.229	0.208	0.174	0.148	0.207	0.179	0.212	0.168
FeO	33.467	33.768	34.842	35.600	32.911	33.938	33.053	32.635	32.487	32.738
Total	94.789	95.554	94.310	95.149	94.086	95.754	97.205	96.022	95.940	96.229
F	0.221	0.265	0.235	0.038	0.056	0.145	0.078	0.097	0.120	0.183
Na	0.029	0.055	0.062	0.028	0.065	0.081	0.086	0.082	0.082	0.065
Mg	0.929	0.940	0.868	0.597	0.755	0.754	0.891	0.941	0.999	1.101
Al	1.966	2.019	1.950	2.001	2.086	2.026	2.128	2.149	2.112	2.076
Si	5.727	5.705	5.753	5.708	5.763	5.768	5.627	5.585	5.621	5.666
K	1.809	1.840	1.535	1.824	1.567	1.648	1.772	1.721	1.748	1.612
Ca	0.027	0.006	0.085	0.004	0.037	0.038	0.004	0.023	0.032	0.053
Ti	0.510	0.476	0.441	0.513	0.571	0.542	0.621	0.629	0.586	0.545
Cr	0.003	0.001	0.000	0.002	0.003	0.001	0.000	0.002	0.000	0.000
Mn	0.018	0.022	0.033	0.030	0.024	0.021	0.028	0.025	0.029	0.023
Fe	4.678	4.693	4.902	4.993	4.565	4.662	4.460	4.457	4.443	4.451
Total cats.	18.055	18.147	18.029	17.810	17.527	17.751	15.695	15.710	15.772	15.774

	MH-KUN-92 28			MH-KUN-92 24		MH-KUN-92 31			
	Bt 5	Bt 1	Bt 2	Bt 1	Bt 2	Bt 3	Bt 1	Bt 2	Bt 3
F	0.333	0.720	1.000	0.227	0.318	0.347	0.374	0.571	0.411
NaO2	0.152	0.070	0.060	0.201	0.120	0.127	0.069	0.054	0.062
MgO	5.654	4.340	6.230	2.265	3.293	3.635	2.416	2.477	3.845
Al2O3	10.776	11.480	10.920	9.506	9.663	9.262	10.177	10.190	9.916
SiO2	35.503	32.810	34.580	34.501	35.293	34.660	34.752	34.754	35.038
K2O	8.739	8.770	9.370	8.437	7.914	8.029	8.250	8.561	8.427
CaO	0.007	0.100	0.000	0.027	0.180	0.189	0.108	0.045	0.025
TiO2	3.897	5.030	4.240	4.305	3.578	3.194	4.057	4.375	3.236
Cr2O3	0.000	No analyses made		0.000	0.000	0.000	0.000	0.000	0.004
MnO	0.169	0.170	0.120	0.297	0.320	0.288	0.152	0.195	0.127
FeO	31.309	33.720	30.400	35.794	34.658	34.589	35.920	34.715	35.107
Total	96.539	97.210	96.920	95.560	95.337	94.320	96.275	95.937	96.198
F	0.170	0.390	0.540	0.120	0.167	0.185	0.196	0.300	0.215
Na	0.047	0.020	0.020	0.065	0.039	0.041	0.022	0.017	0.020
Mg	1.359	1.110	1.570	0.565	0.814	0.913	0.597	0.613	0.947
Al	2.048	2.320	2.180	1.875	1.890	1.840	1.987	1.993	1.931
Si	5.726	5.630	5.860	5.774	5.856	5.841	5.757	5.768	5.790
K	1.798	1.920	2.030	1.801	1.675	1.726	1.743	1.813	1.776
Ca	0.001	0.020	0.000	0.005	0.032	0.034	0.019	0.008	0.005
Ti	0.473	0.650	0.540	0.542	0.446	0.405	0.505	0.546	0.402
Cr	0.000	No analyses made		0.000	0.000	0.000	0.000	0.000	0.001
Mn	0.023	0.020	0.020	0.042	0.045	0.041	0.021	0.027	0.018
Fe	4.223	4.840	4.310	5.010	4.810	4.875	4.976	4.819	4.852
Total cats.	15.870	16.920	17.070	17.884	17.919	18.048	15.823	15.904	15.955

	MH-KUN-92 33			115			116			117
	Bt 1	Bt 2	Bt 3	Bt 1	Bt 2	Bt 3	Bt 1	Bt 2	Bt 3	Bt 1
F	0.323	0.239	0.236	0.219	0.144	0.204	0.000	0.316	0.183	0.357
NaO2	0.046	0.043	0.077	0.197	0.295	0.239	0.135	0.185	0.174	0.155
MgO	1.660	2.645	1.690	4.391	3.650	4.304	0.958	4.293	1.698	3.699
Al2O3	9.574	10.156	9.568	11.284	11.012	10.687	11.484	10.749	11.361	9.389
SiO2	34.320	34.910	34.221	34.874	34.086	35.017	33.620	35.289	34.232	34.429
K2O	7.673	8.521	7.190	8.208	8.002	8.469	8.120	8.456	8.238	8.484
CaO	0.262	0.071	0.396	0.295	0.305	0.084	0.186	0.098	0.087	0.000
TiO2	4.012	3.993	4.155	4.425	4.707	4.439	4.457	3.930	4.474	4.204
Cr2O3	0.026	0.012	0.000	0.032	0.034	0.023	0.023	0.020	0.020	0.001
MnO	0.189	0.207	0.243	0.128	0.132	0.142	0.115	0.170	0.151	0.128
FeO	37.308	35.566	36.984	32.279	32.865	32.642	37.243	32.740	36.340	34.751
Total	95.393	96.363	94.760	96.332	95.232	96.250	96.341	96.246	96.958	95.597
F	0.172	0.125	0.126	0.112	0.075	0.105	0.000	0.163	0.095	0.188
Na	0.015	0.014	0.025	0.062	0.094	0.075	0.043	0.058	0.055	0.050
Mg	0.416	0.651	0.425	1.060	0.896	1.044	0.237	1.042	0.416	0.919
Al	1.900	1.977	1.903	2.155	2.138	2.050	2.248	2.063	2.200	1.844
Si	5.778	5.765	5.776	5.650	5.616	5.698	5.584	5.745	5.625	5.737
K	1.648	1.795	1.548	1.696	1.682	1.758	1.720	1.756	1.727	1.803
Ca	0.047	0.013	0.072	0.051	0.054	0.015	0.033	0.017	0.015	0.000
Ti	0.508	0.496	0.527	0.539	0.583	0.543	0.557	0.481	0.553	0.527
Cr	0.004	0.002	0.000	0.004	0.004	0.003	0.003	0.003	0.003	0.000
Mn	0.027	0.029	0.035	0.018	0.018	0.020	0.016	0.024	0.021	0.018
Fe	5.253	4.912	5.220	4.374	4.529	4.442	5.173	4.458	4.994	4.842
Total cats.	15.766	15.779	15.658	17.778	17.736	17.811	17.670	17.881	17.760	18.001

			138			101			102	
	Bt 2	Bt 3	Bt 1	Bt 2	Bt 3	Bt 1	Bt 2	Bt 3	Bt 1	Bt 2
F	0.345	0.381	0.095	0.440	0.385	0.297	0.275	0.491	0.617	0.605
NaO2	0.166	0.115	0.040	0.084	0.049	0.088	0.179	0.092	0.183	0.120
MgO	2.893	3.391	2.177	2.530	3.507	2.540	3.699	3.318	3.388	3.759
Al2O3	11.048	9.735	9.767	10.364	9.515	9.986	10.177	10.284	9.901	10.698
SiO2	33.902	34.803	34.305	34.350	35.302	34.234	34.893	35.019	34.715	34.901
K2O	8.394	8.569	8.998	9.067	9.150	8.671	8.875	9.053	8.597	8.974
CaO	0.063	0.025	0.020	0.021	0.007	0.008	0.000	0.007	0.334	0.066
TiO2	4.467	4.269	2.377	3.862	3.877	4.130	4.137	3.718	4.319	4.103
Cr2O3	0.006	0.000	0.016	0.019	0.016	0.000	0.019	0.015	0.004	0.015
MnO	0.143	0.116	0.198	0.191	0.235	0.266	0.158	0.266	0.227	0.302
FeO	34.639	34.614	37.454	35.206	34.385	35.952	33.909	34.259	33.467	33.305
Total	96.066	96.018	95.447	96.134	96.428	96.172	96.321	96.522	95.752	96.848
F	0.180	0.199	0.051	0.232	0.201	0.157	0.143	0.256	0.324	0.313
Na	0.053	0.037	0.013	0.027	0.016	0.028	0.057	0.029	0.059	0.038
Mg	0.713	0.836	0.549	0.628	0.862	0.631	0.906	0.815	0.837	0.916
Al	2.153	1.899	1.948	2.034	1.850	1.961	1.971	1.997	1.935	2.062
Si	5.606	5.759	5.805	5.720	5.824	5.704	5.734	5.770	5.756	5.707
K	1.770	1.809	1.942	1.926	1.926	1.843	1.861	1.903	1.818	1.872
Ca	0.011	0.004	0.004	0.004	0.001	0.001	0.000	0.001	0.059	0.012
Ti	0.555	0.531	0.302	0.484	0.481	0.517	0.511	0.461	0.538	0.505
Cr	0.001	0.000	0.002	0.003	0.002	0.000	0.002	0.002	0.001	0.002
Mn	0.020	0.016	0.028	0.027	0.033	0.038	0.022	0.037	0.032	0.042
Fe	4.790	4.790	5.300	4.903	4.744	5.009	4.660	4.721	4.640	4.555
Total cats.	17.910	17.928	17.945	17.985	17.939	17.889	17.868	17.991	17.999	18.023

		103			114			139		
	Bt 3	Bt 1	Bt 2	Bt 3	Bt 1	Bt 2	Bt 3	Bt 1	Bt 2	Bt 3
F	0.644	0.240	0.224	0.429	0.204	0.094	0.223	0.019	0.155	0.718
NaO2	0.106	0.379	0.195	0.214	0.100	0.171	0.144	0.042	0.121	0.065
MgO	2.882	3.212	3.004	4.354	1.834	2.517	1.920	1.255	2.427	2.902
Al2O3	10.961	11.569	11.891	11.445	9.343	9.351	10.829	10.600	10.919	10.330
SiO2	33.644	34.031	33.577	34.018	33.622	34.317	35.201	33.235	33.729	34.031
K2O	8.702	9.493	9.697	9.732	7.350	7.837	7.660	8.771	8.217	9.028
CaO	0.070	0.008	0.013	0.000	0.325	0.327	0.458	0.143	0.199	0.024
TiO2	4.020	5.818	4.807	4.360	3.483	2.964	4.017	4.107	3.423	3.598
Cr2O3	0.000	0.007	0.022	0.015	0.029	0.025	0.025	0.020	0.000	0.016
MnO	0.160	0.213	0.179	0.161	0.325	0.349	0.333	0.124	0.183	0.164
FeO	35.425	32.289	33.570	32.309	37.543	37.050	35.727	37.299	36.323	35.539
Total	96.614	97.259	97.179	97.037	94.158	95.002	96.537	95.615	95.696	96.415
F	0.338	0.123	0.116	0.221	0.110	0.050	0.116	0.010	0.082	0.379
Na	0.034	0.119	0.062	0.068	0.033	0.056	0.046	0.014	0.039	0.021
Mg	0.713	0.776	0.732	1.058	0.468	0.634	0.469	0.316	0.605	0.722
Al	2.145	2.211	2.292	2.199	1.884	1.862	2.093	2.108	2.151	2.032
Si	5.586	5.518	5.491	5.547	5.753	5.798	5.772	5.608	5.637	5.681
K	1.843	1.964	2.023	2.024	1.604	1.689	1.602	1.888	1.752	1.923
Ca	0.012	0.001	0.002	0.000	0.060	0.059	0.080	0.026	0.036	0.004
Ti	0.502	0.709	0.591	0.535	0.448	0.377	0.495	0.521	0.430	0.452
Cr	0.000	0.001	0.003	0.002	0.004	0.003	0.003	0.003	0.000	0.002
Mn	0.023	0.029	0.025	0.022	0.047	0.050	0.046	0.018	0.026	0.023
Fe	4.919	4.378	4.591	4.406	5.372	5.235	4.900	5.264	5.077	4.961
Total cats.	18.115	17.875	17.961	18.124	17.873	17.928	17.705	17.775	17.834	18.200

	140			141		
	Bt 1	Bt 2	Bt 3	Bt 1	Bt 2	Bt 3
F	0.304	0.309	0.441	0.027	0.637	0.255
NaO2	0.081	0.015	0.104	0.127	0.085	0.105
MgO	2.444	2.311	0.904	2.568	2.645	1.033
Al2O3	10.509	9.585	9.795	9.850	10.696	11.027
SiO2	33.892	33.864	33.676	33.635	33.838	33.214
K2O	8.643	8.522	8.572	7.705	9.078	8.780
CaO	0.130	0.241	0.146	0.565	0.010	0.064
TiO2	3.993	3.036	3.912	4.065	4.103	3.730
Cr2O3	0.000	0.023	0.000	0.000	0.025	0.018
MnO	0.320	0.431	0.243	0.136	0.173	0.123
FeO	35.267	36.422	37.685	35.865	35.067	37.580
Total	95.583	94.759	95.478	94.543	96.357	95.929
F	0.161	0.166	0.237	0.014	0.336	0.136
Na	0.026	0.005	0.034	0.041	0.027	0.034
Mg	0.609	0.586	0.229	0.646	0.657	0.260
Al	2.072	1.923	1.963	1.959	2.100	2.193
Si	5.669	5.764	5.728	5.675	5.636	5.603
K	1.844	1.850	1.860	1.658	1.929	1.890
Ca	0.023	0.044	0.027	0.102	0.002	0.012
Ti	0.502	0.389	0.500	0.516	0.514	0.473
Cr	0.000	0.003	0.000	0.000	0.003	0.002
Mn	0.045	0.062	0.035	0.019	0.024	0.018
Fe	4.934	5.185	5.360	5.061	4.884	5.302
Total cats.	17.887	17.977	17.973	17.692	18.111	17.923

Typical amphibole analyses

Unit 2 (Troughs)

	MH-KUN-92 23			MH-KUN-92 25			MH-KUN-92 26			
	Am 1	Am 2	Am 3	Am 1	Am 2	Am 3	Am 1	Am 2	Am 3	Am 4
F	0.533	0.426	0.397	0.542	0.291	0.638	0.176	0.014	0.127	0.183
Na2O	2.518	2.573	2.540	2.487	2.491	2.926	2.025	2.153	2.170	2.112
MgO	3.392	3.348	3.079	2.932	3.028	3.630	5.220	5.022	5.046	5.316
Al2O3	6.281	7.490	7.601	7.819	7.046	4.302	4.004	4.144	4.376	4.542
SiO2	41.142	40.256	39.854	40.055	41.168	44.777	45.519	45.357	45.188	45.250
K	1.223	1.394	1.399	1.379	1.291	0.828	0.625	0.605	0.625	0.658
CaO	10.123	10.396	10.497	10.118	9.912	9.028	9.183	9.099	9.154	9.599
TiO2	1.887	2.747	2.927	3.048	2.529	1.383	1.286	1.353	1.423	1.364
Cr2O3	0.012	0.001	0.013	0.006	0.000	0.013	0.000	0.007	0.013	0.004
MnO	0.467	0.371	0.418	0.430	0.462	0.505	0.464	0.523	0.495	0.482
FeO	29.963	28.937	28.764	29.295	29.687	30.337	29.449	29.588	29.593	28.479
Total	97.541	97.939	97.489	98.111	97.905	98.367	97.951	97.865	98.210	97.989
F	0.276	0.220	0.207	0.280	0.150	0.323	0.089	0.007	0.064	0.092
Na	0.799	0.816	0.811	0.789	0.788	0.908	0.626	0.667	0.670	0.651
Mg	0.827	0.816	0.755	0.715	0.737	0.866	1.239	1.196	1.198	1.259
Al	1.211	1.444	1.475	1.508	1.356	0.812	0.752	0.780	0.822	0.851
Si	6.731	6.584	6.561	6.554	6.720	7.170	7.252	7.245	7.197	7.190
K	0.255	0.291	0.294	0.288	0.269	0.169	0.127	0.123	0.127	0.133
Ca	1.774	1.822	1.852	1.774	1.734	1.549	1.568	1.557	1.562	1.634
Ti	0.232	0.338	0.362	0.375	0.310	0.167	0.154	0.163	0.170	0.163
Cr	0.002	0.000	0.002	0.001	0.000	0.002	0.000	0.001	0.002	0.001
Mn	0.065	0.051	0.058	0.060	0.064	0.068	0.063	0.071	0.067	0.065
Fe	4.099	3.958	3.960	4.009	4.053	4.063	3.924	3.953	3.942	3.784
Total cats.	16.271	16.340	16.338	16.353	16.180	16.098	15.793	15.763	15.821	15.823

Unit 2 (Host)

	MH-KUN-92 28					MH-KUN-92 24				
	Am 5	Am 6	Am 1	Am 2	Am 3	Am 4	Am 1	Am 2	Am 3	Am 4
F	0.194	0.104	0.110	0.080	0.302	0.300	0.271	0.276	0.222	0.605
Na2O	2.142	2.138	2.550	1.580	2.300	2.380	2.719	2.509	2.522	2.502
MgO	4.484	4.719	4.220	2.930	4.019	4.430	2.983	3.427	3.500	2.570
Al2O3	3.849	4.344	6.010	3.620	5.379	4.720	5.744	5.997	5.973	7.768
SiO2	45.896	45.117	39.040	45.290	43.147	45.070	42.667	42.642	42.000	39.341
K	0.511	0.594	1.220	0.730	0.944	0.740	1.073	1.177	1.159	1.384
CaO	9.148	9.358	10.250	9.750	9.751	9.670	9.613	9.691	9.701	10.340
TiO2	1.141	1.373	1.930	0.680	1.495	1.200	1.393	1.915	2.013	2.886
Cr2O3	0.000	0.000			0.000		0.013	0.023	0.006	0.000
MnO	0.487	0.493	0.410	0.430	0.409	0.400	0.504	0.489	0.473	0.424
FeO	30.341	29.975	29.180	32.860	30.246	30.190	31.164	29.701	29.911	29.655
Total	98.193	98.215	94.920	97.950	97.992	99.100	98.144	97.847	97.480	97.475
F	0.098	0.052	0.059	0.041	0.154	0.150	0.139	0.141	0.115	0.316
Na	0.661	0.662	0.839	0.495	0.721	0.731	0.855	0.788	0.798	0.802
Mg	1.064	1.122	1.067	0.706	0.968	1.046	0.721	0.827	0.852	0.633
Al	0.723	0.817	1.202	0.690	1.025	0.881	1.099	1.145	1.150	1.514
Si	7.308	7.201	6.621	7.321	6.973	7.139	6.923	6.907	6.857	6.505
K	0.104	0.121	0.264	0.151	0.195	0.150	0.222	0.243	0.241	0.292
Ca	1.561	1.600	1.863	1.689	1.689	1.641	1.671	1.682	1.697	1.832
Ti	0.137	0.165	0.246	0.083	0.182	0.143	0.170	0.233	0.247	0.359
Cr	0.000	0.000	0.000	0.000	0.000	0.000	0.002	0.003	0.001	0.000
Mn	0.066	0.067	0.059	0.059	0.056	0.054	0.069	0.067	0.065	0.059
Fe	4.041	4.001	4.139	4.443	4.088	4.000	4.229	4.024	4.084	4.101
Total cats.	15.762	15.808	16.358	15.677	16.050	15.935	16.100	16.062	16.108	16.413

	MH-KUN-92 31							MH-KUN-92 33		
	Am 5	Am 6	Am 1	Am 2	Am 3	Am 4	Am 5	Am 6	Am 1	Am 2
F	0.556	0.508	0.467	0.710	0.521	0.475	0.486	0.386	0.673	0.520
Na2O	2.507	2.673	2.413	2.482	2.426	2.480	2.421	2.500	2.699	2.461
MgO	2.603	2.452	2.892	2.686	2.704	3.145	2.542	2.081	2.963	2.787
Al2O3	7.558	7.581	7.976	7.409	7.237	6.345	6.696	5.432	5.563	6.043
SiO2	39.771	39.445	39.706	40.201	40.447	41.775	41.084	42.839	42.389	41.762
K	1.370	1.413	1.393	1.331	1.312	1.203	1.276	0.971	1.023	1.179
CaO	10.221	10.076	10.343	10.196	10.246	10.055	10.036	9.583	9.639	9.806
TiO2	2.842	2.789	3.226	2.617	2.534	1.428	2.240	1.573	1.575	1.770
Cr2O3	0.001	0.009	0.000	0.000	0.007	0.000	0.000	0.000	0.026	0.013
MnO	0.404	0.416	0.407	0.414	0.409	0.462	0.420	0.465	0.473	0.492
FeO	29.893	30.360	29.300	30.426	30.319	30.833	31.127	32.654	31.100	31.235
Total	97.726	97.722	98.123	98.472	98.162	98.201	98.328	98.484	98.123	98.068
F	0.290	0.266	0.242	0.367	0.270	0.244	0.252	0.199	0.346	0.269
Na	0.801	0.857	0.768	0.787	0.771	0.782	0.768	0.790	0.852	0.780
Mg	0.639	0.604	0.707	0.655	0.660	0.762	0.620	0.505	0.719	0.679
Al	1.468	1.478	1.543	1.429	1.398	1.217	1.292	1.043	1.067	1.164
Si	6.553	6.523	6.516	6.577	6.629	6.795	6.723	6.978	6.899	6.826
K	0.288	0.298	0.292	0.278	0.274	0.250	0.266	0.202	0.212	0.246
Ca	1.805	1.786	1.819	1.787	1.799	1.752	1.760	1.673	1.681	1.717
Ti	0.352	0.347	0.398	0.322	0.312	0.175	0.276	0.193	0.193	0.218
Cr	0.000	0.001	0.000	0.000	0.001	0.000	0.000	0.000	0.003	0.002
Mn	0.056	0.058	0.057	0.057	0.057	0.064	0.058	0.064	0.065	0.068
Fe	4.119	4.199	4.021	4.163	4.156	4.194	4.260	4.449	4.233	4.270
Total cats.	16.372	16.418	16.363	16.424	16.329	16.235	16.274	16.095	16.271	16.238

	Unit 3									
			101			102			103	
	Am 3	Am 4	Am 1	Am 2	Am 3	Am 1	Am 2	Am 3	Am 1	Am 2
F	0.531	0.354	0.000	0.194	0.132	0.331	0.429	0.364	0.321	0.349
Na2O	2.610	2.711	2.405	2.438	2.448	2.331	2.956	2.558	3.037	2.484
MgO	1.676	1.864	3.207	3.280	3.076	3.202	3.099	3.207	3.225	3.230
Al2O3	3.403	3.424	8.599	8.671	8.593	8.633	7.972	8.688	8.733	8.593
SiO2	44.873	45.072	39.381	39.225	39.527	39.460	39.963	39.304	39.546	39.557
K	0.915	0.791	1.462	1.505	1.439	1.477	1.371	1.468	1.501	1.562
CaO	8.539	8.601	10.530	10.589	10.571	10.498	10.428	10.505	10.616	10.747
TiO2	1.061	1.066	3.576	3.593	3.500	3.501	2.922	3.546	3.096	3.643
Cr2O3	0.000	0.006	0.000	0.000	0.009	0.000	0.000	0.006	0.006	0.019
MnO	0.669	0.705	0.340	0.381	0.382	0.398	0.382	0.383	0.356	0.365
FeO	34.281	34.193	28.012	27.571	28.168	27.652	28.334	27.512	27.926	28.100
Total	98.558	98.787	97.512	97.447	97.845	97.483	97.856	97.541	98.363	98.649
F	0.273	0.181	0.000	0.101	0.068	0.172	0.222	0.189	0.165	0.180
Na	0.823	0.852	0.768	0.778	0.779	0.742	0.939	0.815	0.959	0.784
Mg	0.406	0.450	0.787	0.805	0.752	0.784	0.756	0.785	0.783	0.784
Al	0.653	0.654	1.669	1.683	1.662	1.672	1.539	1.683	1.677	1.649
Si	7.299	7.306	6.484	6.456	6.485	6.481	6.544	6.457	6.441	6.441
K	0.190	0.164	0.307	0.316	0.301	0.310	0.286	0.308	0.312	0.324
Ca	1.488	1.494	1.858	1.868	1.858	1.848	1.830	1.849	1.853	1.875
Ti	0.130	0.130	0.443	0.445	0.432	0.432	0.360	0.438	0.379	0.446
Cr	0.000	0.001	0.000	0.000	0.001	0.000	0.000	0.001	0.001	0.002
Mn	0.092	0.097	0.047	0.053	0.053	0.055	0.053	0.053	0.049	0.050
Fe	4.663	4.635	3.857	3.795	3.865	3.799	3.880	3.780	3.804	3.826
Total cats.	16.018	15.965	16.219	16.300	16.257	16.295	16.410	16.357	16.423	16.362

	Unit 4									
		114			115			116		
	Am 3	Am 1	Am 2	Am 3	Am 1	Am 2	Am 3	Am 1	Am 2	Am 3
F	0.253	0.293	0.163	0.084	0.146	0.270	0.153	0.200	0.155	0.173
Na2O	2.499	2.680	2.500	2.585	2.544	2.386	2.426	1.992	2.352	2.405
MgO	3.207	2.391	2.699	2.728	2.709	3.059	3.127	2.621	3.094	2.641
Al2O3	8.584	4.612	8.221	8.387	7.575	8.110	8.374	4.971	5.462	8.146
SiO2	39.638	43.662	39.873	39.743	40.513	39.535	39.544	43.181	43.037	39.638
K	1.608	0.754	1.373	1.407	1.390	1.379	1.417	0.800	0.901	1.366
CaO	10.739	9.422	10.246	10.259	9.489	10.210	10.395	9.306	9.705	10.147
TiO2	3.681	1.331	3.234	3.314	2.742	3.254	3.440	1.481	1.710	3.146
Cr2O3	0.001	0.000	0.016	0.009	0.019	0.025	0.004	0.025	0.009	0.016
MnO	0.413	0.613	0.476	0.444	0.358	0.354	0.362	0.576	0.511	0.448
FeO	27.815	31.823	29.215	29.158	29.688	28.725	28.327	32.094	30.998	29.317
Total	98.438	97.581	98.016	98.118	97.173	97.307	97.569	97.247	97.934	97.443
F	0.130	0.151	0.085	0.044	0.076	0.141	0.080	0.104	0.080	0.090
Na	0.790	0.848	0.795	0.822	0.813	0.763	0.774	0.633	0.741	0.769
Mg	0.779	0.582	0.660	0.667	0.665	0.752	0.766	0.640	0.749	0.649
Al	1.650	0.887	1.590	1.621	1.472	1.577	1.623	0.960	1.046	1.585
Si	6.463	7.126	6.539	6.516	6.676	6.521	6.503	7.076	6.990	6.541
K	0.334	0.157	0.287	0.294	0.292	0.290	0.297	0.167	0.187	0.288
Ca	1.876	1.648	1.801	1.802	1.676	1.805	1.832	1.634	1.689	1.794
Ti	0.451	0.163	0.399	0.409	0.340	0.404	0.425	0.183	0.209	0.390
Cr	0.000	0.000	0.002	0.001	0.002	0.003	0.001	0.003	0.001	0.002
Mn	0.057	0.085	0.066	0.062	0.050	0.049	0.050	0.080	0.070	0.063
Fe	3.793	4.344	4.007	3.998	4.092	3.963	3.896	4.398	4.210	4.046
Total cats.	16.324	15.991	16.230	16.235	16.154	16.268	16.246	15.878	15.971	16.217

	Unit 4									
	117		138		139		140		141	
	Am 1	Am 2	Am 1	Am 2	Am 1	Am 2	Am 1	Am 2	Am 1	Am 2
F	0.000	0.000	0.376	0.230	0.495	0.193	0.217	0.411	0.377	0.711
Na2O	2.335	2.476	2.579	2.573	2.484	2.461	2.545	2.503	2.645	2.394
MgO	2.890	2.303	2.147	1.816	2.237	1.776	2.038	2.426	2.227	2.386
Al2O3	8.317	7.800	4.641	8.027	8.191	4.607	6.946	5.434	5.657	7.055
SiO2	39.529	39.967	43.583	38.716	39.073	43.544	40.545	42.667	42.192	40.581
K	1.409	1.352	0.793	1.425	1.509	0.816	1.211	0.978	0.955	1.249
CaO	10.372	10.165	9.498	10.455	10.343	9.568	10.043	9.762	9.796	10.073
TiO2	3.361	3.119	1.309	3.101	3.246	1.158	2.092	1.500	1.596	2.202
Cr2O3	0.000	0.003	0.001	0.007	0.001	0.015	0.022	0.000	0.001	0.004
MnO	0.407	0.341	0.598	0.462	0.449	0.619	0.522	0.566	0.567	0.529
FeO	28.621	29.847	32.653	30.523	30.076	33.392	31.658	31.605	31.397	30.866
Total	97.241	97.373	98.178	97.335	98.104	98.149	97.839	97.852	97.410	98.050
F	0.000	0.000	0.194	0.122	0.259	0.100	0.113	0.212	0.196	0.369
Na	0.748	0.794	0.815	0.834	0.796	0.780	0.815	0.793	0.843	0.762
Mg	0.711	0.568	0.521	0.453	0.551	0.433	0.502	0.591	0.546	0.584
Al	1.620	1.521	0.892	1.582	1.596	0.888	1.352	1.047	1.096	1.365
Si	6.529	6.612	7.102	6.473	6.457	7.119	6.696	6.972	6.936	6.660
K	0.297	0.285	0.165	0.304	0.318	0.170	0.255	0.204	0.200	0.262
Ca	1.836	1.802	1.658	1.873	1.831	1.676	1.777	1.709	1.725	1.771
Ti	0.418	0.388	0.160	0.390	0.403	0.142	0.260	0.184	0.197	0.272
Cr	0.000	0.000	0.000	0.001	0.000	0.002	0.003	0.000	0.000	0.001
Mn	0.057	0.048	0.083	0.065	0.063	0.086	0.073	0.078	0.079	0.074
Fe	3.954	4.129	4.450	4.268	4.157	4.566	4.372	4.319	4.317	4.236
Total cats.	16.168	16.148	16.039	16.365	16.431	15.961	16.218	16.109	16.136	16.354

Typical apatite analyses

	Unit 2 (Troughs)			Unit 2 (Host)			Unit 4			
	MH-KUN-92 28			MH-KUN-92 31			115			113
	Ap 1	Ap 2	Ap 3	Ap 1	Ap 2	Ap 3	Ap 1	Ap 2	Ap 3	Ap 1
F	3.586	5.213	2.836	3.422	3.780	4.165	3.801	4.302	4.435	4.129
Na2O	0.685	0.137	0.113	0.117	0.101	0.109	0.102	0.093	0.115	0.147
SiO2	2.189	0.336	0.359	0.302	0.406	0.355	0.344	0.327	0.312	0.349
P2O5	39.772	42.144	42.061	41.649	41.878	41.992	41.972	42.384	42.996	42.629
Cl	0.057	0.058	0.074	0.010	0.033	0.037	0.028	0.050	0.036	0.029
CaO	52.490	53.686	53.861	53.778	53.783	53.861	54.195	54.167	54.581	54.492
Ce2O3	0.491	0.567	0.679	0.602	0.624	0.520	0.506	0.538	0.485	0.572
Pr2O3	0.125	0.112	0.153	0.000	0.110	0.165	0.000	0.165	0.124	0.098
Nd2O3	0.250	0.278	0.405	0.328	0.378	0.281	0.392	0.359	0.366	0.285
La2O3	0.233	0.315	0.367	0.290	0.285	0.226	0.149	0.290	0.177	0.313
FeO	0.135	0.391	0.269	0.087	0.208	0.252	0.206	0.143	0.109	0.252
MnO	0.039	0.044	0.059	0.031	0.058	0.056	0.035	0.044	0.023	0.048
Total	100.052	103.281	101.236	100.616	101.644	102.019	101.730	102.862	103.759	103.343
F	1.939	2.774	1.508	1.837	2.017	2.220	2.024	2.277	2.323	2.171
Na	0.227	0.045	0.037	0.039	0.033	0.036	0.033	0.030	0.037	0.047
Si	0.374	0.057	0.060	0.051	0.069	0.060	0.058	0.055	0.052	0.058
P	5.757	6.003	5.986	5.986	5.982	5.992	5.983	6.005	6.028	5.999
Cl	0.017	0.017	0.021	0.003	0.009	0.011	0.008	0.014	0.010	0.008
Ca	9.616	9.678	9.701	9.782	9.723	9.727	9.778	9.712	9.684	9.705
Ce	0.031	0.035	0.042	0.037	0.039	0.032	0.031	0.033	0.029	0.035
Pr	0.008	0.007	0.009	0.000	0.007	0.010	0.000	0.010	0.007	0.006
Nd	0.015	0.017	0.024	0.020	0.023	0.017	0.024	0.021	0.022	0.017
La	0.015	0.020	0.023	0.018	0.018	0.014	0.009	0.018	0.011	0.019
Fe	0.019	0.055	0.038	0.012	0.029	0.036	0.029	0.020	0.015	0.035
Mn	0.006	0.006	0.008	0.004	0.008	0.008	0.005	0.006	0.003	0.007
Total cats.	18.024	18.714	17.457	17.789	17.957	18.163	17.982	18.201	18.221	18.107

	Unit 4									
		137		138			140		141	
	Ap 2	Ap 1	Ap 2	Ap 1	Ap 2	Ap 3	Ap 1	Ap 2	Ap 1	Ap 2
F	5.289	3.230	4.349	3.052	3.282	3.697	3.970	4.177	4.179	4.483
Na2O	0.139	0.143	0.115	0.094	0.125	0.092	0.075	0.089	0.093	0.109
SiO2	0.336	1.510	0.475	0.548	0.349	0.449	0.342	0.633	0.445	0.477
P2O5	42.361	41.461	42.054	41.949	42.178	42.004	42.228	41.371	42.066	41.969
Cl	0.058	0.016	0.008	0.022	0.016	0.005	0.025	0.010	0.013	0.000
CaO	54.106	53.042	53.717	54.110	54.491	54.166	54.525	53.892	54.069	54.460
Ce2O3	0.688	0.706	0.719	0.784	0.659	0.591	0.494	0.883	0.630	0.737
Pr2O3	0.136	0.078	0.000	0.205	0.183	0.069	0.119	0.049	0.096	0.165
Nd2O3	0.262	0.366	0.475	0.383	0.401	0.355	0.363	0.383	0.345	0.362
La2O3	0.199	0.428	0.337	0.281	0.190	0.402	0.290	0.372	0.362	0.348
FeO	0.296	0.331	0.179	0.329	0.255	0.183	0.239	0.214	0.059	0.127
MnO	0.045	0.049	0.025	0.056	0.010	0.008	0.043	0.018	0.034	0.023
Total	103.915	101.360	102.453	101.813	102.139	102.021	102.713	102.091	102.391	103.260
F	2.799	1.715	2.313	1.618	1.736	1.964	2.100	2.235	2.220	2.375
Na	0.045	0.047	0.037	0.031	0.041	0.030	0.024	0.029	0.030	0.035
Si	0.056	0.254	0.080	0.092	0.058	0.075	0.057	0.107	0.075	0.080
P	6.000	5.892	5.988	5.951	5.972	5.972	5.979	5.925	5.983	5.951
Cl	0.016	0.005	0.002	0.006	0.005	0.001	0.007	0.003	0.004	0.000
Ca	9.699	9.540	9.680	9.716	9.764	9.746	9.770	9.768	9.732	9.774
Ce	0.042	0.043	0.044	0.048	0.040	0.036	0.030	0.055	0.039	0.045
Pr	0.008	0.005	0.000	0.013	0.011	0.004	0.007	0.003	0.006	0.010
Nd	0.016	0.022	0.029	0.023	0.024	0.021	0.022	0.023	0.021	0.022
La	0.012	0.027	0.021	0.017	0.012	0.025	0.018	0.023	0.022	0.022
Fe	0.041	0.046	0.025	0.046	0.036	0.026	0.033	0.030	0.008	0.018
Mn	0.006	0.007	0.003	0.008	0.001	0.001	0.006	0.003	0.005	0.003
Total cats.	18.740	17.603	18.222	17.569	17.700	17.901	18.053	18.204	18.145	18.335

Typical ilmenite analyses

	Unit2 (Troughs)			Unit 2 (Host)			Unit 4			
	MH-KUN-92 28			MH-KUN-92 31			113			
	Il 1	Il 2	Il 3	Il 1	Il 2	Il 3	Il 1	Il 2	Il 3	Il 4
MgO	0.028	0.030	0.070	0.013	0.015	0.035	0.053	0.051	0.023	0.020
Al2O3	0.032	0.028	0.021	0.004	0.013	0.004	0.013	0.040	0.042	0.025
SiO2	0.026	0.000	0.006	0.002	0.021	0.021	0.009	0.062	0.019	0.043
TiO2	53.111	53.278	52.402	52.904	53.281	53.328	53.264	53.488	53.289	53.718
V2O5	0.299	0.337	0.310	0.355	0.299	0.362	0.362	0.341	0.344	0.378
MnO	1.445	0.944	0.886	0.996	1.015	1.180	1.015	1.109	1.025	1.203
Cr2O3	0.000	0.000	0.000	0.000	0.000	0.000	0.000	0.000	0.000	0.000
FeO	46.010	46.919	46.114	46.309	46.210	46.602	46.552	46.516	46.422	46.434
Fe2O3	0.000	0.266	0.601	0.000	0.000	0.000	0.000	0.000	0.000	0.000
Total	100.951	101.801	100.410	100.582	100.854	101.532	101.268	101.607	101.165	101.820
Mg	0.002	0.002	0.005	0.001	0.001	0.003	0.004	0.004	0.002	0.001
Al	0.002	0.002	0.001	0.000	0.001	0.000	0.001	0.002	0.002	0.001
Si	0.001	0.000	0.000	0.000	0.001	0.001	0.000	0.003	0.001	0.002
Ti	1.995	1.987	1.981	1.996	2.002	1.993	1.995	1.995	1.997	1.999
V	0.012	0.013	0.013	0.014	0.012	0.014	0.014	0.014	0.014	0.015
Mn	0.061	0.040	0.038	0.042	0.043	0.050	0.043	0.047	0.043	0.050
Cr	0.000	0.000	0.000	0.000	0.000	0.000	0.000	0.000	0.000	0.000
Fe2	1.922	1.946	1.939	1.943	1.931	1.937	1.939	1.929	1.935	1.921
Fe3	0.000	0.010	0.023	0.000	0.000	0.000	0.000	0.000	0.000	0.000
Total cats.	3.996	4.000	4.000	3.996	3.990	3.998	3.997	3.994	3.994	3.991

	Unit 4									
	115			137				138		
	Il 1	Il 2	Il 3	Il 1	Il 2	Il 3	Il 4	Il 1	Il 2	Il 3
MgO	0.025	0.032	0.041	0.000	0.017	0.041	0.018	0.007	0.015	0.005
Al2O3	0.002	0.023	0.017	0.019	0.028	0.006	0.032	0.017	0.009	0.017
SiO2	0.000	0.000	0.015	0.011	0.026	0.009	0.030	0.006	0.021	0.011
TiO2	53.591	53.345	53.221	53.907	54.150	53.927	53.516	53.411	53.640	53.701
V2O5	0.319	0.324	0.280	0.281	0.371	0.293	0.305	0.302	0.350	0.291
MnO	0.977	0.968	1.039	1.592	1.668	1.271	1.870	2.103	1.472	1.835
Cr2O3	0.000	0.000	0.086	0.000	0.000	0.000	0.095	0.000	0.000	0.000
FeO	47.157	46.678	46.751	46.071	45.996	45.927	45.615	45.397	46.211	45.767
Fe2O3	0.021	0.000	0.000	0.000	0.000	0.000	0.000	0.000	0.000	0.000
Total	102.093	101.369	101.451	101.880	102.256	101.472	101.481	101.243	101.719	101.627
Mg	0.002	0.002	0.003	0.000	0.001	0.003	0.001	0.000	0.001	0.000
Al	0.000	0.001	0.001	0.001	0.002	0.000	0.002	0.001	0.001	0.001
Si	0.000	0.000	0.001	0.001	0.001	0.000	0.001	0.000	0.001	0.001
Ti	1.993	1.996	1.991	2.004	2.004	2.010	1.998	2.000	1.999	2.002
V	0.013	0.013	0.011	0.011	0.015	0.012	0.012	0.012	0.014	0.012
Mn	0.041	0.041	0.044	0.067	0.070	0.053	0.079	0.089	0.062	0.077
Cr	0.000	0.000	0.003	0.000	0.000	0.000	0.004	0.000	0.000	0.000
Fe2	1.950	1.943	1.945	1.905	1.893	1.904	1.894	1.890	1.915	1.898
Fe3	0.001	0.000	0.000	0.000	0.000	0.000	0.000	0.000	0.000	0.000
Total cats.	4.000	3.996	4.000	3.989	3.986	3.983	3.991	3.993	3.992	3.991

	140		141		
	Il 1	Il 2	Il 1	Il 2	Il 3
MgO	0.003	0.000	0.022	0.028	0.025
Al2O3	0.026	0.038	0.023	0.011	0.008
SiO2	0.024	0.028	0.013	0.011	0.009
TiO2	54.220	53.902	53.947	54.377	53.371
V2O5	0.275	0.363	0.265	0.297	0.312
MnO	1.761	1.779	0.963	1.242	1.096
Cr2O3	0.009	0.050	0.000	0.000	0.000
FeO	46.018	45.345	46.431	46.639	46.147
Fe2O3	0.000	0.000	0.000	0.000	0.000
Total	102.337	101.505	101.663	102.606	100.967
Mg	0.000	0.000	0.002	0.002	0.002
Al	0.002	0.002	0.001	0.001	0.000
Si	0.001	0.001	0.001	0.001	0.000
Ti	2.006	2.008	2.008	2.006	2.003
V	0.011	0.014	0.011	0.012	0.012
Mn	0.073	0.075	0.040	0.052	0.046
Cr	0.000	0.002	0.000	0.000	0.000
Fe2	1.893	1.879	1.922	1.914	1.926
Fe3	0.000	0.000	0.000	0.000	0.000
Total cats.	3.986	3.981	3.985	3.987	3.990

Typical magnetite analyses

Unit 2

	MH-KUN-92 28		115
	Mt 1	Mt 2	Mt 1
MgO	0.000	0.015	0.028
Al2O3	0.493	0.302	0.266
SiO2	0.126	0.113	0.090
TiO2	4.025	7.766	8.891
V2O5	0.025	0.059	0.063
MnO	0.139	0.261	0.289
Cr2O3	0.000	0.000	0.000
FeO	34.060	37.409	38.518
Fe2O3	59.166	52.284	50.426
Total	98.035	98.210	98.572
Mg	0.000	0.007	0.013
Al	0.181	0.111	0.097
Si	0.039	0.035	0.028
Ti	0.944	1.813	2.067
V	0.006	0.015	0.016
Mn	0.037	0.069	0.076
Cr	0.000	0.000	0.000
Fe2	8.885	9.714	9.958
Fe3	13.886	12.216	11.729
Total cats.	23.979	23.980	23.983

Typical zircon analyses

Unit 2 (Troughs)

	MH-KUN-92 25					MH-KUN-92 28				
	Zrn 1a	Zrn 1b	Zrn 1c	Zrn 1d	Zrn 1e	Zrn 1e	Zrn 1a	Zrn 1b	Zrn 1c	Zrn 1d
Al2O3	0.023	0.028	0.017	0.019	0.013	0.008	0.013	0.011	0.009	0.015
SiO2	32.565	31.470	32.788	31.532	31.660	32.769	31.177	32.647	32.910	32.811
ZrO2	65.134	62.537	64.964	62.849	62.537	65.671	66.463	64.996	65.437	64.792
P2O5	0.025	0.078	0.085	0.147	0.066	0.140	0.064	0.030	0.000	0.048
Y2O3	0.650	0.546	0.617	0.776	0.698	0.420	0.173	0.107	0.182	0.154
Ce2O3	0.059	0.073	0.048	0.093	0.089	0.042	0.040	0.041	0.049	0.066
La2O3	0.038	0.008	0.015	0.006	0.001	0.019	0.025	0.043	0.023	0.022
CaO	0.011	0.497	0.018	0.164	0.105	0.022	0.025	0.025	0.025	0.025
ThO2	0.067	0.254	0.101	0.139	0.211	0.121	0.034	0.183	0.112	0.180
HfO2	1.706	2.162	2.033	1.961	1.979	1.823	1.771	1.955	1.749	2.054
FeO	0.040	1.034	0.163	0.635	0.380	0.086	0.043	0.079	0.092	0.089
Nd2O3	0.036	0.000	0.054	0.027	0.016	0.093	0.020	0.044	0.000	0.036
TiO2	0.038	0.087	0.090	0.072	0.110	0.062	0.070	0.068	0.027	0.047
Total	100.393	98.772	100.993	98.418	97.866	101.275	99.918	100.230	100.614	100.339
Al	0.003	0.004	0.002	0.003	0.002	0.001	0.002	0.002	0.001	0.002
Si	3.994	3.940	3.997	3.954	3.988	3.983	3.875	4.007	4.017	4.020
Zr	3.895	3.817	3.862	3.843	3.841	3.893	4.028	3.890	3.895	3.871
P	0.003	0.008	0.009	0.016	0.007	0.014	0.007	0.003	0.000	0.005
Y	0.042	0.036	0.040	0.052	0.047	0.027	0.011	0.007	0.012	0.010
Ce	0.003	0.003	0.002	0.004	0.004	0.002	0.002	0.002	0.002	0.003
La	0.002	0.000	0.001	0.000	0.000	0.001	0.001	0.002	0.001	0.001
Ca	0.001	0.067	0.002	0.022	0.014	0.003	0.003	0.003	0.003	0.003
Th	0.002	0.007	0.003	0.004	0.006	0.003	0.001	0.005	0.003	0.005
Hf	0.060	0.077	0.071	0.070	0.071	0.063	0.063	0.069	0.061	0.072
Fe	0.004	0.097	0.015	0.060	0.036	0.008	0.004	0.007	0.008	0.008
Nd	0.002	0.000	0.002	0.001	0.001	0.004	0.001	0.002	0.000	0.002
Ti	0.004	0.008	0.008	0.007	0.010	0.006	0.007	0.006	0.002	0.004
Total cats.	8.013	8.066	8.014	8.037	8.027	8.008	8.005	8.006	8.007	8.006

Unit 2 (Host)

	MH-KUN-92 35					MH-KUN-92 32			MH-KUN-92 36	
	Zrn 1	Zrn 2a	Zrn 2b	Zrn 2c	Zrn 2d	Zrn 1	Zrn 2a	Zrn 2b	Zrn 1a	Zrn 1b
Al2O3	0.015	0.036	0.017	0.025	0.019	0.008	0.002	0.002	0.028	0.159
SiO2	32.749	32.792	32.052	32.762	31.671	32.801	32.976	32.715	31.966	29.624
ZrO2	65.812	65.340	63.851	64.757	62.815	65.133	65.129	64.643	59.769	54.815
P2O5	0.041	0.105	0.126	0.124	0.078	0.094	0.064	0.105	0.211	0.266
Y2O3	0.032	0.213	0.227	0.246	0.495	0.565	0.338	0.838	1.812	2.330
Ce2O3	0.046	0.061	0.034	0.020	0.015	0.041	0.049	0.055	0.753	1.051
La2O3	0.000	0.038	0.053	0.054	0.036	0.033	0.035	0.027	0.055	0.097
CaO	0.020	0.045	0.027	0.024	0.157	0.035	0.025	0.021	0.013	0.298
ThO2	0.009	0.152	0.189	0.193	0.296	0.034	0.007	0.007	0.440	1.136
HfO2	1.629	1.873	1.906	1.918	1.771	1.439	1.492	1.453	1.744	1.417
FeO	0.104	0.074	0.050	0.050	0.176	0.027	0.026	0.160	0.026	0.886
Nd2O3	0.000	0.023	0.044	0.061	0.044	0.038	0.061	0.065	0.639	0.700
TiO2	0.068	0.077	0.078	0.037	0.072	0.040	0.072	0.075	0.027	0.048
Total	100.525	100.829	98.654	100.270	97.645	100.288	100.275	100.166	97.484	92.828
Al	0.002	0.005	0.002	0.004	0.003	0.001	0.000	0.000	0.004	0.025
Si	3.999	3.998	3.997	4.014	3.994	4.012	4.028	4.008	4.052	3.978
Zr	3.919	3.885	3.883	3.869	3.863	3.884	3.879	3.862	3.694	3.590
P	0.004	0.011	0.013	0.013	0.008	0.010	0.007	0.011	0.023	0.030
Y	0.002	0.014	0.015	0.016	0.033	0.037	0.022	0.055	0.122	0.167
Ce	0.002	0.003	0.002	0.001	0.001	0.002	0.002	0.002	0.035	0.052
La	0.000	0.002	0.002	0.002	0.002	0.001	0.002	0.001	0.003	0.005
Ca	0.003	0.006	0.004	0.003	0.021	0.005	0.003	0.003	0.002	0.043
Th	0.000	0.004	0.005	0.005	0.008	0.001	0.000	0.000	0.013	0.035
Hf	0.057	0.065	0.068	0.067	0.064	0.050	0.052	0.051	0.063	0.054
Fe	0.010	0.007	0.005	0.005	0.017	0.003	0.002	0.015	0.002	0.090
Nd	0.000	0.001	0.002	0.003	0.002	0.002	0.003	0.003	0.029	0.034
Ti	0.006	0.007	0.007	0.003	0.007	0.004	0.007	0.007	0.003	0.005
Total cats.	8.004	8.008	8.005	8.005	8.022	8.011	8.007	8.017	8.044	8.106

Unit 3

					108					111
	Zrn 1c	Zrn 2a	Zrn 2b	Zrn 2c	Zrn 1a	Zrn 1b	Zrn 1c	Zrn 1d	Zrn 1e	Zrn 1a
Al2O3	0.055	0.009	0.000	0.000	0.000	0.006	0.028	0.009	0.026	0.000
SiO2	29.545	32.698	16.315	6.771	31.795	32.997	32.824	32.925	32.858	32.882
ZrO2	52.407	64.328	61.010	16.476	63.829	66.316	65.765	65.418	63.520	65.753
P2O5	0.264	0.131	0.176	0.055	0.099	0.089	0.151	0.092	0.050	0.030
Y2O3	4.226	0.547	0.778	18.046	0.561	0.184	0.023	0.404	0.079	0.502
Ce2O3	0.296	0.047	0.064	1.504	0.052	0.014	0.035	0.057	0.066	0.036
La2O3	0.000	0.033	0.040	0.254	0.026	0.040	0.035	0.045	0.049	0.059
CaO	0.132	0.022	0.239	0.679	0.153	0.017	0.029	0.025	0.036	0.004
ThO2	1.311	0.113	0.338	6.339	0.188	0.104	0.000	0.121	0.053	0.068
HfO2	1.037	1.506	1.524	0.625	1.098	1.190	1.070	1.267	1.052	0.973
FeO	0.994	0.064	0.706	0.458	1.031	0.144	0.026	0.080	0.037	0.009
Nd2O3	0.225	0.028	0.094	1.669	0.000	0.076	0.059	0.000	0.065	0.013
TiO2	0.000	0.040	0.068	0.841	0.065	0.042	0.035	0.067	0.053	0.020
Total	90.490	99.566	81.354	53.716	98.896	101.219	100.081	100.509	97.947	100.348
Al	0.009	0.001	0.000	0.000	0.000	0.001	0.004	0.001	0.004	0.000
Si	4.041	4.024	2.736	2.094	3.953	3.998	4.010	4.014	4.083	4.015
Zr	3.496	3.861	4.989	2.484	3.870	3.918	3.918	3.889	3.849	3.915
P	0.031	0.014	0.025	0.014	0.010	0.009	0.016	0.009	0.005	0.003
Y	0.308	0.036	0.069	2.969	0.037	0.012	0.001	0.026	0.005	0.033
Ce	0.015	0.002	0.004	0.170	0.002	0.001	0.002	0.003	0.003	0.002
La	0.000	0.001	0.002	0.029	0.001	0.002	0.002	0.002	0.002	0.003
Ca	0.019	0.003	0.043	0.225	0.020	0.002	0.004	0.003	0.005	0.001
Th	0.041	0.003	0.013	0.446	0.005	0.003	0.000	0.003	0.002	0.002
Hf	0.040	0.053	0.073	0.055	0.039	0.041	0.037	0.044	0.037	0.034
Fe	0.102	0.006	0.089	0.106	0.096	0.013	0.002	0.007	0.003	0.001
Nd	0.011	0.001	0.006	0.184	0.000	0.003	0.003	0.000	0.003	0.001
Ti	0.000	0.004	0.009	0.195	0.006	0.004	0.003	0.006	0.005	0.002
Total cats.	8.113	8.010	8.057	8.973	8.041	8.006	8.001	8.009	8.006	8.009

							Unit 4 113		Unit 4 135	
	Zrn 1b	Zrn 1c	Zrn 1d	Zrn 1e	Zrn 1e	Zrn 1f	Zrn 1a	Zrn 1b	Zrn 1a	Zrn 1b
Al2O3	0.019	0.015	0.011	0.011	0.011	0.028	0.011	0.047	0.019	0.000
SiO2	32.997	33.087	32.792	32.856	32.987	33.019	32.807	32.381	35.597	32.856
ZrO2	65.321	66.119	64.522	64.262	65.296	65.003	66.293	29.904	68.215	64.798
P2O5	0.021	0.057	0.092	0.089	0.087	0.041	0.094	0.023	0.030	0.080
Y2O3	0.315	0.020	0.977	0.411	0.418	0.217	0.050	0.133	0.119	0.658
Ce2O3	0.019	0.081	0.060	0.046	0.053	0.060	0.060	0.066	0.073	0.000
La2O3	0.055	0.048	0.020	0.034	0.068	0.002	0.035	0.042	0.000	0.000
CaO	0.011	0.022	0.007	0.000	0.015	0.007	0.028	0.234	0.059	0.010
ThO2	0.030	0.028	0.201	0.000	0.061	0.147	0.000	0.164	0.028	0.149
HfO2	0.930	1.169	0.989	1.017	1.063	1.164	0.958	1.008	1.035	1.211
FeO	0.033	0.007	0.026	0.004	0.000	0.047	0.097	0.831	0.154	0.049
Nd2O3	0.001	0.117	0.078	0.001	0.054	0.000	0.058	0.103	0.000	0.083
TiO2	0.050	0.000	0.025	0.000	0.002	0.045	0.022	0.057	0.058	0.047
Total	99.802	100.771	99.800	98.732	100.115	99.781	100.513	64.992	105.388	99.940
Al	0.003	0.002	0.002	0.002	0.002	0.004	0.002	0.009	0.003	0.000
Si	4.038	4.020	4.026	4.058	4.030	4.044	3.997	5.385	4.101	4.027
Zr	3.898	3.918	3.863	3.870	3.890	3.882	3.938	2.425	3.832	3.873
P	0.002	0.006	0.010	0.009	0.009	0.004	0.010	0.003	0.003	0.008
Y	0.021	0.001	0.064	0.027	0.027	0.014	0.003	0.012	0.007	0.043
Ce	0.001	0.004	0.003	0.002	0.002	0.003	0.003	0.004	0.003	0.000
La	0.002	0.002	0.001	0.002	0.003	0.000	0.002	0.003	0.000	0.000
Ca	0.001	0.003	0.001	0.000	0.002	0.001	0.004	0.042	0.007	0.001
Th	0.001	0.001	0.006	0.000	0.002	0.004	0.000	0.006	0.001	0.004
Hf	0.033	0.041	0.035	0.036	0.037	0.041	0.033	0.048	0.034	0.042
Fe	0.003	0.001	0.002	0.000	0.000	0.004	0.009	0.104	0.013	0.004
Nd	0.000	0.005	0.003	0.000	0.002	0.000	0.003	0.006	0.000	0.004
Ti	0.005	0.000	0.002	0.000	0.000	0.004	0.002	0.007	0.005	0.004
Total cats.	8.007	8.003	8.016	8.005	8.007	8.005	8.004	8.054	8.009	8.011

			Unit 4 138				141			
	Zrn 1c	Zrn 1d	Zrn 1a	Zrn 2a	Zrn 2b	Zrn 2c	Zrn 1a	Zrn 1b	Zrn 1c	Zrn 1d
Al2O3	0.023	0.011	0.026	0.025	0.009	0.008	0.017	0.002	0.006	0.006
SiO2	33.047	32.463	33.002	32.980	32.700	32.884	33.059	32.982	32.944	32.935
ZrO2	65.433	64.351	66.259	65.001	63.120	63.490	66.493	65.336	65.078	65.471
P2O5	0.069	0.062	0.085	0.018	0.066	0.108	0.082	0.099	0.080	0.108
Y2O3	0.000	0.128	0.240	0.366	0.897	0.930	0.023	0.290	0.267	0.254
Ce2O3	0.054	0.053	0.046	0.043	0.042	0.084	0.009	0.084	0.001	0.027
La2O3	0.000	0.035	0.016	0.095	0.019	0.025	0.066	0.035	0.045	0.052
CaO	0.035	0.053	0.004	0.011	0.014	0.008	0.020	0.001	0.024	0.027
ThO2	0.066	0.036	0.042	0.063	0.044	0.107	0.000	0.175	0.082	0.019
HfO2	1.281	0.992	1.127	1.190	0.925	0.974	1.305	1.211	1.216	1.085
FeO	0.119	0.239	0.000	0.027	0.037	0.000	0.327	0.180	0.137	0.100
Nd2O3	0.005	0.084	0.000	0.076	0.000	0.042	0.021	0.000	0.000	0.029
TiO2	0.045	0.032	0.048	0.092	0.022	0.042	0.068	0.013	0.035	0.025
Total	100.175	98.539	100.897	99.986	97.895	98.701	101.492	100.409	99.914	100.137
Al	0.003	0.002	0.004	0.004	0.001	0.001	0.002	0.000	0.001	0.001
Si	4.032	4.026	4.006	4.036	4.071	4.065	3.992	4.022	4.031	4.022
Zr	3.893	3.892	3.922	3.879	3.832	3.827	3.916	3.885	3.883	3.898
P	0.007	0.006	0.009	0.002	0.007	0.011	0.008	0.010	0.008	0.011
Y	0.000	0.008	0.016	0.024	0.059	0.061	0.001	0.019	0.017	0.017
Ce	0.002	0.002	0.002	0.002	0.002	0.004	0.000	0.004	0.000	0.001
La	0.000	0.002	0.001	0.004	0.001	0.001	0.003	0.002	0.002	0.002
Ca	0.005	0.007	0.001	0.001	0.002	0.001	0.003	0.000	0.003	0.003
Th	0.002	0.001	0.001	0.002	0.001	0.003	0.000	0.005	0.002	0.001
Hf	0.045	0.035	0.039	0.042	0.033	0.034	0.045	0.042	0.042	0.038
Fe	0.011	0.022	0.000	0.003	0.003	0.000	0.030	0.017	0.013	0.009
Nd	0.000	0.004	0.000	0.003	0.000	0.002	0.001	0.000	0.000	0.001
Ti	0.004	0.003	0.004	0.008	0.002	0.004	0.006	0.001	0.003	0.002
Total cats.	8.004	8.011	8.003	8.010	8.015	8.015	8.008	8.007	8.007	8.006

Appendix D: Representative XRF microprobe analyses

Nunarssuit: Typical pyroxene analyses

	Unit 1			Unit 3			Unit 3			Unit 5
	MH-NUN-92 9			47			51			55
	Px 1	Px 2	Px 3	Px 1	Px 2	Px 3	Px 1	Px 2	Px 3	Px 1
Zn	511.06	494.85	537.29	461.96	406.11	489.58	433.58	450.45	499.88	337.71
Ge	2.36	6.91	14.34	5.09	6.42	3.04	1.27	4.91	5.45	6.64
Rb	180.36	65.66	6.4	6.88	6.93	5.36	3.47	1.17	0.41	1.17
Sr	11.5	13.61	14.02	16.87	57.61	12.82	16.13	15.87	20.27	21.03
Y	187.59	206.55	277.63	145.44	156.15	191.6	151.81	213.97	217.27	137.64
Nb	8.32	15.39	12	26.43	13.71	9.95	18.68	10.54	12.74	12.28
Mo	13.42	7.48	36.56	50.94	25.98	9.44	23.18	18.32	39.79	21.5
Ta	16.36	0.06	6.67	11.14	8.2	8.08	4.18	2.32	0.03	0.8
Ni	1.36	0.07	1.57	2.1	7.64	3.75	5.31	1.61	1.56	2.4
Cu	39.64	4.25	3.48	14.53	4.26	4.82	0.27	1.77	21.93	0.72
Ga	0.75	0.83	6.64	9.76	10.45	6.42	6.18	5.94	7.98	4.71
Zr	346.07	410.28	526.53	286.19	249.74	451.08	301.58	437.38	293.44	228.84
Hf	7.27	20.12	24.92	5.63	10.97	17.04	9.63	4.88	7.27	10.06

			Unit 5			Unit 7				
			56			27		28		
	Px 2	Px 3	Px 1	Px 2	Px 3	Px 1	Px 2	Px 1	Px 2	Px 3
Zn	504.24	366.14	338.01	355.31	344.07	439.6	526.74	414.42	463.82	391.68
Ge	3.57	3.54	3.26	2.43	4.14	4.86	8.41	3.18	5.4	9.76
Rb	13.22	0.04	3.14	8.61	7.3	8.37	15.2	4.05	4.09	1.25
Sr	14.94	35.99	14.74	17.4	16.26	14.49	17.1	16.5	17.93	16.91
Y	166.47	180.59	182.12	234.65	242.01	154.19	286.17	184.61	136.77	156.27
Nb	7.77	11.54	16.72	23.9	16.07	37.32	16.47	18.72	45.54	23.89
Mo	40.55	17.19	42.73	27.66	43.48	47.35	39.5	36.74	23.02	68.09
Ta	18.18	0.01	2.65	7.95	4.5	10.58	4.46	10.9	7.2	3.31
Ni	0.85	2.88	4.92	2.7	3.42	5.47	5.57	7.5	5.28	5.13
Cu	1.02	15.86	6.01	11.08	2.91	1.27	3.64	1.96	16.05	2.85
Ga	8.01	14.35	5.1	5.83	9.52	7.84	17.01	10.32	8.86	6.86
Zr	600.65	577.98	303.31	390.01	587.52	359.6	513.37	331.29	246.86	312.73
Hf	14.71	4.26	5.89	6.02	19.22	5.07	17.74	19.15	13.33	5.81

	Unit 7			Unit 10					
	66			MH-NUN-92 21			MH-NUN-92 1		
	Px 1	Px 2	Px 3	Px 1	Px 2	Px 3	Px 1	Px 2	Px 3
Zn	374.59	382.62	402.64	319.29	345.48	324.42	368.56	381.19	371.49
Ge	6.17	6.33	1.17	0.02	5.39	3.77	0.88	3.02	5.54
Rb	2.14	6.14	4.19	46.19	3.62	5.25	6.68	9.31	4.86
Sr	20.74	21.69	17.91	9.94	69.91	17.17	9.19	7.06	11
Y	152.12	132.73	168.55	128.25	124.67	119.6	137.97	95.97	106.3
Nb	13.57	24.74	29.89	18.85	11.76	17.68	3.01	6.27	6.78
Mo	15.69	36.24	52.96	22.32	25.12	64.66	16.09	15.1	12.64
Ta	4.81	5.69	12.35	4.26	49.24	7.95	0.28	5.31	5.54
Ni	4.73	0.41	5.14	0.08	1.18	11.65	0.35	4.18	5.03
Cu	2.72	9.79	0.07	1.34	20.65	1.01	1.98	5.17	0.81
Ga	2.43	0.98	5.58	4.12	4.19	9.27	5.11	12.29	7.92
Zr	291.62	262	383.31	391.31	335.05	339.46	183.62	172.96	176.7
Hf	9.61	2.64	9.71	9.75	6.07	16.07	3.87	5.29	10.65

Typical olivine analyses

	Unit 1		Unit 3		Unit 5		Unit 5		Unit 7	
	MH-NUN-92 9		51		55		56		27	
	Ol1	Ol 2	Ol1	Ol 2	Ol1	Ol 2	Ol1	Ol 2	Ol1	Ol 2
Zn	480.9	1380.2	1104	565.14	866.52	810.81	705.91	678.32	650.96	836.75
Ge	1.81	1.42	5.86	4.36	3.37	7.74	1.37	0.32	0.4	4.98
Rb	25.73	7.93	11.71	10.88	14	13.98	7.64	0.46	21.16	1.95
Sr	7.49	9.73	16.88	12.35	8.04	9	7.48	12.94	28.84	18.19
Y	47.92	47.39	55.83	23.01	22.33	36.74	42.47	42.3	86.49	79.17
Nb	13.9	23.41	21.95	11.16	18.51	6.92	15.25	10.02	37.88	90.65
Mo	37.99	30.61	40.77	27.29	17.45	14.51	17.56	24.86	39.37	31.96
Ta	1.24	0.78	11.78	2.91	11.24	7.34	0.3	9.61	21.72	8.31
Ni	32.81	22.83	9.19	11.08	45.16	13.6	1.57	3.51	22.38	4.26
Cu	7.07	5.16	19.86	4.26	6.03	2.35	8.58	0.78	36.69	1.98
Ga	0.21	6.59	1.84	2.37	3.24	1.9	4.31	1.85	10.59	9.5
Zr	2.83	13.27	9.41	14.06	18.99	10.92	11.84	14.59	19.45	8.49
Hf	6.46	4.95	1.21	1.51	10.51	4.13	3.83	6.85	4.19	11.29

	Unit 7		Unit 7		Unit 10		Unit 10	
	28		66		MH-NUN-92 21		MH-NUN-92 1	
	Ol1	Ol 2	Ol1	Ol 2	Ol1	Ol 2	Ol1	Ol 2
Zn	977.62	766.44	769.27	1862.09	854.53	870.36	739.98	943.67
Ge	5.82	5.16	7.87	2.49	5.83	7.71	4.5	2.63
Rb	7.28	5.16	2.63	22.46	4.22	8.68	5.28	13.18
Sr	17.37	10.65	38.96	6.39	16.58	12.42	4.81	4.93
Y	40.64	27.72	87.52	27.19	32.56	25.14	57.52	63.58
Nb	13.7	17.49	9	36.68	16.55	27.13	86.35	3.46
Mo	29.83	51.3	27.41	59.81	25.52	32.8	24.89	18.07
Ta	17.02	10.59	7.16	6.7	0.77	6.23	3.87	4.7
Ni	9.37	8.18	12	16.44	20.27	4.57	6.62	31.38
Cu	4.4	11.96	0.19	72.15	36.68	5.82	4.07	8.54
Ga	10.09	5.88	1.25	1.46	2.31	0.89	1.08	1.47
Zr	20.97	11.59	14.19	17.56	14.24	22.14	10.84	59.41
Hf	13.26	8.3	15.61	6.88	53.12	11.3	11.49	16.64

Typical feldspar analyses

	Unit 1						Unit 3			
	9						51			
	Fsp 1	Fsp 2	Fsp 3	Fsp 4	Fsp 5	Fsp 6	Fsp 1	Fsp 2	Fsp 3	Fsp 4
Zn	8.43	6.54	5.59	76.97	7.34	2.58	26.84	3.9	75.25	35.19
Ti	188.81	297.36	151.74	931.74	144.21	180.73	752.92	383.04	1022.39	835.65
Rb	182.23	312.48	193.14	152.09	206.24	200.29	177.18	210.47	200.55	356.54
Sr	4.06	23.79	13.51	31.39	30.16	47.3	289.93	196.25	171.78	196.43
Y	6.85	15.9	9.11	32.89	6.27	15.2	12.9	19.1	20.98	60.12
Nb	7.42	25.11	12.39	35.75	16.16	20.17	20.8	31.07	40.67	29.01
Mo	8.54	38.02	17.19	39	15.49	18.18	83.58	62.76	41.85	53.54
Ni	10.18	13.98	9.13	7.37	12.18	15.64	1.36	0.27	3.39	9.62
Cu	1.52	5.9	3.79	8.81	2.59	2.83	5.31	2.45	13.8	8.16
Ga	29.27	73.11	41.48	110.67	41.74	48.27	79.21	77.77	82.7	69.22
Zr	5.82	14.42	10.83	27.35	8.47	19.08	20.13	5.79	34.17	17.53
Ba	34.45	73.86	41.25	0.1	105.82	164.67	316.15	318.75	16.38	43.63

	Unit 7			Unit 10			
	27		28	MH-NUN-92 21			
	Fsp 1	Fsp 2	Fsp 1	Fsp 2	Fsp 1	Fsp 2	Fsp 3
Zn	8.5	3.32	8.78	18.96	4.87	4.46	4.69
Ti	368.4	520.18	801.11	932.73	485.7	597.82	341.07
Rb	149.59	185.04	193.24	156.32	136.44	166.63	200.35
Sr	136.7	85.53	362.1	233.54	168.58	203.02	216.68
Y	0.47	6.57	8.72	36.52	17.57	19.33	7.26
Nb	28.7	54.43	64.63	50.58	20.57	35.59	19.23
Mo	56.47	78.17	105.01	53.51	72.82	38.11	26.54
Ni	1.99	0.93	4.17	1.12	1.2	1.05	0.74
Cu	3.63	3.26	4.46	8.78	2.51	2.65	2.11
Ga	48.41	50.66	106.09	130.47	48.91	61.16	47.65
Zr	0.41	5.85	21.77	49.94	4.02	11.12	10.37
Ba	295.38	196.37	498.29	122.73	293.46	286.75	261.58

Typical biotite analyses

	Unit 1		Unit 3		Unit 3		Unit 5			
	9		47		51		55		56	
	Bt 1	Bt 2	Bt 1	Bt 2	Bt 1	Bt 2	Bt 1	Bt 2	Bt 1	Bt 2
Zn	700.93	310.27	271.54	220.07	256.61	904.82	1177.83	275.44	665.35	553.56
Ge	7.74	218.92	5.17	2.54	7.33	2.15	15.71	96.66	0.62	1.81
Rb	487.31	791.65	989.77	223.54	226.81	603.74	2111.17	599.89	818.35	496.3
Sr	182.5	25.83	16.93	11.17	21.76	48.59	44.85	19.24	22.27	12.39
Y	209.77	32.26	37.89	19.06	41.51	47.7	111.21	31.07	21.93	32.4
Nb	20.64	360.98	118.55	33.49	28.18	134.73	109.38	42.77	44.2	87.06
Mo	15.73	18.04	35.42	33.11	161.32	184.16	284.7	74.87	44.27	42.37
Ta	7.87	13.92	6.48	0.23	15.17	54.68	15.22	0.54	7.29	0.04
Ni	1.41	4.72	15.75	7.14	7.42	3.89	2.68	2.59	1.57	44.18
Cu	0	11.83	2.88	3.58	26.09	62.08	1.02	17.47	3.61	12.76
Ga	103.87	156.08	84.76	59.42	81.49	220.68	187.6	164.42	120.76	23.71
Zr	413.95	11.68	13.62	5.7	30.58	92.13	78.31	24.09	43.69	64.26
Hf	48.48	0.97	5	5.13	9.34	0.77	31.36	24.58	1.93	8.07

	Unit 7		Unit 7			Unit 10		Unit 10	
	27		28		66	MH-NUN-92 1		MH-NUN-92 21	
	Bt 1	Bt 2	Bt 1	Bt 2	Bt 1	Bt 2	Bt 1	Bt 2	Bt 1
Zn	143.3	111.38	126.95	587.15	602.73	415.51	114.52	417.07	783.45
Ge	3.23	14.67	1.11	59.22	3.79	6.55	0.82	0.24	8.13
Rb	336.96	831.13	44.53	702.47	222.44	333.57	217.37	528.65	511.88
Sr	11.7	215.84	36.03	2987.09	33.57	87.26	12.9	11.01	27.68
Y	14.49	44.14	40.88	119.3	15.65	10	20.46	22.21	35.46
Nb	41.49	164.28	1690.43	163.31	127.54	103.68	13.35	48.69	30.12
Mo	41.68	247.52	105.03	412.53	83	61.7	16	24.61	56.36
Ta	8.98	51.47	15.93	50.27	14.06	7.47	2.29	6.65	7.72
Ni	9.89	71.75	11.65	76.33	4.79	3.23	1.68	5.61	2.76
Cu	4.29	9.8	7.98	152.62	0.18	88	3.73	6.6	78.71
Ga	64.1	296.69	6.17	964.3	80.69	58.9	31.59	103.19	94.63
Zr	9.37	53.92	1032.58	253.44	49.33	8.03	71.52	13.74	43.89
Hf	5.36	36.89	0.33	31.45	116.46	14.67	11.67	3.69	0.79

Typical amphibole analyses

	Unit 1		Unit 3	Unit 3	Unit 3		Unit 5		Unit 5	
	9		47		51		55		56	
	Am 1	Am 2	Am 1	Am 2	Am 1	Am 2	Am 1	Am 2	Am 1	Am 2
Zn	754.69	1119	736.32	838.47	753.04	734.83	5873.6	6091.4	580.8	563.29
Ge	4.57	4.74	7	10.75	3.95	9.34	26.47	17.73	2.16	6.72
Rb	0.86	14.06	5.25	19.11	21.04	7.97	410.63	125.63	12.6	16.55
Sr	15.56	16.86	37.68	26.4	31.15	28.89	182.93	160.54	12.41	15.07
Y	317.89	86.76	97.03	236.33	105.8	300.9	1722.73	2240.35	192.83	219.48
Nb	24.01	84.17	38.16	30.32	36.64	125.67	499.13	206.49	58.76	60.38
Mo	22.48	19.09	24.28	18.08	71.23	58.2	425.57	426.65	49.29	19.33
Ta	0.4	4.41	12.27	7.32	2.44	2.09	134.78	3.85	1.35	5.58
Ni	10.8	4.86	0.58	0.68	2.17	1.39	8	45.49	2.15	5.35
Cu	1.6	2.21	3.73	1.45	2.2	6.51	28.74	133.06	19.49	1.88
Ga	12.38	19.86	16.22	47.58	37.32	54.52	402.13	326.78	43.61	45.41
Zr	439.29	389.53	30.08	847.8	755.46	1041.43	8904.77	7571.39	590.56	255.72
Hf	11.48	12.95	0.53	17.7	21.93	14.5	220.71	154.11	0.45	13.16

	Unit 7			Unit 7		Unit 10				
	27		28		66	MH-NUN-92 21		MH-NUN-92 1		
	Am 1	Am 2	Am 1	Am 2	Am 1	Am 2	Aml	Am 2	Am 1	Am 2
Zn	915.42	925.57	810.66	792.62	779.5	775.48	595.41	585.01	1382.9	909.78
Ge	6.2	2.55	2.73	3.16	4.2	0.57	2.32	3.89	1.54	6.46
Rb	12.53	17.51	13.37	17.86	10.06	22.69	24.25	17.6	10.57	27.24
Sr	26.79	32.94	34.44	22.4	18.42	13.08	20.63	24.69	12.97	23.91
Y	91.04	97.01	108.85	129.92	158.97	136.04	268.79	208.26	153.56	304.62
Nb	86.19	93.1	55.35	35.81	38.13	43.47	50.78	54.22	55.77	91.13
Mo	39.45	15.76	25.8	22.39	39.43	76.52	30.42	49.97	6.58	58.76
Ta	21.26	14.11	15.6	13.44	116.21	17.84	11.65	5.94	5.76	35.87
Ni	5.64	13.1	10.65	3.45	19.34	4.21	3.63	3.92	4.34	9.26
Cu	6.94	5.31	4.41	3.35	45.92	13.34	0.94	2.26	7.17	45.68
Ga	31.6	26	41.17	44.48	26.8	16.95	49.64	48.68	84.93	95.99
Zr	651.08	885.68	1611.35	696.41	538.5	649.21	888.17	580.24	207.61	1345.12
Hf	20.24	19.14	16	7.42	11.2	5.65	19.24	27.42	14.31	10.26

West Kungnat: Typical pyroxene analyses

	Unit 2 (Troughs)						Unit 2 (Host)			
	MH-KUN-92 26			MH-KUN-92 30			MH-KUN-92 31		MH-KUN-92 36	
	Px 1	Px 2	Px 3	Px 1	Px 2	Px 3	Px 1	Px 2	Px 1	Px 2
Zn	215.15	182.44	211.2	191.06	259.55	263.82	252.53	1520.79	354.59	309.98
Ge	1.95	3.15	7.46	4.74	4.36	2.21	4.75	4.01	5.56	5.08
Rb	2.08	0.68	3.14	4.27	1.83	73.19	7.16	2.03	4.7	0.81
Sr	10.02	17.78	9.72	13.37	7.03	34.56	19.55	21.3	13.32	13.93
Y	131.57	50.05	76.44	46.77	139.49	114.77	47.68	81.47	122.81	68.2
Nb	12.18	27.73	32.5	50.3	11.58	17.75	29.58	15.42	144.27	8.78
Mo	10.62	136.98	20.2	84.36	14.48	41.01	66.24	37.12	15.45	11.19
Ta	7.61	6.97	2.96	3.98	4.14	14.46	2.45	3.48	12.52	1.67
Ni	6.45	0.65	0.25	0.07	8.27	2.83	9.46	3.21	2.23	2.01
Cu	8.42	1.46	3.43	5.08	1.71	53.45	16.24	0.03	3.27	4.67
Ga	8.76	7.52	2.13	4.55	11.13	42.74	5.65	0.02	5.19	8.18
Zr	239.46	108.12	168	121.94	338.18	123.21	127.86	184.31	230.74	211.62
Hf	4.41	7.2	7.54	6.07	8.99	2.61	0.14	3.84	12.3	6.61

	Unit 3		Unit 3		Unit 4				Unit 4	
	103		112			119			131	
	Px 1	Px 2	Px 1	Px 2	Px 3	Px 1	Px 2	Px 3	Px 1	Px 2
Zn	375.67	188.18	326.96	306.2	181.09	419.03	232.32	320.19	291.26	272.46
Ge	5.58	3.96	4.52	3.27	3.78	67.8	6.49	7.4	5.36	4.1
Rb	12.68	14.89	4.54	3.04	23.48	4.93	4.41	5.53	105.11	7.7
Sr	40.99	103.49	23.5	32.17	18.93	27.25	14.44	15.62	14.85	21.93
Y	295.8	57.55	100.15	134.06	61.38	288.88	76.94	105.69	74.25	119.44
Nb	100.86	21.75	15.48	13.83	123.96	37.77	11.49	2.9	11.84	124.08
Mo	131.65	35.75	26.53	18.82	65.51	61.1	29.88	33.24	29.32	18.76
Ta	4.11	0.62	6.09	2.22	1.33	32.82	1.49	1.96	0.01	1.98
Ni	4	1.7	4.7	2.31	1.64	7.5	0.5	4.68	1.92	1.95
Cu	10.48	5.12	0.35	2.58	1.5	0.39	2.89	2.34	1.53	0.45
Ga	33.97	7.16	5.58	19.61	4.88	6.78	10.1	6.86	6.28	4.6
Zr	855	167.51	510.09	651.19	524.04	668.14	198.05	316.15	223.29	326.8
Hf	2.74	3.13	14.79	6.53	6.27	31.16	15.18	13.09	10.67	8.82

	Unit 4			
	141			
	Px 3	Px 1	Px 2	Px 3
Zn	295.59	289.99	239.08	323.76
Ge	5.29	2.73	8.05	6.1
Rb	8.62	403.41	51.58	3.55
Sr	100.56	11.42	8.42	27.45
Y	120.77	20.53	48.54	135.13
Nb	19.96	23.34	35.95	25.43
Mo	22.65	27.56	0.23	31.03
Ta	4.8	2.82	4.65	3.03
Ni	2.92	1.86	2	3.86
Cu	1.73	0.35	3.39	2.99
Ga	10.24	3.22	6.55	11.14
Zr	357.89	793.58	607.01	296.1
Hf	8.23	13.68	7.58	6.15

Typical olivine analyses

	Unit 2 (Troughs)			
	MH-KUN-92 26		MH-KUN-92 30	
	Ol 1	Ol 2	Ol 1	Ol 2
Zn	779.22	849.74	832.66	914.3
Ge	3.51	4.8	2.38	5.75
Rb	6.24	10.18	4.94	10.46
Sr	9.29	52.88	9.42	31.23
Y	21.89	16.59	20.93	17.79
Nb	14.01	15.34	13.79	17.19
Mo	16	17.94	14.37	70.93
Ta	3.48	12.52	3.1	3.56
Ni	3.55	7.32	21.53	9.07
Cu	7.41	2.6	6.68	0.1
Ga	0.06	2.25	0.83	4.09
Zr	10.52	0.9	5.8	9.16
Hf	13.53	19.92	3.67	8.95

	Unit 2 (Host)			Unit 3		Unit 3		Unit 4		Unit 4
	36 MH-KUN-92 31			103		112		119		131
	Ol 1	Ol 1	Ol 2	Ol 1	Ol 2	Ol 1	Ol 2	Ol 1	Ol 2	Ol 1
Zn	1127.33	981.75	960.53	730.06	662.47	1041.16	878.07	894.64	822.6	825.16
Ge	1.69	15.26	2.25	2.29	1.31	0.38	1.07	0.74	3.04	0.87
Rb	11.58	16.82	11.84	14.86	5.1	18.39	15.07	137.73	0.45	11.78
Sr	8.51	11.91	18.13	27.02	17.56	14.44	18.95	12.32	10.88	11.91
Y	16.86	17.89	12.69	20.33	56.7	8.09	18.69	0	24.08	23.12
Nb	8.79	23.58	15.35	17.2	27.63	168.67	15.58	258.64	16.11	14.27
Mo	38.25	36.57	24.72	31.56	21.39	8.34	21.23	21.24	31.97	20.98
Ta	2.41	5.96	7.13	6.99	1.51	17.52	5.62	8.12	0	0.94
Ni	32.08	0.4	0.71	18.49	29.64	5.33	1.64	0.48	2.86	18.02
Cu	0.43	6.35	0.7	0.17	1.18	261.46	3.51	0	7.12	15.28
Ga	0.23	2.74	4.86	1.08	1.75	3.72	2.76	0.02	0.01	4.48
Zr	9.21	15.12	5.41	14.26	15.54	8.62	13.06	2.5	10.51	11.91
Hf	4.42	1.88	10.17	5.34	9.34	3.56	8.7	14.11	4.16	1.42

	Unit 4	
	141	
	Ol 1	Ol 2
Zn	886.06	841.19
Ge	5.69	1.98
Rb	14.02	11
Sr	16.35	12.28
Y	69.5	21.02
Nb	16.89	12.47
Mo	24.65	28.3
Ta	0.72	14.3
Ni	20.79	2.23
Cu	12.93	15.98
Ga	0.44	1.74
Zr	9.86	65.28
Hf	1.27	7.54

Typical feldspar analyses

	Unit 2 (Troughs)				
	MH-KUN-92 30				MH-KUN-92 26
	Fsp 1	Fsp 2	Fsp 3	Fsp 4	Fsp 1
Zn	7.86	4.61	49.31	400.23	26.68
Ti	643.8	608	1750.72	2866.66	141.76
Rb	120.13	116.36	374.91	141.3	215.94
Sr	247.58	242.48	625.25	350.8	83.78
Y	14.84	20.18	45.52	162.92	11.41
Nb	43.91	23.46	75.28	86.49	29.44
Mo	101.45	47.5	172.03	148.8	54.18
Ni	0.73	2.67	6.3	62.14	21.88
Cu	8.9	4.25	44.76	449.48	6.79
Ga	46.75	42.67	131.68	47.09	33.76
Zr	7.34	24.04	45.42	48.56	27.16
Ba	1277.34	1327.87	1147.47	853.96	543.47

	Unit 2 (Host)					Unit 3				Unit 4
	MH-KUN-92 31					103				119
	Fsp 1	Fsp 2	Fsp 3	Fsp 4	Fsp 5	Fsp 1	Fsp 2	Fsp 3	Fsp 4	Fsp 1
Zn	32.7	8.01	11.57	68.6	59.16	3.51	32.73	44.15	9.87	4.79
Ti	1175.05	287.23	319.25	1058.71	878.34	160.91	4257.65	8681.36	312.51	201.48
Rb	179.27	258.23	265.69	4110.49	3687.82	217.58	106.51	225.48	164.81	347.77
Sr	399.61	245.36	294.61	3497.6	3677.75	386.62	1121.91	1735.72	514.18	509.7
Y	42.04	8.79	6.93	91.63	121.63	1.71	115.73	134.72	24.55	2.13
Nb	86.86	45.62	30.52	544.01	504.07	32.36	207.5	296.51	67.97	65.33
Mo	212.79	68.7	83.28	808.63	908.1	53.57	483.96	333.44	103.58	95.17
Ni	1.65	1.76	2.2	12.26	9.49	0.85	9.27	5.16	2.05	1.62
Cu	6.04	2.03	4.73	34.15	26.03	3.91	25.18	39.6	8.95	0.71
Ga	148.95	64.31	78.21	866.86	919.76	52.23	108.69	202.48	65.37	54.35
Zr	47.68	25.11	26.51	336.63	415.72	26.93	85.27	482.07	35.16	5.43
Ba	569.23	814.031	856.49	4816.65	4759.76	1526.7	6288.86	5097.72	1980.91	1826.26

	Unit 4				
			141		
	Fsp 2	Fsp 3	Fsp 1	Fsp 2	Fsp 3
Zn	6.83	1.61	17.14	37.19	34.29
Ti	296.01	44.4	923.29	662.14	642.92
Rb	293.2	209.03	392.74	199.05	288.23
Sr	281.13	175.95	518.08	574.98	496.89
Y	11.36	3.88	28.88	44.02	46.35
Nb	36.87	19.97	70.87	114.63	78.45
Mo	36.84	32.14	71.92	105.71	258.42
Ni	0.81	0.71	2.53	1.62	3.54
Cu	4.03	1.79	4.34	18.35	19.39
Ga	49.27	28.88	104.28	139.15	116.11
Zr	12.56	7.36	25.38	13.2	68.59
Ba	1281.79	749.14	567.76	1121.99	2220.5

Typical biotite analyses

	Unit 2 (Troughs)		
	MH-KUN-92 26		30
	Bt 1	Bt 2	Bt 1
Zn	628.02	598.85	771.99
Ge	3.2	2.19	297.3
Rb	677.64	492.58	962.69
Sr	7.39	15.55	12.81
Y	16.01	15.96	14.12
Nb	57	67.67	37.29
Mo	29.05	27.62	22.23
Ta	10.46	22.46	2.99
Ni	2.89	12.72	5.73
Cu	9.03	0.5	1.42
Ga	85.13	75.69	102.61
Zr	16.42	17.03	21.07
Hf	16.73	10.44	8.91

	Unit 2 (Host)					Unit 3		Unit 3		Unit 4
		MH-KUN-92 31		MH-KUN-92 36		103		112		119
	Bt 2	Bt 1	Bt 2	Bt 1	Bt 2	Bt 1	Bt 2	Bt 1	Bt 2	Bt 1
Zn	759	478.91	142.04	918.94	836.27	594.24	553.29	959.88	293.74	632.85
Ge	0.87	2.08	3.55	0.01	1.08	2.94	0.06	0.12	0.15	2.45
Rb	1257.53	834.84	23.27	803.07	2505.28	829.51	819.84	363.05	444.65	20.81
Sr	12.65	17.94	27.18	21.1	16.64	16.52	17.65	25.43	10.97	59.71
Y	34.79	29.05	50.34	35.73	85.84	23.14	23.68	26.75	19.09	260.56
Nb	29.08	27.86	419.53	278.56	386.27	112.35	85.12	258.26	131.46	182.43
Mo	27.91	31.11	40.37	20.22	15.04	35.14	48.12	59.15	12.82	31.26
Ta	1.5	0.1	5.8	12.99	0.25	4.6	0.1	11.84	10.83	7.39
Ni	11.6	0.22	10.41	2.45	0.27	1.12	0.28	22.52	1.52	7.32
Cu	8.65	4.05	1.33	0.38	13.33	1.61	3.36	4.77	0.85	5.63
Ga	180.34	140.89	2	88.72	118.02	59.07	56.83	115.98	79.32	57.18
Zr	12.3	7.16	351.58	21.75	11.96	27.01	23.6	58.8	22.53	786.63
Hf	1.05	9.21	1.95	6.38	5.56	10.83	11.44	15.3	4.84	19.22

	Unit 4	Unit 4	
	131	141	
	Bt 1	Bt 1	Bt 2
Zn	700.18	263.43	686.35
Ge	3.39	163.54	2.31
Rb	719.2	734.82	92.43
Sr	15.49	24.68	30.31
Y	104.72	13.01	321.99
Nb	56.84	82.08	201.14
Mo	35.18	34.38	34.82
Ta	4.8	2.63	6.35
Ni	0.09	4.33	0.3
Cu	4.32	13.87	2.31
Ga	59.63	44.16	42.26
Zr	355.98	294.9	904.22
Hf	9.71	3.27	21.39

Typical ampihoble analyses

	Unit 2 (Troughs)				
	MH-KUN-92 26		MH-KUN-92 30		
	Am 1	Am 2	Am 1	Am 2	Am3
Zn	4527.43	5188.82	570.77	592.06	503.44
Ge	47.55	28.31	2.72	0.82	0.87
Rb	117.27	145.15	13.1	18.7	7.84
Sr	159.68	145.15	12	9.51	6.99
Y	1432.79	986.04	128.33	120.01	181.01
Nb	376	414.36	55.63	58.56	64.84
Mo	215.88	297.01	3.01	29.96	15.01
Ta	60.27	39.26	7.8	11.95	8.45
Ni	28.49	17.98	0.68	13.96	36.81
Cu	196.82	17.27	4.64	1.4	1.29
Ga	6050.04	193.66	66.34	53.06	61.78
Zr	3226.04	1637.87	166.37	176.26	413.33
Hf	108	147.19	4.86	8.09	20.83

	Unit 2 (Host)			Unit 3		Unit 3		Unit 4		
	MH-KUN-92 31			36	103		112		131	
	Am 4	Am 1	Am 2	Am 1	Am 1	Am 2	Am 1	Am 2	Am 1	Am 2
Zn	492.04	497.86	588.88	607.24	432.33	424.38	617.44	561.19	549.1	524.76
Ge	1.24	3.3	3.46	3.75	3.49	1.59	1.2	3.02	0.34	4.52
Rb	13.63	24.27	19.98	12.71	14.46	25.73	4.58	17.62	16.61	17.28
Sr	9.48	18.96	22.65	18.55	13.59	26.83	14.48	39.9	28.08	29.31
Y	158.95	299.34	90.6	212.48	430.28	431.79	249.08	357.36	225.22	276.15
Nb	69.59	173.74	38.98	93.7	192.24	304.76	101.76	227.01	217.94	218.89
Mo	20.87	21.31	32.88	16.55	49.2	53.67	18.71	54.85	45.73	47.06
Ta	0.79	3.96	0.31	16.26	3.26	5.1	13.49	6.56	13.43	0.75
Ni	4.54	0.12	7.38	1.14	8.12	1.32	3.84	7.53	0.37	3.24
Cu	8.07	2.28	1.87	3.34	8.6	2.06	6.42	8.57	5.42	6.58
Ga	69.16	60.63	46.87	50.25	51.55	56.97	56.82	69	44.64	53.6
Zr	406.06	945.41	595.54	322.69	2186.36	2202.94	1285.61	2428.97	966.39	896.7
Hf	21.72	30.96	13.2	22.46	41.41	40.24	31.85	43.78	25.12	18.15

	Unit 4		
		141	
	Am 3	Am 1	Am 2
Zn	541.24	545.58	565.73
Ge	1.86	3.18	2.6
Rb	14.34	14.48	17.42
Sr	22.29	20.69	12.7
Y	191.08	181.39	133.87
Nb	151.47	112.99	99.94
Mo	46.48	13	22.32
Ta	3.14	4.36	2.44
Ni	0.74	0.56	5.71
Cu	1.02	5.62	6.02
Ga	45.27	37.57	41.9
Zr	1018.21	156.04	150.22
Hf	15.87	5.96	9.33

Appendix E: Representative whole rock analyses

Nunarssuit

Sample	9	14	6-41	6-42	6-43	6-44	7-45	7-46	7-47
SiO2	61.87	60.00	53.27	63.29	61.16	63.05	56.63	59.69	61.61
Al2O3	14.43	14.28	10.73	15.61	14.64	15.29	12.95	14.35	15.53
Fe2O3	9.35	10.36	19.56	6.54	8.93	7.33	14.16	9.64	8.15
MgO	0.28	0.39	0.88	0.36	0.46	0.40	0.66	0.50	0.43
CaO	2.55	2.94	4.48	1.96	2.51	2.14	3.77	3.17	2.46
Na2O	5.24	5.42	4.32	5.96	5.55	5.92	4.70	5.16	5.58
K2O	5.01	5.04	3.72	5.15	5.02	5.26	4.47	4.93	5.25
TiO2	0.77	1.02	1.94	0.48	0.87	0.65	1.44	1.17	0.82
MnO	0.18	0.20	0.38	0.12	0.16	0.13	0.25	0.16	0.15
P2O5	0.18	0.24	0.36	0.12	0.18	0.12	0.32	0.22	0.17
Total	99.86	99.89	99.65	99.57	99.47	100.30	99.34	99.00	100.15
LOI	-0.05	-0.03	0.30	0.10	0.10	0.05	0.01	0.12	0.01
Nb	38.00	54.20	92.50	33.10	55.80	46.30	21.60	41.50	50.20
Zr	1815.80	580.40	217.50	240.20	266.90	266.10	421.90	239.20	736.30
Y	89.50	137.40	109.40	70.50	89.00	76.70	46.10	74.50	82.40
Sr	60.60	66.70	53.60	72.00	61.30	63.90	70.40	65.60	62.10
Rb	127.20	159.50	109.00	121.00	130.00	126.50	101.20	102.60	92.10
Th	5.30	6.40	8.00	3.50	6.60	7.10	1.60	3.60	3.80
Pb	18.10	16.80	14.20	22.00	28.10	22.70	10.30	15.80	12.60
Zn	172.20	244.50	306.60	123.90	157.90	136.40	108.10	129.40	226.20
Cu	16.20	19.80	24.40	8.20	12.40	7.20	9.80	13.10	20.10
Ni	3.70	3.80	1.20	3.30	1.50	2.30	1.30	2.80	0.60
Cr				Below detection limits					
Ce	169.00	280.90	252.50	126.20	177.70	144.80	98.00	146.60	156.70
Nd	81.20	137.90	134.40	60.20	87.20	70.70	49.20	75.70	89.60
La	68.60	140.30	105.50	58.60	82.40	66.50	38.50	68.00	70.40
V	5.90	3.40	0.00	0.00	0.00	0.00	0.00	0.00	0.00
Ba	367.20	416.00	337.10	491.00	417.50	428.70	416.00	409.40	398.40
Sc	7.50	12.00	17.10	2.10	8.60	6.00	6.40	7.10	9.20
Quartz	3.96	0.26	0.00	2.69	1.71	1.84	0.00	1.67	1.24
Corundum	0.00	0.00	0.00	0.00	0.00	0.00	0.00	0.00	0.00
Orthoclase	29.90	30.12	22.53	30.73	30.05	31.26	26.92	29.70	31.21
Albite	44.76	45.90	35.37	50.93	47.58	49.60	40.53	44.48	47.48
Anorthite	1.06	0.00	0.00	0.64	0.21	0.00	1.06	1.45	1.83
Leucite	0.00	0.00	0.00	0.00	0.00	0.00	0.00	0.00	0.00
Nephelite	0.00	0.00	0.00	0.00	0.00	0.00	0.00	0.00	0.00
Kaliophyllite	0.00	0.00	0.00	0.00	0.00	0.00	0.00	0.00	0.00
Acmite	0.00	0.31	1.40	0.00	0.00	0.49	0.00	0.00	0.00
Sod Metasil	0.00	0.00	0.00	0.00	0.00	0.00	0.00	0.00	0.00
Pot Metasil	0.00	0.00	0.00	0.00	0.00	0.00	0.00	0.00	0.00
Diopside	9.31	11.58	17.97	7.34	9.83	8.68	13.94	11.49	8.21
Wollastonite	0.00	0.00	0.00	0.00	0.00	0.00	0.00	0.00	0.00
Hypersthene	7.25	7.43	8.22	5.16	6.74	5.48	10.46	6.48	6.46
Olivine	0.00	0.00	6.84	0.00	0.00	0.00	0.68	0.00	0.00
Cal Orthosil	0.00	0.00	0.00	0.00	0.00	0.00	0.00	0.00	0.00
Magnetite	1.88	1.87	3.04	1.31	1.80	1.13	2.87	1.95	1.63
Chromite	0.00	0.00	0.00	0.00	0.00	0.00	0.00	0.00	0.00
Hematite	0.00	0.00	0.00	0.00	0.00	0.00	0.00	0.00	0.00
Ilmenite	1.47	1.96	3.78	0.91	1.66	1.24	2.78	2.26	1.56
Titanite	0.00	0.00	0.00	0.00	0.00	0.00	0.00	0.00	0.00
Perovskite	0.00	0.00	0.00	0.00	0.00	0.00	0.00	0.00	0.00
Rutile	0.00	0.00	0.00	0.00	0.00	0.00	0.00	0.00	0.00
Apatite	0.42	0.57	0.85	0.29	0.43	0.27	0.76	0.52	0.39

Sample	1-8	1-11	15	9-57	10-62	10-63	10-65	10-66	5(trough)
SiO2	41.37	41.20	54.40	41.34	54.67	61.61	61.21	52.96	36.88
Al2O3	4.79	4.77	11.46	4.67	11.93	15.93	15.82	10.97	3.30
Fe2O3	38.43	38.34	18.44	39.65	18.43	6.97	7.61	19.35	45.49
MgO	2.25	2.20	0.91	2.22	1.04	0.49	0.48	1.34	2.17
CaO	7.52	7.56	4.44	7.14	4.21	2.07	2.03	4.82	6.32
Na2O	1.68	1.77	4.26	1.71	4.41	5.61	5.66	4.10	1.10
K2O	1.48	1.52	3.72	1.53	3.98	5.52	5.33	3.48	1.03
TiO2	3.38	3.35	1.76	3.37	1.64	0.59	0.85	1.80	3.59
MnO	0.81	0.82	0.37	0.84	0.37	0.14	0.14	0.43	0.95
P2O5	0.66	0.65	0.35	0.60	0.36	0.14	0.13	0.39	0.60
Total	102.38	102.18	100.10	103.07	101.06	99.07	99.27	99.64	101.42
LOI	-2.06	-2.70	-0.34	-2.08	-0.66	0.88	0.58	0.00	-2.10
Nb	42.90	34.70	41.50	37.80	46.20			51.70	44.80
Zr	261.90	212.40	322.30	181.20	167.40			181.40	187.60
Y	110.20	100.30	71.50	105.20	75.80			85.30	106.90
Sr	32.30	21.80	62.80	36.40	60.80			57.60	18.80
Rb	31.80	35.30	119.80	36.80	68.40			70.30	20.30
Th	17.60	16.70	3.80	20.10	5.90			8.90	0.00
Pb	7.40	4.60	11.20	5.30	11.40			11.80	7.20
Zn	418.00	377.90	142.10	454.70	254.90			265.70	484.30
Cu	42.80	47.50	22.20	43.70	24.30			42.20	40.80
Ni	2.30	4.70	4.00	3.30	2.50			2.90	3.80
Cr		Below detection limits						Below detection limits	
Ce	205.80	179.50	137.20	184.20	164.70			193.20	194.40
Nd	127.00	116.40	75.70	114.30	94.40			104.40	112.70
La	86.10	73.90	54.60	72.90	66.00			81.20	74.90
V	0.00	0.00	6.60	0.00	0.00			0.00	6.60
Ba	410.70	106.60	388.50	129.60	421.50			410.70	80.90
Sc	21.80	35.60	13.70	35.30	16.10			21.80	35.30
Quartz	0.00	0.00	0.00	0.00	0.00	0.84	0.72	0.00	0.00
Corundum	0.00	0.00	0.00	0.00	0.00	0.00	0.00	0.00	0.00
Orthoclase	8.82	9.07	22.33	9.07	23.67	33.14	31.96	20.99	6.22
Albite	14.35	15.18	36.59	14.52	37.52	48.21	48.56	35.41	9.55
Anorthite	1.17	0.59	1.17	0.55	1.00	2.01	2.04	1.28	1.06
Leucite	0.00	0.00	0.00	0.00	0.00	0.00	0.00	0.00	0.00
Nephelite	0.00	0.00	0.00	0.00	0.00	0.00	0.00	0.00	0.00
Kaliophyllite	0.00	0.00	0.00	0.00	0.00	0.00	0.00	0.00	0.00
Acmite	0.00	0.00	0.00	0.00	0.00	0.00	0.00	0.00	0.00
Sod Metasil	0.00	0.00	0.00	0.00	0.00	0.00	0.00	0.00	0.00
Pot Metasil	0.00	0.00	0.00	0.00	0.00	0.00	0.00	0.00	0.00
Diopside	28.15	28.96	16.57	27.21	15.49	6.56	6.38	17.94	23.80
Wollastonite	0.00	0.00	0.00	0.00	0.00	0.00	0.00	0.00	0.00
Hypersthene	12.40	8.80	13.72	11.47	7.77	6.37	6.85	10.59	14.40
Olivine	19.37	21.74	1.69	21.45	6.90	0.00	0.00	5.45	27.28
Cal Orthosil	0.00	0.00	0.00	0.00	0.00	0.00	0.00	0.00	0.00
Magnetite	7.71	7.70	3.72	7.91	3.68	1.41	1.53	3.92	9.27
Chromite	0.00	0.00	0.00	0.00	0.00	0.00	0.00	0.00	0.00
Hematite	0.00	0.00	0.00	0.00	0.00	0.00	0.00	0.00	0.00
Ilmenite	6.48	6.43	3.39	6.42	3.14	1.14	1.64	3.50	6.99
Titanite	0.00	0.00	0.00	0.00	0.00	0.00	0.00	0.00	0.00
Perovskite	0.00	0.00	0.00	0.00	0.00	0.00	0.00	0.00	0.00
Rutile	0.00	0.00	0.00	0.00	0.00	0.00	0.00	0.00	0.00
Apatite	1.55	1.52	0.82	1.40	0.83	0.32	0.31	0.92	1.42

Sample	6	16	1	3	4
SiO2	33.33	60.62	35.57	44.94	30.67
Al2O3	1.76	15.86	2.21	17.34	1.67
Fe2O3	50.71	8.28	51.66	16.79	51.51
MgO	2.90	0.30	2.35	5.82	1.25
CaO	6.18	2.81	5.66	8.19	8.15
Na2O	0.55	5.71	0.52	3.69	0.52
K2O	0.51	4.73	0.98	0.63	0.42
TiO2	3.85	0.85	3.33	2.46	8.02
MnO	1.03	0.16	1.12	0.20	0.97
P2O5	1.10	0.24	0.48	0.38	0.58
Total	101.93	99.56	103.85	100.44	103.75
LOI	-2.38	0.48	-3.77	-0.60	-3.05
Nb	46.00	26.80	56.30	7.90	130.90
Zr	249.60	508.50	351.70	92.20	450.70
Y	121.20	64.60	112.20	29.80	136.30
Sr	15.30	142.10	15.10	575.00	18.60
Rb	17.40	88.40	38.20	8.30	11.40
Th	0.00	2.30	0.50	2.00	0.00
Pb	8.60	12.60	5.90	6.40	3.00
Zn	644.60	140.50	689.80	105.90	754.80
Cu	36.10	12.90	30.40	14.10	49.40
Ni	4.90	3.30	1.50	90.90	3.50
Cr	Below detection limits			56.30	B.d.l.
Ce	228.80	125.20	173.50	29.30	236.60
Nd	134.30	64.70	98.00	19.30	149.90
La	88.10	56.60	66.20	1.80	69.20
V	7.30	2.40	11.20	206.30	27.70
Ba	29.90	864.90	52.50	251.60	38.00
Sc	39.00	11.00	28.50	35.00	24.80
Quartz	0.00	0.95	0.00	0.00	0.00
Corundum	0.00	0.00	0.00	0.00	0.00
Orthoclase	3.08	28.28	5.80	3.74	2.47
Albite	4.77	48.88	4.43	25.14	4.43
Anorthite	0.85	3.71	0.82	29.20	1.00
Leucite	0.00	0.00	0.00	0.00	0.00
Nephelite	0.00	0.00	0.00	3.47	0.00
Kaliophyllite	0.00	0.00	0.00	0.00	0.00
Acmite	0.00	0.00	0.00	0.00	0.00
Sod Metasil	0.00	0.00	0.00	0.00	0.00
Pot Metasil	0.00	0.00	0.00	0.00	0.00
Diopside	20.33	7.76	21.36	7.77	31.72
Wollastonite	0.00	0.00	0.00	0.00	0.00
Hypersthene	18.27	6.55	18.17	0.00	1.55
Olivine	32.26	0.00	31.64	21.70	31.84
Cal Orthosil	0.00	0.00	0.00	0.00	0.00
Magnetite	10.33	1.66	10.32	3.37	10.30
Chromite	0.00	0.00	0.00	0.00	0.00
Hematite	0.00	0.00	0.00	0.00	0.00
Ilmenite	7.49	1.63	6.36	4.72	15.33
Titanite	0.00	0.00	0.00	0.00	0.00
Perovskite	0.00	0.00	0.00	0.00	0.00
Rutile	0.00	0.00	0.00	0.00	0.00
Apatite	2.62	0.56	1.11	0.90	1.36

West Kungnat

Sample no.	23(T)	25(T)	26(T)	28(T)	30(T)	36(T)	24(H)	27(H)	31(H)	33(H)
SiO2	42.26	49.09	43.47	51.29	46.03	59.92	54.61	58.72	57.36	59.63
Al2O3	5.83	9.27	7.32	11.47	8.22	15.64	12.67	15.21	14.47	15.44
Fe2O3	39.53	26.53	36.15	20.44	28.53	8.86	16.78	10.36	12.25	9.33
MgO	1.91	1.4	2.32	1.22	1.93	0.4	0.95	0.58	0.63	0.5
CaO	6.02	5.89	4.6	5.24	6.59	2.51	4.23	3.02	3.31	2.79
Na2O	2.14	3.5	2.62	3.84	3.05	5.54	4.45	5.23	5.06	5.49
K2O	1.948	2.881	2.428	3.775	2.603	5.353	4.461	5.16	4.891	5.093
TiO2	2.308	2.119	2.506	2.875	3.538	0.825	1.479	0.949	1.462	0.993
MnO	0.853	0.54	0.773	0.404	0.537	0.165	0.353	0.207	0.222	0.177
P2O5	0.484	0.458	0.529	0.713	0.814	0.174	0.33	0.194	0.375	0.182
Total	103.28	101.67	102.72	101.27	101.84	99.39	100.31	99.62	100.03	99.62
LOI	-2.87	-1.47	-2.51	-0.78	-1.58	0.07	-0.55	-0.11	-0.49	0.13
Nb	62.7	65.5	64.8	50.4	70.2	82.4	49.4	43	39.2	46.5
Zr	213.2	303	282.2	266.8	292.5	529.8	426.3	209.8	214.5	307.9
Y	70.9	69.8	60	64.5	81.8	49.9	54.1	43.9	46.4	44.8
Sr	38.6	65.1	44.1	76.4	53.5	79.7	74.9	105.4	89.5	92.3
Rb	46.1	63.7	65.7	80.6	63.9	135	121.5	98.7	103.1	145.1
Th	1.7	4.8	2.9	3.9	4.9	9.5	4.4	7.2	4.2	9.5
Pb	8.9	13	11.6	13.6	11.4	14.4	10.1	13.4	13.9	12.8
Zn	413.7	286.2	376.4	220.3	309.2	119.7	192.6	123.7	139.3	125
Cu	43.3	39.2	41.9	35.5	46.2	21.3	21.9	17	22.2	14
Ni	4.1	5	5.3	3	6	2.9	2.7	3.9	5	3.1
Cr	0.7	-2.7	1	0	2.2	-1.7	-1	-0.8	-0.4	-2.4
Ce	134.5	137.6	120.6	146.2	168.8	99.4	102.9	92.3	102.9	100.3
Nd	77.7	78.7	67	79.3	97.8	43	58.8	46.9	53.9	46.5
La	54.6	61.9	47.3	62.6	68	45.3	43.3	44.8	47.2	45.5
V	6.3	7	10.1	11.4	10.1	3.8	6.7	3	7.6	7.3
Ba	362.4	660.9	389	739.3	479.6	837.4	789.7	1120.6	933.3	970.8
Sc	21.4	23.6	22.2	27.7	36.9	8.9	15.3	12.3	13.2	12.6
Quartz	0	0	0	0	0	0	0	0	0	0
Corundum	0	0	0	0	0	0	0	0	0	0
Orthoclase	11.53	17.13	14.41	22.42	15.48	32.08	26.67	30.88	29.2	30.46
Albite	18.13	29.8	22.26	32.65	25.97	47.53	38.09	44.82	43.26	47.01
Anorthite	0.55	1.08	1.05	2.92	1.06	2.02	1.44	2.82	2.35	2.47
Leucite	0	0	0	0	0	0	0	0	0	0
Nephelite	0	0	0	0	0	0	0	0	0	0
Kaliophyllite	0	0	0	0	0	0	0	0	0	0
Acmite	0	0	0	0	0	0	0	0	0	0
Sod Metasil	0	0	0	0	0	0	0	0	0	0
Pot Metasil	0	0	0	0	0	0	0	0	0	0
Diopside	23.02	22.21	16.1	16.2	23.13	8.31	15.44	9.7	10.32	9.06
Wollastonite	0	0	0	0	0	0	0	0	0	0
Hypersthene	3.91	2.95	2.69	4.98	2.05	2.7	0.36	2.36	3.26	4.22
Olivine	29.49	16.41	30.28	9.59	17.95	3.58	11.03	5.05	5.47	2.57
Cal Orthosil	0	0	0	0	0	0	0	0	0	0
Magnetite	7.86	5.3	7.21	4.08	5.7	1.78	3.37	2.08	2.46	1.88
Chromite	0	0	0	0	0	0	0	0	0	0
Hematite	0	0	0	0	0	0	0	0	0	0
Ilmenite	4.39	4.05	4.78	5.49	6.76	1.59	2.84	1.83	2.81	1.91
Titanite	0	0	0	0	0	0	0	0	0	0
Perovskite	0	0	0	0	0	0	0	0	0	0
Rutile	0	0	0	0	0	0	0	0	0	0
Apatite	1.12	1.07	1.23	1.66	1.9	0.41	0.77	0.46	0.88	0.43

Sample no.	34(H)	38	39	40	41
SiO2	58.68	64.29	65.09	60.3	67.26
Al2O3	15.17	15.7	17.08	15.61	15.57
Fe2O3	10.03	6.19	4.59	9.36	4.85
MgO	0.5	0	0.06	0.34	0.07
CaO	2.94	1.1	0.98	2.61	1.05
Na2O	5.4	6.18	7.04	6	6.13
K2O	5.171	5.078	4.588	4.769	4.655
TiO2	1.192	0.449	0.073	0.784	0.117
MnO	0.188	0.177	0.136	0.209	0.138
P2O5	0.267	0.033	0.029	0.185	0.042
Total	99.53	99.15	99.66	100.16	99.88
LOI	0.23	0.21	0.38	-0.04	0.54
Nb	49.1	72.4	20.8	65.8	83.7
Zr	291.6	187.9	151.8	189.1	165.8
Y	46.4	50.9	21.7	38	56.2
Sr	84.6	14.7	40.1	52.1	31.8
Rb	133.8	162.9	112.1	87.8	169.2
Th	7.4	19.2	3.2	0.5	20.3
Pb	14.9	16	13.3	7.3	17.8
Zn	121	151.4	86.1	147	138.9
Cu	16.6	14.3	5.9	13.1	10.9
Ni	4.3	3.7	3.8	3	5.3
Cr	-0.5	0	-1.2	0	2.3
Ce	101.8	688.8	92.1	126.1	565.7
Nd	51.6	230.8	40.2	59.5	195.9
La	46.6	454.1	50.5	55.2	339.4
V	7.3	3.5	2.7	2.1	2.7
Ba	905.9	43.6	132.1	512.1	101.3
Sc	12.2	2.1	0.3	6	1.1
Quartz	0	4.3	2.38	0	9.48
Corundum	0	0	0	0	0
Orthoclase	30.97	30.42	27.31	28.36	27.66
Albite	46.31	53	60.01	51.1	52.15
Anorthite	1.91	0.1	1.46	1.59	1.23
Leucite	0	0	0	0	0
Nephelite	0	0	0	0	0
Kaliophyllite	0	0	0	0	0
Acmite	0	0	0	0	0
Sod Metasil	0	0	0	0	0
Pot Metasil	0	0	0	0	0
Diopside	9.75	4.65	2.88	9.02	3.32
Wollastonite	0	0	0	0	0
Hypersthene	0.5	5.35	4.83	1.43	4.88
Olivine	5.63	0	0	4.7	0
Cal Orthosil	0	0	0	0	0
Magnetite	2.02	1.25	0.92	1.87	0.97
Chromite	0	0	0	0	0
Hematite	0	0	0	0	0
Ilmenite	2.29	0.86	0.14	1.5	0.22
Titanite	0	0	0	0	0
Perovskite	0	0	0	0	0
Rutile	0	0	0	0	0
Apatite	0.63	0.08	0.07	0.43	0.1

Appendix F: Methods for calculating NBO/T ratios magma viscosity and magma density

F.1: NBO/T ratios (after Henderson *et al.*, 1985)

1) Follow method of Deer *et al.* (1966), appendix 1, to recalculate XRF analysis in terms of number of ions for 100 oxygen ions.
2) T = Σ Si + Al + Ti + P ions
3) NBO = 2 x no. oxygen ions (=2 x 100) - 4T

F.2: Viscosity calculation (after Shaw, 1972)

1) Calculate mole fractions (X)
2) Add mole fractions of: TiO_2 + CaO; FeO + Fe_2O_3 + MgO + MnO; Na_2O +K_2O
3) Multiply mole fraction SiO_2 by constants 6.7, 3.4, 4.5, 2.8, 2.0 and by mole fraction of other oxides:

$6.7 \times X_{SiO2} \times X_{Al2O3}$

$3.4 \times X_{SiO2} \times X(TiO2 + MnO)$

$4.5 \times X_{SiO2} \times X_{(FeO + Fe2O3 + MgO + MnO)}$

$2.8 \times X_{SiO2} \times X_{(Na2O + K2O)}$

$2.0 \times X_{SiO2} \times X_{H2O}$

4) Add these numbers together = s
5) Ln $visc_1$ = s(10^4/T in Kelvin) - (1.5s + 6.4)
6) K = (-6.4 - ln $visc_1$)/(1.5-10)
7) Ln $visc_2$ = (K x (10^4/T)) - 6.4
8) Viscosity of melt = $visc_2$

F.3: Density calculation (after Bottinga *et al.*, 1982)

Component	V^0 (cm^3mol^{-1}) at 1400°C	$\alpha^0 \times 10^{-5}$ ($°C^{-1}$)	K (cm^3mol^{-1}) at 1400°C	Additional constants
SiO_2	26.75	0.1	-	$V^* = 41.92$ cm^3mol^{-1} at 1400°C
TiO_2	22.45	37.1	-	
Al_2O_3	-	-	-20.0	
Fe_2O_3	44.40	32.1	-	$\alpha^* = 87.48 \times 10^{-5} °C^{-1}$
MgO	12.32	12.2	-37.8	
CaO	16.59	16.7	-8.5	
MnO	14.13	15.1	-	$K_\alpha = -2.282 \times 10^{-5}$ $cm^3 °C^{-1}$
FeO	13.94	34.7	-58.0	
Na_2O	29.03	25.9	-11.4	
K_2O	46.30	35.9	-48.1	

1) Molar volume = $\{[\Sigma X_i V^0_i + X_A[V^* + X_A(\Sigma XjKj/\Sigma Xj)]] \times \exp\{[\Sigma X_i\alpha^0_i + X_A[\alpha^* + K_\alpha(V^* + X_A(\Sigma XjKj/\Sigma Xj))]](T - 1400)$

where X_i = mole fraction

V_i = molar volume

X_A = mole fraction aluminium

X_j = no. moles

K_j = a constant

α = coefficient of thermal expansion

2) Density =

total percentage weight of oxides/(number of moles of oxide x molar volume)

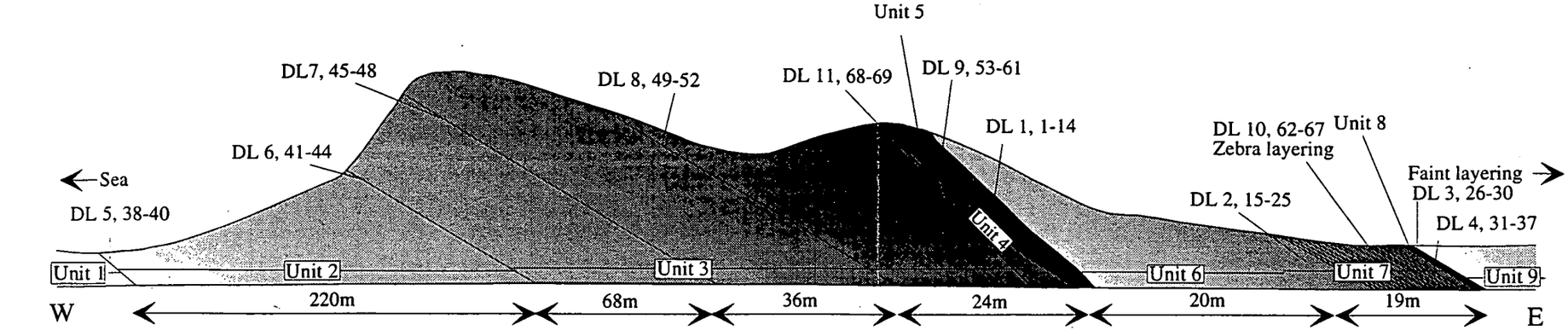

Figure 2.2

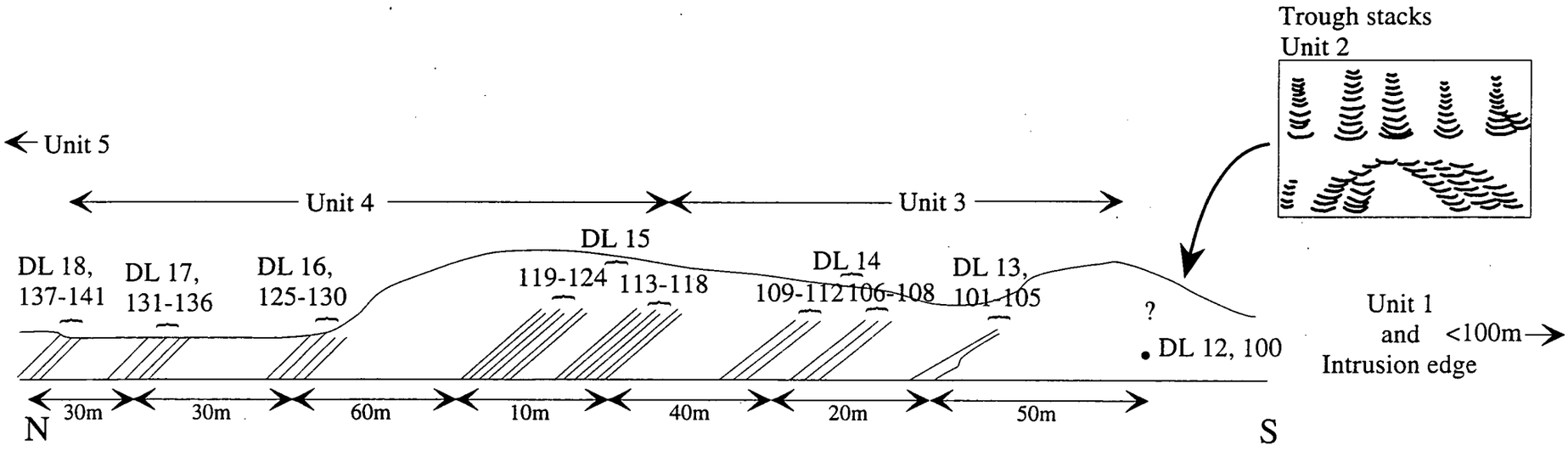

Figure 2.5

Fig. 2.2: Diagrammatic sketch section through the layered sequence of Nunarssuit. Shading represents increase in colour index of the bases of individual rhythms up section. DL indicates a drill locality. N.B. drawing is not to scale. Unit 1 = homogeneous syenite, Unit 2 = lower layered syenite (layers faintly visible and irregularly spaced), Unit 3 = lower layered syenite (layers clearly visible and fairly regularly spaced); Unit 4 = transition unit; Unit 5 = lower melanocratic unit; Unit 6 = middle layered syenite (layers faintly visible and fairly regularly spaced); Unit 7 = middle layered syenite (layers clearly visible and fairly regularly spaced); Unit 8 = middle melanocratic unit; Unit 9 = upper layered syenite (layers faintly visible and fairly regularly spaced); Unit 10 = Upper layered syenite (layers faintly visible and irregularly spaced).

Fig. 2.5: Diagrammatic sketch section through the lower layered series of West Kûngnât. DL indicates drill locality. Question mark above DL 12 indicates lack of certainty over stratigraphic relations between trough stacks and the rest of the stratigraphy. N.B. drawing is not to scale. Unit 1 = homogeneous xenolith-rich syenite; Unit 2 = two series of trough stacks; Unit 3 = poorly layered syenite; Unit 4 = normally graded rhythmically layered syenite; Unit 5 = laminated syenite.